

**Polymeric drug delivery systems: Aspects of core and shell of nanocarriers from
polyesters, poly(ester amide)s or poly(2-oxazoline)s**

**Dissertation
(kumulativ)**

zur Erlangung des akademischen Grades doctor rerum naturalium
(Dr. rer. nat.)

vorgelegt dem Rat der Chemisch-Geowissenschaftlichen Fakultät der
Friedrich-Schiller-Universität Jena
von Irina Muljajew (M.Sc.)
geboren am 05. Mai 1989 in Tscheljabinsk (Russische Föderation)

Gutachter:

1. Prof. Dr. Ulrich S. Schubert, Friedrich-Schiller-Universität Jena
2. Prof. Dr. Thomas Heinze, Friedrich-Schiller-Universität Jena

Tag der öffentlichen Verteidigung: 01.06.2022

Table of contents

Documentation of authorship	3
1 Introduction	7
2 Recent advances in (bio)degradable synthetic polymers – Beyond polyesters	13
3 Tailor-made polyesters with constant hydrophobicity for nanoparticle formation	23
4 Poly(ester amide)s from polyaddition of dicarboxylic acids and 2,2'-bis(2-oxazoline)	27
5 Compatibility of poly(ester amide)s with indomethacin	35
6 PMMA-graft-OEtOx: Backbone end group effect on liver cell-type specificity	41
7 Summary	51
8 Zusammenfassung	57
9 References	63
List of abbreviations	69
Acknowledgement / Danksagung	73
Erklärung zu den Eigenanteilen an Publikationen und Zweitpublikationsrechten bei der kumulativen Dissertation	77
Declaration of authorship / Selbstständigkeitserklärung	79
Curriculum vitae	81
Publication list	83
Publications P1 to P6	89

Table of contents

Documentation of authorship

Documentation of authorship

This section contains a list of the individual contributions to the publications reprinted in this thesis.

P1 Michael Dirauf, ^{1,#} Irina Muljajew, ^{2,#} Christine Weber, ³ Ulrich S. Schubert, ⁴ Recent advances in (bio)degradable polymers – Beyond polyesters, <i>Prog. Polym. Sci.</i> 2021 , under revision. #Authors contributed equally.				
Author	1	2	3	4
Conceptual development	×	×	×	
Preparation of manuscript	×	×		
Correction of manuscript	×	×	×	×
Supervision of M. Dirauf			×	×
Supervision of I. Muljajew			×	×
Proposed publication equivalent		0.5		

P2 Damiano Bandelli, ^{1,#} Christian Helbing, ^{2,#} Christine Weber, ³ Michael Seifert, ⁴ Irina Muljajew, ⁵ Klaus D. Jandt, ⁶ Ulrich S. Schubert, ⁷ Maintaining the hydrophilic–hydrophobic balance of polyesters with adjustable crystallinity for tailor–made nanoparticles, <i>Macromolecules</i> 2018 , <i>51</i> , 5567–5576. #Authors contributed equally.							
Author	1	2	3	4	5	6	7
Conceptual development	×	×	×				
Kinetic studies and interpretation	×						
Polymer synthesis and structural characterization	×						
DSC and TGA studies	×						
PLM and AFM studies		×		×			
Nanoparticle preparation	×						
DLS measurements	×				×		
Preparation of manuscript	×	×	×				
Correction of manuscript			×	×	×	×	×
Supervision of D. Bandelli			×				×
Supervision of C. Helbing						×	
Supervision of I. Muljajew			×				×
Proposed publication equivalent					0.25		

Documentation of authorship

P3 Damiano Bandelli, ¹ Irina Muljajew, ² Karl Scheuer, ³ Johannes B. Max, ⁴ Christine Weber, ⁵ Felix H. Schacher, ⁶ Klaus D. Jandt, ⁷ Ulrich S. Schubert, ⁸ Copolymerization of caprolactone isomers to obtain nanoparticles with constant hydrophobicity and tunable crystallinity, <i>Macromolecules</i> 2020 , <i>53</i> , 5208–5217.								
Author	1	2	3	4	5	6	7	8
Conceptual development	×				×			
Kinetic studies and interpretation	×							
Polymer synthesis and structural characterization	×							
DSC and TGA studies	×							
WAXS analysis				×				
Nanoparticle preparation	×							
Fluorescence measurements		×						
DLS measurements	×							
AFM analysis			×					
Preparation of manuscript	×							
Correction of manuscript		×	×	×	×	×	×	×
Supervision of J. B. Max						×		
Supervision of D. Bandelli					×			×
Supervision of K. Scheuer							×	
Supervision of I. Muljajew					×			×
Proposed publication equivalent		0.25						

Documentation of authorship

P4 Irina Muljajew,¹ Andreas Erlebach,² Christine Weber,³ Johannes R. Buchheim,⁴ Marek Sierka,⁵ Ulrich S. Schubert,⁶ A polyesteramide library from dicarboxylic acids and 2,2'-bis(2-oxazoline): Synthesis, characterization, nanoparticle formulation and molecular dynamics simulations, *Polym. Chem.* **2020**, *11*, 112–124.

Author	1	2	3	4	5	6
Conceptual development	×		×			
Synthesis and characterization of polymers	×					
Nanoparticle preparation	×					
WAXS analysis				×		
Simulations		×				
Preparation of manuscript	×	×				
Correction of manuscript		×	×	×	×	×
Supervision of A. Erlebach					×	
Supervision of I. Muljajew			×			×
Proposed publication equivalent	1					

P5 Irina Muljajew,¹ Mingzhe Chi,² Antje Vollrath,³ Christine Weber,⁴ Baerbel Beringer-Siemers,⁵ Steffi Stumpf,⁶ Stephanie Hoepfner,⁷ Marek Sierka,⁸ Ulrich S. Schubert,⁹ A combined experimental and *in silico* approach to determine the compatibility of poly(ester amide)s and indomethacin in polymer nanoparticles, *Eur. Polym. J.* **2021**, *156*, 110606.

Author	1	2	3	4	5	6	7	8	9
Conceptual development	×			×					
Nanoparticle study			×		×				
SEM measurements						×	×		
DSC study	×								
Simulation		×							
Preparation of manuscript	×	×	×						
Correction of manuscript				×	×	×	×	×	×
Supervision of M. Chi								×	
Supervision of I. Muljajew				×					×
Proposed publication equivalent	1								

Documentation of authorship

Author	1	2	3	4	5	6	7	8	9	10	11	12	13
P6	Irina Muljajew, ^{1,#} Sophie Huschke, ^{2,#} Anuradha Ramoji, ³ Zoltán Cseresnyés, ⁴ Stephanie Hoeppener, ⁵ Ivo Nischang, ⁶ Wanling Foo, ⁷ Jürgen Popp, ⁸ Marc Thilo Figge, ⁹ Christine Weber, ¹⁰ Michael Bauer, ¹¹ Ulrich S. Schubert, ¹² Adrian T. Press, ¹³ Stealth effect of short polyoxazolines in graft copolymers: Minor changes of backbone end group determine liver cell-type specificity, <i>ACS Nano</i> 2021 , <i>15</i> , 12298–12313. #Authors contributed equally.												
Conceptual development	×	×								×			×
Polymer synthesis, micelle formulation, characterization	×												
<i>in vitro</i> and <i>in vivo</i> experiments		×					×						×
Image analysis				×					×				
Raman spectroscopy investigation			×					×					
AUC study						×							
Cryo-TEM imaging					×								
Preparation of manuscript	×	×											
Correction of manuscript			×	×	×	×	×	×	×	×	×	×	×
Supervision of S. Huschke											×		×
Supervision of I. Muljajew										×		×	
Proposed publication equivalent	1												

1 Introduction

Despite the successful development of new active pharmaceutical ingredients (API)s and the understanding of their physiological pathways, the conventional application of free therapeutical agents often reaches efficacy limits exhibiting unspecific toxicity, poor bioavailability, as well as reduced delivery efficiency.^[1] The formulation of the APIs into so-called nanocarriers opens up the access to the research field of nanotechnology and holds great potential to overcome these disadvantages. Nanocarriers typically exhibit a size range from 10 to 500 nm and can improve the delivery of hydrophilic as well as hydrophobic materials, genetic material, proteins and small drugs as well as theragnostic agents.^[2-3] In the resulting field of nanomedicine, among others, two milestones can be named. Firstly, Doxil® was the first nanodrug approved by the U. S. Food and Drug Administration (FDA) as well as European Medicines Agency (EMA) in 1995.^[4] Secondly, the breakthrough development of the mRNA vaccine against the COVID-19 virus based on (polymer) modified lipid nanoparticles through Pfizer-BioNTech must be mentioned.^[5] Both nanomedicines are extraordinary examples of the nanotechnology potential which on itself led to a vibrant research space and a plethora of products in clinical trials.^[6-8]

Based on the carrier material, nanoparticles can be divided into three main classes: Lipid-based nanoparticles, inorganic nanoparticles, and polymeric nanoparticles. Each system exhibits pros and cons, however, polymeric drug delivery systems excel in their precise engineering of particle properties.^[2] Synthetic polymers are highly reproducible with very low batch-to-batch variance representing a major advantage over natural polymers such as polysaccharides. Properties can be controlled through advanced syntheses with predetermined (functional) end groups, molar mass, dispersity and overall comonomer composition. Additional functionalities can be introduced through functional (co)monomers. This enables to control the properties such as solubility, the hydrophilic hydrophobic balance (HHB) and thermal properties, as for example the degree of crystallinity. According to the API at hand, the modular principle allows tailor-made adjustments further facilitating the design of the desired macromolecular architecture such as block copolymers, or graft copolymers. Such a rational conception can, *e.g.*, be pursued by the establishment of polymer libraries. A subsequent formulation of nanocarrier libraries enables detailed investigation of structure-

property relationships. Poly(ethylene glycol) (PEG), poly(methyl methacrylate) (PMMA), poly(glycolic acid) (PGA), poly(lactic acid) (PLA), poly(ϵ -caprolactone) (PCL), as well as copolymers of the polyesters, represent widely established and FDA approved synthetic polymers for drug delivery applications used for that purpose.^[9]

According to the polymer composition and structure, the polymer can be formulated in different ways and a variety of nano-scale systems can be obtained (**Figure 1.1**).

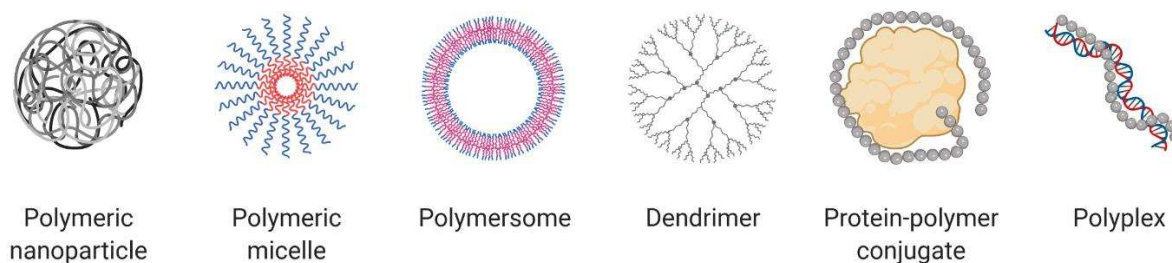


Figure 1.1: Representative variety of polymer-based nanocarriers for drug-delivery application (Figure created with BioRender.com).

Hydrophobic materials can be formulated into micro- and nanoparticles. Amphiphilic block copolymers can be assembled into core-shell nanoparticles, polymer micelles or polymersomes. Precise introduction of linkages enables access to dendrimers, hyperbranched polymers or nanohydrogels. Furthermore, polymers can be conjugated to proteins or complexed to genetic material (polyplex formation) to improve the properties or to elongate the circulation time of the therapeutically active substances.

Nanoparticles as well as polymeric micelles with a hydrophobic core are potential delivery systems for hydrophobic cargos. The development of such carriers is urgently needed as the drug discovery trend leads towards the development of larger, hydrophobic APIs.^[10] Predictions are reported with more than 50% of the new APIs to exhibit poor water solubility.^[11] This undoubtedly leads to difficulties for the preferred form of drug application that is the oral dosage form, *i.e.* tablet application, and overall reduces the bioavailability and delivery efficiency. In this context, also the increasing antibiotic resistance requires higher therapeutical doses as the antibiotic drugs become less effective.^[12]

The encapsulation of APIs by simple nanoprecipitation as well as the direct dissolution method enables fast and mild formulation of different polymers. The resulting drug delivery system

can facilitate a) the reduction of drug degradation, elimination and metabolic clearance, b) the enhancement of bioavailability as well as “effective” solubility, c) accumulation increase at target site through cell or tissue specificity, d) the increase of circulation time and control of the release profile, e) the encapsulation of multiple drugs and thereby enable synergistic effects, f) the reduction of undesired interactions and effects such as plasma protein binding of APIs as well as g) the improvement of permeability profiles through cellular barriers and drug resistance.^[2, 13-14] Every nanocarrier module can be modified thus opening up a large parameter space (**Figure 1.2**). However, this impressive list of potential benefits also includes a list of carrier material requirements, to enable engineering of the respective properties.

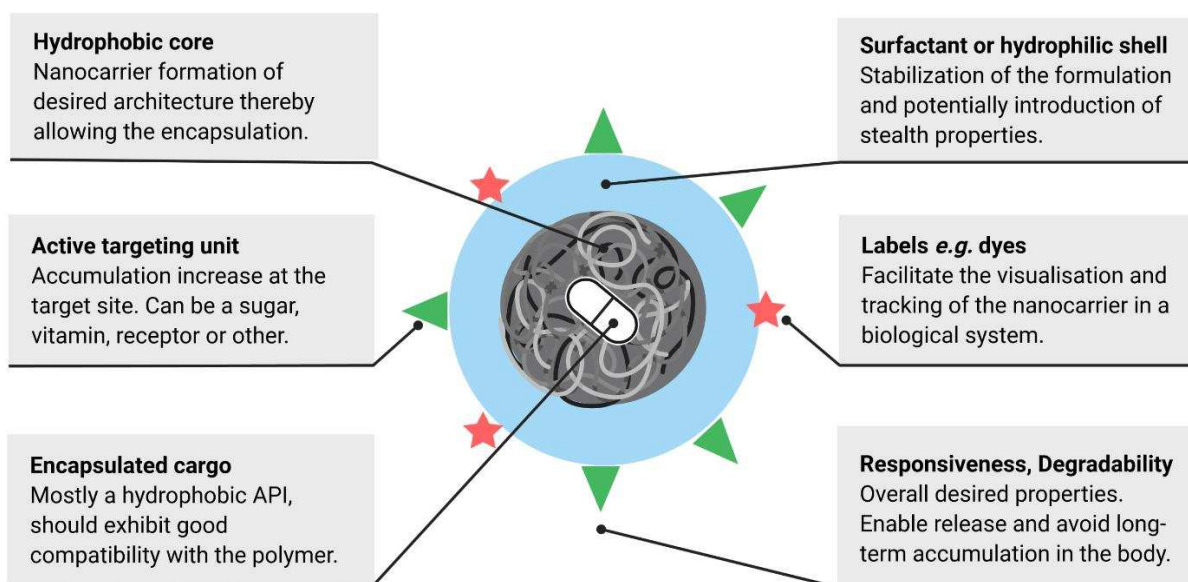


Figure 1.2: Commonly engineered nanocarrier properties that influence its performance as drug delivery system (Figure created with BioRender.com).

The hydrophobic core material should be biocompatible and form stable nanocarrier dispersions of desired size, shape, and surface charge. For efficient delivery, the material should release the cargo upon endogenous (cell environment or enzymatic level) or exogenous (light or sound) triggers. The particle can be stabilized by surfactants and cryo-protectants or by a covalently attached hydrophilic shell further introducing stealth properties. For active targeting, the carrier can be decorated with different ligands, such as receptors, sugars, antibodies, vitamins or small molecules. To facilitate the visualization of the delivery pathway, the carrier should be functionalized with a tracking agent such as radioactive label or dye, latter

within the biological optical window. Last but not most importantly, the API and the polymer material must be compatible to facilitate efficient encapsulation, formulation stability and control of the release profile avoiding API leakage or burst release. The distinct physicochemical properties of each API limit the “one size fits all” approach. Overall, the drug delivery system should be biodegradable, to avoid accumulation of the polymeric material in the body.

The modular approach is very flexible so that different building units of the carrier can be easily “personalized” to the delivery problem at hand. However, the physicochemical properties are strongly intertwined and influence each other. For example, a change in the comonomer composition can influence the overall HHB, crystallinity, phase separation, formulation processing and the formulation stability.^[15] An introduced tracing agent as well as its introduction method (encapsulated or covalently linked) can change the surface properties as well as the biodistribution of the carrier.^[16] As a consequence, changes should be performed with great care and their influence should be investigated in detail to enable proper conclusions about structure–property relationships. Per se, such studies need to be interdisciplinary to illuminate the physicochemical analysis with the respective bio–medical effects.

In this light, the aim of this thesis is the targeted synthesis of new polymeric scaffolds exhibiting great potential to, at least partially, fulfill the variety of requirements discussed above. Secondly, these materials were to be exploited as drug delivery carriers to allow a characterization of structure–property relationships within the large parameter space.

Chapter 2 summarizes the current research efforts on three promising and biodegradable polymer classes beyond the commonly used polyesters. Synthetic developments and applications are reviewed for poly(ester amide)s (PEAs), polyphosphoesters and polyacetals. The polymers appear rather different at first glance, but interesting parallels can be drawn in their development.

Chapter 3 investigates aspects of stability and the HHB for polyesters with defined microstructure. *Chapter 4* and *5* describe the synthesis of hydrophobic PEAs by step–growth polymerization of 2,2’-bis(2-oxazoline)s with differently substituted dicarboxylic acids. The resulting library is subsequently investigated with respect to nanoparticle formulation ability and compatibility with the hydrophobic drug Indomethacin.

Chapter 6 focuses on the characterization of polymeric micelles formed from amphiphilic graft copolymers with a hydrophobic backbone based on PMMA and short hydrophilic side-chains based on oligo(2-ethyl-2-oxazoline) (OEtOx). Here, the polymer end group is varied and its influence is discussed.

2 Recent advances in (bio)degradable synthetic polymers – Beyond polyesters

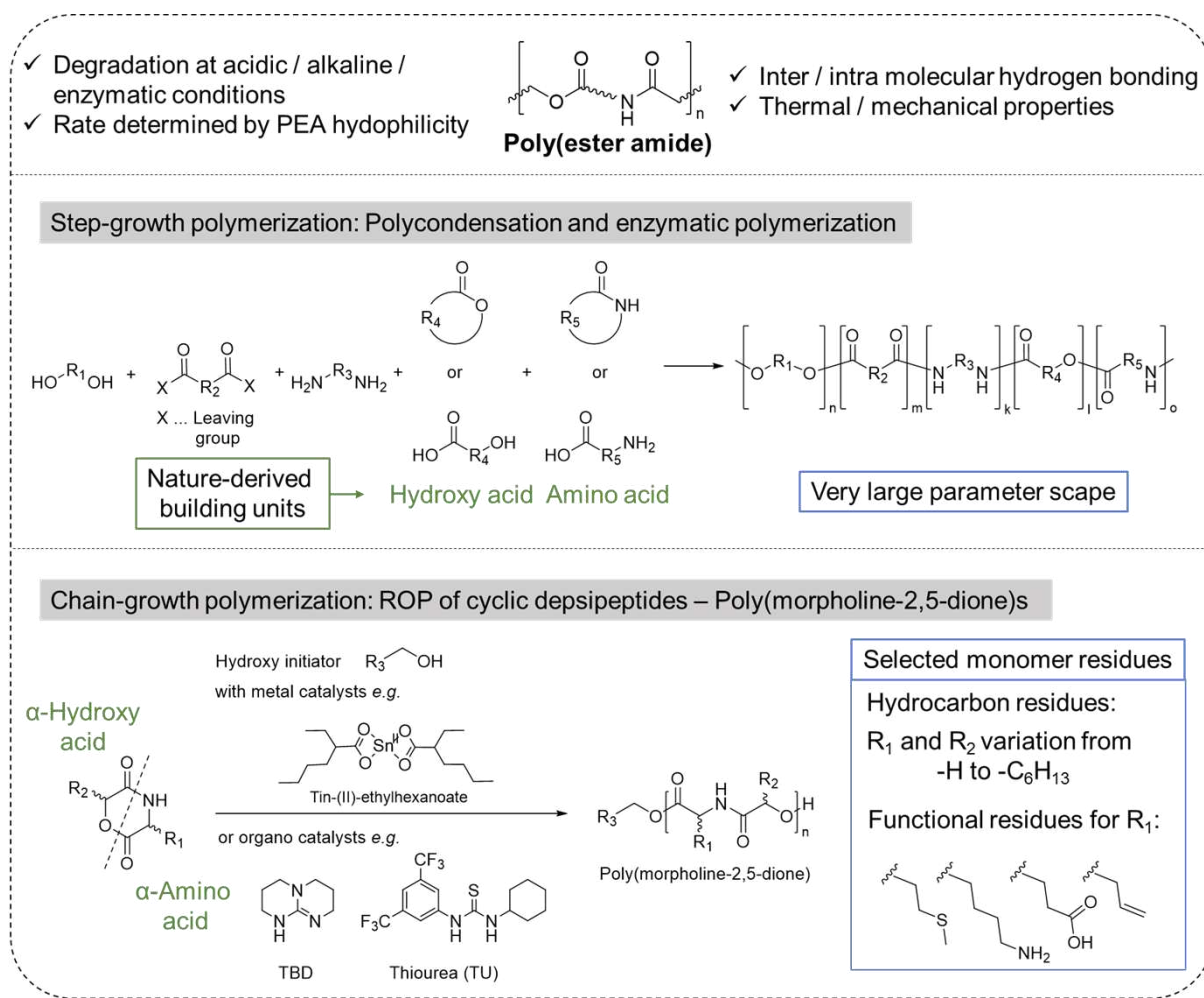
Parts of this chapter will be published: **P1**) M. Dirauf, I. Muljajew, C. Weber, U. S. Schubert, Recent advances in (bio)degradable polymers – Beyond polyesters, *Prog. Polym. Sci.* **2021**, *under revision*.

In 2014, the weight ratio of plastic to fish in the ocean added up to 1:5 and was estimated to increase to 1:1 by 2050.^[17] To tackle urgent issues like this, (bio)degradable polymers are in focus of scientific research. Polyesters are the flagship synthetic polymer class for the alternative use as degradable commodity materials.^[18] Among others, polyhydroxyalkanoates (PHA) or polylactide (PLA) are already widely used in food packaging as well as medical products. In particular, the biodegradation of pharmapolymers is of crucial importance to avoid accumulation in the organism as, *e.g.*, known for poly(ethylene glycol) (PEG) vacuole formation in the liver.^[19] With regards to drug delivery systems from synthetic materials, again polyesters approved by the U. S. Food and Drug Administration (FDA) are mainly on the market or in clinical trials.^[9] However, their degradation can lead to acidification of the microenvironment and, thereby, destabilize proteins or limit the applicability of pH-sensitive active pharmaceutical ingredients (APIs).^[20-22] In drug delivery systems, uncontrolled or unspecific polymer-API interactions can result in cargo leakage or burst release.^[16, 23] Tailor-made, synthetically versatile, degradable as well as bio-inspired alternatives could solve these disadvantages and overall enable a “personalized” application scope. With respect to the synthesis, the current research state for the alternative materials poly(ester amide)s (PEAs), polyphosphoesters and polyacetals is reviewed and their potential as nanosized drug delivery systems for hydrophobic drugs is highlighted.

Poly(ester amide)s

As the polymer name clearly indicates, PEAs combine repeating ester and amide moieties. These functional groups can be incorporated in a statistical way but also in a strictly alternating fashion as discussed below for poly(morpholine-2,5-dione)s (**Figure 2.1**). Amide moieties are often introduced into polyesters to improve the mechanical and thermal properties through inter- and intramacromolecular hydrogen bonds.^[24] Further, the hydrogen bond formation of

the amide groups with an encapsulated drug can facilitate higher drug loadings and formulation stability.^[25-26] *Vice versa* ester groups are introduced into polyamides to facilitate their hydrolysis. The degradation can occur under acidic, alkaline or enzymatic conditions while its rate is dependent on the PEA hydrophilicity.^[27]



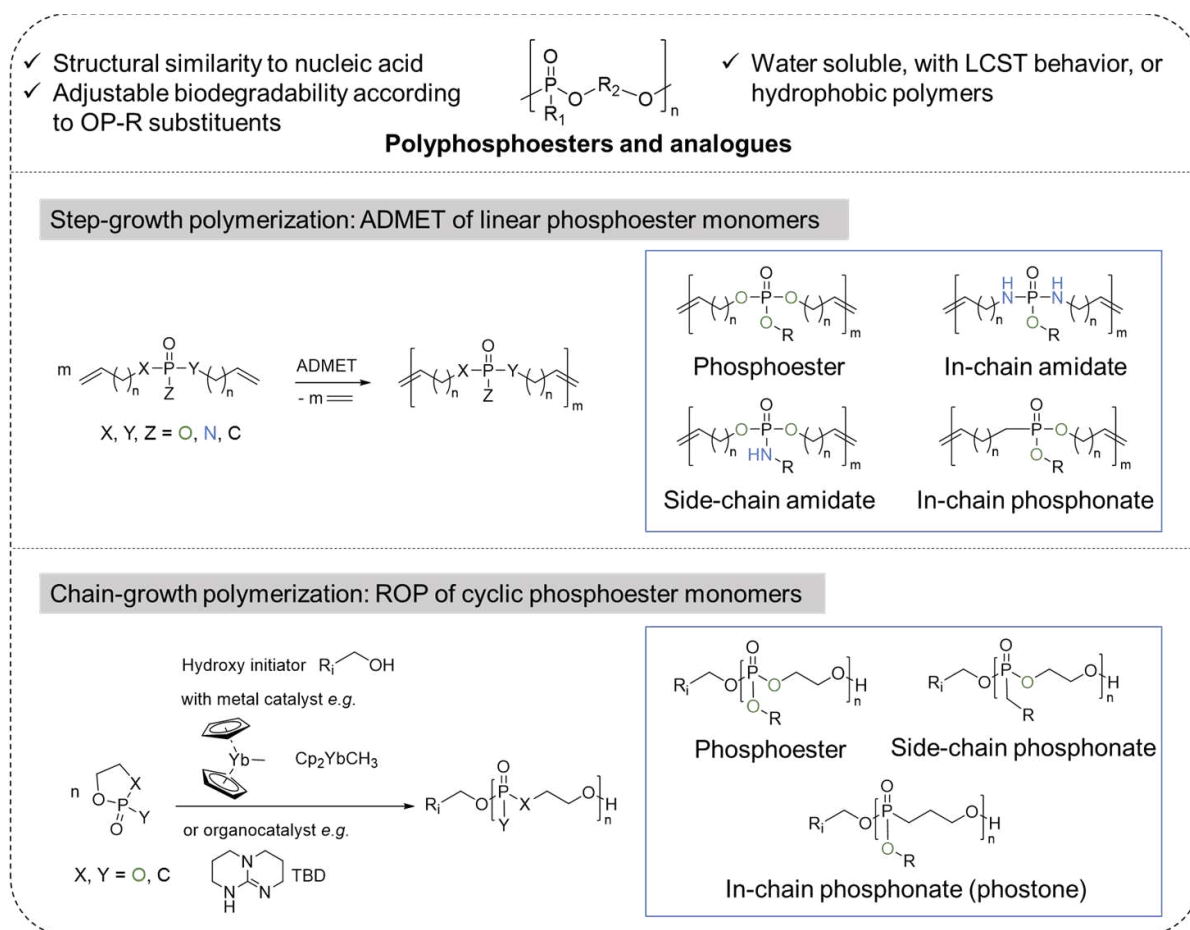
polymerization (ROP).^[30] Acyclic diene metathesis polymerization of suitable olefin monomers is another approach.^[31] PEA synthesis by polyaddition of 2,2'-bis(2-oxazoline) with dicarboxylic acids is detailed in *Chapter 4*. For some strategies, polymerization control is possible yielding alternating structures or block copolymers.^[32-33] In the biomedical field, the resulting PEAs are applied as drug delivery materials, *e.g.*, in topical application for wound healing or matrix tablets.^[34-35]

A common chain-growth strategy for the synthesis of PEAs is the ROP of cyclic depsipeptides to yield poly(morpholine-2,5-dione)s.^[36] The strictly alternating ester and amide moieties in the polymer main chain arise from the monomer structure based on an α -hydroxy acid and an α -amino acid. These two acids are (re)generated upon PEA degradation. Established synthetic routes for the morpholine-2,5-diones enabled access to a large variety of monomers with hydrocarbon substituents of varying hydrophobicity or monomers comprising substituents with additional functional groups.^[37] For the latter protection strategies were required due to the polymerization mechanism. Tin(II)-ethylhexanoate remains the most commonly used catalyst due to its broad monomer polymerization range and its full replacement was not successful yet.^[38] Only recently, organocatalysts such as TBD (1,5,7-triazabicyclo(4.4.0)dec-5-en) and DBU (1,8-diazabicyclo(5.4.0)undec-7-ene) were applied in combination with a suitable thiourea co-catalysts achieving high molar masses and low dispersity values ($\mathcal{D} = 1.15$ to 1.10).^[39-40]

The application driven PEA utilization gave rise to a plethora of different polymer architectures and morphologies. In drug delivery vehicles, hydrophobic poly(morpholine-2,5-dione)s or poly(lactone-*co*-morpholine-2,5-dione)s are used as core materials for nano or microparticle formulation.^[41-42] The latter copolymer is exploited with different monomer ratios to tailor the degradation rate of the nanocarriers or to increase the carrier stability through intramacromolecular hydrogen bonds. Block copolymers are also accessible through the introduction of stealth polymer blocks *via* the macroinitiator strategy as reported for PEG-*block*-PEA or poly(2-ethyl-2-oxazoline)-*block*-PEA.^[43-44] In addition, hydrogen bonds between the PEA nanoparticle core and encapsulated dexamethasone increased the drug loading content in comparison to the analogous poly(lactic-*co*-glycolic acid) (PLGA) system.^[25]

Polyphosphoesters and analogues

Depending on the substituents at the central phosphorus atom, the class can be additionally subdivided into polyphosphonates, polyphostones, and polyphosphoramidates (**Figure 2.2**).^[45-47] Furthermore, additional specification regarding the location of the residue *i.e.* side-chain or in-chain is to be considered. These polymers are at large biocompatible and in particular the polyphosphoesters are investigated as potential synthetic pharmapolymers due to their close structural resemblance to nucleic acids. The degradation of the P–O bond occurs under acidic conditions, the P–N bond under alkaline conditions and the more hydrolytically stable P–C bond can be degraded by microorganisms.^[48-50]



monomers yielded a variety of candidates mainly differing in their alkylene spacer length.^[49] Different side-chain substituents are also reported comprising hydroxyl groups or hydrocarbon groups of varying hydrophobicity. In part, copolymerization strategies were exploited for the incorporation of non-homopolymerizable monomers.^[49]

The chain-growth strategy for the synthesis of polyphosphoesters is the ROP of cyclic phosphoester monomers (**Figure 2.2**, bottom).^[52] Here, the phosphorous atom is substituted by carbon and oxygen residues, with clear literature dominance of the latter (*i.e.* X and Y are oxygen, **Figure 2.2** bottom left). Again, different monomer substituents generate hydrophilic (water soluble) or hydrophobic homopolymers as well as copolymers with lower critical solution temperature (LCST) behavior.^[53] Different side-chain functional groups such as allyl, alkyne or furfuryl moieties were successfully introduced allowing a variety of postpolymerization approaches.^[53-54] Even the introduction of suitable drugs or hydroxyl side-chain groups is possible, sometimes comprising protective group strategies.^[55-56] Amphiphilic block copolymers were accessible through the macroinitiator approach yielding PEG-*block*-polyphosphoesters, which were utilized to encapsulate different hydrophobic drugs.^[57]

Polyacetals

The acetal functional group is characterized by two ether groups at one geminal carbon. Depending on the substituents, acetal moieties degrade under different acidic conditions (re)forming the respective carbonyl compound and alcohol as neutral degradation products. Considering step-growth polymerization, two main synthetic routes are used: (A) The AA+BB polyaddition of diols^[58] and divinyl ethers and (B) the transacetalization polymerization,^[59] which represents a polycondensation-type reaction (**Figure 2.3**). The AA+BB polyaddition enabled access to hydrophilic, hydrophobic as well as amphiphilic polyacetals, depending on the monomer properties (**Figure 2.3**, bottom).^[60-61] Expanding the monomer scope, drugs with diol functionalities were conjugated into the polymer backbone as reported for, *e.g.*, dienestrol (**Figure 2.3**, bottom left).^[62] For side-chain conjugation strategies, different propanediol based monomers (**Figure 2.3**, bottom right) were incorporated allowing conjugation to proteins as well as orthogonal functionalization with targeting ligands and other small molecules.^[63]

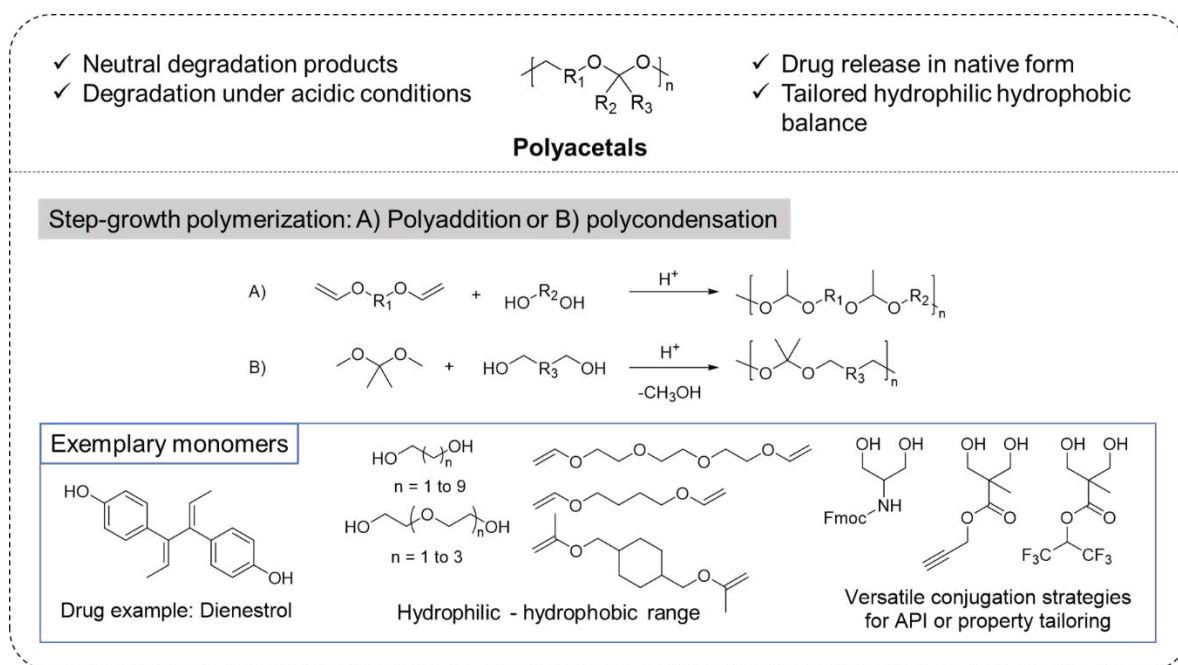


Figure 2.3: Schematic representation of an overview of step-growth polymerizations yielding polyacetals.

The transacetalization polymerization exploits the acetal exchange reaction between a diol and an acetal bearing monomer such as the mostly applied 2,2-dimethoxy propane while the formed methanol is simultaneously removed (**Figure 2.3, B**).^[59] Most research studies utilize an established, hydrophobic polyacetal range based on various compositions of 1,5-pentanediol, 1,4-cyclohexanedimethanol and 1,4-benzenedimethanol. Overall, the hydrophobic polyacetals are investigated intensively as nanosized drug delivery vehicles in a size range between 49 and 500 nm. An increased therapeutic value was observed for the encapsulated APIs such as apoptosis inhibitors,^[64] siRNA^[65] and chemotherapeutic agents.^[66] Degradation studies for the step-growth polyacetals were frequently performed at different pH values *via* a wide range of methods and in different formulations. Therefore, generalizations are omitted.

With respect to the chain-growth polymerization, a variety of strategies were developed over the last decade.^[67] The ROP of cyclic acetal monomers represents a straightforward approach, *e.g.*, using halogenmethyl methyl ethers as initiators and indium(III) bromide as catalyst for the monomers shown in **Figure 2.4, A**.^[68] Polyacetals with high molar masses up to 230,000 g mol⁻¹ were reported. Their tensile strength renders these polyacetals comparable to commodity olefins. Cyclic acetals can further be copolymerized with lactones or vinyl ethers

under cationic polymerization conditions (**Figure 2.4**, B and C).^[69-70] Exemplary monomers are depicted suitable for the copolymerization with frequent crossover reaction between the comonomers for at least one copolymer combination. Partially, the resulting copolymers exhibited unique and adjustable degradation behavior.^[71] It was, *e.g.*, possible to isolate the native acetal monomer from the copolymer through “degradation under vacuum”.^[70]

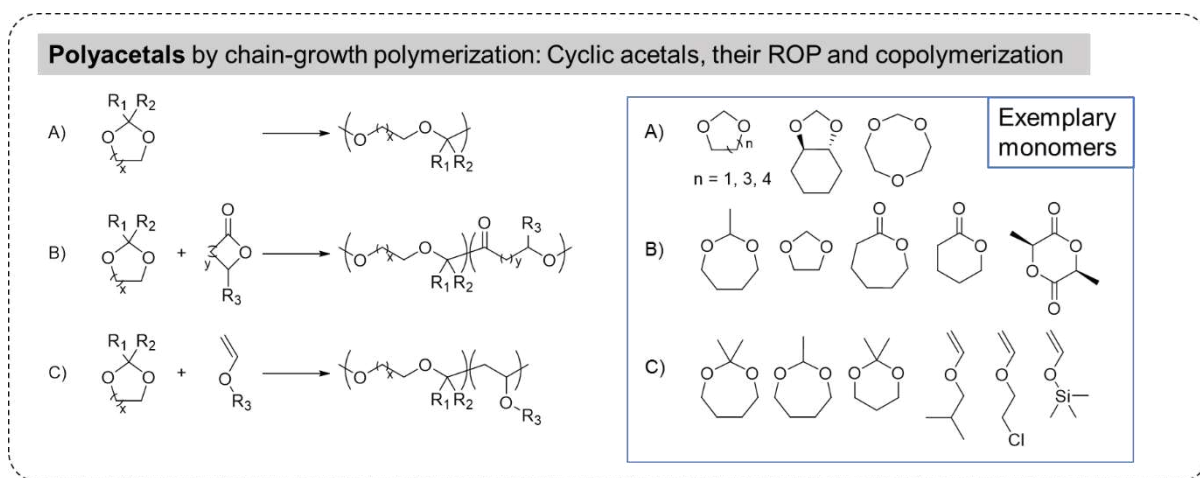


Figure 2.4: Schematic representation of an overview of chain-growth polymerizations for polyacetals including cyclic acetal monomers in A) homopolymerization, B) copolymerization with lactones and C) in copolymerization with vinyl ethers.

With regard to the polymer structure, the acetal functionality remains degradable when one geminal ether group is shifted to the side-chain. Under frequent monomer crossover reaction, this acetal moiety is generated in cationic copolymerizations of vinyl ethers with aldehydes^[72] or oxiranes^[73] as well as in terpolymerization of vinyl ethers with cyclic ethers and ketones (**Figure 2.5**).^[74] The major research was the generation of alternating or sequence-controlled copolymers. For this purpose, a large variety of monomers and reaction conditions was tested.^[75] Several parameters are of crucial importance such as monomer structure and reactivity, the applied Lewis acid, solvent type as well as presence or absence of Lewis bases. For optimized systems, precise sequential arrangement was demonstrated. As an example for poly(vinyl ether)s, acetal breaking points were introduced at predetermined main chain positions through aldehyde introduction, *e.g.*, via generation of alternating or gradient copolymers.^[76] Appropriate choice of protecting as well as functional groups enabled access to poly(vinyl ether-*alt*-aldehyde)s with a large hydrophilicity scope: Hydrophobic, water

soluble, pH-sensitive, copolymers as well as copolymers with LSCT and upper critical solution temperature (UCST) behavior were obtained.^[77-78] The described polymers were frequently hydrolyzed and the degradation products analyzed. However, the obtained information was mainly used to validate the polymer structure.^[79] Potential applications have not been explored so far.

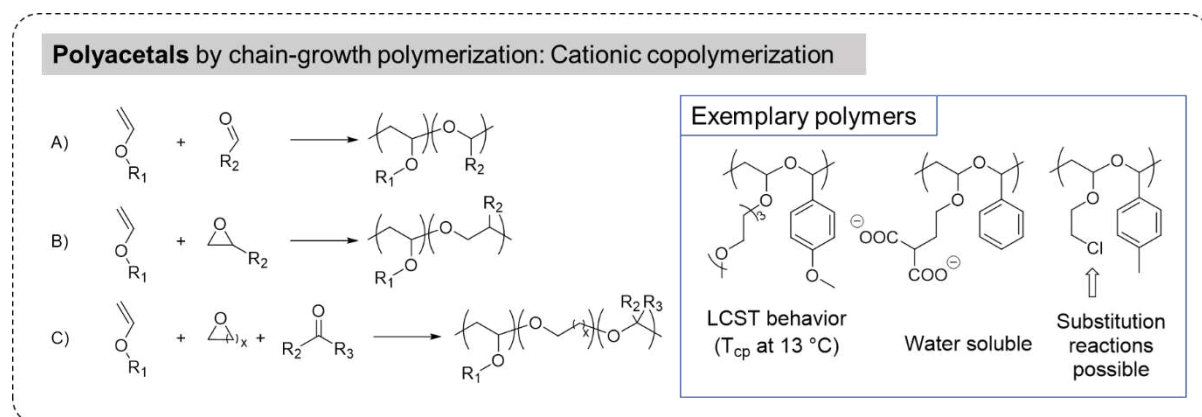


Figure 2.5: Schematic representation of chain-growth polymerizations for the incorporation of side-chain acetal moieties *via* cationic copolymerization of vinyl ethers with A) aldehydes, B) oxiranes and C) with cyclic ethers and ketones.

Lastly, the successful ROP of cyclic hemiacetal ester monomers yields poly(hemiacetal ester)s (**Figure 2.6**).^[80] The polymerization is catalyzed by low amounts of diethylzinc or diphenylphosphoric acid and can proceed with or without additional initiator.^[81] The presence of the latter allowed the introduction of functional groups or hydrophilic blocks.^[82] The obtained amphiphilic PEG-*block*-poly(6-membered hemiacetal ester) formed core-shell micelles facilitating the encapsulation of an amphiphilic drug, thereby increasing its accessibility in *in vitro* studies. These micelles degraded fully after 3 hours at pH 5.7 or 10.8. The 7-membered cyclic hemiacetal esters were also subjected to ROP.^[83] Polymers with less defined properties were obtained due to decreased reaction control. In general, the release of volatile aldehydes yielding the respective polyester represented a major side reaction.

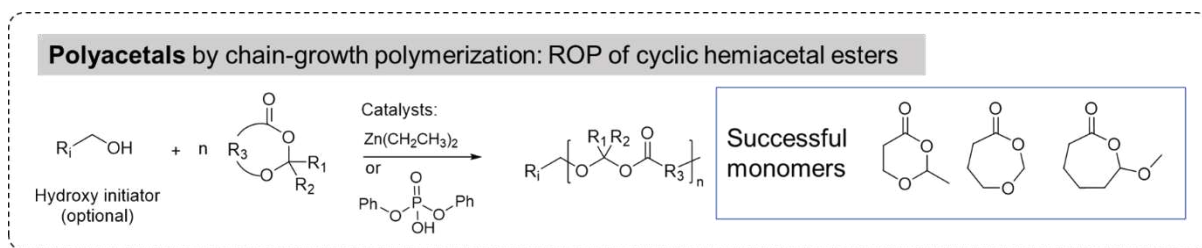


Figure 2.6: Schematic representation of the chain-growth polymerization for poly(hemiacetal ester)s including the monomers successfully polymerized to date.

Over the last decade, PEAs, polyphosphoesters and polyacetals experienced an upsurge in synthetic development, in particular with regards to chain-growth polymerization such as ROP. These new routes opened access to versatile structural design resulting in polymers that cover a large parameter space, *e.g.*, the hydrophilic hydrophobic balance (HHB), functional groups, and conjugation strategies. Concurrently, polymers obtained by more established polymerization routes such as step-growth approaches are frequently investigated in drug delivery application. In combination with the different degradation behavior these polymers will surely yield materials that exhibit efficacy beyond the current *status quo*.

While the polymer classes described above are mostly in their earlier development stages, scientific blind spots still exist even for established polymer classes such as polyesters with regards to their application as drug delivery systems. In particular, the relationship between the physico-chemical properties of the polyesters and their performance during drug delivery is of major interest. Parts of this complex question will be addressed in the following *Chapter 3*.

3 Tailor-made polyesters with constant hydrophobicity for nanoparticle formation

Parts of this chapter are published: **P2)** D. Bandelli, C. Helbing, C. Weber, M. Seifert, I. Muljajew, K. D. Jandt, U. S. Schubert, *Macromolecules* **2018**, *51*, 5567–5576. **P3)** D. Bandelli, I. Muljajew, K. Scheuer, J. B. Max, C. Weber, Felix H. Schacher, K. D. Jandt, U. S. Schubert, *Macromolecules* **2020**, *53*, 5208–5217.

Polymeric nanoparticles can be prepared by different techniques. Among them, the nanoprecipitation method is a very mild and fast process to obtain nanoparticles with controlled physico-chemical properties.^[84] The polymer is homogeneously dissolved in a water-miscible, organic solvent and is added in a controlled way to the aqueous phase under continuous stirring.^[85-86] The aqueous phase may further contain auxiliaries. Through rapid diffusion of the organic solvent into the aqueous phase, the solubility of the polymer decreases yielding a supersaturated solution. Crossing the critical nucleation concentration, the liquid and the solid phase separate and the polymer starts to form nucleation seeds that further grow by, *e.g.*, consuming the dissolved molecules. The formed colloidal precipitate is stabilized by steric and / or electrostatic repulsion. Subsequently, the organic solvent is removed, *e.g.*, by evaporation at room temperature, reduced pressure or similar methods. The nanoprecipitation occurs in the very small region of the solute / solvent / non-solvent ternary phase diagram typically of a triangular shape. This area is also called the “Ouzo” domain and is located in the metastable region between the binodal and spinodal curve.^[87] The desired size range of nanoparticles is typically below 200 nm as it is reported to be beneficial for cell uptake and can potentially increase circulation time in the blood stream avoiding filtration by the spleen or clearance by the kidney.^[88-90]

The physico-chemical properties of polymeric nanoparticles directly influence their performance as drug delivery vehicles. Systematic investigations are required to unravel the complex parameter space and facilitate the design of personalized medicine. The necessary prerequisite is the variation of only one property to obtain legitimate conclusions on structure-property relationships. The hydrophilic hydrophobic balance (HHB) of nanoparticles is one key parameter and known to influence drug release during enzymatic degradation.^[91-92]

The HHB describes the ratio of hydrophilic to hydrophobic molecule parts and was initially introduced as a group contribution method for the calculation of fixed values for low molar mass surfactants.^[93] Due to the high molar mass for polymers and their partially complicated composition, simple addition of attributed group values is not reasonable. However, the consideration of the overall macromolecular composition considering the total ratio of different functional groups is applicable. For example, poly(ϵ -caprolactone) is more hydrophobic compared to poly(δ -valerolactone) because poly(ϵ -caprolactone) exhibits one more methylene group in the monomer repeating unit (**Figure 3.1**). As a consequence, poly(ϵ -caprolactone) and poly(δ -caprolactone) should exhibit the same HHB as the respective monomers are isomers (**Figure 3.3**).

Matching the HHB of poly(ϵ -caprolactone), this design idea was implemented for two studies of copolyesters. The material was synthesized through ring opening polymerization (ROP) using TBD (1,5,7-triazabicyclo(4.4.0)dec-5-en) as catalyst and benzyl alcohol as initiator. In the first approach, two tailor-made copolyesters with the composition of 80 mol% δ -valerolactone (δ VL) and 20 mol% δ -decalactone (δ DL) were obtained with a gradient or a block microstructure (**Figure 3.1**). The monomers and their compositions were chosen to obtain the overall equal ratio of methylene to ester groups as in poly(ϵ -caprolactone), which served as reference material.

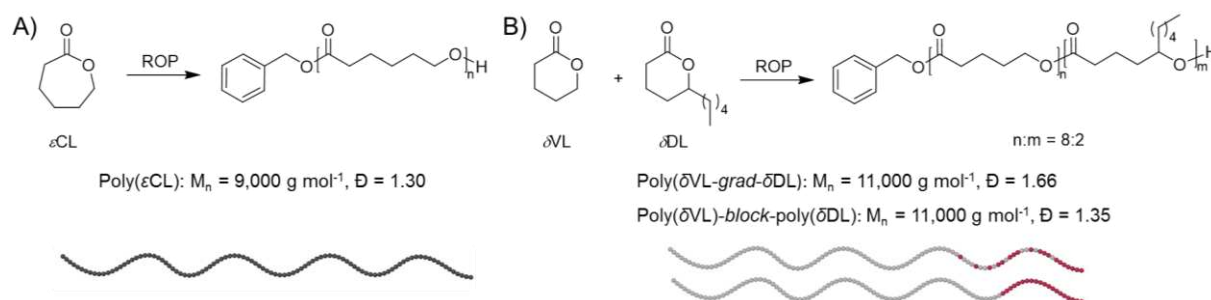


Figure 3.1: Schematic representation of the ring opening polymerization of lactones yielding polyesters with the same hydrophilic hydrophobic balance. A) Poly(ϵ -caprolactone). B) Copolymer of δ -valerolactone and δ -decalactone with different microstructure, *i.e.* gradient and block. M_n and \mathcal{D} obtained by SEC (CHCl_3 , RI detection, PMMA calibration) (Figure partially created with BioRender.com).

These three polyesters were successfully formulated into nanoparticles by nanoprecipitation into water using THF-polymer solutions of different concentrations. Different solvent to

nonsolvent ratios resulted in adjustable sizes between 50 and 230 nm. Without additional surfactants, the nanoparticles were stable over the period of 30 days (**Figure 3.2**). All nanoparticles further revealed zeta (ζ) potentials of approximately -30 mV.^[94-95] The phenomenon is presumably caused by the preferred association of hydroxide ions from neat water on surfaces leading to a negative ζ -potential.^[96]

The tuning of formulation conditions facilitated the formation of nanoparticles with a constant D_h of ≈ 170 nm for every polyester. The fixed size enabled the unambiguous correlation of nanoparticle stiffness with bulk polymer crystallinity.

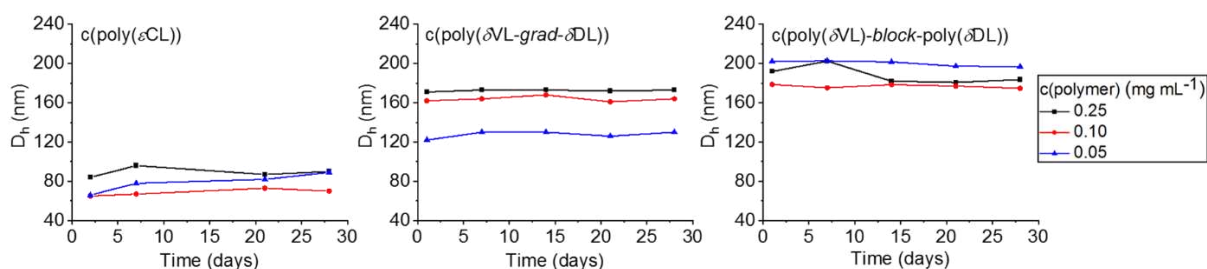


Figure 3.2: Stability of nanoparticles prepared from three polyesters with same hydrophilic hydrophobic balance (HHB) in aqueous suspension. Samples stored at 5 °C between measurements. Hydrodynamic diameters determined by dynamic light scattering.

In the second approach for the synthesis of polyesters with the same HHB, the constitutional isomers ϵ -caprolactone (ϵCL) and δ -caprolactone (δCL) were copolymerized yielding a library of five random copolymers with different composition (**Figure 3.3**). The microstructure was determined by variation of monomer feed ratio and polymerization kinetic studies, additionally supported by application of different kinetic models. Complementary, the respective homopolymers $\text{poly}(\delta\text{CL})$ as well as $\text{poly}(\epsilon\text{CL})$ were also synthesized. All polymers were successfully formulated into nanoparticles of 115 to 138 nm by nanoprecipitation into water using THF-polymer solutions. For $\text{poly}(\epsilon\text{CL})$, $\text{poly}(\delta\text{CL})$ as well as a random copolymer featuring 50% of each repeating unit, the HHB of the polymeric nanoparticles was determined by encapsulation of the solvatochromic dye pyrene. For this purpose, the dye and the respective polymer were coprecipitated with a targeted 1% dye loading. The resulting suspensions revealed a size range from 120 to 160 nm. After subsequent dilution the suspensions were analyzed by fluorescence spectroscopy. The vibrational fine structure in the emission spectrum of pyrene changes depending on the hydrophobicity of the surrounding.^[97-100] However, in the

case of the three copolyesters the ratio of the I_1 and I_3 bands remained at ≈ 1.22 confirming the constant HHB.

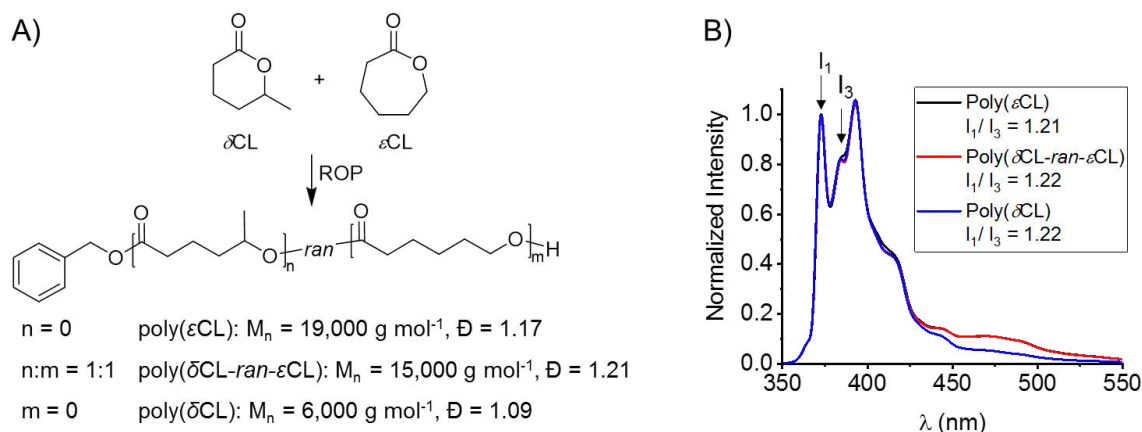


Figure 3.3: A) Schematic representation of the lactones δ -caprolactone and ϵ -caprolactone as well as their ring opening polymerization yielding polyesters with the same hydrophilic hydrophobic balance. B) Normalized emission spectra of nanoparticles from the different polycaprolactone loaded with pyrene ($\lambda_{\text{ex}} = 339 \text{ nm}$, $c(\text{polymer}) = 5 \mu\text{g mL}^{-1}$, $c(\text{pyrene}) = 0.05 \mu\text{g mL}^{-1}$).

In conclusion, the two studies yielded suitable polyester core materials with constant HHB while the respective nanoparticles exhibited long term stability. The constant hydrophobic properties of nanoparticles were validated by encapsulation of a solvatochromic dye. For these polyesters, varied thermal properties and degree of crystallinity were determined allowing their correlation to the nanoparticle stiffness. This set of nanoparticles represents therefore an excellent foundation for further investigations of the relationship between physico-chemical properties and its drug delivery performance.

In other words, eliminating the HHB as a 3rd variable will enable to determine how nanoparticle stiffness or thermal properties influence cell uptake, enzymatic degradation or release of the active pharmaceutical ingredient (API).

So far, attention was put on the polymer design and the resulting nanoparticle properties. Ultimately, also the relationship between polymer and drug will play an important role in the development of drug delivery system. Hydrogen bonding is a prominent way to induce interactions between the core materials as, *e.g.*, possible for poly(ester amide)s. The initial synthesis of such materials is discussed in the following *Chapter 4*.

4 Poly(ester amide)s from polyaddition of dicarboxylic acids and 2,2'-bis(2-oxazoline)

Parts of this chapter are published: **P4**) I. Muljajew, A. Erlebach, C. Weber, J. R. Buchheim, M. Sierka, U. S. Schubert, *Polym. Chem.* **2020**, *11*, 112–124.

Poly(ester amide)s (PEAs) combine the degradability of polyesters and the pronounced thermal and mechanical properties of polyamides.^[24, 101] The current research state was summarized in *Chapter 2*. Gram-scale amounts of new materials are desirable for the evaluation of their potential as drug delivery systems through screening approaches and cross comparison of different methods. The AA+BB polyaddition of commercially available dicarboxylic acids and bis(2-oxazoline) represents a high-yield and versatile approach.^[102] Mechanistically, the oxazoline ring opens by the nucleophilic attack of the carboxylic acid.^[103] Upon rearrangement, the amide functionality is formed. As both monomers are bifunctional, this generates polymers with alternating diester and diamide moieties in the main chain.^[104] Aromatic bis(2-oxazoline)s were have been used occasionally.^[105-106] However, the addition of the 2,2'-bis(2-oxazoline) yielding the repeating oxamide moiety was first investigated in the work at hand. With the constant oxamide moiety, the variation of polymer properties, such as hydrophobicity, was possible through the utilization of dicarboxylic acids with varying linker length and substitution patterns (**Figure 4.1**).

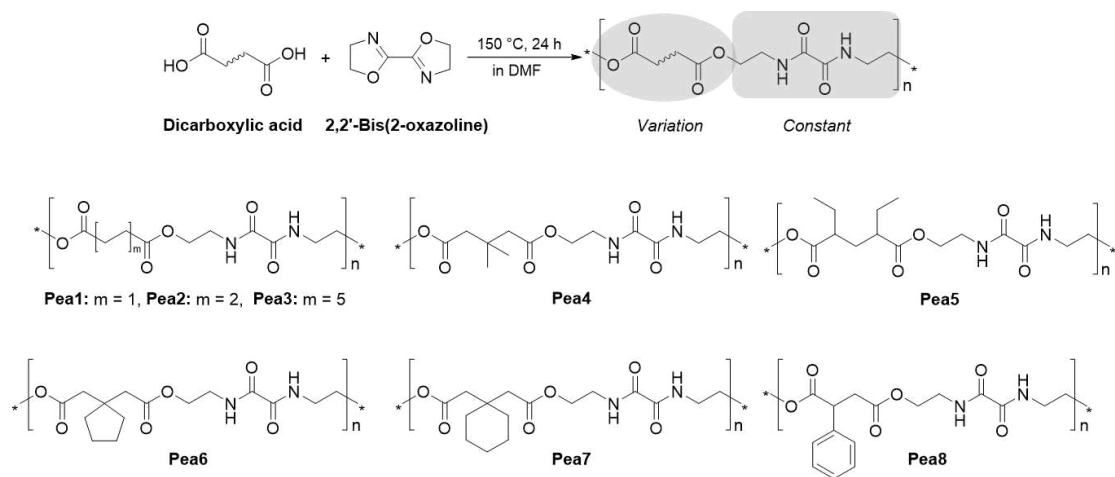


Figure 4.1: Schematic representation of the AA+BB polyaddition and schematic representation of the structures of the obtained poly(ester amide)s **Pea1** to **Pea8**.

For polymers **Pea1** to **Pea3**, the length of the spacer between the ester moieties was varied through the use of unsubstituted, aliphatic dicarboxylic acids as monomers. For **Pea4** to **Pea7**, the spacer length was kept constant but different substituents were introduced, *i.e.*, two methyl substituents, two ethyl substituents, a 5- or 6-membered ring. Noteworthy, **Pea5** and **Pea6** exhibit the same number of methylene / methine groups and should, therefore, exhibit the same hydrophilic hydrophobic balance (HHB). Lastly, **Pea8** was bearing a phenyl side group, thereby additionally varying electron density.

Prior to their investigation as nanoparticle formulation materials, the polymers were characterized by a variety of methods to determine their structure. Ester and amide groups were confirmed by IR spectroscopy through the presence of the respective functional bands. The absence of bands related to the starting material additionally hinted towards the successful polyaddition. The structure was further validated by ^1H NMR spectroscopy in deuterated hexafluoro-*iso*-propanol (HF*i*P), a solvent known for its ability to break strong hydrogen bonds. The exemplary spectrum of **Pea3** confirms the targeted structure revealing the signals related to the dicarboxylate linker as well as the ring-opened oxazoline moieties by the signals 5 and 4 (**Figure 4.2**). Similar conclusions were drawn from the respective ^1H NMR spectra of the other polymers. The signals 5' and 4' were assigned to polymer chain ends $-\text{CONH}-\text{CH}_2-\text{CH}_2-\text{OH}$, presumably created upon opening of the oxazoline ring by nucleophilic attack of water residues. The integrals of these proton peaks were utilized to estimate the degree of polymerization (DP) and thereby also the molar masses. For **Pea1** to **Pea8**, DP values from 4 to 21 and M_n values from 1,200 to 7,100 g mol^{-1} were determined (**Table 4.1**).

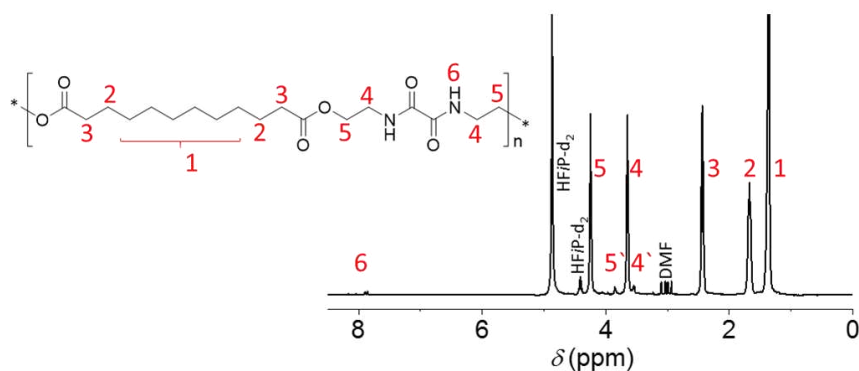


Figure 4.2: ^1H NMR spectrum (400 MHz, HF*i*P- d_2) of **Pea3** with assignment of the signals to the schematic representation of the polymer structure. Peaks 5' and 4' correspond to the polymer end group $-\text{CONH}-\text{CH}_2-\text{CH}_2-\text{OH}$.

The limited solubility of **Pea1** to **Pea3** restricted further analysis in solution. However, the molar mass distribution of **Pea4** to **Pea8** could be investigated by SEC in DMAc. The molar masses ranged from 2,500 to 6,200 g mol⁻¹ while the dispersity values were between 1.3 and 1.9 (Table 4.1). The molar masses determined by SEC and ¹H NMR spectroscopy were in reasonable agreement, while in both cases no trend was observable. In general, the step-growth polymerization enables only limited control over the degree of polymerization.

Table 4.1: Selected characterization data of the poly(ester amide)s **Pea1** to **Pea8** obtained from ¹H NMR spectroscopy, SEC, DSC, WAXS as well as atomistic molecular dynamics simulations.

	M_n^a (g mol ⁻¹)	DP^a	M_n^b (g mol ⁻¹)	\mathcal{D}^b	T_g^c (°C)	T_m^c (°C)	X_c^d (%)	ρ^e (g cm ⁻³)
Pea1	1,200	4	n.a.	n.a.	n.a.	152 / 211 / 222	50	1.296
Pea2	5,000	17	n.a.	n.a.	n.a.	181 / 189	18	1.237
Pea3	7,600	20	n.a.	n.a.	n.a.	149 / 168	39	1.117
Pea4	4,400	14	5,200	1.26	21	n.a.	n.a.	1.214
Pea5	7,100	21	6,200	1.26	14	n.a.	n.a.	1.167
Pea6	3,800	11	4,200	1.36	25	n.a.	n.a.	1.222
Pea7	4,600	13	4,400	1.49	26	132.4 ^f	n.a.	1.200
Pea8	2,600	8	2,500	1.90	50	n.a.	n.a.	1.253

^a Determined by ¹H NMR spectroscopy (400 MHz, HFIP-d₂). ^b Determined by SEC (DMAc, 0.21 wt.% LiCl, RI detection, PS calibration). ^c Determined by DSC in the 2nd heating run, inflection values are reported for T_g . ^d Degree of crystallinity determined by WAXS. ^e Mass densities calculated by atomistic molecular dynamics simulations. ^f Determined by DSC in the 1st heating run, after annealing at 111 °C for 24 hours.

MALDI-ToF mass spectrometry is another powerful method for structural investigation as it provides insights into the repeating unit, end group fidelity and, in general, validates the presence of polymeric species. The exemplary mass spectrum of **Pea7** features peaks spaced by regular intervals of $\Delta m/z = 340$ in agreement with the respective monomers 2,2'-bis(2-oxazoline) and cyclohexanediadic acid (Figure 4.3). Different end groups can be possible with respect to the polyaddition mechanism: **A** – both α and ω ends are carboxylic acids, **B** – both α and ω ends are oxazolines and **C** – one end results from the carboxylic acid and one from the oxazoline. Noteworthy, species **C** is isobar to a potential ring structure. From these

three suggested structures, surprisingly only **C** was identified of lower intensity in the mass spectrum of **Pea7**. Further, two species (**D** and **E**) terminated with $-\text{CONH}-\text{CH}_2-\text{CH}_2-\text{OH}$ instead of 2-oxazoline ring(s) were identified. Both species were ionized with either sodium or potassium counter ions yielding four identified main distributions. In agreement with ^1H NMR spectroscopy, the groups are presumably formed due to the nucleophilic attack of water at the oxazoline ring. Species **B**, initially expected with two terminal oxazoline rings, was thereby transformed into **D** featuring two ring opened ends $-\text{CONH}-\text{CH}_2-\text{CH}_2-\text{OH}$. Similarly, for **C**, the one expected oxazoline ring was detected in its open form leading to species **E**. The assignment of all structures was confirmed by the calculation of the corresponding isotopic patterns, as exemplary shown for the species **D** with a sodium counter ion (**Figure 4.3**).

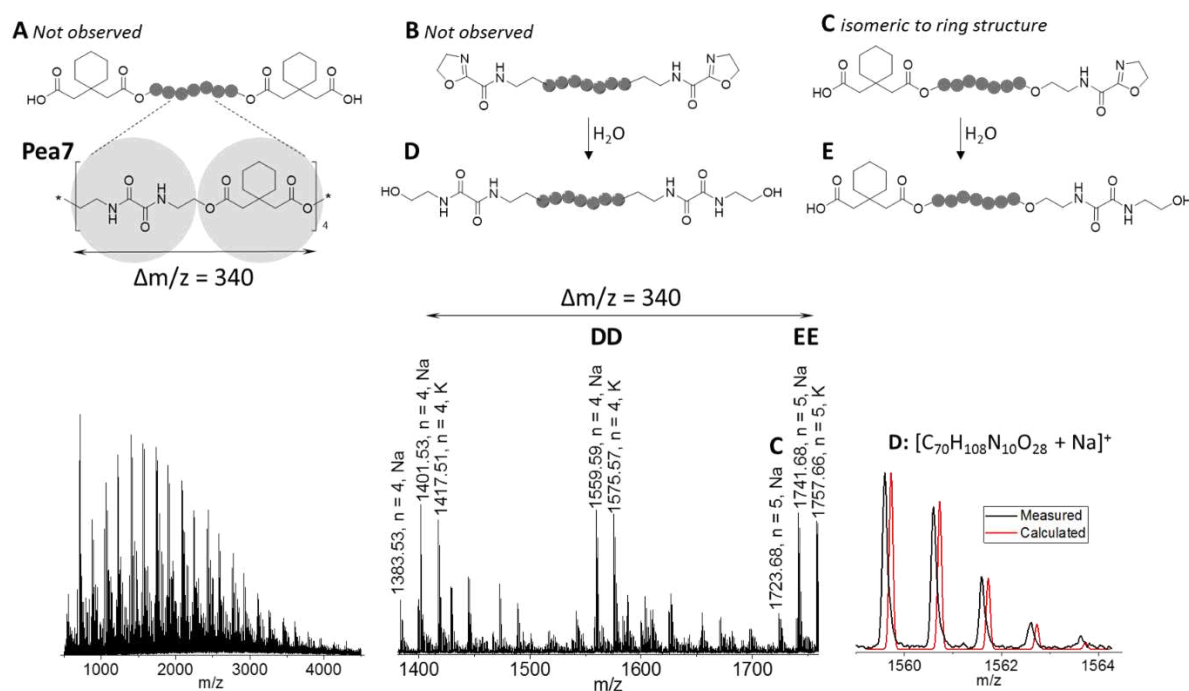


Figure 4.3: MALDI–ToF mass spectrum (matrix: DHB) of **Pea7**. **Top row:** Species **A**, **B**, **C** including end groups expected from the polyaddition mechanism as well as formation of end groups detected in the mass spectrum. **Left bottom:** Full mass spectrum. **Center bottom:** Zoom into the most abundant m/z region and peak assignment. **Right bottom:** Overlay of the calculated and measured isotopic pattern for the exemplary structural assignment of one observed peak corresponding to the **D** species.

The limited solubility of **Pea1** to **Pea3** already indicated hydrogen bonding. Hence thermal as well as wide-angle X-ray scattering (WAXS) analysis of the bulk material was performed to obtain information on the polymer crystallinity. Initially, thermogravimetric analysis (TGA) was applied to determine the temperature range in which the polymer stability was ensured. Differential scanning calorimetry (DSC) measurements for **Pea1** to **Pea3** revealed melting peaks ranging from 149 to 222 °C, clearly indicating the presence of semi-crystalline materials (**Figure 4.4**, **Table 4.1**). Solely for **Pea1**, the polymer with the short aliphatic linker, a third peak at lower temperatures was observed (“c”) potentially caused from less perfect crystals in the form of “bundle chains” due to the reduced chain flexibility. Nevertheless, all three thermograms of **Pea1** to **Pea3** revealed two peaks (“a” and “b”) indicating two different crystalline modifications. The respective melting temperature (T_m) values decrease with increasing linker length between the ester moieties in agreement with literature reports.^[105] Noteworthy, peak “a” and therefore the presence of the respective crystalline domain increased with increasing linker length between the ester moieties.

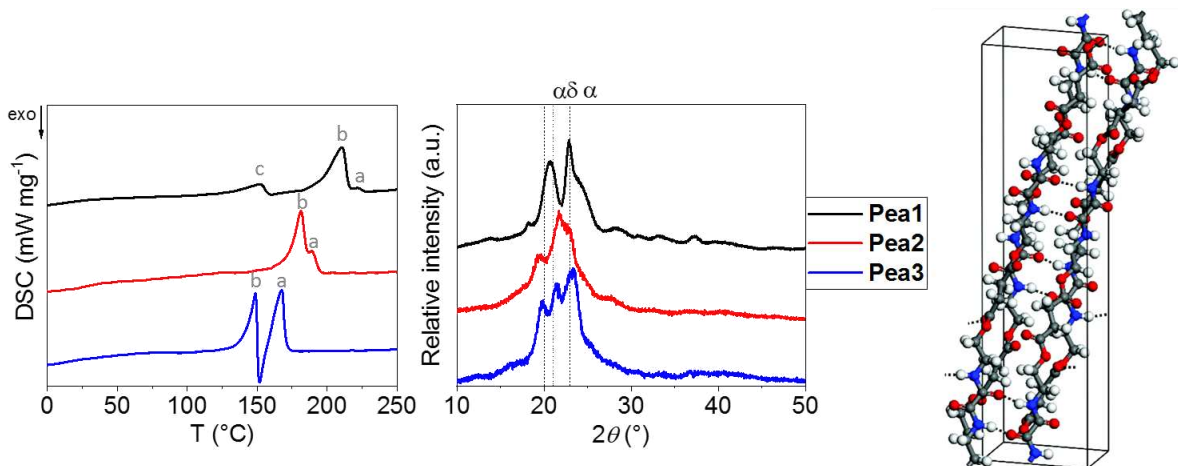


Figure 4.4: Bulk analysis of **Pea1** to **Pea3**. **Left:** Differential scanning calorimetry (DSC) thermograms (second heating run, heating rate: 20 K min⁻¹). **Middle:** Wide-angle X-ray diffractograms. Dotted lines indicate the characteristic Bragg reflections of Nylon11 α and δ forms. **Right:** Structure model of the crystalline structure of **Pea1** obtained by comparison of measured and calculated diffractograms (C: grey, O: red, H: white, N: blue, dotted lines: H bonds).

The three polymeric materials were further investigated by WAXS analysis to gain deeper understanding of their crystalline structures (**Figure 4.4**, right). In agreement with the DSC measurements, the patterns indicated the presence of similar crystalline phases. The positions of the diffraction peak maxima for **Pea1** to **Pea3** and their structural similarity to the well-

studied polyamides (Nylon 6 or 11) suggested similar modifications.^[107-111] From the Bragg reflection positions it was concluded that **Pea1** mainly crystallized in an α -form and **Pea3** was additionally present in a δ -modification. For **Pea2** analogous modification assignment was unfortunately not possible due to the lower degree of crystallinity. However, a calculated diffractogram of **Pea1** allowed access to a structure model of its crystalline structure (**Figure 4.4**, right). Expected to promote ordering, two hydrogen bonds per repeating unit were identified between the amide groups of neighboring polymer chains. Confirming the assumption, these interactions presumably acted as the crystallization driving force.

The other polymers, **Pea4** to **Pea8**, were amorphous as only glass transition events were observed in the respective DSC thermograms with glass transition temperature (T_g) values between 14 and 50 °C (**Table 4.1**). The larger ethyl residues of **Pea5** led to an increased free volume in comparison to the smaller methyl residues of **Pea4** thereby reasoning the T_g values of 14 °C and 21 °C, respectively. For the cyclopentyl and cyclohexyl substituted polymers, **Pea5** and **Pea6**, no significant difference in the T_g values was observed (T_g values \approx 25 °C). The aromatic substituent at **Pea8** led to an increase of the T_g to 50 °C.

The theoretical considerations on polymer hydrophobicity and the observed trends from DSC indicating intramacromolecular forces were further evaluated by atomistic molecular dynamics (MD) simulations. For this purpose, the Hildebrand solubility parameter δ was calculated enabling a rapid ranking of the materials.^[112-113] The obtained δ values agreed with the theoretical consideration and the DSC trends. The δ parameter was therefore sufficiently accurate for the evaluation of the bulk properties, however it provided less accurate predictions on the solubility of the polymers in acetone and THF, two commonly used solvents for nanoprecipitation. As a consequence, more elaborate as well as computationally improved simulations of the Flory–Huggins parameter χ were performed and the solubility was predicted in agreement with experiments: **Pea4** was soluble in acetone and THF, but **Pea8** was not soluble in both solvents.^[114-115]

Conclusively, a polymer library of eight candidates was successfully synthesized by the AA+BB polyaddition and the structures validated by a variety of physico-chemical methods. Semi-crystalline **Pea1** to **Pea3** and amorphous **Pea4** to **Pea8** were obtained as indicated by DSC and WAXS analysis. In combination with MD simulations, this approach clearly

demonstrated a straightforward method for the synthesis of poly(ester amide)s with tunable properties such as hydrophobicity as well as solubility.

The obtained polymers are sufficiently diverse in their features as well as substitution to investigate the respective influences on their nanoparticle formulation ability as performed in detail in the following *Chapter 5*. The materials were further tested as nanocarriers for indomethacin, including detailed bulk miscibility studies.

5 Compatibility of poly(ester amide)s with indomethacin

Parts of this chapter are published: **P5**) I. Muljajew, M. Chi, A. Vollrath, C. Weber, B. Beringer–Siemers, S. Stumpf, S. Hoepfner, M. Sierka, U. S. Schubert, *Eur. Polym. J.* **2021**, *156*, 110606.

Aiming at nanosized polymeric drug delivery systems with potential hydrogen bonding between the core materials, the poly(ester amide)s (PEAs) obtained in *Chapter 4* were investigated according to their nanoparticle formulation ability and their potential to encapsulate a hydrophobic cargo. The focus was to understand the structure–property relationships between polymer and drug and, hence, the compatibility of the core materials. Optimized thermodynamic compatibility enables control of the drug loading and its retention as well as increase the overall stability of the systems.^[16, 23, 25]

The nanoprecipitation method was introduced in *Chapter 3* and represents a very mild and versatile formulation method.^[116] However, the resulting nanoparticles are sensitive to changes of the formulation parameters such as type of organic solvent, concentrations, presence of surfactant, and settings of addition.^[117] Therefore, an initial screening was highly expedient to determine the optimized parameter settings, in particular as the polymers of interest were not yet established in the field. In this light, the polymers (**Figure 4.1**) were subjected to a high–throughput nanoprecipitation study using a liquid handling robot. Up to three organic solvents were tested for each polymer at concentrations between 1 and 20 mg mL⁻¹ which were formulated into pure water or a 0.3% aqueous poly(vinyl alcohol) (PVA) solution. Initial studies on **Pea1** and **Pea2** revealed strong aggregation of the polymers due to the preferred inter– and intramacromolecular forces resulting in their exclusion from detailed screening. Similarly, **Pea3** was a rather unpromising candidate due to the restricted solubility and low formulation stability. Substituted polymers that featured higher density (**Table 4.1**) formed less defined, loaded nanoparticles as for both properties the trend was: **Pea8** > **Pea4** / **Pea6** > **Pea5** / **Pea7**. Nevertheless, the polymers **Pea4** to **Pea8** formed nanoparticles in the desired size range of 100 to 400 nm under optimized conditions utilizing the volatile solvent hexafluoro–*iso*–propanol (HF*i*P) as well as the surfactant.

The nonsteroidal anti-inflammatory drug (NSAID) indomethacin (IMC) (**Figure 5.1**) was chosen for further nanoparticle encapsulation studies.^[118] IMC is hydrophobic and commercially available, can potentially form hydrogen bonds and exhibits a T_m value at 165 °C in the applied experimental setup. The encapsulation studies were performed with reduced surfactant impact, *i.e.*, the PVA was added after the conanoprecipitation was conducted to exclude its effect on the encapsulation efficiency (EE) and loading capacity (LC) (**Figure 5.1**). The loaded nanoparticles Pea@IMC mostly exhibited a smaller size ($120 \text{ nm} < D_h < 167 \text{ nm}$) compared to the unloaded nanoparticles Pea@empty ($178 \text{ nm} < D_h < 329 \text{ nm}$). This behavior was potentially caused by attractive Pea–IMC interactions.^[119-120] The highest EE was obtained for **Pea7@IMC** with 53%. If necessary, this value can probably be increased with an optimized coprecipitation protocol and regular surfactant application. A scanning electron microscopy (SEM) image of exemplary **Pea7@IMC** is shown in **Figure 5.1**. In general, the assessed quality of the Pea@IMC suspensions was in good agreement with the respective images. Overall, the encapsulation study followed the same trend as the formulation study. Polymers that formed the most stable nanoparticles also reached the highest LC.

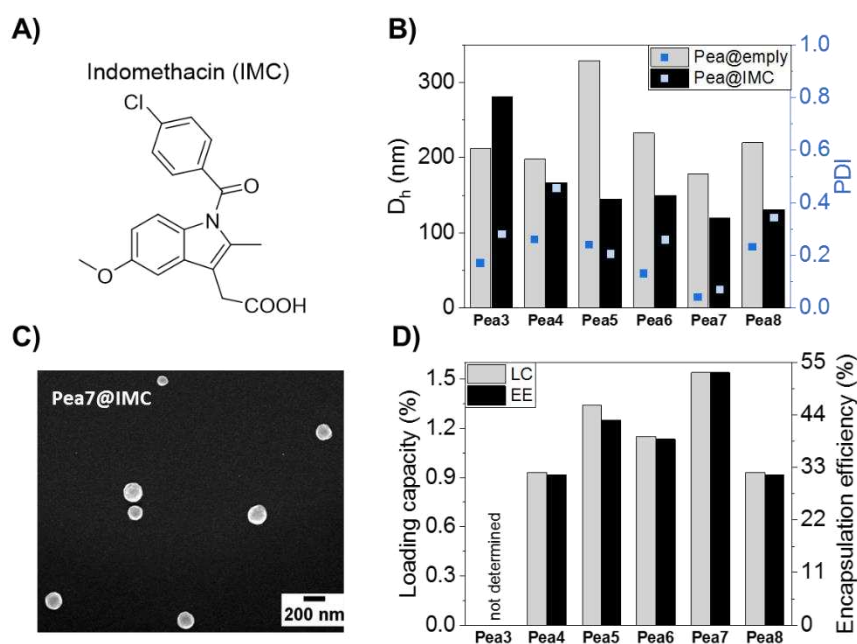


Figure 5.1: **A)** Schematic representation of the drug indomethacin. **B)** Hydrodynamic diameters (D_h) and PDI values determined by dynamic light scattering (DLS) of unloaded poly(ester amide) particles (Pea@empty) and indomethacin loaded particles (Pea@IMC). **C)** Scanning electron microscopy (SEM) image of indomethacin loaded **Pea7** nanoparticles (**Pea7@IMC**). **D)** Loading capacity (LC) and encapsulation efficiency (EE) of Pea@IMC nanoparticles.

Due to the similar formulation behavior with and without drug the question arose if the drug EE was influenced by the nanoparticle stability or the Pea–IMC thermodynamic compatibility. In the following, the formulation effects such as kinetic entrapment were eliminated and only the compatibility of the bulk materials was investigated, *i.e.*, IMC and polymers **Pea3** to **Pea8**. Different methods are known for the determination of solubility or interaction parameters of varying accuracy and experimental complexity.^[121-122] However, many approaches suffer from insufficient consideration of specific, directional interactions such as hydrogen bonding. Therefore, two reinforcing methods based on differential scanning calorimetry (DSC) were chosen due to their experimental accessibility and manifold informational output for the real polymer–drug pairs: 1) Saturation miscibility *via* the melting enthalpy method^[123] and 2) Flory–Huggins interaction parameter from melting point depression.^[124] The sample preparation included hand–milling of polymer–IMC mixtures of the desired mass fractions, annealing of the blends at 111 °C for 24 hours and the subsequent DSC measurement. **Pea8** exhibited a melting event at 132.4 °C upon annealing and was hence excluded from further investigation to avoid the overlapping of melting events of polymer and IMC. The semi–crystalline **Pea3** was not further investigated due to the same reason.

For the other polymers, **Pea4** to **Pea7**, the melting enthalpy of the crystalline IMC was measured depending on its mass fraction within the Pea[IMC] blend (**Figure 5.2, A**). The dissolved amount of the IMC in the polymer matrix did not contribute to the melting endotherm and, hence, could be determined by extrapolation of the enthalpy values to zero enthalpy. At 111 °C, the experimental saturation values increased from 7 to 18 wt% for **Pea4** to **Pea7** thereby indicating an increasing trend for the core materials compatibility with the drug (**Figure 5.2, B**).^[123]

Further, melting point depression of the crystalline IMC was evaluated depending on its mass fraction within the Pea[IMC] blend (**Figure 5.2, C**). In combination with other known blend and drug parameters, the depressed T_m values were used to calculate the respective Flory–Huggins (χ) interaction parameters of drug–polymer pairs.^[124]

On the basis of the Gibbs free energy change, the lattice–based Flory–Huggins theory is well–established for polymer–solvent interactions and was recently expanded to the drug–polymer miscibility.^[113] The threshold χ value for two components to be miscible is 0.5. Interaction parameters below this value indicate stronger heteromolecular interactions and, hence,

miscibility. Contrary, for $\chi > 0.5$ homomolecular interactions are preferred and the components are predicted to phase separate.

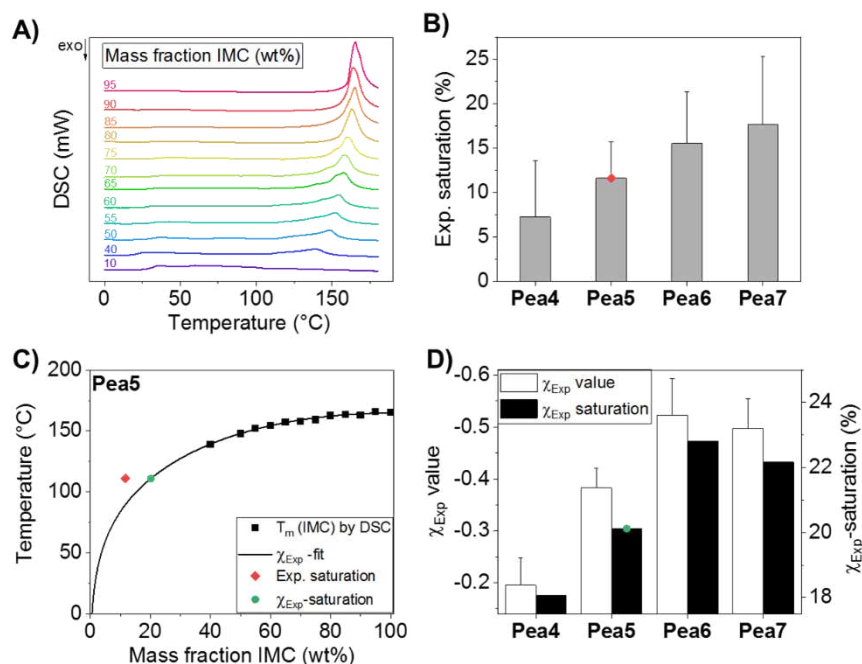


Figure 5.2: **A)** Differential scanning calorimetry (DSC) thermograms of **Pea5[IMC]** blends at different mass fractions. **B)** Experimental saturation values from zero enthalpy extrapolation for the polymer blends **Pea[IMC]**. **C)** Representative melting point depression curve of **Pea5[IMC]**: (Black square) measured melting temperatures by DSC, (solid line) predicted behavior of melting point depression for the experimentally determined χ_{Exp} parameter of -0.40 , (red diamond) experimentally determined saturation from zero enthalpy extrapolation from (B), (green circle) predicted saturation for χ_{Exp} interaction parameter of -0.40 and 111 °C. **F)** Flory–Huggins interaction parameters for **Pea[IMC]** and the predicted saturation values at 111 °C. All **Pea[IMC]** blends were annealed at 111 °C prior to the DSC analysis.

For all **Pea[IMC]** blends, favorable thermodynamic compatibility was determined with parameter values of $-0.20 > \chi_{Exp} > -0.52$ (**Figure 5.2, D**). With the known χ_{Exp} values, the melting point depression curve was completed (**C**, solid line) and the χ_{Exp} –saturation value was read out again for 111 °C. The trends for χ_{Exp} interaction parameters and χ_{Exp} –saturation values agreed as they were based on the same equation (**D**). More relevant, the saturation values from the 1) melting enthalpy method as well as the 2) melting point depression method exhibited a similar trend. Only for **Pea6[IMC]** higher compatibility by the second method was determined. In general, the saturation increased with polymer substituent size and bulkiness. The method–to–method differences decreased from 11% for **Pea4[IMC]** to 5% for **Pea7[IMC]**. The

deviation can be reasoned by blend preparation difficulties of polymers exhibiting T_g values partially close to room temperature.

The comparison of Pea@IMC encapsulation studies (**Figure 5.1**) with the Pea[IMC] blend studies (**Figure 5.2**) revealed different behavior for **Pea6** with IMC: **Pea6@IMC** encapsulated less drug than **Pea5@IMC**, but simultaneously, **Pea6[IMC]** exhibited better compatibility in bulk compared to **Pea5[IMC]**. This indicates a pronounced effect of the formulation ability on the EE of the drug. However, both compatibility and nanoparticle formation ability contribute to the encapsulation efficiency as seen for **Pea7@IMC**.

Combination of experimental compatibility studies with *in silico* simulations can create a feedback loop and reduce the cumbersome trial-and-error design of optimized nanocarrier systems.^[114] Atomistic molecular dynamics (MD) simulations represent a powerful tool for that purpose.^[115] However, due to the complexity of nanoparticle dispersions, their simulation is not feasible. Therefore, MD simulations of the two core components were performed for the worst and best polymer-drug pairs: **Pea4** as well as **Pea7** in combination with IMC. The Flory-Huggins interaction parameters were extracted from simulations. The obtained χ_{Sim} values were in great agreement with the DSC study (**Pea4 and IMC**: $\chi_{\text{Exp}} = -0.20$ vs $\chi_{\text{Sim}} = 0.15$; **Pea7 and IMC**: $\chi_{\text{Exp}} = -0.50$ vs $\chi_{\text{Sim}} = -0.46$). Further insights revealed specific interactions between the polymers and IMC through hydrogen bonding, while their number rationalized the difference in the compatibility values (**Figure 5.3**).

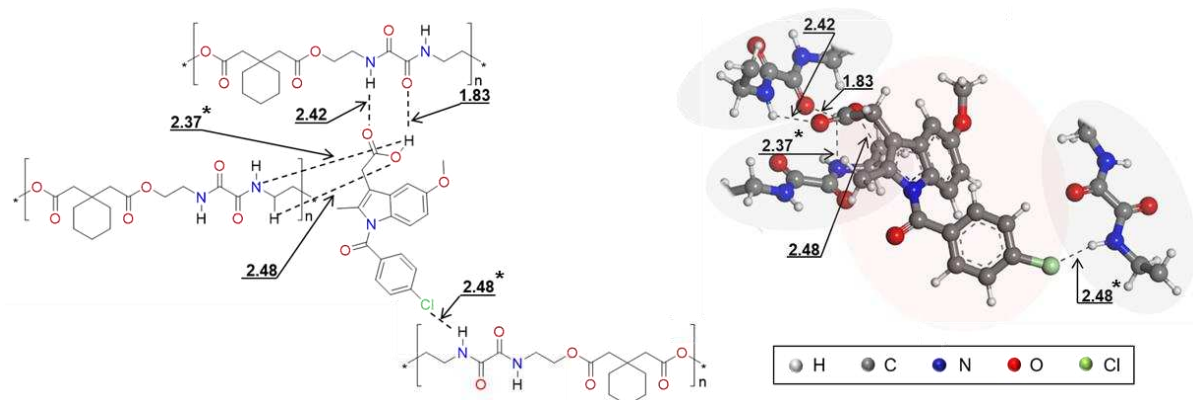


Figure 5.3: Snapshots of molecular dynamics (MD) simulation trajectories showing examples of hydrogen bonds between indomethacin and **Pea7**. **Left:** Chemical structure representation. **Right:** Ball-and-stick representation. Bonds marked with an asterisk (*) were not found in the **Pea4+IMC** combination.

In summary, the semi-crystalline polymers with short linear alkyl spacers (**Pea1**, **Pea2**) were not suitable for the preparation of nanoparticles. Semi-crystalline polymers with increased length of the alkyl spacer (**Pea3**) or introduced phenyl substituent (**Pea8**) were formulated into nanoparticles, however, with rather insufficient suspension and encapsulation performance. In contrast, the substituted and amorphous **Pea4** to **Pea7** were forming nanoparticles of desired quality and were able to encapsulate the hydrophobic cargo IMC (100 to 400 nm) with a pronounced influence of polymer density. Excluding formulation effects, the thermal properties of these four polymers also allowed the investigation of their bulk compatibility with the drug by DSC. Between 7 to 18 wt% of the drug were soluble within the respective polymer matrix while the favorable thermodynamic compatibility was indicated by the Flory-Huggins (χ_{Exp}) interaction parameters of -0.20 to -0.52 . The different compatibilities were rationalized by *in silico* studies revealing different hydrogen bonding in the binary drug-polymer mixtures. Cross comparison of all sequences of the study showed that both compatibility and nanoparticle formation ability contributed to the encapsulation efficiency.

These core materials were represented hydrophobic linear homopolymers such as, polyesters and PEAs. Under partial stabilization by PVA, the formulation of nanosized particles was performed by nanoprecipitation. In the following *Chapter 6*, amphiphilic graft copolymers composed of the hydrophobic pharmapolymer poly(methyl methacrylate) and short hydrophilic poly(2-ethyl-2-oxazoline) chains are discussed. Capable of encapsulation by self-assembly, the influence of small polymer modifications on their behavior *in vivo* is discussed.

6 PMMA–graft–OEtOx: Backbone end group effect on liver cell–type specificity

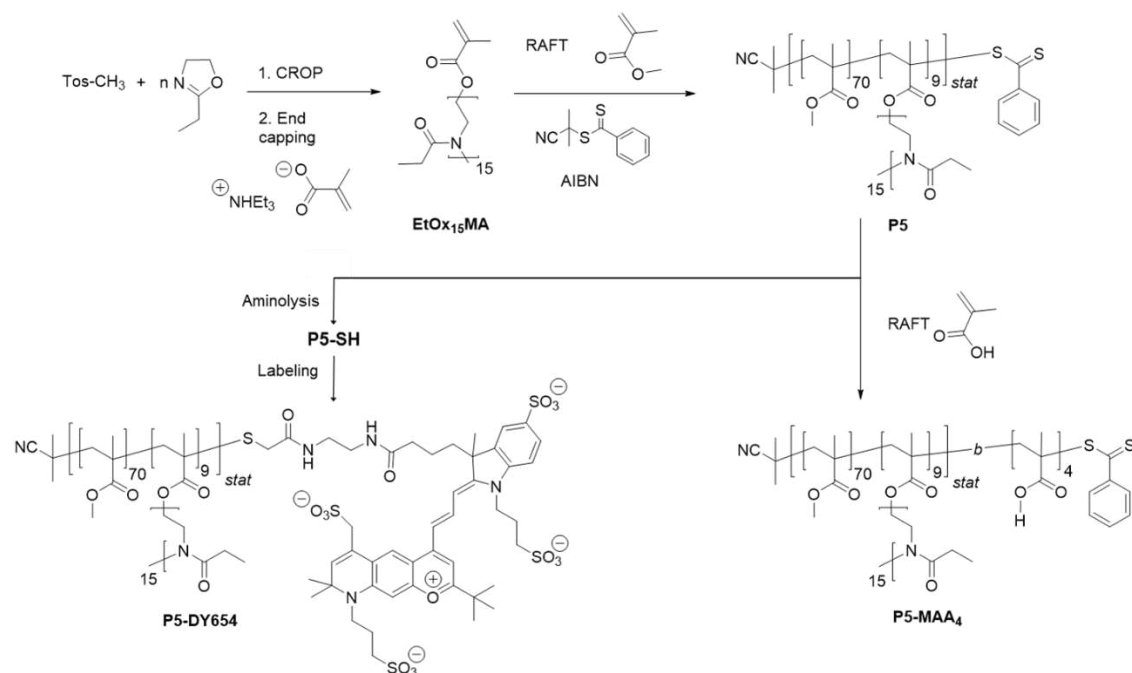
Parts of this chapter are published: **P6** I. Muljajew, S. Huschke, A. Ramoji, Z. Cseresnyés, S. Hoepfner, I. Nischang, W. Foo, J. Popp, M. T. Figge, C. Weber, M. Bauer, U. S. Schubert, A. T. Press, *ACS Nano* **2021**, *15*, 12298–12313.

In the *Chapters 3 to 5*, core materials from hydrophobic polyesters and poly(ester amide)s were introduced and main chain aspects discussed in detail. Among others, *Chapter 2* introduced strategies for the synthesis of amphiphilic block copolymers mainly *via* the macroinitiator approach. The hydrophilic, hydroxy–terminated poly(ethylene glycol) (PEG) was frequently utilized to initiate the ring opening polymerization (ROP) of a variety of hydrophobic, cyclic monomers. These linear block copolymers can then be formulated into, *e.g.*, core–shell nanoparticles or polymeric micelles (**Figure 1.1**) and utilized as drug delivery systems.^[125] Besides the manifold academic research efforts, this principle was already successfully translated into the market, *e.g.*, for Genexol®PM consisting of PEG–*block*–polylactide micelles loaded with the anticancer drug paclitaxel (20 to 50 nm size) approved in 2007 in South Korea.^[126]

The appeal of amphiphilic di– or also triblock copolymers is related to the established correlation between polymer and resulting aggregate properties.^[125] Concurrently, the variation of the assembled structure is limited, hence, making branched structures interesting alternatives to potentially overcome issues such as dissociation.^[127] Utilized as surfactants or nanoparticle materials, graft copolymers based on PEG and polyester revealed reduced protein adsorption compared to their linear analogues.^[128–129]

The reduced recognition by the organism and its reticuloendothelial system (RES) is highly desired for drug delivery vehicles as unspecific side effects can be decreased as well as the necessary amount of the applied drug loaded polymer.^[130] This so–called stealth effect can be achieved by a hydrophilic, polymeric shell, *e.g.*, based on the U. S. Food and Drug Administration (FDA) approved, clinical standard PEG.^[9] However, the manifold use of PEG not only as a pharmapolymer but also in daily cosmetic products caused long–term exposure resulting in the occurrence of PEG antibodies in up to 72% of tested participants.^[131–133] In consequence, PEG is recognized by the immune system reducing the drug carrier effectiveness

and causing in mild or severe side effects.^[133] Therefore, alternative stealth polymers are urgently needed.^[134]



Scheme 6.1: Schematic representation of the synthesis route toward the PMMA-*graft*-OEtOx₁₅ graft copolymers **P5**, **P5-SH**, **P5-DY654**, and **P5-MAA₄**. CROP: Cationic ring opening polymerization. RAFT: Reversible addition-fragmentation chain transfer polymerization. AIBN: 2,2'-Azobis(2-methylpropionitrile).

Poly(2-ethyl-2-oxazoline) (PEtOx) is a promising stealth polymer alternative.^[135] In fact, it is under investigation as a polymer-drug conjugate against early-stage Parkinson's disease in Phase II clinical trials.^[136] PEtOx can be used in different ways to serve in drug delivery systems (**Figure 1.1**).^[135, 137] PEtOx or its oligomer (OEtOx) can be introduced as hydrophilic side-chains to a hydrophobic backbone, thereby generating amphiphilic graft copolymers.^[138] These systems were capable of self-assembly to form core-shell micelles and the encapsulation of hydrophobic cargos.^[139] Beyond its use as plastic glass, the hydrophobic poly(methyl methacrylate) (PMMA) is a widely used pharmapolymer exhibiting excellent biocompatibility.^[9, 140] As a copolymer it is frequently applied in oral dosage coatings. Consequently, the poly(methyl methacrylate)-*graft*-oligo(2-ethyl-2-oxazoline) (PMMA-*graft*-OEtOx) holds great potential as a drug delivery system. A synthetic preliminary study by Muljajew *et al.* demonstrated the flexible design of these graft copolymers, investigating

the influence of grafting degree and side-chain length on the conformation in aqueous solution.^[139] Dominated by the solution behavior of PEtOx, PMMA-*graft*-OEtOx with side-chain lengths of 15 or 24 units exhibited cloud point temperature (T_{cp}) values of 60 to 70 °C rendering them thermally stable in biological studies.^[141-142]

For graft copolymers, additional functional moieties can be introduced as side-chain or backbone end groups.^[143] The latter modification was performed on PMMA-*graft*-OEtOx to understand its influence on *in vitro* and *in vivo* results of the loaded nanocarriers. As the preliminary study indicated its potential as nanocarrier, the graft copolymer **P5** was chosen. All modifications were performed from the same material batch (**Scheme 6.1**). The **P5** polymer was synthesized by the macromonomer approach. First, the hydrophilic OEtOx was synthesized by cationic ROP (CROP). The living character of the polymerization enabled defined adjustment of the degree of polymerization (DP) and further quantitative end-capping introducing a polymerizable methacrylate unit, yielding the macromonomer **EtOx₁₅MA**. This macromonomer was subsequently copolymerized with methyl methacrylate (MMA) by means of reversible addition-fragmentation chain transfer polymerization (RAFT) to yield PMMA-*graft*-OEtOx₁₅, thereby ensuring a similar hydrophilic layer thickness for all subsequently modified polymers. SEC analysis of the statistical copolymer indicated a molar mass of 22,900 g mol⁻¹ and a \bar{D} of 1.10 (**Table 6.1**). ¹H NMR spectroscopy revealed a DP of 70 for MMA and a DP of 9 for the macromonomer, translating to 90 mol% and 10 mol%, respectively.

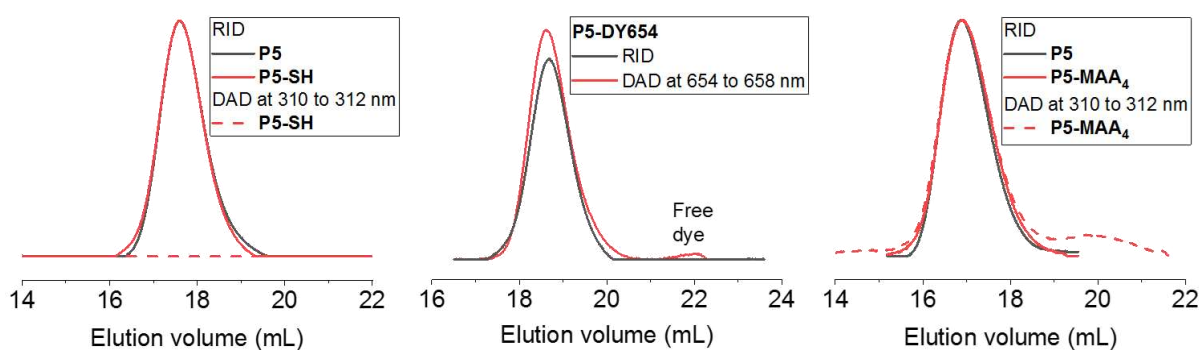


Figure 6.1: SEC elugrams (DMAc, 0.21 wt.% LiCl). **Left:** Overlay of **P5** and **P5-SH** with refractive index (RI) and diode array (DA) detection at 310 to 312 nm. **Middle:** **P5-DY654** overlay of RI and DA detection at 654 to 658 nm. **Right:** Overlay of **P5** and **P5-MAA₄** with RI and DA detection at 310 to 312 nm.

In the following, end group modifications were performed to critically challenge standard labeling protocols. In the first approach, the dithiobenzoate moiety resulting from the chain transfer group (CTA) used during RAFT polymerization was removed quantitatively by aminolysis with hexylamine. The cleavage was validated by SEC with diode array detector (DAD) at the wavelength corresponding to the CTA group. The absence of a polymer signal indicated the presence of a thiol backbone end group in the respective **P5-SH** (**Figure 6.1**).

Table 6.1: Key properties of the PMMA-*graft*-OEtOx₁₅ based polymers and micelles.

Polymer	M _n (g mol ⁻¹) ^a	Đ ^a	D _h empty micelle ^b (nm)	D _h NLO loaded micelle ^b (nm)	Zeta potential (mV) ^c
P5	22,900	1.10	Number av.: 12 Volume av.: 18 Intensity av.: 26	Number av.: 11 Volume av.: 16 Intensity av.: 61	-27
P5-MAA₄	22,100	1.15	Number av.: 7 Volume av.: 9 Intensity av.: 20	Number av.: 9 Volume av.: 12 Intensity av.: 50	-33
P5-DY654	22,700	1.11	Number av.: 9 Volume av.: 11 Intensity av.: 13	Number av.: 11 Volume av.: 12 Intensity av.: 21	n.d.
P5-SH	22,700	1.11	Number av.: 11 Volume av.: 13 Intensity av.: 20	Number av.: 11 Volume av.: 15 Intensity av.: 44	-20
P5+P5-MAA₄ ^d	–	–	Number av.: 12 Volume av.: 16 Intensity av.: 25	Number av.: 10 Volume av.: 12 Intensity av.: 24	-20

^a Determined by SEC (DMAc, 0.21 wt% LiCl, RI detection, PMMA calibration). ^b Determined by dynamic light scattering (DLS). Concentration of polymer $c \approx 1$ mg mL⁻¹ in aqueous solution at 25 °C, filtered samples with 0.45 μm pore nylon membrane. Loaded micelles contained in average ten Neutral Lipid Orange (NLO) molecules per micelle. ^c Concentration of polymer $c = 5$ mg mL⁻¹ in 0.1 mmol L⁻¹ NaCl aqueous solution at 25 °C, filtered samples with 0.45 μm pore nylon membrane. ^d **P5+P5-MAA₄** represents mixed micelles composed of 1% **P5-MAA₄** and 99% of **P5**. n.d.: not detectable

The **P5-SH** was subsequently labeled with the hydrophilic dye DY-654 by nucleophilic substitution at the thiol group using an iodoacetamide derivative. The attachment was validated again by SEC with DAD at the maximum absorption wavelength of the DY-654 (**Figure 6.1**).

The obtained **P5-DY654** revealed a labeling efficiency of 1%, *i.e.*, 99% of polymer chains in the “**P5-DY654** batch” represented the starting material **P5-SH**.

The second modification approach for the introduction of anionic moieties was based on the utilization of the CTA group at **P5**. It was applied as a macro-CTA in combination with methacrylic acid (MAA) under RAFT polymerization conditions. A short block of four MAA repeating units was introduced at the end of the graft copolymer backbone yielding **P5-MAA₄**. The number of MAA repeating units was validated by conversion calculations from ¹H NMR spectroscopy as well as by acid–base titration. Further, the SEC analysis of **P5-MAA₄** with simultaneous DAD at the wavelength of the CTA group revealed its partial presence in agreement with the polymerization mechanism (**Figure 6.1**).

The synthetic motivation for **P5-MAA₄** was to mimic the four sulfonate groups of the DY-654 of **P5-DY654** at the same polymer position. However, as the dye labeling efficiency was only 1%, also the quantitative aspect had to be considered. This was approached by mixing polymeric materials: 99% of **P5** combined with 1% **P5-MAA₄** yielded the mixed micelle **P5+P5-MAA₄** with the same net anionic charge as **P5-DY654**.

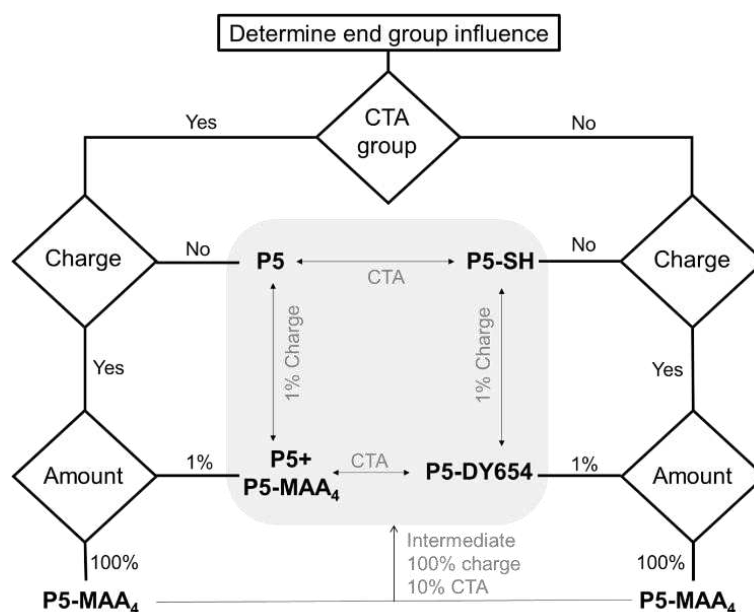


Figure 6.2: Decision tree for the influence determination of the backbone end group of the modified graft copolymers based on PMMA-*graft*-OEtOx₁₅.

Based on these micelles, two end group effects could be deduced independent from each other: Influence of the hydrophobic CTA group was apparent from the comparison of **P5** vs **P5-SH**

as well as **P5+P5–MAA₄** vs **P5–DY654**. Influence of the 1% charged end group was apparent from the comparison of **P5+P5–MAA₄** vs **P5** as well as **P5–DY654** vs **P5–SH** (Figure 6.2).

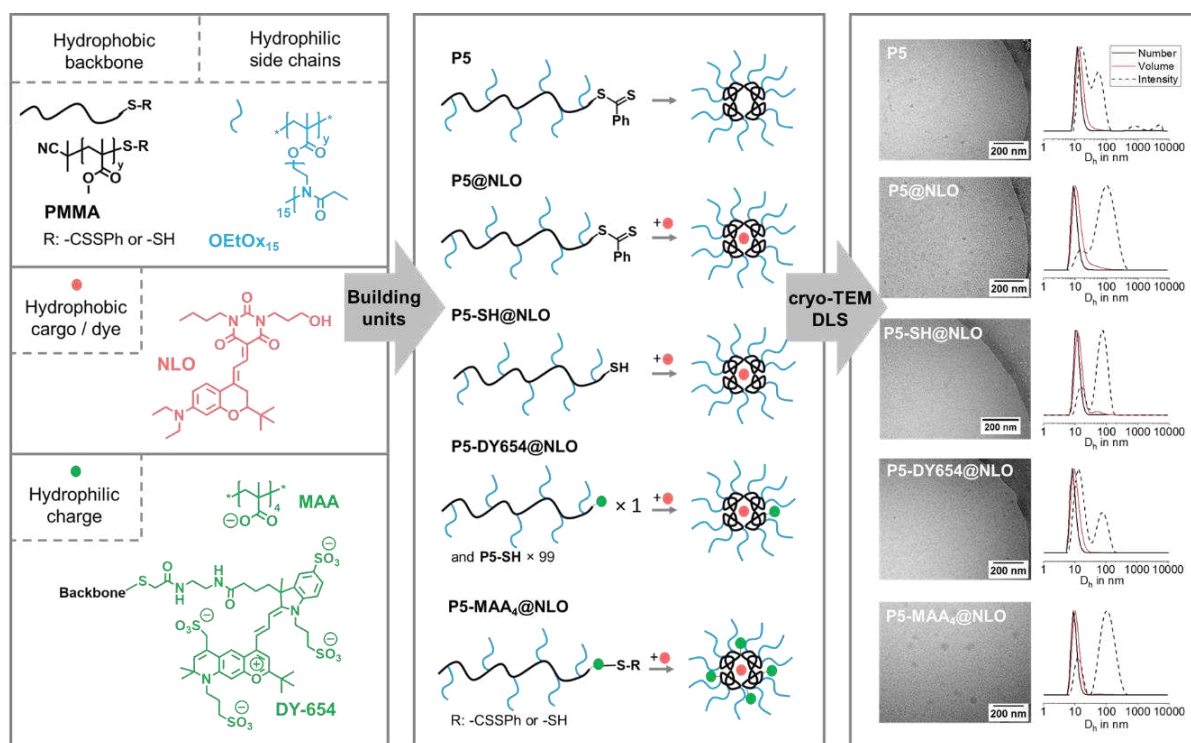


Figure 6.3: **Left:** Schematic representation of different building units used to form micelles with different moieties situated between core and shell. PMMA: Poly(methyl methacrylate). OEtOx: Oligo(2-ethyl-2-oxazoline). NLO: Neutral Lipid Orange. MAA: Methacrylic acid. **Middle:** Simplified schematic overview of the polymer structures and the proposed micelles formed in aqueous solutions. **Right:** Analysis of **P5** micelles and other dye loaded micelles in aqueous solution: Cryo-TEM (c (polymer) = 10 mg mL⁻¹). DLS plots of the respective size distributions (c (polymer) = 1 mg mL⁻¹).

All **P5**-based polymers self-assembled into spherical micelles of roughly 10 nm diameter in water upon direct dissolution as determined by dynamic light scattering (DLS) and cryo-transmission electron microscopy (cryo-TEM) (Table 6.1, Figure 6.3). Previous studies by the absolute method analytical ultracentrifugation revealed an aggregation number of roughly ten polymer chains per micelle for **P5**.^[139] The similarity in the hydrodynamic analysis and chemical structure indicated a similar aggregation number for the other graft copolymers. The amphiphilic architecture enabled the solubilization of the hydrophobic dye Neutral Lipid Orange (NLO) that served as a label in the following biological studies. The amphiphilic nature of the graft copolymers allowed a different encapsulation procedure compared to the solely

hydrophobic materials described in *Chapters 3 to 5* utilizing the thin film method, the dried polymer-cargo blend was simply redissolved in water and the excess of the unencapsulated, hydrophobic NLO was removed by centrifugation. The highest dye uptake was determined for **P5@NLO** with an encapsulation efficiency (EE) of 49% and a loading capacity (LC) of 5.6%. To enable feasible assessment by Raman spectroscopy (*vide infra*) the polymer to dye molar ratio was set to 1:1 yielding a micelle formed from ten polymer chains with ten encapsulated NLO molecules.

The sizes of loaded micelles were in great agreement with the ones of the unloaded micelles as determined by DLS (number and volume distribution) and cryo-TEM (**Figure 6.3**). Solely, the intensity based distribution by DLS indicated a larger hydrodynamic diameter due to its strong sensitivity towards the few, subordinate, slightly larger aggregates. The integrity of the **P5@NLO** micellar structure upon dilution was verified through analytical ultracentrifugation. The *in vivo* blood concentration in animal experiments was expected to be of 103 $\mu\text{g mL}^{-1}$. The structural integrity was validated at concentrations even below 40 $\mu\text{g mL}^{-1}$. In this light, the variation of the backbone end group of the PMMA-*graft*-OEtOx did not influence the micellization in an apparent manner.

Known as a powerful tool for the investigation of molecular bonds and molecules symmetry, Raman spectroscopy was applied to analyze the end group influence on the micelle conformation.^[144] Indeed, changes in the vibrational fingerprint region of the Raman spectra of **P5@NLO**, **P5-MAA4@NLO**, **P5-SH@NLO**, and **P5-DY654@NLO** in aqueous solution were observed. The spectra facilitated their differentiation by the principal component analysis (PCA) yielding well-separated clusters in a 3D score plot. Conclusively, Raman spectroscopy provided experimental evidence of different molecular arrangements within the micelles due to the different end groups, altering the environment of the NLO dye within the carriers.

Primary mouse embryonic fibroblasts (MEFs)^[145-146] were used in *in vitro* studies for the loaded micelles and experiments revealed nontoxic properties for all micelles after 24 hours. Further, different cell culture studies were applied to determine the possible uptake mechanism. Appropriate test procedures were performed applying sodium azide (ATPase inhibitor), Pitstop-2 (inhibitor for clathrin-mediated endocytosis),^[147-148] or MEFs expressing early endosome antigen (a marker for clathrin-mediated endocytosis) as well as cell uptake experiments at 4 °C. The obtained results suggested direct translocation through the cell

membrane, *e.g.*, by penetration, without a rate limitation by active, energy-dependent endocytosis.^[149]

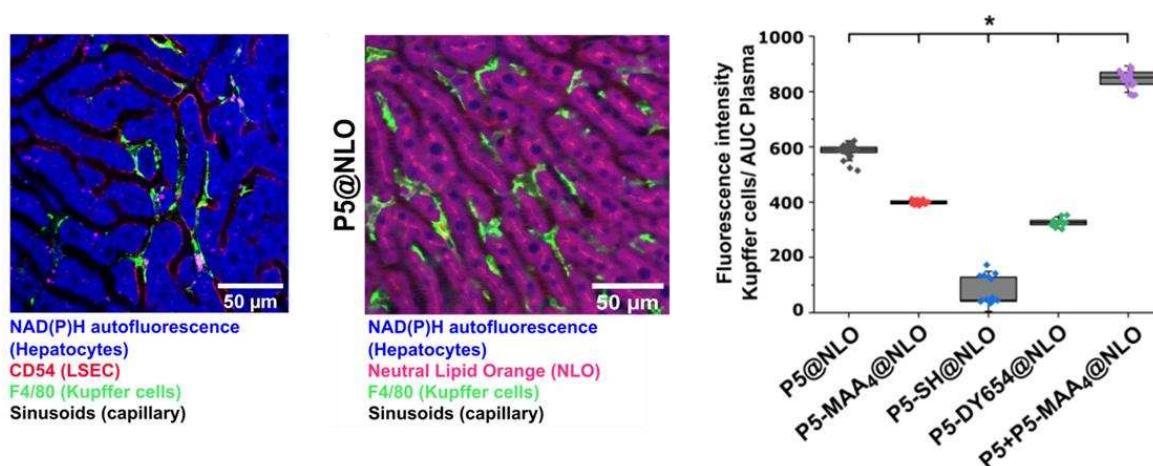


Figure 6.4: Intravital microscopy results of murine liver after 45 min. **Left:** (Co)localization of sinusoids (black) and liver cells commonly contributing to nanocarrier clearance: Hepatocytes were identified by their high NADPH autofluorescence (blue). LSECs stained with anti-CD54 APC (red) and Kupffer cells with anti-F4/80 FITC (green). **Middle:** Exemplary image after injection of **P5@NLO** micelle: Hepatocytes were identified by their high NADPH autofluorescence. Kupffer cells were counterstained with an F4/80-FITC (green) antibody, injected at the end of the experiment. **Right:** End group modifications of graft copolymer micelles influenced uptake in the liver cells, exemplary shown for Kupffer cells.

Differences in cell uptake of the loaded micelles were already observed in cell culture studies. However, the distinct extent of the polymer end group influence was determined in the much more complex *in vivo* systems. As a significant clearance organ, the mouse liver was investigated *via* intravital microscopy to study the pharmacokinetics of the loaded micelles.^[150] The nanocarrier uptake and clearance was determined in hepatocytes, and different RES cells, *e.g.*, circulating immune cells (lymphocytes), Kupffer cells (livers' local macrophages), and liver sinusoidal endothelial cells (LSECs, livers' specialized endothelial cells) (**Figure 6.4**).^[151-158] After the application of the NLO loaded micelles, automated image processing of NLO-stained cells enabled the identification of the cell morphologies and the overall cargo distribution in the mouse liver tissue. Noteworthy, the accumulation of NLO in different cells was normalized to the total amount of NLO passing through the liver large veins. No NLO-stained circulating immune cells (lymphocytes) were identified indicating its subordinate role. For hepatocytes, Kupffer cells and LSECs uptake differences were observed for the loaded

micelles. In relation to **Figure 6.2**, the following conclusions could be made: An increase in cell uptake for hepatocytes and Kupffer cells was seen for 1) the presence of the CTA group **P5+P5-MAA4@NLO** > **P5-DY654@NLO** as well as **P5@NLO** > **P5-SH@NLO** and 2) the presence of 1% of charge **P5+P5-MAA4@NLO** > **P5@NLO** as well as **P5-DY654@NLO** > **P5-SH@NLO**. For LSECs only the uptake of MAA-containing micelles was observed *i.e.* **P5+P5-MAA4@NLO** and **P5-MAA4@NLO**. The intermediate features of **P5-MAA4@NLO** were also indicated in their cell uptake, mostly in between the charge and the end group influence. The different liver cell-type distributions can be the result of direct and indirect effects, such as different interactions of the micelles with cell surfaces and surface factors such as sugars or, *e.g.*, organic anion receptors, or changes in the quality and quantity of adsorbed proteins.^[159-162]

In summary, PMMA-*graft*-OEtOx ($M_n \approx 20 \text{ kg mol}^{-1}$) were modified at their backbone end group with minor implemented changes similar to common labeling procedures, *e.g.*, introduction of (charged) modular units of low molar mass. The amphiphilic nature of the graft copolymers facilitated the formation of core-shell micelles of 10 nm diameter as determined by DLS and cryo-TEM. The synthetically modified moieties are expected to be situated between core and shell for the charged groups or to be located within the hydrophobic core for the hydrophobic moieties. As an alternative to PEG, the OEtOx₁₅ shell formed by short chains introduced stealth properties as well as potentially stabilized the hydrophobic PMMA core by hydrophilic as well as steric shielding. The self-assembled micelles in water enabled encapsulation of the hydrophobic dye NLO into the core that subsequently acted as a fluorescent probe for *in vitro* and *in vivo* investigation. The minor changes at the backbone end group influenced the intravital microscopy results: An efficient stealth effect was observed for micelles formed from polymers with anionically charged or thiol end groups. In contrast, a hydrophobic end group altered the micellar structure sufficiently to adapt cell-type specificity and stealth properties in the liver.

7 Summary

The drug discovery trend indicates the development of larger, hydrophobic active pharmaceutical ingredients (APIs).^[10] Predictions are reported with more than 50% of the new APIs to exhibit poor water solubility.^[11] This undoubtedly gives rise to difficulties for the preferred form of drug application that is oral dosage form, *i.e.* tablet application, and overall leads to poor bioavailability and delivery efficiency. Therefore, drug delivery systems for the encapsulation of hydrophobic cargo such as nanoparticles or micelles are urgently needed. In this light, synthetic polymers hold great promise to generate potent vehicles due to their adjustable properties and high reproducibility.

To fulfill the personalized requirements for the cargo at hand, the nanocarrier can be engineered in many parameters. Examples include core and shell materials, presence of labels or targeting units, degradability or compatibility with an API. However, the change of one parameter can trigger a causal chain and influence other properties of the drug delivery vehicle. Therefore, changes should be performed with great care and the structure property relationships should be well understood.

In this light, the thesis highlighted polymer scaffolds that exhibit promising attributes for their formulation as nanoparticles or polymeric micelles. In addition, these materials were investigated in relation to their application and structure property relationships were assessed. Polyesters are often used as degradable materials for biomedical applications. Representing interesting alternatives, poly(ester amide)s, polyphosphoesters and polyacetals experienced a scientific boost over the last ten years.

7 Summary

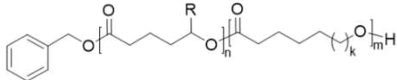

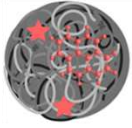
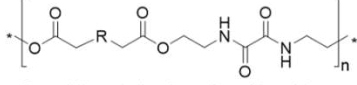
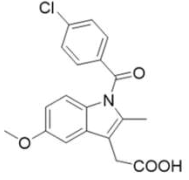

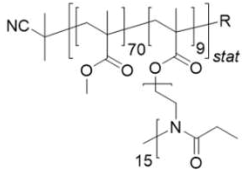
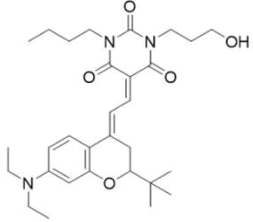
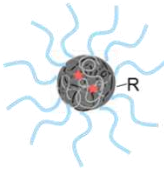
Polymeric core	Hydrophobic cargo	Nanocarrier	Structure property investigation
Polyester  R ... H, CH ₃ , C ₅ H ₁₁	Pyrene, solvatochromic dye 	Nanoparticle (50 to 230 nm) 	Chapter 3 Polymers with different composition and microstructure and its influence on HHB and stability.
Poly(ester amide)  R ... different dicarboxylic acid residues in combination with poly(vinyl alcohol)	Indomethacin, antiinflammatory drug 	Nanoparticle (100 to 400 nm) 	Chapters 4 & 5 Variation of polymer residues (R) and their influence on nanocarrier formulation ability as well as compatibility with indomethacin.
PolyMMA-graft-oligoEtOx  R ... -CSSPh, -SH, -DY654, or -MAA ₄	Neutral Lipid Orange, NIR dye 	Polymeric micelle (≈ 10 nm) 	Chapter 6 Variation of graft copolymer backbone end group (-R) and its influence on the distribution in liver cells.

Figure 7.1: Tabular overview of the schematic representations of the carrier materials investigated in combination with the respective hydrophobic cargo to yield the different nanocarrier systems (Figure partially created with BioRender.com).

Despite the progress on the three polymer classes, for established systems such as polyesters scientific blind spots still exist. In this regard, the question on how the physico-chemical properties influence the drug delivery performance was addressed. The HHB was eliminated as a 3rd variable in two studies covering polyesters with the same overall amount of methylene groups as poly(ϵ -caprolactone) but a different microstructure (**Figure 7.1**). The first study determined excellent long-term stability for nanoparticles from poly(ϵ -caprolactone), poly[(δ -valerolactone)-*grad*-(ϵ -caprolactone)] and poly(δ -valerolactone)-*block*-poly(ϵ -caprolactone). Moreover, these three polymers were formulated into particles of constant $D_h \approx 170$ nm thereby enabling unambiguous correlation of nanoparticle stiffness with bulk polymer crystallinity. The second study validated the constant HHB through encapsulation of the solvatochromic dye pyrene into nanoparticles from the polyesters poly(ϵ -caprolactone), poly(δ -caprolactone) as well as poly[(δ -caprolactone)-*ran*-(ϵ -caprolactone)]. These two sets of nanoparticles form an excellent foundation for the investigation on how

nanoparticle stiffness or thermal properties influence cell uptake, enzymatic degradation or API release.

Despite the great attention to material design, ultimately the interactions of the core components, *i.e.* drug and polymer, will play a decisive role in the development of drug delivery vehicles. The polymeric scaffold of poly(ester amide)s can induce hydrogen bonding with the API and, thereby, stabilize the formulation. The investigation of drug–carrier–interactions benefits from screening approaches and cross comparison of different methods. Therefore, gram amounts of poly(ester amide)s were synthesized by the AA+BB polyaddition of commercially available dicarboxylic acids and 2,2'-bis(2-oxazoline) (**Figure 7.1**). A library of eight polymers with different linker length and substituents was generated and the structures validated by a variety of analytical methods. Semi-crystalline, unsubstituted **Pea1** to **Pea3** and amorphous, substituted **Pea4** to **Pea8** were obtained with variable hydrophobicity as well as solubility. The suppression of crystallinity was decisive as only the amorphous poly(ester amide)s formed nanoparticles of desired qualities, determined by means of an extensive formulation screening. A pronounced influence of the polymer density was observed. In contrast, the HHB exhibited a negligible effect. The polymers performing well in the formulation screening were also able to encapsulate the hydrophobic drug indomethacin with loaded nanoparticles of 100 to 400 nm. To illuminate the critical influence, the formulation effects were excluded and bulk compatibility of the poly(ester amide)s with indomethacin was investigated by thermal analysis. Miscibility with up to 18 wt% of drug within polymer matrix was determined and further favorable thermodynamic compatibility was indicated by the Flory–Huggins interaction parameter. The different compatibilities were rationalized by atomistic molecular dynamics simulations revealing different hydrogen bonding in the binary drug–polymer mixtures. Cross comparison of all sequences of the study showed that both compatibility and nanoparticle formation ability contributed to the encapsulation efficiency. The investigation of the biocompatibility of the synthesized poly(ester amide)s would further facilitate their evaluation as drug delivery systems. The proven hydrogen bonds can be exploited in the encapsulation of APIs that are difficult to formulate in the common polyester nanoparticles due to the lack of favorable carrier–API interactions. In fact, the **Pea5** and **Pea7** are currently investigated as encapsulation materials for the API favipiravir. As a guanin

analogon, favipiravir has low water solubility while structurally it can form hydrogen bonds as it exhibits an amide group, a hydroxy group and two aromatic nitrogen atoms.^[163]

The introduction of a hydrophilic shell covalently linked to the hydrophobic core can increase formulation stability, shielding of the cargo and further introduce stealth properties. This approach is often implemented for linear amphiphilic copolymers. However, the utilization of nanocarriers made from graft copolymers with a hydrophobic backbone and hydrophilic side-chains can further reduce protein adsorption. Therefore, this kind of amphiphilic graft copolymers was synthesized by the macromonomer approach through combination of cationic ring opening polymerization and controlled radical polymerization, *i.e.* reversible addition-fragmentation chain transfer polymerization. The obtained poly(methyl methacrylate)-*graft*-oligo(2-ethyl-2-oxazoline) (PMMA-*graft*-OEtOx₁₅, $M_n \approx 20 \text{ kg mol}^{-1}$) formed micelles of 10 nm size comprising a hydrophilic shell formed by a promising poly(ethylene glycol) (PEG) alternative. The backbone end group of the graft copolymer was synthetically modified through the introduction of (charged) modular units of low molar mass *i.e.* labeling with a hydrophilic dye, introduction of four methacrylic acid repeating units, or formation of a thiol end group. The self-assembly in water and encapsulation of the hydrophobic, fluorescent probe Neutral Lipid Orange (NLO) was not affected by those minor changes similar to common labeling protocols. However, strong differences were observed in the liver cell-type specificity as determined in *in vivo* experiments by means of intravital microscopy. An efficient stealth effect was found for micelles formed from polymers with anionically charged or thiol end groups. In contrast, a hydrophobic end group, present due to the polymerization mechanism, altered the micellar structure sufficiently to adapt cell-type specificity and stealth properties in the liver. In this regards, other biological studies that shed light on the different interactions that result in liver cell type specificity of these micelles would further benefit the understanding and, hence, the rational polymer design. Overall, also other backbone end groups could be introduced such as other dyes or other amounts / type of charge to further deepen the understanding of the influence range. However, all changes could influence the liver cell specificity and should therefore be performed with great care.

Concurrently, the potential of encapsulation and delivery of APIs by the PMMA-*graft*-OEtOx could be further explored, *e.g.*, to hepatocytes. The graft copolymer **P5-DY654**, labeled with a hydrophilic polymethine dye, represents a promising candidate for the respective purpose.

This carrier exhibits high uptake in hepatocytes but low uptake by the stationary macrophages, the Kupffer cells. Further, higher DY654 labeling efficiency would enable the tracking of both carrier and NLO (or appropriate cargo) independently, presumably providing interesting cargo release information as well as insights on the final fate of the polymer. From the synthetic point of view, it would be further interesting to vary the comonomer composition and, *e.g.*, use *n*-butyl methacrylate as the hydrophobic comonomer for the backbone generation. Thereby the overall hydrophobicity of the core would increase, hence, potentially increase its carrier ability. Nonetheless, the encapsulation efficiency of the PMMA-*graft*-OEtOx was already superior in comparison to values often achieved for common nanoparticles.^[119] In this regard, for the encapsulation by the poly(ester amide)s, the nanoprecipitation technique was used while for the polymeric micelles the NLO was encapsulated by direct dissolution, *i.e.* thin film method. In both cases the procedures were not optimized, therefore the comparison should be performed with a grain of salt. Nevertheless, demonstrating its potential, a loading capacity of $\approx 6\%$ for NLO within PMMA-*graft*-OEtOx is higher in comparison to the poly(ester amide)s nanoparticles loaded with indomethacin with a capacity of up to 1.5%.

Independent of the loading, the size of the nanocarriers varied from the nanoparticles ($D_h \approx 200$ nm) to the polymeric micelles ($D_h \approx 10$ nm). This can be used to the advantage for the respective, desired route of administration. The small polymeric micelles were proven to simply translocate through cell membrane while for the nanoparticles endocytosis is proposed as a possible uptake mechanism based on literature.^[88-90]

To conclude, the investigated nanocarriers based on polyesters, poly(ester amide)s and poly(2-oxazoline)s exhibit great potential as nanocarriers. Initially addressing different questions, future research will be directed towards the deepened exploration of the drug delivery application of all materials. For this purpose, synthetic progress with regards to the introduction of a hydrophilic shell and targeting units is of great importance.

Detailed characterization of the synthesized materials as well as thoughtful variation of parameters is the fundamental prerequisite for the possibility to draw correct conclusions on structure property relationships between the drug carrier and its performance.

8 Zusammenfassung

Der Trend in der Wirkstoffforschung führt zur Entwicklung größerer, hydrophober aktiver Wirkstoffe (AWS).^[10] Voraussagen zufolge werden mehr als 50% der neuen AWS eine schlechte Wasserlöslichkeit aufweisen.^[11] Dies führt zweifellos zu Schwierigkeiten in der bevorzugten Form der Arzneimitteleinnahme, welche die orale Dosierung bzw. Tablettenform ist, und führt insgesamt zu einer schlechten Bioverfügbarkeit und Transporteffizienz. Daher werden Wirkstofftransportsysteme zur Verkapselung der hydrophoben Beladung, wie Nanopartikel oder Mizellen, dringend benötigt. In diesem Zusammenhang sind synthetische Polymere aufgrund ihrer einstellbaren Eigenschaften und ihrer hohen Reproduzierbarkeit vielversprechend, um potente Träger zu erzeugen.

Um die personalisierten Anforderungen an die jeweilige Beladung zu erfüllen, können viele Parameter der Nanoträger angepasst werden. Beispiele hierfür sind Kern- und Schalenmaterialien, das Vorhandensein von Markern- oder Targeting-Einheiten, Abbaubarkeit oder Kompatibilität mit einem AWS. Die Änderung eines Parameters kann jedoch eine Kausalkette auslösen und andere Eigenschaften des Wirkstoffträgers beeinflussen. Daher sollten Änderungen mit großer Sorgfalt durchgeführt werden und die Struktur-Eigenschafts-Beziehungen sollten gut verstanden sein.

In diesem Zusammenhang, wurden in der Dissertation Polymere untersucht, die vielversprechende Eigenschaften für ihre Formulierung als Nanopartikel oder Polymermizellen aufweisen. Neben ihrer Synthese wurden diese Materialien hinsichtlich ihrer Anwendung untersucht und Struktur-Eigenschafts-Beziehungen bewertet. Polyester werden häufig als abbaubare Materialien für biomedizinische Anwendungen verwendet. Als interessante Alternativen haben Polyesteramide, Polyphosphoester und Polyacetale in den letzten zehn Jahren einen wissenschaftlichen Aufschwung erfahren.

8 Zusammenfassung

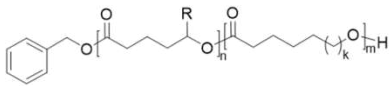
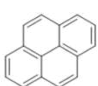
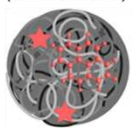
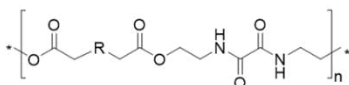
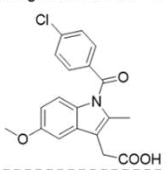

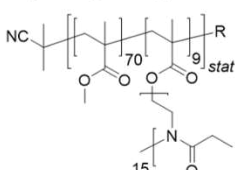
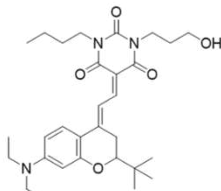
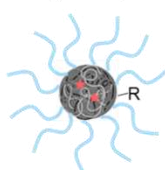
Polymerkern	Hydrophobe Beladung	Nanoträger	Struktur-Eigenschafts-Untersuchung
Polyester  R ... H, CH ₃ , C ₅ H ₁₁	Pyren, solvatochromer Farbstoff 	Nanopartikel (50 bis 230 nm) 	<i>Kapitel 3</i> Polymere mit unterschiedlicher Zusammensetzung und Mikrostruktur und ihr Einfluss auf HHB und Stabilität.
Polyesteramid  R ... verschiedene Dicarbonsäurereste in Kombination mit Polyvinylalkohol	Indometacin, entzündungshemmender Wirkstoff 	Nanopartikel (100 bis 400 nm) 	<i>Kapitel 4 & 5</i> Variation der Polymersubstitution (R) und deren Einfluss auf die Formulierungsfähigkeit von Nanoträgern sowie die Kompatibilität mit Indometacin.
PolyMMA-graft-oligoEtOx  R ... -CSSPh, -SH, -DY654, oder -MAA ₄	Neutral Lipid Orange, NIR-Farbstoff 	Polymermizelle (= 10 nm) 	<i>Kapitel 6</i> Variation der Rückgratendgruppe eines Pfropfcopolymers (-R) und ihr Einfluss auf die Verteilung in Leberzellen.

Abbildung 8.1: Tabellarische Übersicht der schematischen Darstellung der Trägermaterialien, die in Kombination mit der jeweiligen hydrophoben Beladung untersucht wurden, um die verschiedenen Nanoträgersysteme zu erhalten.

Trotz der Fortschritte bei den drei Polymerklassen gibt es bei etablierten Systemen wie den Polyestern, wissenschaftlich betrachtet, noch blinde Flecken. In diesem Zusammenhang wurde die Frage erforscht, wie die physikalisch-chemischen Eigenschaften die Wirkstofftransportleistung beeinflussen. Die HHB wurde als dritte Variable in zwei Studien eliminiert, da Polyester mit der gleichen Gesamtmenge an Methylengruppen wie Poly(ϵ -caprolacton), aber einer anderen Mikrostruktur untersucht wurden (**Abbildung 8.1**). In der ersten Studie wurde eine ausgezeichnete Langzeitstabilität von Nanopartikeln aus Poly(ϵ -caprolacton), Poly[(δ -valerolacton)-*grad*-(ϵ -caprolacton)] und Poly(δ -valerolacton)-*block*-poly(ϵ -caprolacton) festgestellt. Darüber hinaus wurden diese drei Polymere zu Partikeln mit einem konstantem $D_h \approx 170$ nm formuliert, wodurch eine eindeutige Korrelation zwischen der Steifigkeit der Nanopartikel und der Kristallinität der Polymere ermöglicht wurde. Die zweite Studie validierte die konstante HHB durch Einkapselung des solvatochromen Farbstoffs Pyren in Nanopartikel aus den Polyestern Poly(ϵ -caprolacton), Poly(δ -caprolacton) sowie Poly[(δ -caprolacton)-*ran*-(ϵ -caprolacton)]. Diese beiden

Nanopartikelreihen bilden eine hervorragende Grundlage für die Untersuchungen, wie die Steifigkeit oder die thermischen Eigenschaften von Nanopartikeln die Zellaufnahme, den enzymatischen Abbau oder die Wirkstofffreisetzung beeinflussen.

Trotz der großen Beachtung des Materialdesigns werden letztendlich die Wechselwirkungen der Kernkomponenten, d. h. Wirkstoff und Polymer, eine entscheidende Rolle bei der Entwicklung von Wirkstofftransportträgern spielen. Das Polyesteramidgerüst kann Wasserstoffbrückenbindungen mit dem AWS ausbilden und dadurch die Formulierung stabilisieren. Die Untersuchung von Wechselwirkungen zwischen Beladung und Träger profitiert von Screening-Ansätzen und dem Quervergleich verschiedener Methoden. Daher wurden Grammengen von Polyesteramiden durch die AA+BB-Polyaddition von kommerziell erhältlichen Dicarbonsäuren und 2,2'-Bis(2-oxazolin) synthetisiert (**Abbildung 8.1**). Eine Bibliothek von acht Polymeren mit unterschiedlichen Linkerlängen und Substituenten wurde erzeugt und deren Strukturen durch eine Vielzahl von analytischen Methoden validiert. Es wurden teilkristalline, unsubstituierte **Pea1** bis **Pea3** und amorphe, substituierte **Pea4** bis **Pea8** mit unterschiedlicher Hydrophobizität und Löslichkeit erhalten. Entscheidend war die Unterdrückung der Kristallinität, da nur die amorphen Polyesteramide Nanopartikel mit gewünschter Qualität formten. Dies wurde in einem umfangreichen Formulierungsscreening bestimmt. Es wurde ein ausgeprägter Einfluss der Polymerdichte beobachtet. Im Gegensatz dazu zeigte die HHB einen vernachlässigbaren Effekt. Die Polymere, welche im Formulierungsscreening gut abgeschnitten haben, waren auch in der Lage, den hydrophoben Wirkstoff Indometacin einzukapseln und beladene Nanopartikel von 100 bis 400 nm zu bilden. Um dies näher zu untersuchen, wurden Formulierungseffekte ausgeschlossen, indem die Bulk-Kompatibilität der Polyesteramide mit Indometacin durch thermische Analysen untersucht wurde. Eine Mischbarkeit mit bis zu 18 Gew.-% Wirkstoff innerhalb der Polymermatrix wurde bestimmt. Des Weiteren wurde eine günstige thermodynamische Kompatibilität durch den Flory-Huggins-Interaktionsparameter indiziert. Die unterschiedlichen Kompatibilitäten wurden durch atomistische Molekulardynamik-Simulationen erklärt, welche unterschiedliche Wasserstoffbrücken in den binären Wirkstoff-Polymer-Mischungen offenbarten. Der Quervergleich aller Studien zeigte, dass sowohl die Kompatibilität als auch die Fähigkeit zur Bildung von Nanopartikeln zur Einkapselungseffizienz beitragen. Eine Untersuchung der Biokompatibilität der

synthetisierten Polyesteramide würde ihre weitere Bewertung als Wirkstoffträger ermöglichen. Die nachgewiesenen Wasserstoffbrücken könnten bei der Verkapselung von AWS ausgenutzt werden, die aufgrund der fehlenden günstigen Träger–AWS–Wechselwirkungen in üblichen Polyester–Nanopartikeln schwierig zu formulieren sind. Tatsächlich werden deshalb **Pea5** und **Pea7** derzeit als Verkapselungsmaterialien für den Wirkstoff Favipiravir untersucht. Als Guanin–Analogon hat Favipiravir eine geringe Wasserlöslichkeit, während es Wasserstoffbrückenbindungen ausbilden kann, da es eine Amidgruppe, eine Hydroxygruppe und zwei aromatische Stickstoffatome aufweist.^[163]

Die Einführung einer hydrophilen Hülle, die kovalent mit dem hydrophoben Kern verbunden ist, kann die Formulierungsstabilität erhöhen, die Beladung abschirmen und weiterhin Stealth–Eigenschaften einführen. Dieser Ansatz wird häufig für lineare amphiphile Copolymere eingesetzt. Die Verwendung von Nanoträgern aus Pfropfcopolymeren mit hydrophobem Rückgrat und hydrophilen Seitenketten konnte die Proteinadsorption weiter reduzieren. Daher wurde diese Art von amphiphilen Pfropfcopolymeren nach der Makromonomer–Methode durch Kombination von kationischer Ringöffnungspolymerisation und kontrollierter radikalischer Polymerisation, d. h. reversibler Additions–Fragmentierungs–Kettenübertragungspolymerisation, synthetisiert. Das erhaltene Poly(methylmethacrylat)–*graft*–oligo(2–ethyl–2–oxazoline) (PMMA–*graft*–OEtOx₁₅, $M_n \approx 20 \text{ kg mol}^{-1}$) bildete 10 nm große Mizellen mit einer hydrophilen Hülle, welche durch eine vielversprechende Poly(ethylenglycol)–Alternative gebildet wurde. Die Rückgradendgruppe des Pfropfcopolymers wurde synthetisch durch Einführung von (geladenen) Einheiten mit niedriger Molmasse modifiziert, d. h. Markierung mit einem hydrophilen Farbstoff, Einführung von vier Methacrylsäureeinheiten oder Bildung einer Thiol–Endgruppe. Die Selbstorganisation in Wasser und die Verkapselung der hydrophoben, fluoreszierenden Farbstoffs Neutral Lipid Orange (NLO) wurden durch diese geringfügigen Änderungen, wie bei üblichen Labelingsprotokollen, nicht beeinflusst. Es wurden jedoch starke Unterschiede in der Leberzelltyp–Spezifität beobachtet, wie sie in *in-vivo*–Experimenten mittels Intravitalmikroskopie bestimmt wurden. Ein effizienter Stealth–Effekt wurde für Mizellen beobachtet, die aus Polymeren mit anionisch–geladenen Endgruppen oder Thiol–Endgruppen, gebildet wurden. Im Gegensatz dazu veränderte eine hydrophobe Endgruppe, die aufgrund des Polymerisationsmechanismus vorhanden war, die Mizellstruktur ausreichend, um die

Zelltypspezifität und die Stealth-Eigenschaften in der Leber zu verändern. In dieser Hinsicht würden andere biologische Studien, das Verständnis und damit das rationale Polymerdesign erweitern. Insgesamt könnten auch andere Rückgrat-Endgruppen wie andere Farbstoffe oder andere Ladungsarten oder -mengen eingeführt werden, um das Verständnis für den Einflussbereich weiter zu vertiefen. Alle Veränderungen können jedoch die Leberzelltypspezifität beeinflussen und sollten daher mit großer Sorgfalt durchgeführt werden.

Gleichzeitig könnte das Potenzial der AWS-Verkapselung bzw. dessen Transports mittels PMMA-*graft*-OEtOx weiter erforscht werden. Bezüglich Hepatozyten ist das farbstoffmarkierte Pfropfcopolymer **P5-DY654** ein vielversprechender Kandidat, markiert mit einem hydrophilen Methinfarbstoff. Dieser Träger zeigt eine hohe Aufnahme in Hepatozyten, aber eine geringe Aufnahme in die stationären Makrophagen, die Kupffer-Zellen. Darüber hinaus würde eine höhere DY654-Labelingeffizienz die unabhängige Beobachtung von Träger und NLO (oder einer geeigneten Beladung) ermöglichen, was vermutlich interessante Informationen über Wirkstofffreigabe sowie Einblicke in den endgültigen Verbleib des Polymers liefern würde. Aus synthetischer Sicht wäre es weiterhin interessant, die Comonomerzusammensetzung zu variieren und z. B. *n*-Butylmethacrylat als hydrophobes Comonomer für die Rückgratbildung zu verwenden. Dadurch würde die Gesamthydrophobie des Kerns zunehmen und somit möglicherweise seine Trägerfähigkeit erhöht werden.

Nichtsdestotrotz war die Verkapselungseffizienz der PMMA-*graft*-OEtOx im Vergleich zu Werten, die häufig für herkömmliche Nanopartikel erreicht werden, bereits höher.^[119] In dieser Hinsicht wurde für die Verkapselung durch die Polyesteramide die Nanofällungstechnik verwendet, während für die Polymermizellen das NLO durch direktes Auflösen mittels Dünnschichtverfahren eingekapselt wurde. In beiden Fällen wurden die Methoden nicht optimiert, daher sollte der Vergleich mit Vorsicht erfolgen. Dennoch ist die Beladungskapazität von $\approx 6\%$ für NLO in PMMA-*graft*-OEtOx, höher im Vergleich zu den mit Indometacin beladenen Polyesteramid-Nanopartikeln mit einer Kapazität von bis zu 1.5%. Unabhängig von der Beladung variierte die Größe der Nanoträger von Nanopartikeln ($D_h \approx 200$ nm) und Polymermizellen ($D_h \approx 10$ nm). Dies kann für den jeweils gewünschten Aufnahmemechanismus vorteilhaft genutzt werden. Es wurde nachgewiesen, dass die kleinen Polymermizellen einfach durch die Zellmembran translozieren, während für die Nanopartikel,

aufgrund der Literatur, Endozytose als möglicher Aufnahmemechanismus vorgeschlagen wird.
[88-90]

Zusammenfassend lässt sich sagen, dass die untersuchten Nanoträger auf Basis von Polyestern, Polyesteramiden und Poly(2-oxazolin)en ein großes Potenzial als Nanoträger aufweisen. Ursprünglich wurden verschiedene Fragestellungen adressiert, wohingegen die zukünftige Forschung auf das vertiefte Verständnis der Anwendung aller Materialien als Wirkstoffträger gerichtet sein wird. Zu diesem Zweck sind Synthesefortschritte hinsichtlich der Einführung einer hydrophilen Hülle und Targeting-Einheiten von großer Bedeutung.

Eine detaillierte Charakterisierung der synthetisierten Materialien sowie eine wohl überlegte Variation von Parametern ist die grundlegende Voraussetzung, um korrekte Rückschlüsse auf Struktur-Eigenschafts-Beziehungen zwischen dem Wirkstoffträger und seinem Verhalten ziehen zu können.

9 References

- [1] S. A. A. Rizvi, A. M. Saleh, *Saudi Pharm. J.* **2018**, *26*, 64-70.
- [2] M. J. Mitchell, M. M. Billingsley, R. M. Haley, M. E. Wechsler, N. A. Peppas, R. Langer, *Nat. Rev. Drug Discov.* **2021**, *20*, 101-124.
- [3] K. Y. Choi, G. Liu, S. Lee, X. Chen, *Nanoscale* **2012**, *4*, 330-342.
- [4] Y. Barenholz, *J. Control. Release* **2012**, *160*, 117-134.
- [5] E. Dolgin, *Nature* **2021**, *597*, 318-324.
- [6] A. C. Anselmo, S. Mitragotri, *Bioeng. Transl. Med.* **2019**, *4*, 10143.
- [7] A. C. Anselmo, S. Mitragotri, *Bioeng. Transl. Med.* **2021**, *6*, 10246.
- [8] A. E. Nel, *Nano Lett.* **2020**, *20*, 5601-5603.
- [9] C. Englert, J. C. Brendel, T. C. Majdanski, T. Yildirim, S. Schubert, M. Gottschaldt, N. Windhab, U. S. Schubert, *Prog. Polym. Sci.* **2018**, *87*, 107-164.
- [10] J. Zuegg, M. A Cooper, *Curr. Top. Med. Chem.* **2012**, *12*, 1500-1513.
- [11] A. Dahan, J. M. Miller, *AAPS J.* **2012**, *14*, 244-251.
- [12] IACG, "No time to wait: Securing the future from drug resistant infections. Report to the secretary general of the United Nations.", can be found under https://www.who.int/antimicrobial-resistance/interagency-coordination-group/IACG_final_report_EN.pdf?ua=1 last accessed on 01/17/2022.
- [13] L. Milane, Z. Duan, M. Amiji, *PLOS ONE* **2011**, *6*, 24075.
- [14] Z. Gao, L. Zhang, Y. Sun, *J. Control. Release* **2012**, *162*, 45-55.
- [15] L. N. Woodard, M. A. Grunlan, *ACS Macro Lett.* **2018**, *7*, 976-982.
- [16] P. Xu, E. Gullotti, L. Tong, C. B. Highley, D. R. Errabelli, T. Hasan, J.-X. Cheng, D. S. Kohane, Y. Yeo, *Mol. Pharmaceutics* **2009**, *6*, 190-201.
- [17] T. E. M. Foundation, "The New Plastics Economy: Rethinking the future of plastics", can be found under <https://ellenmacarthurfoundation.org/the-new-plastics-economy-rethinking-the-future-of-plastics> last accessed on 01/17/2022.
- [18] T. P. Haider, C. Völker, J. Kramm, K. Landfester, F. R. Wurm, *Angew. Chem. Int. Ed.* **2019**, *58*, 50-62.
- [19] A. Baumann, D. Tuerck, S. Prabhu, L. Dickmann, J. Sims, *Drug Discov. Today* **2014**, *19*, 1623-1631.
- [20] H.-J. Sung, C. Meredith, C. Johnson, Z. S. Galis, *Biomaterials* **2004**, *25*, 5735-5742.
- [21] D. Y. Wong, S. J. Hollister, P. H. Krebsbach, C. Nosrat, *Tissue Eng.* **2007**, *13*, 2515-2523.
- [22] K. Fu, D. W. Pack, A. M. Klibanov, R. Langer, *Pharm. Res.* **2000**, *17*, 100-106.
- [23] K. Trofymchuk, J. Valanciunaite, B. Andreiuk, A. Reisch, M. Collot, A. S. Klymchenko, *J. Mater. Chem. B* **2019**, *7*, 5199-5210.
- [24] G. Rusu, E. Rusu, *J. Polym. Res.* **2013**, *20*, 308.
- [25] N. Brunacci, A. T. Neffe, C. Wischke, T. Naolou, U. Nöchel, A. Lendlein, *J. Control. Release* **2019**, *301*, 146-156.
- [26] Y. Zhao, J. Li, H. Yu, G. Wang, W. Liu, *Int. J. Pharm.* **2012**, *430*, 282-291.
- [27] G. Tsitlanadze, T. Kviria, R. Katsarava, C. C. Chu, *J. Mater. Sci.: Mater. Med.* **2004**, *15*, 185-190.
- [28] M. Winnacker, B. Rieger, *Polym. Chem.* **2016**, *7*, 7039-7046.

-
- [29] A. Douka, S. Vouyiouka, L.-M. Papaspyridi, C. D. Papaspyrides, *Prog. Polym. Sci.* **2018**, *79*, 1-25.
- [30] A. Basterretxea, E. Gabirondo, A. Sanchez-Sanchez, A. Etxeberria, O. Coulembier, D. Mecerreyes, H. Sardon, *Eur. Polym. J.* **2017**, *95*, 650-659.
- [31] F. N. Führer, H. Schlaad, *Macromol. Chem. Phys.* **2014**, *215*, 2268-2273.
- [32] G. Deshayes, C. Delcourt, I. Verbruggen, L. Trouillet-Fonti, F. Touraud, E. Fleury, P. Degée, M. Destarac, R. Willem, P. Dubois, *Eur. Polym. J.* **2011**, *47*, 98-110.
- [33] A. Ali Mohamed, S. Salhi, S. Abid, R. El Gharbi, A. Fradet, *Eur. Polym. J.* **2014**, *53*, 160-170.
- [34] N. Killi, A. T. Pawar, R. V. N. Gundloori, *ACS Appl. Bio Mater.* **2019**, *2*, 3341-3351.
- [35] A. D. B. Martínez, M. V. M. Bellver, I. C. R. Galán, *J. Drug Deliv. Sci. Technol.* **2017**, *42*, 307-314.
- [36] Y. Feng, J. Lu, M. Behl, A. Lendlein, *Macromol. Biosci.* **2010**, *10*, 1008-1021.
- [37] A. Basu, K. R. Kunduru, J. Katzhendler, A. J. Domb, *Adv. Drug Deliv. Rev.* **2016**, *107*, 82-96.
- [38] T. Naolou, A. Lendlein, A. T. Neffe, *Eur. Polym. J.* **2016**, *85*, 139-149.
- [39] J. Lian, M. Li, S. Wang, Y. Tao, X. Wang, *Macromolecules* **2020**, *53*, 10830-10836.
- [40] M. Dirauf, D. Bandelli, C. Weber, H. Görls, M. Gottschaldt, U. S. Schubert, *Macromol. Rapid Commun.* **2018**, *39*, 1800433.
- [41] K. P. Pagar, P. R. Vavia, *Pharm. Dev. Technol.* **2014**, *19*, 385-394.
- [42] K. Pagar, P. Vavia, *Sci. Pharm.* **2013**, *81*, 865-888.
- [43] M. Dirauf, A. Erlebach, C. Weber, S. Hoepfener, J. R. Buchheim, M. Sierka, U. S. Schubert, *Macromolecules* **2020**, *53*, 3580-3590.
- [44] L. Zhang, Y. Feng, H. Tian, C. Shi, M. Zhao, J. Guo, *React. Funct. Polym.* **2013**, *73*, 1281-1289.
- [45] T. Steinbach, F. R. Wurm, *Angew. Chem. Int. Ed.* **2015**, *54*, 6098-6108.
- [46] K. N. Bauer, H. T. Tee, M. M. Velencoso, F. R. Wurm, *Prog. Polym. Sci.* **2017**, *73*, 61-122.
- [47] Z. E. Yilmaz, C. Jérôme, *Macromol. Biosci.* **2016**, *16*, 1745-1761.
- [48] A. Cankaya, M. Steinmann, Y. Bülbül, I. Lieberwirth, F. R. Wurm, *Polym. Chem.* **2016**, *7*, 5004-5010.
- [49] M. Steinmann, M. Wagner, F. R. Wurm, *Chem. Eur. J.* **2016**, *22*, 17329-17338.
- [50] K. N. Bauer, L. Liu, D. Andrienko, M. Wagner, E. K. Macdonald, M. P. Shaver, F. R. Wurm, *Macromolecules* **2018**, *51*, 1272-1279.
- [51] K. N. Bauer, H. T. Tee, I. Lieberwirth, F. R. Wurm, *Macromolecules* **2016**, *49*, 3761-3768.
- [52] G. Becker, Z. Deng, M. Zober, M. Wagner, K. Lienkamp, F. R. Wurm, *Polym. Chem.* **2018**, *9*, 315-326.
- [53] G. Becker, T. A. Marquetant, M. Wagner, F. R. Wurm, *Macromolecules* **2017**, *50*, 7852-7862.
- [54] D. Pranantyo, L. Q. Xu, E.-T. Kang, M. K. Mya, M. B. Chan-Park, *Biomacromolecules* **2016**, *17*, 4037-4044.
- [55] H. Jin, M. Sun, L. Shi, X. Zhu, W. Huang, D. Yan, *Biomater. Sci.* **2018**, *6*, 1403-1413.
- [56] L. K. Müller, T. Steinbach, F. R. Wurm, *RSC Adv.* **2015**, *5*, 42881-42888.
- [57] F. Ding, H.-J. Li, J.-X. Wang, W. Tao, Y.-H. Zhu, Y. Yu, X.-Z. Yang, *ACS Appl. Mater. Interfaces* **2015**, *7*, 18856-18865.

-
- [58] J. Heller, D. W. H. Penhale, R. F. Helwing, *J. Polym. Sci. B Polym. Lett. Ed.* **1980**, *18*, 293-297.
- [59] M. J. Heffernan, N. Murthy, *Bioconjugate Chem.* **2005**, *16*, 1340-1342.
- [60] S. Guo, Y. Nakagawa, A. Barhoumi, W. Wang, C. Zhan, R. Tong, C. Santamaria, D. S. Kohane, *J. Am. Chem. Soc.* **2016**, *138*, 6127-6130.
- [61] S. Samanta, D. R. Bogdanowicz, H. H. Lu, J. T. Koberstein, *Macromolecules* **2016**, *49*, 1858-1864.
- [62] M. J. Vicent, R. Tomlinson, S. Brocchini, R. Duncan, *J. Drug Target.* **2004**, *12*, 491-501.
- [63] A. Moreno, G. Lligadas, J. C. Ronda, M. Galià, V. Cádiz, *Polym. Chem.* **2019**, *10*, 5215-5227.
- [64] W. D. Gray, P. Che, M. Brown, X. Ning, N. Murthy, M. E. Davis, *J. Cardiovasc. Trans. Res.* **2011**, *4*, 631.
- [65] I. Somasuntharam, A. V. Boopathy, R. S. Khan, M. D. Martinez, M. E. Brown, N. Murthy, M. E. Davis, *Biomaterials* **2013**, *34*, 7790-7798.
- [66] K. Mitra, S. K. Hira, S. Singh, N. K. Vishwakarma, S. Vishwakarma, U. Gupta, P. P. Manna, B. Ray, *ChemistrySelect* **2018**, *3*, 8833-8843.
- [67] A. M. J. Coenen, J. A. W. Harings, S. Ghazanfari, S. Jockenhoevel, K. V. Bernaerts, *RSC Adv.* **2020**, *10*, 9623-9632.
- [68] B. A. Abel, R. L. Snyder, G. W. Coates, *Science* **2021**, *373*, 783-789.
- [69] T. Shirouchi, A. Kanazawa, S. Kanaoka, S. Aoshima, *Macromolecules* **2016**, *49*, 7184-7195.
- [70] M. Higuchi, A. Kanazawa, S. Aoshima, *ACS Macro Lett.* **2020**, *9*, 77-83.
- [71] R. Kato, A. Kanazawa, S. Aoshima, *ACS Macro Lett.* **2019**, *8*, 1498-1503.
- [72] Y. Ishido, A. Kanazawa, S. Kanaoka, S. Aoshima, *J. Polym. Sci., Part A: Polym. Chem.* **2014**, *52*, 1334-1343.
- [73] Y. Miyamae, A. Kanazawa, K.-i. Tamaso, K. Morino, R. Ogawa, S. Aoshima, *Polym. Chem.* **2018**, *9*, 404-413.
- [74] A. Kanazawa, S. Aoshima, *ACS Macro Lett.* **2015**, *4*, 783-787.
- [75] M. Mimura, A. Kanazawa, S. Aoshima, *Macromolecules* **2019**, *52*, 7572-7583.
- [76] M. Kawamura, A. Kanazawa, S. Kanaoka, S. Aoshima, *Polym. Chem.* **2015**, *6*, 4102-4108.
- [77] D. Yokota, A. Kanazawa, S. Aoshima, *Macromolecules* **2019**, *52*, 6241-6249.
- [78] S. Aoshima, Y. Oda, S. Matsumoto, Y. Shinke, A. Kanazawa, S. Kanaoka, *ACS Macro Lett.* **2014**, *3*, 80-85.
- [79] Y. Ishido, A. Kanazawa, S. Kanaoka, S. Aoshima, *Polym. Chem.* **2014**, *5*, 43-47.
- [80] A. E. Neitzel, M. A. Petersen, E. Kokkoli, M. A. Hillmyer, *ACS Macro Lett.* **2014**, *3*, 1156-1160.
- [81] A. E. Neitzel, T. J. Haversang, M. A. Hillmyer, *Ind. Eng. Chem. Res.* **2016**, *55*, 11747-11755.
- [82] L. Bixenmann, J. Stickdorn, L. Nuhn, *Polym. Chem.* **2020**, *11*, 2441-2456.
- [83] A. E. Neitzel, L. Barreda, J. T. Trotta, G. W. Fahnhorst, T. J. Haversang, T. R. Hoye, B. P. Fors, M. A. Hillmyer, *Polym. Chem.* **2019**, *10*, 4573-4583.
- [84] S. Schubert, J. J. T. Delaney, U. S. Schubert, *Soft Matter* **2011**, *7*, 1581-1588.
- [85] J. Tao, S. F. Chow, Y. Zheng, *Acta Pharm. Sin. B.* **2019**, *9*, 4-18.

-
- [86] Y. Wang, J. He, C. Liu, W. H. Chong, H. Chen, *Angew. Chem. Int. Ed.* **2015**, *54*, 2022-2051.
- [87] S. A. Vitale, J. L. Katz, *Langmuir* **2003**, *19*, 4105-4110.
- [88] P. Foroozandeh, A. A. Aziz, *Nanoscale Res. Lett.* **2018**, *13*, 1-12.
- [89] C. He, Y. Hu, L. Yin, C. Tang, C. Yin, *Biomaterials* **2010**, *31*, 3657-3666.
- [90] K. Letchford, H. Burt, *Eur. J. Pharm. Biopharm.* **2007**, *65*, 259-269.
- [91] N. Kamaraj, P. Y. Rajaguru, P. k. Issac, S. Sundaresan, *Asian J. Pharm. Sci.* **2017**, *12*, 353-362.
- [92] A. Budhian, S. J. Siegel, K. I. Winey, *Int. J. Pharm.* **2008**, *346*, 151-159.
- [93] W. C. Griffin, *J. Soc. Cosmet. Chem.* **1949**, *1*, 311-326.
- [94] H.-I. Hung, O. J. Klein, S. W. Peterson, S. R. Rokosh, S. Osseiran, N. H. Nowell, C. L. Evans, *Sci. Rep.* **2016**, *6*, 1-13.
- [95] V. Knecht, H. Risselada, A. Mark, S. Marrink, *J. Colloid Interface Sci.* **2008**, *318*, 477-486.
- [96] A. V. Delgado, F. González-Caballero, R. Hunter, L. K. Koopal, J. Lyklema, *Pure Appl. Chem.* **2005**, *77*, 1753-1805.
- [97] E. M. S. Castanheira, J. M. G. Martinho, *Chem. Phys. Lett.* **1991**, *185*, 319-323.
- [98] E. Goddard, N. Turro, P. Kuo, K. Ananthapadmanabhan, *Langmuir* **1985**, *1*, 352-355.
- [99] K. Kalyanasundaram, J. Thomas, *J. Am. Chem. Soc.* **1977**, *99*, 2039-2044.
- [100] G. B. Ray, I. Chakraborty, S. P. Moulik, *J. Colloid Interface Sci.* **2006**, *294*, 248-254.
- [101] A. Ghaffar, G. Draaisma, G. Mihov, A. Dias, P. Schoenmakers, S. Van Der Wal, *Biomacromolecules* **2011**, *12*, 3243-3251.
- [102] B. M. Culbertson, *Prog. Polym. Sci.* **2002**, *27*, 579-626.
- [103] C. Weber, T. Neuwirth, K. Kempe, B. Ozkahraman, E. Tamahkar, H. Mert, C. R. Becer, U. S. Schubert, *Macromolecules* **2012**, *45*, 20-27.
- [104] K. Kempe, *Macromol. Chem. Phys.* **2017**, *218*, 1700021.
- [105] J. Kronek, J. Nedbal, H. Valentová, M. Neubert, I. Janigová, N. Petrenčíková, P. Šrámková, K. Csomorová, L. Petra, *Polym. Test.* **2018**, *68*, 1-7.
- [106] J. Lustoň, J. Kronek, A. Kleinová, I. Janigová, H. Valentová, J. Nedbal, *J. Polym. Sci., Part A: Polym. Chem.* **2012**, *50*, 3936-3943.
- [107] H. Arimoto, M. Ishibashi, M. Hirai, Y. Chatani, *J. Polym. Sci., Part A: Gen. Pap.* **1965**, *3*, 317-326.
- [108] J. P. Parker, P. H. Lindenmeyer, *J. Appl. Polym. Sci.* **1977**, *21*, 821-837.
- [109] Q. Zhang, Z. Mo, H. Zhang, S. Liu, S. Z. D. Cheng, *Polymer* **2001**, *42*, 5543-5547.
- [110] J. O. Fernandez, G. M. Swallowe, S. F. Lee, *J. Appl. Polym. Sci.* **2001**, *80*, 2031-2038.
- [111] H. Shanak, K. H. Ehses, W. Götz, P. Leibenguth, R. Pelster, *J. Mater. Sci.* **2009**, *44*, 655-663.
- [112] A. Erlebach, T. Ott, C. Otzen, S. Schubert, J. Czaplewska, U. S. Schubert, M. Sierka, *J. Comput. Chem.* **2016**, *37*, 2220-2227.
- [113] A. O. Kasimova, G. M. Pavan, A. Danani, K. Mondon, A. Cristiani, L. Scapozza, R. Gurny, M. Möller, *J. Phys. Chem. B* **2012**, *116*, 4338-4345.
- [114] X. D. Guo, L. J. Zhang, Y. Qian, *Ind. Eng. Chem. Res.* **2012**, *51*, 4719-4730.
- [115] L. Huynh, C. Neale, R. Pomès, C. Allen, *Nanomedicine* **2012**, *8*, 20-36.
- [116] C. J. M. Rivas, M. Tarhini, W. Badri, K. Miladi, H. Greige-Gerges, Q. A. Nazari, S. A. G. Rodríguez, R. Á. Román, H. Fessi, A. Elaissari, *Int. J. Pharm.* **2017**, *532*, 66-81.
- [117] C. I. Crucho, M. T. Barros, *Mater. Sci. Eng., C* **2017**, *80*, 771-784.

-
- [118] F. D. Hart, P. Boardman, *Br. Med. J.* **1963**, *2*, 965-970.
- [119] B. Shkodra, A. T. Press, A. Vollrath, I. Nischang, S. Schubert, S. Hoepfener, D. Haas, C. Enzensperger, M. Lehmann, P. Babic, *Pharmaceutics* **2020**, *12*, 1110.
- [120] A. Reisch, A. Runser, Y. Arntz, Y. Mely, A. S. Klymchenko, *ACS Nano* **2015**, *9*, 5104-5116.
- [121] S. Jankovic, G. Tsakiridou, F. Ditzinger, N. J. Koehl, D. J. Price, A.-R. Ilie, L. Kalantzi, K. Kimpe, R. Holm, A. Nair, *J. Pharm. Pharmacol.* **2019**, *71*, 441-463.
- [122] M. M. Lübtow, M. S. Haider, M. Kirsch, S. Klisch, R. Luxenhofer, *Biomacromolecules* **2019**, *20*, 3041-3056.
- [123] Y. Amharar, V. Curtin, K. H. Gallagher, A. M. Healy, *Int. J. Pharm.* **2014**, *472*, 241-247.
- [124] P. J. Marsac, S. L. Shamblin, L. S. Taylor, *Pharm. Res.* **2006**, *23*, 2417-2426.
- [125] H. Cabral, K. Miyata, K. Osada, K. Kataoka, *Chem. Rev.* **2018**, *118*, 6844-6892.
- [126] C. Oerlemans, W. Bult, M. Bos, G. Storm, J. F. W. Nijssen, W. E. Hennink, *Pharm. Res.* **2010**, *27*, 2569-2589.
- [127] P. Maksym-Bębenek, D. Neugebauer, *Macromol. Biosci.* **2015**, *15*, 1616-1624.
- [128] J. Rieger, C. Passirani, J. P. Benoit, K. Van Butsele, R. Jérôme, C. Jerome, *Adv. Funct. Mater.* **2006**, *16*, 1506-1514.
- [129] S. Sant, S. Poulin, P. Hildgen, *J. Biomed. Mater. Res., Part A* **2008**, *87*, 885-895.
- [130] D. Papahadjopoulos, T. Allen, A. Gabizon, E. Mayhew, K. Matthay, S. Huang, K. Lee, M. Woodle, D. Lasic, C. Redemann, *Proc. Natl. Acad. Sci. U. S. A.* **1991**, *88*, 11460-11464.
- [131] Q. Yang, T. M. Jacobs, J. D. McCallen, D. T. Moore, J. T. Huckaby, J. N. Edelstein, S. K. Lai, *Anal. Chem.* **2016**, *88*, 11804-11812.
- [132] B.-M. Chen, Y.-C. Su, C.-J. Chang, P.-A. Burnouf, K.-H. Chuang, C.-H. Chen, T.-L. Cheng, Y.-T. Chen, J.-Y. Wu, S. R. Roffler, *Anal. Chem.* **2016**, *88*, 10661-10666.
- [133] G. T. Kozma, T. s. Mészáros, I. Vashegyi, T. s. Fülöp, E. Örfi, L. s. Dézsi, L. s. Rosivall, Y. Bavli, R. Urbanics, T. E. Mollnes, *ACS Nano* **2019**, *13*, 9315-9324.
- [134] A. Rimmel, *Nature* **2021**, *590*, 538-540.
- [135] T. Lorson, M. M. Lübtow, E. Wegener, M. S. Haider, S. Borova, D. Nahm, R. Jordan, M. Sokolski-Papkov, A. V. Kabanov, R. Luxenhofer, *Biomaterials* **2018**, *178*, 204-280.
- [136] S. Therapeutics, "Serina Therapeutics Pipeline", can be found under <https://serinatherapeutics.com/pipeline/> last accessed on 01/17/2022.
- [137] R. Victor, *J. Mater. Sci.: Mater. Med.* **2014**, *25*, 1211-1225.
- [138] P. Wilson, P. C. Ke, T. P. Davis, K. Kempe, *Eur. Polym. J.* **2017**, *88*, 486-515.
- [139] I. Muljajew, C. Weber, I. Nischang, U. S. Schubert, *Materials* **2018**, *11*, 528.
- [140] A. Vollrath, A. Schallon, C. Pietsch, S. Schubert, T. Nomoto, Y. Matsumoto, K. Kataoka, U. S. Schubert, *Soft Matter* **2013**, *9*, 99-108.
- [141] D. Christova, R. Velichkova, W. Loos, E. J. Goethals, F. Du Prez, *Polymer* **2003**, *44*, 2255-2261.
- [142] H. M. Lambermont-Thijs, R. Hoogenboom, C. A. Fustin, C. Bomal-D'Haese, J. F. Gohy, U. S. Schubert, *J. Polym. Sci., Part A: Polym. Chem.* **2009**, *47*, 515-522.
- [143] G. G. Alvaradejo, H. V.-T. Nguyen, P. Harvey, N. M. Gallagher, D. Le, M. F. Ottaviani, A. Jasanoff, G. Delaître, J. A. Johnson, *ACS Macro Lett.* **2019**, *8*, 473-478.
- [144] A. T. Press, A. Ramoji, M. vd Lühe, A. C. Rinkenauer, J. Hoff, M. Butans, C. Rössel, C. Pietsch, U. Neugebauer, F. H. Schacher, *NPG Asia Mater.* **2017**, *9*, 444.

-
- [145] L.-Q. Qiu, W. S. Lai, D. J. Stumpo, P. J. Blackshear, *Bio-protocol* **2016**, *6*, 1859.
- [146] M. V. Recouvreux, C. Comisso, *Front. Endocrinol.* **2017**, *8*, 261.
- [147] D. Dutta, C. D. Williamson, N. B. Cole, J. G. Donaldson, *PLOS ONE* **2012**, *7*, 45799.
- [148] I. Liashkovich, D. Pasrednik, V. Prystopiuk, G. Rosso, H. Oberleithner, V. Shahin, *Sci. Rep.* **2015**, *5*, 9994.
- [149] G. Sahay, W. Querbes, C. Alabi, A. Eltoukhy, S. Sarkar, C. Zurenko, E. Karagiannis, K. Love, D. Chen, R. Zoncu, Y. Buganim, A. Schroeder, R. Langer, D. G. Anderson, *Nat. Biotechnol.* **2013**, *31*, 653-658.
- [150] Y.-N. Zhang, W. Poon, A. J. Tavares, I. D. McGilvray, W. C. W. Chan, *J. Control. Release* **2016**, *240*, 332-348.
- [151] F. Alexis, E. Pridgen, L. K. Molnar, O. C. Farokhzad, *Mol. Pharmaceutics* **2008**, *5*, 505-515.
- [152] W. Poon, Y.-N. Zhang, B. Ouyang, B. R. Kingston, J. L. Y. Wu, S. Wilhelm, W. C. W. Chan, *ACS Nano* **2019**, *13*, 5785-5798.
- [153] T. M. Rogoff, P. E. Lipsky, *Gastroenterology* **1981**, *80*, 854-860.
- [154] E. Sadauskas, H. Wallin, M. Stoltenberg, U. Vogel, P. Doering, A. Larsen, G. Danscher, *Part. Fibre Toxicol.* **2007**, *4*, 10.
- [155] C. D. Walkey, J. B. Olsen, H. Guo, A. Emili, W. C. W. Chan, *J. Am. Chem. Soc.* **2012**, *134*, 2139-2147.
- [156] J. Poisson, S. Lemoine, C. Boulanger, F. Durand, R. Moreau, D. Valla, P.-E. Rautou, *J. Hepatol.* **2017**, *66*, 212-227.
- [157] K. K. Sørensen, P. McCourt, T. Berg, C. Crossley, D. L. Couteur, K. Wake, B. Smedsrød, *Am. J. Physiol.* **2012**, *303*, 1217-1230.
- [158] A. T. Press, A. Traeger, C. Pietsch, A. Mosig, M. Wagner, M. G. Clemens, N. Jbeily, N. Koch, M. Gottschaldt, N. Bézière, V. Ermolayev, V. Ntziachristos, J. Popp, M. M. Kessels, B. Qualmann, U. S. Schubert, M. Bauer, *Nat. Commun.* **2014**, *5*, 5565.
- [159] A. C. Rinkenauer, A. T. Press, M. Raasch, C. Pietsch, S. Schweizer, S. Schwörer, K. L. Rudolph, A. Mosig, M. Bauer, A. Traeger, U. S. Schubert, *J. Control. Release* **2015**, *216*, 158-168.
- [160] M. Schroffenegger, N. S. Leitner, G. Morgese, S. N. Ramakrishna, M. Willinger, E. M. Benetti, E. Reimhult, *ACS Nano* **2020**, *14*, 12708-12718.
- [161] C. Corbo, R. Molinaro, A. Parodi, N. E. T. Furman, F. Salvatore, E. Tasciotti, *Nanomedicine* **2016**, *11*, 81-100.
- [162] C. C. Fleischer, C. K. Payne, *J. Phys. Chem. B* **2012**, *116*, 8901-8907.
- [163] E. De Clercq, *Chem. Asian J.* **2019**, *14*, 3962-3968.

List of abbreviations

List of abbreviations

^1H NMR	Proton nuclear magnetic resonance
ADMET	Acyclic diene metathesis
AIBN	2,2'-Azobis(2-methylpropionitrile)
API	Active pharmaceutical ingredient
AUC	Area under the curve
av.	Average
<i>c</i>	Concentration
CD54	APC-labeled CD54 (clone: YN1/1.7.4) antibody
CROP	Cationic ring opening polymerization
Cryo-TEM	Cryogenic-transmission electron microscopy
CTA	Chain transfer agent
<i>D</i>	Dispersity
DA(D)	Diode array (detector)
DBU	1,8-Diazabicyclo(5.4.0)undec-7-en
D_h	Hydrodynamic diameter
DHB	2,5-Dihydroxybenzoic acid
DLS	Dynamic light scattering
DMAc	<i>N,N</i> -Dimethylacetamide
DMF	<i>N,N</i> -Dimethylformamide
DP	Degree of polymerization
DSC	Differential scanning calorimetry
EE	Encapsulation efficiency
EMA	European Medicines Agency
F4/80	FITC-labeled F4/80 (clone: BM8) antibody
FDA	U. S. Food and Drug Administration
HF <i>i</i> P	Hexafluoro- <i>iso</i> -propanol
HHB	Hydrophilic hydrophobic balance
IMC	Indomethacin
IR	Infrared

List of abbreviations

LC	Loading capacity
LCST	Lower critical solution temperature
LSEC	Liver sinusoidal endothelial cells
MAA	Methacrylic acid
MALDI–ToF MS	Matrix–assisted laser–desorption time of flight mass spectroscopy
MD	Molecular dynamics
MEF	Mouse embryonic fibroblasts
MMA	Methyl methacrylate
M_n	Molar mass
mRNA	Messenger ribonucleic acid
n.d.	Not detectable
NADP	Nicotinamide adenine dinucleotide phosphate
NIR	Near infrared
NLO	Neutral Lipid Orange
NSAID	Nonsteroidal anti–inflammatory drug
NY	Nylon 66
OEtOx	Oligo(2–ethyl–2–oxazoline)
PCA	Principal component analysis
PCL	Poly(ϵ –caprolactone)
PDI	Polydispersity index
PEA	Poly(ester amide)
PEG	Poly(ethylene glycol)
PEtOx	Poly(2–ethyl–2–oxazoline)
PGA	Poly(glycolic acid)
Ph	Phenyl
PHA	Polyhydroxyalkanoates
PLA	Polylactide
PLGA	Poly(lactic– <i>co</i> –glycolic acid)
PMMA	Poly(methyl methacrylate)
PS	Polystyrene
PVA	Poly(vinyl alcohol)
RAFT	Reversible addition–fragmentation chain transfer polymerization
RES	Reticuloendothelial system
RI(D)	Refractive index (detector)
ROP	Ring opening polymerization

List of abbreviations

SEC	Size exclusion chromatography
SEM	Scanning electron microscopy
siRNA	Small interfering ribonucleic acid
TBD	1,5,7-Triazabicyclo(4.4.0)dec-5-en
T _{cp}	Cloud point temperature
T _g	Glass transition temperature
TGA	Thermogravimetric analysis
THF	Tetrahydrofuran
T _m	Melting point
Tos	Tosylate
UCST	Upper critical solution temperature
WAXS	Wide-angle X-ray scattering
X _c	Degree of crystallinity
εCL	ε-Caprolactone
δ	Hildebrand solubility parameter
δCL	δ-Caprolactone
δDL	δ-Decalactone
δVL	δ-Valerolactone
χ	Flory-Huggins interaction parameter

List of abbreviations

Acknowledgement / Danksagung

First, I acknowledge my doctoral supervisor Prof. Dr. Ulrich. S. Schubert for giving me the opportunity to work in his extraordinary group. I was able to learn and grow so much during my time in your group not only as a chemist, but also as a communicator, supervisor, project manager, colleague, public speaker, and not at least person. Through all of the countless opportunities that you provided, you created an environment every PhD candidate can only dream of. Thank you for always supporting and encouraging me. I am honored to be part of your “academic tree”.

Dear Dr. Christine Weber, I could not have wished for a better supervisor than you. You balanced continuous challenges and constant support in such an astonishing, down-to-earth way that made me thrive throughout my whole time in the group. Thank you for taking me with you to the ACS Meeting, it was one of so many highlights. I think in my work future I am going to look back and think “What would Christine do in a situation like this?”.

I would further like to acknowledge Michael Dirauf for writing the review together with Christine and me.

I thank Damiano Bandelli for introducing me to the exciting field of polyesters, it was my great pleasure to work with and learn from you. Many thanks to the other “polyester project” partners for the same reason: Dr. Christian Helbing, Michael Seifert, Karl Scheuer, Dr. Johannes B. Max, Prof. Dr. Felix H. Schacher, Prof. Dr. Klaus D. Jandt.

I would like to express acknowledgement to the “computational scientist” from the SFB 1278 A01 project: Mingzhe Chi, Dr. Andreas Erlebach, and Prof. Dr. Marek Sierka. Thank you all for the fruitful collaborations, valuable data and this extraordinary introduction to the field of atomistic molecular dynamics simulations.

Dr. Johannes R. Buchheim, thank you for working together with me (us) on the WAXS investigation of the poly(ester amide)s. Your contribution increased the value of the manuscript very much.

I would like to further express my gratitude for the intense collaboration to the “formulation team”: Dr. Antje Vollrath, Baerbel Beringer–Siemers, and Johannes Schenk. You made the polymers “come to life” and actually fulfil their purpose of forming nanoparticles. Antje, thank you for kindly answering all of my beginner questions on the topic of formulation.

Dr. Ivo Nischang, thank you for the characterization of the P5 micelles by such an advanced technique as AUC and the connection to the FFE team. Both approaches shed immense light on the behavior of the polymers in solution and contributed substantially to the understanding and the success of the project.

I further express my gratitude to the coauthors of the “ACS Nano project”. Many thanks for the biological investigation and conceptional design to Sophie Huschke, Wanling Foo, Prof. Dr. Michael Bauer, and Jun–Prof. Dr. Adrian T. Press. Especially to Sophie and Adrian, thank you for the enthusiastic and passionate exchange. Without your strong believe and vision for those micelles this would not have been possible. I thank Dr. Anuradha Ramoji and Prof. Dr. Jürgen Popp for the Raman analysis. Anu, thank you for the exceptional PCA 3D score plot and your kind and many explanations. Dear Dr. Zoltán Cseresnyés and Prof. Dr. Marc Thilo Figge, thank you for the image analysis. Dare I say it almost felt like “magic” what you did with the image data.

For the different microscopy images, I would like to acknowledge Steffi Stumpf, Dr. Pelin Sungur, Dr. Stephanie Hoepfener. Thank you for making the nanocarriers real “super models”. Dear Dr. Grit Festag, thank you for keeping the SEC’s running, *the* polymer scientist instrument. Dear Nicole Fritz, thank you for the MS investigations. Dear Renzo Paulus, thank you for the introduction to the thermal analysis devices and refilling the N₂–tank with me countless times. Renzo, also, so many thanks for all those IT related things, I am not sure what the group would do without you. Dear Sandra Köhn, Alexander Meier and Dr. Jürgen Vitz, for being reliable contact persons in so many fields. I further thank the NMR Department for your continuous efforts, help and measurements. Thank you, Dr. Peter Bellstedt, Friederike Pielenz, and Rica Patzschke. Further I would like to thank Jens Ulbrich for providing the poly(methyl methacrylate), and Dr. Robert Wildgruber and Markart Meckel from the FFE Service GmbH for free flow electrophoresis measurements.

For exceptional organizational work, I would like to acknowledge Doreen Kückler, Franca Frister, Katja Gattung, Mandy Necke, Sylvia Braunsdorf, and Ulrike Kaiser.

I would further like to thank the Postdocs in the group for keeping those hierarchies flat and for always being supportive through discussion and piece of advice, many thanks to Dr. Johannes Brendel, Dr. Michael Gottschaldt, Dr. Martin Hager, Dr. Uwe Köhn, Dr. David Pretzel, Dr. Stephanie Schubert, Dr. Anja Träger, and Dr. Jürgen Vitz.

To students and “HIWIs” who contributed to the projects, thank you for making me grow as a supervisor and also find fulfillment in teaching: Sandra Kröll, Tommy Melzer, Samuel Brashaw, and Nicolas Müller.

I had the great pleasure of participating in the coaching series funded by the PolyTarget CRC 1278 and guided by Dr. Anne–Christin Warskulat. Thank you, Anne, for creating “The Awesome Women in Science” and many thanks to those awesome female scientists for your insights and inspiration: Anna, Annemarie, Blerina, Ceren, Gauri, Kathy, Maren, and Maria.

My everyday PhD life was shaped by big and small interactions, on professional and personal level. Especially the latter did not end up on any scientific contribution, but that does not mean they were of lesser personal value to me. I would like to thank lab / office / group mates: Caro, Christoph, Damiano, Dulce, Fabi, Florian, Gauri, Grit, Ilknur, Jana, Julien, Justyna, Kate, Leanne, Liên, Lukas, Martin, Michael, Michi, Natalie, Nora, Olenka, Paul, Peng, Prosper, Renzo, Rieke, Simon, Susanne, Tanja, Thomas, Tobi and Ursula (I refrain from listing the whole Schubert group even though I am very tempted ;)).

I thank my family, friends and my partner. You are the roots that keep me grounded and the sun that keeps me growing.

My work was funded by the Deutsche Forschungsgemeinschaft (DFG, German Research Foundation) – number 316213987 – SFB 1278 “PolyTarget” (project A01). To me, it was a great privilege to be part of this extraordinary CRC.

Declaration of authorship / Selbstständigkeitserklärung

Ich erkläre, dass ich die vorliegende Arbeit selbstständig und unter Verwendung der angegebenen Hilfsmittel, persönlichen Mitteilungen und Quellen angefertigt habe.

I certify that the work presented here is, to the best of my knowledge and belief, original and the results of my own investigations, except as acknowledged, and was not submitted, either in part or whole, for a degree at this or any other university.

Jena, den __ . __ . 2022

Irina Muljajew

Curriculum vitae

07/2017 – Present

PhD candidate

Friedrich Schiller University Jena, Germany

- Laboratory of Organic and Macromolecular Chemistry (IOMC)
- Doctorate supervisor Prof. Dr. Ulrich S. Schubert
- Within the Collaborative Research Center (CRC) 1278 „PolyTarget“. Thesis title: „Polymeric drug delivery systems: Aspects of core and shell for nanocarriers from polyesters, poly(ester amide)s and poly(2-oxazoline)s“
- Postgraduate courses: Nanotoxicology and Nanobiopharmacy, Simulation and Modelling
- *Cancelled research stay at IBM with Prof. Hedrick due to the COVID-19 pandemic*

Jena, __. __. ____

Publication list

Peer-reviewed publications

1. I. Muljajew, C. Weber, I. Nischang, U. S. Schubert, *Materials* **2018**, *11*, 528.

“PMMA-g-OEtOx graft copolymers: Influence of grafting degree and side-chain length on the conformation in aqueous solution“

2. D. Bandelli, C. Helbing, C. Weber, M. Seifert, I. Muljajew, K. D. Jandt, U. S. Schubert, *Macromolecules* **2018**, *51*, 5567–5576.

“Maintaining the hydrophilic–hydrophobic balance of polyesters with adjustable crystallinity for tailor-made nanoparticles“

3. D. Bandelli, I. Muljajew, K. Scheuer, J. B. Max, C. Weber, F. H. Schacher, K. D. Jandt, U. S. Schubert, *Macromolecules* **2020**, *53*, 5208–5217.

“Copolymerization of caprolactone isomers to obtain nanoparticles with constant hydrophobicity and tunable crystallinity“

4. I. Muljajew, A. Erlebach, C. Weber, J. R. Buchheim, M. Sierka, U. S. Schubert, *Polym. Chem.* **2020**, *11*, 112–124.

“A polyesteramide library from dicarboxylic acids and 2,2'-bis(2-oxazoline): Synthesis, characterization, nanoparticle formulation and molecular dynamics simulations“

5. A. Erlebach, I. Muljajew, M. Chi, C. Bückmann, C. Weber, U. S. Schubert, M. Sierka, *Adv. Theory Simul.* **2020**, *3*, 2000001.

“Predicting solubility of small molecules in macromolecular compounds for nanomedicine application from atomistic simulations”

6. I. Muljajew, S. Huschke, A. Ramoji, Z. Cseresnyés, S. Höppener, I. Nischang, W. Foo, J. Popp, M. T. Figge, C. Weber, M. Bauer, U. S. Schubert, A. T. Press, *ACS Nano* **2021**, *15*, 12298–12313.

“Stealth effect of short polyoxazolines in graft copolymers: Minor changes of backbone end group determine liver cell–type specificity“

7. I. Muljajew, M. Chi, A. Vollrath, C. Weber, B. Beringer–Siemers, S. Stumpf, S. Hoepfener, M. Sierka, U. S. Schubert, *Eur. Polym. J.* **2021**, *156*, 110606.

“A combined experimental and *in silico* approach to determine the compatibility of poly(ester amide)s and indomethacin in polymer nanoparticles“

Submitted manuscripts

1. M. Dirauf, I. Muljajew, C. Weber, U. S. Schubert, *Prog. Polym. Sci.* **2021**, *under revision*.

“Recent advances in (bio)degradable polymers – Beyond polyesters”

Oral presentations

1. Retreat meeting of the CRC 1278 PolyTarget, 7th and 8th November 2018, Weimar, Germany

U. S. Schubert, I. Muljajew, M. Sierka, A. Erlebach

“Tailor-made multifunctional polymers and nanoparticles with optimized compatibility between biodegradable core and encapsulated drug”

2. ACS Spring National Meeting, 31st March to 4th April 2019, Orlando, U.S.A.

I. Muljajew, C. Weber, U. S. Schubert

“PMMA-g-OEtOx graft copolymers: Influence of the advanced polymer architecture and the development of a two-dye-system“

3. Summer School “Nanomedicine: Formulation, characterization, translation” of the CRC 1066 (Mainz) and the CRC 1278 (Jena), 24th to 28th June 2019, Dipperz / Fulda, Germany

U. S. Schubert, I. Muljajew, M. Sierka, A. Erlebach, M. Chi

“Poly(ester amide)s with tailor-made hydrophilicity“

4. Retreat meeting of the CRC 1278 PolyTarget, 6th and 7th November 2019, Apolda, Germany

U. S. Schubert, I. Muljajew, M. Sierka, A. Erlebach, M. Chi

“Tailor-made multifunctional polymers and nanoparticles with optimized compatibility between biodegradable core and encapsulated drug”

5. Retreat meeting of the CRC 1278 PolyTarget, 7th and 8th October 2021, Jena, Germany

U. S. Schubert, I. Muljajew, M. Sierka, M. Chi

“Tailor-made multifunctional polymers and nanoparticles with optimized compatibility between biodegradable core and encapsulated drug”

Poster presentations

1. Retreat meeting of the CRC 1278 PolyTarget, 7th and 8th November 2018, Weimar, Germany

U. S. Schubert, I. Muljajew, M. Sierka, A. Erlebach

“Tailor-made multifunctional polymers and nanoparticles with optimized compatibility between biodegradable core and encapsulated drug”

2. ACS Spring National Meeting, 31st March to 4th April 2019, Orlando, U.S.A.

I. Muljajew, M. Dirauf, C. Weber, U. S. Schubert

“Poly(ester amide)s by advanced step growth and chain growth polymerization“

3. Summer School “Nanomedicine: Formulation, characterization, translation” of the CRC 1066 (Mainz) and the CRC 1278 (Jena), 24th to 28th June 2019, Dipperz / Fulda, Germany

U. S. Schubert, I. Muljajew, M. Sierka, A. Erlebach

“Tailor-made multifunctional polymers and nanoparticles with optimized compatibility between biodegradable core and encapsulated drug“

4. Symposium on innovative polymers for nanomedicine of the 21st century, 15th to 17th July 2019, Jena, Germany

U. S. Schubert, I. Muljajew, M. Sierka, A. Erlebach

“Tailor-made multifunctional polymers and nanoparticles with optimized compatibility between biodegradable core and encapsulated drug“

5. Retreat meeting of the CRC 1278 PolyTarget, 6th and 7th November 2019, Apolda, Germany

U. S. Schubert, I. Muljajew, M. Sierka, A. Erlebach, M. Chi, T. Schrader

“Tailor-made multifunctional polymers and nanoparticles with optimized compatibility between biodegradable core and encapsulated drug”

6. Freiburg Macromolecular Colloquium, 26th February 2021, digital

I. Muljajew, M. Chi, A. Vollrath, C. Weber, J. R. Buchheim, B. Beringer–Siemers, S. Stumpf, S. Hoepfner, M. Sierka, U. S. Schubert

“Poly(ester amide)s by step growth polymerization of 2,2’-bis(2-oxazoline) and their compatibility with the hydrophobic anti-inflammatory drug Indomethacin“

7. Retreat meeting of the CRC 1278 PolyTarget, 7th and 8th October 2021, Jena, Germany

U. S. Schubert, I. Muljajew, M. Sierka, M. Chi,

“Tailor-made multifunctional polymers and nanoparticles with optimized compatibility between biodegradable core and encapsulated drug”

Publications **P1** to **P6**

P1: Reprinted with permission from M. Dirauf, C. Weber, U. S. Schubert.

P2: Reprinted with permission from *Macromolecules* **2018**, 51, 5567–5576. Copyright (2018) American Chemical Society.

P3: Reprinted with permission from *Macromolecules* **2020**, 53, 5208–5217. Copyright (2020) American Chemical Society.

P4: Reprinted with permission from Copyright (2020) Royal Society of Chemistry.

P5: Reprinted with permission from *Eur. Polym. J.* **2021**, 156, 110606. Copyright (2021) Elsevier Ltd. Formal publication on ScienceDirect <https://doi.org/10.1016/j.eurpolymj.2021.110606>.

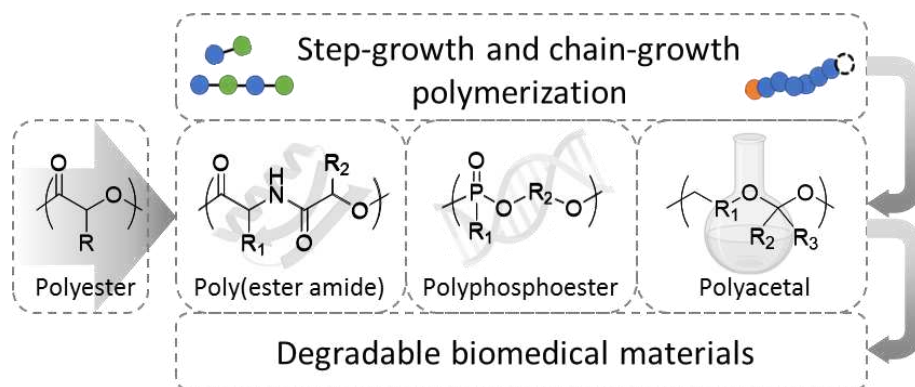
P6: Reprinted with permission from *ACS Nano* **2021**, 15, 12298–12313. Copyright (2021) American Chemical Society.

Publication 1

Recent advances in (bio)degradable polymers – Beyond polyesters

M. Dirauf, I. Muljajew, C. Weber, U. S. Schubert

Prog. Polym. Sci. **2021**, under revision.



Recent advances in (bio)degradable polymers – Beyond polyesters

*Michael Dirauf^{ab}, Irina Muljajew^{ab}, Christine Weber^{ab}, Ulrich S. Schubert^{ab} **

^a Laboratory of Organic and Macromolecular Chemistry (IOMC) Friedrich Schiller University Jena, Humboldtstr. 10, 07743 Jena, Germany.

^b Jena Center for Soft Matter (JCSM), Friedrich Schiller University Jena, Philosophenweg 7, 07743 Jena, Germany.

E-mail: ulrich.schubert@uni-jena.de

ABSTRACT: Polyesters have been studied intensely over the last few decades and proved to be suitable for a wide range of applications. Despite all benefits, drawbacks such as *e.g.* the acidification of the microenvironment during degradation, represent ongoing issues. Therefore, the necessity of developing alternative materials in *e.g.* drug delivery systems represents an emerging field in polymer science. In that regard, this review covers the latest developments of (bio)degradable synthetic polymers beyond polyesters. In spite of seemingly different on first glance, poly(ester amide)s, polyphosphoesters as well as polyacetals have recently experienced a boost with respect to the development of new synthetic routes that enable access to more tailored materials. The successful synthesis and characterization of the new materials represent fundamental premises for the understanding of structure-property relationships which, in turn, form the basis for the development of reasonable tailored pharmapolymers. The review hence scrutinizes the recent synthetic developments of these polymer classes throughout the last 10 years, putting them into the context of applications that have arisen for less novel materials.

KEYWORDS: Poly(ester amide)s, polyphosphoesters, polyacetals, polyketals degradable polymers, step-growth polymerization, ring-opening polymerization.

ABBREVIATIONS:

^1H NMR	Proton nuclear magnetic resonance
ADMET	Acyclic diene metathesis
AL	Aldehyde
API	Active pharmaceutical ingredient
ATRP	Atom-transfer radical polymerization
Boc	<i>tert</i> -Butyloxycarbonyl protective group
<i>b</i> PEI	Branched poly(ethylene imine)
CA	Cyclic acetal
CAGW	Cys-Ala-Gly-Trp
Cbz	Benzyloxycarbonyl protection group
CE	Cyclic ether
CIM	Cyclic imidate mechanism
CM	Comonomer
cPE	Cyclic phosphoester monomer
CREDV	Cys-Arg-Glu-Asp-Val
CROP	Cationic ring-opening polymerization
Cryo-TEM	Cryo-transmission electron microscopy
CTA	Chain transfer agent
DBU	1,8-Diazabicyclo(5.4.0)undec-7-ene
D_h	Hydrodynamic diameter
DLS	Dynamic light scattering
DMAEMA	2- <i>N,N</i> -Dimethylaminoethyl methacrylate
DMP	2,2-dimethoxy propane
DO	Diol
DOTAP	<i>N</i> -[1-(2,3-Dioleoyloxy)propyl]- <i>N,N,N</i> -trimethylammonium methylsulfate

DOX	Doxorubicin
DP	Degree of polymerization
DPP	Diphenylphosphoric acid
DTBP	2,6-Di- <i>tert</i> -butylpyridine
ECs	Endothelial cells
ESI MS	Electrospray ionization mass spectrometry
EtAlCl ₂	Ethylaluminum dichloride
EtSO ₃ H	Ethanesulfonic acid
Fmoc	Fluorenylmethyloxycarbonyl
GlcNAc	<i>N</i> -Acetylglucosamine
HAE	Hemiacetal ester
HCPT	10-Hydroxycamptothecin
HPLC	High performance liquid chromatography
HSAB	Hard and soft acids and bases
HUVEC	Human vascular endothelial cells
IBEA	1-(Isobutoxy)ethyl acetate
IBU	Ibuprofen
IBVE	Isobutyl vinyl ether
IUPAC	International union of pure and applied chemistry
KE	Ketone
LCST	Lower critical solution temperature
LNCaP	Lymph node carcinoma of the prostate
IPE	Linear phosphoester monomer
/PEI	Linear poly(ethylene imine)
M/cat.	Monomer to catalyst ratio
M/I	Monomer to initiator ratio
MALDI MS	Matrix-assisted laser-desorption mass spectrometry

MD	Morpholine-2,5-dione
mPEG	α -Methoxy-poly(ethylene glycol)
N/P	Nitrogen to phosphorous ratio
NADPH	Nicotinamide adenine denucleotide phosphate
NHS	<i>N</i> -Hydroxyl succinimide
OTf	Triflate
PBS	Phosphate-buffered saline
PCL	Poly(ϵ -caprolactone)
PDLA	Poly(D-lactide)
pDNA	Plasmid DNA
PDO	<i>p</i> -Dioxanone
PEA	Poly(ester amide)
PEG	Poly(ethylene glycol)
PEGMA	Poly(ethylene glycol) methacrylate
PEI	Poly(ethylene imine)
PEO	Poly(ethylene oxide)
PEtOx	Poly(2-ethyl-2-oxazoline)
PLA	Poly(lactide)
PLGA	Poly(lactide- <i>co</i> -glycolide)
PLLA	Poly(L-lactide)
PMD	Poly(morpholine-2,5-dione)
PMDETA	N^1 -[2-(Dimethylamino)ethyl]- N^3,N^3 -trimethylethane-1,2-diamine
PNVP	Poly(<i>N</i> -vinyl pyrrolidone)
POx	Poly(2-oxazoline)
PPDO	Poly(<i>p</i> -dioxanone)
PPE	Polyphosphoester
PPEGMA	Poly(poly(ethylene glycol) methacrylate)

PTX	Paclitaxel
REDV	Arg-Glu-Asp-Val
RGD	Arg-Gly-Asp
RGDS	Arg-Gly-Asp-Ser
ROMP	Ring-opening metathesis polymerization
ROP	Ring-opening polymerization
SEC	Size-exclusion chromatography
SEM	Scanning electron microscope
siRNA	Small interfering ribonucleic acid
Sn(Oct) ₂	Tin-(II)-ethyl hexanoate
TBD	1,5,7-Triazabicyclo(4.4.0)dec-5-ene
T _{cp}	Cloud point temperature
TEM	Transmission electron microscopy
TFA	Trifluoroacetic acid
T _g	Glass-transition temperature
THF	Tetrahydrofuran
TIM	Thioimidate mechanism
T _m	Melting point
TMEDA	<i>N,N,N',N'</i> -Tetramethylethan-1,2-diamine
TU	Thiourea
UCST	Upper critical solution temperature
UV	Ultra violet
VE	Vinyl ether
ZnEt ₂	Diethyl zinc

CONTENTS

1. Introduction.....	8
2. Poly(ester amide)s.....	11
2.1. Step-growth polymerization	11
2.2. ROP of cyclic depsipeptides – Poly(morpholine-2,5-dione)s.....	14
2.2.1. Monomer synthesis.....	14
2.2.2. Recent developments regarding the catalysis of the ROP of MD	21
2.2.2.1. Recent developments in the metal-catalyzed ROP of MD.....	22
2.2.2.2. The emerging field of the organo-catalyzed ROP of MD	23
2.2.3. Application guided synthesis of MD containing polymers	28
2.2.3.1. Bulk applications of MD containing polymers.....	29
2.2.3.2. MD containing polymers as drug delivery vehicles	33
2.2.3.3. MD containing polymers for gene delivery.....	40
3. Polyphosphoesters and analogues.....	45
3.1. Phosphoester monomers for acyclic diene metathesis polymerization (IPE).....	46
3.2. PPE derived from ADMET polymerization of IPE	50
3.3. Cyclic phosphoester monomers (cPE)	52
3.4. ROP of cPE monomers	56
4. Polyacetals.....	62
4.1. Step-growth polymerization.....	63
4.1.1. Linear polyacetals from polyaddition of diols and divinyl ethers.....	64
4.1.2. Linear polyacetals from transacetalization polymerization	76
4.1.3. Linear polymers from polyaddition of acetal containing monomers	80
4.2. Chain growth polymerization.....	82
4.2.1. Polymerization of cyclic acetals	83
4.2.2. Copolymerization of cyclic acetals with lactones or vinyl ethers	85
4.2.3. Copolymerization of vinyl ethers with aldehydes.....	89
4.2.4. Copolymerization of vinyl ethers with oxiranes.....	101
4.2.5. Terpolymerization of vinyl ethers with cyclic ethers and ketones.....	104
4.2.6. Ring opening polymerization of hemiacetal esters	108
5. Summary	111

1. Introduction

Nowadays, the global production of plastic based devices is of excessive growth.[1] This is due to the availability of a broad variety of (functional) polymers featuring different mechanical or chemical properties.[2-4] However, most of these materials are not (bio)degradable. In consequence, plastic waste production also increases which, in return, contributes to the pollution of the environment.[5, 6] The logical prerequisite to tackle this issue is the utilization of degradable plastics, ideally derived from renewable resources. In this regard, the class of polyesters is dominating the different application fields with (bio)degradable properties.[7] Considering commodity materials,[8] a range of polyesters are produced on industrial scale, including poly(ethylene terephthalate) (PET), poly(lactic acid) (PLA), poly(butylene succinate), poly(butylene adipate terephthalate) (PBAT, Ecoflex) and polyhydroxyalkonates (PHAs). Such materials that are already serving in numerous applications in textiles or food packaging.[9]

In particular when used in medical or pharmaceutical applications, degradability of polymeric materials represents a crucial factor to avoid accumulation in the organism.[11] Poly(ethylene glycol) (PEG) vacuole formation in the liver represents one example.[10] Potentially, the non-degradable nature of some pharmapolymers hampers their successful transition to pharmaceutical products.[11] Also considering degradable, synthetic polymers for tissue engineering or nanoscaled drug delivery systems, mainly polyesters are on the market or in clinical trials.[11-13] The variety of approved materials includes PLA, poly(glycolic acid) (PGA), poly(ϵ -caprolactone) (PCL), their copolymers, as well as less prominent polyesters such as polyoxalate, poly(butylene terephthalate) or poly(bis-(*p*-carboxyphenoxy)propane-*co*-sebacic acid).[14] The strong research focus on polyesters is possibly due to a faster “bench to bedside” translation as it is more cost and time efficient if the polymeric materials are already used in other pharmaceutical products.

However, there is a clear need for improved approaches and materials. For example, acidification of the microenvironment upon ester degradation can lead to protein destabilization[15, 16] as well as autocatalytic degradation[17] for some polyesters.[18] Pronounced control of degradation pathways are required to avoid short service life times of pharmaceutical products.[19] When poorly water-soluble active pharmaceutical ingredients (API) are encapsulated into hydrophobic polyesters, uncontrolled or unspecific polymer-API interactions can result in API leakage or burst release.[20, 21] In addition, the occurrence of acidic degradation products limits the applicability of such systems to API tolerating decreased pH values in the microenvironment.[18]

Whereas several properties such as crystallinity or hydrophilic-hydrophobic balance (HHB) can be adjusted for polyesters,[22, 23] additional functional moieties can only be introduced as α - or ω -end groups. In view of pharmapolymers with tailor-made adjustments for “personalized” applications, current literature frequently reports alternative (bio)degradable polymer classes that could serve as substitute materials.[24-26] Some of these, such as poly(ester amide)s (PEA) or poly(hemiacetal ester)s maintain the advantages of polyesters and approach such disadvantages through incorporation of additional functional groups in the polymer backbone. The latter may either tailor the degradation behavior or broaden the range of applicable API through possibilities of specific interactions such as, *e.g.*, hydrogen bonding. Other new degradable materials such as poly(2,5-morpholine-dione)s, or polyphosphoesters (PPE) are inspired by natural building units such as amino acids or DNA, which seems promising in terms of bioresorbability.

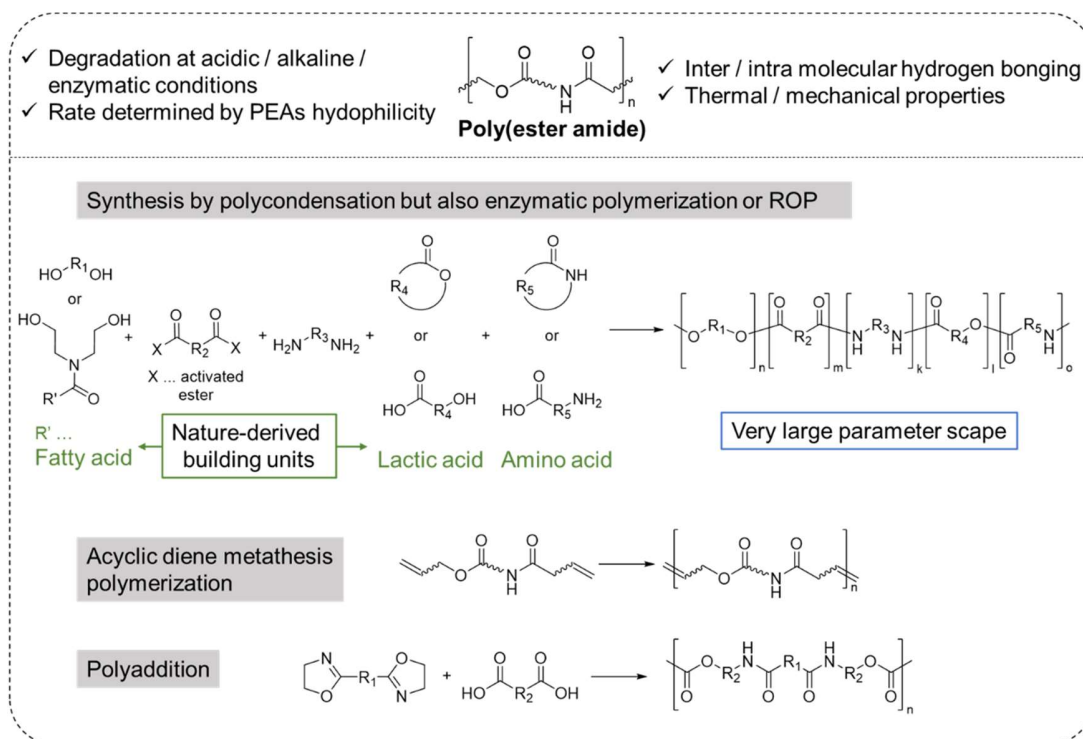
In fact, such advantages of polyester alternatives have been exploited for several years, often with strong focus on exploiting their use as pharmapolymers.[27] In spite of seemingly different on first glance, PEA, polyacetals as well as PPE have recently experienced a boost with respect to the development of new synthetic routes that enable access to more tailored materials. The successful

synthesis and characterization of the new materials represent fundamental premises for the understanding of structure-property relationships which, in turn, form the basis for the development of reasonable tailored pharmapolymers. The review hence scrutinizes the recent synthetic developments of these polymer classes throughout the last 10 years, putting them into the context of applications that have arisen for less novel materials.

2. Poly(ester amide)s

2.1. Step-growth polymerization

Step-growth polymerization represents a versatile approach to yield a manifold of PEAs *via* a variety of methods. The polycondensation of mixtures of commonly used monomers that yield polyesters or polyamides in homopolymerizations represents the simplest approach. AB or AA / BB monomers include diols, diamines, dicarboxylic acids, hydroxy acids or amino acids and their derivatives, which enables an immense parameter space (**Scheme 1**).[28-30] The resulting PEAs are frequently used as prepolymers for, *e.g.* polyurethane[31] synthesis or other coupling methods to increase the molar masses.[32] Whereas typical polycondensation procedures involve harsh reaction conditions, in particular when carboxylic acids are applied as monomers, mild enzymatic polymerization approaches offer several advantages, as has recently been reviewed.[33]



Scheme 1: Advantages of poly(ester amide)s and schematic representation of an overview step-growth polymerizations yielding poly(ester amide)s.

Facilitating intra- and intermolecular hydrogen bonding, amide moieties are incorporated into polyester-based materials to alter the mechanical properties.[34] In turn, polyamides are often modified with ester moieties to accelerate their degradation behavior. The latter is particularly important with respect to avoiding long-term contamination of the environment with commodity plastics. In view of sustainability, current efforts are directed towards development of recyclable materials, at best through depolymerization or hydrolysis yielding the monomers.

Nature provides a range of building blocks that enables the production of PEA from renewable materials. In addition to bifunctional monomers that can be directly used for PEA synthesis, a steadily increasing amount of promising materials based on vegetable oils is currently developed.[35-37] Most approaches rely on a fatty acid amide with diethanolamine, which subsequently acts as a diol monomer to produce ester functionalities with varying dicarboxylic acid derivatives. The biocompatibility and mechanical properties of such materials have led to biomedical applications, *e.g.* for wound healing when loaded with antifungals.[36] Thereby, hydrogen bonding to drugs such as lovastatin or the use of branched materials with decreased glass transition temperature were beneficial for the formulation characteristics.[38]

Besides several hydroxy acids obtained from renewable resources, as *e.g.*, lactic acid, natural amino acids represent obvious biocompatible monomers and have long been applied in several copolymerizations to yield PEA *via* step-growth polymerizations.[39, 40] An adjustment of material properties such as hydrophilicity or hydrolysis rate is possible *via* the dicarboxylic acid (derivatives) and diol used as comonomers.[41] Degraded *via* surface erosion mechanism into less acidic products compared to the standard PLGA, such materials are becoming widely used in various forms for drug delivery. Examples include matrix tablets loaded with ketoprofen,[42] or microspheres for intravitreal drug delivery[43, 44] as well as treatment of arthritis.[45-47]

Replacement of the dicarboxylic acid and diol by ϵ -caprolactone as an AB monomer yielded PEA with the accordingly altered structures as random copolymers with a tendency to alternate. Harsh polymerization conditions ($T > 200\text{ }^{\circ}\text{C}$) were required, in particular when the neat amino acids β -alanine[48] and alanine[49] were used. Use of the glycine and alanine ethyl esters and 1,5,7-triazabicyclo(4.4.0)dec-5-ene (TBD) as catalyst reduced reaction temperatures to $120\text{ }^{\circ}\text{C}$ but racemization could not be fully circumvented.[50] When also the amino acid monomer is replaced by a cyclic monomer, the PEA are in fact obtained *via* a chain-growth polymerization, as *e.g.* reported for the copolymerizations of ϵ -caprolactam / lactide[51] or ϵ -caprolactam / ϵ -caprolactone.[34] Such approaches enabled access to PEA block copolymer architectures through the use of Jeffamines®, an amino endfunctionalized polyether, as macroinitiators and sequential monomer addition.[52, 53]

Other less common functional moieties also enable access to PEA *via* step growth polymerizations. Often used for coupling of precursors to achieve high molar mass polymers,[54-58] the AA+BB polyaddition of bisoxazolines and dicarboxylic acids facilitates access to PEAs without the need to remove condensation products.[59-62] The advantage holds true also for the polyaddition using analogous AB[63] or AB₂ monomers.[64, 65] Mainly, the polymerization of aromatic bis(2-oxazolines) is exploited focusing on the thermal properties of the resulting polymers.[66-71] In contrast, the application of the simple 2,2'-bis(2-oxazoline) as monomer resulted in PEAs with an oxamide repeating unit. These polymers were investigated as nanocarriers for the hydrophobic drug indomethacin.[61, 62, 72]

Another alternative approach towards PEA is the polymerization of monomers containing the respective esters and amides *via* reaction of other functional groups, as reported in the acyclic diene metathesis (ADMET) polymerization of a diglycine diene derivative with ethyleneglycol

dimethacrylate.[73] Also a hyperbranched PEA featuring hydroxyl moieties is commercially available and opens avenues for the straightforward introduction of other functional groups *via* post-polymerization reactions.[74]

2.2. ROP of cyclic depsipeptides – Poly(morpholine-2,5-dione)s

Chain-growth polymerization represents a powerful tool to synthesize high molar mass polymers. Regarding the PEA synthesis, particularly the ring-opening polymerization (ROP) of cyclic monomers, the morpholine-2,5-diones (MD), represents the most commonly applied polymerization procedure. The resulting materials feature strictly alternating ester and amide moieties along the polymer backbone. Their degradation products are based on α -hydroxy and α -amino acids. Since Helder *et al.* reported the first successful homopolymerization of 6-methylmorpholine-2,5-dione in 1985,[75] this synthesis approach has become the most commonly applied strategy to obtain PEA from MD. This review covers the latest developments of this research aspect. Further information can be found in other reviews.[76-78] In particular, the review by Feng *et al.* presents a comprehensive summary of the literature until 2010.[77] Due to the rapidly growing interest and latest developments in PEA research, we aim for closing this gap and provide a summary of the recent reports.

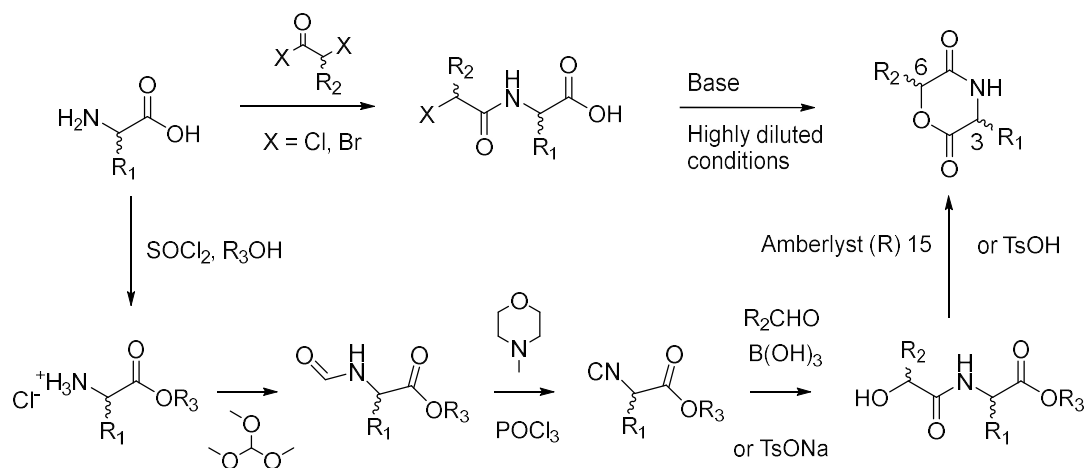
2.2.1. Monomer synthesis

Different strategies towards the synthesis of MD monomers have been developed, as detailed in the review article by Basu *et al.*[76] Generally, MD are synthesized from α -amino acids as starting materials. In a first step, a linear precursor is generated through covalent attachment of an α -hydroxy acid derivative. This can be either done *via* the carboxylic acid moiety of the α -amino acid to result in an ester precursor, or *via* the carboxylic acid moiety of the α -hydroxy acid leading

to an amide moiety. The latter approach is frequently performed in recent literature reports and will therefore be highlighted in the following (**Scheme 2**, top). The amino acid is reacted with chloroacyl chlorides or bromoacyl bromides, yielding the respective *N*-(α -haloacyl)- α -amino acid precursor. The subsequent cyclization is performed in highly diluted solution at moderate temperatures in order to avoid the formation of oligomers. The purified monomers are typically obtained after column chromatography, recrystallization, or a combination of both. However, the comparably low final yields of the MD monomers represent a drawback of this established synthesis procedure. Although varying significantly from report to report, rather poor to moderate yields ranging from 7% for highly sterically hindered MD (*vide infra*, **MD15**),^[79] up to about 50% for the mostly utilized 3-methyl-morpholine-2,5-dione (*vide infra*, **MD8**) were reported.^[80-83]

Aiming at overcoming this limitation, Zi-Chen and coworkers demonstrated a new approach providing MD monomers in excellent yields (**Scheme 2**, bottom).^[84] Instead of utilizing the α -amino acids directly for the precursor synthesis, the amino moieties are converted to their corresponding isocyanides and subsequently reacted with aldehydes in a Passerini type reaction, yielding the *N*-(α -hydroxyacyl)- α -amino acid precursors in yields from 82 to 91%. Different substituents in 3- and 6-position were introduced by choice of the amino acid and the aldehyde, whereby the stereocenter in 3-position was retained and therefore pre-determined by the α -amino acid. The subsequent cyclization of the precursor was achieved under reflux conditions in toluene utilizing catalytic amounts of Amberlyst (R) 15 ion-exchange resin or *p*-toluenesulfonic acid (TsOH). Nine MD monomers, ultimately derived from glycine, L-leucine or L-phenylalanine were obtained with respective cyclization yields varying between 71 and 90%. The respective overall yields from 60 to 77% thus emphasize the great potential and variability of this new approach. It

should be noted that the stereocenter in 6-position cannot be pre-determined because this carbon atom generates a prochiral center throughout the reaction, resulting in a mixture of diastereomers.



Scheme 2. Schematic representation of the different synthesis routes towards MD monomers.

MD can generally be categorized in monomers with hydrocarbon substituents (**Figure 1**, **MD1** to **MD16**), and heterocycles comprising substituents with additional functional moieties (**Table 1**, **MD17** to **MD30**). For clarity, each MD is assigned to a specific number herein, which is defined in **Figure 1** or **Table 1**. The individual numbers will be referred to in the following text.

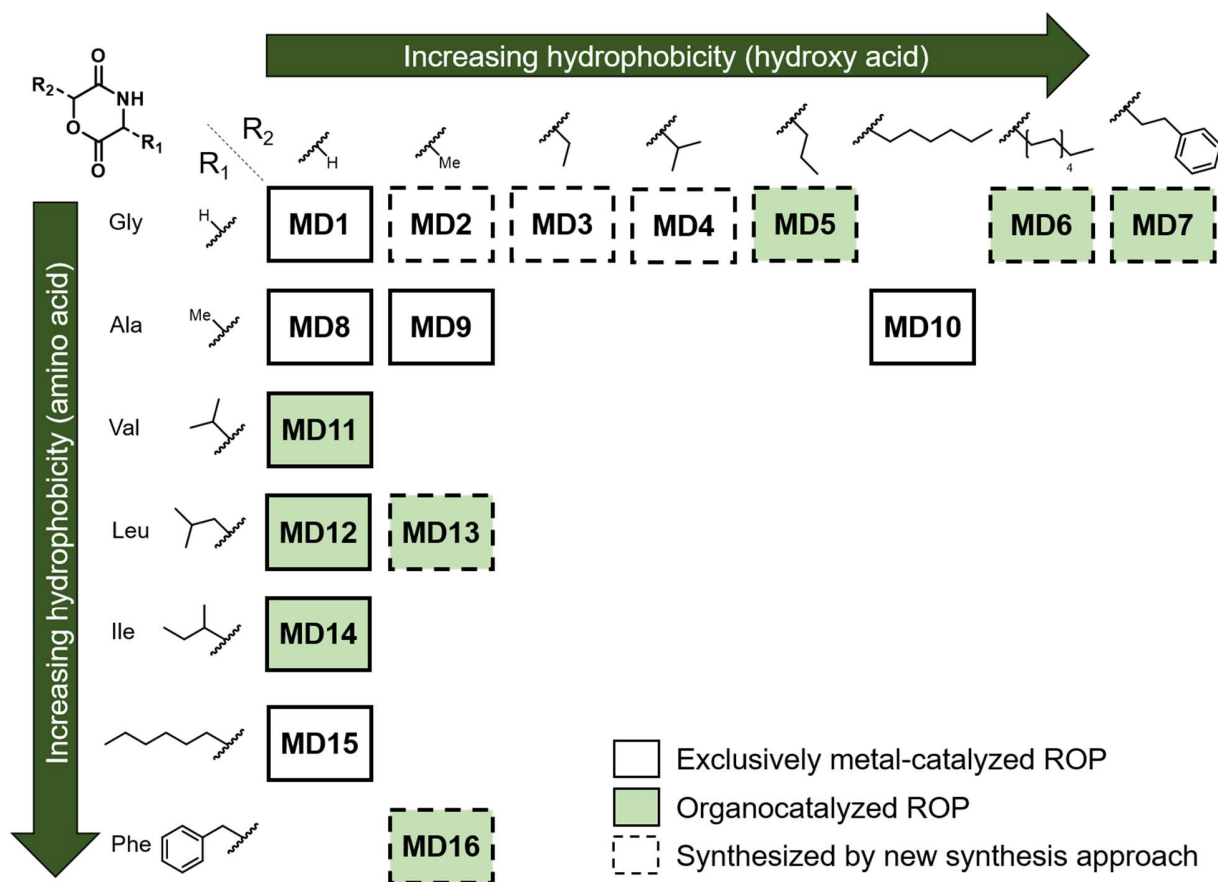


Figure 1. General schematic overview of MD monomers with hydrocarbon substituents reported in the last decade. The color indicates the application of the individual MD in organo- or metal-catalyzed ROP. MD with dashed frames were obtained *via* the monomer synthesis pathway as reported by Zi-Chen and coworkers.[84]

As shown in **Figure 1**, a broad variety of MD with varying hydrophilicity or hydrophobicity has been reported and polymerized *via* ROP throughout the last decade. Interestingly, at least one site of the heterocyclic monomer comprises a non-sterically demanding moiety (such as hydrogen or methyl), whereas the other substituent can be of higher steric demand. However, no reports on monomers with two sterically demanding groups were published. This might be due to a low reactivity caused by the steric hindrance of such monomers potentially hampering the ROP

process. In addition, already **MD10** and **MD15** featuring only one highly sterically demanding substituent were accessible in low yields of 7 and 15%, respectively.[79]

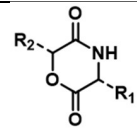
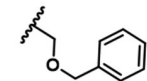
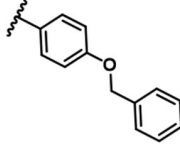
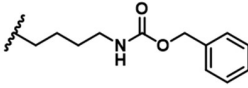
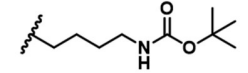
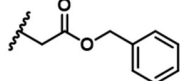
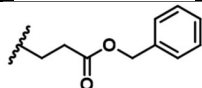
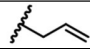
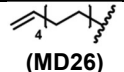
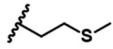
Aiming at materials that can be readily functionalized in post-polymerization modification approaches, thioethers (**MD27** to **MD30**) as well as allyl groups (**MD25** and **MD26**) have been incorporated into MD monomers. The latter was used to functionalize PEA by radical thiol-ene additions using various thiols featuring additional reactive groups, including amines, carboxylic acids and alcohols.[85] However, the conversions varied significantly dependent on the applied thiol (quantitative for the carboxylic acid and alcohol decorated thiols, < 25% for sterically hindered non-functional thiols). Most PEA retained an intact backbone structure during the post-polymerization functionalizations. However, the amino moiety at the respective thiol induced backbone degradation. In contrast, the PEA chains of the methionine based **PMD26** remained intact during oxidation utilizing hydrogen peroxide in formic acid.[86] The nucleophilic character of methionin's sulfur atom was furthermore exploited in nucleophilic substitutions using propargyl bromide or propylene oxide resulting in polymers featuring positively charged sulfonium sidechains.[86]

On the other hand, functional groups such as amines, alcohols or carboxylic acids can also be present in MD monomers by choice of the amino acid used for the monomer synthesis. However, neither the ROP of MD, nor the monomer synthesis tolerate these functional groups. As a consequence, protection prior to monomer synthesis, and deprotection subsequent to polymerization is mandatory. However, synthetic methods benefit from protection group chemistry that has been well-established within peptide research. The commercial availability of various *tert*-butyloxycarbonyl (Boc), benzyl- or benzyloxycarbonyl (Cbz)-protected α -amino

acids has thus promoted the frequent introduction of functional moieties in 3-position of the MD monomer (R1 in **Table 1**).

For instance, a copolymer composed of the benzyl protected serine-based **MD18** and lactide was deprotected in a hydrogenation approach without notable main chain degradation at degrees of deprotection of about 90%, yielding a PEA with pendant hydroxyl moieties.[87] The deprotection strategies for Cbz-protected lysine containing PEA was accomplished either by treatment with HBr/HOAc, or by hydrogenations. Klok *et al.* utilized both methodologies aiming to gain access to a quantitatively deprotected **PMD20** homopolymer, however, either resulting in incomplete deprotection or in backbone degradation.[85] Similar difficulties occurred during deprotection of the Boc protected **PMD22** homopolymer. In contrast, Ohya and coworkers reported successful deprotection of copolymers composed of lactide and either the Cbz-protected lysine-based **MD20** or the benzyl protected asparagine-based **MD23** (5 mol%, respectively) with degrees of deprotection of 70 to 85%.[88] Copolymers featuring the glutamic acid-derived benzyl-protected **MD24** (up to 30% **MD24**) were deprotected by hydrogenation in a quantitative manner without degradation.[89] Apparently, high degrees of deprotection without main chain degradation can be achieved for statistical copolymers featuring a comparably low molar fraction of MD, whereas the deprotection of PEA homopolymers derived from MD based on functional amino acids is not straightforward.

Table 1. Overview of functional MD monomers including protective groups, deprotection strategies as well as possible post-polymerization modification reactions.

	R ₁ (Amino acid)	R ₂ (Hydroxy acid)	Deprotection	Function	Possible modifications	Homopolymer	Copolymer (mol% feed)	Ref.
L-Ser		H (MD17)	Hydrogenation	-OH	Esterification	x	/	[90]
		Me (MD18)				/	x (up to 10%)	[87]
L-Tyr		H (MD19)	Hydrogenation	-OH	Esterification	x	/	[90]
L-Lys		H (MD20)	HBr/AcOH	-NH ₂	Amidation	x	x (5%)	[85, 88]
		Me (MD21)	Hydrogenation			/	x	[91]
L-Lys		H (MD22)	TFA	-NH ₂	Amidation	x	/	[85]
L-Asp		H (MD23)	TFA/ thioanisole	-COOH	Amidation, esterification	/	x (5%)	[88, 89, 92, 93]
L-Glu		H (MD24)	Hydrogenation			/	x (up to 30%)	
allyl-Gly		H (MD25)	Not necessary	Allyl	Radical thiol-ene addition	x	/	[85]
Gly	H	 (MD26)				x	/	[84]
D,L-Met		H (MD27)	Not necessary	Thio-ether	Oxidation, addition	x	/	[86]
		Me (MD28)				x	/	
		Et (MD29)				x	/	
		nBu (MD30)				x	/	

2.2.2. Recent developments regarding the catalysis of the ROP of MD

In general, the ROP of MD proceeds in a similar fashion as that of cyclic ester monomers such as, *e.g.*, lactide or glycolide. Besides early enzyme mediated polymerizations as detailed by Feng,[77] recently applied ROP catalysts can be categorized into metal- or organo-based systems. Nowadays, in particular the utilization of organocatalysts represents an emerging field. On the other hand, a significant push towards the optimization of the metal-catalyzed ROP is clearly evident from current reports. The following section highlights the individual approaches and details the achieved developments. **Figure 2** illustrates recently applied catalysts and **Table 2** summarizes characterization data as well as reaction conditions.

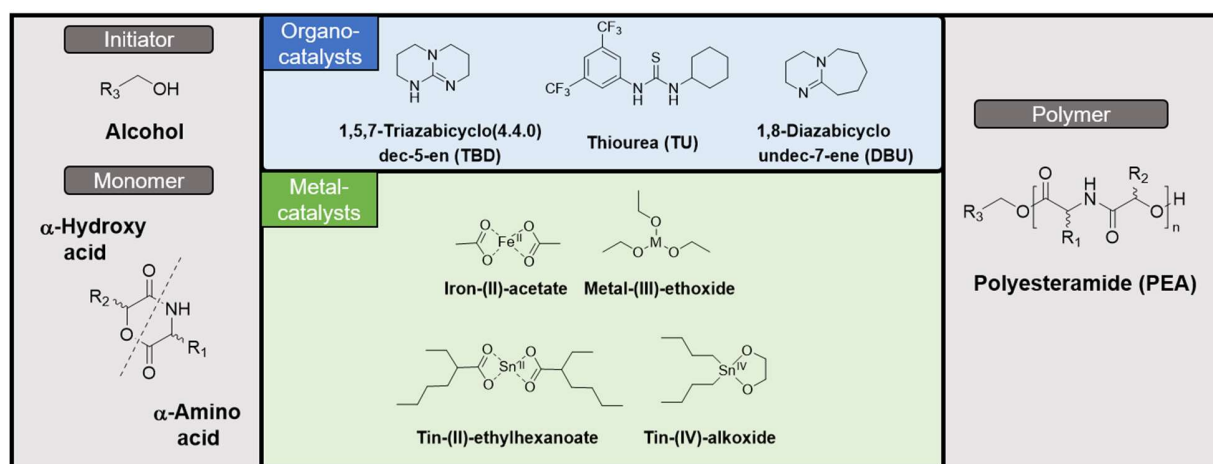


Figure 2. Left: Schematic representation of applicable initiators and MD monomers. Middle top: Schematic representation of utilized organo-catalysts. Middle bottom: Schematic representation of recently applied metal-based catalysts. Right: Schematic representation of PEA structures derived from ROP of MDs.

2.2.2.1. Recent developments in the metal-catalyzed ROP of MD

Tin(II)-ethylhexanoate ($\text{Sn}(\text{Oct})_2$) still represents the most common catalyst in a broad variety of ROPs, also for the preparation of PEA derived from MD. This is due to its robustness, commercial availability as well as ease of handling. For instance, Lendlein and coworkers utilized this catalyst to gain access to PEA with varying aliphatic sidechains ranging from low (**MD8**) up to higher sterical demand (**MD14**, **MD10** and **MD15**) by applying typically used bulk polymerization conditions.[79, 94] Noteworthy, the authors additionally tested a polymerization in toluene but conversions and final yields were rather poor. This observation demonstrates one key restriction of this catalyst, which is the necessity of high reaction temperatures to actively catalyze the ROP, limiting potential solvents to those featuring high boiling points. Apart from this, severe drawbacks such as the broadening of the molar mass distributions and rather long reaction times (up to days) intrinsically hamper the preparation of tailor-made well-defined polymeric materials. Therefore, recent metal-catalyzed ROPs aim to overcome these issues.

The $\text{Sn}(\text{Oct})_2$ catalyzed ROP of MD featuring functional groups in 3-position in bulk was optimized for the Cbz protected lysine-based **MD20**. [85] In a broad screening of the monomer to catalyst (M/cat.) ratio without additional initiator, the highest molar masses were achieved by applying a low M/cat. ratio of 40. Although this came to the cost of limited molar masses ($\text{DP} \approx 60$) and broad dispersity ($\text{Đ} \approx 2$) values due to chain-transfer reactions occurring at higher conversions, this ROP represents one of the few homopolymerizations reported for functional MD monomers. It was further applied using the Boc-protected lysine based monomer **MD22** and **MD25** comprising a double bond.

In another approach, the HSAB principle was considered as a key factor for the catalytic activity of metal-based catalysts in the ROP of MD.[90] In a screening of different metal complexes (see

Table 2), the authors observed that $\text{Fe}(\text{OAc})_2$, featuring a softer metal center than $\text{Sn}(\text{Oct})_2$, was more efficient in the 1,8-octanediol initiated ROP of **MD14** and **MD17** (based on isoleucine and benzyl-protected serine, respectively). This behavior was explained by a weaker metal-oxygen bonding promoting the propagation. However, $\text{Sn}(\text{Oct})_2$ was superior for the ROP of **MD19** based on benzyl-protected tyrosine, most likely due to the larger ion radius of Sn^{2+} enhancing the interaction of the catalyst center with the ester moiety of the more sterically hindered monomer. In addition, various metal-ethoxides (In^{II} , Fe^{III} , Mg^{II} and Al^{III}) were tested, however, without sufficiently catalyzing the ROP. In contrast, a Sn^{IV} alkoxide prepared from ethylene glycol acted as efficient catalyst / initiator in the ROP of **MD14**.^[95] Even at high temperatures, PEA with two defined hydroxyl ω -end groups were produced *via* this bifunctional initiator, as confirmed by matrix-assisted laser-desorption mass spectrometry (MALDI MS). The catalytic system was furthermore applied for various copolymers comprising **MD8**, **MD14** and **MD12**. These studies clearly demonstrate the achieved progress in the development of optimized metal-based ROP of MD, however also showing that the replacement of $\text{Sn}(\text{Oct})_2$ can be cumbersome due to its versatility being able to polymerize most MD.

2.2.2.2. *The emerging field of the organo-catalyzed ROP of MD*

On the other hand, highly active organocatalysts have gained considerable attention among the community opening a novel synthesis procedure that circumvents problems affiliated with the usage of $\text{Sn}(\text{Oct})_2$.

Pioneering this strategy back in 2005, Hedrick and coworkers utilized *N*-heterocyclic carbenes and a combination of (-)-sparteine with a thiourea (TU) cocatalyst for the polymerization of **MD9** or **MD13**.^[96, 97] Interestingly, this approach was only revisited recently applying the “super-base” catalyst TBD.^[98] Five MD based on glycolic acid and aliphatic α -amino acids were polymerized

at room temperature in solution. Narrowly dispersed PEA were obtained from the soluble **MD11**, **MD12** and **MD14**, respectively. Although hampered by inter- and intramolecular transesterification processes at higher conversions, precise molar mass, α - and ω - end group control was possible through choice of the initiating alcohol BnOH up to moderate monomer conversions. Shortly after, Zi-Chen and coworkers found that the loss of control was avoided when a TU based co-catalyst was added, enabling access towards various high molar mass PEA with low dispersity values ($\mathcal{D} < 1.1$) even at quantitative conversions. In addition, a block copolymer was obtained by sequential monomer addition.[84] Similar findings were reported for the 1,8-diazabicyclo(5.4.0)undec-7-ene (DBU) catalyzed ROP of **MD12**. [99] In detail, a dispersity drop from 3.06 to 1.15 was achieved when 10 eq. TU were applied. In terms of the homopolymerization kinetics, an increased amount of TU led to a decrease of the polymerization rate because it promoted a thioimidate mediated (TIM) polymerization mechanism. Whereas TIM is somewhat slower compared to the cyclic imidate mechanism (CIM) mainly occurring without TU, it grants good control over the polymerization. Additionally, the authors demonstrated that the use of primary alcohols as initiators resulted in a faster initiation when compared to secondary ones.

Also the organocatalytic polymerization of methionine based MD (**MD27** - **MD30**) was investigated in detail.[86] Firstly, **MD27** was polymerized in different chain lengths using a DBU/TU binary catalyst system, yielding well defined materials ($\mathcal{D} \leq 1.11$). When the more sterically demanding and less reactive monomers **MD28** and **MD29** were used, a weaker TU needed to be applied to promote the polymerization. The bulkiest **MD30** could, however, not be polymerized.

MD monomers also allow the inclusion of isolated L-alanine units into PLA through copolymerization with lactide. This was comprehensively investigated for the DBU and TBD

catalyzed, BnOH initiated copolymerization of L-lactide with 20 mol% **MD9**.^[100] Detailed kinetic and thermodynamic analyses were based on variation of key parameters such as the temperature, initial total monomer concentration and solvent polarity. In-depth NMR studies of the resulting materials proved the absence of isolated PEA blocks in the copolymer. The combination of DBU and TU as a catalyst system was also applied in a copolymerization of **MD12** with L-lactide in feed fractions from 25 to 75 mol%.^[99] The introduction of secondary alcohol-based chain ends through the lactide comonomer significantly decreased the polymerization rate of the MD monomer. As MD chain ends based on glycolic acid were more reactive compared to lactide chain ends, this resulted in gradient copolymers enriched with lactide in the beginning of the chain ($r_{LA} = 1.94 > 1 > r_{MD} = 0.26$, Finemann-Ross method). Noteworthy, creatinine acetate as a biogenic catalyst was also successfully utilized in the copolymerization of L-lactide with up to 10 mol% of the benzyl protected serine based **MD18**.^[87]

Table 2. Reaction conditions and selected characterization data of the PEA homopolymers.

Monomer	Initiator	Catalyst	Solvent	T (°C)	t (h)	M/I	M _n ^a (g mol ⁻¹)	Đ ^a	Ref.
MD15	Ethylene glycol	Sn(Oct) ₂	Bulk	140	18	30	5,600	1.2	[79]
MD10	Ethylene glycol	Sn(Oct) ₂	Bulk/toluene ^c	140	12	28	5,400	1.2	
MD8	Ethylene glycol	Sn(Oct) ₂	Bulk/toluene ^c	140	16	46	5,700	1.4	
MD20	None	Sn(Oct) ₂	Bulk	110	20	40 ^b	24,400	2.5	[85]
MD22	None	Sn(Oct) ₂	Bulk	110	20	40 ^b	21,700	2.0	
MD25	None	Sn(Oct) ₂	Bulk	110	20	40 ^b	13,300	1.8	
MD14	1,8-Octane diol	Fe(OAc) ₂ Sn(Oct) ₂ In(OEt) ₃ Mg(OEt) ₂ Al(OEt) ₃ Fe(OEt) ₃	Bulk	135 to 160	3.5 to 24	29	3,100 to 5,800	1.13 to 1.19	[90]
MD18	1,8-Octane diol	Fe(OAc) ₂ Sn(Oct) ₂	Bulk	135	5 to 24	29	4,700 to 7,800	1.26 to 1.45	
MD19	1,8-Octane diol	Fe(OAc) ₂ Sn(Oct) ₂	Bulk	150	5 to 24	29	6,000 to 8040	1.27 to 1.41	

Table 2. Continued.

MD8	Ethylene glycol	Sn ^{IV} salt	Bulk	140	24	n.a.	13,000	1.7	[95]
MD14	Ethylene glycol	Sn ^{IV} salt	Bulk	140	24	n.a.	14,000	1.5	
MD12	Ethylene glycol	Sn ^{IV} salt	Bulk/toluene ^d	140	24	n.a.	11,000	1.5	
MD1	Benzyl alcohol	TBD	THF ^c	RT	1	100	4,500	1.41	[98]
MD8	Benzyl alcohol	TBD	THF ^c	RT	1	100	6,500	1.27	
MD11	Benzyl alcohol	TBD	THF	RT	0 to 1	100	9,500 to 16,600	1.12 to 1.27	
MD12	Benzyl alcohol	TBD	THF	RT	0 to 1	100	7,600 to 16,300	1.10 to 1.17	
MD14	Benzyl alcohol	TBD	THF	RT	0 to 1	100	10,200 to 21,000	1.13 to 1.34	
MD5	Benzyl alcohol	DBU/TU	CH ₂ Cl ₂	25	0 to 5	100	5,000 to 12,500	1.06 to 1.12	Selected examples from [84]
MD26	Benzyl alcohol	DBU/TU	CH ₂ Cl ₂	25	0 to 5	100	5,000 to 22,500	1.06 to 1.10	
MD16	Benzyl alcohol	DBU/TU	CH ₂ Cl ₂	25	0 to 5	100	4,000 to 13,500	1.06 to 1.07	
MD12	Benzyl alcohol	DBU/TU	CH ₂ Cl ₂	40	5 to 20 min	50 to 150	8,600 to 25,200	1.15 to 1.49	[99]
MD27	Benzyl alcohol	DBU/TU	CHCl ₃	RT	3 to 6	25 to 100	8,100 to 25,600	1.07 to 1.11	[86]
MD28	Benzyl alcohol	DBU/TU	CHCl ₃	RT	8	100	23,700	1.11	
MD29	Benzyl alcohol	DBU/TU	CHCl ₃	RT	24	100	28,200	1.10	

a) SEC values; b) M/cat. ratio; c) not/partially soluble; d) low conversion.

2.2.3. Application guided synthesis of MD containing polymers

Combining the individual features of different polymer classes enables the synthesis of tailor-made materials and can, therefore, be beneficial when targeting specific physicochemical properties. Besides solely relying on copolymerization, also more sophisticated morphologies such as (multi)block copolymers, covalently crosslinked hydrogels or material blends have been utilized to serve numerous purposes. The recent developments in the fabrication of polymers featuring MD are mostly application driven (**Figure 3**), e.g. tailoring the of the degradation rates of polyesters, tissue engineering or shape memory materials, gene delivery platforms, or the encapsulation or conjugation of API. Such covalent functionalizations rely on post-polymerization modification reactions of PEA obtained through incorporation of MD monomers featuring functional moieties.

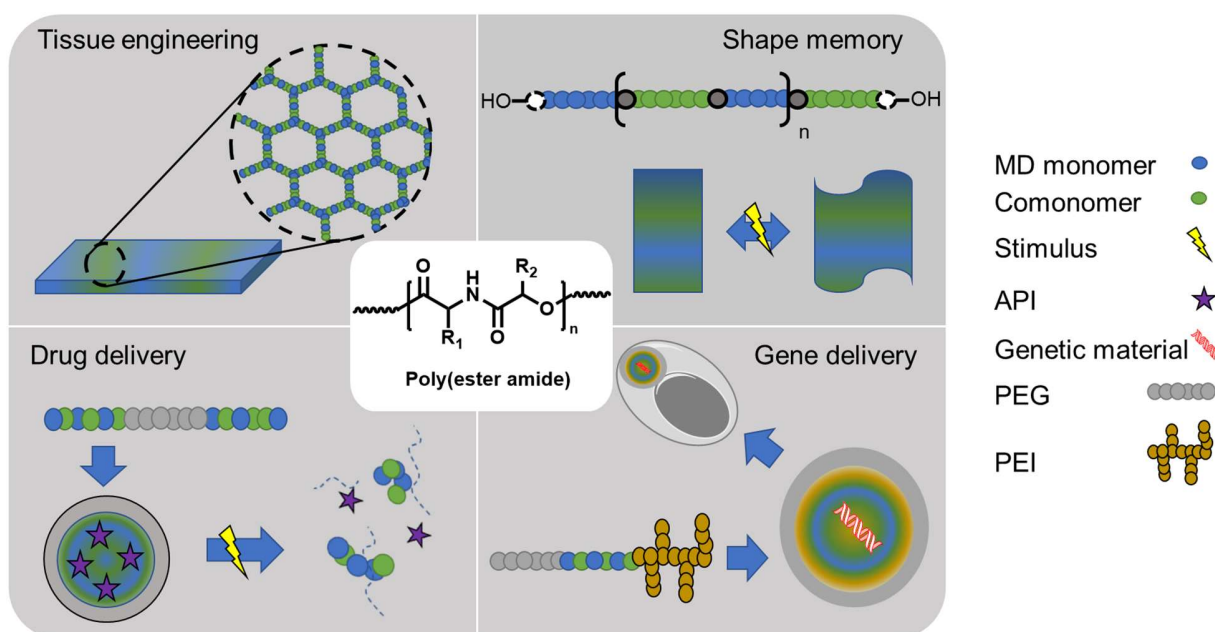


Figure 3. Schematic overview of recent application fields of polymers derived from MD monomers.

2.2.3.1. Bulk applications of MD containing polymers

Thermal properties, such as the glass transition temperature (T_g) or melting events of homo- or stereocrystallites represent macroscopic properties that have been tailored for MD containing polymers. Depending on the substituents (**MD1**, **MD8**, **MD11**, **MD12** and **MD14**) PEA are either amorphous or partially crystalline.[101-104] Among these PEA featuring either no or C_1 to C_4 substituents, only **PMD11** with an isopropyl substituent is unable to crystallize. PEA based on glycine (**PMD1**), alanine (**PMD8**) and leucine (**PMD12**) feature T_m values above 190 °C, whereas the T_m value of the isoleucine-derived **PMD14** is significantly lower at 74 °C. Expanding the field of MD based homopolymers, a study by Lendlein and coworkers described PEA with hexyl substituents featuring a relatively low T_g of around 35 °C.[79] This was achieved by the $Sn(Oct)_2$ catalyzed bulk ROP of **MD15** and **MD10**, carrying a hexyl substituent in 3- or 6-position, respectively.

The copolymerization of **MD8** with a sterically demanding cyclic carbonate monomer resulted in thermal properties that were adjustable through **MD8** mass fractions from 18.5 to 100 wt%.[81] T_g values of the amorphous copolymers increased significantly with higher carbonate monomer content due to its rigid character. Tsuji *et al.* recently demonstrated the stereocomplexation of PLLA/PDLA comprising featuring up to 13 mol% alanine units obtained by copolymerization of lactide with 20 mol% **MD9** featuring the respective stereocenter.[105] As typical for stereocomplexation, stereocrystallites featured increased T_m values compared to homocrystallites. Depending on the stereocomplexation conditions, the alanine units could be selectively included or excluded from the stereocrystallites.

The partial crystallinity of PEA derived from **MD12** was exploited for the generation of shape memory polymers. In this regard, Lendlein and coworkers focused on the development of

multiblock copolymers fabricated by polyaddition of **PMD12** ($M_n = 9,300 \text{ g mol}^{-1}$) and oligo- ϵ -caprolactone (PCL, $M_n = 2,700 \text{ g mol}^{-1}$) polyols with trimethylhexamethylene diisocyanate (**Figure 4**).[106] The crystalline domains of the **PMD12** represented anchor points defining the permanent shape due to their high T_m value, whereas the crystalline PCL domains as well as the T_g of the **PMD12** were used for temporary shape fixation. After deformation to 200% strain, the material recovered efficiently the initial shape. Follow-up studies described the influence of the physical programming parameters on the shape memory ability of the multiblock copolymer,[107] the tuning of the surface morphology,[108] and potential applications in modern compression textiles.[109] **PMD12**-PCL multiblock copolymer based fibers were also modified with peptides aiming at enhanced HUVEC adhesion and proliferation and to reduce protein adsorption.[110] In addition, the multiblock copolymers were utilized as a matrix material for polyester-based microparticles for gene delivery.[111] The system was further improved by the incorporation of spider fibroin, thereby enhancing the mechanical properties and biocompatibility.[112].

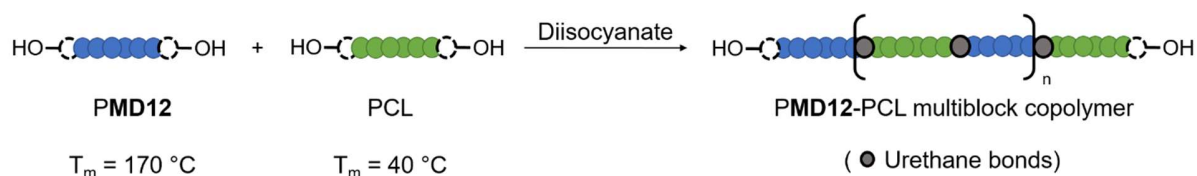


Figure 4. Schematic representation of the synthesis approach towards **PMD12**-PCL multiblock copolymers.

Materials for tissue engineering represent another application of MD containing polymers. **Figure 5** summarizes the applied synthetic strategies. Statistical copolymers comprising either hydrophobic or functional MD monomers were directly used for this purpose. Covalently crosslinked materials have been accessed through star-shaped MD containing macromonomers with methacrylate end groups.

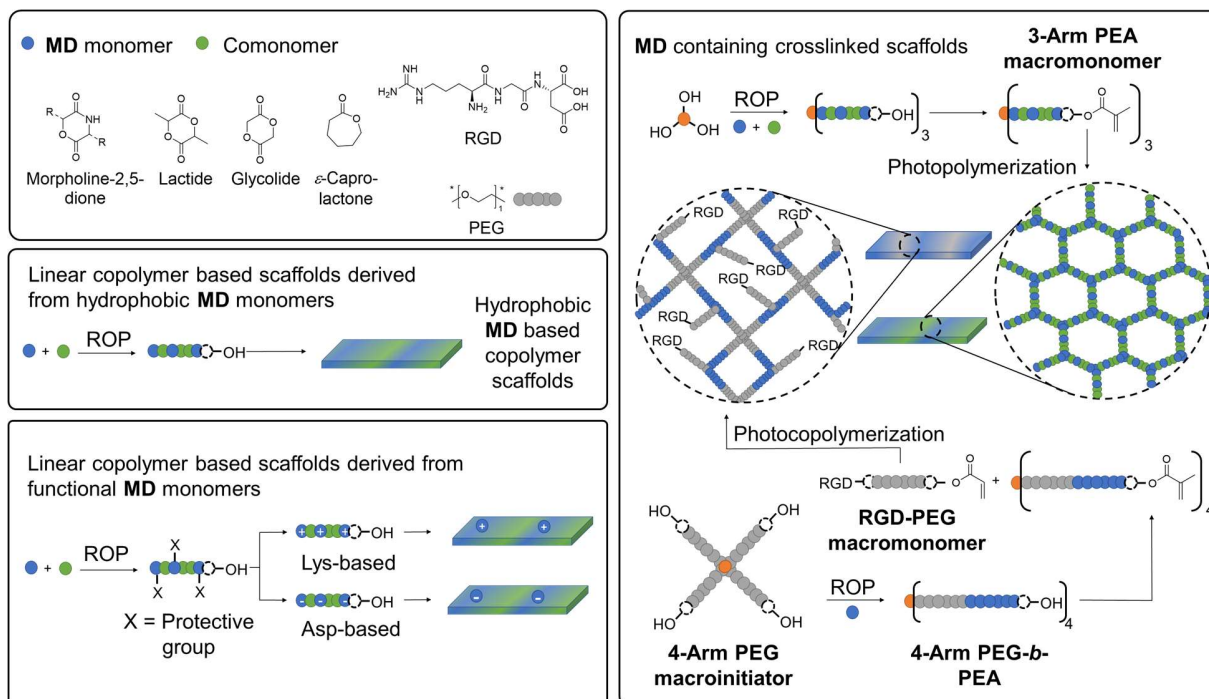


Figure 5. Schematic depiction of recent synthesis strategies towards MD containing materials used for tissue engineering. Schematic representations of the key structural elements for the fabrication of such materials are depicted in the top left corner.

The alanine-based **MD8** was utilized to improve the mechanical properties of PLGA nanofibers applied for vascular tissue engineering.[113] Introduction of up to 17.4 wt% **MD8** in a statistical copolymer lowered the tensile strength in the wet state and significantly increased the elongation at break. Cell proliferation of human vascular endothelial cells (HUVEC cells) was also improved, and cells penetrated the partially degraded subcutaneous implant prepared from the material.

MD monomers based on of L-Lys or L-Asp (**MD20** or **MD23**, respectively) were used to introduce 5% charged moieties in PLA.[88] PEA containing scaffolds loaded with physically entrapped growth factors for tissue regeneration indeed revealed a faster release than solely PLLA based scaffolds, presumably due to a higher hydrolysis rate of the PEA containing polymers. This

resulted in enhanced cell proliferation and superior attachment of rat PC12 pheochromocytoma cells. In particular, the slightly positively charged L-Lys based copolymer scaffold promoted differentiation into nerve-like cells, emphasizing a potential use of this material for enhanced nerve regeneration.

Elomaa *et al.* reported the fabrication of crosslinked three-dimensional polymer scaffolds for tissue engineering by photopolymerization of **MD8** containing macromonomers.[80] Firstly, a three-arm macromonomer was synthesized by copolymerization of ϵ -caprolactone with up to 10 wt% **MD8**. Subsequent methacrylation of the hydroxyl end-groups enabled the photopolymerization process, resulting in a highly crosslinked polymeric scaffold. Biocompatibility was proven by incubation of the material with HUVEC. After treatment for seven days, a 10-fold amount of the initial cells was reported. For testing of the bone regeneration ability, C3H10T1/2 bone cells were seeded on the scaffolds, also revealing enhanced cell proliferation.

A four-arm PEG-*b*-(**MD8**-methacrylate)₄ macromonomer was utilized to fabricate high-density crosslinked hydrogels by visible light stereolithography.[114] For this purpose, a methacryl functionalized PEG-RGDS conjugate was copolymerized with the star-shaped macromonomer to enhance cell attachment due to the presence of the integrin-specific RGDS functions. In general, these hydrogels were softer compared to PEG hydrogels and their stiffness was in the range of natural tissue material. Initial *in vitro* degradation experiments revealed that the mass loss could be tailored by the applied photopolymerization time, *i.e.* the crosslinking density. The degradation of cell-laden hydrogels occurred throughout cell proliferation, thus enabling cell penetration into the scaffold.

2.2.3.2. MD containing polymers as drug delivery vehicles

The application of PEA made from MD monomers as drug delivery vehicles represents a highly emerging field. In general, the MD monomers serve two purposes (**Figure 6**): a) Hydrophobic MD are utilized for particle formulation of PEA homopolymers or to tailor the degradation rate of polyester based materials through copolymerization. b) Functional MD allow access to macromolecular prodrugs, and the attachment of targeting functions or hydrophilic “stealth” polymers *via* post-polymerization modifications. Alternatively, the latter can be introduced by using PEG or poly(2-oxazoline)s (POx) with hydroxyl end groups as macroinitiators for the ROP of MD monomers.

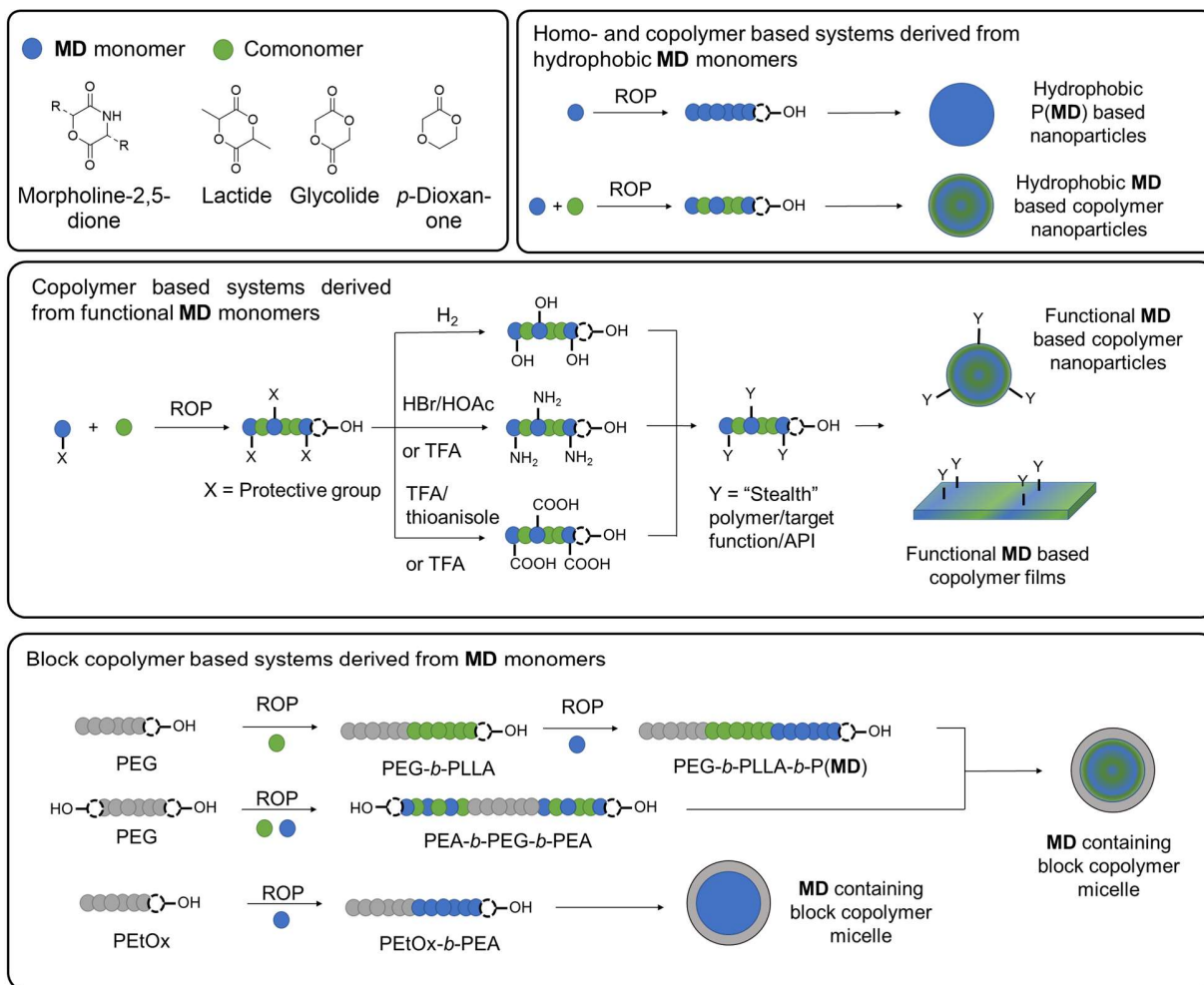


Figure 6. Schematic representation of the synthesis strategies towards PEA based drug delivery systems derived from MD.

The bioavailability of hydrophobic API can be increased through formulation in nanoparticles composed of degradable hydrophobic polymers. PLGA represents the standard material utilized for this purpose. Nanoparticles made of PLA comprising 5 mol% of the leucine-based MD12 (1 in **Figure 7**) and ciprofloxacin hydrochloride facilitated similar drug release profiles as PLGA.[115] An initial burst release was followed by a sustained release over the course of 24 h, but the drug release rate was lower. A similar release profile was evident when rivastigmine[116]

was encapsulated. In contrast, when naltrexone[117] was encapsulated, the release from the PEA based microparticles was faster than for the PLGA control. Switching from nanoparticles to microparticles prolonged the sustained release to a period of 28 days.[117] Also nanoparticles composed of the homopolymer of the isoleucine-based **MD14** and dexamethasone featured similarly altered release properties.[94] The formation of hydrogen bonds between the PEA units and the drug significantly increased the drug content in the delivery vehicle, in particular when polymer films were compared. These films retained the drug much longer compared to PLGA films, most likely due to the slower degradation of the PEA as well as a deformation of the film throughout degradation. These studies highlight the possibility of the formation of stable nanocarriers that retain the drugs longer than the gold standard PLGA *via* the use of PEA derived from MD monomers.

Suitably protected MD monomers based on aspartic and glutamic acid (**MD23** and **MD24**, respectively) enabled access to PLA comprising 8 to 16% carboxylic acid groups after deprotection.[89, 92, 93] These were subsequently utilized to attach PEG sidechains *via* DCC/DMAP coupling (**4** in **Figure 7**).[89, 93] The release rate of doxorubicin (DOX) encapsulated in micelles formed from these PLA-*graft*-PEG graft copolymers increased when longer PEG chains were used, presumably due to an enhanced permeation of water into the micelle core. When the grafting of PEG was only performed to 90% of the carboxylic acid groups, the residual 10% enabled the coupling of other, additional molecules.[92] Ohya and coworkers used these to couple levofloxacin resulting in a macromolecular prodrug (**3** in **Figure 7**). The material was designed as an injectable gel, transitioning from the sol phase to the gel phase at physiological temperature and releasing the API in a sustained manner.

Aiming at a qualitative comparison of the release behavior of these PEA based drug delivery systems, **Figure 7** summarizes the API release regarding burst release and normalized sustained release. The following conclusions should be taken with a grain of salt due to the variety of applied API and polymer structures: (i) The sustained release rate of hydrogels and microparticles is lower compared to that of nanoparticles. (ii) The initial burst release can be suppressed by the incorporation of PEG. (iii) The overall release behavior of DOX is faster from micelles featuring longer PEG chains.

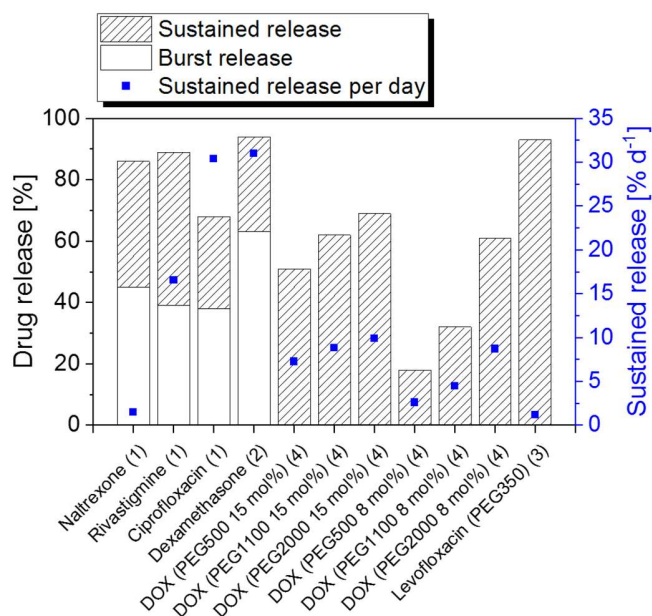
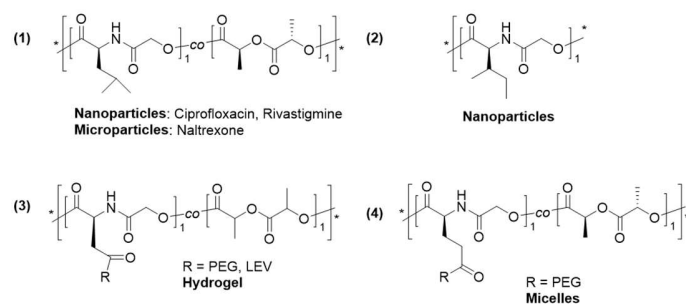


Figure 7. API release behavior of drug delivery systems composed of polymers made by ROP of MD monomers (phosphate-buffered saline (PBS), pH = 7.4) and schematic representation of the polymer structures.[89, 92-94, 115-117] The sustained release was normalized to release per day

since most studies performed *in vitro* drug release experiments in different timeframes. A linear course of the sustained release was assumed to simplify the calculation.

“Stealth” polymers such as PEG help to increase the blood circulation time of drug delivery vehicles. The fact that the ROP of MD monomers is initiated by alcohols enables the attachment of PEA to PEG in a straightforward manner *via* macroinitiator approaches. This methodology has already been applied in earlier literature as summarized by Feng.[77] Briefly, monohydroxyl or dihydroxyl end functional PEGs can be used as macroinitiators to result in AB or ABA block copolymers, respectively. Recent research is directed towards more sophisticated tri- or pentablock copolymers, as well as the replacement of PEG by alternative materials. The latter originates from drawbacks afflicted with the use of PEG such as, *e.g.*, the occurrence of PEG antibodies or anaphylaxis, presumably induced by this polymer. These issues are in addition recently observed subsequent to administration of the new vaccines against COVID-19, thus, highlighting the urgency to develop suitable alternative polymers.[118]

Exposing a PEtOx shell from nanocarriers, in this regard, results in a similar “stealth” effect as that of the gold standard PEG.[119] Recently, poly(2-ethyl-2-oxazoline) (PEtOx) featuring an ω -hydroxyl end group was applied as a macroinitiator for the ROP of **MD11** and **MD14**.[120] For each monomer, three different block copolymers with varied fraction of the PEA block were synthesized (**MD11**: 71 to 87 wt%; **MD14**: 56 to 88 wt%). Although these materials have not yet been applied as nanocarriers, the PEtOx-*b*-PMD materials fulfilled the basic requirements since they formed well-defined nanostructures in aqueous suspension exposing the “stealth” polymer toward the outside, as confirmed by cryo-TEM.

Exploiting PEG as ROP macroinitiator enabled access to varying more sophisticated block copolymer structures. mPEG-*b*-PLLA-*b*-PMD8 ABC triblock copolymers were accessed utilizing

mPEG as an initiator for the consecutive ROP of L-lactide and **MD8**. [121] Paclitaxel (PTX) as a hydrophobic anti-tumoral API was encapsulated in micelles formed from these triblock copolymers. The PEA block prevented drug leakage that occurred for mPEG-*b*-PLLA diblock copolymer micelles, enhanced their stability, and increased the cytotoxicity on the investigated cancer cell lines. Similar triblock copolymers, composed of PLGA instead of PLLA, were utilized to stabilize PEG-PLGA micelles containing 10-hydroxycamptothecin (HCPT) through preparation of mixed micelles. [122]

The use of PEG-diol as macroinitiator for the ROP provides ABA triblock copolymers with a central PEG block in one step. DOX was successfully encapsulated and released from PEA-*b*-PEG-*b*-PEA ABA triblock copolymer nanoparticles. [83, 123] The PEG fraction was kept constant as 20 wt% and the PEA blocks in these studies were composed of the hydrophobic **MD14** or **MD8**, either as homopolymer blocks or statistical copolymers with *p*-dioxanone (PDO). These combinations were favored, since pure PPDO revealed a rather slow hydrolytic degradation kinetics in earlier studies. [124] In addition, interactions between the amino acids helped to stabilize the nanocarriers. In a follow-up study, the material was further modified by attachment of a P(*N,N*-dimethylaminoethylmethacrylate) (PDMAEMA) block through atom-transfer radical polymerization (ATRP) using an ABA triblock copolymer based on PEG and statistical copolymers comprising **MD12** and PDO. [125] The resulting pentablock copolymers were utilized for the co-encapsulation of ibuprofen (IBU) and DOX.

All these nanomaterials revealed sustained release, which could be controlled by the MD contents, and the polymer degradation was monitored utilizing size exclusion chromatography (SEC). Aiming at a direct comparison of these investigated systems, the respective block copolymers with the highest and the lowest MD weight fractions were selected (**Figure 8**). For the triblock

copolymers (**Figure 8a** and b), three general statements can be made. (i) The fastest degradation occurred for the block copolymers composed of PEG and the PEA homopolymer, (ii) the PEA segment bearing the methyl substituents hydrolyzed faster compared to that comprising *sec*-butyl substituents and (iii) the hydrolysis rate can be tailored by the weight fractions of PDO and MD in the respective PEA block. For the pentablock copolymers (**Figure 8c**), a substantially higher relative molar mass remained due to the non-degradable P(DMAEMA) segments. However, the lowest and highest MD weight fractions (2 and 25 wt%) revealed rather similar degradation rates, pointing towards less adjustable hydrolysis rates compared to the ABA triblock copolymers.

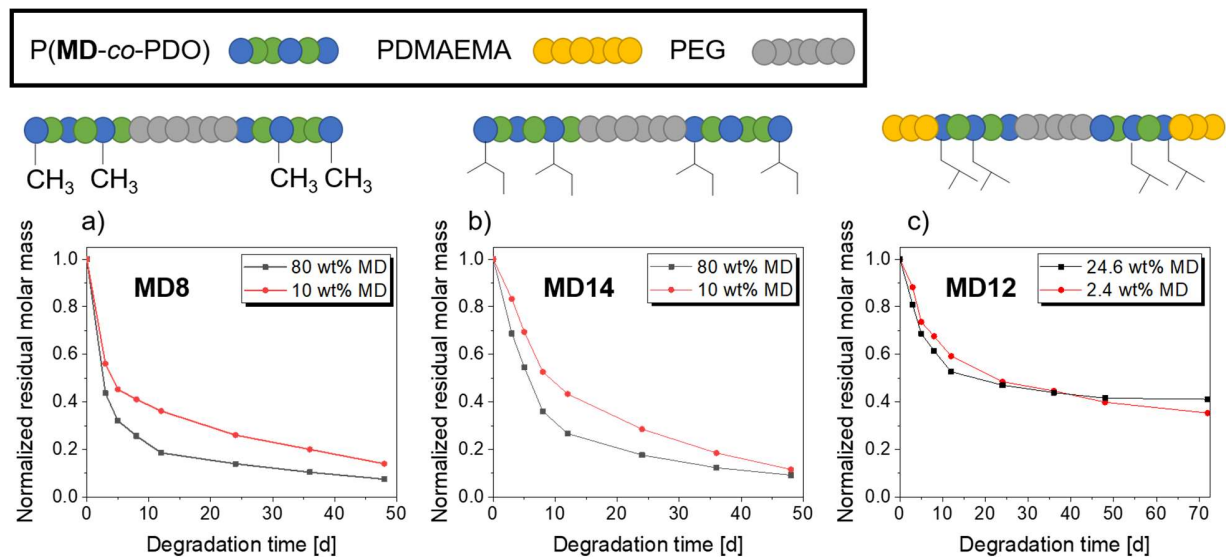


Figure 8. Normalized residual molar masses of the PEA containing block copolymers obtained during *in vitro* degradation experiments in PBS buffer (pH = 7.4, T = 37 °C).[83, 123, 125]

2.2.3.3. MD containing polymers for gene delivery

Poly(ethylene imine) (PEI) is a commonly applied polymer for the immobilization of genetic material, either as linear (*l*PEI) or branched (*b*PEI) polymer. A hydrophobic segment is however advantageous when designing gene delivery vehicles. **Figure 9** illustrates recently applied synthesis strategies toward MD containing polymers for gene delivery purposes. Mostly, the hydroxyl end groups of the PEA are converted into isocyanates, which are subsequently coupled to PEI. The approach has been followed with mono- as well as bifunctional initiators for the ROP, PEA homopolymers and statistical copolymers with cyclic ester monomers, or with block copolymers comprising the “stealth” polymer PEG. To ultimately enhance cellular uptake of these gene delivery vehicles, defined peptide sequences such as REDV or CAGW were attached additionally to the PEI building blocks of the materials.

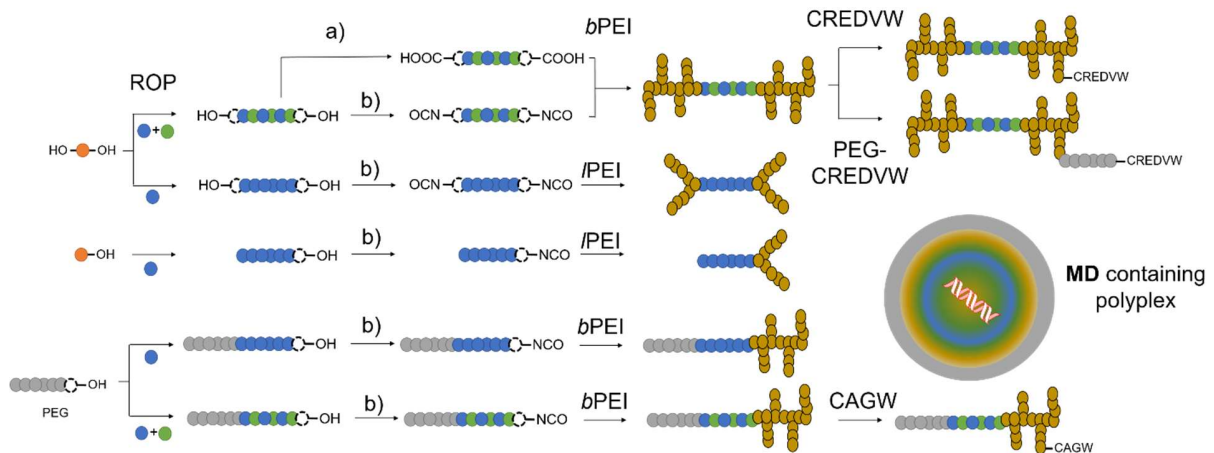


Figure 9. Schematic representation of synthetic strategies towards MD containing materials for gene delivery. a) Succinic anhydride functionalization of the hydroxyl end groups and subsequent *b*PEI attachment by *N*-hydroxyl succinimide (NHS) coupling. b) Diisocyanate functionalization of the hydroxyl end groups.

Transfection using *l*PEI based conjugates to a PEA homopolymer composed of **MD14** was investigated.[126] The strong interaction of the isoleucine-based PEA segments with each other on an intermolecular level enhanced the stability of the polyplexes. The materials were synthesized by ROP of **MD14** in the presence of either benzyl alcohol or 1,8-octanediol, resulting in the respective mono- or di-hydroxyl end-functional PEA. In a second step, these moieties were converted to isocyanates and subsequently reacted with *l*PEI. Although *l*PEI represents a linear polymer, the conjugation reaction most likely occurred at secondary amines along the backbone, thereby resulting in swallowtail end groups. The best results regarding assembly parameters, plasmid DNA (pDNA) binding and transfection behavior were obtained for the material obtained from a bifunctional ROP initiator and 10 kDa *l*PEI, featuring the highest *l*PEI content.

Several consecutive studies by Wencheng and coworkers were concerned with optimization of the selective transport of pZNF580 DNA towards endothelial cells, thus enabling rapid endothelialization of artificial vascular implants by overexpression of the ZNF580 protein, which represents a key protein for cell migration. In order to access the migration and proliferation enhancement through the utilization of PEA based gene delivery materials, the recovery of artificial scratch tests of cell films as well as the protein overexpression was monitored. The materials consisted of the following segments: *b*PEI as the gold standard cationic polymer, PEG as a stealth polymer to reduce the cytotoxicity, and biodegradable MD containing polymers to enhance the polyplex stability. Initially, the hydrophobic block consisted of glycolide and the alanine-based **MD8**, and *b*PEI ($M_w = 1,800 \text{ g mol}^{-1}$) was used.[127] The material self-assembled into sub 200 nm objects that were successfully loaded with the selected gene at various nitrogen to phosphorous (N/P) ratios. *In vitro* tests revealed a decreasing release rate with an increasing N/P ratio. Transfection in ECs was successful, thereby increasing the ZNF580 protein expression

which led to an enhanced cell proliferation and migration behavior. In the following, hydrophobic cores ranging from pure P(MD8) over MD8-co-lactide to MD8-co-lactide-co-glycolide were compared systematically.[128] **Figure 10** summarizes the pDNA release, protein overexpression enhancement factors as well as the recovered areas from scratch tests. When a copolymer with glycolide was used (1), *i.e.* the least sterically demanding hydrophobic copolymer block, the release of the pDNA as well as the corresponding protein expression exhibited the lowest overall values, whereas these low values did not affect the endothelialization and cell migration, reaching values about 80% recovery. Utilization of the PEA homopolymer as hydrophobic core (2) resulted in an enhancement of the cumulative pDNA release and overexpression of the factor. Additional improvement was achieved when copolymers with lactide (3) or a combination of lactide and glycolide (4) were used. The release rates and protein expression further accelerated, which also resulted in enhanced healing ability, reaching values up to 90%.

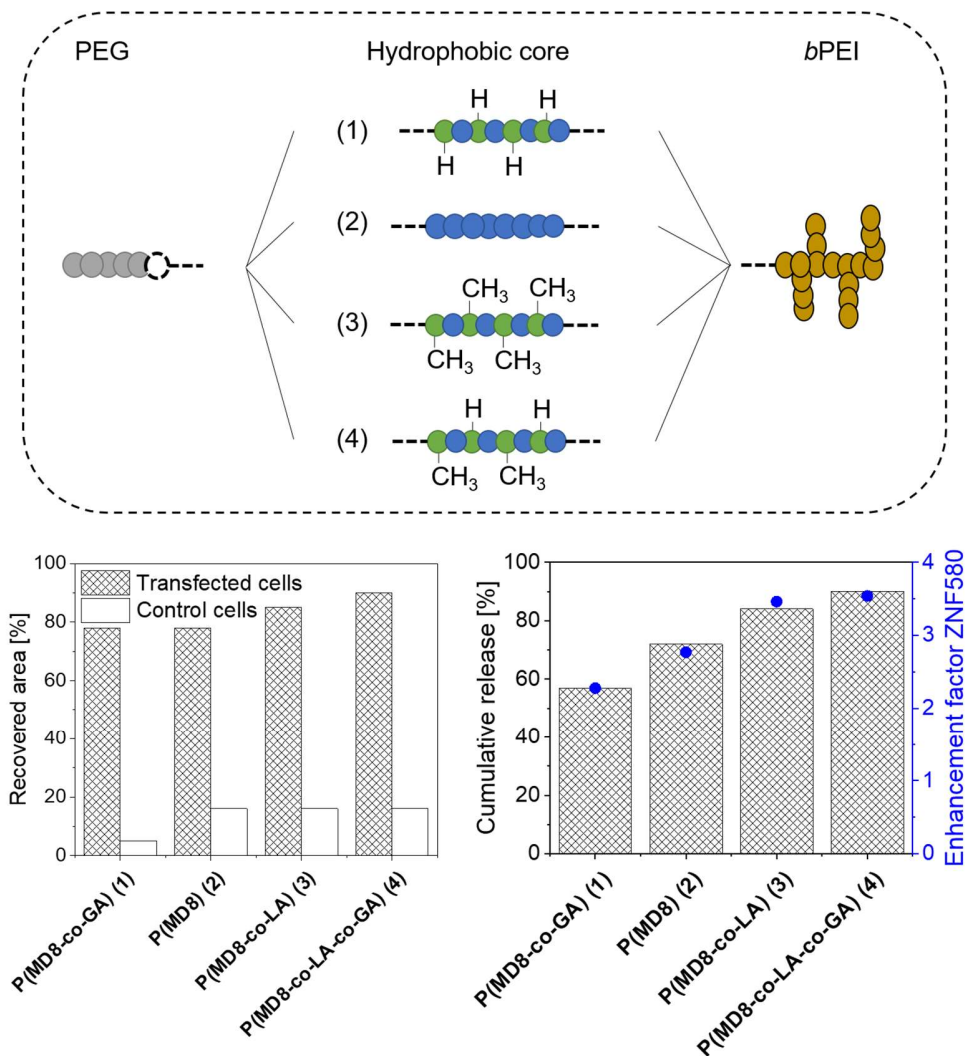


Figure 10. Comparison of the efficiency of pZNF580 DNA loaded gene delivery vehicles featuring different MD containing hydrophobic cores.[127, 128] **Bottom left:** Recovered area after scratching experiments compared to the respective control groups. **Bottom right:** Cumulative pDNA release (columns) and protein overexpression (dots).

The CREDVW peptide sequence was attached to polyplex materials consisting of **PMD8** and *b*PEI by a Michael addition.[129] As the REDV peptide sequence enabled selective binding to the $\alpha_4\beta_1$ integrin receptor of endothelial cells (ECs), cellular uptake was enhanced. Cytotoxicity assays

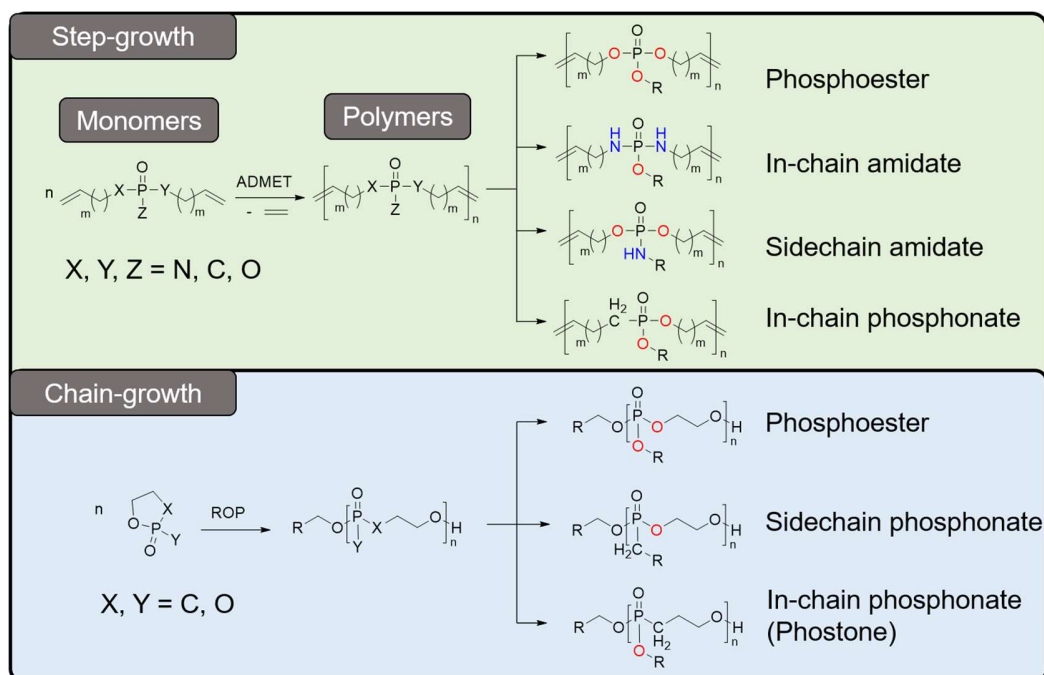
proved the biocompatibility of the material up to concentrations of 100 $\mu\text{g mL}^{-1}$. In artificial scratch-healing tests, up to 95% of the scratch area were recovered by ECs within a timeframe of 12 h when PEA containing polyplexes were used for transfection (PLGA based control: 85% were recovered). The promising carrier system was further modified by incorporation of PEG spacers[130] and through attachment the alternative active peptide CAGW to enhance adhesion of ECs.[131] For the latter, **MD8** containing materials proved superior to controls comprising only PLGA as hydrophobic segment.

Co-assembly of two different polymers simplifies the synthesis, purification and characterization. In such approaches, components composed of the hydrophobic block and PEI are mixed with block copolymers comprising the same hydrophobic block and the stealth polymer PEG. A micellar co-assembly of *b*PEI-P(**MD8-co-lactide**)-*b*PEI and mPEG-P(**MD8-co-lactide**) was utilized to investigate the impact of the polymer ratio on the efficacy of mixed micelle carriers.[82] It was demonstrated that high PEG contents decreased the DNA binding ability, presumably due to shielding of pDNA-*b*PEI interactions. Cytotoxicity and transfection efficiency could be adjusted by the mPEG and *b*PEI amount in the polyplexes. A subsequent study replaced linear PEG segments by poly(poly(ethyleneglycol)methacrylate) (PPEGMA).[132] After an initial ROP of **MD8** and L-lactide initiated by 1,8-octanediol, the hydroxyl end groups were converted into bromides, thus enabling a subsequent ATRP of PEGMA. The polymer was additionally decorated with REDV units at the sidechain end groups of the PPEGMA block. A *b*PEI-P(**MD8-co-lactide**)-*b*PEI was used for micellar co-assembly and loading with the pZNF580 gene. As expected, the peptide decorated polyplexes revealed superior transfection and proliferation when compared to the unmodified control group.

3. Polyphosphoesters and analogues

PPEs and analogues represent highly interesting materials as *e.g.* as flame retardants[133] or in biomedical research. Especially the latter is in focus here due to the biocompatibility as well as the adjustable biodegradability of these materials. The polymer backbone or sidechain can be varied by utilization of ester (P-O), amidate (P-NH) or phosphonate/phostone (P-C) based monomers, opening a broad variety of accessible phosphorous based polymers (**Scheme 3**). P-O bonds are degradable under alkaline conditions, whereas P-N bonds are labile in acidic environments.[134, 135] In contrast, P-C bonds feature enhanced hydrolytic stability but can be degraded by microorganisms.[136]

The most commonly applied syntheses of such materials can be categorized into step-growth polymerizations by metathesis polymerization and chain-growth polymerization by ROP. Recently, Wurm and coworkers published a review highlighting the usage of hydrophilic PPE.[137] Because PPE have recently been reviewed comprehensively,[24, 133, 138] the following chapter only briefly highlights latest reports about hydrophobic PPE synthesis and their biomedical applications.



Scheme 3. Schematic representation of the most commonly applied synthesis routes towards PPE and analogues.

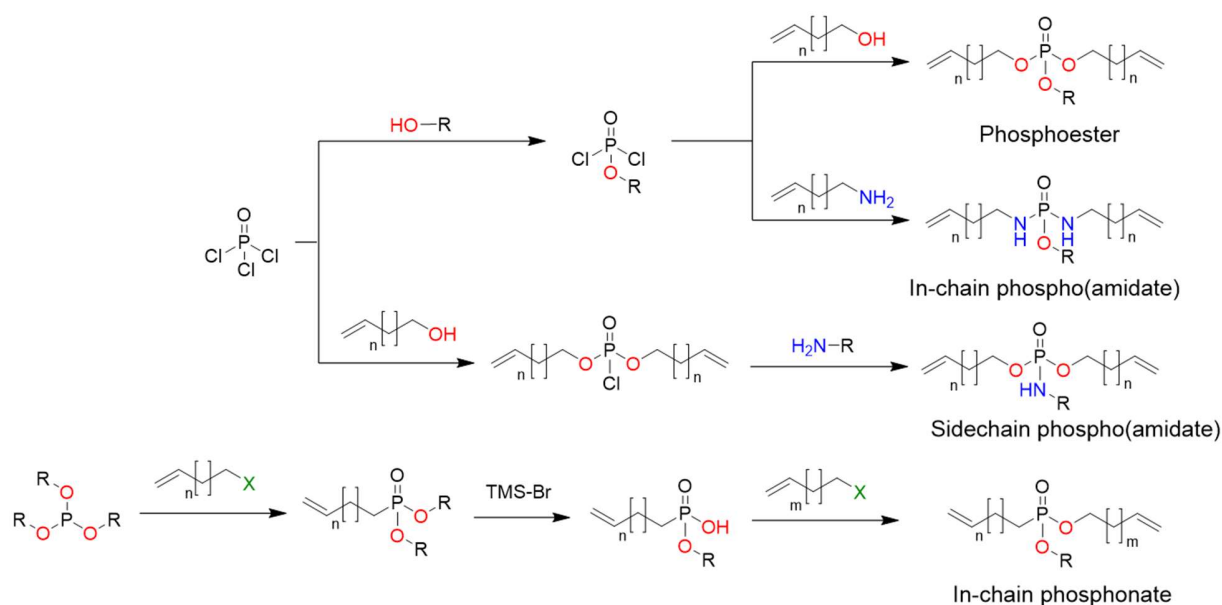
3.1. Phosphoester monomers for acyclic diene metathesis polymerization (IPE)

In general, PPE derived from ADMET can feature adjustable degradability, interesting thermal as well as mechanical properties. Therefore, some recent reports focus on the synthesis and thorough characterization of the polymers without specifying on a particular application since the materials are potentially suited for biomedical research as well as flame retardants.

From a structural perspective, IPE facilitate a broad variability in terms of building blocks. Besides adjustable methylene spacer lengths between the central phosphorous atom and the polymerizable alkene moieties, the covalent binding at the phosphorous atom can be based on different structural elements, such as esters, amides and phosphonates. These can be obtained by mainly two different synthesis routes (**Scheme 4**). Monomers featuring solely ester bonds and in-chain phosphoamidates featuring pendant ester functions are obtained in a two-step reaction starting

from phosphoryl chloride. The initial step is a nucleophilic substitution of one chlorine atom by an alcohol. The remaining two chlorine atoms are subsequently exchanged utilizing ω -alkylene alcohols or amines. When aiming at sidechain phosphoamidates, the polymerizable groups are introduced prior to the pendant substituent.

For non-symmetrical in-chain phosphonates, phosphitesters serve as starting materials.[139] Initially, the P-C bond is formed through a Michaelis-Arbuzow reaction, whereby the trivalent phosphorous is oxidized to a pentavalent form. One of the remaining ester bonds is cleaved by stoichiometric amounts of trimethylsilyl bromide and subsequently reacted with a halide functionalized alkene.



Scheme 4. Schematic representation of synthesis approaches towards IPE.

The reader is directed to other reviews for a broader overview of the applied monomers as well as a summary about metathesis polymerizations, including ring-opening metathesis (ROMP).[24, 133] **Table 3** only depicts IPE reported since 2015. Phosphoester monomers were varied regarding the methylene spacer lengths as well as the pendant substituents. The latter ranged from hydroxyl

or methyl ester moieties of low sterical demand to bulky hydrophobic phenyl esters. **IPE13** featured an isopropylidene protected catechol moiety that was deprotected in an acidic environment without backbone degradation subsequent to polymerization.[140] **IPE11** represents a cyclic 7-membered monomer that was polymerized by ring-opening metathesis polymerization for the synthesis of phosphorous based block and miktoarm polymers (*vide infra*).[141]

Recently polymerized in-chain phosphoamidate monomers comprise methylene spacers of varying lengths, whereas the pendant substituents were of low sterical demand. Only one sidechain phosphoamidate monomer was utilized for ADMET polymerization. In-chain phosphonate dienes featured pendant ethyl esters with varying alkyl spacer lengths. The PPE resulting from polymerization of the IPE monomers contain main chain double bonds, which are usually hydrogenated to result in a fully saturated backbone, mostly to improve the flame-retardant properties of the materials. Other post-polymerization modifications such as triazolinedione-ene coupling enable further modification of the PPE properties.[142]

Table 3. Schematic representation of recently applied IPE for the synthesis of PPE *via* ADMET polymerization.

n = 1 (IPE1)	[135]	n = 1 (IPE4)	[135]	n = 1 (IPE7)	[140]	n = 1 (IPE8)	[134]
n = 5 (IPE2)	[135]	n = 5 (IPE5)	[135]				
n = 8 (IPE3)	[135, 143]	n = 8 (IPE6)	[135]				
n = 1 (IPE9)	[144]	IPE11	[141]	IPE12	[141]	IPE13	[140]
n = 8 (IPE10)	[143, 144]						
n = 1 (IPE14)	[135]	n = 1 (IPE17)	[135]	n = 8 (IPE20)	[134]	n = 1; m = 1 (IPE21)	[139]
n = 5 (IPE15)	[135]	n = 5 (IPE18)	[135]			n = 3; m = 3 (IPE22)	[139]
n = 8 (IPE16)	[135]	n = 8 (IPE19)	[135]			n = 8; m = 8 (IPE23)	[139]
						n = 8; m = 6 (IPE24)	[139]

3.2. PPE derived from ADMET polymerization of IPE

The ADMET polymerization represents a step-growth polymerization. A variety of transition metal based catalysts were reported to catalyze this polymerization type, including tungsten-, molybdenum- and ruthenium complexes.[145] In particular, Ru-based Grubbs and Grubbs-Hoveyda catalysts facilitate selectivity towards olefins and tolerate many functional groups such as alcohols and carbonyl containing compounds.[146] During the polymerization, stoichiometric amounts of ethylene are formed. The removal of this gaseous byproduct represents the driving force of the polymerization. The resulting polymers always feature α,ω -terminal double bonds. Addition of suitable alkenes subsequent to polymerization enables the introduction of tailored end groups. The approach was exploited for quenching of the homopolymerizations of **IPE9** or **IPE10**, respectively, to obtain alcohol, carboxylic acid, halide, epoxide, or thioacetate PPE homotelechelic.[144]

The enhanced hydrolytic stability of P-C bonds was exploited for the synthesis of in-chain phosphonate IPE with varying aliphatic spacer lengths (**IPE21** to **IPE24**).[139] Similar to the corresponding cyclic phosphonate monomers (*vide infra*), these monomers were stable at room temperature for several months. The polymerization of **IPE21**, featuring the shortest alkyne spacer, only resulted in the formation of oligomers, presumably since the short distance between the central phosphorous atom and the catalyst center subsequent to attachment of the monomer hampered further propagation. However, PPE with molar masses $> 10 \text{ kg mol}^{-1}$ were obtained from the non-symmetric monomers.

ADMET of the side-chain phosphoramidate **IPE20** and the corresponding phosphoester based **IPE8** resulted in materials with similar crystallization behavior.[134] However, the material comprising the pendant amidate moiety featured enhanced thermal stability. In addition, selective cleavage of

the pendant amidate moieties under mild acidic conditions enabled access to pendant hydroxyl groups, making the resulting polymers polyphosphodiester.

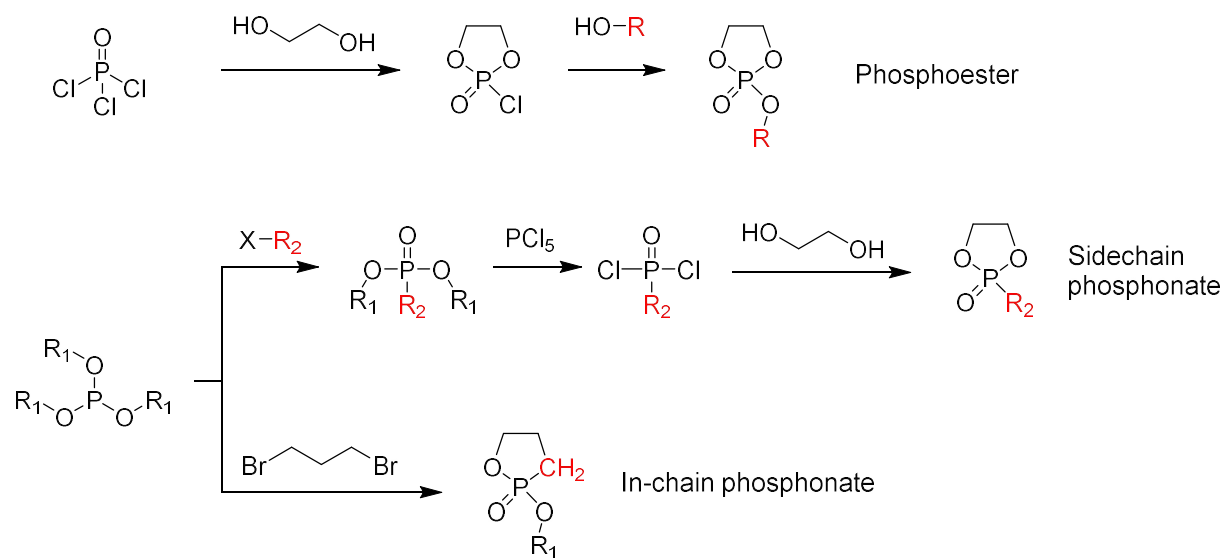
Despite the excellent group tolerance of the catalysts, these materials may be difficult to obtain by direct polymerization of the respective monomers **IPE1-3** or **IPE14-16**.^[135] In contrast to monomers with pendant methyl ester moieties (**IPE4** to **IPE6**, **IPE17** to **IPE19**), the monomers with a free hydroxyl group failed to homopolymerize due to catalyst deactivation. However, copolymerization of the two monomer types was successful. The incorporation of phosphodiester moieties is useful because they act as hydrogen bond donors. As shown for copolymers of **IPE3** and **IPE10**, this enabled self-healing and shape memory properties, and enhanced adhesion to alumina devices.^[143] Besides exploiting adhesive properties to magnetite particles, pendant hydroxyl moieties through incorporation of the catechol-based **IPE13** have also been used for covalent crosslinking reactions.^[140]

ADMET also allows the copolymerization with non-phosphorous containing monomers, as reported for the copolymerization of **IPE10** with a diacrylamide based on lysine.^[147] The reactivity differences of the two monomer types resulted in alternating copolymers and molar masses up to 18,000 g mol⁻¹. The hydrophobic materials were used to encapsulate rifampicin in sub-100 nm particles.

3.3. Cyclic phosphoester monomers (cPE)

Although the key structural elements of different types of cPE are similar, the synthesis of solely phosphoester based monomers and the regioselective introduction of P-C bonds require individual synthesis strategies (**Scheme 5**). Phosphotriester monomers are synthesized starting from phosphoryl chloride. Reaction with ethylene glycol results in a five membered ring precursor, which can be readily functionalized with various alcohols at the phosphorous atom.

The Michaelis-Arbuzow reaction represents the most commonly applied synthesis towards monomers featuring P-C bonds using phosphite esters as starting materials.[148] Sidechain phosphonate synthesis comprise of three steps: A nucleophilic attack of the lone electron pair of phosphite esters at an alkyl halide to introduce the P-C bond, chlorination using PCl_5 and subsequent ring closure with ethylene glycol. In contrast, in-chain phosphonates can be accessed in a one-step reaction by direct ring closure of phosphite esters using 1,3-dibromopropane.



Scheme 5. Schematic representation of synthesis strategies towards cPE monomers.

Scheme 6 depicts the respective cPE monomers recently applied for ROP. Phosphotriesters featuring alkyl substituents (**cPE1** to **cPE7**) comprise linear and branched moieties. Among these, **cPE1** and **cPE2** with methyl- or ethyl-ester moieties are hydrophilic. The hydrophobic character increases from the propyl substituted **cPE3** on. Their ROP, thus, potentially enables access toward PPE with tailored hydrophobicity.

In order to fabricate PPE materials featuring lower critical solution temperatures (LCST), the furfuryl functionalized **cPE9** was copolymerized with the hydrophilic **cPE1** or **cPE2** in various molar ratios (5 to 25 mol% **cPE9**, respectively).[149] The cloud point temperature (T_{cp}) decreased with an increasing amount of the hydrophobic **cPE9**. The same concept was applied for sidechain phosphonate-based PPE through DBU catalyzed copolymerization of the hydrophilic **cPE19**, the hydrophobic **cPE20** and the allyl functionalized **cPE21**. [150]

Since the ROP of cPE monomers proceeds in a similar fashion as that of MD, the utilization of functional monomers is limited. Non-saturated pendant substituents (**cPE10** to **cPE11**) are preferably introduced to enable post-polymerization modifications of PPE. For instance, a **cPE10** homopolymer featuring pendant allyl substituents was quantitatively modified by UV induced thiol-ene addition without the necessity of purification.[151] This kind of modification was also utilized for a copolymer comprising the propargyl functionalized **cPE11** for the attachment of protein repelling peptides.[152] The propargyl moiety of **cPE11** was moreover functionalized in a copper-catalyzed azide-alkyne reaction in order to introduce tertiary amino moieties.[153] The furfuryl moiety of **cPE9** allowed post-polymerization modification with a variety of maleimides *via* Diels-Alder reactions.[149]

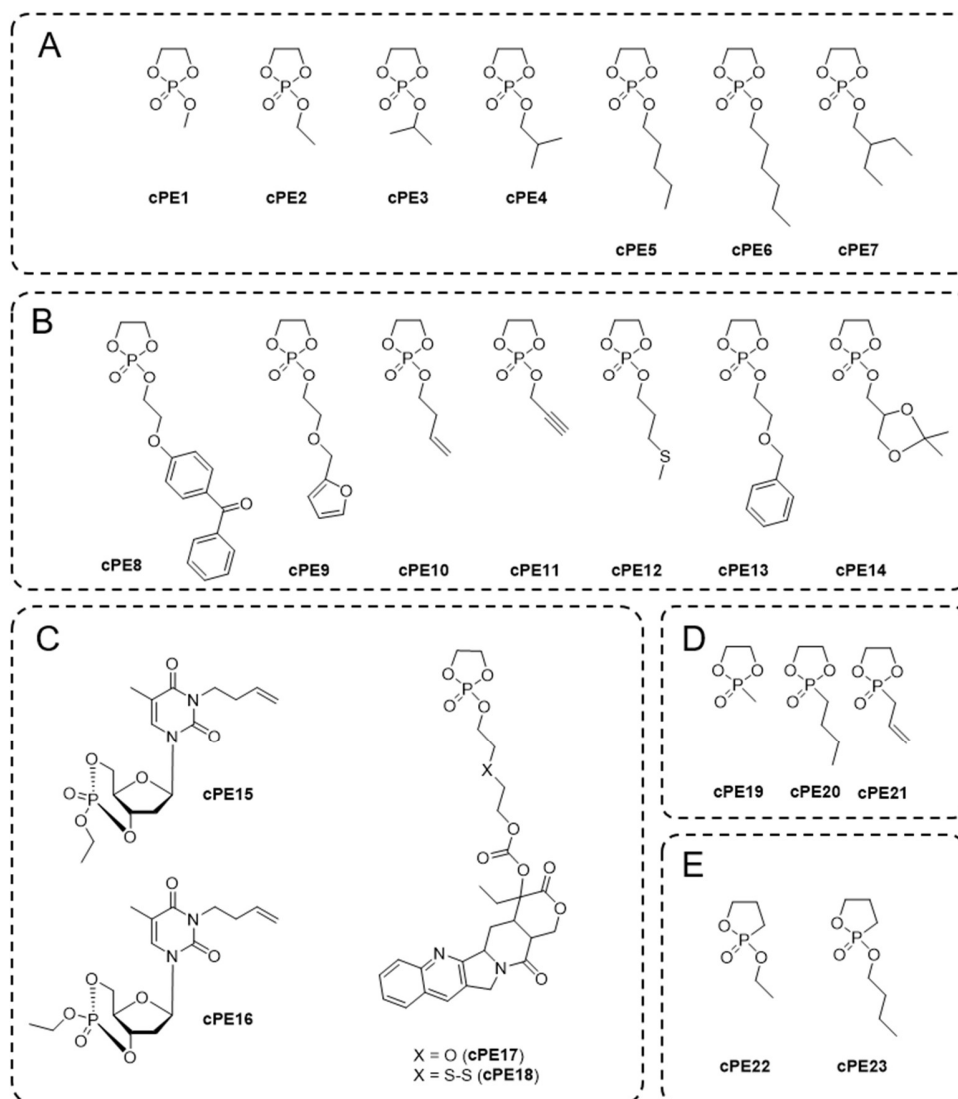
Due to the degradability of solely phosphoester-based materials under basic conditions, protection / deprotection strategies need to be based on orthogonal reaction conditions. **cPE13** featuring a

benzyl protected hydroxyl moiety can be deprotected by hydrogenation, whereas the acetal moieties in **cPE14** can be removed in slightly acidic media. Both have been utilized to introduce pendant hydroxyl moieties into PPE.[154] In addition, a copolymer comprising both functional monomers was selectively deprotected without backbone degradation, allowing a potential stepwise functionalization.

The benzophenone decorated **cPE8** enabled crosslinking of PPE terpolymers and simultaneous covalent attachment to benzophenone modified glass substrates, gaining access to studies conducted with the interactions of various PPE with proteins.[155]

The camptothecin conjugates **cPE17** and **cPE18** were copolymerized with **cPE2**, yielding copolymers comprising up to 10 mol% of the prodrug monomer.[156] The API was connected to a spacer *via* a carbonate moiety and, therefore, released from both systems. The disulfide containing linker of **cPE18** additionally enabled a reduction triggered release, thereby enhancing the release rate. Thymidine functionalized cPE (**cPE15** and **cPE16**) were polymerized aiming at macromolecules with structural elements similar to DNA.[157, 158]

Also cyclic phosphonate monomers featuring P-C bonds have been reported, resulting in side-chain (**cPE19** to **cPE21**)[150, 159] or in-chain polyphosphonates (phostones, **cPE22** and **cPE23**)[136].



Scheme 6. Schematic representation of recently utilized cPE. A) Cyclic phosphotriesters featuring pendant alkyl esters. B) Cyclic phosphotriesters featuring functional moieties. C) Bulky cyclic phosphotriesters for the synthesis of artificial DNA or macromolecular prodrugs. D) Sidechain phosphonate cPE. E) In-chain phosphonate (phostone) cPE.

3.4. ROP of *cPE* monomers

When aiming at the synthesis of PPE derived from ROP, typically low temperatures (–40 °C to room temperature) and high monomer concentrations (4 M) are applied, whereby the targeted molar masses can be adjusted by the applied monomer to initiator (M/I). However, higher molar masses often come to the cost of slightly increased dispersity values (**Table 4**). In general, α -end groups can be pre-determined by choice of the initiating alcohol which can be either small molecule- or polymer-based. However, the end groups can also be intrinsically derived from the catalyst, as shown for methyl ytterbocene (Cp_2YbMe), which was applied in the ROP of aliphatic ester-based cyclic phosphates (**cPE1** and **cPE3**) and sidechain phosphonates (**cPE19** and **cPE20**).^[159] The successful group transfer from the catalyst was evident from MALDI MS measurements.

Similar to the organocatalyzed polymerization of MD, current literature is mainly focused on the utilization of “super-base” catalysts such as TBD or DBU, partly in combination with co-catalysts. Kinetics of the binary DBU/TU system for the ROP of **cPE4** and **cPE10** were particularly suited to develop continuous flow polymerization in microreactors, whereas the TBD catalyzed ROP of **cPE10** could not be adopted to the reaction setup.^[151] Similarly, the binary catalysts DBU/TU and DBU/tris-urea efficiently catalyzed the ROP of the in-chain phosphonates **cPE22** and **cPE23** (pseudo-first order kinetics, $D \approx 1.5$).^[136] When solely TBD or metal-based catalysts ($\text{Sn}(\text{Oct})_2$, ^{*t*}bu[salen]AlMe) were applied, ill-defined polymers were obtained.




Table 4. Summary of the polymerization conditions and selected polymer characterization data of recent homopolymerizations of cPE (for the chemical structure refer to **Scheme 6**).

Monomer	Initiator	Cat.	T (°C)	t (min)	M/I	M _n (g mol ⁻¹)	Đ	Ref.
cPE4	Benzyl alcohol	DBU/TU or TBD	0 to 40	1 to 20	30	1,100 to 2,440	1.10 to 1.19	[151]
cPE10	Benzyl alcohol	DBU/TU or TBD	0 to 40	3 to 20	30	1,400 to 3,580	1.08 to 1.21	
cPE22	2-(Benzyloxy)ethanol	DBU/TU or	0	ca. 24 h	20 to	3,000 to 25,100	1.24 to 1.56	[136]
		DBU/Tris-urea			170			
cPE23	2-(Benzyloxy)ethanol	TBD	-20 to 0	ca. 5 d	20 to 50	3,900 to 8,500	1.56 to 1.61	
cPE15	4-Methoxybenzyl alcohol	TBD	RT	6 to 24 (h)	10 to 30	3,200 to 6,200	1.06 to 1.09	[157]
cPE19	-	Cp ₂ YbMe	-40	2 to 60	50	11,400 to 33,400	1.15 to 1.47	[159]
cPE20	-	Cp ₂ YbMe	-40	2 to 180	50	800 to 31,500	1.03 to 1.28	
cPE1	-	Cp ₂ YbMe	-40	10	50	1,900	1.21	
cPE3	-	Cp ₂ YbMe	-40	2 to 60	50	500 to 8,200	1.01 to 1.22	

Whereas recent literature regarding the homopolymerizations of cPE focused on aspects such as the polymerization behavior and access towards new PPE classes, copolymerization approaches focus on the incorporation of functional moieties to enable post-polymerization modifications of the resulting copolymers. In contrast to MD, which are mostly copolymerized with cyclic ester monomers, different cPE monomers are preferably copolymerized with each other utilizing the established metal- or organo-based catalysts (**Table 5**).

Table 5. Summary of recently synthesized statistical co- and terpolyphosphoesters. Schematic representations of the monomer structures are illustrated in **Scheme 6**. The color indicates the recently reported compositions of the copolymers (Green: Composed of two monomers. Orange: Composed of three monomers. Blue: Copolymers composed either of two or three monomers.). Monomer compositions that have not yet been explored are represented by the non-colored fields in the table.

cPE	1	2	5	7	8	9	10	11	13	14	17	18	19	20	21
1						[149]									
2			[155]	[155]	[155]	[149]	[155]	[152]	[154]	[154]	[156]	[156]			
5					[155]										
7					[155]										
8							[155]								
9															
10															
11															
13															
14										[154]					
17															
18															
19														[150]	[150]
20														[150]	
21															

	Statistical copolymers
	Statistical terpolymers
	Co- and terpolymers

As the ROP of cPE monomers can be initiated by alcohols, utilization of PEG macroinitiators allows access to amphiphilic block copolymers featuring hydrophobic PPE blocks. This was exploited for photodynamic therapy, where the photosensitizer chlorin e6 was encapsulated in nanocarriers composed of a PEG-*b*-P(**cPE6**) block copolymer.[160] Similarly, PEG-*b*-(**cPE12**) was used for the encapsulation of chlorin e6 and PTX.[161] The chlorin e6 catalyzed singlet oxygen generation resulted in the *in situ* oxidation of the **cPE12** thioether moieties, thereby increasing the hydrophilicity of the carrier. Due to the triggered disassembly of the micelles, the PTX release was accelerated.

Besides application oriented research, PPE synthesis strategies have become sufficiently reliable enough to enable access to sophisticated polymer architectures, as was demonstrated by a combination of ROP, ROMP and ADMET yielding fully PPE based ABC block and miktoarm star terpolymers (**Figure 11**).[141] In contrast to ADMET of symmetrical monomers, ROMP allows the synthesis of heterotelechelic polymers. The initial ROMP of **IPE11** was terminated utilizing 1,4-diacrylate-*cis*-2-butene to introduce an acrylate ω -end group. For the linear ABC block copolymer, the resulting material was used in a subsequent ADMET polymerization of the heterobifunctional **IPE11** that comprises an allyl as well as an acrylate moiety, thereby ensuring a selective head-to-tail orientation throughout the polymerization. Post-polymerization modification of the remaining acrylate ω -end group utilizing mercaptoethanol enabled the ROP of cyclic phosphate monomer **cPE2**. For the miktoarm star polymer synthesis, the ROMP polymer was modified with 3-mercapto-1,2-propanediol. One hydroxyl moiety was subsequently esterified utilizing acryloyl chloride, and the polymer was applied as macroinitiator for the ROP of **cPE2**. The **IPE12** segment was introduced through ADMET polymerization.

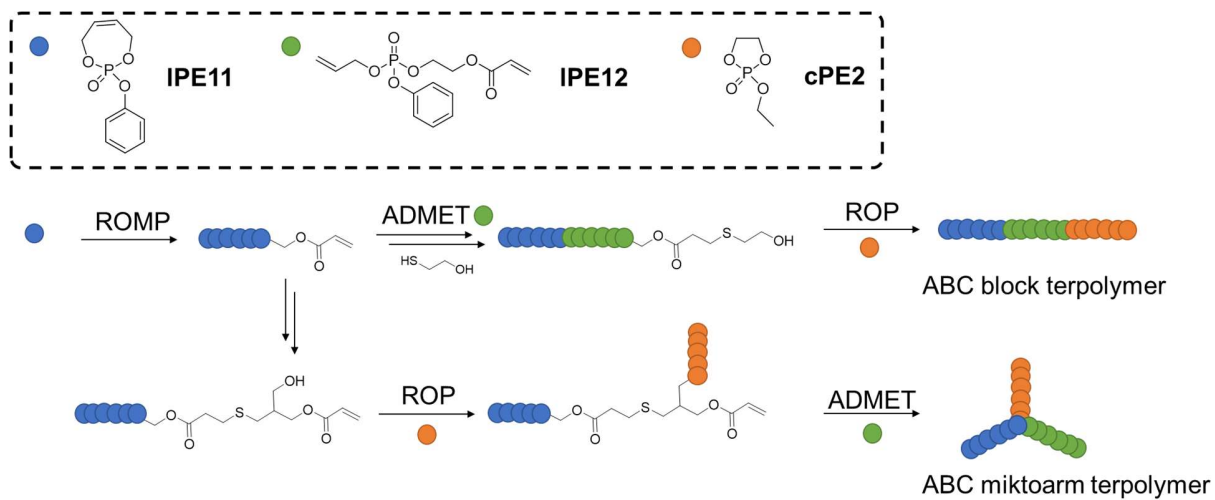


Figure 11. Schematic representation of synthesis strategies applied for the generation of fully PPE based ABC block and miktoarm terpolymers.[141]

4. Polyacetals

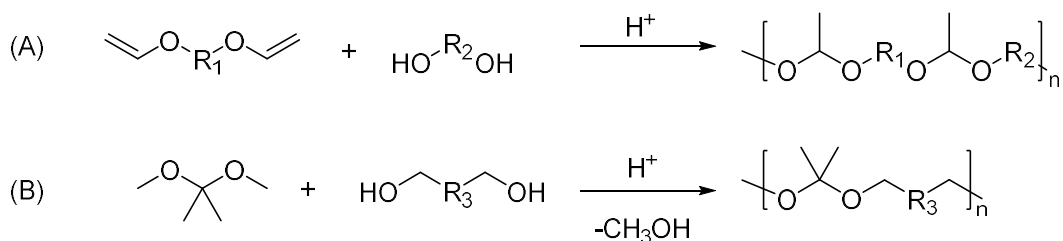
The nucleophilic addition of an alcohol to the carbonyl moiety of an aldehyde produces unstable hemiacetals, which usually react with a second alcohol molecule, thereby directly forming an acetal through condensation. When the reaction is performed starting with a ketone as carbonyl compound, a ketal is formed *via* the same mechanism. According to IUPAC, ketals are considered now a subclass of acetals.[162] We will hence use the term “ketal” to highlight significant structural effects but refer to both moieties as acetals for the sake of simplicity. Acetals are stable under basic conditions but hydrolysable under acidic conditions forming neutral degradation products, *i.e.* the initial carbonyl compound and alcohol.

Polyoxymethylene, also named polyformaldehyde, is one of the simplest and oldest polyacetals. The first report goes back to studies by A. M. Butlerov in 1859[163] and was followed by extensive studies, among others by H. Staudinger in the 1920s.[164] The role of polyoxymethylene and developments in this field are summarized elsewhere and recommended to the interested reader.[165, 166] Since then, a variety of other polyaldehydes has been developed,[167] and also polysaccharides such as, *e.g.* acetalated dextran[168] might be considered as polyacetals.

A variety of methods for the synthesis of manifold polyacetals was developed, ranging from straightforward step-growth polymerizations to controlled / living chain growth polymerizations. The utilized monomers cover a large parameter space facilitating access to hydrophilic as well as hydrophobic materials featuring different hydrolysis behavior. In consequence, different kinds of application exist that range from thermoplastics[25] to drug delivery systems.[169, 170] Due to the immense recent progress with respect to development of polyacetals designed for the latter, we focused our attention on new developments in the field of degradable main-chain polyacetals.

4.1. Step-growth polymerization

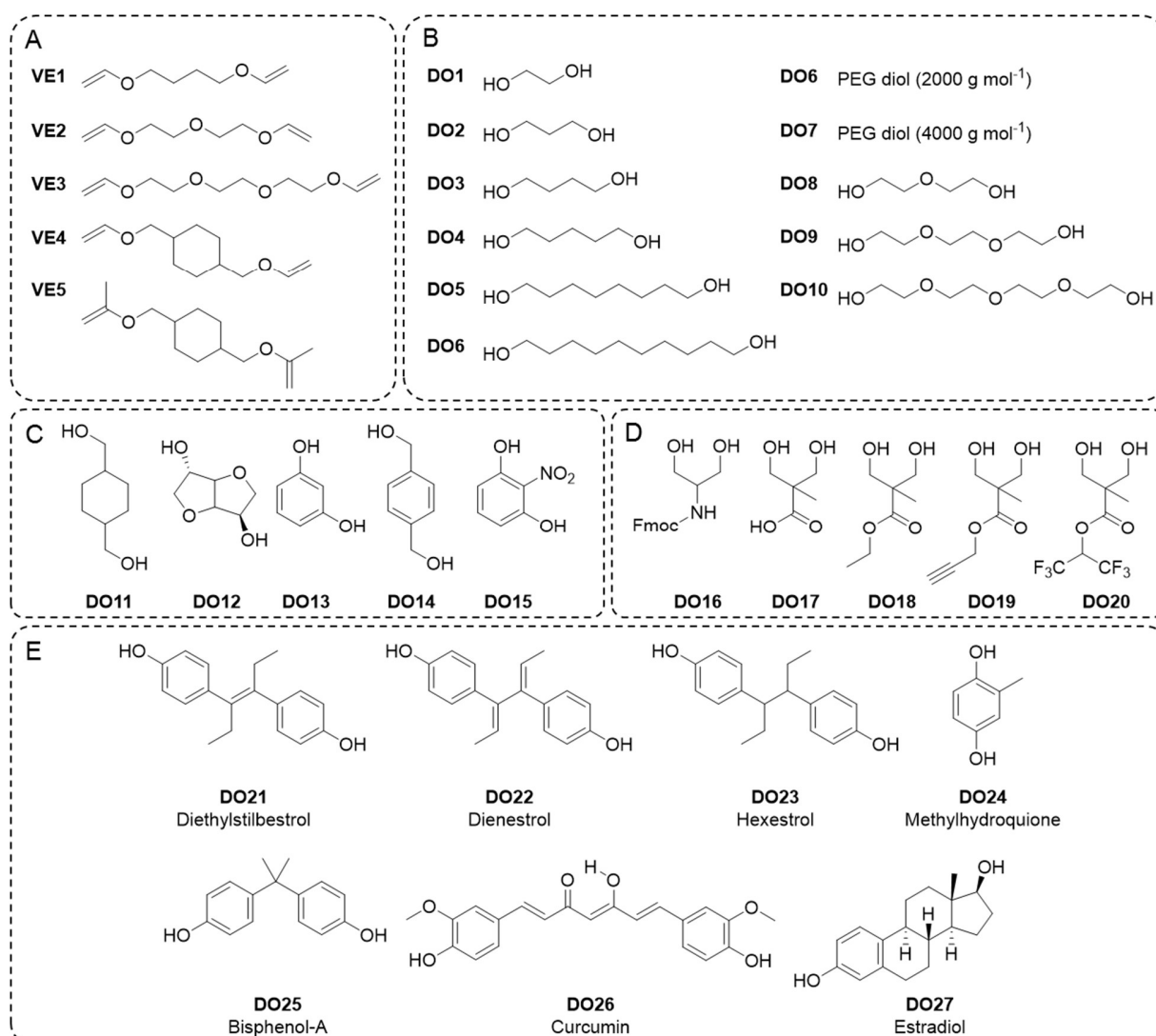
Polyacetals can be obtained by step-growth polymerization *via* two main synthetic strategies (**Scheme 7**). The acetal moieties can be directly incorporated through polyaddition of diols to divinyl ethers, as initially reported by Heller *et al.* in 1980.[171] Established by Murthy and co-workers in 2004,[172] transacetalization polymerization proceeds through an acetal exchange reaction between a diol compound and an acetal containing monomer such as 2,2-dimethoxypropane (DMP) (*i.e.* acetone dimethyl ketal). The newly formed volatile alcohol is removed from the reaction by simultaneous distillation thereby shifting the reaction equilibrium towards polymeric species. Both approaches rely on acidic catalysts such as toluene sulfonic acid or its pyridinium salt, as reviewed in 2013.[169, 170]



Scheme 7. Schematic representation of the two main reaction pathways for acid-catalyzed step-growth polymerization yielding polyacetals. (A) Polyaddition of divinyl ethers and diols. (B) Polycondensation of 2,2-dimethoxypropane and diols.

4.1.1. Linear polyacetals from polyaddition of diols and divinyl ethers

By AA+BB polyaddition of diols and divinyl ethers, hydrophilic, hydrophobic or amphiphilic polymers are accessible (**Table 6**). Aside from variation of properties through simple monomers, drugs with diol functionalities can directly be used as monomers (**Scheme 8**), as established in 2004 by Duncan and co-workers.[173] Further functional moieties such as esters or Fmoc protected amines were introduced through the diol monomer. Similarly, reactive ester or alkyne containing monomers enabled access to additional conjugation of proteins, drugs as well as targeting units *via* post polymerization modifications. If the monomer features a vinyl and a hydroxy function at the same molecule an AB step-growth polymerization can proceed, as reported for macromonomers.



Scheme 8. Schematic representation of recently utilized monomers for polyacetal synthesis. A) Divinyl ethers. B) and C) Hydrophobic and hydrophilic diols. D) Diols with functional groups. E) Diols used as active pharmaceutical ingredients.

Table 6. Selected characterization data of the polyacetals obtained *via* polyaddition of divinyl ethers and diols. Molar masses determined by SEC.

VE	DO	Drug or 2nd diol	M_n (g mol⁻¹)	Application	Acidic degradation ^{a)}	Ref.
VE1 –3	DO1–4, DO8–10		1,000 to 17,300	LCST	VE1/DO10: 50% of original M _n after 4 h at pH 5.5 (SEC)	[174]
VE1	DO1		12,400	Film forming	–	[175]
VE3	DO10_{20%}	DO5_{80%}	12,280	Film forming	–	[175]
VE3	DO10	DO21, DO24, DO25	7,000 to 18,300	Drug conjugate	VE3/DO10_{85%}/DO21_{15%}: 50% of original M _n after 5 h at pH 5 (SEC)	[176]
VE2	DO6	DO21_{2wt%}	17,600	Drug conjugate	50% drug release after 3 days at pH 5.5 (HPLC)	[177]
VE2	DO6	DO21_{5wt%}	22,000	Drug conjugate	50% drug release after 15 days at pH 5.5 (HPLC)	[177]
VE	DO6	DO21_{9wt%}	25,300	Drug conjugate	30% drug release after 45 days at pH 5.5 (HPLC)	[177]
VE2	DO7	DO22_{4wt%}	25,800	Drug conjugate	–	[177]

VE2	DO7	DO23 _{4wt%}	22,700	Drug conjugate	–	[177]
VE2	DO7	DO21 _{5wt%}	22,500	Drug conjugate	50% drug release after 7 days at pH 5.5 (HPLC)	[177]
VE2	DO7	DO25 _{5wt%}	24,300	Drug conjugate	50% drug release after 13 days at pH 5.5 (HPLC)	[177]
VE3	DO7	DO21	20,800 to 24,400	Drug conjugate (Statistical structure)	VE3/DO7/DO21 _{4wt%} : 50% drug release after 3 days at pH 5.5 (HPLC)	[178]
VE3	DO7	DO21	16,700 to 24,200	Drug conjugate (Block structure)	VE3/DO7/DO21 _{4wt%} : 50% drug release after 3 days at pH 5.5 (HPLC)	[178]
VE2	DO7	DO26	26,600 to 45,400 (M _w)	Drug conjugate	VE2/DO7/DO26 _{4wt%} : 50% drug release after 24 h at pH 5.5 (HPLC)	[179]
VE2	DO6	DO21 DO26	11,200 to 40,100	Drug conjugate	VE2/DO6/DO21 _{1wt%} / DO26 _{5wt%} : Drug release at pH 5.5 after 7 days: 40% for DO26 and 10% for DO21 (HPLC)	[180]
VE5	DO27		6,500	Drug conjugate	–	[181]

VE5	DO11	DO27 _{11wt%}	23,300	Drug conjugate	50% drug release after 3 days at pH 5.0 (HPLC)	[181]
VE5	DO11		–		–	[181]
VE5	DO11	DO6	49,800		–	[181]
VE5	DO3		47,800		–	[181]
VE5	DO6		193,100		–	[181]
VE5	DO12		45,300		–	[181]
VE3	DO7 _{60%}	DO16 _{40%}	6,500	Protein conjugation	–	[182]
VE3	DO7 _{64%}	DO17 _{36%}	4,900	Protein conjugation	–	[182]
VE1	DO18		16,000		–	[183]
VE1	DO20		5,600	Drug conjugation	–	[183]
VE1	DO19		17,500	Drug conjugation	–	[183]
VE1	DO19 _{48%}	DO20 _{52%}	19,500	Drug conjugation	–	[183]

VE4	DO15	–	2,800	For block copolymer synthesis		[184]
VE4	DO13		–	For block copolymer synthesis		[185]

^{a)} Additional degradation conditions and profiles are reported.

Polyacetals comprising drugs in the backbone

The wide variety of diols and divinyl ethers represents an excellent platform for the variation of properties of polyacetals in a combinatorial manner, as reported by Koberstein and co-workers, who synthesized a 21-membered library.[174] A variety of hydrophobic aliphatic diols (**DO1** to **DO4**) as well as oligo(ethylene oxide) diols (**DO8** to **DO10**) and three divinyl ethers (**VE1** to **VE3**) were used for that purpose. The combination of hydrophilic and hydrophobic monomers resulted in polyacetals featuring LCST behavior in water in a temperature range from 6 to 80 °C. This behavior was further exploited in wound care applications in a triple polymer-gel matrix additionally including chitosan, hydroxypropylmethylcellulose-stearoxyether and antimicrobial compounds such as silver sulfadiazine.[175]

The oligo(ethylene oxide) based monomers **VE3** and **DO10** represented the basis for the incorporation of hydrophobic Hypoxia Inducible Factor-1 (HIF-1) inhibitors for anti-cancer therapy into the polyacetal chains through copolymerization of the drug diols **DO21**, **DO24** and **DO25**. [176] Drug contents varied from 5 to 40%. Whereas **DO24** and **DO25** polymerized with full conversion, **DO21** was less reactive, resulting in polyacetals with only 20% drug content. The hydrophobicity of the drugs in the PEG-like polymer led to LCST behavior, which could be adjusted by the copolymer composition. Promising candidates for hyperthermia-based targeting included poly(**VE3-co-DO10/DO14**_{15%}) with a T_{cp} of 40.7 °C, poly(**VE3-co-DO10/DO25**_{7.5%}) with a T_{cp} of 39.4 °C, and poly(**VE3-co-DO10/DO21**_{15%}) with a T_{cp} of 39.5 °C. As the drug formed part of the polymer chain, drug release was achieved by complete degradation of the polyacetal. Whereas the molar mass decreased by 50% after 5 h in a pH 5 PBS solution, the drug release was delayed. Only 20% of **DO21** were released after three days.

Vicent and coworkers reported similar polyacetals based on PEG (**DO6** or **DO7**) and **VE2** comprising between 2.4 and 8.9 wt% **DO21**, **DO22**, **DO23** as well as **DO25**.^[177] Detailed release studies of designed copolymer pairs showed that the release of bisphenol A (**DO25**) was significantly slower compared to that of diethylstilberol (**DO21**), and that the degradation of polyacetals with lower drug content or longer PEG spacers was faster. In contrast to the free drugs, the polymeric prodrugs were not or only slightly cytotoxic, thereby enhancing the drug therapeutic index.

In a follow-up study, the influence of the distribution of the of **DO21** with respect to its position in the polyacetal chain was investigated.^[178] In contrast to simple direct copolymerization of all comonomers to result in a statistical distribution of the drug in the polymer chain, a block-like architecture was achieved by a consecutive polymerization of **DO7** and **DO21** with **VE3**. Thereby, the drug content of water soluble polyacetals was increased from 6 to 9 wt%. A different assembly behavior of the two copolymers in water resulted in altered **DO21** release profiles: It was gradually released from the statistical copolymer but in a stepwise fashion from the block-like copolymer. The latter also featured enhanced cytotoxicity in selected prostate cancer cell lines.

Relying on the established PEG-based polyacetal formed from **VE2** and **DO7**, the antioxidant and anti-inflammatory drug curcumin (**DO26**) was copolymerized in drug loadings from 2 to 6 wt%.^[179] Due to the hydrophobicity of the drug, well-defined nanocarriers of 90 nm size (DLS) were formed. Similar to diethylstilberol, the conjugation of curcumin improved solubility, blood bioavailability, cytotoxicity as well as stability in comparison to the free drug to potentially enable treatment for acute and chronic spinal cord injury recovery.

To exploit a synergistic cytotoxic effect against LNCaP cells of both drugs, *i.e.* curcumin (**DO26**) and diethylstilbestrol (**DO21**) were copolymerized in a PEG-based matrix formed from **DO6** and

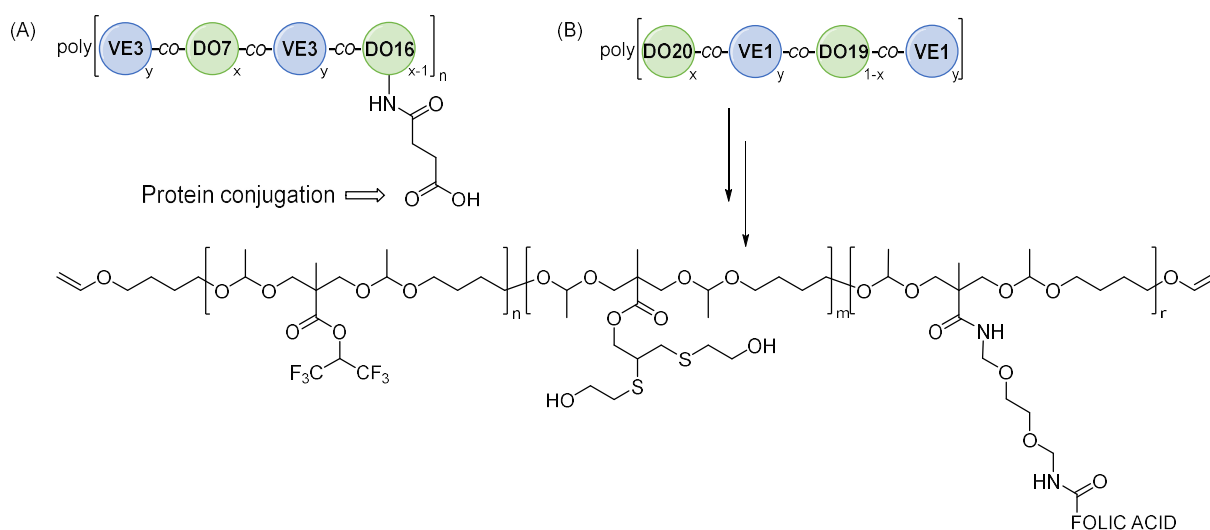
VE2.^[180] Due to the less stable curcumin acetal moieties, copolymers comprising increasing **DO26** amounts featured lower molar masses ($40,100 \text{ g mol}^{-1} > M_n > 11,200 \text{ g mol}^{-1}$) and assembled into smaller nanocarriers ($33 \text{ nm} > D_h > 9 \text{ nm}$). Accordingly, **DO26** was released faster from the copolymers than **DO21**.

The substituent variation at the vinyl double bond would result in a different acetal or ketal repeating units than the simple acetaldehyde-based acetal. Guo *et al.* reported the respective **VE5** to form acetone as degradation product of polyketals synthesized *via* polyaddition with a range of hydrophobic diol monomers (**DO3**, **DO6**, **DO11**, **DO12**).^[181] The catalyst pyridinium *p*-toluenesulfonate yielded polymers with high molar masses between 45 and 193 kg mol⁻¹ ($1.7 < \bar{M}_n < 2.2$) at room temperature. Estradiol (**DO27**) was used as a model drug for copolymerization, either as sole diol or with **DO11**. Degradation of microparticles formed from the terpolymer released the estradiol, avoiding or reducing the formation of acidic degradation products, as was shown by fluorescence mapping of the pH sensitive cargo LysoSensor Yellow/Blue dextran. Biocompatibility of the terpolymer microparticles was confirmed by *in vivo* experiments in rat with benign tissue reaction.

Whereas the approach represents an elegant way to release the drug through backbone degradation in its native form, it is intrinsically limited to drugs comprising two hydroxyl moieties. Reactivity differences of the hydroxyl moieties further complicate predictions of the final copolymer composition, which directly corresponds to the drug loading in this approach. However, detours such as functionalization of such drugs with acetal moieties that are additionally linked to other polymerizable moieties represent promising alternatives circumventing such problems, as recently reported for gemcitabine.^[186]

Polyacetals for conjugation of bioactive molecules

The incorporation of diol monomers with additional functional moieties enables access to polyacetals that can be used for the conjugation of bioactive molecules *via* post-polymerization modification approaches (**Scheme 9**). In particular, Fmoc protected serinol (**DO16**) was frequently applied to yield amino functionalities to be exploited for fluorescence labelling, *e.g.* through NHS ester coupling.[178, 179] In addition, other functional diols such as the alkyne containing **DO19** or the active ester containing **DO20** offer alternative synthetic possibilities.



Scheme 9. Schematic representation of conjugation strategies for the attachment of bioactive molecules to polyacetals obtained by step-growth polymerization.

The serinol strategy was applied for conjugation of trypsin to a PEG-based polyacetal formed from the polyaddition of **VE3** and **DO7**. [182] The resulting polymer comprised 40% of the Fmoc-protected serinol (**DO16**) and was subject to a series of post-polymerization modifications involving the deprotection of the Fmoc group, the ring-opening of succinic anhydride through the nucleophilic amino moieties, and the conjugation of trypsin to the carboxylic acid functionalities

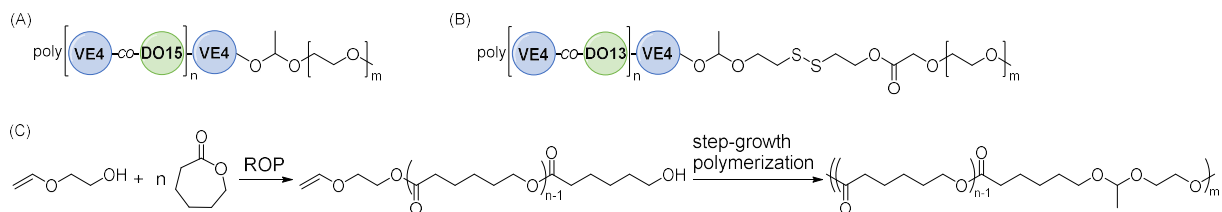
with a C4-spacer (**Scheme 9A**). A terpolymerization of **VE3**, **DO7** and **DO17** yielded a corresponding polyacetal without the C4-spacer, which was less efficiently conjugated due to steric hindrance. Both integer polymers inhibited the enzymatic activity of trypsin at pH 7.4 due to a masking effect, and released the protein at pH 6.5 due to polymer degradation, thereby restoring its activity. The so-called “polymer masked – unmasked protein therapy” (PUMPT) effect was also compared to a common PEGylated trypsin, with 2 to 3-fold higher activity for the polyacetal-based systems.

A conjugation strategy based on the use of ester functionalized diols was reported by Moreno *et al.* (**Scheme 9B**).^[183] The utilized monomers in the polyaddition included **VE1** and diols based on 2,2-bis(hydroxymethyl) propionic acid with different ester groups such as ethyl ester (**DO18**), propargyl ester (**DO19**) as well as hexafluoroisopropyl ester (**DO20**). These monomers enabled chemically orthogonal postpolymerization modifications. **DO19** was reacted with 2-mercaptoethanol by thiol-yne reaction in varying degrees of modification to tune the polymer hydrophilicity, size and critical aggregation concentration (CAC) of nanoparticles, which were used to encapsulate and release curcumin. Based on detailed development of the orthogonal functionalization of the active ester containing monomer **DO20**, a folic acid derivative was attached by amidation to decorate the nanocarriers with a targeting ligand.

Utilization of end groups

The polyaddition of diols and divinyl ethers results in polymers featuring hydroxyl or vinyl ether end groups. While reducing the molar mass,^[174] the use of one monomer in slight excess enables certain control of the end group type. However, a mixture of both end groups will likely be present when the two monomers are used in an equimolar ratio. Nevertheless, terminal vinyl ether moieties

were utilized for attachment of a hydrophilic PEG block through addition of hydroxyl end functional PEG (**Scheme 10A and B**).



Scheme 10. Schematic representation of acetal-copolymer structures obtained by utilization of end groups.

The approach was initially investigated using a polyacetal from **VE4** and **DO15** as light-controlled drug delivery system for photo-chemotherapy.[184] The coupling of mPEG (2,000 g mol⁻¹) resulted in a clear shift of the SEC elugram, however, also in a range of degradation products, most likely formed through transacetalization or hydrolysis of the initial polyacetal. The amphiphilic block copolymer (5,000 g mol⁻¹) was used to encapsulate camptothecin and hematoporphyrin, which were released through pH value and light as triggers (photolysis at single (365 nm) and double (532 nm) photon excitation). The synthetic approach was adopted by Wang *et al.* who additionally included disulfide linkages between the two blocks, *i.e.* a hydrophobic polyacetal from **VE4** and **DO13** and mPEG (2,000 g mol⁻¹) (**Scheme 10B**).[185] The acetal and disulfide functionalities rendered the carriers acid and reductions sensitive, respectively, as demonstrated by degradation studies at various pH values and glutathione concentrations.

Fuoco obtained acetal and ester copolymers by a straightforward one pot polymerization with two subsequent steps combining a heterotelechelic macromonomer synthesis and AB polyaddition (**Scheme 10C**).[187] The first step included ROP of ϵ -caprolactone yielding oligo(ϵ -caprolactone) with TBD as catalyst and ethylene glycol vinyl ether as initiator, introducing the

vinyl ether functionality at the α -end and a hydroxyl functionality at the ω -end. These AB-monomers with molar masses between 300 and 10,200 g mol⁻¹ were then polymerized in a step growth approach by switching the catalyst through addition of an excess of diphenyl phosphate (DPP). The resulting multiblock copolymers featured increased M_n values from 2,300 to 78,400 g mol⁻¹ ($1.6 < D < 2.4$). To expand the proof of concept also other cyclic monomers such as trimethylene carbonate, *p*-dioxanone and L-lactide were utilized in the one pot approach. The degradation behavior of films formed from the poly(oligo(ϵ -caprolactone)-*co*-acetal)s with different DP of the ϵ -caprolactone sequences (6, 10, 18, 33) was investigated over eight days. The according mass losses were between 8% and 16%, whereby films with shorter ϵ -caprolactone sequences degraded faster.

4.1.2. Linear polyacetals from transacetalization polymerization

Recently published transacetalization polymerizations yielding polyacetals rely on DMP and hydrophobic diols initially utilized by Murthy in 2004,[172] *i.e.* **DO4**, **DO11**, and **DO14** (compare **Scheme 8**, **Table 7**). Hence, recent developments are mainly focused on exploiting their properties for new applications, such as the encapsulation and release of apoptosis inhibitors, siRNA, or chemotherapeutic agents.

Table 7. Selected characterization data of the polyacetals obtained *via* transacetalization of 2,2-dimethoxypropane (DMP) and diols. Molar masses determined by SEC.

Polyacetal	M_n (g mol⁻¹)	API	Application	Acidic degradation	Ref.
DO11 + DMP	4,100 (Đ of 1.54)	SB239063	Loaded particles of 370 nm (SEM)	t _{1/2} of 24.1 days at pH 4.5 by ¹ H NMR sample	[188, 189]
0.13 DO4 / 0.87 DO11 + DMP	2,500 (Đ of 1.43)	siRNA / microRNA	Loaded particles of 500 nm (SEM)	t _{1/2} of 1.8 days at pH 4.5 by ¹ H NMR sample	[190-193]
DO14 + DMP	6,700 (Đ of 1.8)	–	Polymer film	Photochemical degradation after 10 min by UV irradiation	[194]
DO4, DO11 + DMP (ABA–block with PNVP)	5,500 (Đ of 1.16)	DOX, imatinib	Loaded particles of 42 to 49 nm (TEM)	M _n change by SEC: Detection of the mass for the hydrophilic block after 24 h	[195]
DO4, DO11 + DMP	8,500 (Đ of 1.05)	DOX	Loaded particles of 70 nm (TEM)	M _n change by SEC: Detection of the mass for the	[196]

(ABA–block with PEG)				hydrophilic block after 24 h	
-------------------------	--	--	--	---------------------------------	--

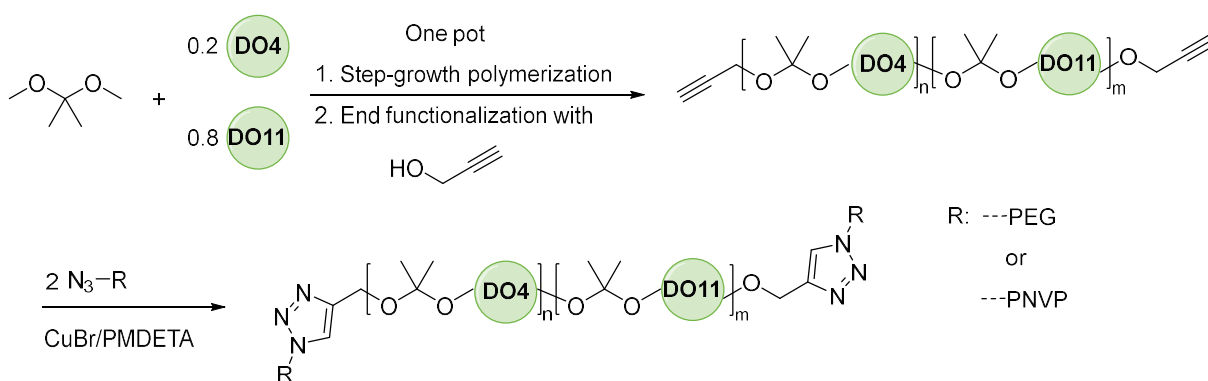
The polyacetal from the condensation of **DO11** and DMP[188] was formulated into *N*-acetylglucosamine (GlcNAc) decorated particles through use of the sugar functionalized surfactant.[189] A decoration degree of 9 wt% was achieved benefitting from the interaction of the surfactant's hydrophobic alkyl chain with the particle exposing the hydrophilic carbohydrate head group to the aqueous phase. The GlcNAc decoration of particles loaded with the apoptosis inhibitor SB239063 led to increased cellular uptake into cardiomyocytes when compared to unfunctionalized particles. A reduction in apoptotic events as well as infarct size, and improved acute cardiac function were found in rats treated with the particles, whereas no acute effects of non-sugar-decorated particles were found.[197]

For the delivery of genetic material such as siRNA, a copolymer based on two diols **DO4** as well as **DO11** with DMP[191, 192] was coformulated with the cationic lipid DOTAP and chloroquine to increase the endosomal escape.[190] An improvement of cardiac function of mice following myocardial infarction was achieved through uptake by cardiac macrophages, where released siRNA specifically silenced the Nox2 gene and inactivated the NADPH oxidase, thereby restoring acute cardiac function at a low dose of 5 $\mu\text{g kg}^{-1}$ animal. The same polyacetal was also applied to deliver microRNA for the reprogramming of cultured mouse bone marrow-derived mononuclear cells.[193] The microRNA released from particles containing 0.9 wt% of genetic material was specific towards embryonic stem cells and successfully activated pluripotency-associated genes (Oct4, Sox2 and Nanog) without permanent genetic manipulation after only eight days of treatment.

Polyacetals are also potentially photochemically degradable.[194] This was intensely investigated for polymers prepared *via* both step growth mechanisms, *i.e.* for a polymer from polycondensation of **DO14** and DMP as well as a polymer obtained *via* the polyaddition of **VE4** and **DO14** (compare Chapter 4.1.1.). Films from both polymers of roughly similar molar mass degraded fully after 10 min exposure to low energy UV irradiation at 193 nm as well as 248 nm. A photolysis mechanism was proposed, based on the heterolytic cleavage of the benzylic acetal moieties and subsequent rearrangement to carbonyl and hydroxyl products. The polymer films were used as photodegradable substrates for laser-mediated cell detachment and direct patterning of mouse fibroblasts sheets through postculture laser ablation.

The step-growth synthesis was further expanded by the introduction of alkyne groups at both ends of the polyacetal backbone thereby enabling postpolymerization modification (**Scheme 11**).[195, 196] For this purpose, the transacetalization polymerization was performed as already established with a feed ratio of 20 mol% **DO4** and 80 mol% of **DO11**. After monomer conversion, propargyl alcohol was added in large excess to produce oligomeric acetals with claimed end groups ($M_n \approx 1,800 \text{ g mol}^{-1}$; $\bar{D} = 1.15$). Subsequently, ABA copolymers were synthesized by the alkyne-azide-click reaction with N_3 -poly(ethylene glycol) and N_3 -poly(*N*-vinyl pyrrolidone), respectively. Both ABA polymers formed nanocarriers of 4 to 6 nm size (TEM), which considerably increased upon loading with hydrophobic drugs such as DOX or imatinib (42 to 70 nm). Strong decrease of M_n was observed at pH values between 1.4 and 7.4 after 4 h. Despite complete degradation of the hydrophobic segments of the carrier polymers, drug release reached a plateau after ~ 10 h independent of the utilized polymer, drug or the pH value. This might point towards aggregation of the hydrophobic drugs upon degradation of the carrier, thereby impeding quantification in the

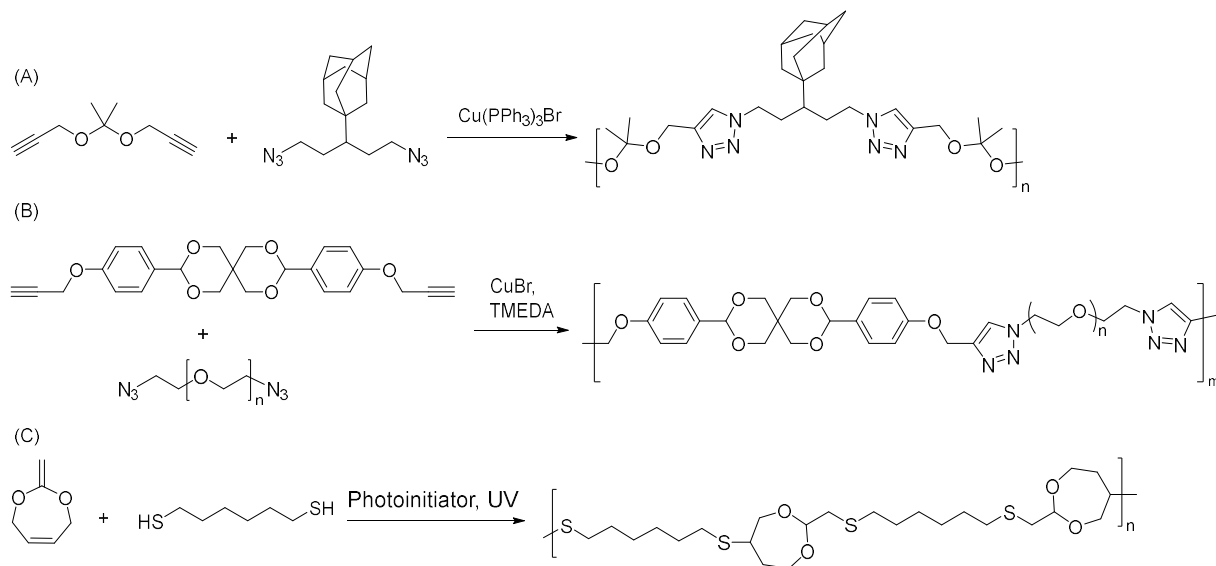
used setup. *In vitro*, the loaded nanocarriers demonstrated tumoricidal activities against the parental and drug resistant lymphoma cells of murine and human origin with significant effects on cellular uptake, cytotoxicity, growth inhibition and apoptosis. *In vivo*, PEG-*b*-PA-*b*-PEG+DOX reduced the lymphoma size and increased the life span of the treated mice with improved histopathological parameters.



Scheme 11. Schematic representation of the synthetic strategy towards ABA polymers with a hydrophobic polyacetal middle block and hydrophilic outer blocks.

4.1.3. Linear polymers from polyaddition of acetal containing monomers

In addition to synthesis of polyacetals by formation of the acetal moiety throughout the polymerization process, the acetal/ketal unit can already be present within the monomer structure and stay unaltered during the polymerization, thereby introducing the ketal into the polymer backbone while other functional groups react in a step-wise manner (**Scheme 12**).



Scheme 12. Schematic representation of linear polyacetals from polyaddition of acetal containing monomers.

This synthetic approach was successfully implemented by Murthy and coworkers (**Scheme 12A**).^[198] The alkyne–azide–cycloaddition was used to polymerize a diazide adamantane monomer together with a dialkyne ketal monomer to yield polyacetals with M_n of $49,500 \text{ g mol}^{-1}$ and D of 1.74. The adamantane group embedded into the backbone formed host guest complexes with β -cyclodextrin modified with *b*PEI (1800 g mol^{-1}). pDNA polyplexes of these materials increased transfection efficiency 60-fold in comparison to the uncomplexed β -cyclodextrin modified with *b*PEI while also reducing the cytotoxicity.

A similar approach was reported by Andrade–Gagnon *et al.* (**Scheme 12B**).^[199] The spirocyclic acetal monomer based on pentaerythritol was further functionalized with two (ethynyloxy)aryl groups to be subsequently polymerized with diazide–PEG in a step–growth manner by the Cu(I)–catalyzed cycloaddition. Nanoaggregates with sizes of 400 to 460 nm formed from these amphiphilic polymers were hydrolysable at acidic pH value but stable at physiological pH value.

However, the similar Nile Red release profiles at both pH values pointed towards the presence of leakage effects, although the carriers were cytocompatible and taken up by epithelial cells.

The bifunctional monomer 2-methylene-1,3-dioxane-5-one was used to synthesize a poly(acetal thioether).[200] First, the anti-Markovnikov thiol-ene addition of the acetal ketene functionality with 1,6-hexanedithiol led to dimeric intermediates (**Scheme 12C**). Subsequently, the photoinitiated, radical polyaddition of the remaining endocyclic double bonds with the dithiol yielded polymers with backbone acetal functionalities. After reduction and capping of the thiol end groups, a polymer of M_n of 5,900 g mol⁻¹ and \bar{D} of 3.8 was obtained.

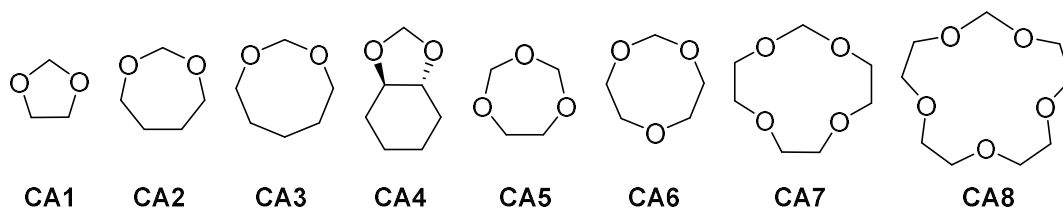
4.2. Chain growth polymerization

Over the last decade a range of different synthetic strategies was reported for the incorporation of acetal moieties into the polymer backbone. Besides the direct ROP of cyclic monomers, their copolymerization with lactones or vinyl ethers open access to polymers with adjustable degradation behavior. In this regard, acetal functionalities in the polymer backbone are also formed in copolymerizations of vinyl ethers with carbonyl compounds or cyclic ethers when a crossover of the monomers takes place. In addition, cyclic hemiacetal esters enable access to polymers with repeating acetal and ester moieties. As many of these synthetic strategies are new, recent publications in this field mainly focus on polymerization mechanism, the design of new polymers as well as on detailed characterization approaches. The few applications reported so far include solid electrolytes in batteries, recyclable thermoplastics or drug delivery systems but rely mainly on well-established synthesis strategies such as the ROP of cyclic acetals based on formaldehyde.

4.2.1. Polymerization of cyclic acetals

Cyclic acetal monomers (**Scheme 13**) represent a straightforward choice for obtaining polyacetals in a direct ROP approach. In fact such syntheses were already reported in the 1930s for the cationic ROP (CROP) of the seven-membered formaldehyde-based acetal **CA2** and the analogous eight membered ring **CA3** by Hill and Carothers.[201] The homopolymerization of **CA1** was patented in the 1940s.[202] Cyclic acetals based on (substituted) **CA1** and **CA2** were found to copolymerize with formaldehyde or 1,2,5-trioxane yielding polyoxymethylene copolymers with high industrial success and are today known as POM-C.[165, 166, 203-210]

In addition to these formaldehyde and acetaldehyde based materials, additional early reports exist on the copolymerization of other substituted 1,3-dioxacycloalkanes with 1,2,5-trioxane.[211-213] Since then, aspects of polymerization conditions and mechanistic pathways have remained of great interest. The activated chain end mechanism during Brønsted or Lewis acid catalyzed CROP of such monomers promotes formation of cyclic polymers with overall low molar masses, which causes dispersity broadening and hampers the access to end-functionalized polyacetals. Intermacromolecular transacetalization represents another challenge to be met during the synthesis of tailor-made polyacetals.[209]



Scheme 13. Schematic representation of cyclic acetal monomers successfully polymerized *via* chain-growth processes to homopolymers.

The access to α,ω -hydroxy telechelic polyCA1 was recently optimized in the triflic acid / ethylene glycol initiated CROP.[214] Low catalyst to initiator ratios in the solution polymerization were favorable. However, inter- and intramacromolecular transacetalization could not be avoided at conversions above 20%.

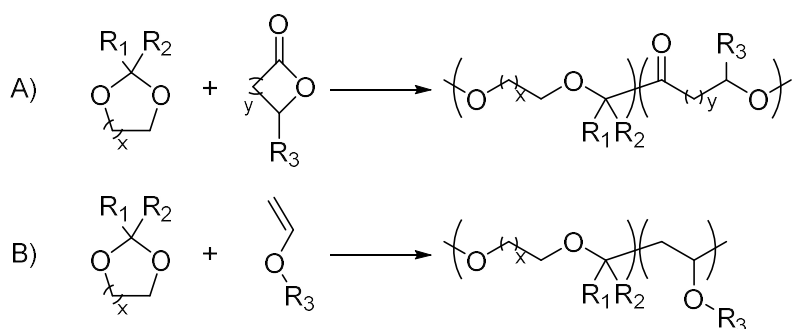
Other recent reports are concerned with achieving high molar mass polyCA1. The use of rare-earth triflates [RE(OTf)₃] (RE = Sc, Y, Gd, Tm, and Lu) led to polyCA1 with molar masses up to 44,300 g mol⁻¹ as well as $\bar{D} < 1.71$. [215] Coates and coworkers described reversible-deactivation conditions during the CROP of cyclic acetals using halogenmethyl methyl ethers as initiators and indium(III) bromide as catalyst.[216] The living polymerization of five different cyclic acetals (CA1 to CA4, CA6) based on formaldehyde yielded polymers with high conversions (up to 85%) and molar masses up to 230,000 g mol⁻¹. Dispersity values ranged between 1.51 and 1.74 due to the transacetalization as described above. PolyCA1 was investigated in detail as a chemically recyclable thermoplastic, as it exhibited tensile strength comparable to commodity olefins such as isotactic polypropylene or high-density polyethylene. Depolymerization catalyzed by a strong acid was impressively shown as it was possible to recover the CA1 monomer quantitatively by distillation from polymer bulk material or plastic waste mixtures.

In particular, the more hydrophilic poly(ether acetals) (CA1, CA5 to CA8) are currently discussed as poly(ethylene oxide) (PEO) alternatives as polymer electrolytes in lithium-ion batteries.[217-222] The polymers can be synthesized from cyclic acetals containing increased amounts of ethylene oxide in the ring structure, predetermining the ratio of ethylene oxide and methylene oxide repeating moieties in the resulting polymers.[217] The variation of the Li⁺ coordination in the electrolyte, as in comparison to PEO, enhances the cation self-diffusion and, hence, influences the conductivity. Further optimizations are potentially possible through the use of miscible blends

of, e.g., polyCA6 and PEO.[219] In this context, it should also be noted that the monomer CA1 can be used as solvent in Li ion batteries, whereby its electro- or cationic polymerization within the device creates a protective solid electrolyte interphase layer.[220-223]

4.2.2. Copolymerization of cyclic acetals with lactones or vinyl ethers

The fact that cyclic acetals can be polymerized *via* CROP facilitates their copolymerization with other cationically polymerizable monomers such as lactones or vinyl ethers (**Scheme 14, Figure 12**).

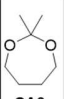
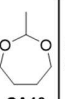
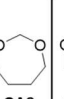
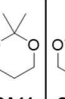
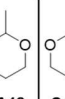
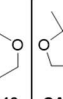
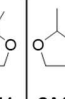
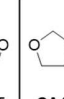
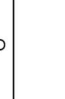


Scheme 14. Schematic representation of the cationic copolymerization of cyclic acetals with A) lactones and B) vinyl ethers.

The copolymerization of L-lactide with CA1 yielded copolymers comprising up to 27 mol% acetal moieties leading to increased acid sensitivity compared to the pure polyester.[224] For instance, a copolymer featuring a molar mass of 7,500 g mol⁻¹ degraded to oligomers of 1,400 g mol⁻¹ after 72 hours.

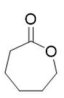
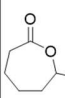
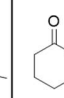
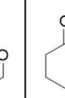
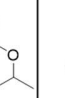
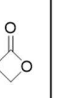
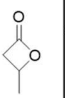
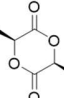
Cyclic acetals represent isomers of hydroxyl functionalized vinyl ethers. 4-Hydroxybutyl vinyl ether (VE21) isomerized forming 2-methyl-1,3-dioxepane (CA10) within 5 min at 0 to 30 °C in the presence of ethanesulfonic acid (EtSO₃H), *i.e.* under cationic polymerization conditions.[225] Its copolymerization with ε-caprolactone yielded a variety of copolymers with tunable

compositions and sequences depending on the initial monomer concentration. Poly(ϵ -caprolactone-*alt*-**VE21**) was obtained by removal of **CA10** at reduced pressure from a copolymer comprising 80 mol% **CA10**. During this degradation under vacuum *via* depolymerization as well as random transacetalization, the molar mass decreased from 6,300 g mol⁻¹ to 1,900 g mol⁻¹. However, such copolymerizations were only possible with a few lactones.[226] Copolymerizations of **CA15** and L-lactide, β -butyrolactone, as well as β -hexanolactone failed; copolymerizations with ϵ -heptanolactone and β -propiolactone proceeded slowly yielding cyclic, low molar mass products. In contrast, δ -valerolactone and ϵ -caprolactone were copolymerizable with **CA10**. Other cyclic acetals were incorporated only in low amounts into PCL. Poly(δ -valerolactone-*co*-**CA15**) was subjected to a polymerization-depolymerization study controlled by the reaction temperature between 30 and 90 °C. Sequence transformation was achieved at higher temperatures shifting from 2:1 [**CA15**]:[δ -valerolactone] towards a 1:1 ratio of the monomers. Interestingly, this behavior was reversible, whereas the **CA15** monomer was reintroduced into the polymer backbone upon cooling.

M_n kg mol ⁻¹ /Đ	 CA9	 CA10	 CA2	 CA11	 CA12	 CA13	 CA14	 CA15	 CA1
VE9	15.6 /1.41	6.8 /1.65	11.2 /1.84	16.5 /1.85	7.2 /1.19		9.9 /1.19	5.2 /1.37	
VE8	13.0 /1.16	8.6 /1.36	4.5 /1.34	12.8 /1.16			9.9 /1.09		
VE14	8.5 /1.54						1.0 /1.26		
ϵ -Caprolactone	2.5 /2.20	15.2 /1.9	1.6 /3.24		16.1 /1.37			10.0 /3.10	23.3 /1.79
L-Lactide									7.5 /2.0*

Behavior in copolymerization

- Copolymer via frequent crossover
- Occasional crossover / reduced polymerization control
- Vinyl homopolymers
- No data

								
CA10 (VE21)	14.5 /1.90**	1.3 /2.17	8.8 /1.92**			0.5 /2.21		

- Copolymer via frequent crossover
- Occasional crossover / slow reaction
- Not successful

* No crossover information, [L-lactide]/[CA1]:1.4
** Main peak value

Figure 12. Top: Summary of copolymerization studies of a variety of cyclic acetals with the vinyl ethers and lactones. **Bottom:** Summary of the copolymerization study of 2-methyl-1,3-dioxepane (CA10) (generated *in situ* from 4-hydroxybutyl vinyl ether (VE21)) with a variety of lactones. Molar masses determined by SEC.

The cationic copolymerization of several cyclic acetals derived from formaldehyde, acetaldehyde and acetone with the vinyl ethers **VE8** and **VE9** was intensively investigated (**Figure 12**).[227, 228] Among them, the 5-membered heterocycle **CA1** as well as the 7-membered rings **CA2** and **CA10** underwent homopolymerization or oligomerization under the conditions used in the copolymerizations (IBEA / TiCl₄ / SnCl₄ / ethyl acetate / DTBP, in toluene / CH₂Cl₂ at -78 °C), which is in agreement with earlier reports.[201, 209] In copolymerizations with the vinyl ethers, vinyl ether homopolymers were obtained for non-compatible VE-cyclic acetal combinations. However, several copolymer sequences such as multiblock, random, or nearly alternating were realized for suitable monomer combinations. For copolymers with **VE9**, an increasing stability of the acetal-generated carbocation (primary < secondary < tertiary) also increased the efficiency of

the crossover reaction as well as the polymerization rate. The more reactive **VE8** exhibiting a higher tendency to homopolymerize led to fewer successful **VE8**–cyclic acetal combinations with less frequent crossover reactions.

Trimethylsilyl vinyl ether (**VE14**) enabled access to polyvinyl alcohol through deprotection of the resulting polymer, which can be achieved at weak basic or acidic conditions but also with fluorides.[229] In a copolymerization with a cyclic acetal such as **CA9** (**Figure 13**), the resulting vinyl alcohol repeating units form an unstable hemiacetal at positions in the polymer chain where a crossover took place. Applicable also in terpolymers of **VE14**, **CA9** and **VE9**, the strategy hence facilitated selective cleavage of these predetermined breaking points with fluoride ions, whereas the acetal moieties could be further degraded under acidic conditions.

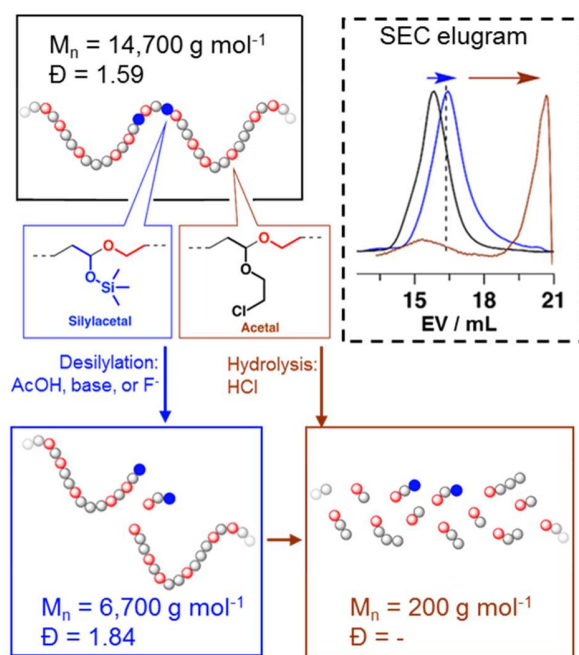
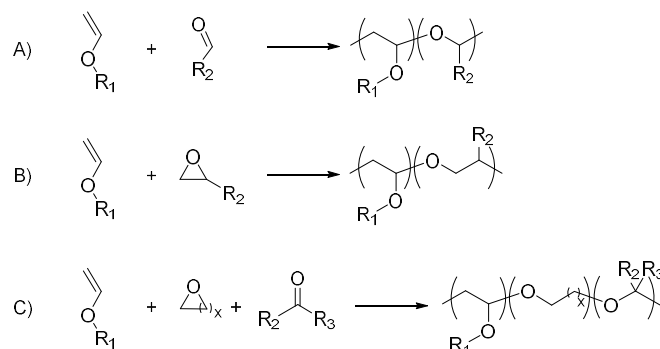


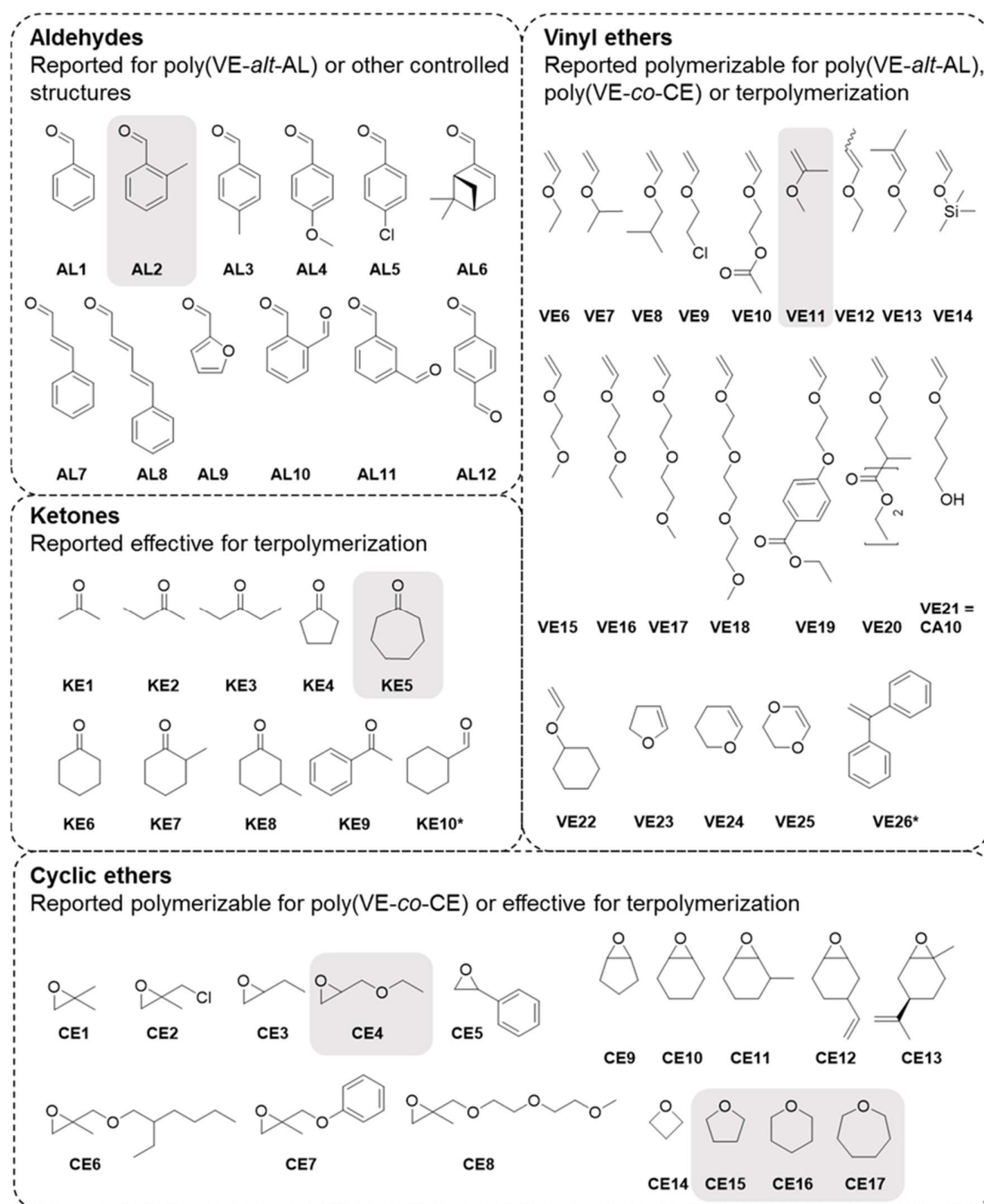
Figure 13. Schematic representation the selective cleavage of hemiacetal moieties formed upon desilylation of trimethylsilyl vinyl ether repeating units the terpolymer poly(**VE9**–*co*–**CA9**–*co*–**VE14**) as confirmed by SEC (EV: elution volume). Adapted with permission from [Kato R. *et al* ACS Macro Lett. 2019;8:1498-503]. [229] Copyright 2019 American Chemical Society.

4.2.3. Copolymerization of vinyl ethers with aldehydes

Over the last years, Aoshima and coworkers produced a large body of work on cationic copolymerization of vinyl ethers with aldehydes, oxiranes (as well as other cyclic ethers), and ketones as well as the combination thereof. Review articles concentrate mainly on mechanistic aspects of that research area and focus on living cationic polymerization in general as well as Lewis acid–base pair catalysis, and are recommended to the interested reader.[230, 231] Whereas their degradability is seen as a tool to elucidate monomer sequences within these copolymers, biomedical use of the materials is not focused upon. The acetal functionality is introduced by the consecutive polymerization of a vinyl ether and, *e.g.*, an aldehyde. Thereby one acetal oxygen atom is located in the backbone and one in the sidechain (**Scheme 15**). The degradability is not affected by this positioning and can even yield recyclable degradation products. In more recent studies a large variety of monomers was tested, mainly with the focus on achieving alternating or sequence controlled polymers (**Scheme 16**). In particular, the cyclotrimerizations represent frequent side reactions to be avoided. For that purpose, control parameters such as monomer structure and reactivity, Lewis acid, solvent, presence or absence of Lewis bases represent crucial factors.



Scheme 15. Schematic representation of vinyl ether copolymerizations yielding polymers featuring acetal moieties.



Scheme 16. Schematic representation of monomers tested for different chain growth polymerizations. Compounds marked in grey reported unsuccessful in the respective polymerization attempts. Compounds marked with an asterisk (*) are sorted according to their use in the polymerization instead of functionality. **VE21** isomerizes forming the cyclic acetal **CA10**.

Table 8. Copolymerizations of vinyl ethers and aldehydes. Schematic representation of the monomer structures is depicted in **Scheme 16**. Deviations from the standard polymerization conditions (EtSO₃H / GaCl₃ / 1,4-dioxane in toluene at -78 °C) are noted accordingly. DTBP: 2,6-Di-*tert*-butylpyridine. Molar masses determined by SEC, unless indicated otherwise.

VE	AL	M_n (g mol⁻¹)	D	Reaction conditions	Content AL (%)	M_n of degradatio n product (g mol⁻¹)	Ref.
VE11	AL1 / AL3 / AL4	4,700 to 6,500	1.40 to 1.59	Standard	<1	–	[232]
VE12	AL1 / AL3 / AL4	17,800 to 20,300	1.17 to 1.59	Standard	42 to 48	150 to 210	[232]
VE13	AL1 / AL3 / AL4	300 to 380	–	Standard	–	–	[232]
VE23	AL1 / AL3 / AL4	6,000 to 18,400	1.72 to 2.40	Standard	44 to 48	190 to 200	[232]
VE24	AL1 / AL3 /	3,500 to 13,000	1.38 to 1.90	Standard	48 to 50	100 to 1000	[232]

	AL4						
VE25	AL4	21,100	1.62	GaCl ₃ in CH ₂ Cl ₂ at -78 °C	49	–	[232]
VE9	AL7	22,400	1.15	Standard	47	160	[233]
VE9	AL8	18,000	1.27	EtSO ₃ H / GaCl ₃ / 1,4-dioxane / DTBP in toluene at -78 °C	48	180	[233]
VE8	AL6	22,100	1.12	Standard	48%	180	[234]
VE9	AL1	10,000	1.08	Standard	5 (short block) ⁴⁾	5,100	[235]
VE8	AL6	5,100	1.17	Standard	~25 (block) ⁴⁾	3,300	[235]
1. VE8 2. VE4	AL6	11,300	1.53	1. EtSO ₃ H / GaCl ₃ / 1,4-dioxane in toluene at -78 °C, 2. -40 °C	n.d.	1,500	[235]
VE9	AL11	13,700 ¹⁾	1.65	Standard	n.d.	690	[235]
VE18	AL4	33,900	1.27	EtSO ₃ H / GaCl ₃ / DTBP / 1,4-dioxane in toluene at -78 °C	48 (alt) ⁴⁾	170	[236]

VE18	AL4	17,900	1.21	EtSO ₃ H / GaCl ₃ / DTBP / 1,4-dioxane in toluene at -78 °C	14 (block) ⁴⁾	13,400	[236]
VE18	AL4	31,200	1.30	EtSO ₃ H / GaCl ₃ / DTBP / 1,4-dioxane in toluene at -78 °C	7 (gra- dient) ⁴⁾	3,300	[236]
VE10	AL9	8,100	1.51	Standard	48	285 / 389 / 433 ³⁾	[237]
VE10	AL9	5,900	1.56	EtSO ₃ H / GaCl ₃ / 1,4-dioxane in CH ₂ Cl ₂ at -78 °C	40		[237]
VE9	AL9	5,700	1.75	Standard	48		[237]
VE8	AL10	17,500	1.21	Standard	48	360	[238]
VE23	AL10	5,400	2.12	Standard	–	–	[238]
VE24	AL10	9,000	2.06	Standard	52	–	[238]
VE13	AL10	5,800	1.69	Standard	50	260	[238]
VE9	AL11	2,200	1.77	EtAlCl ₂ with THF or ethyl acetate in CH ₂ Cl ₂ at 0 °C	90 ⁴⁾	100	[239]

VE9	AL12	3,600	2.39	EtAlCl ₂ with THF or ethyl acetate in CH ₂ Cl ₂ at 0 °C	87 ⁴⁾	–	[239]
VE13	AL11	3,100	2.21	EtAlCl ₂ with THF or ethyl acetate in CH ₂ Cl ₂ at 0 °C	95 ⁴⁾	–	[239]
VE13	AL12	2,500	1.99	EtAlCl ₂ with THF or ethyl acetate in CH ₂ Cl ₂ at 0 °C	n.d. ⁴⁾	–	[239]
VE26	AL11	2,300	1.65	GaCl ₃ in CH ₂ Cl ₂ at –78 °C	n.d. ⁴⁾	–	[239]
VE18	AL4	33,900	1.27	EtSO ₃ H / GaCl ₃ / 1,4–dioxane / DTBP in toluene at –78 °C	48	170	[240]
VE19	AL1	14,800	1.15	EtSO ₃ H / GaCl ₃ / THF in toluene / CH ₂ Cl ₂ at –78 °C	42	190/150	[240]
VE20	AL1	12,700	1.12	GaCl ₃ / THF in toluene at –78 °C	46	150	[240]
VE9	AL1	16,700	1.19	Standard	45	–	[241]
VE9	AL3	27,300	1.28	Standard	49	–	[241]
VE9	AL4	5,500	1.75	Standard	50	–	[241]

VE9	AL5	11,000	1.31	Standard	43	100	[241]
------------	------------	--------	------	----------	----	-----	-------

¹⁾ Indicative of the copolymer microstructure.

²⁾ Determined by laser light scattering.

³⁾ Determined by electrospray ionization mass spectrometry (ESI MS).

⁴⁾ % Cyclic trimerization.

General reaction scope / living polymerization

Earlier reports describe the establishment of the base-assisted cationic copolymerization of isobutyl vinyl ether (**VE8**) and benzaldehyde (**AL1**) initially utilizing EtSO₃H and EtAlCl₂ in toluene in the presence of 1,4-dioxane at -78 °C.[242, 243] A subsequent systematic study investigating the structural effects was performed for cationic copolymerizations of benzaldehyde derivatives and various enol ethers with different structures under standard reaction conditions (**Table 8**).[232] In addition to simple vinyl ethers such as **VE6** and **VE8**, acyclic monomers with methyl substituents involved the α -methyl substituted **VE11**, the β -monomethyl substituted **VE12**, and the β,β -dimethyl substituted **VE13**. Additionally, five- and six-membered cyclic enol ethers such as **VE23**, **VE24**, and **VE25** were investigated. Several benzaldehyde-based monomers (**AL1** / **AL3** / **AL4**) successfully copolymerized with **VE6**, **VE12**, **VE8**, **VE23** and **VE24**. Some copolymerizations were even well controlled, yielding alternating copolymers with controlled molar masses and dispersity values. However, monomers such as **VE11**, **VE13** or **VE25** either homopolymerized, underwent exclusive cyclotrimerizations with one benzaldehyde-based monomer, or prohibited any polymerization. Nevertheless, the possibility to achieve a successful alternating copolymerization in such cases through variation of the polymerization conditions was demonstrated for the copolymerization of **VE25** and **AL4**. In general, the molar masses of the

poly(VE-co-AL) increased with increasing reactivity of the benzaldehyde-based monomer following **AL1** < **AL3** < **AL4** due to the increasing ability to stabilize the cationic charge. In contrast, an ortho-substitution of the benzaldehyde-based monomer (**AL2**) resulted in loss of the defined properties, increase of side products, in particular for copolymerizations with β -substituted enol ethers. Among a variety of plant-derived, non-aromatic enals, in particular the copolymerization of **VE8** and myrtenal (**AL6**) was well controlled.[234, 244]

The controlled cationic copolymerization of cinnamaldehyde (**AL7**) with **VE8** proceeded *via* the specific 1,2-carbonyl addition of the enal fragment and resulted in the alternating copolymer poly(**VE8-alt-AL7**).[233] Its acidic hydrolysis yielded, among others, **AL8** as a degradation product. Despite the additional conjugated double bond, the copolymerization of **AL8** with **VE8** also proceeded mainly *via* the 1,2-carbonyl addition. The resulting copolymer likewise hydrolyzed to yield the extended conjugated aldehyde (*E,E,E*)-7-phenylhepta-(2,4,6)-trienal with ~ 80% yield. A chemical recycling system was hence established as overall three copolymerization-hydrolysis rounds were achieved taking into account the synthesis of poly(**VE8-alt-AL1**) and its hydrolysis giving the **AL7** monomer.[242]

The synthetic sequence control was demonstrated through the controlled cationic copolymerization of **VE9** and **AL3** as well as **VE8** and **AL6**. [235] Up to three predetermined breaking points in form of alternating VE-AL sequences (*i.e.* acetal moieties) were introduced in the main chain by addition of at least five equivalents of the highly reactive **AL3** to the living cationic polymerization of **VE9**. Thereby, the fast aldehyde consumption facilitated the formation of homo-VE-sequences before and after aldehyde addition. Block-type copolymers with degradable VE-AL blocks were obtained by addition of 1.5 equivalents of **AL6** to the living

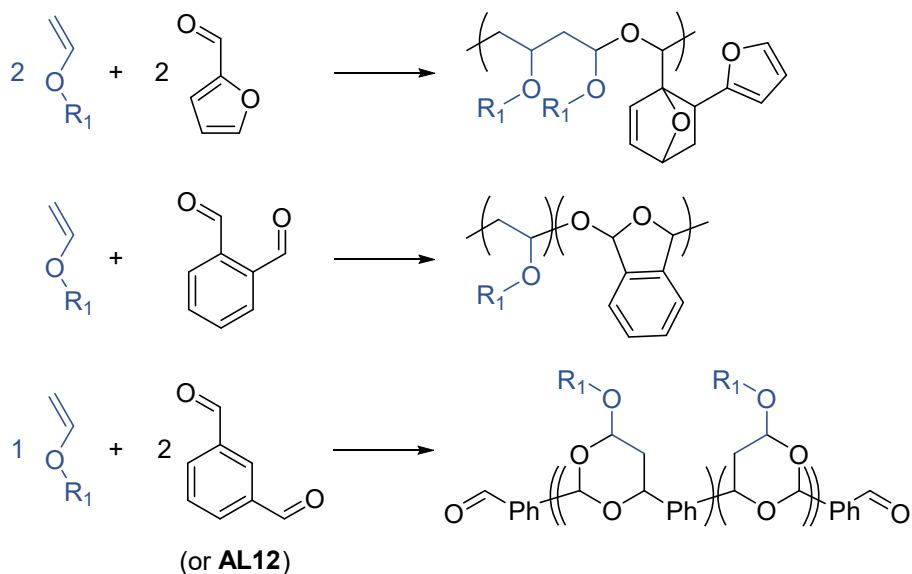
cationic polymerization of the monomer **VE8**. Subsequently, the two monomers were consumed at the same rate yielding poly(**VE8**)–*block*–(**VE8**–*alt*–**AL6**). The livingness of such polymerizations was further exploited in order to obtain core–degradable star–shaped polymers, through addition of a bifunctional VE or aldehyde in the second step to enable crosslinking of the second block.

The sequential arrangement of monomeric units was further expanded to gradient copolymers made of tri(ethylene glycol) methyl vinyl ether (**VE18**) and **AL4**.^[236] Use of a large excess of **VE18** ($[\text{VE18}]_0/[\text{AL4}]_0 = 11/1$) caused a gradual decrease in the instantaneous composition of the aldehyde units along the polymer. Alternating as well as block copolymers with the same monomers were obtained as described above. However, less reactive **AL6** as well as **AL1** hindered the crossover reaction the VE–derived propagation end to the aldehyde monomer.

In addition to being evident from the thermoresponsive properties of the materials, the successful synthesis of such tailored polymer architectures was confirmed by SEC after acidic hydrolysis of the respective breaking points at the specific positions.^[235, 236] Whereas alternating copolymers fully degraded into low molar mass products, according polyVE fragments of higher molar mass were clearly evident for block, gradient and star–shaped polymers.

More complex poly(VE–co–AL) from various aldehydes

The aldehyde monomer scope was further expanded to more complex monomers such as furfural (**AL9**),^[237] *o*–phthalaldehyde (**AL10**),^[238] isophthalaldehyde (**AL11**) and terephthalaldehyde (**AL12**) (**Scheme 17**).^[239]



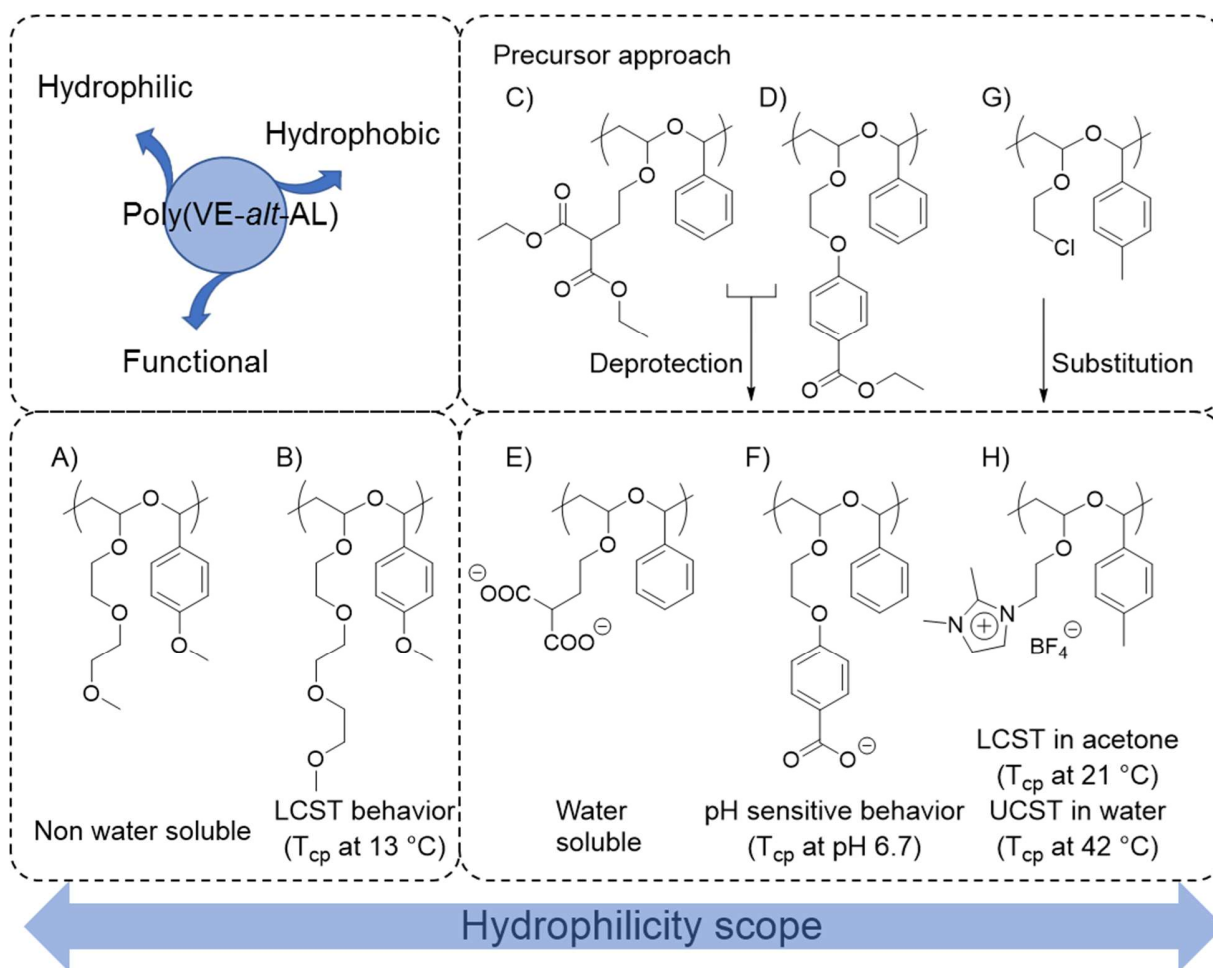
Scheme 17. Schematic representation of the copolymerization of vinyl ethers and furfural (**AL9**), *o*-phthalaldehyde (**AL10**), isophthalaldehyde (**AL11**) and terephthalaldehyde (**AL12**) yielding more complex structures.

The use of **AL9** in the copolymerization with 2-acetoxyethyl vinyl ether (**VE10**) as well as **VE9** resulted in a 2:(1 + 1)-type repeating sequence because every second **AL9** monomer reacted as dienophile in a Diels-Alder reaction with the pendant furan ring adjacent to the growing carbocation.[237] In contrast, the use of dialdehydes resulted in a variation of the backbone structure. The living copolymerization of **AL10** with **VE8** proceeded *via* the intramolecular cyclization of the two aldehyde moieties of **AL10** and frequent crossover propagation between **AL10** and **VE8**. [238] However, **AL10**'s tendency to form five-membered-rings also in cationic homopolymerization[245] was reduced when copolymerized with **VE23** as approximately 15% of the aldehyde units did not undergo intramolecular cyclization. On the other hand, **VE24** and **AL10** yielded a nearly alternating copolymer. Here, **AL10** probably helped to overcome the low homopolymerizability of the sterically hindered **VE24**. Furthermore, the sterically hindered **VE13**,

which does not homo- or copolymerize with benzaldehyde derivatives, was also copolymerizable with **AL10** in an alternating fashion. **AL11** and **AL12** yielded six-membered rings when copolymerized with vinyl monomers such as **VE9**, **VE13** or **VE26**.^[239] However, the use of the more reactive vinyl ethers **VE8** and **VE7** resulted in side reactions such as VE-homopolymerization and termination of the linear poly(cyclic acetal) chain.

Functional and stimuli responsive copolymers

Most copolymers of aldehydes and vinyl ethers represent hydrophobic materials, which is due to the use of the hydrophobic aldehydes during copolymerization that decreases the water solubility of the polyvinyl ether analogs, as the case for 2-(2-methoxyethoxy)ethyl vinyl ether (**VE17**) (A in **Scheme 18**).^[236] However, increased length of the pendant oligo(ethylene glycol) chain resulted in copolymers featuring LCST behavior in water (B in **Scheme 18**).^[240] Also hydrophilic copolymers featuring carboxylate moieties were accessible through use of ethyl ester functional vinyl ethers and subsequent deprotection at alkaline conditions (C-F in **Scheme 18**). The detour was necessary because the cationic polymerization mechanism prohibited the direct polymerization of the carboxylic acid functional monomers. Whereas F in **Scheme 18** was water soluble only at $\text{pH} > 6.7$, *i.e.* featured pH value responsive solubility behavior, the two carboxylate functionalities made (E) fully water soluble over the whole temperature range, potentially the only poly(VE-*alt*-AL) reported so far.



Scheme 18. Schematic representation of responsive and functionalized alternating copolymers of vinyl ethers and aldehydes.

The use of the standard vinyl ether monomer **VE9** enabled access to further post-polymerization modifications through nucleophilic substitution of the pendant chlorine atom.[241] The approach was exploited for the attachment of dimethylimidazolium functionalities to copolymers of **VE9** with several aldehydes (96 to 100% efficiency). The resulting alternating polymeric ionic liquids featured UCST-type phase transitions in water, and several also LCST behavior, as investigated in detail by the authors. The LCST behavior of several copolymers in acetone was exploited for

thermo-induced micelle and aggregate formation of a block copolymer comprising a polyVE8 segment as a corona.

4.2.4. Copolymerization of vinyl ethers with oxiranes

Similar to the reaction of vinyl ethers with aldehydes, the strictly alternating polymerization of vinyl ethers and oxiranes would yield copolymers with an acetal group in the repeating unit by concurrent cationic vinyl-addition and ring-opening copolymerization (**Scheme 15 B**).

The excellent focus review[246] by Kanazawa *et al.* summarized different strategies for this polymerization approach. We hence briefly summarize key aspects and focus on very recent work (**Figure 14**). So far poly(VE-co-oxirane) were obtained by copolymerization *via* frequent crossover reaction. Although the comonomers were not incorporated in a strictly alternating fashion, the VE-oxirane crossover per chain was sufficient to yield low molar mass degradation products after hydrolysis. The generation of a stabilized carbocation resulting from the ring opening of the oxonium ion derived from an oxirane was essential for successful crossover (**Figure 14**, top). By implication, the frequency of crossover reactions in copolymerization depended on the frequency of the ring-opening reactions of oxonium ions and the nucleophilicity of the monomers. Substituents at the oxirane ring were hence found to be crucial for the successful copolymerization with alkyl VEs. In addition, a suitable Lewis acid catalyst generating a weakly coordinating counter anion was necessary. For instance, $B(C_6F_5)_3$ effectively initiated through the reaction with water traces, producing $B(C_6F_5)_3(OH)^-$ and a proton that initiated the VE and/or oxirane polymerization.[247-249] Other parameters such as solvent polarity as well as the presence of additives also had a significant influence. A weak Lewis base such as ethyl acetate promoted the carbocation stability of the chain end and, thereby, facilitated the cross over reaction.[250]

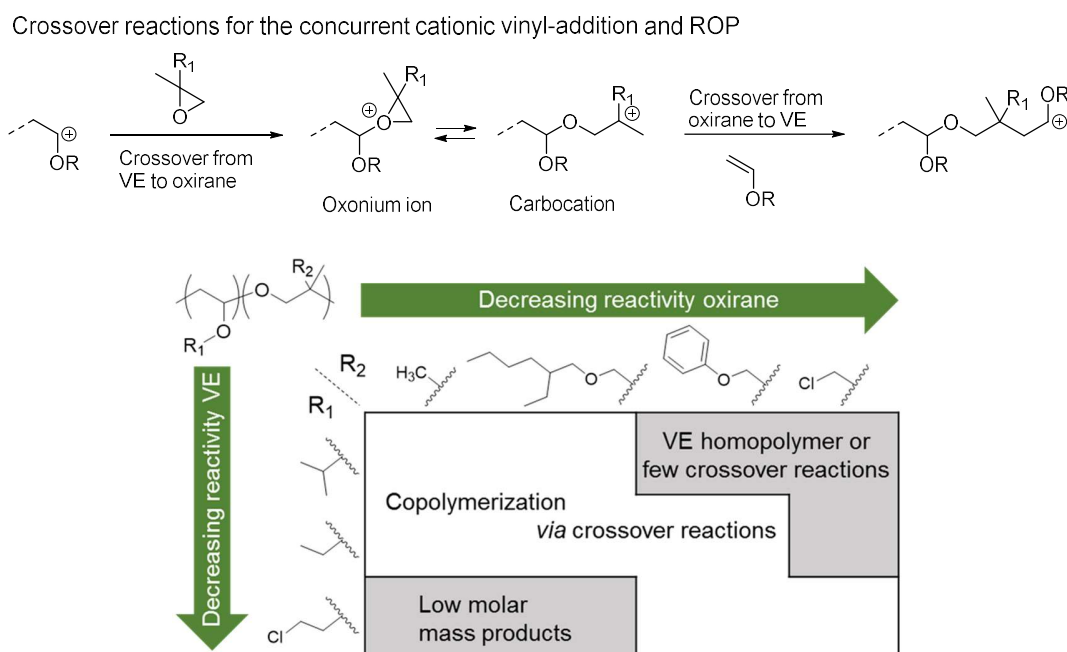


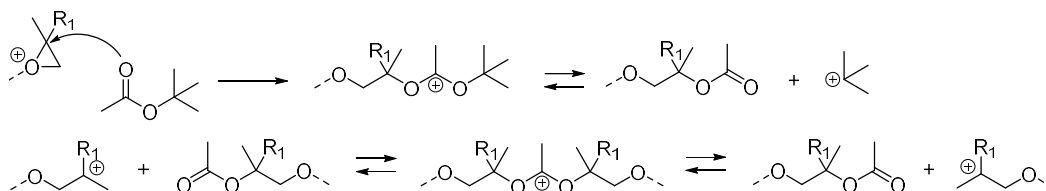
Figure 14. Copolymerization of vinyl ethers and oxiranes *via* concurrent cationic vinyl–addition and ring–opening polymerization. (**Top**) Schematic representation of the monomer propagation in the different crossover reactions. (**Bottom**) The influence of the monomer substituents and reactivities on the copolymerization products. Triphenylmethylm tetrakis(pentafluorophenyl)borate ($\text{Ph}_3\text{CB}(\text{C}_6\text{F}_5)_4$) was used as initiator at $-78\text{ }^\circ\text{C}$ in CH_2Cl_2 (with 5 vol% hexane).

The scope of monomer reactivities was recently further expanded to combinations of alkyl VE and 2,2–disubstituted oxiranes featuring a methyl and a weakly electron–withdrawing substituent (**Figure 14**, bottom).[251] For the used oxirane monomers, the reactivity (or nucleophilicity) decreased in relation to the electron withdrawing effect of the substituents in the following order: **CE1 > CE8 > CE7 > CE2**. Analogously, the reactivity of the VE monomers decreased following **VE7 > VE6 > VE9**. For the successful copolymerization *via* crossover reaction the comonomer reactivities had to match. However, VE homopolymers with few crossover reactions were obtained

when the reactivity of the VE was higher compared to that of the oxirane. Accordingly, low molar mass products with short homooxirane sequences were isolated when the reactivity of the oxirane exceeded that of the vinyl ether. **Table 9** summarizes selected successful copolymerization results including the sequences from efficient crossover reactions.

Current efforts are directed to improve the copolymerization of vinyl ethers and oxiranes by screening of initiators aiming at generation of a “living” species during the cationic polymerization.[252] Among the variety of initiators or catalysts such as $\text{CF}_3\text{SO}_3\text{H}$, $(\text{CF}_3\text{SO}_2)_2\text{NH}$, 1,1,2,2,3,3-hexafluoropropane-1,3-disulfonimide, $\text{B}(\text{C}_6\text{F}_5)_3$, $\text{Ph}_3\text{C}^+\text{B}(\text{C}_6\text{F}_5)_4^-$, $\text{Ph}_3\text{C}^+\text{PF}_6^-$, IBVE-HCl / SnCl_4 , $\text{CF}_3\text{SO}_3\text{H} / n\text{-Bu}_4\text{NI}$, only trifluoromethyl sulfonate decreased the frequency of side reactions, thereby enabling molar mass control of the copolymers. A reversibly cleavable, covalent carbon-triflate bond formed exclusively at the **CE1**-derived propagating end of for poly**VE7-co-CE1** and generated a dormant state. Whereas the reaction conditions were optimized for the monomer pair **VE7 / CE1**, the copolymerization of several other monomer pairs involving cyclohexyl VE (**VE22**), limonene oxide (**CE13**), and styrene oxide (**CE5**) remained to be improved. Another strategy to increase the control of the cationic copolymerization of oxiranes and vinyl ethers included the use of *tert*-butyl esters as reversible chain transfer agents (CTA) (**Scheme 19**).[253] The proposed mechanism was based on nucleophilic attack of the ester at the **CE1**-derived oxonium species, the formation of an intermediate cation and the subsequent generation of a relatively stable *tert*-butyl cation that initiated a new chain. The ester derived polymer ω -chain end acted as a CTA and promoted reversible chain transfer. Among a variety of potential CTAs, in particular *tert*-butyl acetate efficiently decreased the polymerization rate, was able to control the molar mass and produced up to 94% acetoxy ω -end groups, thereby validating

the proposed mechanism. Besides being successful for the monomer pairs **VE7 / CE1** and **VE9 / CE2**, the approach was also applicable with acetoxy endfunctional poly(*p*-methylstyrene) as a macro CTA enabling access to block copolymers.



Scheme 19. Schematic representation of the reversible chain transfer mechanism in the *tert*-butyl acetate mediated cationic copolymerization of vinyl ethers and oxiranes.

4.2.5. Terpolymerization of vinyl ethers with cyclic ethers and ketones

As described above, esters such as ethyl acetate acted as weak Lewis bases and promoted the ROP of the oxirane-derived carbocation or acted as CTAs as stated prior for *tert*-butyl acetate. However, carbonyl compounds such as ketones were also able to act as comonomers in combination with VEs and cyclic ethers (**Scheme 15C**).^[246] The polymerization mechanism includes the concurrent cationic vinyl-addition, ring-opening and carbonyl-addition terpolymerization through crossover reactions in, potentially, a one-way cycle (**Figure 15**, right). The sequence control occurs from the preferential reaction of vinyl ethers with cyclic ethers, cyclic ethers with ketones and ketones with vinyl ethers. However, vinyl ethers as well as cyclic ethers are also homopolymerizable, resulting in a possible occurrence of short homoblocks of these monomers and a general sequence block for the terpolymer according to [(vinyl ether)_x – (cyclic ether)_y – (ketone)₁]_n. Usually performed with B(C₆F₅)₃ in CH₂Cl₂ at –78 °C, other initiators^[254] or reaction conditions were also favorable to suppress homopropagation yielding ABC-type terpolymers.^[255] As described above, the VE–cyclic ether crossover reaction introduces an acetal

functionality in the main chain rendering the terpolymers hydrolysable. However, also the utilization of hydrolysable monomers such as **HAE2**[256] (**Figure 15**, left) or crossover reactions from carbonyl compound to oxiranes can introduce hydrolysable moieties to the main chain. A summary of promising monomer combinations is provided in **Table 9**.

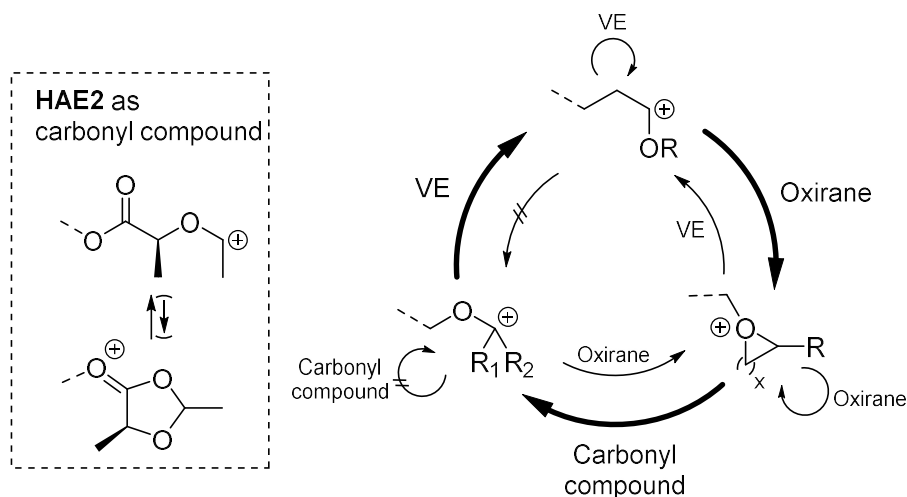


Figure 15. Schematic representation of the propagation reactions during the cationic terpolymerization of vinyl ethers, oxiranes (as well as cyclic ethers) and carbonyl compounds. Mostly ketones were reported, but also an aldehyde and cyclic hemiacetal esters such as, *e.g.*, **HAE2** were applied. Targeted reactions to achieve sequence control in a one-way-cycle are depicted in bold (clockwise direction). Counter clockwise side reactions were (mostly) suppressed.

Table 9. Selected results of cationic co- and terpolymerization of vinyl ethers, cyclic ethers and carbonyl compounds. DP indicates number of repeating units per chain divided by the number of crossover events per chain. Molar masses determined by SEC.

VE_{DP}	Cyclic ether_{DP}	Carbonyl compound_{DP}	M_n (g mol⁻¹)	Đ	M_n of the degradation product (g mol⁻¹)	Ref.
VE7₃₀	CE1_{5.1}	–	9,500	2.20	2,800	[251]
VE7₉₅	CE6_{3.5}	–	16,200	1.97	7,300	[251]
VE6_{4.6}	CE1_{6.6}	–	1,900	2.04	900	[251]
VE6_{7.4}	CE6_{3.2}	–	7,500	1.94	900	[251]
VE6₄₁	CE7_{0.9}	–	4,900	1.95	1,900	[251]
VE9_{2.9}	CE7_{4.5}	–	2,100	1.76	700	[251]
VE9₃₄	CE2₇	–	11,200	2.15	3,300	[251]
VE6	CE8	–	3,000	1.53	800	[251]
VE7₁₃	CE1_{2.3}	–	5,700	1.57	1,500	[252]
VE7₁₇	CE1₃	–	4,900	1.72	1,700	[253]
VE9	CE2	–	5,600	2.57	–	[253]
VE7_{2.3}	CE10_{2.1}	KE2_{0.96}	2,100	1.96	300	[257]
VE7_{6.8}	CE1_{1.6}	KE2_{0.79}	4,000	1.83	400	[257]
VE7_{0.49}	CE10_{7.3}	KE10_{1.1}	9,200	2.05	700	[257]
VE6_{1.2}	CE12_{1.4}	KE2₁	17,300	1.74	300	[255]
VE7₂₄	CE14₁₈	KE2_{0.82}	17,600	1.82	3,400	[254]

VE6 ₁₂	CE14 ₁₇	KE2 _{0.77}	12,000	1.94	–	[254]
–	CE1 _{2.7}	HAE2 ₁	4,500	1.83	300	[256]
–	CE12 ₁₁	HAE1 ₁	13,600	2.24	1,200	[256]
–	CE12 _{6.7}	HAE2 _{0.95}	18,800	2.21	1,100	[256]
–	CE12 _{9.9}	HAE3 ₁	6,900	1.62	1,300	[256]
VE7 _{6.3}	CE1 _{1.6}	HAE2 ₁	19,900	1.79	1,800	[256]
VE7 ₁₂	CE12 _{3.8}	HAE3 ₁	12,600	1.20	1,200	[256]

Initially successful for the comonomer combination **VE7**, cyclohexene oxide (**CE10**) and methyl ethyl ketone (**KE2**), which yielded poly(**VE7**_{~2}– **CE10**_{~2}– **KE2**) ($M_n = 2.100 \text{ g mol}^{-1}$; $\bar{D} = 1.96$), other monomer combinations such as **CE1** / **VE7** / **KE2** or **CE10** / **VE7** / **KE10** resulted in terpolymers featuring longer polyoxiran or poly(vinyl ether) sequences.[257] The orthogonality of the terpolymerization was hence screened using a large variety of monomers (ten VEs, nine cyclic ethers and nine ketones).[255] Substitution pattern and the thereby induced steric hindrance, ring strain, intrinsic homopolymerizability, and nature of the generated cationic propagation chain end affected the ability of each monomer type to be terpolymerized in ABC periodic sequences. Moderate but sufficiently high relative reactivities were required for VEs and cyclic ethers to suppress homopropagation, facilitate the frequent crossover reactions and generate polymers with sufficiently high molar masses. In particular cyclic ketones such as cyclohexanone (**KE6**) promoted the formation of ketals in the main chain. The frequency of cross over reactions increased at high ketone concentrations and when polymerizations were performed in less polar solvents such as toluene at lower temperatures (–100 °C). Under such optimized conditions, the cationic

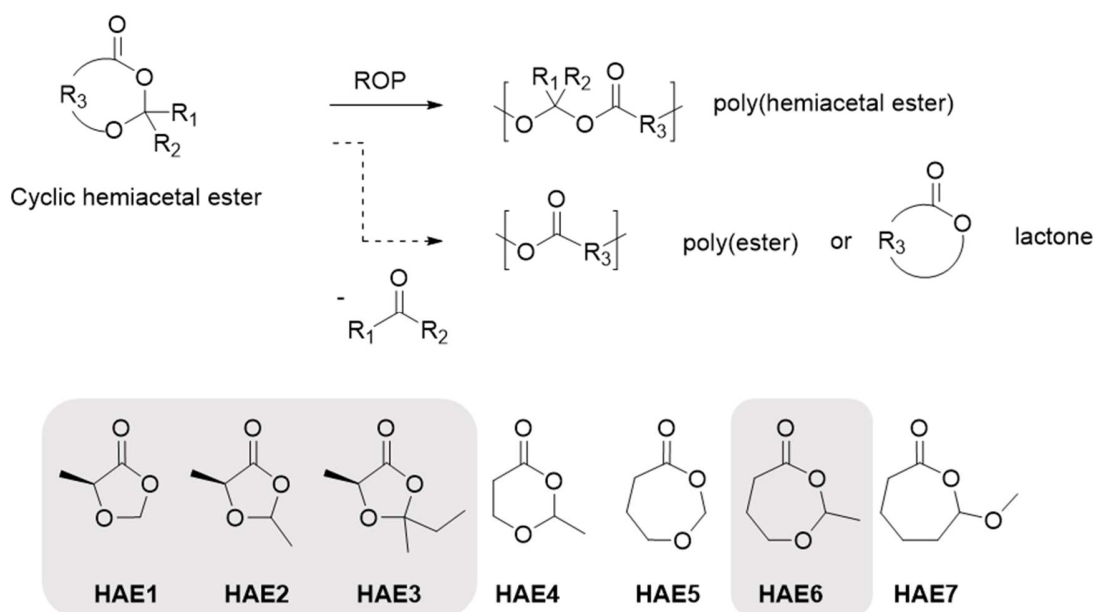
terpolymerization of **VE6**, **CE12** and **KE2** yielded the ABC pseudo-periodic poly(**VE6**_{1.2}–**CE12**_{1.4}–**KE2**_{1.0}) with a high molar mass of $M_n = 17,300 \text{ g mol}^{-1}$ ($\mathcal{D} = 1.74$).

The scope of the carbonyl-based monomer was further expanded to 1,3-dioxolan-4-ones, *i.e.* lactic acid derivatives with formaldehyde, acetaldehyde and methyl ethylketone, respectively (**HAE1** to **HAE3**, **Scheme 20**).^[256] Although these cyclic hemiacetal esters did not homopolymerize cationically, and copolymerizations with **VE7**, **VE9**, **VE6** or styrene derivatives failed, copolymerizations with **CE1** and **CE12**, or the terpolymerization **VE7** / **CE1** / **HAE2** were successful.

4.2.6. Ring opening polymerization of hemiacetal esters

The ring-opening polymerization of hemiacetal esters would enable the synthesis of poly(hemiacetal ester)s (**Scheme 20**). As mentioned above, the homopolymerization of **HAE1** to **HAE3** *via* cationic ROP using different Lewis acid catalysts or reaction temperatures was unsuccessful.^[256] In fact, also homopolymerization using aluminum salen catalysts^[258, 259] or Sn(II)octanoate^[260] failed or yielded polyesters due to elimination of the carbonyl compound.^[261] Similar problems arose when high catalyst amounts of diethylzinc (ZnEt_2) were used for the ROP of 2-methyl-1,3-dioxan-4-one (**HAE4**).^[262] However, a reduction of the catalyst amount facilitated access to the poly(hemiacetal ester)s with M_n 's of 8,000 to 34,000 g mol^{-1} . Whereas a variety of other catalysts caused monomer decomposition, DPP was identified as a very versatile catalyst for the ROP of **HAE4**. Polymerizations without additional initiators proceeded *via* an activated chain end mechanism, where initially high molar mass polymers were formed that decreased their molar mass due to backbiting reactions throughout the course of the reaction. Addition of various alcohols as initiators introduced a competing activated monomer mechanism, enabling access to well-defined poly(hemiacetal ester)s with pre-determined end

groups. DPP was hence further utilized for the synthesis of block copolymers utilizing mPEG–OH as macroinitiator.[263] The variation of the DP of the hydrophobic block resulted in micellar assemblies of varying sizes (26 to 142 nm) in aqueous phosphate buffer solution. Whereas polyHAE4 alone degraded surprisingly slow (half the original M_n at pH 4.4 after 75 h),[262] the micelles degraded considerably faster. For instance, complete degradation occurred after 3 hours at pH 5.7 as well as pH 10.8. The core shell micelles were able to solubilize the hydrophobic Nile Red (94 nm by DLS) as well as AdiFectin™, an amphiphilic immune stimulatory TLR–7 agonist. The drug accessibility was thereby increased and hence increased TLR stimulation activity of the RAW blue macrophages as determined in *in vitro* studies in comparison to the free drug alone.



Scheme 20. (Top) Schematic representation of the ROP of cyclic hemiacetal esters yielding poly(hemiacetal ester)s. Release of the carbonyl compound as side reaction (dashed arrow) results in polyesters or lactones. (Bottom) Schematic representation of the cyclic hemiacetal ester monomers. Compounds marked in grey reported unsuccessful for homopolymerization.

Aiming at favorable ROP thermodynamics, Neitzel *et al.* further continued their studies on 7-membered ring analogues of **HAE4**, *i.e.*, 2-methyl-1,3-dioxepan-4-one (**HAE6**), 1,3-dioxepan-4-one (**HAE5**) as well as 7-methoxyoxepan-2-one (**HAE7**).^[264, 265] Although the high reactivity due to the ring strain of **HAE6** as well as **HAE5** complicated their handling as frequent decomposition or autopolymerization occurred during monomer purification, **HAE5** was successfully polymerized applying DPP and benzyl alcohol yielding the respective poly**HAE5** with a molar mass of 6,000 g mol⁻¹ ($\bar{M}_n = 1.3$). In contrast, the polymerization of **HAE5** with diethylzinc and benzyl alcohol failed and instead yielded γ -butyrolactone and formaldehyde. To avoid the release of a volatile aldehyde during its ROP, **HAE7** featuring an exocyclic hemiacetal ester was investigated.^[265] Whereas poly**HAE7** was successfully obtained by the cationic ROP using HCl / benzyl alcohol or triflic acid, the molar mass could not be controlled. However, cationic reversible addition-fragmentation chain-transfer polymerization with a photocatalyst and three different dithiocarbamate or trithiocarbonate CTAs was successful in this respect, also in a copolymerization with **VE8**.

5. Summary

Poly(ester amide)s (PEA), polyphosphoesters (PPE) and polyacetals represent promising alternative polymer classes for the substitution of polyesters in biomedical applications. This is due to a broad parameter space, enabled by the highly variable structural design and, in return, adjustable degradation behavior. For all three polymer classes, well-established step growth syntheses exist that have led to materials that are currently broadly applied. Whereas there is a clear focus on materials for biomedical applications in particular for PEA and polyacetals, the use of PPE in this respect is in its infancy.

A considerable variety of polymer architectures exists within the polymer classes, which is due to the necessity to attach stealth polymers or biologically active molecules in materials potentially applicable in drug delivery applications. However, multi-step syntheses approaches make the exact structural identification of the final polymers difficult, in particular due to their degradability. The fact that biological data are sometimes nevertheless reported might cause misleading interpretation regarding their performance. We hence encourage the complementation of a spectroscopic characterization with at least size exclusion chromatography during each step to verify the covalent attachment of all building blocks.

In fact, this point of view seems to find its way into the community and is strengthened through the current immense progress in the development of chain growth polymerizations for all three polymer classes. This is due to the use of organocatalysts for ring-opening polymerizations (ROP) enabling access to well-defined PEA, PPE, and to a certain extent also to polyacetals. For the latter, in particular cationic copolymerizations of vinyl ethers with cyclic ethers, aldehydes or cyclic ketals represents a very promising alternative route. As such new synthetic developments are usually accompanied by in-depth structural characterization approaches, we expect the variety of well-defined polymer architectures to thrive.

The question of degradability is addressed from different viewpoints within the polymer classes: Whereas the hydrolysis of acetal moieties is often used to determine the copolymer microstructures of new copolymers from vinyl ethers with, *e.g.*, carbonyl compounds, it is often seen as a prerequisite to promote drug release from more established carrier materials. The reasoning is straightforward when API's are covalently attached, *e.g.*, within the main chain of polyacetals. However, additional leakage effects are likely to contribute when actives are encapsulated. At this point, the additional hydrogen bonding options in PEAs are promising, either to increase drug loading or to sustain the release in comparison to standard polyester materials. In particular, the option to tailor the degradability of PPEs through incorporation of P–O, P–N or P–C bonds is expected to be exploited in future with respect to release kinetics.

Such future studies will likely be accompanied by a careful characterization of degradation products, which is a necessity taking into account that they will be of biological relevance as well. Additional upcoming biological investigations utilizing such new materials will clearly benefit from that viewpoint, bringing the application of polyester alternatives to the next level.

Funding Sources

The work was financially supported by the Deutsche Forschungsgemeinschaft (DFG, German Research Foundation) – project number 316213987 – SFB 1278 (projects A01 and Z01) and the Federal Ministry for Education and Research of Germany (BMBF) (project NextPEG, 13XP5049C).

REFERENCES

- [1] Geyer R, Jambeck JR, Law KL. Production, use, and fate of all plastics ever made. *Sci Adv*. 2017;3:e1700782. DOI: 10.1126/sciadv.1700782.
- [2] Aklonis JJ. Mechanical properties of polymers. *J Chem Educ*. 1981;58:892-7. <https://doi.org/10.1021/ed058p892>.
- [3] Nunes RW, Martin JR, Johnson JF. Influence of molecular weight and molecular weight distribution on mechanical properties of polymers. *Polym Eng Sci*. 1982;22:205-28. <https://doi.org/10.1002/pen.760220402>.
- [4] Bicerano J. Prediction of the properties of polymers from their structures. *J Macromol Sci, Part C: Polym Rev*. 1996;36:161-96. <https://doi.org/10.1080/15321799608009645>.
- [5] Li WC, Tse HF, Fok L. Plastic waste in the marine environment: A review of sources, occurrence and effects. *Sci Total Environ*. 2016;566-567:333-49. <https://doi.org/10.1016/j.scitotenv.2016.05.084>.
- [6] Miloloža M, Kučić Grgić D, Bolanča T, Ukić Š, Cvetnić M, Ocelić Bulatović V, et al. Ecotoxicological assessment of microplastics in freshwater sources—A review. *Water*. 2021;13:e56. <https://doi.org/10.3390/w13010056>.
- [7] Schneiderman DK, Hillmyer MA. 50th anniversary perspective: There is a great future in sustainable polymers. *Macromolecules*. 2017;50:3733-49. 10.1021/acs.macromol.7b00293.
- [8] Haider TP, Völker C, Kramm J, Landfester K, Wurm FR. Plastics of the future? The impact of biodegradable polymers on the environment and on society. *Angew Chem Int Ed*. 2019;58:50-62. <https://doi.org/10.1002/anie.201805766>.
- [9] Ikada Y, Tsuji H. Biodegradable polyesters for medical and ecological applications. *Macromol Rapid Commun*. 2000;21:117-32. [https://doi.org/10.1002/\(SICI\)1521-3927\(20000201\)21:3<117::AID-MARC117>3.0.CO;2-X](https://doi.org/10.1002/(SICI)1521-3927(20000201)21:3<117::AID-MARC117>3.0.CO;2-X).
- [10] Baumann A, Tuerck D, Prabhu S, Dickmann L, Sims J. Pharmacokinetics, metabolism and distribution of PEGs and PEGylated proteins: Quo vadis? *Drug Discov Today*. 2014;19:1623-31. <https://doi.org/10.1016/j.drudis.2014.06.002>.
- [11] Englert C, Brendel JC, Majdanski TC, Yildirim T, Schubert S, Gottschaldt M, et al. Pharmapolymers in the 21st century: Synthetic polymers in drug delivery applications. *Prog Polym Sci*. 2018;87:107-64. <https://doi.org/10.1016/j.progpolymsci.2018.07.005>.

- [12] Molavi F, Barzegar-Jalali M, Hamishehkar H. Polyester based polymeric nano and microparticles for pharmaceutical purposes: A review on formulation approaches. *J Control Release*. 2020;320:265-82. <https://doi.org/10.1016/j.jconrel.2020.01.028>.
- [13] Pappalardo D, Mathisen T, Finne-Wistrand A. Biocompatibility of resorbable polymers: A historical perspective and framework for the future. *Biomacromolecules*. 2019;20:1465-77. [10.1021/acs.biomac.9b00159](https://doi.org/10.1021/acs.biomac.9b00159).
- [14] Maitz MF. Applications of synthetic polymers in clinical medicine. *Biosurf Biotribol*. 2015;1:161-76. <https://doi.org/10.1016/j.bsbt.2015.08.002>.
- [15] Sung H-J, Meredith C, Johnson C, Galis ZS. The effect of scaffold degradation rate on three-dimensional cell growth and angiogenesis. *Biomaterials*. 2004;25:5735-42. <https://doi.org/10.1016/j.biomaterials.2004.01.066>.
- [16] Wong DY, Hollister SJ, Krebsbach PH, Nosrat C. Poly(ϵ -caprolactone) and Poly (L-lactic-co-glycolic acid) degradable polymer sponges attenuate astrocyte response and lesion growth in acute traumatic brain injury. *Tissue Eng*. 2007;13:2515-23. [10.1089/ten.2006.0440](https://doi.org/10.1089/ten.2006.0440).
- [17] Li S. Hydrolytic degradation characteristics of aliphatic polyesters derived from lactic and glycolic acids. *J Biomed Mater Res*. 1999;48:342-53. [https://doi.org/10.1002/\(SICI\)1097-4636\(1999\)48:3<342::AID-JBM20>3.0.CO;2-7](https://doi.org/10.1002/(SICI)1097-4636(1999)48:3<342::AID-JBM20>3.0.CO;2-7).
- [18] Fu K, Pack DW, Klibanov AM, Langer R. Visual evidence of acidic environment within degrading poly(lactic-co-glycolic acid) (PLGA) microspheres. *Pharm Res*. 2000;17:100-6. <https://doi.org/10.1023/A:1007582911958>.
- [19] Woodard LN, Grunlan MA. Hydrolytic degradation and erosion of polyester biomaterials. *ACS Macro Lett*. 2018;7:976-82. [10.1021/acsmacrolett.8b00424](https://doi.org/10.1021/acsmacrolett.8b00424).
- [20] Trofymchuk K, Valanciunaite J, Andreiuk B, Reisch A, Collot M, Klymchenko AS. BODIPY-loaded polymer nanoparticles: Chemical structure of cargo defines leakage from nanocarrier in living cells. *J Mater Chem B*. 2019;7:5199-210. [10.1039/C8TB02781A](https://doi.org/10.1039/C8TB02781A).
- [21] Xu P, Gullotti E, Tong L, Highley CB, Errabelli DR, Hasan T, et al. Intracellular drug delivery by poly(lactic-co-glycolic acid) nanoparticles revisited. *Mol Pharmaceutics*. 2009;6:190-201. [10.1021/mp800137z](https://doi.org/10.1021/mp800137z).
- [22] John J, Mani R, Bhattacharya M. Evaluation of compatibility and properties of biodegradable polyester blends. *J Polym Sci, Part A: Polym Chem*. 2002;40:2003-14. <https://doi.org/10.1002/pola.10297>.

- [23] Ostafinska A, Fortelny I, Nevoralova M, Hodan J, Kredatusova J, Slouf M. Synergistic effects in mechanical properties of PLA/PCL blends with optimized composition, processing, and morphology. *RSC Adv.* 2015;5:98971-82. <https://doi.org/10.1039/C5RA21178F>.
- [24] Steinbach T, Wurm FR. Poly(phosphoester)s: A new platform for degradable polymers. *Angew Chem Int Ed.* 2015;54:6098-108. <https://doi.org/10.1002/anie.201500147>.
- [25] Hufendiek A, Lingier S, Du Prez FE. Thermoplastic polyacetals: Chemistry from the past for a sustainable future? *Polym Chem.* 2019;10:9-33. <https://doi.org/10.1039/C8PY01219A>
- [26] Pirsá S, Kurush AS. A review of the applications of bioproteins in the preparation of biodegradable films and polymers. *J Chem Lett.* 2020;1:47-58. DOI: 10.22034/jchemlett.2020.111200.
- [27] Manavitehrani I, Fathi A, Badr H, Daly S, Negahi Shirazi A, Dehghani F. Biomedical applications of biodegradable polyesters. *Polymers.* 2016;8:20.
- [28] de Jongh PAJM, Paul PKC, Khoshdel E, Wilson P, Kempe K, Haddleton DM. High Tg poly(ester amide)s by melt polycondensation of monomers from renewable resources; citric acid, D-glucono- δ -lactone and amino acids: A DSC study. *Eur Polym J.* 2017;94:11-9. <https://doi.org/10.1016/j.eurpolymj.2017.06.040>.
- [29] Triki R, Bougarech A, Tessier M, Abid S, Fradet A, Abid M. Furanic–aliphatic polyesteramides by bulk polycondensation between furan-based diamine, aliphatic diester and diol. *J Polym Environ.* 2018;26:1272-8. <https://doi.org/10.1007/s10924-017-1037-y>.
- [30] Winnacker M, Rieger B. Poly(ester amide)s: Recent insights into synthesis, stability and biomedical applications. *Polym Chem.* 2016;7:7039-46. <https://doi.org/10.1039/C6PY01783E>
- [31] Nyambo C, Misra M, Mohanty AK. Toughening of brittle poly(lactide) with hyperbranched poly(ester-amide) and isocyanate-terminated prepolymer of polybutadiene. *J Mater Sci.* 2012;47:5158-68. <https://doi.org/10.1007/s10853-012-6393-3>.
- [32] Yin T, Sun HY, Zhao JB, Zhang ZY, Yang WT. Synthesis and characterization of aliphatic polyesteramides mainly composed of alternating diester diamide units from N,N'-bis(2-hydroxyethyl)-oxamide and diacids. *Polym Eng Sci.* 2014;54:756-65. <https://doi.org/10.1002/pen.23612>.
- [33] Douka A, Vouyiouka S, Papaspyridi L-M, Papaspyrides CD. A review on enzymatic polymerization to produce polycondensation polymers: The case of aliphatic polyesters,

- polyamides and polyestaramides. *Prog Polym Sci.* 2018;79:1-25. <https://doi.org/10.1016/j.progpolymsci.2017.10.001>.
- [34] Rusu G, Rusu E. Evaluation of thermal and mechanical behavior of some anionic polyestaramide copolymers. *J Polym Res.* 2013;20:e308. doi: 10.1007/s10965-013-0308-0.
- [35] Ahmad S, Ashraf SM, Zafar F. Development of linseed oil based polyestaramide without organic solvent at lower temperature. *J Appl Polym Sci.* 2007;104:1143-8. <https://doi.org/10.1002/app.25774>.
- [36] Killi N, Pawar AT, Gundloori RVN. Polyestaramide of neem oil and its blends as an active nanomaterial for tissue regeneration. *ACS Appl Bio Mater.* 2019;2:3341-51. <https://doi.org/10.1021/acsabm.9b00354>.
- [37] Pin J-M, Misra M, Mohanty AK. Cross-linkable liquid-crystalline biopolyestaramide as a multifunctional polymeric platform designed from corn oil side-stream product of bioethanol industry. *Macromol Rapid Commun.* 2019;40:e1900093. <https://doi.org/10.1002/marc.201900093>.
- [38] Muniandy A, Lee CS, Lim WH, Pichika MR, Mak KK. Hyperbranched poly(glycerol esteramide): A biocompatible drug carrier from glycerol feedstock and dicarboxylic acid. *J Appl Polym Sci.* 2021;138:e50126. <https://doi.org/10.1002/app.50126>.
- [39] Guo K, Chu CC. Synthesis, characterization, and biodegradation of novel poly(ether ester amide)s based on l-phenylalanine and oligoethylene glycol. *Biomacromolecules.* 2007;8:2851-61. <https://doi.org/10.1021/bm070158c>.
- [40] Lu D-D, Yuan J-C, Lei Z-Q. High molecular weight biodegraded poly(lactic acid-glycolic acid- ϵ -caprolactam) copolymer: Direct polycondensation of lactic acid, glycolic acid and ϵ -caprolactam using Sn(II)-organic anhydride as catalysts. *Polym Adv Technol.* 2009;20:536-40. <https://doi.org/10.1002/pat.1378>.
- [41] Tsitlanadze G, Kviria T, Katsarava R, Chu CC. In vitro enzymatic biodegradation of amino acid based poly(ester amide)s biomaterials. *J Mater Sci: Mater Med.* 2004;15:185-90. <https://doi.org/10.1023/B:JMSM.0000011821.46166.1e>.
- [42] Bonillo Martínez AD, Margarit Bellver MV, Rodríguez Galán IC. Matrix tablets based on amino acid-derived polyestaramide containing release modifiers. *J Drug Deliv Sci Technol.* 2017;42:307-14. <https://doi.org/10.1016/j.jddst.2017.05.003>.

- [43] Andrés-Guerrero V, Zong M, Ramsay E, Rojas B, Sarkhel S, Gallego B, et al. Novel biodegradable polyesteramide microspheres for controlled drug delivery in ophthalmology. *J Control Release*. 2015;211:105-17. <https://doi.org/10.1016/j.jconrel.2015.05.279>.
- [44] Peters T, Kim S-W, Castro V, Stingl K, Strasser T, Bolz S, et al. Evaluation of polyesteramide (PEA) and polyester (PLGA) microspheres as intravitreal drug delivery systems in albino rats. *Biomaterials*. 2017;124:157-68. <https://doi.org/10.1016/j.biomaterials.2017.02.006>.
- [45] Tellegen AR, Rudnik-Jansen I, Pouran B, de Visser HM, Weinans HH, Thomas RE, et al. Controlled release of celecoxib inhibits inflammation, bone cysts and osteophyte formation in a preclinical model of osteoarthritis. *Drug Delivery*. 2018;25:1438-47. <https://doi.org/10.1080/10717544.2018.1482971>.
- [46] Rudnik-Jansen I, Schrijver K, Woike N, Tellegen A, Versteeg S, Emans P, et al. Intra-articular injection of triamcinolone acetonide releasing biomaterial microspheres inhibits pain and inflammation in an acute arthritis model. *Drug Delivery*. 2019;26:226–36. DOI: 10.1080/10717544.2019.1568625.
- [47] Rudnik-Jansen I, Woike N, de Jong S, Versteeg S, Kik M, Emans P, et al. Applicability of a modified rat model of acute arthritis for long-term testing of drug delivery systems. *Pharmaceutics*. 2019;11:e70. <https://doi.org/10.3390/pharmaceutics11020070>.
- [48] Ali Mohamed A, Salhi S, Abid S, El Gharbi R, Fradet A. Random and quasi-alternating polyesteramides deriving from ϵ -caprolactone and β -alanine. *Eur Polym J*. 2014;53:160-70. <https://doi.org/10.1016/j.eurpolymj.2014.01.023>.
- [49] Salhi S, Mahfoudh J, Abid S, Atanase L-I, Popa M, Delaite C. Random poly(ϵ -caprolactone-L-alanine) by direct melt copolymerization. *Polym Int*. 2020;69:1161-8. <https://doi.org/10.1002/pi.6085>.
- [50] Ali Mohamed A, Salhi S, Abid S, El Gharbi R, Fradet A. Quasi-alternating polyesteramides from ϵ -caprolactone and α -amino acids. *J Appl Polym Sci*. 2016;133:e44220. <https://doi.org/10.1002/app.44220>.
- [51] Basterretxea A, Gabirondo E, Sanchez-Sanchez A, Etxeberria A, Coulembier O, Mecerreyes D, et al. Synthesis and characterization of poly(ϵ -caprolactam-co-lactide) polyesteramides using Brønsted acid or Brønsted base organocatalyst. *Eur Polym J*. 2017;95:650-9. <https://doi.org/10.1016/j.eurpolymj.2017.05.023>.

- [52] Deshayes G, Delcourt C, Verbruggen I, Trouillet-Fonti L, Touraud F, Fleury E, et al. Novel polyesteramide-based diblock copolymers: Synthesis by ring-opening copolymerization and characterization. *Macromol Chem Phys.* 2009;210:1033-43. <https://doi.org/10.1002/macp.200900065>.
- [53] Deshayes G, Delcourt C, Verbruggen I, Trouillet-Fonti L, Touraud F, Fleury E, et al. Novel polyesteramide-based di- and triblock copolymers: From thermo-mechanical properties to hydrolytic degradation. *Eur Polym J.* 2011;47:98-110. <https://doi.org/10.1016/j.eurpolymj.2010.07.005>.
- [54] Douhi A, Fradet A. Study of bulk chain coupling reactions. III. Reaction between bisoxazolines or bisoxazines and carboxy-terminated oligomers. *J Polym Sci, Part A: Polym Chem.* 1995;33:691-9. <https://doi.org/10.1002/pola.1995.080330410>.
- [55] Huang CQ, Luo SY, Xu SY, Zhao JB, Jiang SL, Yang WT. Catalyzed chain extension of poly(butylene adipate) and poly(butylene succinate) with 2,2'-(1,4-phenylene)-bis(2-oxazoline). *J Appl Polym Sci.* 2010;115:1555-65. <https://doi.org/10.1002/app.31160>.
- [56] Néry L, Lefebvre H, Fradet A. Chain extension of carboxy-terminated aliphatic polyamides and polyesters by arylene and pyridylene bisoxazolines. *Macromol Chem Phys.* 2004;205:448-55. <https://doi.org/10.1002/macp.200300054>.
- [57] Seppälä JV, Helminen AO, Korhonen H. Degradable polyesters through chain linking for packaging and biomedical applications. *Macromol Biosci.* 2004;4:208-17. <https://doi.org/10.1002/mabi.200300105>.
- [58] Xu SY, Shi YH, Zhao JB, Jiang SL, Yang WT. Chain extension of adipic acid and (or) succinic acid/butanediol polyesters with 2,2'-(1,4-phenylene)-bis(2-oxazoline) and adipoylbiscaprolactamate combined chain extenders. *Polym Adv Technol.* 2011;22:2360-7. <https://doi.org/10.1002/pat.1771>.
- [59] Kagiya T, Narisawa S, Maeda T, Fukui K. Preparation of a crystalline poly(ester-amide) by the polyaddition reaction of bisoxazoline and a dicarboxylic acid. *J Polym Sci B Polym Lett.* 1966;4:257-60. <https://doi.org/10.1002/pol.1966.110040405>.
- [60] Wilsens CHRM, Wullems NJM, Gubbels E, Yao Y, Rastogi S, Noorderover BAJ. Synthesis, kinetics, and characterization of bio-based thermosets obtained through polymerization of a 2,5-furandicarboxylic acid-based bis(2-oxazoline) with sebacic acid. *Polym Chem.* 2015;6:2707-16. <https://doi.org/10.1039/C4PY01609B>

- [61] Muljajew I, Erlebach A, Weber C, Buchheim JR, Sierka M, Schubert US. A polyesteramide library from dicarboxylic acids and 2,2'-bis(2-oxazoline): Synthesis, characterization, nanoparticle formulation and molecular dynamics simulations. *Polym Chem.* 2020;11:112-24. <https://doi.org/10.1039/C9PY01293A>
- [62] Muljajew I, Chi M, Vollrath A, Weber C, Beringer-Siemers B, Stumpf S, et al. A combined experimental and in silico approach to determine the compatibility of poly(ester amide)s and indomethacin in polymer nanoparticles. *Eur Polym J.* 2021;156:e110606. <https://doi.org/10.1016/j.eurpolymj.2021.110606>.
- [63] Lustoň J, Kronek J, Kleinová A, Janigová I, Valentová H, Nedbal J. Synthesis and polymerization reactions of cyclic imino ethers. VI. Polymers with biphenyl structure. *J Polym Sci, Part A: Polym Chem.* 2012;50:3936-43. <https://doi.org/10.1002/pola.26199>.
- [64] Culbertson BM. Cyclic imino ethers in step-growth polymerizations. *Prog Polym Sci.* 2002;27:579-626. [https://doi.org/10.1016/S0079-6700\(01\)00053-3](https://doi.org/10.1016/S0079-6700(01)00053-3).
- [65] Kempe K. Chain and step growth polymerizations of cyclic imino ethers: From poly(2-oxazoline)s to poly(ester amide)s. *Macromol Chem Phys.* 2017;218:e1700021. <https://doi.org/10.1002/macp.201700021>.
- [66] Chevallier P, Soutif J-C, Brosse J-C, Rincón-Guerrero A. Poly(amide-ester)s from 2,6-pyridine dicarboxylic acid and ethanolamine derivatives for metal ion complexation. Synthesis via bis(2-oxazoline)-diacid reaction. *Eur Polym J.* 1998;34:767-78. [https://doi.org/10.1016/S0014-3057\(97\)00186-9](https://doi.org/10.1016/S0014-3057(97)00186-9).
- [67] Kronek J, Nedbal J, Valentová H, Neubert M, Janigová I, Petrenčíková N, et al. Thermal stability and structural anisotropy of semiaromatic poly(ester amides) from aromatic bis(2-oxazolines) and aliphatic dicarboxylic acids. *Polym Test.* 2018;68:1-7. <https://doi.org/10.1016/j.polymertesting.2018.02.005>.
- [68] Li S, Tao M. Preparation and properties of copolymer resins based on phenolphthalein benzoxazine–benzoic acid and bisoxazoline. *J Therm Anal Calorim.* 2013;113:633-9. <https://doi.org/10.1007/s10973-012-2758-8>.
- [69] Lustoň J, Kronek J, Markus O, Janigová I, Böhme F. Synthesis and polymerization reactions of cyclic imino ethers. 3. Poly(ester amide)s of the AA + BB type on the basis of 2-oxazolines. *Polym Adv Technol.* 2007;18:165-72. <https://doi.org/10.1002/pat.801>.

- [70] Mansour IB, Alouani K, Chauveau E, Martin V, Schiets F, Mercier R. Synthesis and characterisation of poly(ester-amide)s from aromatic bisoxazoline precursors. *Eur Polym J*. 2010;46:814-20. <https://doi.org/10.1016/j.eurpolymj.2009.12.014>.
- [71] Sano Y. Polymerization of bis(2-oxazoline) compounds with dicarboxylic acids. *J Polym Sci, Part A: Polym Chem*. 1989;27:2749-60. <https://doi.org/10.1002/pola.1989.080270820>.
- [72] Erlebach A, Muljajew I, Chi M, Bückmann C, Weber C, Schubert US, et al. Predicting solubility of small molecules in macromolecular compounds for nanomedicine application from atomistic simulations. *Adv Theory Simul*. 2020;3:e2000001. <https://doi.org/10.1002/adts.202000001>.
- [73] Führer FN, Schlaad H. ADMET Polymerization of amino-acid-based diene. *Macromol Chem Phys*. 2014;215:2268-73. <https://doi.org/10.1002/macp.201400166>.
- [74] Medel S, Martínez-Campos E, Acitores D, Vassileva-Tonkova E, Grabchev I, Bosch P. Synthesis and spectroscopic properties of a new fluorescent acridine hyperbranched polymer: Applications to acid sensing and as antimicrobial agent. *Eur Polym J*. 2018;102:19-29. <https://doi.org/10.1016/j.eurpolymj.2018.03.008>.
- [75] Helder J, Kohn FE, Sato S, van den Berg JW, Feijen J. Synthesis of poly[oxyethylidenecarbonylimino(2-oxoethylene)] [poly(glycine-D,L-lactic acid)] by ring opening polymerization. *Macromol Rapid Commun*. 1985;6:9-14. <https://doi.org/10.1002/marc.1985.030060103>.
- [76] Basu A, Kunduru KR, Katzhendler J, Domb AJ. Poly(α -hydroxy acid)s and poly(α -hydroxy acid-co- α -amino acid)s derived from amino acid. *Adv Drug Delivery Rev*. 2016;107:82-96. <https://doi.org/10.1016/j.addr.2016.08.003>.
- [77] Feng Y, Lu J, Behl M, Lendlein A. Progress in depsipeptide-based biomaterials. *Macromol Biosci*. 2010;10:1008-21. <https://doi.org/10.1002/mabi.201000076>.
- [78] Fonseca AC, Gil MH, Simões PN. Biodegradable poly(ester amide)s – A remarkable opportunity for the biomedical area: Review on the synthesis, characterization and applications. *Prog Polym Sci*. 2014;39:1291-311. <https://doi.org/10.1016/j.progpolymsci.2013.11.007>.
- [79] Peng X, Behl M, Zhang P, Mazurek-Budzyńska M, Razzaq MY, Lendlein A. Hexyl-modified morpholine-2,5-dione-based oligodepsipeptides with relatively low glass transition temperature. *Polymer*. 2016;105:318-26. <https://doi.org/10.1016/j.polymer.2016.10.033>.

- [80] Elomaa L, Kang Y, Seppälä JV, Yang Y. Biodegradable photocrosslinkable poly(depsipeptide-co- ϵ -caprolactone) for tissue engineering: Synthesis, characterization, and in vitro evaluation. *J Polym Sci, Part A: Polym Chem.* 2014;52:3307-15. <https://doi.org/10.1002/pola.27400>.
- [81] Feng Y, Chen C, Zhang L, Tian H, Yuan W. Synthesis and characterization of novel copolymers based on 3(S)-methyl-morpholine-2,5-dione. *Trans Tianjin Univ.* 2012;18:315-9. <https://doi.org/10.1016/j.ijpharm.2012.03.043>.
- [82] Lv J, Yang J, Hao X, Ren X, Feng Y, Zhang W. Biodegradable PEI modified complex micelles as gene carriers with tunable gene transfection efficiency for ECs. *J Mater Chem B.* 2016;4:997-1008. <https://doi.org/10.1039/C5TB02310F>
- [83] Zhang L, Feng Y, Tian H, Shi C, Zhao M, Guo J. Controlled release of doxorubicin from amphiphilic depsipeptide-PDO-PEG-based copolymer nanosized microspheres. *React Funct Polym.* 2013;73:1281-9. <https://doi.org/10.1016/j.reactfunctpolym.2013.06.012>.
- [84] Shi C-X, Guo Y-T, Wu Y-H, Li Z-Y, Wang Y-Z, Du F-S, et al. Synthesis and controlled organobase-catalyzed ring-opening polymerization of morpholine-2,5-dione derivatives and monomer recovery by acid-catalyzed degradation of the polymers. *Macromolecules.* 2019;52:4260-9. <https://doi.org/10.1021/acs.macromol.8b02498>.
- [85] Franz N, Klok H-A. Synthesis of functional polydepsipeptides via direct ring-opening polymerization and post-polymerization modification. *Macromol Chem Phys.* 2010;211:809-20. <https://doi.org/10.1002/macp.200900521>.
- [86] Lian J, Li M, Wang S, Tao Y, Wang X. Organocatalytic polymerization of morpholine-2,5-diones toward methionine-containing poly(ester amide)s: Preparation and facile functionalization. *Macromolecules.* 2020;53:10830-6. <https://doi.org/10.1021/acs.macromol.0c02065>.
- [87] Pang Z, Li H, He P, Wang Y, Ren H, Wang H, et al. Controllable ring-opening copolymerization of L-lactide and (3S)-benzyloxymethyl-(6S)-methyl-morpholine-2,5-dione initiated by a biogenic compound creatinine acetate. *J Polym Sci, Part A: Polym Chem.* 2012;50:4004-9. <https://doi.org/10.1002/pola.26196>.
- [88] Ohya Y, Matori J, Ouchi T. Preparation of growth factor-loaded biodegradable matrices consisting of poly(depsipeptide-co-lactide) and cell growth on the matrices. *React Funct Polym.* 2014;81:33-9. <https://doi.org/10.1016/j.reactfunctpolym.2014.04.003>.

- [89] Yu Z, He B, Long C, Liu R, Sheng M, Wang G, et al. Synthesis, characterization, and drug delivery of amphiphilic poly{(lactic acid)-co-[(glycolic acid)-alt-(L-glutamic acid)]}-g-poly(ethylene glycol). *Macromol Res.* 2012;20:250-8. <https://doi.org/10.1007/s13233-012-0055-9>.
- [90] Naolou T, Lendlein A, Neffe AT. Influence of metal softness on the metal-organic catalyzed polymerization of morpholine-2,5-diones to oligodepsipeptides. *Eur Polym J.* 2016;85:139-49. <https://doi.org/10.1016/j.eurpolymj.2016.10.011>.
- [91] Yu H, Guo X, Qi X, Liu P, Shen X, Duan Y. Synthesis and characterization of arginine-glycine-aspartic peptides conjugated poly(lactic acid-co-l-lysine) diblock copolymer. *J Mater Sci: Mater Med.* 2008;19:1275-81. <https://doi.org/10.1007/s10856-007-3237-9>.
- [92] Takahashi A, Umezaki M, Yoshida Y, Kuzuya A, Ohya Y. A macromolecular prodrug-type injectable polymer composed of poly(depsipeptide-co-lactide)-g-PEG for sustained release of drugs. *Polym Adv Technol.* 2014;25:1226-33. <https://doi.org/10.1002/pat.3265>.
- [93] Yu Z, He B, Sheng M, Wang G, Gu Z. Novel PLGGE graft polymeric micelles for doxorubicin delivery. *Chin Sci Bull.* 2012;57:3994-4004. <https://doi.org/10.1007/s11434-012-5307-8>.
- [94] Brunacci N, Neffe AT, Wischke C, Naolou T, Nöchel U, Lendlein A. Oligodepsipeptide (nano)carriers: Computational design and analysis of enhanced drug loading. *J Control Release.* 2019;301:146-56. <https://doi.org/10.1016/j.jconrel.2019.03.004>.
- [95] Peng X, Behl M, Zhang P, Mazurek-Budzyńska M, Feng Y, Lendlein A. Synthesis of well-defined dihydroxy telechelics by (co)polymerization of morpholine-2,5-diones catalyzed by Sn(IV) alkoxide. *Macromol Biosci.* 2018;18:e1800257. <https://doi.org/10.1002/mabi.201800257>.
- [96] Pratt R, Dove A, Lohmeijer B, Culkun D, Waymouth R, Hedrick J. Extending the reactivity of N-heterocyclic carbenes to polymerization of functional and biomimetic monomers. *Polym Prepr (Am Chem Soc, Div Polym Chem).* 2005;46:902.
- [97] Pratt RC, Lohmeijer BG, Mason AF, Waymouth RM, Hedrick JL. Organocatalytic ring-opening polymerizations of morpholine-2, 6-diones: A route to functionalized poly (lactide) s and pseudopeptides. *Polym Prepr (Am Chem Soc, Div Polym Chem).* 2006;47:101-2.
- [98] Dirauf M, Bandelli D, Weber C, Görls H, Gottschaldt M, Schubert US. TBD-catalyzed ring-opening polymerization of alkyl-substituted morpholine-2,5-dione derivatives. *Macromol Rapid Commun.* 2018;39:e1800433. <https://doi.org/10.1002/marc.201800433>.

- [99] Burton TF, Pinaud J, Giani O. Rapid and controlled organocatalyzed ring-opening polymerization of 3S-(isobutyl)morpholine-2,5-dione and copolymerization with lactide. *Macromolecules*. 2020;53:6598-607. <https://doi.org/10.1021/acs.macromol.0c00940>.
- [100] Kivijärvi T, Pappalardo D, Olsén P, Finne-Wistrand A. Inclusion of isolated α -amino acids along the polylactide chain through organocatalytic ring-opening copolymerization. *Eur Polym J*. 2020;131:e109703. <https://doi.org/10.1016/j.eurpolymj.2020.109703>.
- [101] Feng Y, Klee D, Höcker H. Synthesis and characterization of new ABA triblock copolymers with poly[3(S)-isobutylmorpholine-2,5-dione] and poly(ethylene oxide) blocks. *Macromol Chem Phys*. 1999;200:2276-83. [https://doi.org/10.1002/\(SICI\)1521-3935\(19991001\)200:10<2276::AID-MACP2276>3.0.CO;2-N](https://doi.org/10.1002/(SICI)1521-3935(19991001)200:10<2276::AID-MACP2276>3.0.CO;2-N).
- [102] Feng Y, Klee D, Höcker H. Lipase-catalyzed ring-opening polymerization of 3(S)-sec-butylmorpholine-2,5-dione. *Macromol Biosci*. 2001;1:66-74. [https://doi.org/10.1002/1616-5195\(20010301\)1:2<66::AID-MABI66>3.0.CO;2-M](https://doi.org/10.1002/1616-5195(20010301)1:2<66::AID-MABI66>3.0.CO;2-M).
- [103] In 't Veld PJA, Dijkstra PJ, van Lochem JH, Feijen J. Synthesis of alternating polydepsipeptides by ring-opening polymerization of morpholine-2,5-dione derivatives. *Makromol Chem*. 1990;191:1813-25. <https://doi.org/10.1002/macp.1990.021910808>.
- [104] In 't Veld PJA, Shen Z-R, Takens GAJ, Dijkstra PJ, Feijen J. Glycine/glycolic acid based copolymers. *J Polym Sci, Part A: Polym Chem*. 1994;32:1063-9. <https://doi.org/10.1002/pola.1994.080320608>.
- [105] Tsuji H, Sato S, Masaki N, Arakawa Y, Kuzuya A, Ohya Y. Synthesis, stereocomplex crystallization and homo-crystallization of enantiomeric poly(lactic acid-co-alanine)s with ester and amide linkages. *Polym Chem*. 2018;9:565-75. <https://doi.org/10.1039/C7PY02024D>
- [106] Yan W, Fang L, Noechel U, Kratz K, Lendlein A. Influence of deformation temperature on structural variation and shape-memory effect of a thermoplastic semi-crystalline multiblock copolymer. *Express Polym Lett*. 2015;9:624-35. DOI: 10.3144/expresspolymlett.2015.58.
- [107] Yan W, Fang L, Noechel U, Kratz K, Lendlein A. Influence of programming strain rates on the shape-memory performance of semicrystalline multiblock copolymers. *J Polym Sci B Polym Phys*. 2016;54:1935-43. <https://doi.org/10.1002/polb.24097>.
- [108] Yan W, Fang L, Weigel T, Behl M, Kratz K, Lendlein A. The influence of thermal treatment on the morphology in differently prepared films of a oligodepsipeptide based multiblock copolymer. *Polym Adv Technol*. 2017;28:1339-45. <https://doi.org/10.1002/pat.3953>.

- [109] Yan W, Rudolph T, Noechel U, Gould O, Behl M, Kratz K, et al. Reversible actuation of thermoplastic multiblock copolymers with overlapping thermal transitions of crystalline and glassy domains. *Macromolecules*. 2018;51:4624-32. <https://doi.org/10.1021/acs.macromol.8b00322>.
- [110] Bai L, Zhao J, Li Q, Guo J, Ren X, Xia S, et al. Biofunctionalized electrospun PCL-PIBMD/SF vascular grafts with PEG and cell-adhesive peptides for endothelialization. *Macromol Biosci*. 2019;19:e1800386. <https://doi.org/10.1002/mabi.201800386>.
- [111] Feng Y, Liu W, Ren X, Lu W, Guo M, Behl M, et al. Evaluation of electrospun PCL-PIBMD meshes modified with plasmid complexes in vitro and in vivo. *Polymers*. 2016;8:e58. <https://doi.org/10.3390/polym8030058>.
- [112] Bai L, Li Q, Duo X, Hao X, Zhang W, Shi C, et al. Electrospun PCL-PIBMD/SF blend scaffolds with plasmid complexes for endothelial cell proliferation. *RSC Adv*. 2017;7:39452-64. <https://doi.org/10.1039/C7RA06253B>
- [113] Feng Y, Lu W, Ren X, Liu W, Guo M, Ullah I, et al. Electrospun poly(lactide-co-glycolide-co-3(S)-methyl-morpholine-2,5-dione) nanofibrous scaffolds for tissue engineering. *Polymers*. 2016;8:e13. <https://doi.org/10.3390/polym8020013>.
- [114] Elomaa L, Pan C-C, Shanjani Y, Malkovskiy A, Seppälä JV, Yang Y. Three-dimensional fabrication of cell-laden biodegradable poly(ethylene glycol-co-depsipeptide) hydrogels by visible light stereolithography. *J Mater Chem B*. 2015;3:8348-58. <https://doi.org/10.1039/C5TB01468A>.
- [115] Pagar KP, Vavia PR. Poly[LA-(Glc-Leu)] copolymer as a carrier for ocular delivery of ciprofloxacin: Formulation, characterization and in vivo biocompatibility study. *Ther Deliv*. 2013;4:553-65. <https://doi.org/10.4155/tde.13.29>.
- [116] Pagar K, Vavia P. Rivastigmine-loaded L-lactide-depsipeptide polymeric nanoparticles: Decisive formulation variable optimization. *Sci Pharm*. 2013;81:865-88. <https://doi.org/10.3797/scipharm.1211-20>.
- [117] Pagar KP, Vavia PR. Naltrexone-loaded poly[La-(Glc-Leu)] polymeric microspheres for the treatment of alcohol dependence: In vitro characterization and in vivo biocompatibility assessment. *Pharm Dev Technol*. 2014;19:385-94. <https://doi.org/10.3109/10837450.2013.784334>.
- [118] Remmel A. COVID vaccines and safety: What the research says. *Nature*. 2021;590:538-40. <https://doi.org/10.1038/d41586-021-00290-x>.

- [119] Fam SY, Chee CF, Yong CY, Ho KL, Mariatulqabiah AR, Tan WS. Stealth coating of nanoparticles in drug-delivery systems. *Nanomaterials*. 2020;10:e787. <https://doi.org/10.3390/nano10040787>.
- [120] Dirauf M, Erlebach A, Weber C, Hoeppener S, Buchheim JR, Sierka M, et al. Block copolymers composed of PEO and polyesteramides based on glycolic acid, L-valine, and L-isoleucine. *Macromolecules*. 2020;53:3580-90. <https://doi.org/10.1021/acs.macromol.0c00282>.
- [121] Zhao Y, Li J, Yu H, Wang G, Liu W. Synthesis and characterization of a novel polydepsipeptide contained tri-block copolymer (mPEG-PLLA-PMMD) as self-assembly micelle delivery system for paclitaxel. *Int J Pharm*. 2012;430:282-91. <https://doi.org/10.1016/j.ijpharm.2012.03.043>.
- [122] Yin S, Li J, Li N, Wang G, Gu X. Preparation and characterization of long-circulating PELMD/mPEG-PLGA-mixed micelles for 10-hydroxycamptothecin. *J Nanoparticle Res*. 2014;16:e2274. <https://doi.org/10.1007/s11051-014-2274-9>.
- [123] Lv J, Zhang L, Khan M, Ren X, Guo J, Feng Y. Biodegradable depsipeptide-PDO-PEG-based block copolymer micelles as nanocarriers for controlled release of doxorubicin. *React Funct Polym*. 2014;82:89-97. <https://doi.org/10.1016/j.reactfunctpolym.2014.06.005>.
- [124] Bai W, Chen D, Li Q, Chen H, Zhang S, Huang X, et al. In vitro hydrolytic degradation of poly(para-dioxanone) with high molecular weight. *J Polym Res*. 2009;16:471-80. <https://doi.org/10.1007/s10965-008-9250-y>.
- [125] Zhang L, Feng Y, Tian H, Zhao M, Khan M, Guo J. Amphiphilic depsipeptide-based block copolymers as nanocarriers for controlled release of ibuprofen with doxorubicin. *J Polym Sci, Part A: Polym Chem*. 2013;51:3213-26. <https://doi.org/10.1002/pola.26713>.
- [126] Wang W, Naolou T, Ma N, Deng Z, Xu X, Mansfeld U, et al. Polydepsipeptide block-stabilized polyplexes for efficient transfection of primary human cells. *Biomacromolecules*. 2017;18:3819-33. <https://doi.org/10.1021/acs.biomac.7b01034>.
- [127] Shi C, Yao F, Huang J, Han G, Li Q, Khan M, et al. Proliferation and migration of human vascular endothelial cells mediated by ZNF580 gene complexed with mPEG-b-P(MMD-co-GA)-g-PEI microparticles. *J Mater Chem B*. 2014;2:1825-37. <https://doi.org/10.1039/C3TB21601B>
- [128] Shi C, Yao F, Li Q, Khan M, Ren X, Feng Y, et al. Regulation of the endothelialization by human vascular endothelial cells by ZNF580 gene complexed with biodegradable microparticles. *Biomaterials*. 2014;35:7133-45. <https://doi.org/10.1016/j.biomaterials.2014.04.110>.

- [129] Shi C, Li Q, Zhang W, Feng Y, Ren X. REDV peptide conjugated nanoparticles/pZNF580 complexes for actively targeting human vascular endothelial cells. *ACS Appl Mater Interfaces*. 2015;7:20389-99. <https://doi.org/10.1021/acsami.5b06286>.
- [130] Yang J, Liu W, Lv J, Feng Y, Ren X, Zhang W. REDV–polyethyleneimine complexes for selectively enhancing gene delivery in endothelial cells. *J Mater Chem B*. 2016;4:3365-76. <https://doi.org/10.1039/C6TB00686H>.
- [131] Hao X, Li Q, Wang H, Muhammad K, Guo J, Ren X, et al. CAGW modified polymeric micelles with different hydrophobic cores for efficient gene delivery and capillary-like tube formation. *ACS Biomater Sci Eng*. 2018;4:2870-8. <https://doi.org/10.1021/acsbiomaterials.8b00529>.
- [132] Li Q, Hao X, Lv J, Ren X, Zhang K, Ullah I, et al. Mixed micelles obtained by co-assembling comb-like and grafting copolymers as gene carriers for efficient gene delivery and expression in endothelial cells. *J Mater Chem B*. 2017;5:1673-87. <https://doi.org/10.1039/C6TB02212J>.
- [133] Bauer KN, Tee HT, Velencoso MM, Wurm FR. Main-chain poly(phosphoester)s: History, syntheses, degradation, bio-and flame-retardant applications. *Prog Polym Sci*. 2017;73:61-122. <https://doi.org/10.1016/j.progpolymsci.2017.05.004>.
- [134] Cankaya A, Steinmann M, Bülbül Y, Lieberwirth I, Wurm FR. Side-chain poly(phosphoramidate)s via acyclic diene metathesis polycondensation. *Polym Chem*. 2016;7:5004-10. <https://doi.org/10.1039/C6PY00999A>
- [135] Steinmann M, Wagner M, Wurm FR. Poly(phosphorodiamidate)s by olefin metathesis polymerization with precise degradation. *Chem Eur J*. 2016;22:17329-38. <https://doi.org/10.1002/chem.201603990>.
- [136] Bauer KN, Liu L, Andrienko D, Wagner M, Macdonald EK, Shaver MP, et al. Polymerizing phosphonates: A fast way to in-chain poly(phosphonate)s with adjustable hydrophilicity. *Macromolecules*. 2018;51:1272-9. <https://doi.org/10.1021/acs.macromol.7b02473>.
- [137] Pelosi C, Tinè MR, Wurm FR. Main-chain water-soluble polyphosphoesters: Multifunctional polymers as degradable PEG-alternatives for biomedical applications. *Eur Polym J*. 2020;141:e110079. <https://doi.org/10.1016/j.eurpolymj.2020.110079>.
- [138] Yilmaz ZE, Jérôme C. Polyphosphoesters: New trends in synthesis and drug delivery applications. *Macromol Biosci*. 2016;16:1745-61. <https://doi.org/10.1002/mabi.201600269>.

- [139] Bauer KN, Tee HT, Lieberwirth I, Wurm FR. In-chain poly(phosphonate)s via acyclic diene metathesis polycondensation. *Macromolecules*. 2016;49:3761-8. <https://doi.org/10.1021/acs.macromol.6b00366>.
- [140] Becker G, Ackermann L-M, Schechtel E, Klapper M, Tremel W, Wurm FR. Joining two natural motifs: Catechol-containing poly(phosphoester)s. *Biomacromolecules*. 2017;18:767-77. <https://doi.org/10.1021/acs.biomac.6b01613>.
- [141] Qiu J, Zhang J, Yu F, Wei J, Ding L. Novel ABC miktoarm star terpolyphosphoesters: Facile construction and high-flame retardant property. *J Polym Sci, Part A: Polym Chem*. 2016;54:692-701. <https://doi.org/10.1002/pola.27895>.
- [142] Becker G, Vlaminck L, Velencoso MM, Du Prez FE, Wurm FR. Triazolinedione-“clicked” poly(phosphoester)s: Systematic adjustment of thermal properties. *Polym Chem*. 2017;8:4074-8. <https://doi.org/10.1039/C7PY00813A>.
- [143] Tee HT, Koynov K, Reichel T, Wurm FR. Noncovalent hydrogen bonds tune the mechanical properties of phosphoester polyethylene mimics. *ACS Omega*. 2019;4:9324-32. <https://doi.org/10.1021/acsomega.9b01040>.
- [144] Steinmann M, Marsico F, Wurm FR. Reactive poly(phosphoester)-telechelics. *J Polym Res*. 2015;22:e143. <https://doi.org/10.1007/s10965-015-0788-1>.
- [145] Hilf S, Kilbinger AFM. Functional end groups for polymers prepared using ring-opening metathesis polymerization. *Nat Chem*. 2009;1:537-46. <https://doi.org/10.1038/nchem.347>.
- [146] Grubbs RH. The development of functional group tolerant ROMP catalysts. *J Macromol Sci A*. 1994;31:1829-933. <https://doi.org/10.1080/10601329408545884>.
- [147] Peres LB, Preiss LC, Wagner M, Wurm FR, de Araújo PHH, Landfester K, et al. ALTMET polymerization of amino acid-based monomers targeting controlled drug release. *Macromolecules*. 2016;49:6723-30. <https://doi.org/10.1021/acs.macromol.6b01530>.
- [148] Bhattacharya AK, Thyagarajan G. Michaelis-Arbuzov rearrangement. *Chem Rev*. 1981;81:415-30. <https://doi.org/10.1021/cr00044a004>.
- [149] Becker G, Marquetant TA, Wagner M, Wurm FR. Multifunctional poly(phosphoester)s for reversible Diels–Alder postmodification to tune the LCST in water. *Macromolecules*. 2017;50:7852-62. <https://doi.org/10.1021/acs.macromol.7b01716>.

- [150] Wolf T, Rheinberger T, Wurm FR. Thermoresponsive coacervate formation of random poly(phosphonate) terpolymers. *Eur Polym J.* 2017;95:756-65. <https://doi.org/10.1016/j.eurpolymj.2017.05.048>.
- [151] Baeten E, Vanslambrouck S, Jérôme C, Lecomte P, Junkers T. Anionic flow polymerizations toward functional polyphosphoesters in microreactors: Polymerization and UV-modification. *Eur Polym J.* 2016;80:208-18. <https://doi.org/10.1016/j.eurpolymj.2016.02.012>.
- [152] Pranantyo D, Xu LQ, Kang E-T, Mya MK, Chan-Park MB. Conjugation of polyphosphoester and antimicrobial peptide for enhanced bactericidal activity and biocompatibility. *Biomacromolecules.* 2016;17:4037-44. <https://doi.org/10.1021/acs.biomac.6b01452>.
- [153] Yao X, Du H, Xu N, Sun S, Zhu W, Shen Z. Fully degradable antibacterial poly(ester-phosphoester)s by ring-opening polymerization, “click” chemistry, and quaternization. *J Appl Polym Sci.* 2015;132:e42647. <https://doi.org/10.1002/app.42647>.
- [154] Müller LK, Steinbach T, Wurm FR. Multifunctional poly(phosphoester)s with two orthogonal protective groups. *RSC Adv.* 2015;5:42881-8. <https://doi.org/10.1039/C5RA07167D>
- [155] Becker G, Deng Z, Zober M, Wagner M, Lienkamp K, Wurm FR. Surface-attached poly(phosphoester)-hydrogels with benzophenone groups. *Polym Chem.* 2018;9:315-26. <https://doi.org/10.1039/C7PY01777D>
- [156] Jin H, Sun M, Shi L, Zhu X, Huang W, Yan D. Reduction-responsive amphiphilic polymeric prodrugs of camptothecin–polyphosphoester for cancer chemotherapy. *Biomater Sci.* 2018;6:1403-13. <https://doi.org/10.1039/C8BM00162F>.
- [157] Tsao Y-YT, Wooley KL. Synthetic, functional thymidine-derived polydeoxyribonucleotide analogues from a six-membered cyclic phosphoester. *J Am Chem Soc.* 2017;139:5467-73. <https://doi.org/10.1021/jacs.7b01116>.
- [158] Tsao Y-YT, Smith TH, Wooley KL. Regioisomeric preference in ring-opening polymerization of 3',5'-cyclic phosphoesters of functional thymidine DNA analogues. *ACS Macro Lett.* 2018;7:153-8. <https://doi.org/10.1021/acsmacrolett.7b00858>.
- [159] Wang Q, Chen S, Deng B, Wang Y, Dong D, Zhang N. Rare earth metal-mediated ring-opening polymerisation of cyclic phosphoesters. *Polym Chem.* 2019;10:2101-5. <https://doi.org/10.1039/C9PY00025A>.

- [160] Ding F, Li H-J, Wang J-X, Tao W, Zhu Y-H, Yu Y, et al. Chlorin e6-encapsulated polyphosphoester based nanocarriers with viscous flow core for effective treatment of pancreatic cancer. *ACS Appl Mater Interfaces*. 2015;7:18856-65. <https://doi.org/10.1021/acsami.5b05724>.
- [161] Wang J, Li D, Tao W, Lu Y, Yang X, Wang J. Synthesis of an oxidation-sensitive polyphosphoester bearing thioether group for triggered drug release. *Biomacromolecules*. 2019;20:1740-7. <https://doi.org/10.1021/acs.biomac.9b00101>.
- [162] Moss GP, Smith PAS, Tavernier D. Glossary of class names of organic compounds and reactivity intermediates based on structure (IUPAC Recommendations 1995). *Pure and Applied Chemistry*. 1995;67:1307-75. doi:10.1351/pac199567081307.
- [163] Butlerow A. Ueber einige Derivate des Jodmethylens. *Justus Liebigs Annalen der Chemie*. 1859;111:242-52. <https://doi.org/10.1002/jlac.18591110219>.
- [164] Staudinger H, Lüthy M. Hochpolymere Verbindungen. 3. Mitteilung. Über die Konstitution der Poly-oxymethylene. *Helvetica Chimica Acta*. 1925;8:41-64. <https://doi.org/10.1002/hlca.19250080111>.
- [165] Kern W, Jaacks V. Die Bedeutung der Polyoxymethylene für die Entwicklung der makromolekularen Chemie. *Kolloid-Z u Z Polymere*. 1967;216:286-98. <https://doi.org/10.1007/BF01525094>.
- [166] Vogl O. Addition polymers of aldehydes. *J Polym Sci, Part A: Polym Chem*. 2000;38:2293-9. [https://doi.org/10.1002/1099-0518\(20000701\)38:13<2293::AID-POLA10>3.0.CO;2-M](https://doi.org/10.1002/1099-0518(20000701)38:13<2293::AID-POLA10>3.0.CO;2-M).
- [167] Köstler S. Polyaldehydes: Homopolymers, block copolymers and promising applications. *Polym Int*. 2012;61:1221-7. <https://doi.org/10.1002/pi.4245>.
- [168] Bachelder EM, Pino EN, Ainslie KM. Acetalated dextran: A tunable and acid-labile biopolymer with facile synthesis and a range of applications. *Chem Rev*. 2017;117:1915-26. <https://doi.org/10.1021/acs.chemrev.6b00532>.
- [169] Binauld S, Stenzel MH. Acid-degradable polymers for drug delivery: A decade of innovation. *Chem Commun*. 2013;49:2082-102. <https://doi.org/10.1039/C2CC36589H>
- [170] Carmali S, Brocchini S. Polyacetals. In: Kumbar SG, Laurencin CT, Deng M, editors. *Natural and Synthetic Biomedical Polymers*. Burlington, MA: Elsevier Inc.; 2014. p. 219-33.
- [171] Heller J, Penhale D, Helwing R. Preparation of polyacetals by the reaction of divinyl ethers and polyols. *J Polym Sci B Polym Lett Ed*. 1980;18:293-7. <https://doi.org/10.1002/pol.1980.130180410>.

- [172] Heffernan MJ, Murthy N. Polyketal nanoparticles: A new pH-sensitive biodegradable drug delivery vehicle. *Bioconjugate Chem.* 2005;16:1340-2. <https://doi.org/10.1021/bc050176w>.
- [173] Vicent MJ, Tomlinson R, Brocchini S, Duncan R. Polyacetal-diethylstilboestrol: A polymeric drug designed for pH-triggered activation. *J Drug Target.* 2004;12:491-501. <https://doi.org/10.1080/10611860400011885>.
- [174] Samanta S, Bogdanowicz DR, Lu HH, Koberstein JT. Polyacetals: Water-soluble, pH-degradable polymers with extraordinary temperature response. *Macromolecules.* 2016;49:1858-64. <https://doi.org/10.1021/acs.macromol.5b02304>.
- [175] De Silva CC, Israni N, Zanzwar A, Jagtap A, Leophairatana P, Koberstein JT, et al. "Smart" polymer enhances the efficacy of topical antimicrobial agents. *Burns.* 2019;45:1418-29. <https://doi.org/10.1016/j.burns.2019.04.013>.
- [176] Samanta S, De Silva CC, Leophairatana P, Koberstein JT. Main-chain polyacetal conjugates with HIF-1 inhibitors: Temperature-responsive, pH-degradable drug delivery vehicles. *J Mater Chem B.* 2018;6:666-74. <https://doi.org/10.1039/C7TB01417A>
- [177] England RM, Masiá E, Giménez V, Lucas R, Vicent MJ. Polyacetal-stilbene conjugates—The first examples of polymer therapeutics for the inhibition of HIF-1 in the treatment of solid tumours. *J Control Release.* 2012;164:314-22. <https://doi.org/10.1016/j.jconrel.2012.08.017>.
- [178] Giménez V, James C, Armiñán A, Schweins R, Paul A, Vicent MJ. Demonstrating the importance of polymer-conjugate conformation in solution on its therapeutic output: Diethylstilbestrol (DES)-polyacetals as prostate cancer treatment. *J Control Release.* 2012;159:290-301. <https://doi.org/10.1016/j.jconrel.2011.12.035>.
- [179] Requejo-Aguilar R, Alastrue-Agudo A, Cases-Villar M, Lopez-Mocholi E, England R, Vicent MJ, et al. Combined polymer-curcumin conjugate and ependymal progenitor/stem cell treatment enhances spinal cord injury functional recovery. *Biomaterials.* 2017;113:18-30. <https://doi.org/10.1016/j.biomaterials.2016.10.032>.
- [180] Plyduang T, Armiñán A, Movellan J, England RM, Wiwattanapatapee R, Vicent MJ. Polyacetal-based combination therapy for the treatment of prostate cancer. *Macromol Rapid Commun.* 2018;39:e1800265. <https://doi.org/10.1002/marc.201800265>.
- [181] Guo S, Nakagawa Y, Barhoumi A, Wang W, Zhan C, Tong R, et al. Extended release of native drug conjugated in polyketal microparticles. *J Am Chem Soc.* 2016;138:6127-30. <https://doi.org/10.1021/jacs.6b02435>.

- [182] Escalona GR, Sanchis J, Vicent MJ. pH-responsive polyacetal – protein conjugates designed for Polymer Masked–Unmasked Protein Therapy (PUMPT). *Macromol Biosci.* 2018;18:e1700302. <https://doi.org/10.1002/mabi.201700302>.
- [183] Moreno A, Lligadas G, Ronda JC, Galia M, Cadiz V. Orthogonally functionalizable polyacetals: A versatile platform for the design of acid sensitive amphiphilic copolymers. *Polym Chem.* 2019;10:5215-27. <https://doi.org/10.1039/C9PY01107B>
- [184] Pasparakis G, Manouras T, Vamvakaki M, Argitis P. Harnessing photochemical internalization with dual degradable nanoparticles for combinatorial photo–chemotherapy. *Nat Commun.* 2014;5:e3623. <https://doi.org/10.1038/ncomms4623>.
- [185] Wang P, Wang JX, Tan HW, Weng SF, Cheng LY, Zhou ZP, et al. Acid- and reduction-sensitive micelles for improving the drug delivery efficacy for pancreatic cancer therapy. *Biomater Sci.* 2018;6:1262-70. <https://doi.org/10.1039/C7BM01051F>
- [186] Zhong H, Mu J, Du Y, Xu Z, Xu Y, Yu N, et al. Acid-triggered release of native gemcitabine conjugated in polyketal nanoparticles for enhanced anticancer therapy. *Biomacromolecules.* 2020;21:803-14. <https://doi.org/10.1021/acs.biomac.9b01493>.
- [187] Fuoco T. Degradation in order: Simple and versatile one-pot combination of two macromolecular concepts to encode diverse and spatially regulated degradability functions. *Angew Chem Int Ed.* 2021;60:15482-9. <https://doi.org/10.1002/anie.202103143>.
- [188] Lee S, Yang SC, Heffernan MJ, Taylor WR, Murthy N. Polyketal microparticles: A new delivery vehicle for superoxide dismutase. *Bioconjugate Chem.* 2007;18:4-7. <https://doi.org/10.1021/bc060259s>.
- [189] Gray WD, Che P, Brown M, Ning X, Murthy N, Davis ME. N-Acetylglucosamine conjugated to nanoparticles enhances myocyte uptake and improves delivery of a small molecule p38 inhibitor for post-infarct healing. *J Cardiovasc Transl Res.* 2011;4:631-43. <https://doi.org/10.1007/s12265-011-9292-0>.
- [190] Somasuntharam I, Boopathy AV, Khan RS, Martinez MD, Brown ME, Murthy N, et al. Delivery of Nox2-NADPH oxidase siRNA with polyketal nanoparticles for improving cardiac function following myocardial infarction. *Biomaterials.* 2013;34:7790-8. <https://doi.org/10.1016/j.biomaterials.2013.06.051>.

- [191] Lee S, Yang SC, Kao C-Y, Pierce RH, Murthy N. Solid polymeric microparticles enhance the delivery of siRNA to macrophages in vivo. *Nucleic Acids Res.* 2009;37:e145. <https://doi.org/10.1093/nar/gkp758>.
- [192] Yang SC, Bhide M, Crispe IN, Pierce RH, Murthy N. Polyketal copolymers: A new acid-sensitive delivery vehicle for treating acute inflammatory diseases. *Bioconjugate Chem.* 2008;19:1164-9. <https://doi.org/10.1021/bc700442g>.
- [193] Sohn Y-D, Somasuntharam I, Che P-L, Jayswal R, Murthy N, Davis ME, et al. Induction of pluripotency in bone marrow mononuclear cells via polyketal nanoparticle-mediated delivery of mature microRNAs. *Biomaterials.* 2013;34:4235-41. <https://doi.org/10.1016/j.biomaterials.2013.02.005>.
- [194] Pasparakis G, Manouras T, Selimis A, Vamvakaki M, Argitis P. Laser-induced cell detachment and patterning with photodegradable polymer substrates. *Angew Chem Int Ed.* 2011;50:4142-5. <https://doi.org/10.1002/anie.201007310>.
- [195] Mitra K, Hira SK, Singh S, Vishwakarma NK, Vishwakarma S, Gupta U, et al. In vitro anticancer drug delivery using amphiphilic poly(N-vinylpyrrolidone)-b-polyketal-b-poly(N-vinylpyrrolidone) block copolymer as micellar nanocarrier. *ChemistrySelect.* 2018;3:8833-43. <https://doi.org/10.1002/slct.201801399>.
- [196] Hira SK, Mitra K, Srivastava P, Singh S, Vishwakarma S, Singh R, et al. Doxorubicin loaded pH responsive biodegradable ABA-type amphiphilic PEG-b-aliphatic polyketal-b-PEG block copolymer for therapy against aggressive murine lymphoma. *Nanomedicine: NBM.* 2020;24:e102128. <https://doi.org/10.1016/j.nano.2019.102128>.
- [197] Sy JC, Seshadri G, Yang SC, Brown M, Oh T, Dikalov S, et al. Sustained release of a p38 inhibitor from non-inflammatory microspheres inhibits cardiac dysfunction. *Nat Mater.* 2008;7:863-8. <https://doi.org/10.1038/nmat2299>.
- [198] Maity S, Choudhary P, Manjunath M, Kulkarni A, Murthy N. A biodegradable adamantane polymer with ketal linkages in its backbone for gene therapy. *Chem Commun.* 2015;51:15956-9. <https://doi.org/10.1039/C5CC05242D>
- [199] Andrade-Gagnon B, Belanger-Bouliga M, Nguyen PT, Nguyen THD, Bourgault S, Nazemi A. Degradable spirocyclic polyacetal-based core-amphiphilic assemblies for encapsulation and release of hydrophobic cargo. *Nanomaterials.* 2021;11:e161. <https://doi.org/10.3390/nano11010161>.

- [200] Herwig G, Dove AP. Synthesis of rapidly surface eroding polyorthoesters and polyacetals using thiol–ene click chemistry. *ACS Macro Lett.* 2019;8:1268-74. <https://doi.org/10.1021/acsmacrolett.9b00463>.
- [201] Hill JW, Carothers WH. Cyclic and polymeric formals. *J Am Chem Soc.* 1935;57:925-8. <https://doi.org/10.1021/ja01308a045>.
- [202] Gresham WF. Preparation of polydioxolane. 1946;US2394910A.
- [203] Jaacks VV. Über die thermische Stabilität von Copolymeren des 1,3,5-Trioxans. *Makromol Chem.* 1965;84:250-60. <https://doi.org/10.1002/macp.1965.020840123>.
- [204] Jaacks VV. Anomalien bei der kationischen Copolymerisation von Trioxan. *Makromol Chem.* 1967;101:33-57. <https://doi.org/10.1002/macp.1967.021010103>.
- [205] Kern W, Jaacks V. Some kinetic effects in the polymerization of 1,3,5-trioxane. *J Polym Sci.* 1960;48:399-404. <https://doi.org/10.1002/pol.1960.1204815040>.
- [206] Lüftl S, Visakh P. Polyoxymethylene: State of art, new challenges and opportunities. In: Lüftl S, Chandran S, Visakh P, editors. *Polyoxymethylene Handbook*. Scrivener Publishing; 2014. p. 1-19.
- [207] Offermanns H. C 1-Chemie: Formaldehyd und seine Polymere. *Chem Unserer Zeit.* 2020;54:242-8. <https://doi.org/10.1002/ciuz.201900042>.
- [208] Price MB, McAndrew FB. The polymerization and copolymerization of trioxane. *J Macromol Sci A.* 1967;1:231-42. <https://doi.org/10.1080/10601326708053968>.
- [209] Reibel LC, Durand CP, Franta E. Cationic polymerization of 1,3-dioxolane and 1,3-dioxepane. Application to graft and block copolymer synthesis. *Can J Chem.* 1985;63:264-9. <https://doi.org/10.1139/v85-043>.
- [210] Walling CT, Brown F, Bartz KW. Copolymers. 1962;US3027352A.
- [211] Weissermel VK, Hermann HD, Burg KH. Die Copolymerisation des Trioxans mit substituierten 1,3-Dioxacycloalkanen. *Makromol Chem.* 1967;107:149-57. <https://doi.org/10.1002/macp.1967.021070115>.
- [212] Penczek S. Cationic ring-opening polymerization (CROP) major mechanistic phenomena. *J Polym Sci, Part A: Polym Chem.* 2000;38:1919-33. [https://doi.org/10.1002/\(SICI\)1099-0518\(20000601\)38:11<1919::AID-POLA10>3.0.CO;2-W](https://doi.org/10.1002/(SICI)1099-0518(20000601)38:11<1919::AID-POLA10>3.0.CO;2-W).
- [213] Szymanski R, Kubisa P, Stpenczek. Mechanism of cyclic acetal polymerization. End of a controversy? *Macromolecules.* 1983;16:1000-8. <https://doi.org/10.1021/ma00240a034>.

- [214] Coenen AM, Harings JA, Ghazanfari S, Jockenhoevel S, Bernaerts KV. Formation of cyclic structures in the cationic ring-opening polymerization of 1,3-dioxolane. *RSC Adv.* 2020;10:9623-32. <https://doi.org/10.1039/D0RA00904K>
- [215] Qiu H, Yang Z, Köhler M, Ling J, Schacher FH. Synthesis and solution self-assembly of poly(1,3-dioxolane). *Macromolecules.* 2019;52:3359-66. <https://doi.org/10.1021/acs.macromol.9b00302>.
- [216] Abel BA, Snyder RL, Coates GW. Chemically recyclable thermoplastics from reversible-deactivation polymerization of cyclic acetals. *Science.* 2021;373:783-9. DOI: 10.1126/science.abh0626.
- [217] Halat DM, Snyder RL, Sundararaman S, Choo Y, Gao KW, Hoffman ZJ, et al. Modifying Li⁺ and anion diffusivities in polyacetal electrolytes: A pulsed-field-gradient NMR study of ion self-diffusion. *Chem Mater.* 2021;33:4915-26. <https://doi.org/10.1021/acs.chemmater.1c00339>.
- [218] Zheng Q, Pesko DM, Savoie BM, Timachova K, Hasan AL, Smith MC, et al. Optimizing ion transport in polyether-based electrolytes for lithium batteries. *Macromolecules.* 2018;51:2847-58. <https://doi.org/10.1021/acs.macromol.7b02706>.
- [219] Gao KW, Loo WS, Snyder RL, Abel BA, Choo Y, Lee A, et al. Miscible polyether/poly(ether-acetal) electrolyte blends. *Macromolecules.* 2020;53:5728-39. <https://doi.org/10.1021/acs.macromol.0c00747>.
- [220] Sahadeo E, Wang Y, Lin C-F, Li Y, Rubloff G, Lee SB. Mg²⁺ ion-catalyzed polymerization of 1,3-dioxolane in battery electrolytes. *Chem Commun.* 2020;56:4583-6. <https://doi.org/10.1039/D0CC01769H>
- [221] Zhong H, Wang C, Xu Z, Ding F, Liu X. A novel quasi-solid state electrolyte with highly effective polysulfide diffusion inhibition for lithium-sulfur batteries. *Sci Rep.* 2016;6:e25484. <https://doi.org/10.1038/srep25484>.
- [222] Liu F-Q, Wang W-P, Yin Y-X, Zhang S-F, Shi J-L, Wang L, et al. Upgrading traditional liquid electrolyte via in situ gelation for future lithium metal batteries. *Sci Adv.* 2018;4:eaat5383. DOI: 10.1126/sciadv.aat5383.
- [223] Wang Y, Sahadeo E, Rubloff G, Lin C-F, Lee SB. High-capacity lithium sulfur battery and beyond: A review of metal anode protection layers and perspective of solid-state electrolytes. *J Mater Sci.* 2019;54:3671-93. <https://doi.org/10.1007/s10853-018-3093-7>.

- [224] Kost B, Basko M. Synthesis and properties of l-lactide/1,3-dioxolane copolymers: Preparation of polyesters with enhanced acid sensitivity. *Polym Chem.* 2021;12:2551-62. <https://doi.org/10.1039/D1PY00358E>
- [225] Higuchi M, Kanazawa A, Aoshima S. Tandem unzipping and scrambling reactions for the synthesis of alternating copolymers by the cationic ring-opening copolymerization of a cyclic acetal and a cyclic ester. *ACS Macro Lett.* 2019;9:77-83. <https://doi.org/10.1021/acsmacrolett.9b00874>.
- [226] Higuchi M, Kanazawa A, Aoshima S. Unzipping and scrambling reaction-induced sequence control of copolymer chains via temperature changes during cationic ring-opening copolymerization of cyclic acetals and cyclic esters. *J Polym Sci.* 2021. <https://doi.org/10.1002/pol.20210197>.
- [227] Shirouchi T, Kanazawa A, Kanaoka S, Aoshima S. Controlled cationic copolymerization of vinyl monomers and cyclic acetals via concurrent vinyl-addition and ring-opening mechanisms. *Macromolecules.* 2016;49:7184-95. <https://doi.org/10.1021/acs.macromol.6b01565>.
- [228] Maruyama K, Kanazawa A, Aoshima S. Controlled cationic copolymerization of vinyl monomers and cyclic acetals via concurrent vinyl-addition and ring-opening mechanisms: The systematic study of structural effects on the copolymerization behavior. *Polym Chem.* 2019;10:5304-14. <https://doi.org/10.1039/C9PY01024F>.
- [229] Kato R, Kanazawa A, Aoshima S. Desilylation-triggered degradable silylacetal polymers synthesized via controlled cationic copolymerization of trimethylsilyl vinyl ether and cyclic acetals. *ACS Macro Lett.* 2019;8:1498-503. <https://doi.org/10.1021/acsmacrolett.9b00745>.
- [230] Aoshima S, Kanaoka S. A renaissance in living cationic polymerization. *Chem Rev.* 2009;109:5245-87. <https://doi.org/10.1021/cr900225g>.
- [231] Hong M, Chen J, Chen EY-X. Polymerization of polar monomers mediated by main-group Lewis acid–base pairs. *Chem Rev.* 2018;118:10551-616. <https://doi.org/10.1021/acs.chemrev.8b00352>.
- [232] Ishido Y, Kanazawa A, Kanaoka S, Aoshima S. Controlled cationic alternating copolymerization of various enol ethers and benzaldehyde derivatives: Effects of enol ether structures. *J Polym Sci, Part A: Polym Chem.* 2014;52:1334-43. <https://doi.org/10.1002/pola.27122>.

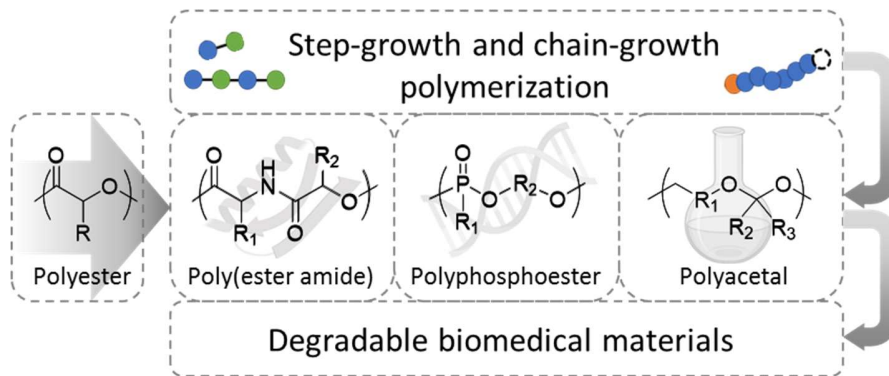
- [233] Ishido Y, Kanazawa A, Kanaoka S, Aoshima S. Chemically recyclable alternating copolymers with low polydispersity from conjugated/aromatic aldehydes and vinyl ethers: Selective degradation to another monomer at ambient temperature. *Polym Chem.* 2014;5:43-7. <https://doi.org/10.1039/C3PY00842H>.
- [234] Ishido Y, Kanazawa A, Kanaoka S, Aoshima S. New degradable alternating copolymers from naturally occurring aldehydes: Well-controlled cationic copolymerization and complete degradation. *Macromolecules.* 2012;45:4060-8. <https://doi.org/10.1021/ma3004828>.
- [235] Kawamura M, Kanazawa A, Kanaoka S, Aoshima S. Sequence-controlled degradable polymers by controlled cationic copolymerization of vinyl ethers and aldehydes: Precise placement of cleavable units at predetermined positions. *Polym Chem.* 2015;6:4102-8. <https://doi.org/10.1039/C5PY00493D>.
- [236] Matsumoto S, Kanazawa A, Kanaoka S, Aoshima S. Dual stimuli-responsive copolymers with precisely arranged degradable units: Synthesis by controlled alternating copolymerization of oxyethylene-containing vinyl ethers and conjugated aldehydes. *Polym Chem.* 2019;10:4134-41. <https://doi.org/10.1039/C9PY00513G>
- [237] Matsumoto S, Kanazawa A, Kanaoka S, Aoshima S. Tandem reaction of cationic copolymerization and concertedly induced hetero-Diels–Alder reaction preparing sequence-regulated polymers. *J Am Chem Soc.* 2017;139:7713-6. <https://doi.org/10.1021/jacs.7b03526>.
- [238] Hayashi K, Kanazawa A, Aoshima S. Exceptional copolymerizability of o-phthalaldehyde in cationic copolymerization with vinyl monomers. *Polym Chem.* 2019;10:3712-7. <https://doi.org/10.1039/C9PY00547A>
- [239] Naito T, Kanazawa A, Aoshima S. Polyaddition of vinyl ethers and phthalaldehydes via successive cyclotrimerization reactions: Selective model reactions and synthesis of acid-degradable linear poly(cyclic acetal)s. *Polym Chem.* 2019;10:1377-85. <https://doi.org/10.1039/C9PY00043G>
- [240] Aoshima S, Oda Y, Matsumoto S, Shinke Y, Kanazawa A, Kanaoka S. Efficient design for stimuli-responsive polymers with quantitative acid-degradability: Specifically designed alternating controlled cationic copolymerization and facile complete degradation. *ACS Macro Lett.* 2014;3:80-5. <https://doi.org/10.1021/mz400563v>.
- [241] Yokota D, Kanazawa A, Aoshima S. Alternating degradable copolymers of an ionic liquid-type vinyl ether and a conjugated aldehyde: Precise synthesis by living cationic copolymerization

- and dual rare thermosensitive behavior in solution. *Macromolecules*. 2019;52:6241-9. <https://doi.org/10.1021/acs.macromol.9b00634>.
- [242] Ishido Y, Aburaki R, Kanaoka S, Aoshima S. Well-defined alternating copolymers of benzaldehydes with vinyl ethers: Precision synthesis by cationic copolymerization and quantitative degradation to cinnamaldehydes. *Macromolecules*. 2010;43:3141-4. <https://doi.org/10.1021/ma902840d>.
- [243] Ishido Y, Aburaki R, Kanaoka S, Aoshima S. Controlled cationic copolymerization of benzaldehyde with isobutyl vinyl ether using base-assisting system. *J Polym Sci, Part A: Polym Chem*. 2010;48:1838-43. <https://doi.org/10.1002/pola.23945>.
- [244] Ishido Y, Kanazawa A, Kanaoka S, Aoshima S. Selectively degradable alternating copolymers of isobutyl vinyl ether and plant-derived aldehydes with acyclic side chains: Effects of side group structures on copolymerization behaviors. *J Polym Sci, Part A: Polym Chem*. 2013;51:4684-93. <https://doi.org/10.1002/pola.26890>.
- [245] Aso C, Tagami S, Kunitake T. Polymerization of aromatic aldehydes. II. Cationic cyclopolymerization of phthalaldehyde. *J Polym Sci, Part A: Polym Chem*. 1969;7:497-511. <https://doi.org/10.1002/pol.1969.150070208>.
- [246] Kanazawa A, Aoshima S. Concurrent cationic vinyl-addition and ring-opening copolymerization of vinyl ethers and oxiranes. *Polym J*. 2016;48:679-87. <https://doi.org/10.1038/pj.2016.27>.
- [247] Piers WE, Chivers T. Pentafluorophenylboranes: From obscurity to applications. *Chem Soc Rev*. 1997;26:345-54. <https://doi.org/10.1039/CS9972600345>
- [248] Ishihara K, Yamamoto H. Arylboron compounds as acid catalysts in organic synthetic transformations. *Eur J Org Chem*. 1999;1999:527-38. [https://doi.org/10.1002/\(SICI\)1099-0690\(199903\)1999:3<527::AID-EJOC527>3.0.CO;2-R](https://doi.org/10.1002/(SICI)1099-0690(199903)1999:3<527::AID-EJOC527>3.0.CO;2-R).
- [249] Erker G. Tris(pentafluorophenyl)borane: A special boron Lewis acid for special reactions. *Dalton Trans*. 2005:1883-90. <https://doi.org/10.1039/B503688G>
- [250] Kanazawa A, Aoshima S. Frequency control of crossover reactions in concurrent cationic vinyl-addition and ring-opening copolymerization of vinyl ethers and oxiranes: Specific roles of weak Lewis bases and solvent polarity. *Polym Chem*. 2015;6:5675-82. <https://doi.org/10.1039/C5PY00152H>.

- [251] Miyamae Y, Kanazawa A, Tamaso K-i, Morino K, Ogawa R, Aoshima S. The influence of the substituents of oxiranes on copolymerization with vinyl ethers via concurrent cationic vinyl-addition and ring-opening mechanisms. *Polym Chem.* 2018;9:404-13. <https://doi.org/10.1039/C7PY01292F>
- [252] Hotta D, Kanazawa A, Aoshima S. Generation of “living” species using perfluoroalkylsulfonic acids in concurrent cationic vinyl-addition and ring-opening copolymerization via crossover reactions. *Macromolecules.* 2018;51:7983-92. <https://doi.org/10.1021/acs.macromol.8b01686>.
- [253] Hotta D, Kanazawa A, Aoshima S. tert-Butyl esters as potential reversible chain transfer agents for concurrent cationic vinyl-addition and ring-opening copolymerization of vinyl ethers and oxiranes. *Macromol Rapid Commun.* 2021;42:e2000479. <https://doi.org/10.1002/marc.202000479>.
- [254] Kanazawa A, Aoshima S. Cationic terpolymerization of vinyl ethers, oxetane, and ketones via concurrent vinyl-addition, ring-opening, and carbonyl-addition mechanisms: Multiblock polymer synthesis and mechanistic investigation. *Macromolecules.* 2017;50:6595-605. <https://doi.org/10.1021/acs.macromol.7b01250>.
- [255] Mimura M, Kanazawa A, Aoshima S. ABC pseudo-periodic sequence control by cationic orthogonal terpolymerization of vinyl ether, oxirane, and ketone. *Macromolecules.* 2019;52:7572-83. <https://doi.org/10.1021/acs.macromol.9b01573>.
- [256] Hyoui K, Kanazawa A, Aoshima S. Cationic ring-opening co- and terpolymerizations of lactic acid-derived 1,3-dioxolan-4-ones with oxiranes and vinyl ethers: Nonhomopolymerizable monomer for degradable co- and terpolymers. *ACS Macro Lett.* 2019;8:128-33. <https://doi.org/10.1021/acsmacrolett.8b00868>.
- [257] Kanazawa A, Aoshima S. Exclusive one-way cycle sequence control in cationic terpolymerization of general-purpose monomers via concurrent vinyl-addition, ring-opening, and carbonyl-addition mechanisms. *ACS Macro Lett.* 2015;4:783-7. <https://doi.org/10.1021/acsmacrolett.5b00365>.
- [258] Cairns SA, Schultheiss A, Shaver MP. A broad scope of aliphatic polyesters prepared by elimination of small molecules from sustainable 1, 3-dioxolan-4-ones. *Polym Chem.* 2017;8:2990-6. <https://doi.org/10.1039/C7PY00254H>

- [259] Xu Y, Perry MR, Cairns SA, Shaver MP. Understanding the ring-opening polymerisation of dioxolanones. *Polym Chem.* 2019;10:3048-54. <https://doi.org/10.1039/C8PY01695J>
- [260] Martin RT, Camargo LP, Miller SA. Marine-degradable polylactic acid. *Green Chem.* 2014;16:1768-73. <https://doi.org/10.1039/C3GC42604A>.
- [261] Bandelli D, Alex J, Weber C, Schubert US. Polyester stereocomplexes beyond PLA: Could synthetic opportunities revolutionize established material blending? *Macromol Rapid Commun.* 2020;41:e1900560. <https://doi.org/10.1002/marc.201900560>.
- [262] Neitzel AE, Petersen MA, Kokkoli E, Hillmyer MA. Divergent mechanistic avenues to an aliphatic polyesteracetal or polyester from a single cyclic esteracetal. *ACS Macro Lett.* 2014;3:1156-60. <https://doi.org/10.1021/mz5005794>.
- [263] Bixenmann L, Stickdorn J, Nuhn L. Amphiphilic poly(esteracetal)s as dual pH- and enzyme-responsive micellar immunodrug delivery systems. *Polym Chem.* 2020;11:2441-56. <https://doi.org/10.1039/C9PY01716J>
- [264] Neitzel AE. Ring-opening polymerization of cyclic hemiacetal esters for the preparation of hydrolytically and thermally degradable polymers [Ph.D. Dissertation]. Minneapolis, MN: University of Minnesota; 2018.
- [265] Neitzel AE, Barreda L, Trotta JT, Fahnhorst GW, Haversang TJ, Hoye TR, et al. Hydrolytically-degradable homo-and copolymers of a strained exocyclic hemiacetal ester. *Polym Chem.* 2019;10:4573-83. <https://doi.org/10.1039/C9PY00797K>

Table of Contents (ToC) entry:

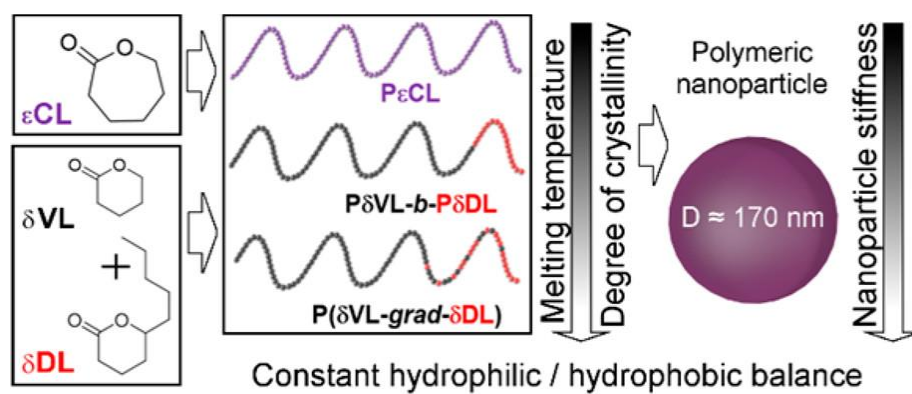


Publication 2

Maintaining the hydrophilic–hydrophobic balance of polyesters with adjustable crystallinity
for tailor–made nanoparticles

D. Bandelli, C. Helbing, C. Weber, M. Seifert, I. Muljajew, K. D. Jandt, U. S. Schubert

Macromolecules **2018**, *51*, 5567–5576.



Maintaining the Hydrophilic–Hydrophobic Balance of Polyesters with Adjustable Crystallinity for Tailor-Made Nanoparticles

Damiano Bandelli,^{†,‡} Christian Helbing,^{‡,§} Christine Weber,^{†,‡} Michael Seifert,[§] Irina Muljajew,^{†,‡} Klaus D. Jandt,^{*,‡,§} and Ulrich S. Schubert^{*,†,‡}

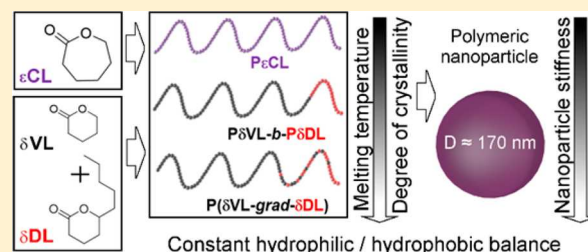
[†]Laboratory of Organic and Macromolecular Chemistry (IOMC), Friedrich Schiller University Jena, Humboldtstr. 10, 07743 Jena, Germany

[‡]Jena Center for Soft Matter (JCSM), Friedrich Schiller University Jena, Philosophenweg 7, 07743 Jena, Germany

[§]Chair of Materials Science (CMS), Department of Materials Science and Technology, Otto Schott Institute of Materials Research, Faculty of Physics and Astronomy, Friedrich Schiller University Jena, Löbdergraben 32, 07743 Jena, Germany

Supporting Information

ABSTRACT: To explore the relationship between thermal properties of a polymer and the biological performance of the resulting nanoparticle, all other parameters, including the hydrophobicity, should be kept constant. For this purpose, a gradient and a block copolyester were tailor-made via the triazabicyclodecene catalyzed ring-opening copolymerization of δ -valerolactone (δ VL) and δ -decalactone (δ DL) to match the hydrophobicity of poly(ϵ -caprolactone) (P ϵ CL). The degree of crystallinity of the semicrystalline materials was significantly reduced due to the incorporation of amorphous P δ DL segments, as confirmed by dynamic scanning calorimetry. Atomic force microscopy revealed short and randomly oriented crystals in the gradient copolymer but longer and parallel aligned crystals for the block copolymer and P ϵ CL. The stiffness of nanoparticles ($D_h \approx 170$ nm) prepared from the polyesters correlated to the bulk crystallinity. The set of nanoparticles with constant hydrophobicity and size will facilitate direct access to the influence of the nanoparticle crystallinity on biological processes such as enzymatic degradation, drug release, and cellular uptake.



INTRODUCTION

Polymeric nanoparticles represent highly promising materials for the targeted delivery of actives. They are often composed of a biodegradable polymer core serving as a reservoir for pharmaceutically active compounds, while stealth polymers¹ or targeting ligands² can be attached to its shell.³ The interdisciplinary field and the modularity of the concept offer a vast parameter landscape, rendering strict systematic investigations extremely complex. However, the latter are required to understand nanoparticle mediated drug delivery, which is one key factor for the development of a truly personalized medicine. Although the physicochemical characterization of nanoparticle carrier systems alone has been established,⁴ investigations of structure–property relationships with a predicting character regarding, e.g., release profiles of actives are still missing.

The vast majority of degradable nanocarriers is composed of polyesters such as poly(ϵ -caprolactone) (P ϵ CL) or polylactide (PLA).⁵ Encapsulated actives are released by enzymatic degradation.⁶ Besides other factors such as the hydrophobicity, the molar mass, or the chemical composition of the polymers, the crystallinity of polyesters influences the enzymatic degradation rate and, hence, the release from polyester-based nanoparticles.^{7–9} However, a clear statement can only be made

if only one parameter is varied, but all other parameters are kept constant. Although such investigations exist regarding the influence of the degree of crystallinity for PLA stereocomplexes in thin films,¹⁰ the issue is more complex for aqueous nanoparticle suspensions and has, to the best of our knowledge, not been clarified yet.

Whereas, e.g., the size of a polymer nanoparticle can be easily varied by using the identical polymer material,¹¹ a variation of the polyester crystallinity is often accompanied by a variation of the chemical composition. Unfortunately, a constant hydrophilic–hydrophobic balance (HHB) of the materials is difficult to maintain because polyesters with elongated alkyl spacers are more crystalline but also more hydrophobic than polyesters with shorter alkyl spacers.^{12,13}

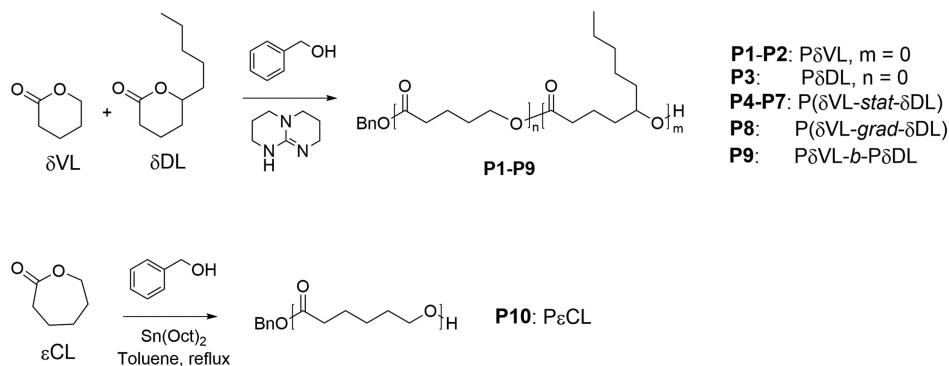
We therefore selected P ϵ CL as a well-known semicrystalline reference material and approached the issue by developing polyesters that would feature a different degree of crystallinity but the same hydrophobicity, i.e., the same fraction of ester moieties per polymer chain. The copolymerization concept relies on δ -lactones as monomers (Scheme 1). Lacking one

Received: April 30, 2018

Revised: June 19, 2018

Published: July 18, 2018

Scheme 1. Schematic Representation of the Ring-Opening Polymerization of ϵ -Caprolactone (ϵ CL), δ -Valerolactone (δ VL), and δ -Decalactone (δ DL) Yielding the Homo- and Copolyesters P1 to P10



methylene unit compared to $P\epsilon$ CL, poly(δ -valerolactone) ($P\delta$ VL) represents a semicrystalline polyester with a similar melting temperature as the reference material. Substituents at the six-membered monomer ring are known to significantly decrease the crystallinity of the corresponding polyesters, which in fact are often amorphous.¹³ We hence selected δ -decalactone (δ DL), comprising four additional methylene moieties compared to ϵ CL, as a second monomer to compensate for the “missing” methylene moiety of δ VL. A copolymer consisting of 80 mol % of δ VL and 20 mol % of δ DL would hence feature the same fraction of ester moieties as $P\epsilon$ CL.

δ -Lactones can be polymerized via ring-opening polymerization (ROP) using cationic initiators,¹⁴ the standard catalyst tin(II) octoate ($\text{Sn}(\text{Oct})_2$),¹⁵ and organic base catalysts.^{16–20} The negative free enthalpy and entropy of the ROP of δ -lactones make the resulting polyesters polymers featuring a classical ceiling temperature.¹³ In view of this fact, we relied on the highly active catalyst triazabicyclodecene (TBD), which has already been successfully applied for the homopolymerization of δ VL²¹ and δ DL^{22,23} at room temperature.

The synthetic development of the tailor-made copolyesters we describe herein includes detailed kinetic studies to elucidate the microstructure and is complemented by an extensive characterization of the thermal and mechanical properties of the materials. Dynamic scanning calorimetry and polarized light microscopy were applied as integrating methods²⁴ to bulk samples. Atomic force microscopy^{25,26} was applied to correlate the bulk properties with the mechanical properties of nanoparticles prepared from the materials.

EXPERIMENTAL SECTION

Materials. δ -Valerolactone (δ VL, 98%) and δ -decalactone (δ DL, 97%) were purchased from TCI. ϵ -Caprolactone (ϵ CL, 97%) was purchased from Sigma-Aldrich and dried over calcium hydride. Benzyl alcohol (BnOH, 99.8%, water content <0.003%), 1,5,7-triazabicyclo[4.4.0]dec-5-ene (TBD), tin octanoate ($\text{Sn}(\text{Oct})_2$), and anhydrous toluene were purchased from Sigma-Aldrich. All other chemicals were purchased from standard suppliers and used without further purification. All glassware was dried at 110 °C for 24 h prior to use for polymerization.

Instruments. All polymerizations were prepared in a MBraun UNILab Plus glovebox workstation under a nitrogen atmosphere (<0.1 ppm of H_2O ; <0.1 ppm of O_2). Proton nuclear magnetic resonance (^1H NMR) spectra were recorded at room temperature in CDCl_3 on a Bruker Avance 300 MHz using the residual solvent resonance as internal standard. The chemical shifts are given in ppm relative to tetramethylsilane (TMS).

Size exclusion chromatography (SEC) measurements were performed on a Shimadzu system equipped with a CBM-20A system controller, a LC-10AD VP pump, a RID-10A refractive index detector, a SPD-10AD VP UV detector, and a SDV linear S column from PSS (Polymer Standards Service GmbH, Mainz, Germany) at 40 °C using chloroform:triethylamine:2-propanol (94:4:2) as eluent at a flow rate of 1 mL min⁻¹. The system was calibrated against PMMA standards (410–88 000 g mol⁻¹), which were purchased from PSS.

For the measurements of the matrix-assisted laser desorption/ionization time-of-flight (MALDI-ToF) mass spectra, an Ultraflex III ToF/ToF instrument (Bruker Daltonics, Bremen, Germany) was used. The instrument is equipped with a Nd:YAG laser and a collision cell. All spectra were measured in the positive reflector mode using *trans*-2-[3-(4-*tert*-butylphenyl)-2-methyl-2-propenylidene] (DCTB) as matrix and sodium iodide (NaI) as doping salt. The instrument was calibrated prior to each measurement with an external PMMA standard (2500 g mol⁻¹) from PSS.

Thermogravimetric analysis (TGA) was performed under a nitrogen atmosphere on a Netzsch TG 209 F1 Iris from room temperature to 600 °C at a heating rate of 10 K min⁻¹. Differential scanning calorimetry (DSC) measurements were performed on a Netzsch DSC 204 F1 Phoenix under a nitrogen atmosphere from –150 to 210 °C. Three cycles were recorded for each sample using a cooling rate of 20 K min⁻¹ between the heating runs. The first and the second heating run were conducted at a heating rate of 20 K min⁻¹. For the third heating run, a heating rate of 10 K min⁻¹ was applied. The glass transition temperature (T_g , inflection value reported) and the melting temperature (T_m) values are reported from the second heating run.

Dynamic light scattering (DLS) and ζ -potential measurements were performed on a Zetasizer Nano ZS (Malvern Instruments, Herrenberg, Germany) at 25 °C ($\lambda = 633$ nm) at an angle of 173°. Each measurement was performed five times. The mean particle size was approximated as the effective (Z-average) diameter and the width of the distribution as the dispersity index (PDI) of the particles obtained by the cumulants method assuming a spherical shape.

A Leica DM 2700 equipped with a linkam heating stage was used to prepare polymeric spherulites. For this purpose, a small amount of the polymer was placed on a clean glass slide and heat-treated with the same temperature profile as described for the DSC measurements. The formation of spherulites was clarified by light microscopy with crossed polarizers.

Shape and dimensions of the nanoparticles were investigated by scanning electron microscopy (SEM) with an AURIGA 60 Cross-Beam workstation (Carl Zeiss AG, Oberkochen, Germany). Additionally, atomic force microscopy (AFM) measurements were performed with a Dimension 3100 and Catalyst (both from Bruker, Veeco, Santa Barbara, CA) equipped with a nanoscope IV and VIII controller, respectively, to determine the nanoparticle shape and stiffness. Measurements were performed at room temperature by using standard tapping mode silicon cantilevers from Bruker (model RTESP, Veeco, Santa Barbara, CA) with a resonance frequency in the

Table 1. Selected Structural Characterization Data of the Synthesized (Co)polymers

sample	polymer	$\delta VL/\delta DL$			NMR ^c [mol %]	NMR		SEC
		feed [mol %]	conv ^a [%]	theor ^b [mol %]		M_n^c [kg mol ⁻¹]	M_n^d [kg mol ⁻¹]	
P1 ^e	P δVL	100/0	98/–	100/0	100/0	2.7	3.8	1.47
P2	P δVL	100/0	93/–	100/0	100/0	9	9	1.33
P3	P δDL	0/100	–/84	0/100	0/100	14	14	1.55
P4	P(δVL -stat- δDL)	80/20	99/82	83/17	85/15	11	14	2.33
P5	P(δVL -stat- δDL)	70/30	99/84	73/27	77/23	11	13	2.31
P6	P(δVL -stat- δDL)	60/40	99/85	64/36	67/33	12	14	1.94
P7	P(δVL -stat- δDL)	50/50	99/84	54/46	58/42	12	13	1.66
P8	P(δVL -grad- δDL)	75/25	98/82	78/22	80/20	11	11	1.66
P9	P δVL -b-P δDL	n.a.	70/17	80/20	82/18	11	11	1.35
P10	PeCL	n.a.	99 (eCL)	n.a.	n.a.	9	9	1.30

^aDetermined by integration of suitable signals in the ¹H NMR spectra of the reaction solution. ^bCalculated from feed ratio and monomer conversion. ^cDetermined by integration of suitable signals in the ¹H NMR spectra of the purified polymers. ^dEluent CHCl₃, RI detection, PMMA calibration. ^eMALDI-ToF MS: $M_n = 2.8$ kg mol⁻¹, $\bar{D} = 1.14$.

range 315–364 kHz in air, a spring constant in the range 20–80 N m⁻¹, and a typical tip radius of less than 10 nm (typically 7 nm). The peak-force tapping mode was used to capture force–distance curves simultaneously to height profiles. To avoid a movement of the nanoparticles during the measurements, silicon substrates were modified with a thin layer of polyethylenimine (PEI).

Ring-Opening Polymerization. All polymerization mixtures were prepared in a glovebox at room temperature under a nitrogen atmosphere (<0.1 ppm of H₂O; <0.1 ppm of O₂). For the polymerizations catalyzed by TBD, a stock solution of initiator and catalyst was used. The stock solution contained 28 mg (0.2 mmol) of TBD, 20 μ L (0.2 mmol) of BnOH, and 180 μ L of anhydrous toluene for polymerizations conducted at a [BnOH]:[TBD] ratio of 1:1.

Polymerization Kinetics. For the kinetic studies of the homopolymerization of δVL and δDL , five vials were each charged with 1 mmol of monomer (corresponding to 110 μ L of δVL and 179 μ L of δDL). For the polymerization of δDL , 0.01 mmol of BnOH and 0.01 mmol of TBD were added to each vial from a stock solution in toluene to reach a ratio of [δDL]:[TBD]:[BnOH] = 100:1:1. According to a ratio of [δVL]:[TBD]:[BnOH] = 100:0.1:1, 0.01 mmol of BnOH and 0.001 mmol of TBD were used for the polymerization of δVL . The ROP proceeded at room temperature under stirring, and the reactions were quenched by addition of 1 mL of a solution of benzoic acid (1 equiv with respect to TBD) in chloroform after varying time intervals. ¹H NMR and SEC analyses were performed from the quenched reaction mixtures in order to assess the monomer conversion, the molar mass, and the dispersity (\bar{D}). The P δVL kinetics were conducted directly inside the glovebox. For the P δDL kinetics, the sample vials were prepared and sealed inside the glovebox and subsequently stirred outside of the glovebox at 23 °C.

For the kinetic studies of the statistical copolymerization, 0.75 mmol (70 μ L) of δVL and 0.25 mmol (45 μ L) of δDL were mixed inside each vial, and BnOH and TBD were added as described above to reach a ratio of [δVL]:[δDL]:[TBD]:[BnOH] = 75:25:1:1. The vials were transferred out of the glovebox, and kinetic samples were quenched and analyzed as described above.

Homopolymerization of δVL and δDL (P1 to P3). Corresponding to an initial ratio of [M]:[TBD]:[BnOH] of 20:0.1:1, P1 was obtained as described above using 110 μ L (1 mmol) of δVL and 10 μ L of the stock solution containing TBD and BnOH. The polymerizations of P2 to P3 were conducted as described above (see kinetic studies). After the polymerization time indicated below, the polymerization mixtures were quenched, and a sample for the determination of the monomer conversion was taken. The crude polymers were precipitated into cold methanol (–22 °C), and the purified polyesters were dried at 40 °C in a vacuum oven overnight.

P δVL (P1). $t_{pol} = 13$ min; conv = 98%. ¹H NMR (300 MHz, CDCl₃): δ /ppm = 1.68 (broad, $-\text{CH}_2\text{CH}_2-$), 2.35 (t, $-\text{OC}(\text{O})\text{CH}_2-$), 4.08 (t, $-\text{CH}_2\text{O}-$), 5.15 (s, C₆H₅(CH₂)OC(O)-), 7.36 (m,

C₆H₅-). SEC (CHCl₃, PMMA calibration): $M_n = 3.8$ kg mol⁻¹; $\bar{D} = 1.47$. MALDI MS: $M_n = 2.8$ kg mol⁻¹, $\bar{D} = 1.14$.

P δVL (P2). $t_{pol} = 50$ min; conv = 93%; yield 90%. ¹H NMR (300 MHz, CDCl₃): δ /ppm = 1.68 (broad, $-\text{CH}_2\text{CH}_2-$), 2.35 (t, $-\text{OC}(\text{O})\text{CH}_2-$), 4.08 (t, $-\text{CH}_2\text{O}-$), 5.15 (s, C₆H₅(CH₂)OC(O)-), 7.36 (m, C₆H₅-). SEC (CHCl₃, PMMA calibration): $M_n = 9$ kg mol⁻¹; $\bar{D} = 1.33$.

P δDL (P3). $t_{pol} = 24$ h; conv = 84%; yield 50%. ¹H NMR (300 MHz, CDCl₃): δ /ppm = 0.86 (t, CH₃-), 1.28 (t, $-\text{CH}_2-\text{CH}_2-\text{CH}_2-$), 1.57 (broad, $-\text{CH}_2-\text{CH}_2-\text{CH}(\text{OH})-\text{CH}_2-$), 2.30 (t, $-\text{OC}(\text{O})-\text{CH}_2-$), 5.12 (s, C₆H₅(CH₂)OC(O)-), 7.36 (m, C₆H₅-). SEC (CHCl₃, PMMA calibration): $M_n = 14$ kg mol⁻¹; $\bar{D} = 1.55$.

Statistical Copolymerization of δVL and δDL (P4 to P8). The statistical copolymers comprising δVL and δDL P4 to P7 were obtained as described above for the homopolymers P2 to P3. Keeping a constant ratio of [M]_{total}: [TBD]: [BnOH] = 100:1:1, the feed ratio of δDL and δVL was varied as indicated in Table 1. In an exemplary reaction for P4, 74 μ L (0.8 mmol) of δVL was mixed with 36 μ L (0.20 mmol) of δDL , 0.01 mmol of BnOH, and 0.01 mmol of TBD. The polymerization was conducted at room temperature for 18 h, and the analysis and purification were performed as described above.

Corresponding to a ratio of [δVL]:[δDL]:[TBD]:[BnOH] = 75:25:1:1, P8 was obtained using 69.6 μ L (0.75 mmol) of δVL , 44.6 μ L (0.25 mmol) of δDL , and 10 μ L of the stock solution containing TBD and BnOH.

P(δVL -stat- δDL) (P8). $t_{pol} = 7.5$ h; conv(δVL) = 98%; conv(δDL) = 82%; yield 82%. ¹H NMR (300 MHz, CDCl₃): δ /ppm = 0.89 (t, CH₃-(DL)), 1.28 (t, CH₃-CH₂-CH₂-CH₂-(DL)), 1.63 (broad, $-\text{CH}_2-\text{CH}(\text{OH})-\text{CH}_2-\text{CH}_2-$ -(DL)), 2.35 (t, $-\text{OC}(\text{O})\text{CH}_2-$), 4.09 (t, $-\text{CH}_2\text{O}-$ (VL)), 4.88 (t, $-\text{CH}_2\text{O}-$ (DL)), 5.13 (s, C₆H₅(CH₂)OC(O)-), 7.36 (m, C₆H₅-). SEC (CHCl₃, PMMA calibration): $M_n = 11$ kg mol⁻¹; $\bar{D} = 1.66$.

Synthesis of P δVL -b-P δDL (P9). 20 μ L of the stock solution and 185.8 μ L (2 mmol) of δVL were used for the synthesis of the first block corresponding to a [M]:[TBD]:[BnOH] = 100:0.1:1. The polymerization was quenched after 32 min by the addition of 1 mL of a solution of benzoic acid (1 equiv in comparison with TBD) in chloroform. The first block was purified and analyzed as described above.

Conv = 70%; yield 53%; $M_{n,theo} = 7.1$ kg mol⁻¹. ¹H NMR (300 MHz, CDCl₃): δ /ppm = 1.68 (broad, $-\text{CH}_2\text{CH}_2-$), 2.35 (t, $-\text{OC}(\text{O})\text{CH}_2-$), 4.08 (t, $-\text{CH}_2\text{O}-$), 5.15 (s, C₆H₅(CH₂)OC(O)-), 7.36 (m, C₆H₅-); $M_{n,NMR} = 7.7$ kg mol⁻¹. SEC (CHCl₃, PMMA calibration): $M_n = 10$ kg mol⁻¹; $\bar{D} = 1.18$.

For the chain extension, 75 mg (0.01 mmol) of the P δVL block was dissolved in 177 μ L (1 mmol) of δDL by stirring for 2 h. Subsequently, 10 μ L of a solution of TBD in toluene was added to result in an initial ratio of [M]:[TBD]:[P δVL] = 100:1:1. The reaction was performed at room temperature and quenched after 260

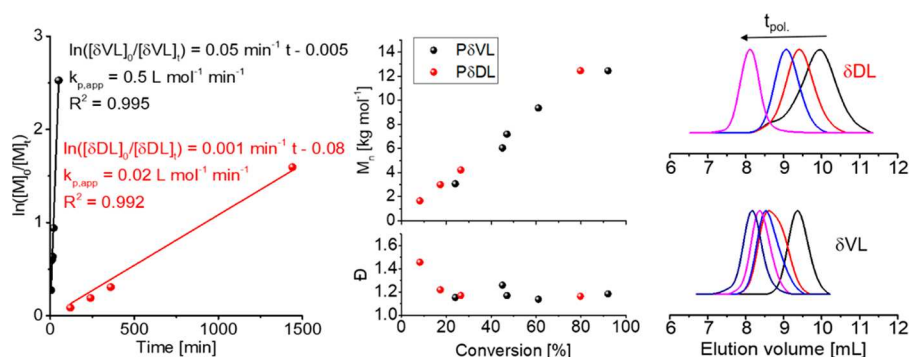


Figure 1. Kinetic studies of the homopolymerization of δ VL and δ DL conducted in bulk at room temperature using BnOH as initiator and TBD as catalyst ($[\delta$ DL]:[TBD]:[I] = 100:1:1; $[\delta$ VL]:[TBD]:[I] = 100:0.1:1). Left: first-order kinetic plot with a linear fit according to $\ln([M]_0/[M]) = k_{p,app}[I]_0 t$. Center: evolution of the molar mass with monomer conversion. Right: overlay of the SEC elugrams of the samples taken (CHCl_3 , RI detection).

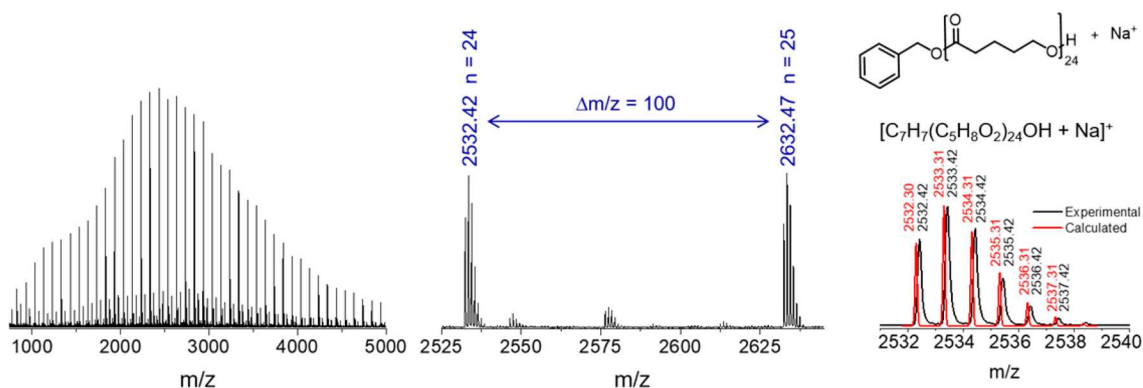


Figure 2. MALDI-ToF MS analysis of P δ VL (P1, DCTB, NaI). Left: full mass spectrum. Center: zoom into the most abundant m/z region. Right: overlay of the calculated and measured isotopic pattern for the structural assignment of the observed peaks.

min. The block copolymer **P9** was purified and analyzed as described above.

P δ VL-*b*-P δ DL (P9). Conv = 17%; yield 24%. $^1\text{H NMR}$ (300 MHz, CDCl_3): δ/ppm = 0.89 (t, CH_3 -(DL)), 1.28 (t, CH_3 - $\text{CH}_2\text{CH}_2\text{CH}_2$ -(DL)), 1.63 (broad, $-\text{CH}_2-\text{CH}(\text{OH})-\text{CH}_2\text{CH}_2$ -(DL)), 2.35 (t, $-\text{OC}(\text{O})\text{CH}_2$ -), 4.09 (t, $-\text{CH}_2\text{O}$ -(VL)), 4.88 (t, $-\text{CH}_2\text{O}$ -(DL)), 5.13 (s, $\text{C}_6\text{H}_5(\text{CH}_2)\text{OC}(\text{O})$ -), 7.36 (s, C_6H_5 -). SEC (CHCl_3 , PMMA calibration): $M_n = 11 \text{ kg mol}^{-1}$; $\bar{D} = 1.35$.

Poly(ϵ -caprolactone) (P ϵ CL, **P10**) was prepared charging 1108 μL (1 mol) of ϵ -CL, 10 μL (10 mmol) of BnOH, and 40 mg (10 mmol) of $\text{Sn}(\text{Oct})_2$ in a Schlenk round-bottom flask inside the glovebox. The flask was moved out of the glovebox, and 19 mL of anhydrous toluene was added under argon flux ($[M]_0 = 0.5 \text{ mol L}^{-1}$). The polymerization was performed at reflux conditions for 24 h. Aliquots of 200 μL were taken periodically and analyzed by means of SEC and $^1\text{H NMR}$ spectroscopy to monitor the evolution of the molar mass and the monomer conversion. Subsequent to cooling to room temperature, the final sample was taken, and the polymer solution was precipitated into cold methanol ($-22 \text{ }^\circ\text{C}$). The purified P ϵ CL was dried at $40 \text{ }^\circ\text{C}$ under reduced pressure overnight.

P ϵ CL (P10). Conv = 99%; yield 93%. $^1\text{H NMR}$ (300 MHz, CDCl_3): δ/ppm = 1.41 (broad, $-\text{CH}_2\text{CH}_2\text{C}(\text{O})\text{O}$ -), 1.47 (broad, $-\text{OCH}_2\text{CH}_2\text{CH}_2$ -), 2.32 (t, $-\text{CH}_2\text{C}(\text{O})\text{O}$ -), 4.10 (t, $-\text{CH}_2\text{O}$ -), 5.13 (s, $\text{C}_6\text{H}_5(\text{CH}_2)\text{OC}(\text{O})$ -), 7.37 (m, C_6H_5 -). SEC (CHCl_3 , PMMA calibration): $M_n = 9 \text{ kg mol}^{-1}$; $\bar{D} = 1.30$.

Nanoparticle Preparation. Aqueous nanoparticle suspensions were prepared by dropping a polymer solution in THF into deionized water (see the [Supporting Information](#) for details). In a representative example, 5 mg of polymer was dissolved in 1 mL of THF and then 0.5 mL of this solution were dropped into 5 mL of deionized water under stirring (1000 rpm) at room temperature. The samples were left stirring for 3 h in order to evaporate the THF. DLS analyses were

performed 24 h after preparation. The samples were stored at $5 \text{ }^\circ\text{C}$, and DLS analyses were regularly performed for a period of 1 month in order to evaluate the stability of the nanoparticles.

RESULTS AND DISCUSSION

Homopolymerization of δ VL and δ DL. Prior to the synthesis of copolymers comprising δ VL and δ DL, kinetic studies of the homopolymerization of both monomers were conducted in bulk at room temperature utilizing TBD as a catalyst. Benzyl alcohol was used as initiator at an initial ratio of $[M]:[\text{TBD}]:[I]$ of 100:1:1 for the polymerization of δ DL (Scheme 1). The significantly more reactive unsubstituted monomer δ VL was polymerized using a lower amount of catalyst ($[M]:[\text{TBD}]:[I] = 100:0.1:1$). SEC analysis of the kinetic samples revealed mostly monomodal molar mass distributions for P δ DL as well as P δ VL. In particular, the dispersity (\bar{D}) of the P δ VL samples remained low ($\bar{D} = 1.04$ – 1.12). For P δ DL, the dispersity significantly decreased from $\bar{D} = 1.47$ to $\bar{D} = 1.09$ during the course of the polymerization. The molar masses of both polymers increased in a linear fashion with the monomer conversion, indicating that the molar mass of P δ DL and P δ VL can be well controlled under similar polymerization conditions. The linear kinetic plots depicted in Figure 1 (left) revealed that both ROP followed pseudo-first-order kinetics. Despite a 10-fold lower amount of catalyst used, the apparent polymerization rate constant $k_{p,app}$ is 25 times higher for δ VL ($k_{p,app} = 0.5 \text{ L mol}^{-1} \text{ min}^{-1}$) compared to δ DL ($k_{p,app} = 0.02 \text{ L mol}^{-1} \text{ min}^{-1}$), suggesting that a

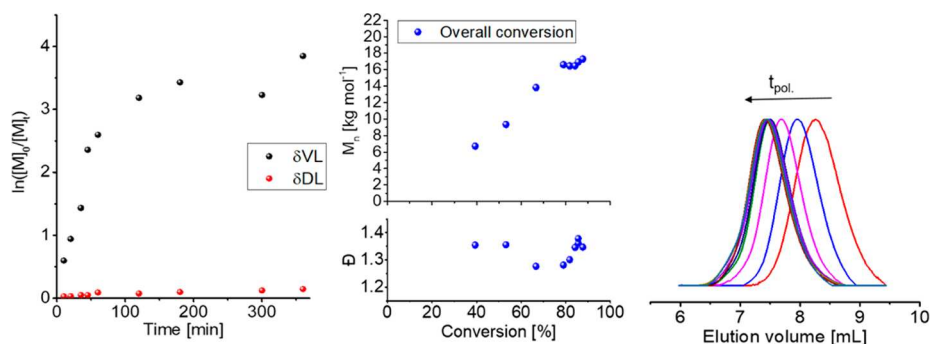


Figure 3. Kinetic studies of the statistical copolymerization of δ VL and δ DL conducted in bulk at room temperature using BnOH as initiator and TBD as catalyst ($[\delta$ VL]: $[\delta$ DL]:[TBD]:[I] = 75:25:1:1). Left: first-order kinetic plot for both monomers. Center: evolution of the molar mass with the overall monomer conversion. Right: overlay of the SEC elugrams of the samples taken (CHCl_3 , RI detection).

statistical copolymerization of the two monomers would result in copolymers with a strong gradient.

With respect to the synthesis of well-defined block copolymers comprising P δ VL and P δ DL, a high end group fidelity of the first block is of utmost importance for the reinitiation of the second block, i.e., the chain extension. For this purpose, MALDI-ToF MS analysis was performed for a P δ VL with a degree of polymerization (DP) of 20 (P1). The mass spectrum revealed a main distribution spaced by regular intervals of $\Delta m/z = 100$, corresponding to the mass of one repeating unit (Figure 2). The species could be assigned to sodiated P δ VL chains initiated by benzyl alcohol and terminated with a proton, as is demonstrated by the overlapping calculated and measured isotopic patterns. An additional less abundant m/z series could not be assigned to any water-initiated or cyclic polymer chains. In consequence, the obtained P δ VL would be suitable to act as a macroinitiator for a subsequent ROP of δ DL.

Statistical Copolymerization of δ VL and δ DL. In an initial screening, several statistical copolymerizations of δ VL and δ DL were performed to gain insight into a reasonable feed ratio of the monomers required to obtain a copolymer comprising 20 mol % δ DL. For this purpose, the fraction of δ DL in the feed was varied from 20 to 50 mol %. To account for the low reactivity of δ DL, the catalyst concentration was selected accordingly, resulting in an overall ratio of $[M]_{\text{total}}:[\text{TBD}]:[I]$ of 100:1:1 (Table 1). SEC analysis of the resulting copolymers P4 to P7 (see the Supporting Information) revealed rather broad molar mass distributions ($1.6 < \bar{D} < 2.4$) after a polymerization time of 16 h, most likely due to transesterification reactions. In particular, the SEC traces of P4 and P5, i.e., the copolymers comprising high molar fractions of the more reactive monomer δ VL, featured pronounced low molar mass tailing. Accordingly, the dispersity increases within the polymer series from P7 to P4. The individual monomer conversions were estimated from the ^1H NMR spectra of the unpurified samples. Because of overlapping signals in the spectra, the initial feed ratio of the two monomers was used as additional information (see the Supporting Information for details). Almost quantitative conversions of δ VL were reached, whereas around 80–85% of the less reactive δ DL was incorporated to the copolymers, as expected for the statistical copolymerization of two monomers with different reactivity. The final composition of P4 to P7 was determined via the integration of the methylene (δ VL repeating units) or methine (δ DL repeating units) proton signals neighboring the ester functionalities in the ^1H NMR spectra of the purified

copolyesters (Figure S3). As shown in Table 1, the resulting compositions are in good agreement with the values calculated from the feed ratio and the monomer conversions for all copolymers.

To obtain a copolyester with the targeted composition of 80 mol % δ VL and 20 mol % δ DL, the feed ratio of the monomers was hence set to 75:25. Kinetic studies were performed to obtain detailed information about the expected compositional gradient along the polymer chain (Figure 3). In agreement with the kinetic plot for the homopolymerization of the two monomers, δ VL revealed a higher reactivity than δ DL, resulting in the formation of a gradient copolymer that is strongly enriched with δ VL repeating units at the beginning of the growing chain (see the Supporting Information). The linear increase of the molar mass with the overall monomer conversion and the unimodal molar mass distributions revealed that transesterifications were avoided despite the almost quantitative conversion of the more reactive δ VL. These polymerization conditions were hence applied to obtain a gradient copolyester with the same HHB of P ϵ CL (P8) that is composed of 80 mol % δ VL and 20 mol % δ DL.

Block Copolymerization. The targeted copolymer composition was achieved in a straightforward manner for the P δ VL-*b*-P δ DL block copolymer P9. To enable a fast initiation of the second block, the first block was synthesized via ROP of the more reactive δ VL. The resulting P δ VL with a DP of ≈ 76 served as macroinitiator for the less reactive δ DL. To avoid possible chain transfer reactions at high monomer conversions, the initial $[M]/[I]$ was set to 100 during the chain extension, which was driven to a conversion of 17%. In accordance with the monomer ratio thus expected, ^1H NMR spectroscopy revealed the targeted composition comprising 80 mol % δ VL and 20 mol % δ DL for the purified block copolymer. In addition, a clearly shifted molar mass distribution was observed by means of SEC measurements upon chain extension of the first block (see the Supporting Information).

In consequence, two tailor-made copolyesters with different microstructure were obtained that match the HHB of P ϵ CL (P10): the P δ VL-*b*-P δ DL block copolymer P9 and the P(δ VL-*grad*- δ DL) gradient copolymer P8. In addition, all three polymers featured a similar molar mass of around 9–11 kg mol^{-1} , making them perfect candidates for further investigation.

Bulk Properties. A differing degree of crystallinity or melting temperature of these tailor-made polyesters represented the next prerequisite to make them suitable materials

for our purpose. DSC measurements were hence performed using the bulk materials in the temperature range from -100 to 200 °C as the polyesters comprising P δ DL degraded above 200 °C (see the Supporting Information). As expected, the amorphous P δ DL **P3** revealed a low glass transition temperature T_g of -56 °C, whereas the P δ VL **P2** and the P ϵ CL **P10** represented semicrystalline materials with a melting temperature T_m of 57 °C (Figure 4). The fact that the T_m of the

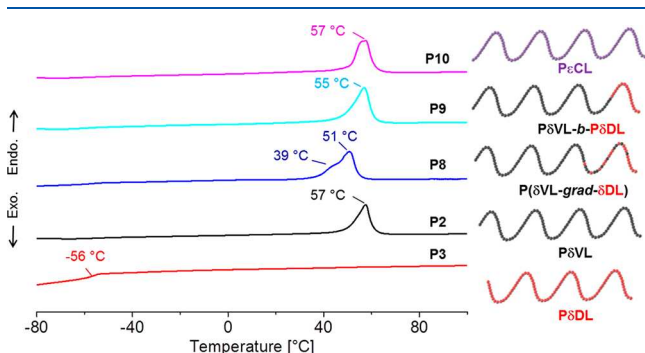


Figure 4. DSC thermograms of the polyesters **P8** to **P10** with constant HHB and the P δ VL and P δ DL homopolymers **P2** to **P3**. The measurement was performed from -100 to 200 °C (second heating run, heating rate 20 K min^{-1}).

P δ VL-*b*-P δ DL block copolymer **P9** remained almost unchanged ($T_m = 55$ °C) compared to that of the P δ VL homopolymer hints toward a phase segregation of the two building blocks in bulk. In contrast, the DSC thermogram of the P(δ VL-*grad*- δ DL) gradient copolymer **P8** revealed a nonsymmetrical broad endothermal peak at a significantly lower temperature. Although the crystallization of the P δ VL is impaired due to the incorporation of δ DL repeating units along the polymer chain, the strong gradient of **P9** allowed the formation of crystalline domains in the bulk material. Presumably, domains of varying composition melt at slightly different temperatures, explaining the broad transition.

The crystallinity of the materials is only resulting from the P δ VL segments, whereas the amorphous P δ DL fractions do not contribute. In consequence, the degree of crystallinity $X_{c,uw}$ was estimated from the DSC data using the melting enthalpies of fully crystalline P δ VL ΔH_f^0 .²⁷ As shown in Table 2, the three polyesters with constant HHB differ significantly with respect to their overall degree of crystallinity (from 24 to 52%). The P ϵ CL **P10** features the highest $X_{c,uw}$ and the $X_{c,uw}$ of the two copolymers is reduced. To compare the degree of crystallinity of the P δ VL domains of **P8** and **P9** to that of the P δ VL homopolymer, the δ VL mass fraction of the copolymers w_c was taken into account (eq 1).²⁸

$$X_{c,w} = \frac{\Delta H_f}{\Delta H_f^0 w_c} \quad (1)$$

Remarkably, the P δ VL domains in the P δ VL-*b*-P δ DL block copolymer **P9** revealed a similar $X_{c,w}$ as the P δ VL homopolymer, showing that the amorphous P δ DL domains do not interfere with the crystallization of the P δ VL block. In agreement with the broad melting transition, the $X_{c,w}$ is lowered for the P(δ VL-*grad*- δ DL) gradient copolymer **P8**. Here, the integration of δ DL mers in the crystalline P δ VL reduces the crystallizable domain size of the polymer chain and, thus, the bulk crystallinity.

The observations made by DSC measurements were supported by PLM measurements (Figure 5, left). For this purpose, polymer spherulites were prepared with the same temperature profiles as used for DSC measurements. The resulting light microscopy images confirmed the crystallinity of all three polymers because structures are visible due to a polarization of the light by birefringence induced by the polymeric crystals.²⁹

To obtain further information, we used AFM to investigate the surface in a more detailed fashion (Figure 5). Already the overview scans revealed that the alteration of the polymer chemistry significantly affected the bulk structure of the polyesters with constant HHB. The P ϵ CL homopolymer formed small spherulites, whereas a defined spherulite structure was not observable in the AFM images for the copolyesters **P8** and **P9**. The variation in the polymer chain composition and, thus, the resulting varied crystallization behavior, visible in the DSC curves (Figure 4), are the reasons for the different surface structures. A closer look at the resulting crystalline surface morphology revealed that the differences in the chemical polymer structure from **P8** to **P10** not only induced different lamellar thicknesses (Table 2); furthermore, the lamellar crystal length and distribution changed. The gradient copolymer **P8** formed short and randomly oriented crystals. This observation explains the broad melting peak in the DSC, which correlates with a broad distribution of different crystal species.^{30,31} Likewise, the uniform long and parallel aligned crystals of the block copolymer **P9** and the P ϵ CL homopolymer **P10** are in agreement with the narrower DSC peak. The comparison of the lamella widths with the calculated polymer chain length (Table 2) revealed that the crystal domains are created by chain folds, which is typical for polymers.³²

Nanoparticles in Aqueous Suspension. Having successfully gained access to three polyesters with constant hydrophobicity but varied crystallinity, aqueous nanoparticle suspensions were prepared from **P8** to **P10** via nano-

Table 2. Bulk Properties of the Polyesters **P8**–**P10** with Constant HHB

polymer	$m\%$ δ VL	T_m^a [°C]	T_c^c [°C]	ΔH_f^a [J g^{-1}]	$X_{c,uw}^d$ [%]	$X_{c,w}^e$ [%]	l_{chain}^f [nm]	l_{lamella} [nm]
P2	P δ VL	57	22	72	40	40		
P3	P δ DL	$-^b$	–	–	0	0		
P8	P(δ VL- <i>grad</i> - δ DL)	51	4	43	24	34	71	21.5 ± 2.6
P9	P δ VL- <i>b</i> -P δ DL	55	28	57	31	43	71	23.2 ± 7.2
P10	P ϵ CL	57	25	70	52	52	69	14.8 ± 2.0

^aDetermined by DSC in the second heating run. ^b $T_g = -56$ °C (inflection value, second heating run). ^cCrystallization temperature determined by DSC in the first cooling run. ^dEstimated from DSC using the ΔH_f of the fully crystalline materials from the literature ($\Delta H_f^0(\text{P}\delta\text{VL}) = 181.8$ J g^{-1} , $\Delta H_f^0(\text{P}\epsilon\text{CL}) = 136.1$ J g^{-1}).²⁷ ^eDegree of crystallinity of the P δ VL domains taking into account the mass fraction of δ VL in the copolymers. ^fCalculated for a completely extended chain considering the bond lengths and bond angles.

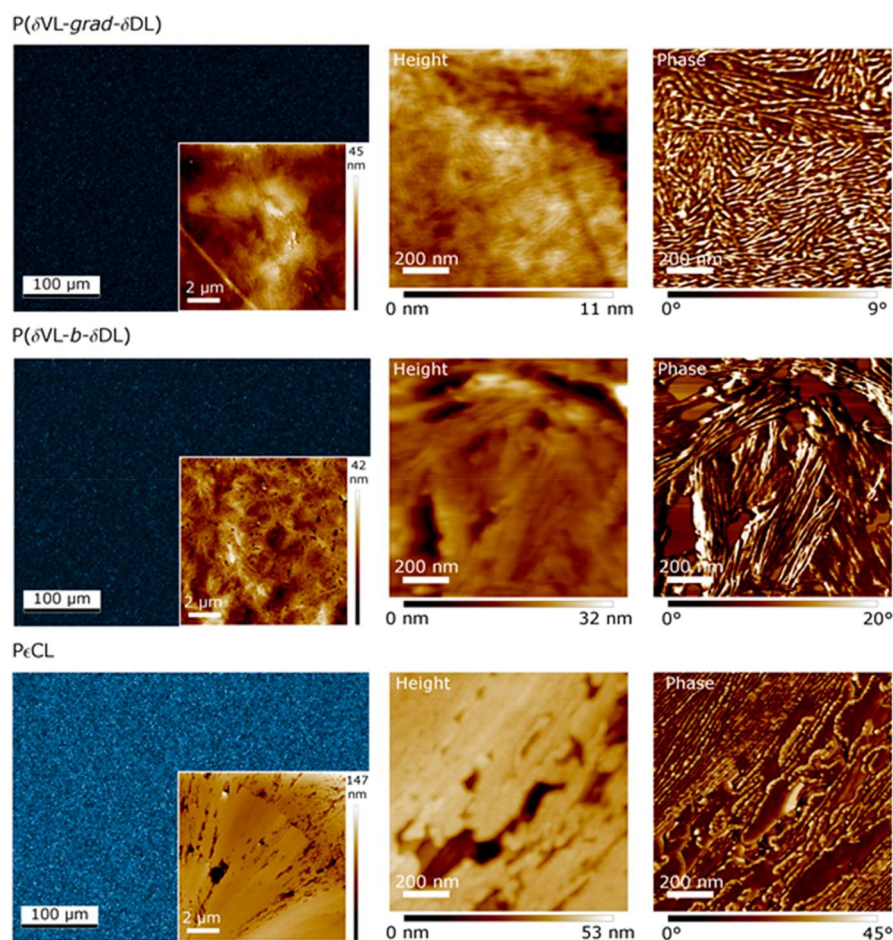


Figure 5. Left: polarized light microscopy images of **P8** to **P10** spherulites between polarizer and analyzer with a changed position of 90° . Overview AFM height images are shown as insets in the light microscopy pictures. Only for **P10**, a spherulite is recognizable. Center: magnified AFM height images (scale bars represent 200 nm). Right: magnified AFM phase images (scale bars represent 200 nm). The crystalline lamellae are visible for all three polymers (**P8**–**P10**).

precipitation according to a published protocol for polyesters with long alkyl spacers.³³ For this purpose, a solution of the polymer in THF was slowly dropped into water under vigorous stirring. Variation of the polymer concentration in the THF solution and the volume ratio of solvent (THF) to nonsolvent (water) facilitated access to particles with tailor-made hydrodynamic diameters (*Z*-average) between 50 and 230 nm (DLS analysis, see the [Supporting Information](#)). The utmost majority of the nanoparticle suspensions remained stable within a period of 4 weeks without the need of further stabilizers. In general, the nanoparticles formed from the copolyesters **P8** and **P9** revealed larger D_h if prepared under the same conditions as the corresponding **PεCL** nanoparticles. However, an adjustment of the nanoprecipitation conditions of the individual polymers allowed to prepare nanoparticles of the same sizes from all three polyesters **P8** to **P10**. To simplify the investigation of the physical properties of the nanoparticles, a D_h of around 170 nm was selected for this purpose ([Table 3](#)). In accordance with the preliminary stability tests, all nanoparticles revealed negative zeta potentials (ζ) of approximately -30 mV, as common for polyester nanoparticles in aqueous suspension.^{34,35}

To assess whether the variation in crystallinity of the bulk materials was retained in the corresponding nanoparticles, they were investigated in detail by means of SEM and AFM ([Figure 6](#)). To avoid a movement of the nanoparticles during the

Table 3. DLS Data, ζ Potential, and Stiffness of Polymeric Nanoparticles Prepared in THF from Polymers with the Same HHB

	P(δ VL- <i>grad</i> - δ DL) (P8)	P δ VL- <i>b</i> -P δ DL (P9)	P ϵ CL (P10)
D_h^a [nm]	176	179	162
PDI	0.075	0.073	0.149
ζ [mV]	-28.6	-31.0	-27.8
stiffness ^b [$N m^{-1}$]	2.2 ± 0.6	4.4 ± 1.6	7.4 ± 2.0

^a D_h denotes the *Z*-average. ^bDetermined by AFM.

characterization, the substrates were functionalized with PEI. This polyelectrolyte layer induces a positive surface charge, immobilizing the nanoparticles electrostatically due to their negative ζ potential. SEM revealed a spherical shape of all polymeric nanoparticles. However, the diameters (around 200 nm) were found to be increased compared to the D_h from DLS. This effect was most significant for the polymer featuring the lowest degree of crystallinity (the gradient copolymer **P8**) and can be explained by collapsing of the nanoparticles onto the surface during the drying process. This is supported by the AFM images, which revealed a nanoparticle height that is lower than the nanoparticle diameter.

The degree of crystallinity of the nanoparticles is difficult to investigate in a direct manner. However, the stiffness and the

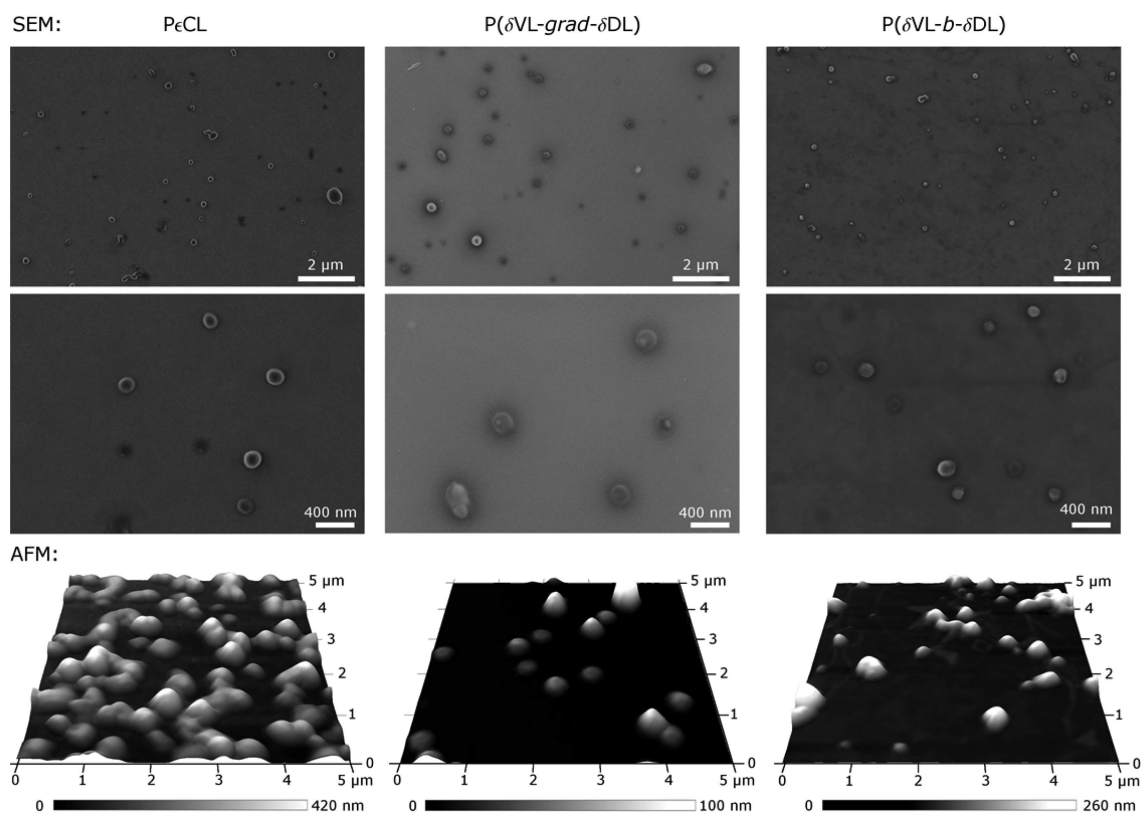


Figure 6. SEM images (upper part) and 3D AFM height images (lower part) of dried nanoparticles prepared from the three polymers (P8 to P10) by nanoprecipitation.

Young's modulus, which correlate with each other, are affected by the crystallinity of nanoparticles and can be deduced from AFM measurements.^{36,37} It should be noted that the cellular uptake of nanoparticles is directly affected by the stiffness of the materials and represents an additional key factor for successful nanoparticle-induced drug delivery.^{38,39} Force–distance curves were hence collected by means of AFM investigations. The resulting nanoparticle stiffness ranges from 2.2 to 7.4 N m⁻¹ and increases from the gradient copolymer P8, over the block copolymer P9, to the PεCL homopolymer P10 (Table 3). The degree of crystallinity of the bulk polymers follows the same trend (Table 2). On the basis of this comparison, we assume a correlation between the polymer bulk and nanoparticle crystallinity. In particular for the copolyesters P8 and P9, the mer sequences in the chemical structure represent the only chemical difference. Hence, the differences in the observed stiffness can only be induced by the increased degree of crystallinity from P8 to P9. It is expected that the degradation and, thus, the release rate of a drug from our polymeric nanoparticles will decrease with increasing degree of crystallinity. In contrast to the loosely packed amorphous domains, the close packing in the crystalline domains impairs the enzyme adsorption and, consequently, the enzymatic cleavage of the polyester chains in the bulk materials.⁷ The controlled HHB of our polymeric nanoparticles allows to develop direct structure–property relationships between crystallinity and degradation behavior and, hence, to adjust release profiles in the future.

CONCLUSION

The copolymerization of δVL and δDL enabled access to tailor-made polyester materials that feature the same hydro-

phobicity as PεCL but a varied degree of crystallinity. Stable nanoparticles in aqueous suspension of similar sizes were prepared from the three tailored materials. AFM measurements revealed that the bulk crystallinity correlates with the nanoparticle stiffness. The former can hence be directly applied as a first hint to deduce the nanoparticle crystallinity as additional influencing factors have been excluded by the copolymer design. Our future research will include the assessment of the nanoparticle crystallinity directly in suspension to investigate whether this observation can be generalized. The tailor-made nanoparticles presented here form the basis for studies regarding the enzymatic degradation, release profiles of encapsulated actives, and cellular uptake. The future utilization of a variety of actives and other designed polyesters will allow a clear statement about the effect of crystallinity on the release behavior.

ASSOCIATED CONTENT

Supporting Information

The Supporting Information is available free of charge on the ACS Publications website at DOI: 10.1021/acs.macromol.8b00925.

An additional kinetic study, NMR spectra, SEC elograms, TGA curves, nanoparticle preparation details and stability tests (PDF)

AUTHOR INFORMATION

Corresponding Authors

*(K.D.J.) E-mail k.jandt@uni-jena.de.

*(U.S.S.) E-mail ulrich.schubert@uni-jena.de.

ORCID

Klaus D. Jandt: 0000-0002-7537-5603

Ulrich S. Schubert: 0000-0003-4978-4670

Author Contributions

D.B. and C.H. contributed equally.

Notes

The authors declare no competing financial interest.

ACKNOWLEDGMENTS

This project was funded by the Thüringer Ministerium für Wirtschaft, Wissenschaft, und Digitale Gesellschaft (Thuringian Ministry for Economic Affairs, Science and Digital Society, ProExzellenz II, NanoPolar). Moreover, the work was supported by the DFG-funded Collaborative Research Centre PolyTarget (SFB 1278, projects A06 and Z01). We gratefully acknowledge the partial financial support of the Thüringer Ministerium für Wirtschaft, Wissenschaft und Digitale Gesellschaft and the Deutsche Forschungsgemeinschaft (DFG), grant reference INST 275/389-1 FUGG; AOBJ: 640980.

REFERENCES

- (1) Knop, K.; Hoogenboom, R.; Fischer, D.; Schubert, U. S. Poly(ethylene glycol) in drug delivery: Pros and cons as well as potential alternatives. *Angew. Chem., Int. Ed.* **2010**, *49*, 6288–6308.
- (2) Press, A. T.; Traeger, A.; Pietsch, C.; Mosig, A.; Wagner, M.; Clemens, M. G.; Jbeily, N.; Koch, N.; Gottschaldt, M.; Beziere, N.; Ermolayev, V.; Ntziachristos, V.; Popp, J.; Kessels, M. M.; Qualmann, B.; Schubert, U. S.; Bauer, M. Cell type-specific delivery of short interfering RNAs by dye-functionalised theranostic nanoparticles. *Nat. Commun.* **2014**, *5*, 13.
- (3) Farokhzad, O. C.; Cheng, J. J.; Teply, B. A.; Sherifi, I.; Jon, S.; Kantoff, P. W.; Richie, J. P.; Langer, R. Targeted nanoparticle-aptamer bioconjugates for cancer chemotherapy in vivo. *Proc. Natl. Acad. Sci. U. S. A.* **2006**, *103*, 6315–6320.
- (4) Müller-Goymann, C. C. Physicochemical characterization of colloidal drug delivery systems such as reverse micelles, vesicles, liquid crystals and nanoparticles for topical administration. *Eur. J. Pharm. Biopharm.* **2004**, *58*, 343–356.
- (5) Czaplewski, J. A.; Majdanski, T. C.; Barthel, M. J.; Gottschaldt, M.; Schubert, U. S. Functionalized PEG-b-PAGE-b-PLGA triblock terpolymers as materials for nanoparticle preparation. *J. Polym. Sci., Part A: Polym. Chem.* **2015**, *53*, 2163–2174.
- (6) Azevedo, H. S.; Reis, R. L. Understanding the enzymatic degradation of biodegradable polymers and strategies to control their degradation rate. In *Biodegradable Systems in Tissue Engineering and Regenerative Medicine*; CRC Press: 2005; pp 177–201.
- (7) Buchholz, V.; Agarwal, S.; Greiner, A. Synthesis and enzymatic degradation of soft aliphatic polyesters. *Macromol. Biosci.* **2016**, *16*, 207–213.
- (8) Karavelidis, V.; Giliopoulos, D.; Karavas, E.; Bikiaris, D. Nanoencapsulation of a water soluble drug in biocompatible polyesters. Effect of polyesters melting point and glass transition temperature on drug release behavior. *Eur. J. Pharm. Sci.* **2010**, *41*, 636–643.
- (9) Karavelidis, V.; Karavas, E.; Giliopoulos, D.; Papadimitriou, S.; Bikiaris, D. Evaluating the effects of crystallinity in new biocompatible polyester nanocarriers on drug release behavior. *Int. J. Nanomed.* **2011**, *6*, 3021–3032.
- (10) Tsuji, H. Poly(lactide) stereocomplexes: Formation, structure, properties, degradation, and applications. *Macromol. Biosci.* **2005**, *5*, 569–597.
- (11) Perevyazko, I. Y.; Delaney, J. T.; Vollrath, A.; Pavlov, G. M.; Schubert, S.; Schubert, U. S. Examination and optimization of the self-assembly of biocompatible, polymeric nanoparticles by high-throughput nanoprecipitation. *Soft Matter* **2011**, *7*, 5030–5035.
- (12) Ceccorulli, G.; Scandola, M.; Kumar, A.; Kalra, B.; Gross, R. A. Cocrystallization of random copolymers of ω -pentadecalactone and ϵ -caprolactone synthesized by lipase catalysis. *Biomacromolecules* **2005**, *6*, 902–907.
- (13) Schneiderman, D. K.; Hillmyer, M. A. Aliphatic polyester block polymer design. *Macromolecules* **2016**, *49*, 2419–2428.
- (14) Lou, X.; Detrembleur, C.; Jérôme, R. Living cationic polymerization of δ -valerolactone and synthesis of high molecular weight homopolymer and asymmetric telechelic and block copolymer. *Macromolecules* **2002**, *35*, 1190–1195.
- (15) Kasyapi, N.; Bhowmick, A. K. Nanolamellar triblock of poly-d,l-lactide- δ -valerolactone-d,l-lactide with tuneable glass transition temperature and crystallinity for use as a drug-delivery vesicle. *RSC Adv.* **2014**, *4*, 27439–27451.
- (16) Dove, A. P. Organic catalysis for ring-opening polymerization. *ACS Macro Lett.* **2012**, *1*, 1409–1412.
- (17) Naumann, S.; Thomas, A. W.; Dove, A. P. Highly polarized alkenes as organocatalysts for the polymerization of lactones and trimethylene carbonate. *ACS Macro Lett.* **2016**, *5*, 134–138.
- (18) Lohmeijer, B. G. G.; Pratt, R. C.; Leibfarth, F.; Logan, J. W.; Long, D. A.; Dove, A. P.; Nederberg, F.; Choi, J.; Wade, C.; Waymouth, R. M.; Hedrick, J. L. Guanidine and amidine organocatalysts for ring-opening polymerization of cyclic esters. *Macromolecules* **2006**, *39*, 8574–8583.
- (19) Zhang, L.; Nederberg, F.; Pratt, R. C.; Waymouth, R. M.; Hedrick, J. L.; Wade, C. G. Phosphazene bases: A new category of organocatalysts for the living ring-opening polymerization of cyclic esters. *Macromolecules* **2007**, *40*, 4154–4158.
- (20) Kamber, N. E.; Jeong, W.; Waymouth, R. M.; Pratt, R. C.; Lohmeijer, B. G. G.; Hedrick, J. L. Organocatalytic ring-opening polymerization. *Chem. Rev.* **2007**, *107*, 5813–5840.
- (21) Pratt, R. C.; Lohmeijer, B. G. G.; Long, D. A.; Waymouth, R. M.; Hedrick, J. L. Triazabicyclodecene: A simple bifunctional organocatalyst for acyl transfer and ring-opening polymerization of cyclic esters. *J. Am. Chem. Soc.* **2006**, *128*, 4556–4557.
- (22) Bansal, K. K.; Kakde, D.; Purdie, L.; Irvine, D. J.; Howdle, S. M.; Mantovani, G.; Alexander, C. New biomaterials from renewable resources - amphiphilic block copolymers from δ -decalactone. *Polym. Chem.* **2015**, *6*, 7196–7210.
- (23) Martello, M. T.; Burns, A.; Hillmyer, M. Bulk ring-opening transesterification polymerization of the renewable δ -decalactone using an organocatalyst. *ACS Macro Lett.* **2012**, *1*, 131–135.
- (24) Meeus, J.; Scurr, D. J.; Chen, X.; Amssoms, K.; Davies, M. C.; Roberts, C. J.; Van den Mooter, G. Combination of (M)DSC and surface analysis to study the phase behaviour and drug distribution of ternary solid dispersions. *Pharm. Res.* **2015**, *32*, 1407–1416.
- (25) Armini, S.; Vakarelski, I. U.; Whelan, C. M.; Maex, K.; Higashitani, K. Nanoscale indentation of polymer and composite polymer-silica core-shell submicrometer particles by atomic force microscopy. *Langmuir* **2007**, *23*, 2007–2014.
- (26) Sitterberg, J.; Ozcetin, A.; Ehrhardt, C.; Bakowsky, U. Utilising atomic force microscopy for the characterisation of nanoscale drug delivery systems. *Eur. J. Pharm. Biopharm.* **2010**, *74*, 2–13.
- (27) Lorient, M.; Linossier, I.; Vallée-Réhel, K.; Fay, F. Syntheses, characterization, and hydrolytic degradation of P(ϵ -caprolactone-co- δ -valerolactone) copolymers: Influence of molecular weight. *J. Appl. Polym. Sci.* **2016**, *133*, 43007.
- (28) Arias, V.; Olsen, P.; Odelius, K.; Høglund, A.; Albertsson, A.-C. Selective degradation in aliphatic block copolyesters by controlling the heterogeneity of the amorphous phase. *Polym. Chem.* **2015**, *6*, 3271–3282.
- (29) Tagaya, A.; Koike, Y. Compensation and control of the birefringence of polymers for photonics. *Polym. J.* **2012**, *44*, 306–314.
- (30) Hölzer, S.; Büttner, T. N.; Schulze, R.; Arras, M. M. L.; Schacher, F. H.; Jandt, K. D.; Schubert, U. S. Mechanisms and kinetics of the crystal thickening of poly(butadiene)-block-poly(ethylene oxide) during annealing within the melting range. *Eur. Polym. J.* **2015**, *68*, 10–20.

(31) Schulze, R.; Arras, M. M. L.; Helbing, C.; Hoelzer, S.; Schubert, U. S.; Keller, T. F.; Jandt, K. D. How the calorimetric properties of a crystalline copolymer correlate to its surface nanostructures. *Macromolecules* **2014**, *47*, 1705–1714.

(32) He, W.-N.; Xu, J.-T. Crystallization assisted self-assembly of semicrystalline block copolymers. *Prog. Polym. Sci.* **2012**, *37*, 1350–1400.

(33) Herzog, K.; Müller, R. J.; Deckwer, W. D. Mechanism and kinetics of the enzymatic hydrolysis of polyester nanoparticles by lipases. *Polym. Degrad. Stab.* **2006**, *91*, 2486–2498.

(34) Hung, H.-I.; Klein, O. J.; Peterson, S. W.; Rokosh, S. R.; Osseiran, S.; Nowell, N. H.; Evans, C. L. PLGA nanoparticle encapsulation reduces toxicity while retaining the therapeutic efficacy of EtNBS-PDT in vitro. *Sci. Rep.* **2016**, *6*, 33234.

(35) Knecht, V.; Risselada, H. J.; Mark, A. E.; Marrink, S. J. Electrophoretic mobility does not always reflect the charge on an oil droplet. *J. Colloid Interface Sci.* **2008**, *318*, 477–486.

(36) Guo, D.; Xie, G.; Luo, J. Mechanical properties of nanoparticles: Basics and applications. *J. Phys. D: Appl. Phys.* **2014**, *47*, 013001.

(37) Paik, P.; Kar, K. K.; Deva, D.; Sharma, A. Measurement of mechanical properties of polymer nanospheres by atomic force microscopy: Effects of particle size. *Micro Nano Lett.* **2007**, *2*, 72–77.

(38) Banquy, X.; Suarez, F.; Argaw, A.; Rabanel, J.-M.; Grutter, P.; Bouchard, J.-F.; Hildgen, P.; Giasson, S. Effect of mechanical properties of hydrogel nanoparticles on macrophage cell uptake. *Soft Matter* **2009**, *5*, 3984–3991.

(39) Sun, J.; Zhang, L.; Wang, J.; Feng, Q.; Liu, D.; Yin, Q.; Xu, D.; Wei, Y.; Ding, B.; Shi, X.; Jiang, X. Tunable rigidity of (polymeric core)-(lipid shell) nanoparticles for regulated cellular uptake. *Adv. Mater.* **2015**, *27*, 1402–1407.

Supporting information for

Maintaining the hydrophilic hydrophobic balance of polyesters with adjustable crystallinity for tailor-made nanoparticles

*Damiano Bandelli,^{1,2#} Christian Helbing,^{2,3#} Christine Weber,^{1,2} Michael Seifert,³ Irina Muljajew,^{1,2} Klaus D. Jandt,^{2,3} * Ulrich S. Schubert^{1,2*}*

¹ Laboratory of Organic and Macromolecular Chemistry (IOMC), Friedrich Schiller University Jena, Humboldtstr. 10, 07743 Jena, Germany

² Jena Center for Soft Matter (JCSM), Friedrich Schiller University Jena, Philosophenweg 7, 07743 Jena, Germany

³ Chair of Materials Science (CMS), Department of Materials Science and Technology, Otto Schott Institute of Materials Research, Faculty of Physics and Astronomy, Friedrich Schiller University Jena, Löbdergraben 32, 07743 Jena, Germany

Both authors contributed equally.

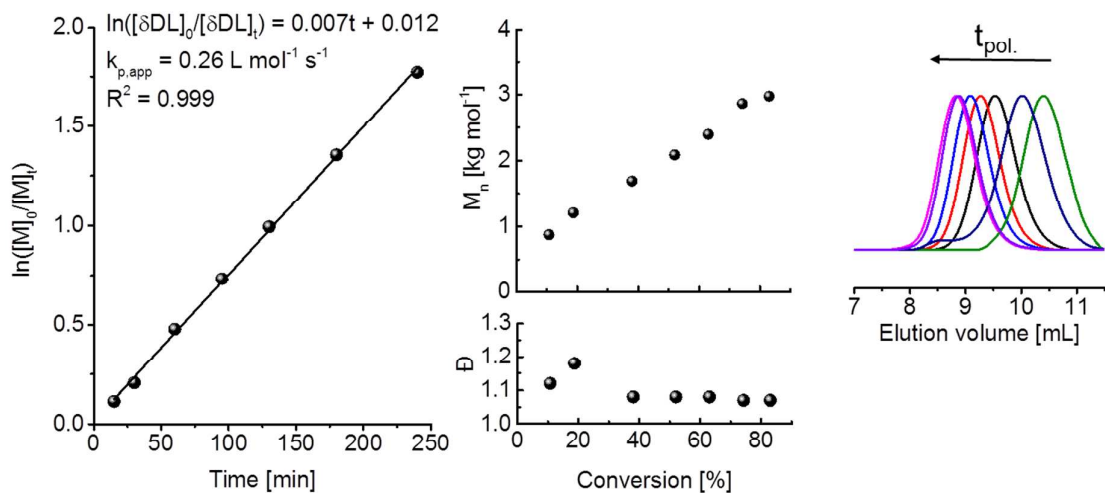


Figure S1: Kinetic studies of the homopolymerization of δDL conducted in bulk at room temperature using BnOH as initiator and TBD as catalyst ($[M]:[TBD]:[I] = 20:1:1$). **Left:** First-order kinetic plot with a linear fit according to $\ln([M]_0/[M]_t) = k_{p,app} [I]_0 t$. **Center:** Evolution of the molar mass with monomer conversion. **Right:** Overlay of the SEC elugrams of the samples taken (CHCl_3 , RI detection).

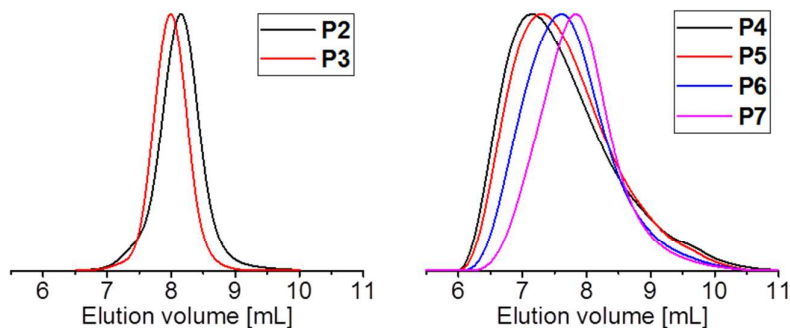


Figure S2: SEC elugrams (CHCl_3 , RI detection) of the P δVL (**P2**) and P δDL (**P3**) homopolymers and the statistical copolymers **P4** to **P7**.

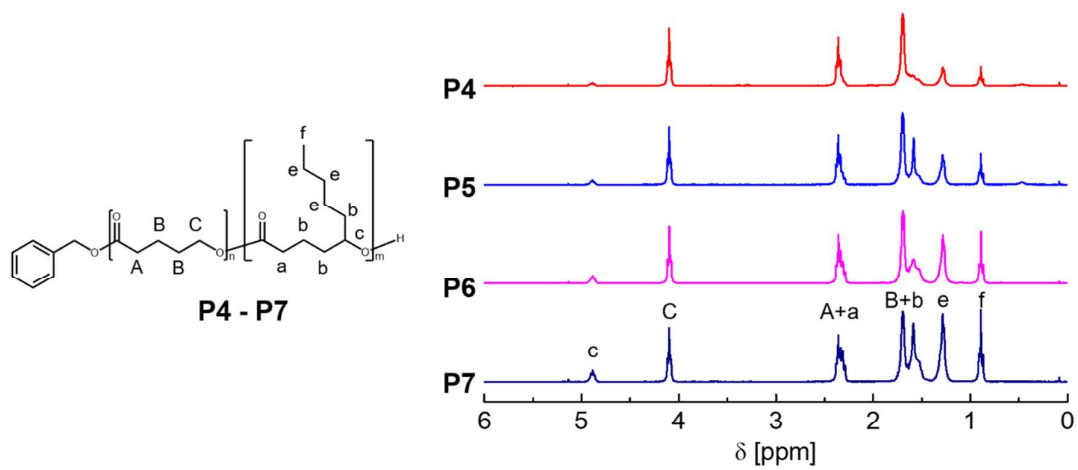


Figure S3: ^1H NMR spectra (300 MHz, CDCl_3) of the polymer series **P4** to **P7** after purification and structural assignment of the peaks. Signals **c** and **C** were used for the determination of the copolymer composition.

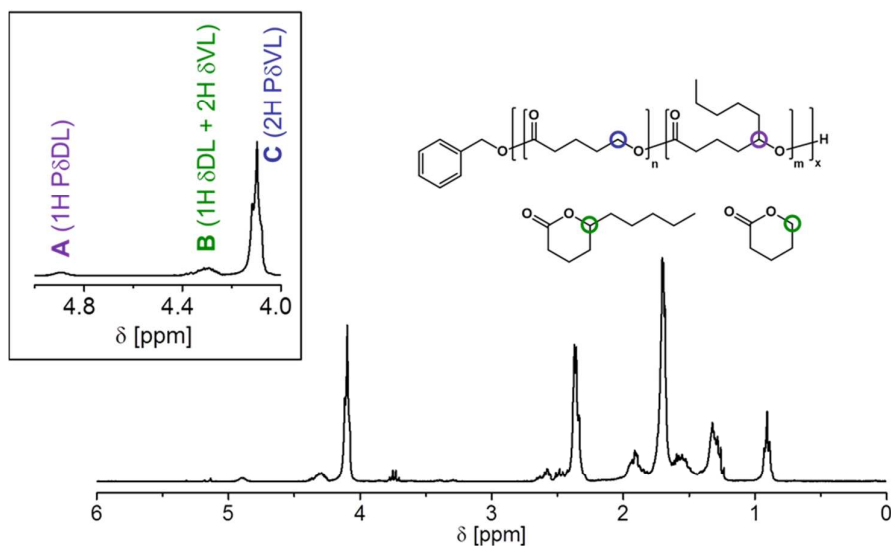


Figure S4: ^1H NMR spectrum (300 MHz, CDCl_3) of the kinetic sample taken after six hours during the copolymerization of δVL and δDL . The inset shows a zoom into the region of the spectrum used to determine the monomer conversions. The respective signals A-C are assigned to the structure of the polymer and the monomers.

Calculation of the monomer conversions

The overall conversion was calculated using the signal integrals assigned in **Figure S4** according to:

$$\text{conv}_{\text{Overall}} = \frac{\int A + \int C}{\int A + \int B + \int C} \quad (1)$$

To obtain the separate conversions of the two monomers, the following set of equations was used:

$$\int A = [\text{P}\delta\text{DL}] \quad (2)$$

$$\int C = 2[\text{P}\delta\text{VL}] \quad (3)$$

$$\int B = 2[\delta\text{VL}] + [\delta\text{DL}] \quad (4)$$

$$\frac{[\delta\text{VL}]_0}{[\delta\text{DL}]_0} = \frac{[\delta\text{VL}] + [\text{P}\delta\text{VL}]}{[\delta\text{DL}] + [\text{P}\delta\text{DL}]} \quad (5)$$

$[\delta\text{DL}]$ and $[\delta\text{VL}]$ denote the residual amounts of both monomers, whereas $[\text{P}\delta\text{DL}]$ and $[\text{P}\delta\text{VL}]$ denote the amounts of both monomers incorporated to the polymer. $[\delta\text{VL}]_0/[\delta\text{DL}]_0$ corresponds to the feed molar ratio of the two comonomers, which is known.

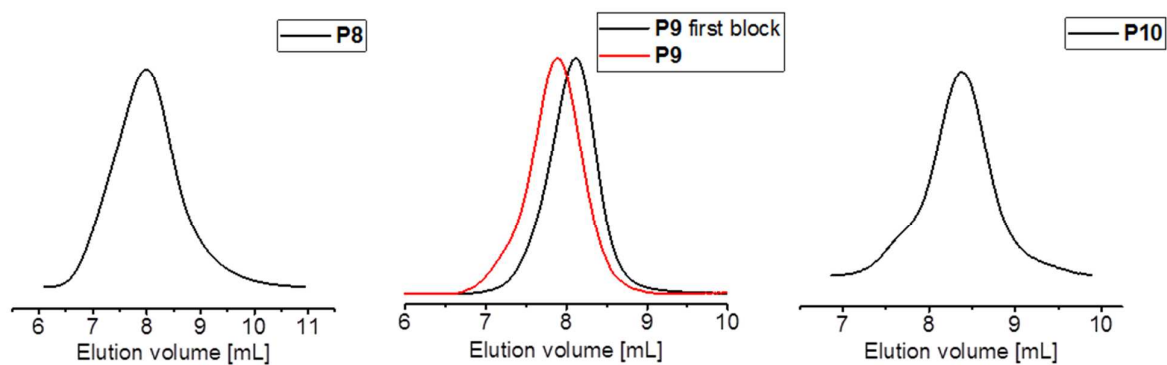


Figure S5: SEC elugrams (CHCl_3 , RI detection) of the three polyesters **P8** to **P10** featuring the same HHB.

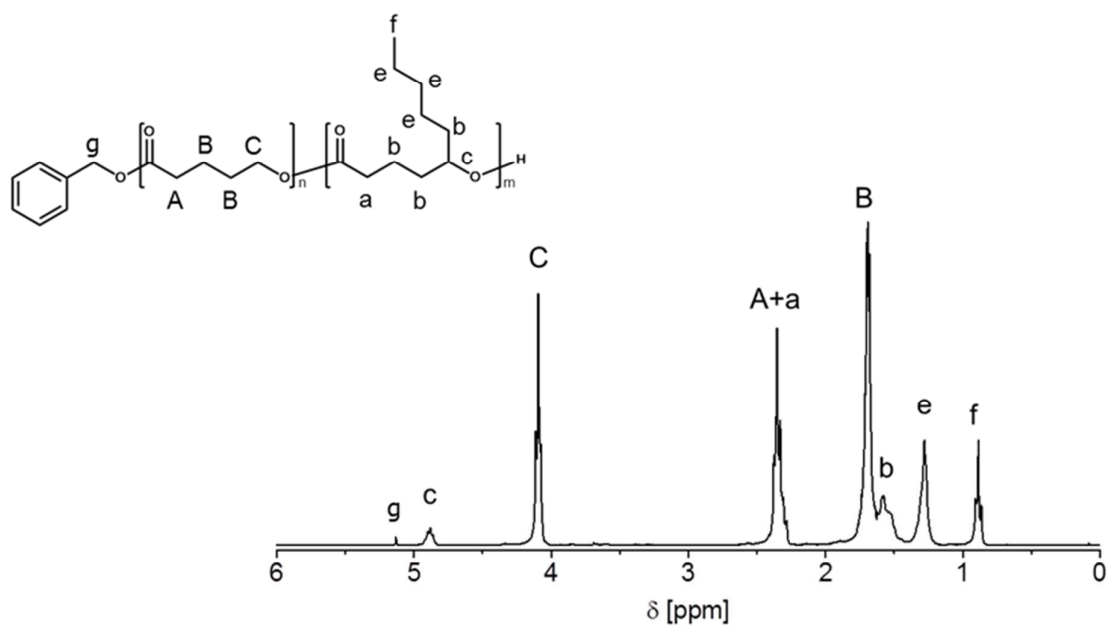


Figure S6: ^1H NMR spectrum (300 MHz, CDCl_3) of $\text{P}(\delta\text{VL-grad-}\delta\text{DL})$ (**P8**) and assignment of the signals to the structure of the polymer.

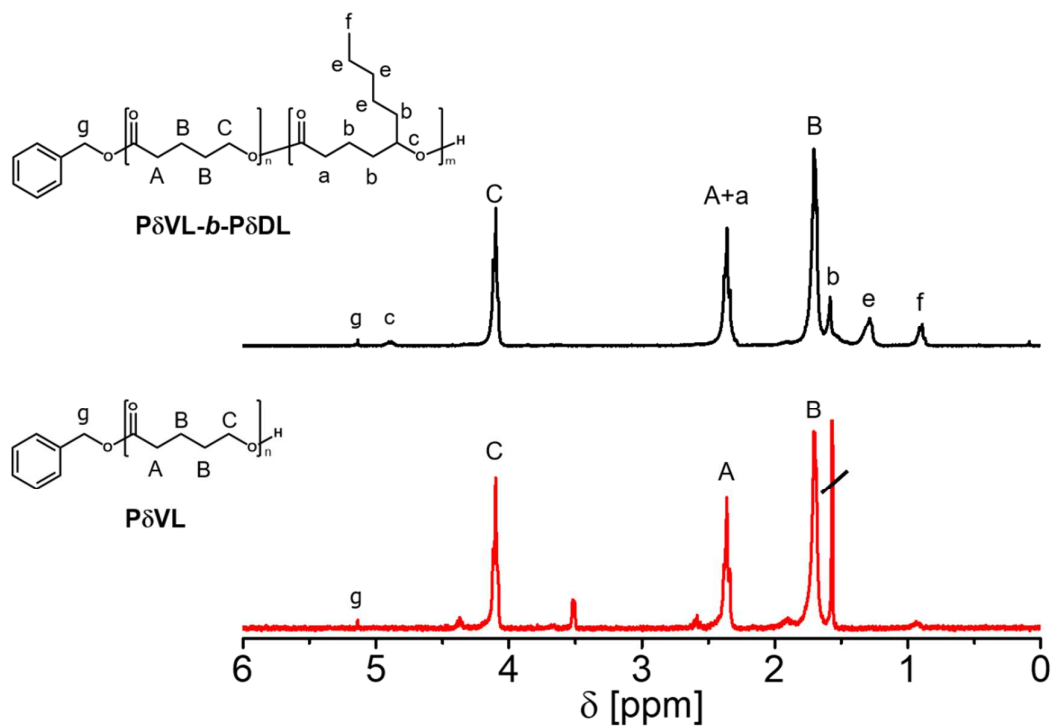


Figure S7: ^1H NMR spectra (300 MHz, CDCl_3) of $\text{P}\delta\text{VL-}b\text{-P}\delta\text{DL}$ (**P9**), the initial $\text{P}\delta\text{VL}$ macroinitiator and assignment of the signals to the structure of the polymer.

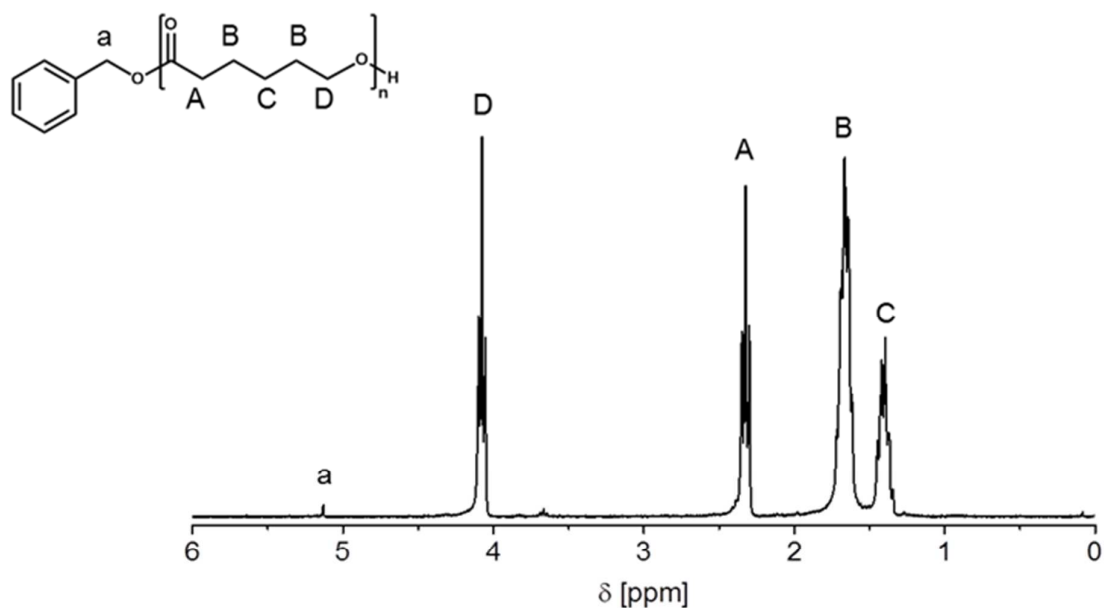


Figure S8: ^1H NMR spectrum (300 MHz, CDCl_3) of $\text{P}\epsilon\text{CL}$ (**P10**) and assignment of the signals to the structure of the polymer.

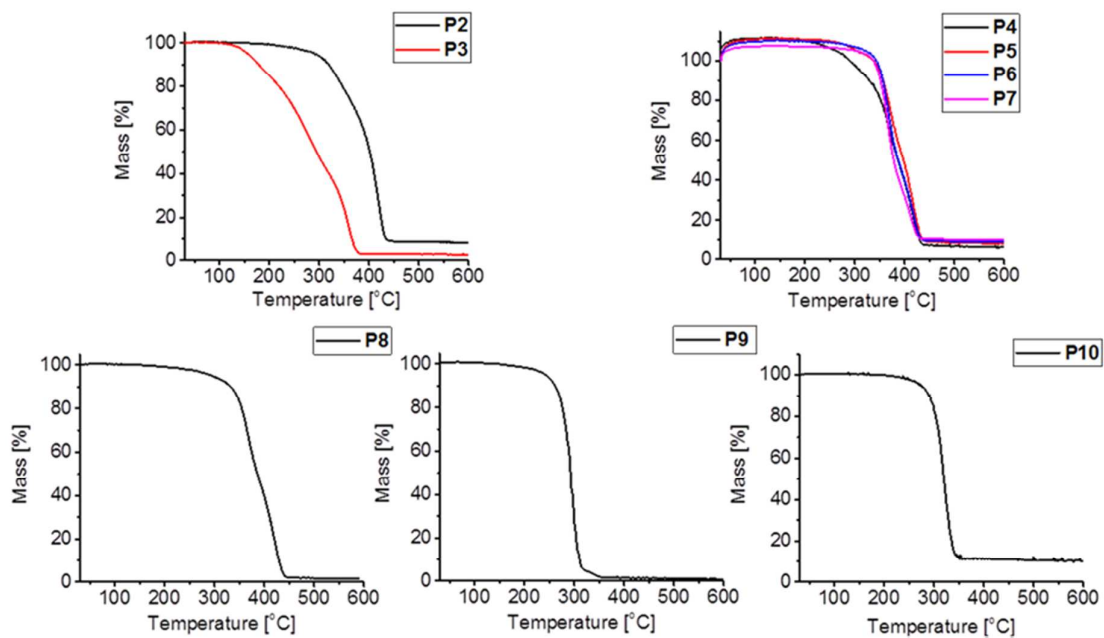


Figure S9: TGA thermograms of **P2** to **P10** (nitrogen atmosphere, heating rate 20 K min⁻¹).

Table S1: Detailed description of the nanoparticle screening performed from **P8-P10**.

Polymer	Sample	c(P) in THF [mg mL ⁻¹]	V(THF) [mL]	V(H ₂ O) [mL]	c(P) in H ₂ O [mg mL ⁻¹]
P ϵ CL	P10-NP 1	5	0.5	5	0.5
P ϵ CL	P10-NP 2	2.5	0.5	5	0.25
P ϵ CL	P10-NP 3	1	0.5	5	0.1
P ϵ CL	P10-NP 4	0.5	0.5	5	0.05
P ϵ CL	P10-NP 5	5	0.5	10	0.25
P ϵ CL	P10-NP 6	2.5	0.5	10	0.125
P ϵ CL	P10-NP 7	1	0.5	10	0.05
P ϵ CL	P10-NP 8	0.5	0.5	10	0.025
P(δ VL-grad- δ DL)	P8-NP 1*	5	0.5	5	0.5
P(δ VL-grad- δ DL)	P8-NP 2	2.5	0.5	5	0.25
P(δ VL-grad- δ DL)	P8-NP 3	1	0.5	5	0.1
P(δ VL-grad- δ DL)	P8-NP 4	0.5	0.5	5	0.05
P δ VL- <i>b</i> -P δ DL	P9-NP 2	2.5	0.5	5	0.25
P δ VL- <i>b</i> -P δ DL	P9-NP 3	1	0.5	5	0.1
P δ VL- <i>b</i> -P δ DL	P9-NP 4	0.5	0.5	5	0.05

* No stable nanoparticles were formed.

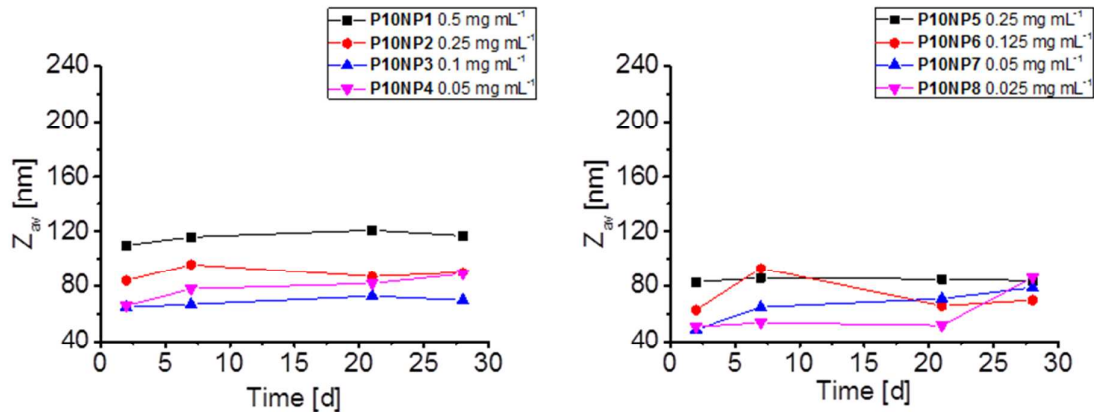


Figure S10: Stability of the nanoparticles prepared from PaCL **P10** in aqueous suspension upon storage at 5 °C. **Left:** Hydrodynamic diameters (DLS, Z-average) of the nanoparticle batches **P10NP1-4**. **Right:** Hydrodynamic diameters (DLS, Z-average) of the nanoparticle batches **P10NP5-8**.

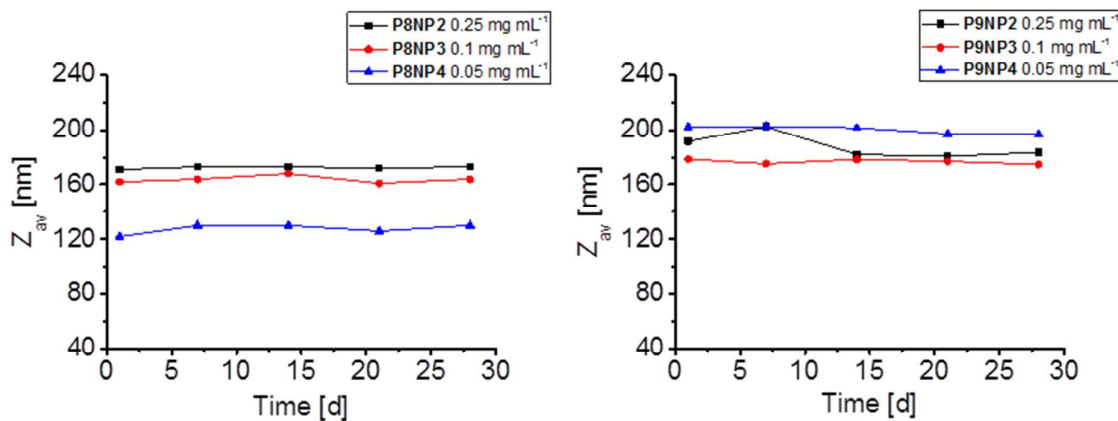


Figure S11: Stability of the nanoparticles prepared from P(δ VL-grad- δ DL) **P8** (left) and P(δ VL-*b*-P δ DL) **P9** (right) in aqueous suspension upon storage at 5 °C. Hydrodynamic diameters represent the Z-average as determined by DLS.

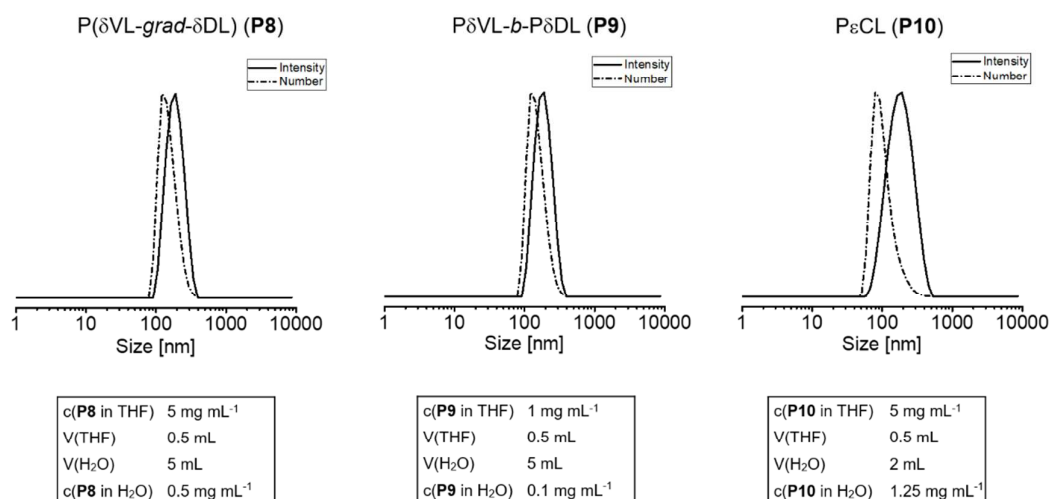


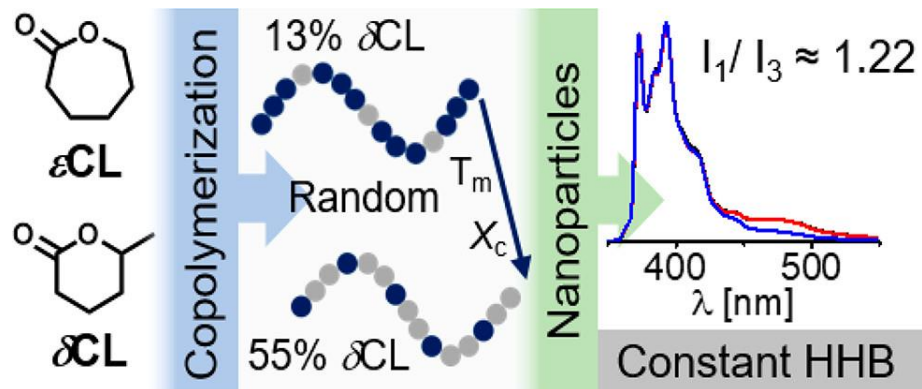
Figure S12: DLS size distributions of the nanoparticles prepared from **P8** to **P10** with hydrodynamic diameters of ≈ 170 nm. The full lines represent the intensity-weighted data, the dotted lines represent the number-weighted data.

Publication 3

Copolymerization of caprolactone isomers to obtain nanoparticles with constant hydrophobicity and tunable crystallinity

D. Bandelli, I. Muljajew, K. Scheuer, J. B. Max, C. Weber, F. H. Schacher, K. D. Jandt, U. S. Schubert

Macromolecules **2020**, *53*, 5208–5217.



Copolymerization of Caprolactone Isomers to Obtain Nanoparticles with Constant Hydrophobicity and Tunable Crystallinity

Damiano Bandelli, Irina Muljajew, Karl Scheuer, Johannes B. Max, Christine Weber, Felix H. Schacher, Klaus D. Jandt, and Ulrich S. Schubert*

Cite This: *Macromolecules* 2020, 53, 5208–5217

Read Online

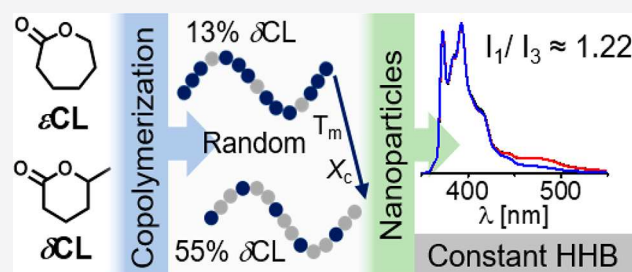
ACCESS |

Metrics & More

Article Recommendations

Supporting Information

ABSTRACT: To obtain a set of polycaprolactones (PCL) with varying crystallinity, the triazabicyclodecene-catalyzed copolymerization of the two constitutional isomers ϵ -caprolactone (ϵ CL) and δ -caprolactone (δ CL) was carried out at room temperature in toluene. Variation of the feed fraction of ϵ CL from 50% to 80% and the detailed kinetic studies accompanied by application of terminal as well as nonterminal kinetic models suggested the formation of random copolymers. Differential scanning calorimetry and wide-angle X-ray scattering investigations revealed the decrease of melting temperatures and degree of crystallinity with the ϵ CL fraction in the PCL. All copolymers were suited to obtain aqueous nanoparticle dispersions by means of nanoprecipitation. Encapsulation of the fluorescent probe pyrene confirmed a constant hydrophilic/hydrophobic balance of the nanoparticles.



INTRODUCTION

The preparation of polymeric nanoparticle carriers is a central subject for the development of compelling and personalized medicine.^{1,2} Already commercially available polymers can serve for the formulation of loaded nanoparticles as carriers for drug delivery applications,^{3–5} where the precise variation of the particle features, e.g., size, morphology, and eventual further compartmentalization,^{6,7} affect the targeting area.⁸ As a consequence, nanoparticles represent complex systems to be exploited systematically.^{4,9,10} The polymer design already plays a central role and is often accompanied by functionalization, enabling the preparation of well-defined polymers bearing biologically active labels,¹¹ fluorescent markers, or stealth polymers.^{12,13}

In this regard, polyesters represent an extremely versatile polymer class that can be obtained from natural and renewable resources.^{14–16} Due to the ester linkages, polyesters are also degradable via enzymatic catalysis.¹⁷ As a consequence, they are employed in the biomedical field not only within academic research, but also for industrial purposes.^{18–20} Currently, the majority of commercially available formulations are based on poly(lactic acid) (PLA), poly(lactic acid-co-glycolic acid) (PLGA), and polycaprolactone (PCL). These polyesters feature different thermal and mechanical properties, as well as different hydrophilic hydrophobic balance (HHB), resulting in different release activities during enzymatic degradation.^{21,22} However, the variation of a complete set of properties does not allow us to unambiguously decouple the effect of a single feature. The polymer design already enables constant selected properties, e.g., molar mass and HHB, making the synthesis of

the polyesters a central aspect in the multidimensional parameter space to be taken into account.²³

From a synthetic perspective, the fine-tuning of molar mass and dispersity is achieved via the ring opening polymerization (ROP) of the corresponding lactone, employing metal complexes as well as organobases as catalysts.^{24–27} However, the HHB of a resulting nanoparticle is more difficult to maintain while varying thermal properties.

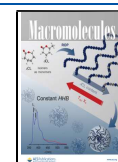
Taking advantage of the known bulk properties of several homopolymers,¹⁶ the copolymerization of established monomers already allows us to predict a variation of macroscopic properties. For instance, the addition of a comonomer during a statistical copolymerization results in the variation of thermal as well as mechanical properties of a given material.^{28–30} On the other hand, the incorporation of different amounts of comonomer in the copolymer will mostly alter the final HHB. The employment of constitutional isomers as monomers can prevent that if the general structure as a polyester is kept unchanged. This is because the proportion of ester vs methine, methylene, and methyl moieties is kept constant according to Davie's method.³¹

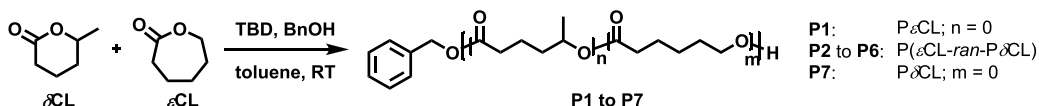
In this regard, the copolymerization of the two isomers ϵ -caprolactone (ϵ CL) and δ -caprolactone (δ CL) represents a

Received: March 1, 2020

Revised: May 13, 2020

Published: June 16, 2020



Scheme 1. ROP of δ -Caprolactone (δ CL) and ϵ -Caprolactone (ϵ CL) Yielding the Homo- and Co-polyesters P1 to P7

useful tool to access a library of materials featuring the same HHB. To the best of our knowledge, both monomers have only been copolymerized by Song et al., who focused on the enzymatic degradation of three statistical copolymers.³² However, detailed insights into the copolymerization kinetics and, hence, the copolymer microstructure remain unknown to date.

Representing a methyl-substituted lactone, δ CL featured a lower polymerizability compared to the unsubstituted ϵ CL when diphenylphosphate was used as a catalyst.¹⁶ As a consequence, one might expect the formation of gradient copolymers during a statistical copolymerization of ϵ CL and δ CL. As an efficient catalyst for the ROP of ϵ CL at room temperature,³³ we selected triazabicyclodecene (TBD), although it or other guanidinium base catalysts have, to the best of our knowledge, not yet been employed for the ROP of δ CL (Scheme 1).

We present an in-depth study of the copolymerization kinetics of ϵ CL and δ CL including the calculation of reactivity ratios. With the microstructure in hand, a set of copolymers with varied comonomer composition was studied with respect to bulk crystallinity by means of differential scanning calorimetry (DSC) and wide-angle X-ray scattering (WAXS). Representing a key toward future encapsulation of active pharmaceutical ingredients, stable nanoparticle dispersions were prepared and investigated regarding their HHB by fluorescence spectroscopy of encapsulated pyrene.

EXPERIMENTAL SECTION

Materials. ϵ -Caprolactone (ϵ CL, > 99%, TCI) and δ -caprolactone (δ CL, > 99%, TCI) were dried over calcium hydride and distilled at reduced pressure. The reaction solvent toluene (extra dry, Aldrich), the catalyst 1,5,7-triazabicyclo[4.4.0]dec-5-ene (TBD, 98%, Aldrich), and the initiator benzyl alcohol (BnOH, anhydrous, 99.8%, Aldrich) were stored under nitrogen atmosphere. Tetrahydrofuran (THF) for nanoparticle preparation was purified in a solvent purification system (SPS; Pure solv EN, InnovativeTechnology). All other chemicals were purchased from standard suppliers and were used without any further purification, unless stated otherwise.

Instruments. Polymerizations were conducted under nitrogen atmosphere in a MBraun UNILab Plus glovebox equipped with high efficiency box filters HEPA H13, a UNILab inert gas purification system and a vacuum pump.

Proton nuclear magnetic resonance (¹H NMR) spectra were measured in CDCl₃ at room temperature on a 300 MHz Bruker Avance I spectrometer. The residual ¹H peak of the deuterated solvent was used for chemical shift referencing.

Size-exclusion chromatography (SEC) measurements were performed utilizing a Shimadzu system equipped with a CBM-20A system controller, a LC-10AD pump, an RID-10A refractive index detector, and PSS (Polymer Standards Service GmbH, Mainz, Germany) SDV guard/linear S columns with chloroform/triethylamine (NEt₃)/*iso*-propanol (94:4:2) as eluent with a flow rate of 1 mL min⁻¹. The Techlab column oven was set to a constant temperature of 40 °C. Polystyrene (PS, 0.16 kg mol⁻¹ < M_n < 128 kg mol⁻¹) samples were used for calibration.

Matrix-assisted laser desorption ionization time-of-flight mass spectrometry (MALDI TOF MS) investigations were performed using an Ultraflex III ToF/ToF instrument from Bruker Daltonics equipped with a Nd:YAG laser. All spectra were measured in the

linear positive mode using *trans*-2-[3-(4-*tert*-butylphenyl)-2-methyl-2-propenyldene]malononitrile (DCTB) as a matrix and sodium iodide as the doping salt. The instrument was calibrated with an external PMMA standard from PSS.

Thermogravimetric analysis (TGA) was performed under nitrogen atmosphere on a Netzsch TG 209 F1 Iris. Data were recorded from 30 to 600 °C at a heating rate of 20 °C min⁻¹. Differential scanning calorimetry (DSC) measurements were performed with a Netzsch 204 F1 Phoenix instrument under a nitrogen atmosphere from -100 to 210 °C applying a heating rate of 20 °C min⁻¹ in the first and second run and 10 °C min⁻¹ in the third run. The cooling rate between the heating runs was 20 °C min⁻¹.

Wide angle X-ray scattering (WAXS) measurements were performed on a Bruker AXS Nanostar, equipped with an Incoatec I μ SCu E025 microfocus X-ray source, operating at $\lambda = 1.54$ Å and a VANTEC 2000 detector. A pinhole setup with 750, 400, and 1000 μ m (in the order from source to sample) was used, and the sample-to-detector distance was 12 cm. The samples were fixed on a tape, and a corresponding baseline measurement was subtracted.

Dynamic light scattering (DLS) measurements were performed on a Zetasizer Nano ZS (Malvern Instruments, Herrenberg, Germany) at 25 °C ($\lambda = 633$ nm) at an angle of 173°. For each measurement, 3 \times 30 s runs were carried out in triplicate after an equilibration time of 30 s. The mean particle size was approximated as the effective (*Z*-average) diameter and the width of the distribution as the dispersity index (PDI) of the particles obtained by the cumulants method assuming a spherical shape.

Fluorescence spectra were recorded on a Jasco FP-8300 instrument using quartz cuvettes (Hellma analytics, 1 cm pathway). Measurements were performed at an excitation wavelength λ_{ex} of 339 nm from 350 to 550 nm with a scan speed of 20 nm min⁻¹ at an interval of 0.2 nm.

Atomic force microscopy (AFM) was performed with a Dimension 3100 and Multimode (both from Bruker, Veeco, Santa Barbara, CA) equipped with a nanoscope IV controller, as well as with a JPK-Nanowizard 3 (JPK BioAFM, Bruker Nano GmbH, Berlin, Germany) to determine the nanoparticle shape. Prior to each measurement, nanoparticle suspensions were deposited on Mica substrates, and the residual water was allowed to evaporate at room temperature. Measurements were performed at room temperature using standard tapping mode silicon cantilevers from Bruker (model RTESP, Veeco, Santa Barbara, CA) with a resonance frequency from 315 to 364 kHz in air, a spring constant in the range of 20 to 80 N m⁻¹, and a typical tip radius of less than 10 nm (typically 7 nm).

Ring Opening Polymerization. All polymerizations were performed at 23 °C in a glovebox under nitrogen atmosphere (<0.1 ppm of H₂O; < 0.1 ppm of O₂).

Homopolymerization Kinetics for ϵ CL and δ CL. The monomer was transferred into a vial and mixed with toluene. Afterward a solution containing BnOH, TBD, and toluene was added to adjust the initial monomer concentration [M]₀ and [M]₀: [BnOH]₀: [TBD]₀ ratio (Table S1 of the Supporting Information, SI). The ROP proceeded at room temperature. Aliquots were regularly withdrawn, quenched with a 4-fold excess of benzoic acid, and analyzed by means of ¹H NMR spectroscopy (Figure S1) and SEC to determine monomer conversions, molar masses, and dispersity values. In an exemplary reaction ([ϵ CL]: [BnOH]: [TBD] = 200:1:1; [ϵ CL]₀ = 2 mol L⁻¹), 444 μ L (4 mmol) of ϵ CL and 1.456 mL of toluene were transferred in a vial and stirred at room temperature to obtain a homogeneous solution. Subsequently, 100 μ L of a toluene solution containing 2.8 mg (0.02 mmol) of TBD and 2.2 mg (0.02 mmol) of BnOH were added to the mixture to start the reaction. Samples were

Table 1. Selected Structural Characterization Data of the Synthesized (Co)polyesters

sample	polymer	$\epsilon\text{CL}/\delta\text{CL}$			NMR			SEC ^d	
		feed [mol %]	conversion ^a [%]	theor. ^b [mol %]	NMR ^c [mol %]	$M_{n, \text{theo}}^b$ [kg mol ⁻¹]	$M_{n, \text{NMR}}^c$ [kg mol ⁻¹]	$M_{n, \text{SEC}}$ [kg mol ⁻¹]	\bar{D}
P1 ^e	P ϵCL	100/0	47/0	100/0	100/0	11	13	19	1.17
P2 ^f	P($\epsilon\text{CL-ran-}\delta\text{CL}$)	80/20	89/62	85/15	87/13	9	13	21	1.57
P3 ^f	P($\epsilon\text{CL-ran-}\delta\text{CL}$)	75/25	81/63	79/21	81/19	9	10	19	1.41
P4 ^f	P($\epsilon\text{CL-ran-}\delta\text{CL}$)	70/30	75/62	74/26	75/25	8	10	19	1.30
P5 ^f	P($\epsilon\text{CL-ran-}\delta\text{CL}$)	60/40	64/64	59/41	61/39	7	9	16	1.26
P6 ^f	P($\epsilon\text{CL-ran-}\delta\text{CL}$)	50/50	51/67	43/57	45/55	7	7	15	1.21
P7 ^g	P δCL	0/100	0/44	0/100	0/100	10	9	6	1.09

^aDetermined by the integration of monomer and polymer signals from the ¹H NMR spectra of the reaction solution between 4 and 5 ppm.

^bCalculated from the single monomer conversions and the feed ratio. ^cDetermined by the integration of suitable signals from the ¹H NMR spectra of the purified polyesters. ^dEluent CHCl₃, RI detection, PS calibration. ^e[ϵCL]₀: [BnOH]₀: [TBD]₀ = 200:1:1; [ϵCL]₀ = 2 mol L⁻¹. ^f[ϵCL]₀: [BnOH]₀: [TBD]₀ = 100:1:2; [CL]₀ = 4 mol L⁻¹. ^g[δCL]₀: [BnOH]₀: [TBD]₀ = 200:1:4; [δCL]₀ = 4 mol L⁻¹.

taken after 1, 4, 5, 7.5, and 8 h, quenched with a 4-fold excess of benzoic acid, and analyzed as described above.

For bulk polymerizations, various vials were charged with the same amount of monomer, catalyst, and initiator. After varying the reaction time at room temperature, each vial was quenched by addition of a 4-fold excess of benzoic acid in toluene and analyzed as described above.

Statistical Copolymerization Kinetics for ϵCL and δCL . The two monomers were transferred into a vial to achieve five different monomer feed ratios [ϵCL]₀: [δCL]₀ of 80:20, 75:25, 70:30, 60:40, and 50:50. The overall monomer molar amount was fixed to 456 mg (4 mmol). Subsequently, 0.36 mL of toluene was added. The mixture was stirred at room temperature to obtain a homogeneous solution. Afterward 0.2 mL of a solution containing 4.3 mg (0.04 mmol) of BnOH and 11.1 mg (0.08 mmol) of TBD in toluene was added to adjust the overall initial monomer concentration [M]_{0,ovr} to 4 mol L⁻¹ and [M]_{0,ovr}: [BnOH]₀: [TBD]₀ ratio to 100:1:2 (Table S1). The ROP proceeded at room temperature. Aliquots were regularly withdrawn, quenched with a 4-fold excess of benzoic acid, and analyzed by means of ¹H NMR spectroscopy and SEC to determine monomer conversions, molar masses, and dispersity values.

In an exemplary reaction ([ϵCL]₀: [δCL]₀ = 70:30), 310 μL (2.8 mmol) of ϵCL , 132 μL (1.2 mmol) of δCL , 4.3 mg (0.04 mmol) of BnOH, 11.1 mg (0.08 mmol) of TBD, and 0.56 mL of toluene were used. The ROP proceeded at room temperature. Samples were withdrawn after 1, 2, 3, and 5 h, quenched with a 4-fold excess of benzoic acid, and analyzed via ¹H NMR spectroscopy and SEC.

Homopolymerization of ϵCL and δCL (P1 and P7). Corresponding to a ratio of [ϵCL]: [BnOH]: [TBD] of 200:1:1 and a [ϵCL]₀ of 2 mol L⁻¹, P ϵCL (P1) was obtained by adding 19.4 mL (175 mmol) of ϵCL and 67.2 mL of toluene to a round-bottom flask. Subsequent to complete dissolution at room temperature, 1 mL of a toluene solution containing 90.5 μL (0.87 mmol) of BnOH and 122 mg (0.87 mmol) of TBD was added to initiate the polymerization. Samples were withdrawn after 5, 7, and 8 h to monitor conversion, molar mass, and dispersity value. After 9 h of stirring at room temperature, the reaction mixture was quenched with a 4-fold excess of benzoic acid dissolved in toluene and a sample was taken to determine the monomer conversion. After a first precipitation of the polymers in cold methanol (-22 °C) followed by filtration, the polymer was redissolved in chloroform, reprecipitated in cold methanol (-22 °C), filtered, and dried in vacuum at 40 °C overnight to yield a white powder.

P ϵCL (P1): Conv. = 47%; yield: 7.6 g (38%). ¹H NMR (300 MHz, CDCl₃): δ /ppm = 1.39 (m, 209 H, -CH₂CH₂C(O)O-), 1.65 (m, 420 H, -OCH₂CH₂CH₂-), 2.31 (t, 208 H, -OC(O)-CH₂-), 4.06 (t, 207 H, -CH₂-O-), 5.11 (s, 2 H, C₆H₅-CH₂-), 7.35 (br, 5 H, C₆H₅-); SEC (CHCl₃, PS calibration): M_n = 19 kg mol⁻¹; \bar{D} = 1.17.

P δCL (P7) was synthesized employing a [δCL]: [BnOH]: [TBD] ratio of 200:1:4 at a [δCL]₀ of 4 mol L⁻¹. For this purpose, 19.29 mL (175.2 mmol) of δCL were dissolved in 19.5 mL of toluene at room

temperature. Subsequently, 5 mL of a toluene solution containing 90.66 μL (0.88 mmol) of BnOH and 488 mg (3.5 mmol) of TBD were added. After 2 h of stirring at room temperature, the reaction was terminated by addition of 1.5 equiv of benzoic acid in toluene. The mixture was stored at -22 °C for 3 days, forming a gel precipitate that was separated from the solution by decanting. The gel was dissolved in chloroform and precipitated from a 1/3 water/methanol mixture at room temperature. The precipitate was collected by centrifugation (5 °C, 7500 rpm, 5 min). The process was repeated twice, and the purified P7 was dried in vacuo at 40 °C overnight yielding a glassy gel.

P δCL (P7): Conv. = 44%; yield: 3.9 g (20%). ¹H NMR (300 MHz, CDCl₃): δ /ppm = 1.20 (d, 308 H, -CH₃), 1.59 (m, 473 H, -OCH(CH₃)CH₂CH₂-), 2.28 (t, 198 H, -OC(O)-CH₂-), 4.90 (m, 95 H, -CH(CH₃)-O-), 5.11 (s, 2 H, C₆H₅-CH₂-), 7.35 (br, 5 H, C₆H₅-); SEC (CHCl₃, PS calibration): M_n = 6.0 kg mol⁻¹; \bar{D} = 1.09.

General Procedure for the Statistical Copolymerization (P2 to P6). The reaction mixtures for the statistical copolymers of ϵCL and δCL were prepared in a similar fashion as that described above for the statistical copolymer kinetics. Corresponding to an [M]_{0,ovr}: [BnOH]: [TBD] ratio of 100:1:2 and an initial monomer concentration of 4 mol L⁻¹, 487 mg (3.5 mmol) of TBD, 181 μL (1.75 mmol) of BnOH and 4.877 mL of toluene were used. The feed ratio of ϵCL and δCL was varied as indicated below and in Table 1. Subsequent to polymerization at room temperature for 5 h, the reactions were terminated by addition of a 4-fold excess of benzoic acid. Aliquots of 200 μL were withdrawn from the solutions and used for SEC and ¹H NMR analyses. The remaining reaction mixtures were precipitated from cold methanol (-22 °C), kept at -22 °C for 1 h, and centrifuged (-10 °C, 8000 rpm, 5 min). Subsequent to removal of the supernatants, the copolymers were dissolved in 5 mL of THF, precipitated from 5 mL of water at room temperature, stored at 5 °C for 30 min, and centrifuged (5 min, 5 °C, 8000 rpm). Subsequent to removal of the supernatants, the precipitates were dried in vacuum at 40 °C overnight.

P($\epsilon\text{CL-ran-}\delta\text{CL}$) (P2): Corresponding to a [ϵCL]/[δCL] feed ratio of 80/20, 3.103 mL (28 mmol) of ϵCL and 0.77 mL (7 mmol) of δCL were used according to the general procedure.

Overall conv. = 81%; conv.(ϵCL) = 89%; conv.(δCL) = 62%; yield = 2.13 g (53%).

¹H NMR (300 MHz, CDCl₃): δ /ppm = 1.21 (d, 37 H, P δCL , -CH₃-), 1.39 (m, 153 H, P ϵCL , -CH₂CH₂C(O)O-), 1.62 (m, 426 H, P($\epsilon\text{CL-co-}\delta\text{CL}$), -OCH₂CH₂CH₂-), 2.30 (m, 172 H, P($\epsilon\text{CL-co-}\delta\text{CL}$), -OC(O)-CH₂-), 4.06 (t, 147 H, P ϵCL , -CH₂-O-), 4.90 (m, 11 H, P δCL , -CH₂-O-), 5.11 (s, 2 H, C₆H₅-CH₂-), 7.35 (br, 5 H, C₆H₅-); SEC (CHCl₃, PS calibration): M_n = 21 kg mol⁻¹; \bar{D} = 1.57.

P($\epsilon\text{CL-ran-}\delta\text{CL}$) (P3): Corresponding to a [ϵCL]/[δCL] feed ratio of 75/25, 2.909 mL (26.25 mmol) of ϵCL and 0.963 mL (8.75 mmol) of δCL were used according to the general procedure.

Overall conv. = 77%; conv.(ϵ CL) = 81%; conv.(δ CL) = 63%; yield = 1.58 g (40%).

^1H NMR (300 MHz, CDCl_3): δ /ppm = 1.21 (d, 55 H, $\text{P}\delta\text{CL}$, CH_3), 1.39 (m, 149 H, $\text{P}\epsilon\text{CL}$, $-\text{CH}_2\text{CH}_2\text{C}(\text{O})\text{O}-$), 1.62 (m, 455 H, $\text{P}(\epsilon\text{CL}-\text{co}-\delta\text{CL})$, $-\text{OCH}_2\text{CH}_2\text{CH}_2-$), 2.30 (m, 185 H, $\text{P}(\epsilon\text{CL}-\text{co}-\delta\text{CL})$, $-\text{OC}(\text{O})-\text{CH}_2-$), 4.06 (t, 147 H, $\text{P}\epsilon\text{CL}$, $-\text{CH}_2-\text{O}-$), 4.90 (m, 17 H, $\text{P}\delta\text{CL}$, $-\text{CH}_2-\text{O}-$), 5.11 (s, 2H, $\text{C}_6\text{H}_5-\text{CH}_2-$), 7.35 (br, 5H, C_6H_5-); SEC (CHCl_3 , PS calibration): $M_n = 19 \text{ kg mol}^{-1}$; $\bar{D} = 1.41$.

$\text{P}(\epsilon\text{CL}-\text{ran}-\delta\text{CL})$ (P4): Corresponding to a $[\epsilon\text{CL}]/[\delta\text{CL}]$ feed ratio of 70/30, 2.715 mL (24.5 mmol) of ϵCL and 1.156 mL (10.5 mmol) of δCL were used according to the general procedure.

Overall conv. = 72%; conv.(ϵ CL) = 75%; conv.(δ CL) = 62%; yield = 2.02 g (50%).

^1H NMR (300 MHz, CDCl_3): δ /ppm = 1.21 (d, 72 H, $\text{P}\delta\text{CL}$, CH_3), 1.39 (m, 145 H, $\text{P}\epsilon\text{CL}$, $-\text{CH}_2\text{CH}_2\text{C}(\text{O})\text{O}-$), 1.62 (m, 429 H, $\text{P}(\epsilon\text{CL}-\text{co}-\delta\text{CL})$, $-\text{OCH}_2\text{CH}_2\text{CH}_2-$), 2.30 (m, 187 H, $\text{P}(\epsilon\text{CL}-\text{co}-\delta\text{CL})$, $-\text{OC}(\text{O})-\text{CH}_2-$), 4.06 (t, 139 H, $\text{P}\epsilon\text{CL}$, $-\text{CH}_2-\text{O}-$), 4.90 (m, 22 H, $\text{P}\delta\text{CL}$, $-\text{CH}_2-\text{O}-$), 5.11 (s, 2H, $\text{C}_6\text{H}_5-\text{CH}_2-$), 7.35 (br, 5H, C_6H_5-); SEC (CHCl_3 , PS calibration): $M_n = 19 \text{ kg mol}^{-1}$; $\bar{D} = 1.30$.

$\text{P}(\epsilon\text{CL}-\text{ran}-\delta\text{CL})$ (P5): Corresponding to a $[\epsilon\text{CL}]/[\delta\text{CL}]$ feed ratio of 60/40, 2.327 mL (21 mmol) of ϵCL and 1.541 mL (14 mmol) of δCL were used according to the general procedure.

Overall conv. = 63%; conv.(ϵ CL) = 62%; conv.(δ CL) = 64%; yield = 1.74 g (44%).

^1H NMR (300 MHz, CDCl_3): δ /ppm = 1.21 (d, 94 H, $\text{P}\delta\text{CL}$, CH_3), 1.39 (m, 100 H, $\text{P}\epsilon\text{CL}$, $-\text{CH}_2\text{CH}_2\text{C}(\text{O})\text{O}-$), 1.62 (m, 470 H, $\text{P}(\epsilon\text{CL}-\text{co}-\delta\text{CL})$, $-\text{OCH}_2\text{CH}_2\text{CH}_2-$), 2.30 (m, 145 H, $\text{P}(\epsilon\text{CL}-\text{co}-\delta\text{CL})$, $-\text{OC}(\text{O})-\text{CH}_2-$), 4.06 (t, 86 H, $\text{P}\epsilon\text{CL}$, $-\text{CH}_2-\text{O}-$), 4.90 (m, 28 H, $\text{P}\delta\text{CL}$, $-\text{CH}_2-\text{O}-$), 5.11 (s, 2H, $\text{C}_6\text{H}_5-\text{CH}_2-$), 7.35 (br, 5H, C_6H_5-); SEC (CHCl_3 , PS calibration): $M_n = 16 \text{ kg mol}^{-1}$; $\bar{D} = 1.26$.

$\text{P}(\epsilon\text{CL}-\text{ran}-\delta\text{CL})$ (P6): Corresponding to a $[\epsilon\text{CL}]/[\delta\text{CL}]$ feed ratio of 50/50, 1.939 mL (17.5 mmol) of ϵCL and 1.926 mL (17.5 mmol) of δCL were used according to the general procedure.

Overall conv. = 59%; conv.(ϵ CL) = 51%; conv.(δ CL) = 67%; yield = 1.10 g (28%).

^1H NMR (300 MHz, CDCl_3): δ /ppm = 1.21 (d, 127 H, $\text{P}\delta\text{CL}$, CH_3), 1.39 (m, 75 H, $\text{P}\epsilon\text{CL}$, $-\text{CH}_2\text{CH}_2\text{C}(\text{O})\text{O}-$), 1.62 (m, 361 H, $\text{P}(\epsilon\text{CL}-\text{co}-\delta\text{CL})$, $-\text{OCH}_2\text{CH}_2\text{CH}_2-$), 2.30 (m, 154 H, $\text{P}(\epsilon\text{CL}-\text{co}-\delta\text{CL})$, $-\text{OC}(\text{O})-\text{CH}_2-$), 4.06 (t, 68 H, $\text{P}\epsilon\text{CL}$, $-\text{CH}_2-\text{O}-$), 4.90 (m, 41 H, $\text{P}\delta\text{CL}$, $-\text{CH}_2-\text{O}-$), 5.11 (s, 2H, $\text{C}_6\text{H}_5-\text{CH}_2-$), 7.35 (br, 5H, C_6H_5-); SEC (CHCl_3 , PS calibration): $M_n = 15 \text{ kg mol}^{-1}$; $\bar{D} = 1.21$.

Nanoparticle Preparation. P1 to P7 were dissolved in THF to provide a concentration of 1 mg mL^{-1} . 0.5 mL of the solution were dropped into 5 mL of Milli-Q water while stirring. The suspensions were stirred (1000 rpm) for 3 h at room temperature. The vials were left open overnight to allow evaporation of THF yielding aqueous dispersions of a final concentration of 0.1 mg mL^{-1} . Afterward DLS measurements were performed. The pyrene loaded nanoparticles were prepared by mixing 0.4 mL of polymeric THF solutions ($c = 1.25 \text{ mg mL}^{-1}$) and 0.1 mL of a pyrene solution in THF ($c = 50 \mu\text{g mL}^{-1}$). 0.5 mL of the combined solution was dropped into 5 mL of Milli-Q water while stirring. The vials were left open overnight to allow evaporation of THF yielding aqueous dispersions of a final polymer concentration of 0.1 mg mL^{-1} and a pyrene concentration of $1 \mu\text{g mL}^{-1}$. After DLS measurements, the nanoparticle suspensions of P1, P6, and P7 were diluted 20 times and fluorescence spectra were measured ($\lambda_{\text{ex}} = 339 \text{ nm}$, $c(\text{pyrene}) = 2.4 \times 10^{-7} \text{ mol L}^{-1}$).

Kinetic Modeling. Kinetic modeling was performed using Origin version Pro 2015. For the calculation of reactivity ratios, least-squares analysis based on standard functions was implemented for the kinetic models. The visual representations of the copolymer microstructures obtained employing the Meyer–Lowry (ML) and Beckingham (BSL) models were based on the calculation of conditional probabilities and the average block length of both ϵCL and δCL segments.^{34–36}

RESULTS AND DISCUSSION

The aim of our study was to obtain PCL with varied degrees of crystallinity. Since δCL is rarely focused on, even in academic research,^{16,32,37} a broad screening of the homopolymerization conditions represented the initial step of this study. Therefore, the organobase TBD was used as a catalyst at room temperature and parameters such as $[\text{monomer}]$ to $[\text{initiator}]$ ratio and monomer concentration in toluene were varied (see the SI for details). Irrespective of the initial monomer concentration, the monomer concentration approached a threshold value of 0.55 mol L^{-1} that represents the monomer equilibrium concentration $[\delta\text{CL}]_{\text{eq}}$ at room temperature (Figure 1). The value is in accordance with thermodynamic

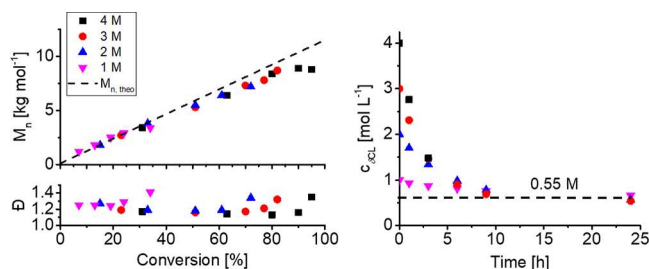


Figure 1. Kinetic plots for the TBD-catalyzed ROP of δCL in toluene at room temperature employing an initial $[\delta\text{CL}]_0$: $[\text{BnOH}]_0$: $[\text{TBD}]_0$ ratio of 100:1:2 at initial monomer concentrations $[\delta\text{CL}]_0$ of 4, 3, 2, and 1 mol L^{-1} . Left: Dependence of the molar mass $M_{n,\text{SEC}}$ and dispersity on the monomer conversion. The dotted line represents the theoretical molar mass $M_{n,\text{theo}}$ calculated according to $M_{n,\text{theo}} = M_{\delta\text{CL}} \times ([\delta\text{CL}]_0/[\text{BnOH}]_0) \times \text{conversion} + M_{\text{BnOH}}$. Right: Evolution of the residual monomer concentration $[\delta\text{CL}]$ over time. The dotted line represents the monomer equilibrium concentration $[\delta\text{CL}]_{\text{eq}}$ of 0.55 mol L^{-1} .

data reported for the diphenyl phosphate catalyzed ROP of δCL reported by Hillmyer and co-workers.¹⁶ Briefly, optimized polymerization conditions required at least 2 equiv of TBD with respect to the initiator BnOH. Similar to Lohmeijer et al.,³³ we observed that $\text{P}\epsilon\text{CL}$ with low dispersity required a reduced amount of TBD, i.e., $[\text{BnOH}]$: $[\text{TBD}]$ ratios of 1:1 or 1:0.5 (see SI for details). A $[\text{BnOH}]$: $[\text{TBD}]$ ratio of 1:2 as a compromise between the optimum ROP conditions of both monomers was selected for the statistical copolymerization. To account for $[\delta\text{CL}]_{\text{eq}}$, a rather high initial monomer concentration $[\text{CL}]_0$ of 4 mol L^{-1} was investigated further.

Statistical Copolymerization of δCL and ϵCL . As Song et al. reported that a δCL fraction in the feed $f_{\delta\text{CL},0}$ of 50% resulted in amorphous materials,³² we varied the feed ratio of ϵCL and δCL between 80:20 and 50:50. For this purpose, the kinetics of five different statistical copolymerizations were examined applying the conditions described above ($[\text{CL}]_0$: $[\text{BnOH}]_0$: $[\text{TBD}]_0 = 100$:1:2; $[\text{CL}]_0 = 4 \text{ mol L}^{-1}$ in toluene at room temperature, Figures S15–S19).

Irrespective of the initial feed ratio, SEC revealed the occurrence of high molar mass tailing for conversions above 50%, in line with the results obtained for the homopolymerization of ϵCL . However, dispersity values remained below 1.4 and the molar masses increased with conversion in a linear fashion. Because a monomer equilibrium concentration was not reached, the semilogarithmic plots suggested pseudo-first order polymerization kinetics up to such conversions. As evident from the apparent polymerization rate constants of the individual monomers $k_{p,\text{app}}$ (Table S3), the polymerizability of

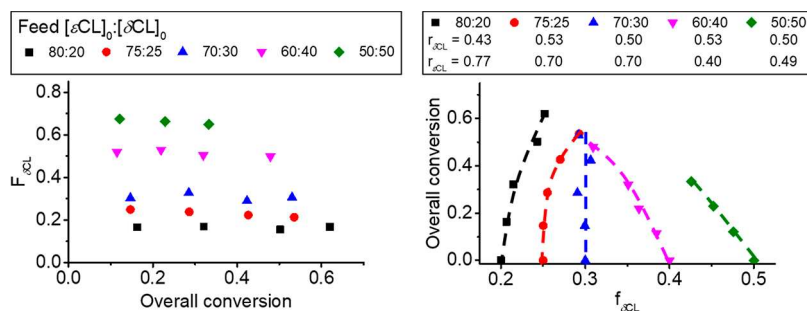


Figure 2. Monomer reactivity of ϵ CL and δ CL. Left: Evolution of the δ CL fraction in the copolymer ($F_{\delta\text{CL}}$) vs overall conversion. Right: Overall monomer conversion vs molar fraction of δ CL in the feed ($f_{\delta\text{CL}}$). The dotted lines represent fits according to the Meyer–Lowry equation.³⁹ Estimated reactivity ratios are indicated in the legend.

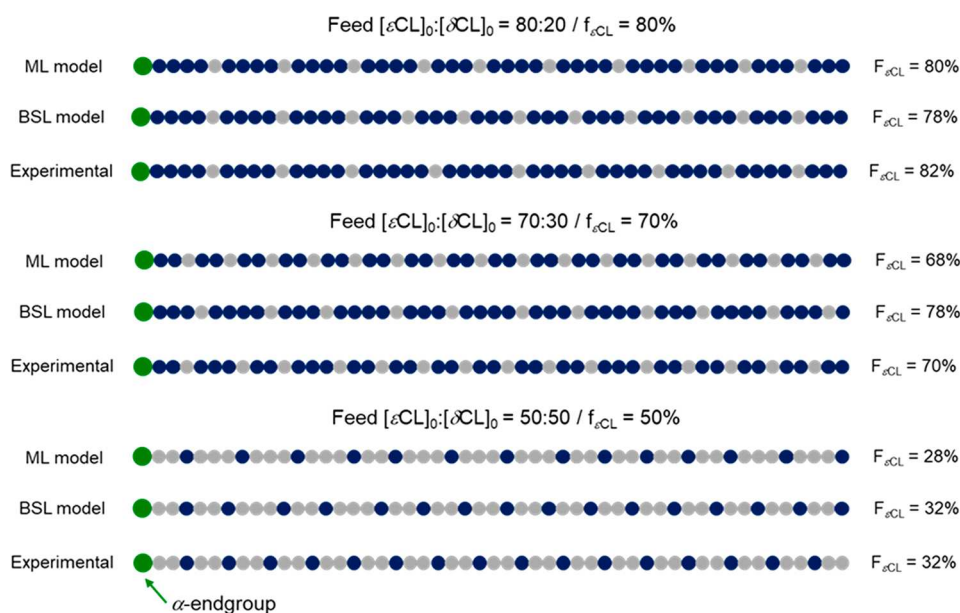


Figure 3. Schematic representation of the microstructures obtained from experimental data and probability calculations based on the Meyer–Lowry (ML) and Beckingham (BSL) models for a DP value of 50 employing an initial $[\epsilon\text{CL}]_0:[\delta\text{CL}]_0$ ratio of 80:20, 70:30, and 50:50. The benzyl α -end group is depicted in green, the ϵ CL and δ CL units are depicted in blue and gray, respectively.

the substituted lactone δ CL was increased in the copolymerization with ϵ CL compared to its homopolymerization.

In order to clarify the role of ϵ CL in the copolymerization with δ CL, the monomer reactivity ratios were of interest, reasoning the focus on low conversions during the kinetic studies. A range of analytical models can be used for this purpose and are often applied for irreversible polymerizations.^{38–40} Although equilibrium processes play a role in the ROP of lactones, the copolymerization of ϵ CL and δ CL resembled an irreversible reaction in the low conversion range investigated here. The Mayo–Lewis method³⁸ pointed toward a tendency of homopropagation for both monomers ($r_{\delta\text{CL}} = 7.1$ and $r_{\epsilon\text{CL}} = 3.1$). However, the overall conversions of around 18% were relatively high for this classical method (Figure S20). However, the wealth of data from the kinetic studies enabled a much clearer picture of the copolymer microstructure (Figure 2). For all copolymerizations, no significant variation of the δ CL fraction in the copolymer $F_{\delta\text{CL}}$ during the course of polymerization was observed. For the reactions up to a δ CL feed fraction $f_{\delta\text{CL},0}$ of 30%, the δ CL fraction was maintained in the copolymer. In contrast, increasing the $f_{\delta\text{CL},0}$ to 40% or 50% resulted in an elevated δ CL fraction in the copolymer ($F_{\delta\text{CL}} = 52\%$ or 66% , respectively). The observation is in agreement

with fitting results according to the Meyer–Lowry (ML) model,³⁹ which showed an almost constant reactivity ratio of δ CL for all copolymerizations ($r_{\delta\text{CL}} \approx$ of 0.50). In contrast, the estimated reactivity ratio of ϵ CL $r_{\epsilon\text{CL}}$ slightly changed throughout the series of kinetic studies but consistently remained below 1. In addition, the simple nonterminal method proposed by Beckingham et al.⁴⁰ in 2015 (BSL model) was tested although it assumes an ideal copolymerization taking place (Figure S21). Also in this case, slightly different reactivity ratios were found comparing the individual kinetic studies with varied comonomer feed fraction ($0.80 \leq r \leq 2.13$).

In summary, the ML as well as the BSL model hinted toward the presence of a random copolymerization of ϵ CL and δ CL. That is in line with observations made by Song et al., who investigated the copolymer microstructure by ¹³C NMR studies.³² The more accurate terminal ML model⁴¹ giving two independent reactivity ratios pointed toward a minor tendency to alternate as all reactivity ratios were below 1. However, none of the models took into account any equilibrium processes, and small differences in reactivity ratios might not be straightforward to picture as they could simply result from experimental error. The calculations were hence complemented with visual representations of selected copoly-

mer microstructures (Figure 3). The microstructures based on the ML and BSL models, respectively, were obtained on the basis of the conditional probabilities followed by the calculation of the average block length of both ϵ CL and δ CL segments estimated from the reactivity ratios.^{34–36} The average block length of the ϵ CL mers decreased from four ($f_{\epsilon\text{CL}} = 0.8$) to one ($f_{\epsilon\text{CL}} = 0.5$) within the copolymer series. The depictions of the microstructures labeled as “experimental” were directly and solely based on the $[\epsilon\text{CL}]_0:[\delta\text{CL}]_0:[\text{BnOH}]_0$ ratio of the two monomers and the individual monomer conversions after each time interval between sampling.

All three microstructures closely resembled each other, irrespective of the initial comonomer feed ratio. One can hence conclude that (a) the simplified BSL model gave similar results as the mathematically more challenging terminal ML model; and (b) despite the actual presence of equilibria during the ROP of ϵ CL and δ CL, our initial disregard of that fact was valid. Models developed for solely chain growth polymerization were hence reasonable to be applied here. It should, however, be stressed that maintaining monomer concentrations significantly above the monomer equilibrium concentrations $[M]_{\text{eq}}$ was an important prerequisite. These conclusions might not hold true for higher monomer conversions where $[M]_{\text{eq}}$ cannot be neglected anymore.

Synthesis of PCL Materials. The extensive kinetic investigations on the ROP of caprolactones described above enabled us to identify optimum polymerization conditions suited for the preparation of various PCL homo- and copolyesters on a gram scale. In order to exclude additional variation of properties due to molar mass effects, a DP value of 100 (corresponding to a molar mass M_n of 11 kg mol⁻¹) was targeted. To avoid broadening of the molar mass distributions at higher conversions, the two homopolymers P ϵ CL **P1** and P δ CL **P7** were synthesized employing a $[\text{CL}]_0:[\text{BnOH}]_0$ of 200:1 and terminated at conversions of around 50% (Table 1). In contrast, kinetic studies for the copolymers revealed low dispersity values also at higher conversions. Therefore, a $[\text{CL}]_0:[\text{BnOH}]_0$ of 100:1 was employed for the synthesis of **P2** to **P6**. In line with the kinetic studies, the conversion of ϵ CL increased from 50 to 90% with increasing molar fraction of ϵ CL in the feed, whereas the δ CL conversion was around 65% for all copolymers. In consequence, the molar fraction of ϵ CL in the purified copolymers was mostly increased in comparison with the feed.

Analyses of the purified copolyesters by means of ¹H NMR spectroscopy confirmed that. As depicted in Figure 4, signals assigned to both repeating units were seen, albeit mostly as overlapping signals. However, the methylene or methine proton signals neighboring the oxygen atoms of the ester moieties (peaks “d” and “D” in Figure 4) were well separated and hence used to determine the composition of **P2** to **P6**. The resulting values are in agreement with the values expected from the individual monomer conversions, confirming that the purification procedure did not alter the composition of the initial samples. In addition, the molar mass of the polyesters **P1** to **P7** was estimated from the ¹H NMR spectra utilizing peak integrals assigned to the benzylic methylene protons (“e” vs “d” and/or “D” in Figure 4). The resulting $M_{n,\text{NMR}}$ values tended to be slightly higher than $M_{n,\text{theo}}$, i.e., the molar mass expected from feed and conversion. This is most likely due to the accuracy of the end group determination method for molar masses around 10 kg mol⁻¹, because SEC analysis did not

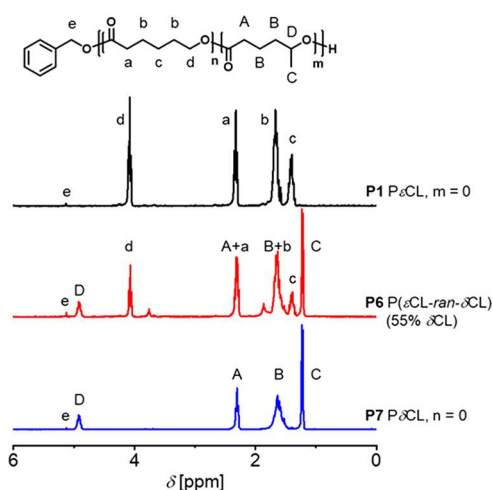


Figure 4. ¹H NMR spectra of P ϵ CL (**P1**), P δ CL (**P7**), the copolymer **P6** (300 MHz, CDCl₃), and assignment of the signals to the schematic representation of the structure of the copolyesters.

indicate any loss of low molar mass fractions throughout the purification process.

In line with the increased hydrodynamic volume of P ϵ CL compared to P δ CL in the chloroform based eluent used for SEC analysis, the molar masses $M_{n,\text{SEC}}$ were found to increase with the ϵ CL content throughout the polyester library. Also the dispersity value \bar{D} increased from 1.21 to 1.57 with the ϵ CL fraction for the copolymers **P2** to **P6**. This is most likely due to the formation of cyclic macromolecules through transesterification at higher conversions, as indicated by MALDI TOF mass spectrometry. Additional presence of TBD-initiated chains^{42,43} could neither be excluded nor be confirmed due to the resolution of the spectra (see SI). However, the two P ϵ CL and P δ CL homopolymers **P1** and **P7**, which were obtained under carefully optimized polymerization conditions, featured narrow molar mass distributions with dispersity values \bar{D} of 1.17 and 1.09, respectively.

Bulk Properties. As the crystallinity of polyesters can influence their degradation kinetics,³² analysis of the bulk materials by means of DSC and WAXS represented the next step to enable the determination of properties such as the melting temperature (T_m) and the degree of crystallinity (X_c). Subsequent to ensuring the thermal stability of the materials by means of TGA, DSC measurements were performed in the temperature range from -100 to 210 °C using three consecutive heating and cooling cycles (Table 2).

During the first heating run, the semicrystalline **P1** featured a melting temperature of 68 °C. Upon increasing the δ CL content in the copolymer, T_m decreased in a linear fashion to 24 °C for **P5** with a δ CL fraction $F_{\delta\text{CL}}$ of 39% (Figure 5). Although slightly lower T_m values were found for the semicrystalline **P1** to **P5** during the second and third heating run, the trend remained the same for polyesters with erased thermal prehistory. This observation is in line with the exothermic crystallization peaks recorded during the cooling runs for the samples **P1** to **P4**. Also here, an increased δ CL fraction resulted in a decreased T_c , suggesting that the comonomer δ CL affected the crystallization of the P ϵ CL domains. It should be noted that **P4** and **P5** additionally displayed cold crystallization during the second and third heating run. In addition, the enthalpy of melting decreased linearly with $F_{\epsilon\text{CL}}$, pointing toward a reduced degree of

Table 2. Bulk Properties of the Copolyesters Obtained by Means of DSC and WAXS Analysis

sample	polymer	$F_{\delta\text{CL}}$ [mol %]	first heating run ^a		WAXS ^b	first cooling run ^c		second heating run ^a	
			T_m [°C]	ΔH_f [J g ⁻¹]	X_c [%]	T_c [°C]	ΔH_c [J g ⁻¹]	T_m [°C]	$\Delta H_f - \Delta H_{cc}$ [J g ⁻¹]
P1	P ϵ CL	0	69	140	73	26	-93	60	87
P2	P(ϵ CL- <i>ran</i> - δ CL)	13	54	80	44	-4	-71	46	54
P3	P(ϵ CL- <i>ran</i> - δ CL)	19	52	50	38	-14	-43	42	49
P4	P(ϵ CL- <i>ran</i> - δ CL)	25	42	43	28	-29	-11	38	13
P5	P(ϵ CL- <i>ran</i> - δ CL)	39	24	2	4				
P6	P(ϵ CL- <i>ran</i> - δ CL)	55			0				
P7	P δ CL	100		n.d.	8				

^aPerformed from -100 to 210 °C with a heating rate of 20 °C min⁻¹. ^bPerformed at room temperature. ^cPerformed from 210 to -100 °C with a cooling rate of -20 °C min⁻¹.

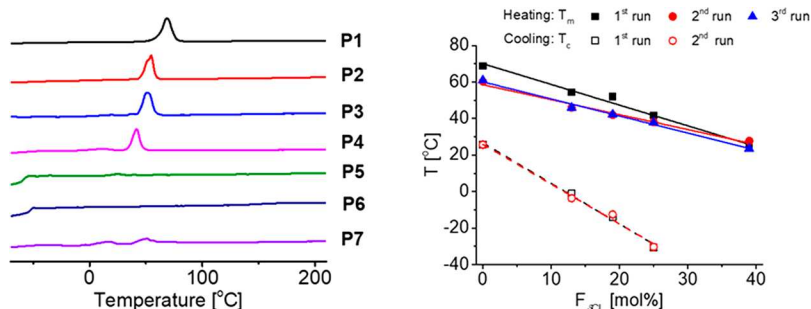


Figure 5. Left: DSC thermograms of the homo and copolyesters P1 to P7 (N₂, first heating run -100 to 210 °C, heating rate 20 °C min⁻¹). Right: Dependence of the melting temperature (T_m) and the crystallization temperature (T_c) on the fraction of δ CL in the copolymer ($F_{\delta\text{CL}}$).

crystallinity through incorporation of δ CL units in the P ϵ CL matrix (see SI).

Increasing the $F_{\delta\text{CL}}$ further resulted in the absence of a melting point, showing that a $F_{\delta\text{CL}}$ of 55% (P6) is sufficient to suppress the crystallinity induced by the P ϵ CL domains, which is in line with the average P ϵ CL block length of one determined by conditional probability calculations (Figure 3). However, the DSC thermogram of the P δ CL homopolymer P7 revealed multiple endothermic events in the first heating run, which were not visible in the second or third heating runs anymore.

WAXS analyses were performed to unambiguously determine the degree of crystallinity of the bulk materials P1 to P7. As reported in literature,^{44,45} the P ϵ CL P1 was semicrystalline with a degree of crystallinity of 73% and typical reflections at 2θ of 21.7 and 23.9 (Figure 6). The scattering pattern remained unaltered for the copolymers P2 to P5, suggesting that the introduction of δ CL comonomers did not affect the crystal structure of the P ϵ CL domains. However, increasing the

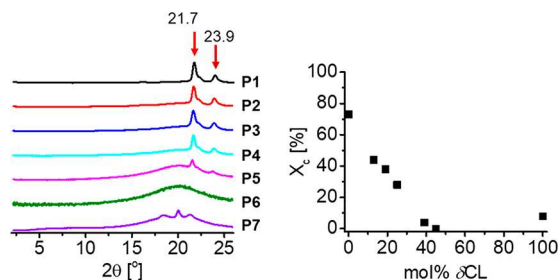


Figure 6. WAXS analysis for the homo and copolyesters P1 to P7. Left: WAXS diffractograms and assignment of the typical reflexes of P ϵ CL (P1). Right: Dependence of the degree of crystallinity (X_c) on the fraction of δ CL in the copolymer ($F_{\delta\text{CL}}$).

δ CL content resulted in lower scattering intensities, and, in consequence, lowered the degree of crystallinity. In fact, X_c of the polyesters P1 to P5 linearly decreased with the ϵ CL content (Figure 6). In line with DSC analyses, the copolyester P6 with a δ CL content of 55% represented an amorphous material.

WAXS analysis of the P δ CL homopolymer P7 showed the presence of low intensity scattering reflexes at 2θ of 18.4, 20.0, and 21.3 and a degree of crystallinity of 8%. The three new reflections did not superimpose with the scattering pattern of P1, suggesting that both polymers can, indeed, crystallize assuming different chain packing. However, the absence of the signals related to P7 in the WAXS diffractograms of P2 to P6 suggests an absence of such crystallites in the copolymers.

Nanoparticle Formulation. Having established a copolyester library with similar molar mass but varying degree of crystallinity, the preparation of stable aqueous nanoparticle dispersions represented the next step. Nanoprecipitation was hence performed according to an established protocol^{28,29} to yield dispersions of a final polymer concentration of 0.1 mg mL⁻¹ in water, avoiding the formation of agglomerates or polymer films. DLS measurements indicated hydrodynamic diameters between 115 and 138 nm and low to moderate dispersity (Table 3, SI). AFM was used as complementary technique to investigate the polymer nanoparticles from P1 to P7, revealing structures with an increased average size of 190 nm in diameter. However, the average height of 20 nm suggested that the nanoparticles collapsed on the surface of the substrate.

As final proof of concept for the preparation of polyester nanoparticles featuring the same HHB, pyrene was encapsulated employing the homopolymer P1 and P7 and the copolyester P6 (featuring a ϵ CL to δ CL ratio of 45 to 55). Frequently applied for the determination of the critical micellar concentration,^{46,47} pyrene can serve as a tool to determine the

Table 3. DLS Data of the Nanoparticles Obtained from the Polyesters P1 to P7

sample	P1	P2	P3	P4	P5	P6	P7
$F_{\epsilon\text{CL}}:F_{\delta\text{CL}}$ [mol %]	100:0	87:13	81:19	75:25	61:39	55:45	0:100
D_h^a [nm]	137	138	137	129	137	130	115
PDI	0.109	0.055	0.085	0.071	0.076	0.074	0.133

^a D_h denotes the Z-average.

hydrophobicity of its surrounding due to variation of the vibrational fine structure in its fluorescence spectrum. For this purpose, pyrene and the polymers were coprecipitated from THF into water keeping the pyrene to polymer mass ratio at 1% for all the samples. DLS analyses revealed hydrodynamic diameters between 120 and 160 nm and low to moderate dispersity ($0.084 < \text{PDI} < 0.103$; see SI). After a 20-fold dilution, the resulting pyrene-loaded nanoparticles were analyzed by means of fluorescence spectroscopy. The hydrophobicity of the nanoparticles was evaluated via the ratio of the I_1 and I_3 bands, resulting in a value of around 1.22 for all samples (Figure 7). This did not only confirm the constant

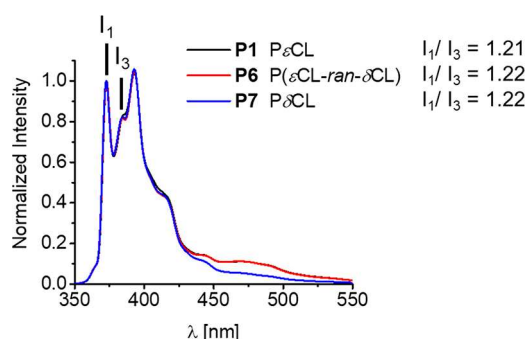


Figure 7. Normalized fluorescence spectra of pyrene loaded nanoparticles formed from P1, P6, and P7 ($\lambda_{\text{ex}} = 339$ nm, $\text{co}(\text{polymer}) = 5 \mu\text{g mL}^{-1}$, $\text{co}(\text{pyrene}) = 0.05 \mu\text{g mL}^{-1}$).

HHB for the PCL nanoparticles, but also hinted toward an increased hydrophobicity of the PCL particles in comparison to PLA ($I_1/I_3 \approx 1.3$),²⁹ thereby demonstrating the significance of a careful polymer design before structure property relationships with respect to nanoparticle performance can be drawn.

CONCLUSIONS

The copolymerization of the two constitutional isomers ϵCL and δCL represented a suitable approach to access a library of tailor-made polyesters with the same hydrophilic hydrophobic balance (HHB). An in-depth evaluation of the homo and copolymerization kinetics and application of the ML and BSL models suggested the presence of random copolymers. A comparison of the resulting microstructure estimated by conditional probability calculations with the microstructure directly obtained from kinetic data hinted toward the applicability of the kinetic models well below the monomer equilibrium concentration.

The copolymer microstructure and composition directly influenced the bulk crystallinity and melting temperature of the copolyesters, which both decreased in a linear fashion with the δCL fraction. The materials were suited to prepare stable aqueous nanoparticle dispersions of similar size and constant HHB, as indicated by encapsulation of the probe pyrene.

These carefully adjusted materials are currently investigated with respect to release of encapsulated active pharmaceutical ingredients to unambiguously clarify the effect of the crystallinity of polyester nanoparticles on enzymatic degradation.

ASSOCIATED CONTENT

Supporting Information

The Supporting Information is available free of charge at <https://pubs.acs.org/doi/10.1021/acs.macromol.0c00486>.

Additional description of the homopolymerization optimization and kinetic studies, calculation details, ¹H NMR spectra, SEC elugrams, MALDI TOF mass spectra including discussion, TGA and DSC thermograms, DLS and AFM data, and nanoparticle preparation details (PDF)

AUTHOR INFORMATION

Corresponding Author

Ulrich S. Schubert – Laboratory of Organic and Macromolecular Chemistry (IOMC) and Jena Center for Soft Matter (JCSM), Friedrich Schiller University Jena, 07743 Jena, Germany; orcid.org/0000-0003-4978-4670; Email: ulrich.schubert@uni-jena.de

Authors

Damiano Bandelli – Laboratory of Organic and Macromolecular Chemistry (IOMC) and Jena Center for Soft Matter (JCSM), Friedrich Schiller University Jena, 07743 Jena, Germany

Irina Muljajew – Laboratory of Organic and Macromolecular Chemistry (IOMC) and Jena Center for Soft Matter (JCSM), Friedrich Schiller University Jena, 07743 Jena, Germany

Karl Scheuer – Chair of Materials Science (CMS), Department of Materials Science and Technology, Otto Schott Institute of Materials Research, Faculty of Physics and Astronomy, Friedrich Schiller University Jena, 07743 Jena, Germany

Johannes B. Max – Laboratory of Organic and Macromolecular Chemistry (IOMC) and Jena Center for Soft Matter (JCSM), Friedrich Schiller University Jena, 07743 Jena, Germany

Christine Weber – Laboratory of Organic and Macromolecular Chemistry (IOMC) and Jena Center for Soft Matter (JCSM), Friedrich Schiller University Jena, 07743 Jena, Germany

Felix H. Schacher – Laboratory of Organic and Macromolecular Chemistry (IOMC) and Jena Center for Soft Matter (JCSM), Friedrich Schiller University Jena, 07743 Jena, Germany; orcid.org/0000-0003-4685-6608

Klaus D. Jandt – Jena Center for Soft Matter (JCSM) and Chair of Materials Science (CMS), Department of Materials Science and Technology, Otto Schott Institute of Materials Research, Faculty of Physics and Astronomy, Friedrich Schiller University Jena, 07743 Jena, Germany; orcid.org/0000-0002-7537-5603

Complete contact information is available at:

<https://pubs.acs.org/10.1021/acs.macromol.0c00486>

Notes

The authors declare no competing financial interest.

ACKNOWLEDGMENTS

The work was funded by the Deutsche Forschungsgemeinschaft (DFG, German Research Foundation)—project number 316213987—SFB 1278 (projects A01, A03, A06, Z01) and SCHA1640/18-1. We gratefully acknowledge the additional financial support of the Thüringer Ministerium für Wirtschaft, Wissenschaft, und Digitale Gesellschaft (Thuringian Ministry for Economic Affairs, Science and Digital Society, ProExzellenz II, NanoPolar) and the Deutsche Forschungsgemeinschaft (DFG), grant reference INST 275/389-1 FUGG; AOBJ: 640980. F.H.S. and U.S.S. acknowledge support from the Thuringian Ministry for Education, Science, and Culture (TMBWK, #B515-11028, SWAXS-JCSM).

REFERENCES

- (1) Fornaguera, C.; García-Celma, M. J. Personalized nanomedicine: A revolution at the nanoscale. *J. Pers. Med.* **2017**, *7*, 12.
- (2) Facklam, A. L.; Volpatti, L. R.; Anderson, D. G. Biomaterials for personalized cell therapy. *Adv. Mater.* **2020**, *32*, 1902005.
- (3) Casalini, T.; Rossi, F.; Castrovinci, A.; Perale, G. A perspective on polylactic acid-based polymers use for nanoparticles synthesis and applications. *Front. Bioeng. Biotechnol.* **2019**, *7*, 259.
- (4) Mir, M.; Ahmed, N.; Rehman, A. u. Recent applications of PLGA based nanostructures in drug delivery. *Colloids Surf., B* **2017**, *159*, 217–231.
- (5) Englert, C.; Brendel, J. C.; Majdanski, T. C.; Yildirim, T.; Schubert, S.; Gottschaldt, M.; Windhab, N.; Schubert, U. S. Pharmapolymer in the 21st century: Synthetic polymers in drug delivery applications. *Prog. Polym. Sci.* **2018**, *87*, 107–164.
- (6) Xu, Z.; Wang, D.; Cheng, Y.; Yang, M.; Wu, L.-P. Polyester based nanovehicles for siRNA delivery. *Mater. Sci. Eng., C* **2018**, *92*, 1006–1015.
- (7) Liu, X.; Fan, X.; Jiang, L.; Loh, X. J.; Wu, Y.-L.; Li, Z. Biodegradable polyester unimolecular systems as emerging materials for therapeutic applications. *J. Mater. Chem. B* **2018**, *6*, 5488–5498.
- (8) Peres, C.; Matos, A. I.; Conniot, J.; Sainz, V.; Zupančič, E.; Silva, J. M.; Graça, L.; Sá Gaspar, R.; Prêat, V.; Florindo, H. F. Poly(lactic acid)-based particulate systems are promising tools for immune modulation. *Acta Biomater.* **2017**, *48*, 41–57.
- (9) Gao, S.; Tang, G.; Hua, D.; Xiong, R.; Han, J.; Jiang, S.; Zhang, Q.; Huang, C. Stimuli-responsive bio-based polymeric systems and their applications. *J. Mater. Chem. B* **2019**, *7*, 709–729.
- (10) Elsabahy, M.; Wooley, K. L. Design of polymeric nanoparticles for biomedical delivery applications. *Chem. Soc. Rev.* **2012**, *41*, 2545–2561.
- (11) Ekladios, I.; Colson, Y. L.; Grinstaff, M. W. Polymer–drug conjugate therapeutics: advances, insights and prospects. *Nat. Rev. Drug Discovery* **2019**, *18*, 273–294.
- (12) Cabral, H.; Miyata, K.; Osada, K.; Kataoka, K. Block copolymer micelles in nanomedicine applications. *Chem. Rev.* **2018**, *118*, 6844–6892.
- (13) Michalski, A.; Brzezinski, M.; Lapienis, G.; Biela, T. Star-shaped and branched polylactides: Synthesis, characterization, and properties. *Prog. Polym. Sci.* **2019**, *89*, 159–212.
- (14) Hillmyer, M. A.; Tolman, W. B. Aliphatic polyester block polymers: Renewable, degradable, and sustainable. *Acc. Chem. Res.* **2014**, *47*, 2390–2396.
- (15) Zhang, X.; Fevre, M.; Jones, G. O.; Waymouth, R. M. Catalysis as an enabling science for sustainable polymers. *Chem. Rev.* **2018**, *118*, 839–885.
- (16) Schneiderman, D. K.; Hillmyer, M. A. Aliphatic polyester block polymer design. *Macromolecules* **2016**, *49*, 2419–2428.
- (17) Bartnikowski, M.; Dargaville, T. R.; Ivanovski, S.; Huttmacher, D. W. Degradation mechanisms of polycaprolactone in the context of chemistry, geometry and environment. *Prog. Polym. Sci.* **2019**, *96*, 1–20.
- (18) Attia, M. F.; Brummel, B. R.; Lex, T. R.; Van Horn, B. A.; Whitehead, D. C.; Alexis, F. Recent advances in polyesters for biomedical imaging. *Adv. Healthcare Mater.* **2018**, *7*, 1800798.
- (19) Zhao, J.; Weng, G.; Li, J.; Zhu, J.; Zhao, J. Polyester-based nanoparticles for nucleic acid delivery. *Mater. Sci. Eng., C* **2018**, *92*, 983–994.
- (20) Castro-Aguirre, E.; Iñiguez-Franco, F.; Samsudin, H.; Fang, X.; Auras, R. Poly(lactic acid)—Mass production, processing, industrial applications, and end of life. *Adv. Drug Delivery Rev.* **2016**, *107*, 333–366.
- (21) Kamaraj, N.; Rajaguru, P. Y.; Issac, P. k.; Sundaresan, S. Fabrication, characterization, in vitro drug release and glucose uptake activity of 14-deoxy, 11, 12-didehydroandrographolide loaded polycaprolactone nanoparticles. *Asian J. Pharm. Sci.* **2017**, *12*, 353–362.
- (22) Budhian, A.; Siegel, S. J.; Winey, K. I. Controlling the in vitro release profiles for a system of haloperidol-loaded PLGA nanoparticles. *Int. J. Pharm.* **2008**, *346*, 151–159.
- (23) Bandelli, D.; Alex, J.; Weber, C.; Schubert, U. S. Polyester stereocomplexes beyond PLA: Could synthetic opportunities revolutionize established material blending? *Macromol. Rapid Commun.* **2020**, *41*, 1900560.
- (24) Lyubov, D. M.; Tolpygin, A. O.; Trifonov, A. A. Rare-earth metal complexes as catalysts for ring-opening polymerization of cyclic esters. *Coord. Chem. Rev.* **2019**, *392*, 83–145.
- (25) Bandelli, D.; Weber, C.; Schubert, U. S. Strontium isopropoxide: A highly active catalyst for the ring-opening polymerization of lactide and various lactones. *Macromol. Rapid Commun.* **2019**, *40*, 1900306.
- (26) Ottou, W. N.; Sardon, H.; Mecerreyes, D.; Vignolle, J.; Taton, D. Update and challenges in organo-mediated polymerization reactions. *Prog. Polym. Sci.* **2016**, *56*, 64–115.
- (27) Kamber, N. E.; Jeong, W.; Waymouth, R. M.; Pratt, R. C.; Lohmeijer, B. G. G.; Hedrick, J. L. Organocatalytic ring-opening polymerization. *Chem. Rev.* **2007**, *107*, 5813–5840.
- (28) Bandelli, D.; Helbing, C.; Weber, C.; Seifert, M.; Muljajew, I.; Jandt, K. D.; Schubert, U. S. Maintaining the hydrophilic–hydrophobic balance of polyesters with adjustable crystallinity for tailor-made nanoparticles. *Macromolecules* **2018**, *51*, 5567–5576.
- (29) Bandelli, D.; Alex, J.; Helbing, C.; Ueberschaar, N.; Görls, H.; Bellstedt, P.; Weber, C.; Jandt, K. D.; Schubert, U. S. Poly(3-ethylglycolide): a well-defined polyester matching the hydrophilic hydrophobic balance of PLA. *Polym. Chem.* **2019**, *10*, 5440–5451.
- (30) Liénard, R.; Zaldua, N.; Josse, T.; Winter, J. D.; Zubitur, M.; Mugica, A.; Iturrospe, A.; Arbe, A.; Coulembier, O.; Müller, A. J. Synthesis and characterization of double crystalline cyclic diblock copolymers of poly(ϵ -caprolactone) and poly(l(d)-lactide) (c(PCL-b-PL(D)LA)). *Macromol. Rapid Commun.* **2016**, *37*, 1676–1681.
- (31) Guo, X.; Rong, Z.; Ying, X. Calculation of hydrophile–lipophile balance for polyethoxylated surfactants by group contribution method. *J. Colloid Interface Sci.* **2006**, *298*, 441–450.
- (32) Song, Q.; Xia, Y.; Hu, S.; Zhao, J.; Zhang, G. Tuning the crystallinity and degradability of PCL by organocatalytic copolymerization with δ -hexalactone. *Polymer* **2016**, *102*, 248–255.
- (33) Lohmeijer, B. G. G.; Pratt, R. C.; Leibfarth, F.; Logan, J. W.; Long, D. A.; Dove, A. P.; Nederberg, F.; Choi, J.; Wade, C.; Waymouth, R. M.; Hedrick, J. L. Guanidine and amidine organocatalysts for ring-opening polymerization of cyclic esters. *Macromolecules* **2006**, *39*, 8574–8583.
- (34) Harwood, H. J.; Ritchey, W. M. The characterization of sequence distribution in copolymers. *J. Polym. Sci., Part B: Polym. Lett.* **1964**, *2*, 601–607.
- (35) Galvan, R.; Tirrell, M. On the average sequence length in copolymers. *J. Polym. Sci., Part A: Polym. Chem.* **1986**, *24*, 803–807.

(36) Harrison, S.; Ercole, F.; Muir, B. W. Living spontaneous gradient copolymers of acrylic acid and styrene: One-pot synthesis of pH-responsive amphiphiles. *Polym. Chem.* **2010**, *1*, 326–332.

(37) Save, M.; Schappacher, M.; Soum, A. Controlled ring-opening polymerization of lactones and lactides initiated by lanthanum isopropoxide, 1. General aspects and kinetics. *Macromol. Chem. Phys.* **2002**, *203*, 889–899.

(38) Mayo, F. R.; Lewis, F. M. Copolymerization. I. A basis for comparing the behavior of monomers in copolymerization; the copolymerization of styrene and methyl methacrylate. *J. Am. Chem. Soc.* **1944**, *66*, 1594–1601.

(39) Meyer, V. E.; Lowry, G. G. Integral and differential binary copolymerization equations. *J. Polym. Sci., Part A: Gen. Pap.* **1965**, *3*, 2843–2851.

(40) Beckingham, B. S.; Sanoja, G. E.; Lynd, N. A. Simple and accurate determination of reactivity ratios using a nonterminal model of chain copolymerization. *Macromolecules* **2015**, *48*, 6922–6930.

(41) Lynd, N. A.; Ferrier, R. C.; Beckingham, B. S. Recommendation for accurate experimental determination of reactivity ratios in chain copolymerization. *Macromolecules* **2019**, *52*, 2277–2285.

(42) Pascual, A.; Sardón, H.; Ruipérez, F.; Gracia, R.; Sudam, P.; Veloso, A.; Mecerreyes, D. Experimental and computational studies of ring-opening polymerization of ethylene brassylate macrolactone and copolymerization with ϵ -caprolactone and TBD-guanidine organic catalyst. *J. Polym. Sci., Part A: Polym. Chem.* **2015**, *53*, 552–561.

(43) Simón, L.; Goodman, J. M. The mechanism of TBD-catalyzed ring-opening polymerization of cyclic esters. *J. Org. Chem.* **2007**, *72*, 9656–9662.

(44) Muñoz-Bonilla, A.; Cerrada, M. L.; Fernández-García, M.; Kubacka, A.; Ferrer, M.; Fernández-García, M. Biodegradable polycaprolactone-titania nanocomposites: Preparation, characterization and antimicrobial properties. *Int. J. Mol. Sci.* **2013**, *14*, 9249–9266.

(45) Li, L.; Meng, F.; Zhong, Z.; Byelov, D.; de Jeu, W. H.; Feijen, J. Morphology of a highly asymmetric double crystallizable poly(ϵ -caprolactone-*b*-ethylene oxide) block copolymer. *J. Chem. Phys.* **2007**, *126*, 024904.

(46) Gu, L.; Shen, Z.; Zhang, S.; Lu, G.; Zhang, X.; Huang, X. Novel amphiphilic centipede-like copolymer bearing polyacrylate backbone and poly(ethylene glycol) and polystyrene side chains. *Macromolecules* **2007**, *40*, 4486–4493.

(47) Weber, C.; Wagner, M.; Baykal, D.; Hoepfener, S.; Paulus, R. M.; Festag, G.; Altuntas, E.; Schacher, F. H.; Schubert, U. S. Easy access to amphiphilic heterografted poly(2-oxazoline) comb copolymers. *Macromolecules* **2013**, *46*, 5107–5116.

Supporting information for

Copolymerization of caprolactone isomers to obtain nanoparticles with constant hydrophobicity and tunable crystallinity

*Damiano Bandelli,^{1,2} Irina Muljajew,^{1,2} Karl Scheuer,³ Johannes B. Max,^{1,2} Christine Weber,^{1,2}
Felix H. Schacher,^{1,2} Klaus D. Jandt,^{2,3} Ulrich S. Schubert^{1,2*}*

¹ Laboratory of Organic and Macromolecular Chemistry (IOMC), Friedrich Schiller University
Jena, Humboldtstr. 10, 07743 Jena, Germany

² Jena Center for Soft Matter (JCSM), Friedrich Schiller University Jena, Philosophenweg 7,
07743 Jena, Germany

³ Chair of Materials Science (CMS), Department of Materials Science and Technology, Otto Schott
Institute of Materials Research, Faculty of Physics and Astronomy, Friedrich Schiller University
Jena, Löbdergraben 32, 07743 Jena, Germany

* Correspondence to U. S. Schubert (ulrich.schubert@uni-jena.de)

Table S1: Details on the homopolymerization kinetics and test reactions for the ROP of ε -caprolactone and δ -caprolactone.

Entry	Monomer	[M] ₀ [mol L ⁻¹]	[M]:[BnOH]:[TBD]	n _M [mmol]	V _{ov} [mL]	Conversion [%] (time [h])	M _{n,SEC} [kg mol ⁻¹] (\bar{M})
1	δ CL	8.3	50:1:1	8.3	0.12	92 (4)	7 (1.13)
2	δ CL	8.3	100:1:1	8.3	0.12	2 (3)	n.d.
3	δ CL	8.3	100:1:2	8.3	0.12	67 (4)	7 (1.12)
4	δ CL	1	100:1:2	1	1	34 (24)	3 (1.41)
5	δ CL	2	100:1:2	2	1	72 (24)	7 (1.34)
6	δ CL	3	100:1:2	3	1	82 (24)	9 (1.32)
7	δ CL	4	100:1:2	4	1	83 (24)	9 (1.35)
8	δ CL	2	200:1:1	4	2	4 (24)	1 (1.17)
9	δ CL	2	200:1:2	4	2	7 (5.5)	1 (1.23)
10	δ CL	4	201:1:2	4	1	15 (48)	2 (1.21)
11	δ CL	4	200:1:4	4	1	51 (2)	7 (1.09)
12	δ CL	4	200:1:6	4	1	65 (2)	9 (1.10)
13	δ CL	4	200:1:8	4	1	73 (2)	9 (1.11)
14	ε CL	1	100:1:2	1	1	95 (24)	14 (1.95)
15	ε CL	2	100:1:2	2	1	92 (4.5)	13 (2.27)
16	ε CL	3	100:1:2	3	1	97 (4.5)	14 (2.62)
17	ε CL	4	100:1:2	4	1	68 (1)	14 (1.41)
18	ε CL	2	200:1:0.5	4	2	36 (24)	15 (1.15)
19	ε CL	4	200:1:0.5	4	1	48 (6)	18 (1.23)
20	ε CL	2	200:1:1	4	2	50 (8)	20 (1.17)

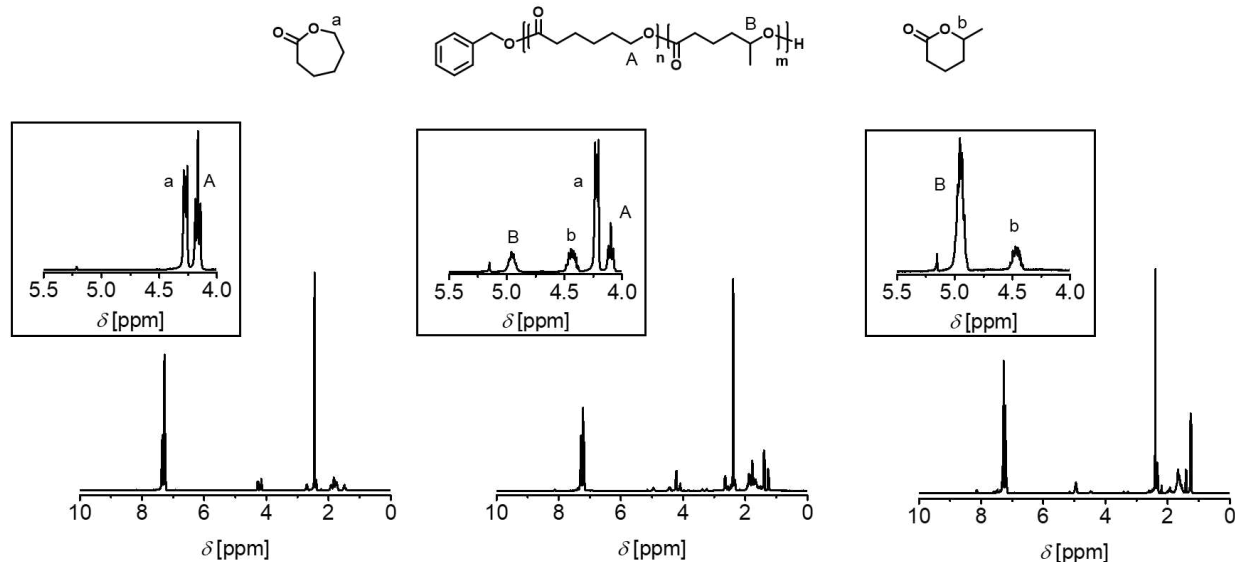


Figure S1: Exemplary ^1H NMR spectra (300 MHz, CDCl_3) of reaction mixtures of the ROP of ϵCL and δCL used to determine the monomer conversions. The zooms depict the chemical shift region used for the calculation assignments of the utilized signals to the schematic representation of monomers and polymers. **Left:** ^1H NMR spectrum of the homopolymerization reaction of ϵCL employing a $[\epsilon\text{CL}]_0:[\text{BnOH}]_0:[\text{TBD}]_0$ of 200:1:1, $[\epsilon\text{CL}]_0$ of 4 mol L^{-1} , collected after a reaction time of 8 h. **Center:** ^1H NMR spectrum of the statistical copolymerization reaction of ϵCL and δCL employing a $[\epsilon\text{CL}]_0 : [\delta\text{CL}]_0$ feed ratio of 50:50, a $[\text{CL}]_0:[\text{BnOH}]_0:[\text{TBD}]_0$ of 100:1:2 and $[\text{CL}]_0$ of 4 mol L^{-1} , collected after a reaction time of 3 h. **Right:** ^1H NMR spectrum of the homopolymerization reaction of δCL employing a $[\delta\text{CL}]_0:[\text{BnOH}]_0:[\text{TBD}]_0$ of 100:1:2, $[\delta\text{CL}]_0$ of 4 mol L^{-1} , collected after a reaction time of 9 h.

Homopolymerization kinetics of δ CL

First experiments were conducted in the bulk (**Figure S2-S3**) because the high initiator concentration during the ROP increases the overall polymerization rate. Although a low $[\delta\text{CL}]_0:[\text{BnOH}]_0:[\text{TBD}]_0$ ratio of 50:1:1 resulted in a linear increase of molar mass with respect to monomer conversion and a first order kinetic behavior, only low conversions were obtained at an increased feed ratio of 100:1:1. Also an increased catalyst amount (100:1:2) failed to increase the monomer conversion above 67%.

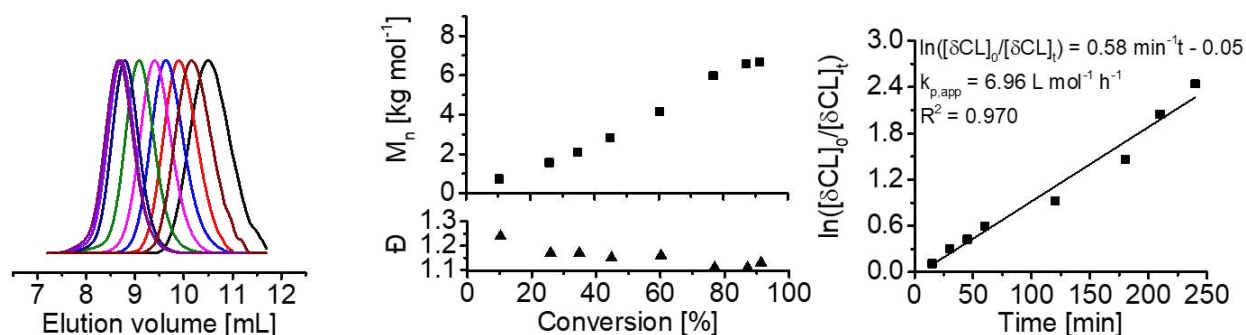


Figure S2: Kinetic studies of the ROP of δ CL in bulk employing a $[\delta\text{CL}]:[\text{BnOH}]:[\text{TBD}]$ of 50:1:1 (**Table S1**, entry **1**). **Left:** Overlay of SEC elugrams (CHCl_3 , RID). **Center:** Molar mass and dispersity evolution over conversion. **Right:** First order kinetic plot and linear extrapolation of experimental data (black line).

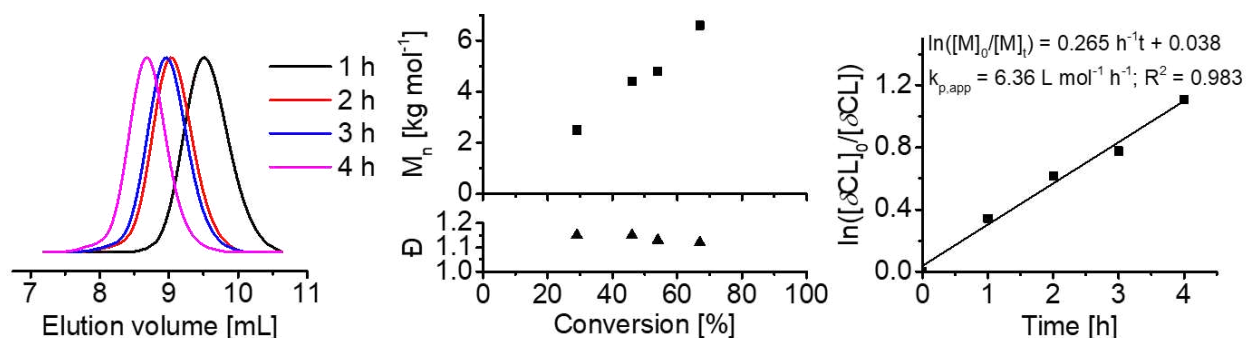


Figure S3: Kinetic studies of the ROP of δCL in bulk employing a $[\delta\text{CL}]:[\text{BnOH}]:[\text{TBD}]$ of 100:1:2 (**Table S1**, entry 3). **Left:** Overlay of SEC elugrams (CHCl_3 , RID). **Center:** Molar mass and dispersity evolution over conversion. **Right:** First order kinetic plot and linear extrapolation of experimental data (black line).

We hence focused on the ROP of δCL in toluene. The feed ratio of 100:1:2 was kept constant, but the initial monomer concentration $[\delta\text{CL}]_0$ was varied ($[\delta\text{CL}]_0 = 1, 2, 3$ and 4 mol L^{-1} ; **Figure 1**, **Figure S4-S5**). SEC analyses revealed monomodal molar mass distributions for all samples, while the linear increase of the molar masses with respect to monomer conversion suggested a polymerization that was controlled with respect to molar mass. Low to moderate dispersity values (\bar{D}) below 1.4 were obtained. Besides, P δCL revealed a similar hydrodynamic volume as the calibration standard polystyrene (PS) in the chloroform-based eluent because the measured molar masses $M_{n,\text{SEC}}$ were in agreement with the values expected from the monomer to initiator ratio and conversion.

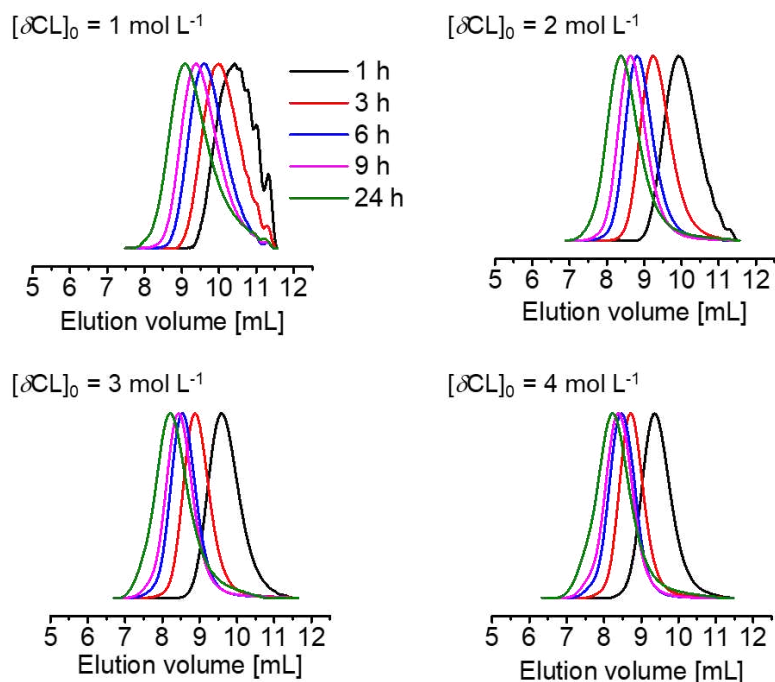


Figure S4: Overlay of SEC elugrams (CHCl_3 , RID) of the homopolymerization kinetics of δCL employing a $[\delta\text{CL}]:[\text{BnOH}]:[\text{TBD}]$ ratio of 100:1:2 and $[\delta\text{CL}]_0$ from 1 to 4 mol L^{-1} (**Table S1**, entries 4 to 7).

All solution ROP kinetics revealed a deviation from first-order behavior. The polymerization rate decreased throughout the course of the reaction. In principle, this may be due to termination, deactivation of the catalyst, or due to an equilibrium process. Irrespective of the initial monomer concentration, the monomer concentration approached a threshold value of 0.55 mol L^{-1} that represents the monomer equilibrium concentration $[\delta\text{CL}]_{\text{eq}}$ at room temperature. The value is in accordance with thermodynamic data reported for the diphenyl phosphate catalyzed ROP of δCL reported by Hillmyer and coworkers.¹ The respective kinetic equations describing the equilibrium process²⁻⁴ were hence applied to calculate the apparent polymerization rate constant ($k_{\text{p, app}}$ average value of $5.4 \text{ L mol}^{-1} \text{ h}^{-1}$).

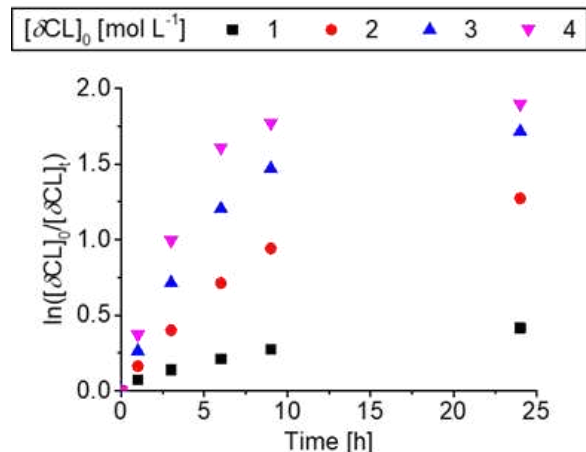


Figure S5: First order kinetic plots for the polymerization of δCL employing a $[\delta\text{CL}]:[\text{BnOH}]:[\text{TBD}]$ of 100:1:2 and $[\delta\text{CL}]_0$ from 1 to 4 mol L⁻¹ (**Table S1**, entries 4 to 7).

As the monomer equilibrium concentration prohibited a quantitative conversion of δCL , the monomer to initiator feed ratio was increased to 200:1 in order to obtain P δCL with higher degrees of polymerization (DP) and lower dispersity values. However, conversions remained low for polymerizations conducted using 1 or 2 equivalents of TBD. In contrast, an increased catalyst amount of 4, 6 or 8 equivalents enabled conversions above 50% as well as the synthesis of P δCL with narrow molar mass distribution ($\mathcal{D} \approx 1.10$, **Figure S6**). In conclusion, higher catalyst amounts were needed to obtain well-defined P δCL homopolymers.

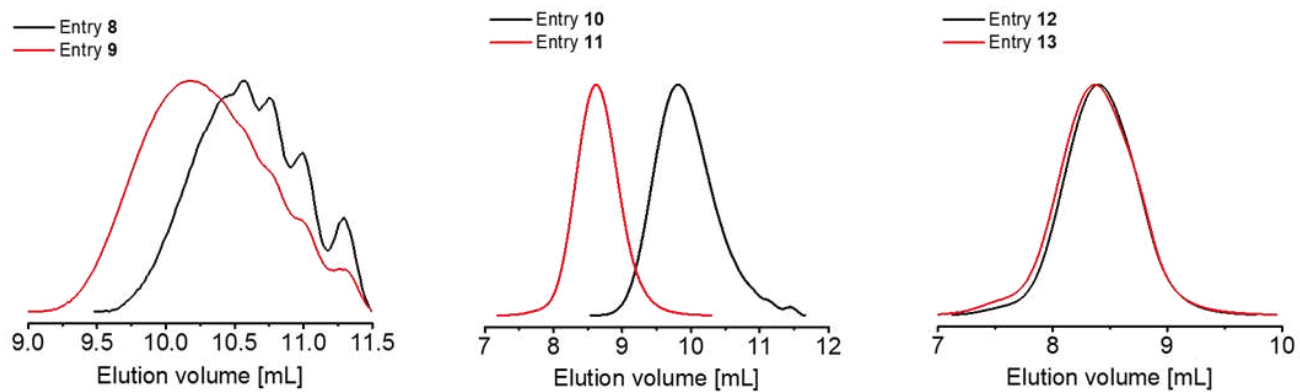


Figure S6: Overlay of SEC elugrams (CHCl_3 , RID) of the homopolymerization of δCL employing a $[\delta\text{CL}]:[\text{BnOH}]$ ratio of 200:1 (**Table S1**, entries **8** to **13**).

Homopolymerization kinetics of ϵ CL

Unfortunately, the trend was reversed for the homopolymerization of ϵ CL. Similar to Lohmeijer *et al.*,⁵ we observed that P ϵ CL with low dispersity required a reduced amount of TBD, *i.e.* [BnOH]:[TBD] ratios of 1:1 or 1:0.5. A [BnOH]:[TBD] ratio of 1:2 as a compromise between the optimum ROP conditions of both monomers, *i.e.* ϵ CL and δ CL was selected for the statistical copolymerization and, hence, studied in detail with respect to an optimization of the monomer concentration $[\epsilon\text{CL}]_0$ in toluene. For this purpose, similar homopolymerization kinetics were conducted as described above for δ CL (**Figures S7-S13**). The unsubstituted ϵ CL polymerized faster ($k_{p, \text{app}}$ average value of $13.7 \text{ L mol}^{-1} \text{ h}^{-1}$) than the substituted lactone δ CL. In particular, for ROP at lower initial monomer concentration, rather high dispersity values ($\bar{D} \geq 1.9$) were observed. A $[\text{CL}]_0$ of 4 mol L^{-1} was also favorable with respect to the monomer equilibrium concentration of δ CL, as it allowed higher monomer conversions maintaining low dispersity. These conditions were hence selected for the statistical copolymerization of ϵ CL and δ CL.

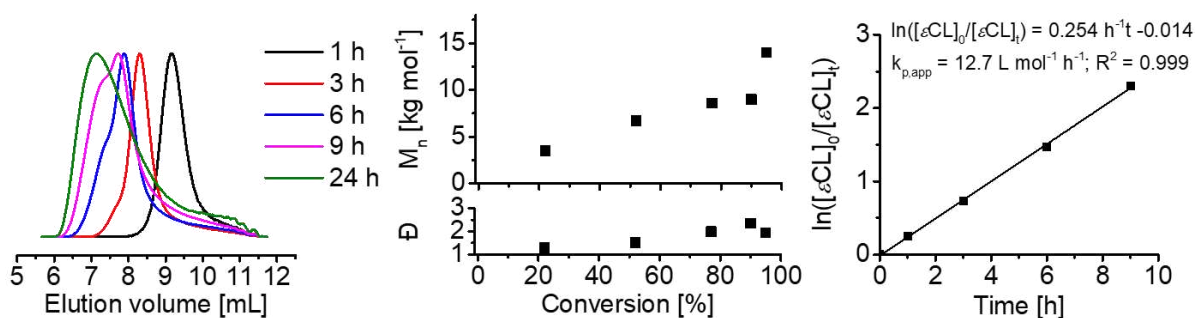


Figure S7: Kinetic studies of the ROP of ϵ CL employing a $[\epsilon\text{CL}]:[\text{BnOH}]:[\text{TBD}]$ of 100:1:2 and $[\epsilon\text{CL}]_0 = 1 \text{ mol L}^{-1}$ in toluene at room temperature (**Table S1**, entry 14). **Left:** Overlay of SEC elugrams (CHCl_3 , RID). **Center:** Dependence of the molar mass and dispersity on monomer conversion. **Right:** First order kinetic plot and linear extrapolation of experimental data (black line).

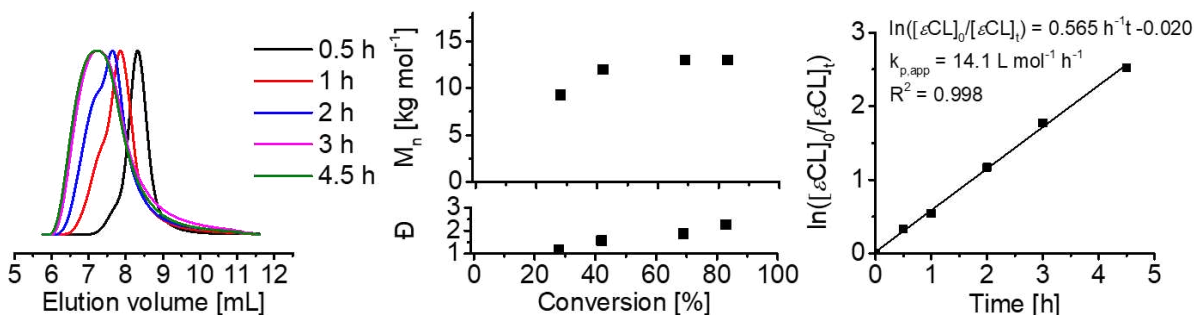


Figure S8: Kinetic studies of the ROP of ϵ CL employing a $[\epsilon\text{CL}]:[\text{BnOH}]:[\text{TBD}]$ of 100:1:2 and $[\epsilon\text{CL}]_0 = 2 \text{ mol L}^{-1}$ in toluene at room temperature (Table S1, entry 15). **Left:** Overlay of SEC elugrams (CHCl_3 , RID). **Center:** Dependence of the molar mass and dispersity on monomer conversion. **Right:** First order kinetic plot and linear extrapolation of experimental data (black line).

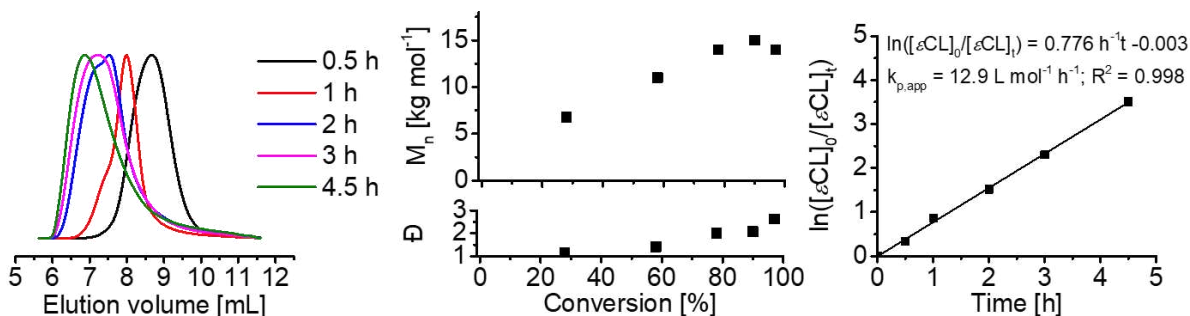


Figure S9: Kinetic studies of the ROP of ϵ CL employing a $[\epsilon\text{CL}]:[\text{BnOH}]:[\text{TBD}]$ of 100:1:2 and $[\epsilon\text{CL}]_0 = 3 \text{ mol L}^{-1}$ in toluene at room temperature (Table S1, entry 16). **Left:** Overlay of SEC elugrams (CHCl_3 , RID). **Center:** Dependence of the molar mass and dispersity on monomer conversion. **Right:** First order kinetic plot and linear extrapolation of experimental data (black line).

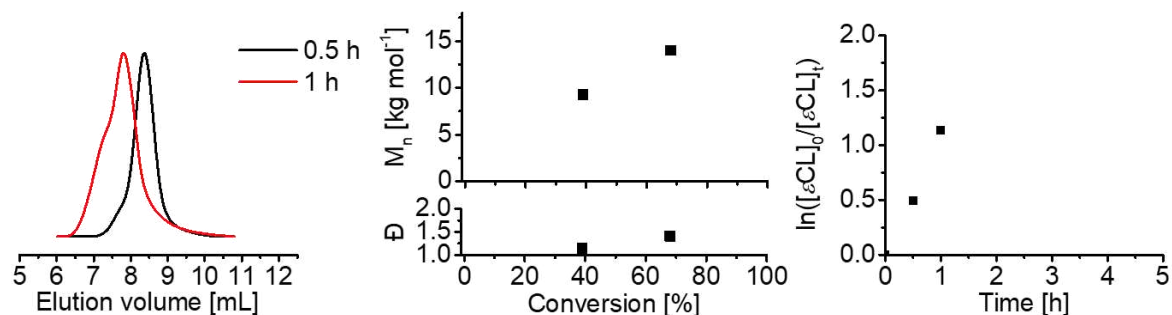


Figure S10: Test reactions of the ROP of ϵCL employing a $[\epsilon\text{CL}]:[\text{BnOH}]:[\text{TBD}]$ of 100:1:2 and $[\epsilon\text{CL}]_0 = 4 \text{ mol L}^{-1}$ in toluene at room temperature (Table S1, entry 17). **Left:** Overlay of SEC elugrams (CHCl_3 , RID). **Center:** Dependence of the molar mass and dispersity on monomer conversion. **Right:** First order kinetic plot.

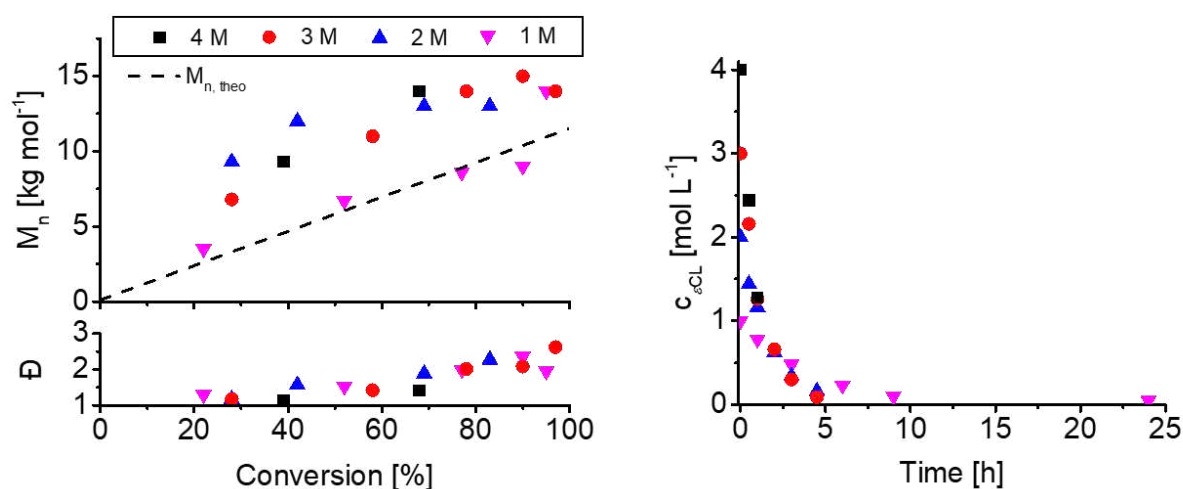


Figure S11: Kinetic plots for the TBD-catalyzed ROP of ϵCL in toluene at room temperature employing an initial $[\epsilon\text{CL}]_0:[\text{BnOH}]_0:[\text{TBD}]_0$ ratio of 100:1:2 at initial monomer concentrations $[\epsilon\text{CL}]_0$ of 4, 3, 2 and 1 mol L^{-1} . **Left:** Dependence of the molar mass $M_{n, \text{SEC}}$ and dispersity \bar{D} on the monomer conversion. The dotted line represents the theoretical molar mass $M_{n, \text{theo}}$ calculated according to $M_{n, \text{theo}} = M_{\epsilon\text{CL}} \times ([\epsilon\text{CL}]_0/[\text{BnOH}]_0) \times \text{conversion} + M_{\text{BnOH}}$. **Right:** Evolution of the residual monomer concentration $[\epsilon\text{CL}]$ over time.

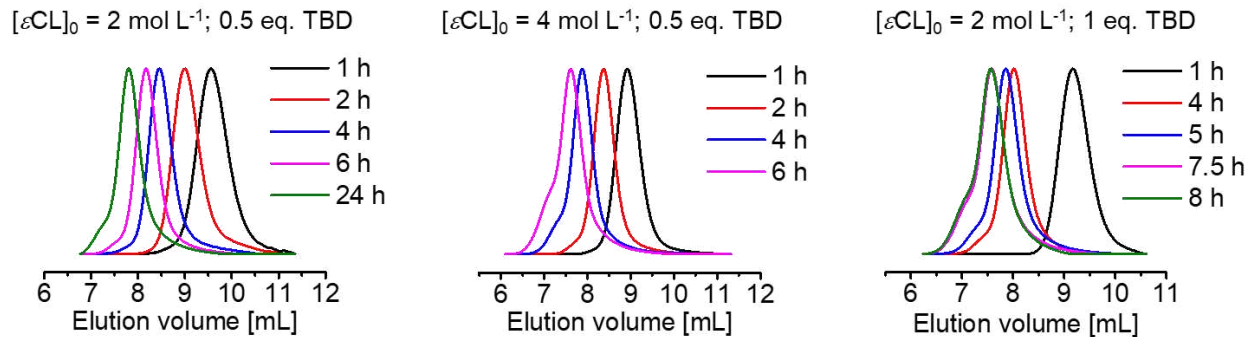


Figure S12: Overlay of SEC elugrams taken during the ϵCL homopolymerization in toluene at room temperature employing a $[\epsilon\text{CL}]:[\text{BnOH}]$ ratio of 200:1. Initial monomer concentration $[\epsilon\text{CL}]_0$ and catalyst concentration were varied as indicated.

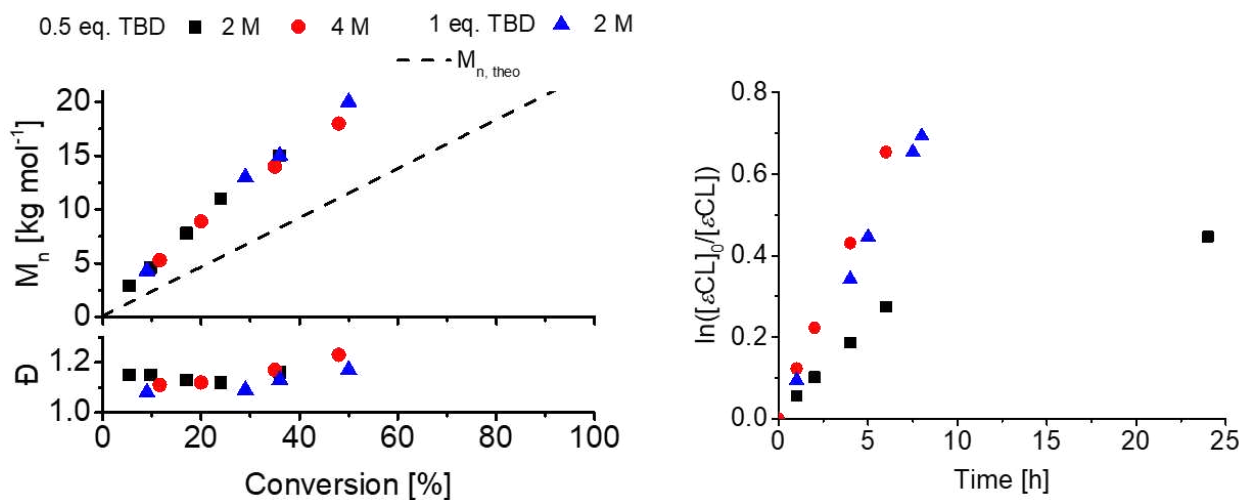


Figure S13: Kinetic plots for the polymerization of ϵCL in toluene at room temperature employing a $[\epsilon\text{CL}]:[\text{BnOH}]$ of 200:1. Initial monomer concentration $[\epsilon\text{CL}]_0$ and catalyst concentration were varied as indicated in the legend. **Left:** Dependence of the molar mass $M_{n, \text{SEC}}$ and dispersity \bar{D} on the monomer conversion. **Right:** First order kinetic plots.

Additional discussion of the monomer equilibrium concentration

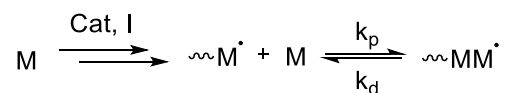
From a thermodynamic perspective, the homopolymerization of ε and δ -lactones show negative values for both enthalpy and entropy of polymerization. The latter results in a ceiling temperature for each monomer and a monomer equilibrium concentration ($[M]_{eq}$) that is dependent on the reaction temperature. The $[M]_{eq}$ can be hence calculated according to **equation 1**:

$$[M]_{eq} = \frac{\overline{DP}_n - 1}{\overline{DP}_n} \times e^{\left(\frac{\Delta H_p^0}{RT} - \frac{\Delta S_p^0}{R}\right)} \quad (\text{equation 1})$$

The homopolymerization kinetics of δ CL employing an initial monomer concentration of 1, 2, 3 and 4 mol L⁻¹ show that after an initial monomer conversion, a plateau in the monomer concentration is reached at 0.55 mol L⁻¹. The comparison with the value calculated from literature data show that 0.54 mol L⁻¹ represents the monomer equilibrium concentration for the polymerization of δ CL at 23 °C.³ The latter suggests that the plateau seen during polymerizations is related to equilibrium processes, and therefore the monomer consumption cannot proceed any further. Similarly to δ CL, also the consumption of ε CL proceeded with the development of a plateau in the monomer concentration vs. time plots. The low monomer equilibrium concentration of ε CL (1.2x10⁻² mol L⁻¹) enabled the high conversions reached during polymerization (**Figure S13**).⁴

Kinetic evaluation for the homopolymerization of δ CL and ϵ CL

Representing a reversible polymerization, the ROP of lactones is defined from a kinetic perspective, by a polymerization rate constant k_p as well as a depolymerization rate constant k_d .



The kinetic equation related to the reversible polymerization can be written as:

$$\frac{d[M]}{dt} = k_p[M][M^*] - k_d[MM^*] \quad (\text{equation 2})$$

where $[M]$, $[M^*]$ and $[MM^*]$ are the concentration of the monomer and the propagating species at time t , respectively. The resolution of **equation 2** leads to **equation 3**:²

$$[M] = [M]_{eq} + ([M]_0 - [M]_{eq}) \times e^{-k_{p,app}[I]_0 t} \quad (\text{equation 3})$$

where $[M]_0$ and $[I]_0$ are the initial concentration of monomer and initiator respectively, while $[M]_{eq}$ is the monomer equilibrium concentration.

However, the ROP of lactones catalyzed by mTBD/thioureas was dependent on the initial concentration of the catalyst. Equation 2 can be therefore rearranged as follows:⁵

$$[M] = [M]_{eq} + ([M]_0 - [M]_{eq}) \times e^{-k_{p,app}[C]_0 t} \quad (\text{equation 4})$$

The latter can be written as:

$$\text{Conversion [\%]} = 100 \times \left(1 - \frac{[M]_{eq}}{[M]_0}\right) \times (1 - e^{-k_{p,app}[C]_0 t}) \quad (\text{equation 5})$$

In principle, fitting of kinetic data to **equation 5** enables the calculation of parameters such as $[M]_{eq}$ and the apparent polymerization rate constant $k_{p,app}$. Aiming to calculate the kinetic constants of homopolymerization for δ CL as well as for ε CL, the conversion vs. time plot were fitted according to equation 4 (**Figure S14, Table S2**).

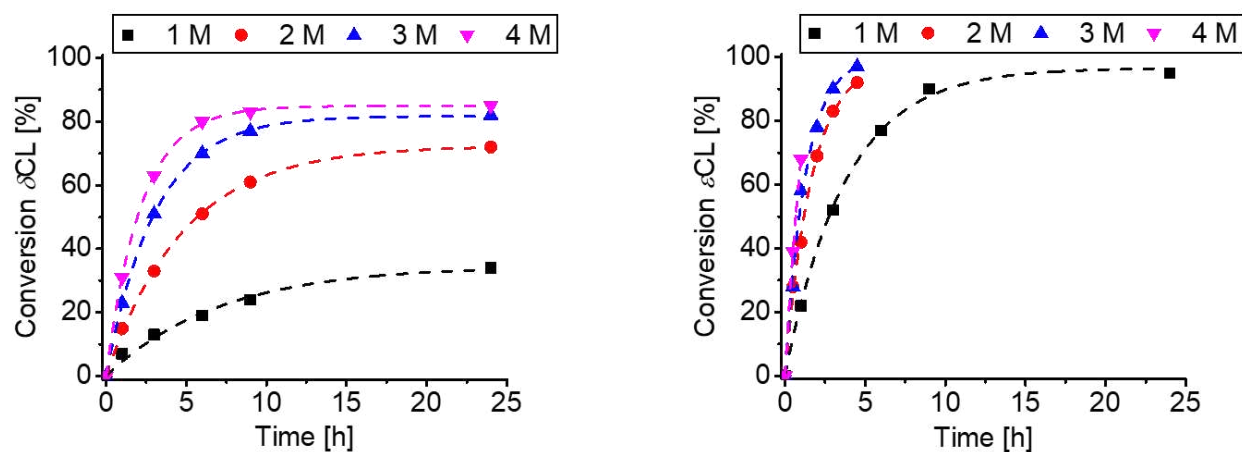


Figure S14: Fitting of kinetic data of the polymerization of δ CL and ε CL in toluene according to **equation 5** (room temperature, $[CL]:[BnOH]:[TBD] = 100:1:2$) (**Table S1**, entries **5 to 8** and **15 to 18**, respectively).

Table S2: Apparent polymerization rate constants and monomer equilibrium concentrations obtained from fitting of the kinetic data of the ROP of δ CL (entry 5 to 8) and ε CL (entry 15 to 17). The corresponding fits are depicted in **Figure S14**.

Entry ^{a)}	R ² ^{b)}	k _{p, app} ^{b)} [L mol ⁻¹ h ⁻¹]	[M] _{eq} ^{b)} [mol L ⁻¹]	[M] _{eq} ^{c)} [mol L ⁻¹]
5	0.985	7.05	0.65	0.54
6	0.999	5.15	0.55	0.54
7	0.999	5.43	0.55	0.54
8	0.999	5.67	0.60	0.54
15	0.998	13.3	0.034	0.015
16	0.997	14.8	0.017	0.015
17	0.994	12.9	0.015	0.015

^{a)} According to **Table S1**.

^{b)} Fitting the conversion over time plots according to **equation 5**.

^{c)} Calculated according to **equation 1** from literature data.

Copolymerization kinetics of ϵ CL and δ CL

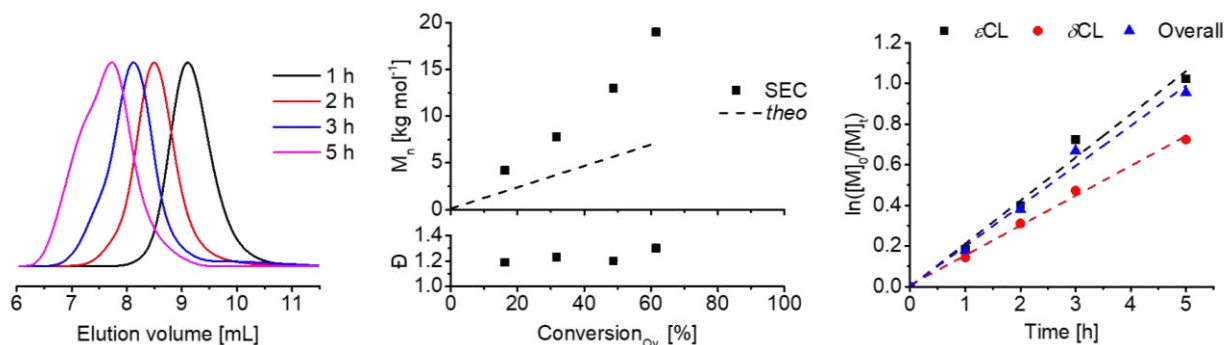


Figure S15: Kinetic studies of the copolymerization of ϵ CL and δ CL employing a $[\epsilon$ CL]: $[\delta$ CL]: $[\text{BnOH}]$: $[\text{TBD}]$ of 80:20:1:2 ($[\text{CL}]_0 = 4 \text{ mol L}^{-1}$ in toluene at room temperature). **Left:** Overlay of SEC elugrams (CHCl_3 , RID). **Center:** Dependence of the molar mass $M_{n,\text{SEC}}$ and dispersity \bar{D} on the overall monomer conversion. **Right:** First order kinetic plot and linear extrapolation of experimental data (dotted lines).

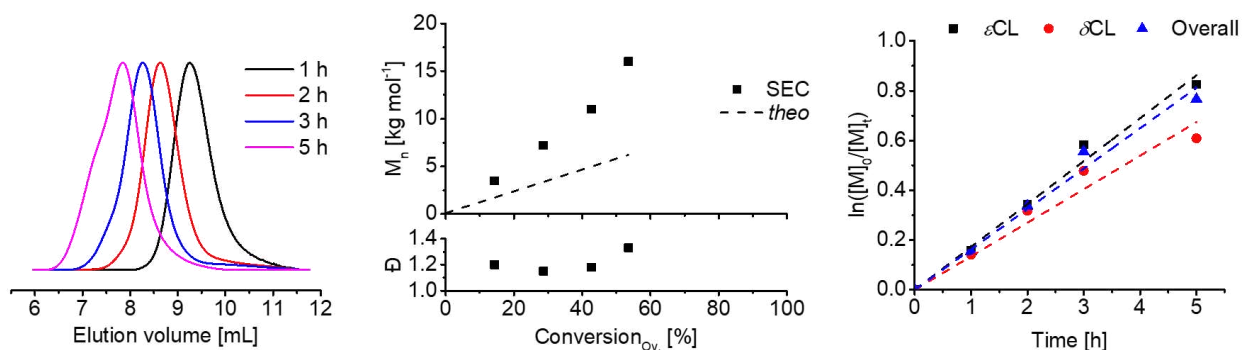


Figure S16: Kinetic studies of the copolymerization of ϵ CL and δ CL employing a $[\epsilon$ CL]: $[\delta$ CL]: $[\text{BnOH}]$: $[\text{TBD}]$ of 75:25:1:2 ($[\text{CL}]_0 = 4 \text{ mol L}^{-1}$ in toluene at room temperature) **Left:** Overlay of SEC elugrams (CHCl_3 , RID). **Center:** Dependence of the molar mass $M_{n,\text{SEC}}$ and dispersity \bar{D} on the overall monomer conversion **Right:** First order kinetic plot and linear extrapolation of experimental data (dotted lines).

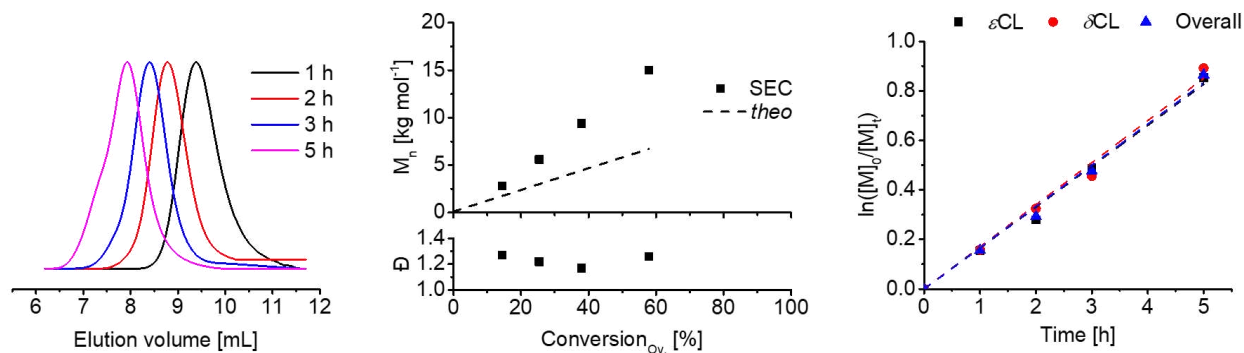


Figure S17: Kinetic studies of the copolymerization of ϵ CL and δ CL employing a $[\epsilon\text{CL}]:[\delta\text{CL}]:[\text{BnOH}]:[\text{TBD}]$ of 70:30:1:2 ($[\text{CL}]_0 = 4 \text{ mol L}^{-1}$ in toluene at room temperature). **Left:** Overlay of SEC elugrams (CHCl_3 , RID). **Center:** Dependence of the molar mass $M_{n,\text{SEC}}$ and dispersity \mathcal{D} on the overall monomer conversion **Right** First order kinetic plot and linear extrapolation of experimental data (dotted lines).

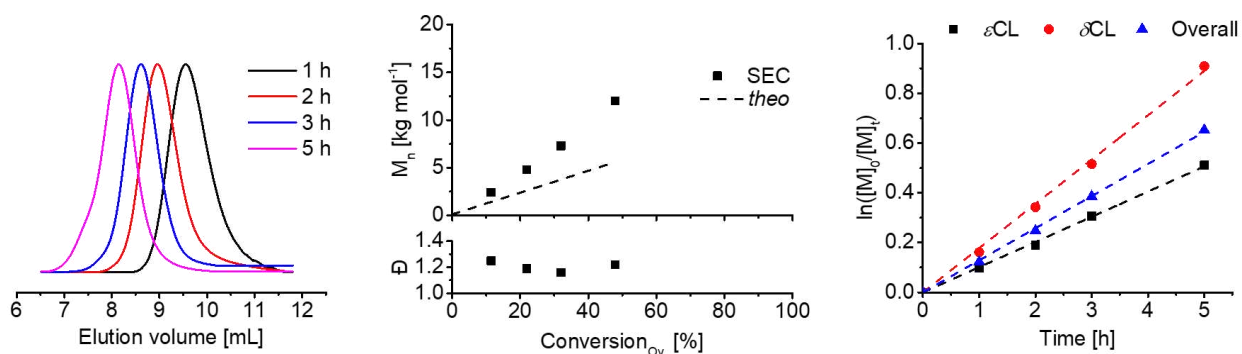


Figure S18: Kinetic studies of the copolymerization of ϵ CL and δ CL employing a $[\epsilon\text{CL}]:[\delta\text{CL}]:[\text{BnOH}]:[\text{TBD}]$ of 60:40:1:2 ($[\text{CL}]_0 = 4 \text{ mol L}^{-1}$ in toluene at room temperature). **Left:** Overlay of SEC elugrams (CHCl_3 , RID). **Center:** Dependence of the molar mass $M_{n,\text{SEC}}$ and dispersity \mathcal{D} on the overall monomer conversion **Right:** First order kinetic plot for the single and the overall monomer conversion and linear fitting (dotted lines).

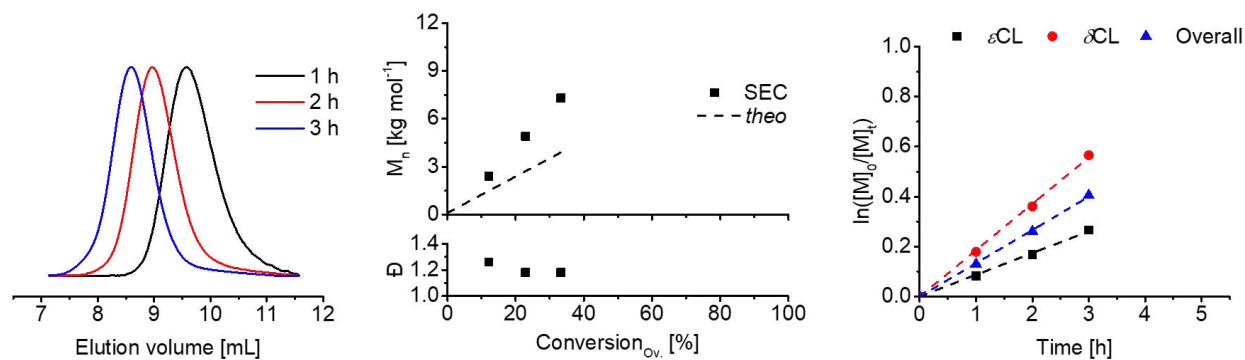


Figure S19: Kinetic studies of the copolymerization of ϵ CL and δ CL employing a $[\epsilon\text{CL}]:[\delta\text{CL}]:[\text{BnOH}]:[\text{TBD}]$ of 50:50:1:2 ($[\text{CL}]_0 = 4 \text{ mol L}^{-1}$ in toluene at room temperature). **Left:** Overlay of SEC elugrams (CHCl_3 , RID). **Center:** Dependence of the molar mass $M_{n,\text{SEC}}$ and dispersity \bar{D} on the overall monomer conversion **Right:** First order kinetic plot and linear extrapolation of experimental data (dotted lines).

Table S3: Calculations of the apparent polymerization rate ($k_{p, \text{app}}$) for the copolymerization studies (**Figure S15 to S19**) according to linear fitting of the semilogarithmic plot.

$[\epsilon\text{CL}]: [\delta\text{CL}]$	$k_{p, \text{app}, \epsilon\text{CL}} [\text{L mol}^{-1} \text{h}^{-1}]$	$k_{p, \text{app}, \delta\text{CL}} [\text{L mol}^{-1} \text{h}^{-1}]$	$k_{p, \text{app}, \text{ov.}} [\text{L mol}^{-1} \text{h}^{-1}]$
80:20	10.60	7.35	9.85
75:25	8.60	6.75	8.10
70:30	8.25	8.50	8.30
60:40	5.10	8.85	6.45
50:50	4.35	9.25	6.65

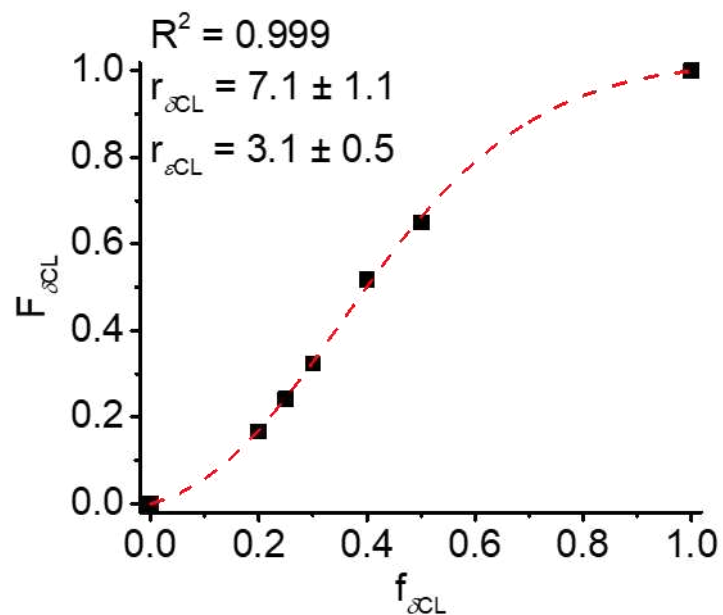


Figure S20: Dependence of the molar fraction of δCL in the copolymers ($F_{\delta\text{CL}}$) on the molar fraction of δCL in the feed ($f_{\delta\text{CL}}$) at an overall conversion of 18% and fitting according to Mayo-Lewis equation.

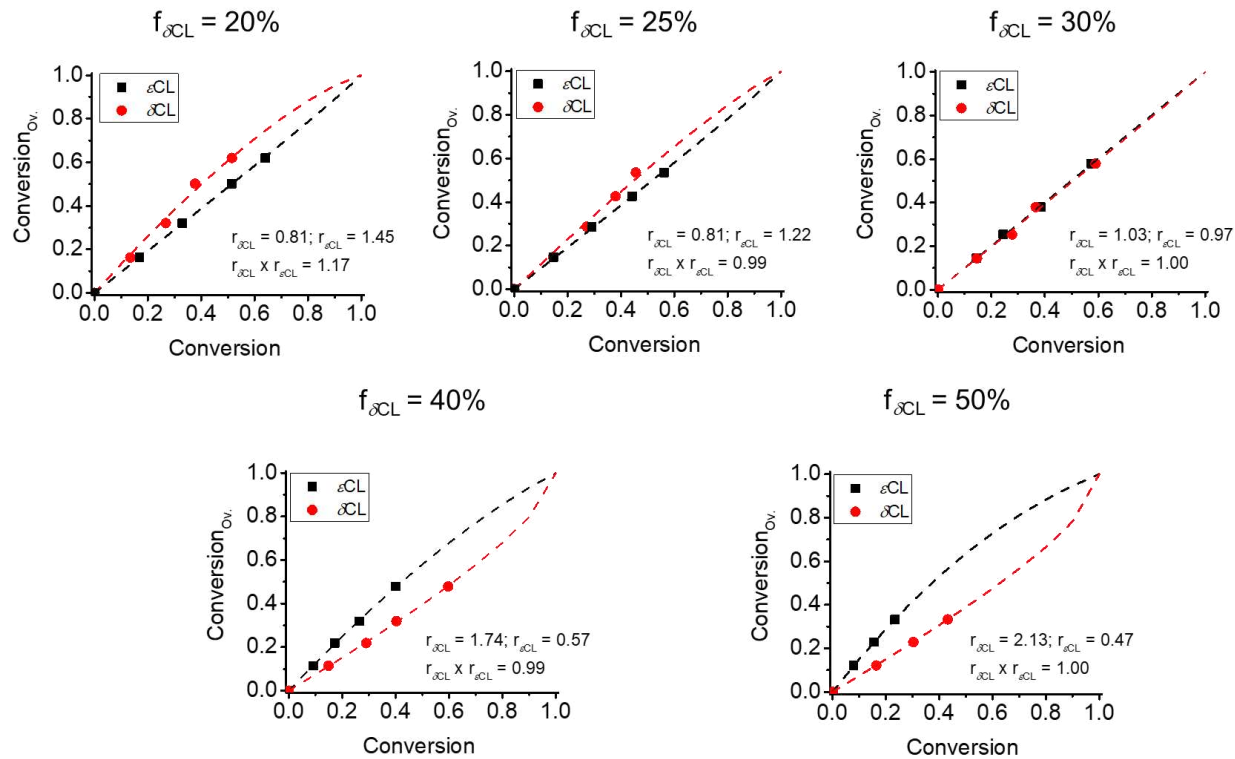


Figure S21: Evolution of the overall conversion over single monomer conversion for the copolymerization studies, fitting according to the Beckingham model, reactivity ratios obtained for each monomer feed investigated and estimation of the ideality of the copolymerization.

Characterization of PCL materials

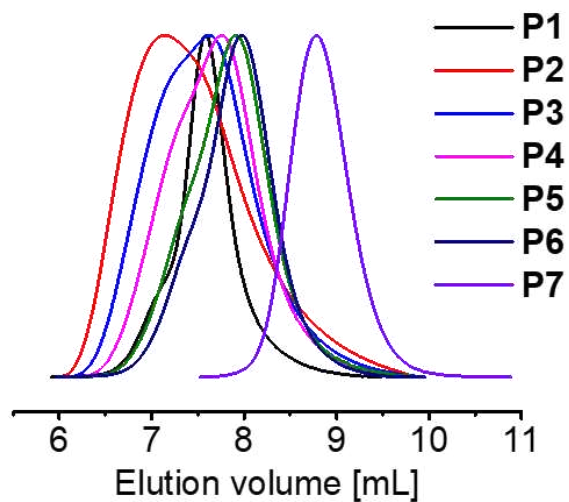


Figure S22: SEC elugrams of the purified homo and copolyesters **P1** to **P7** (CHCl_3 , RI detection).

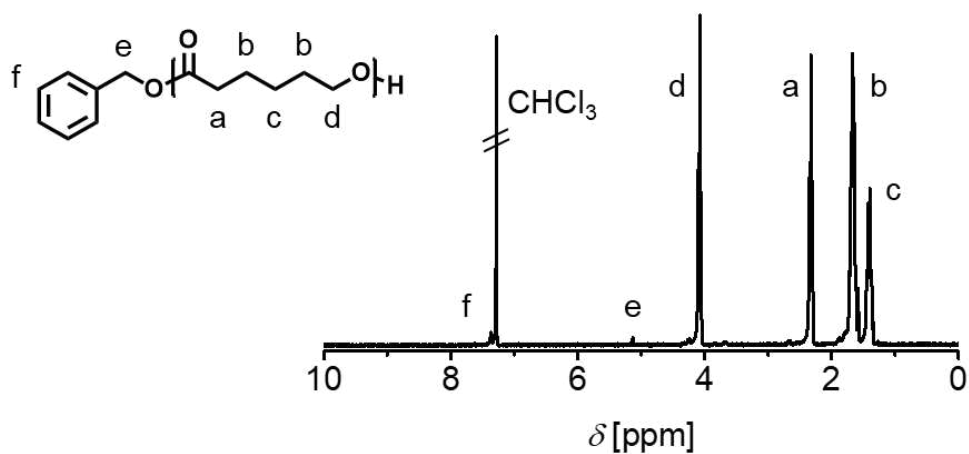


Figure S23: ^1H NMR spectrum (CDCl_3 , 300 MHz) of the purified $\text{P}\epsilon\text{CL}$ **P1** and assignment of the signals to the schematic representation of the structure.

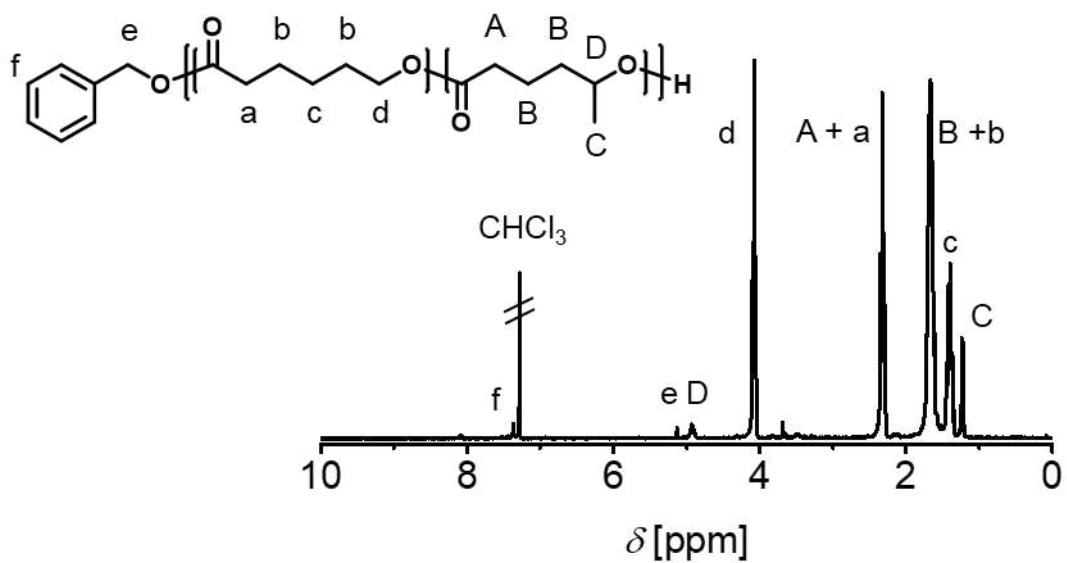


Figure S24: ^1H NMR spectrum (CDCl_3 , 300 MHz) of the purified $\text{P}(\epsilon\text{CL-}ran\text{-}\delta\text{CL})$ **P2** and assignment of the signals to the schematic representation of the structure.

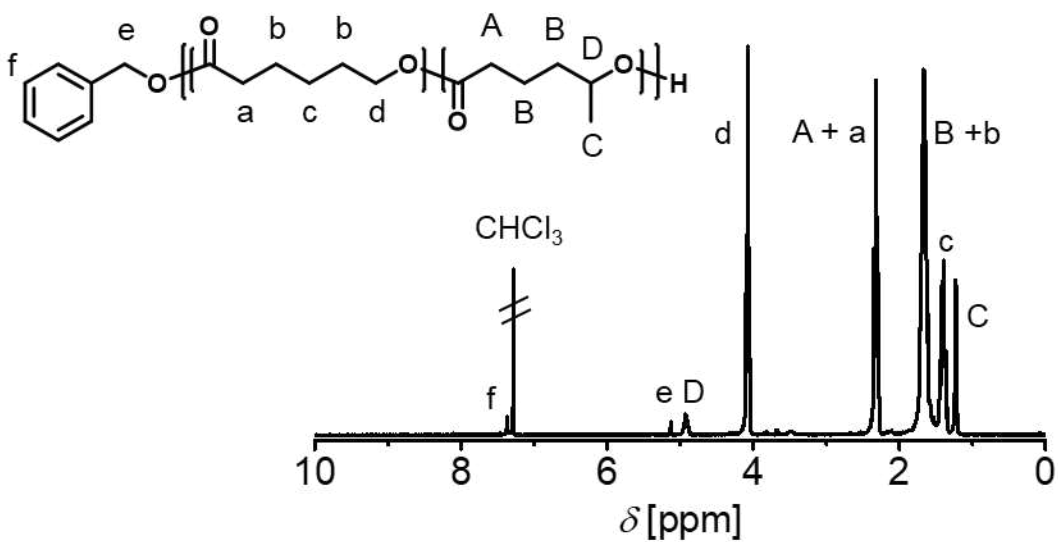


Figure S25: ^1H NMR spectrum (CDCl_3 , 300 MHz) of the purified $\text{P}(\epsilon\text{CL-}ran\text{-}\delta\text{CL})$ **P3** and assignment of the signals to the schematic representation of the structure.

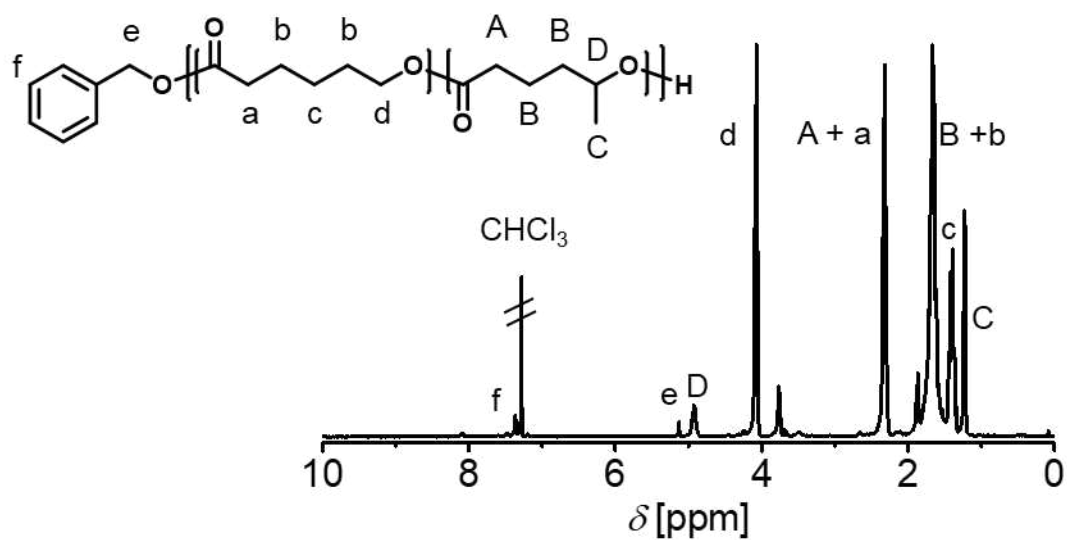


Figure S26: ^1H NMR spectrum (CDCl_3 , 300 MHz) of the purified $\text{P}(\epsilon\text{CL-ran-}\delta\text{CL})$ **P4** and assignment of the signals to the schematic representation of the structure.

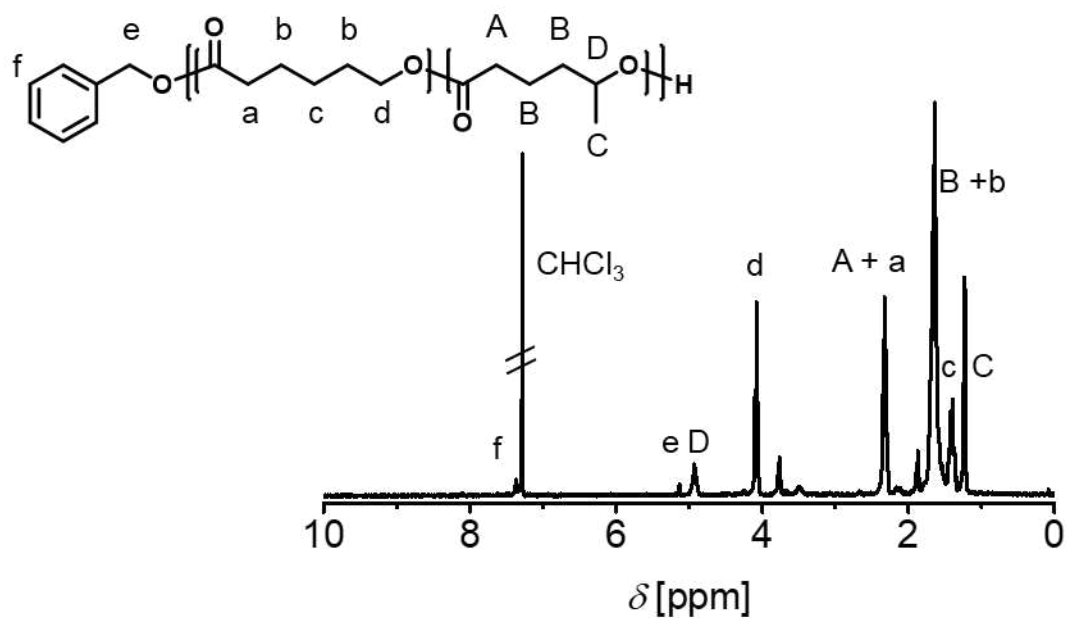


Figure S27: ^1H NMR spectrum (CDCl_3 , 300 MHz) of the purified $\text{P}(\epsilon\text{CL-ran-}\delta\text{CL})$ **P5** and assignment of the signals to the schematic representation of the structure.

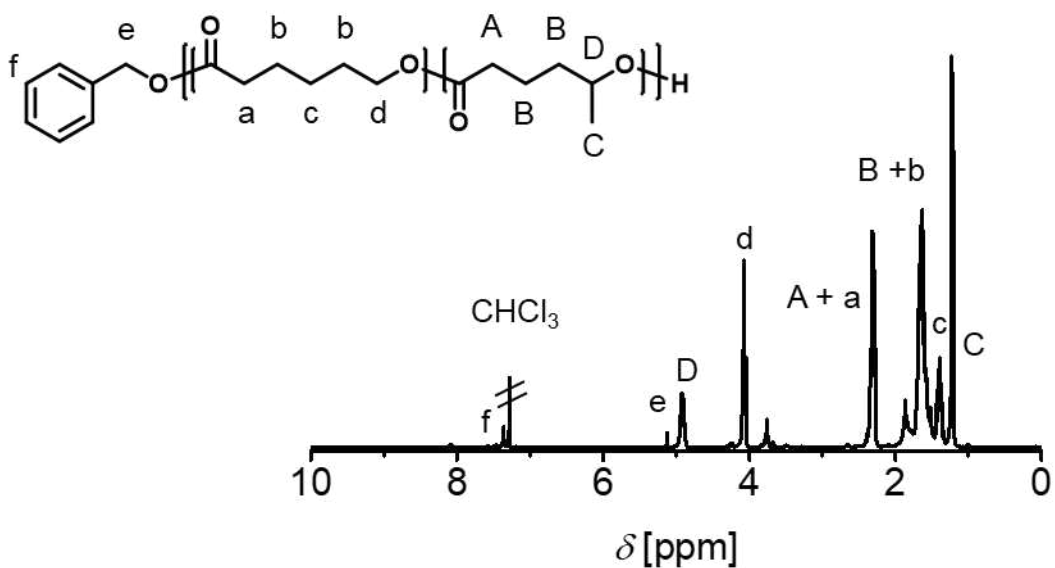


Figure S28: ¹H NMR spectrum (CDCl₃, 300 MHz) of the purified P(εCL-ran-δCL) P6 and assignment of the signals to the schematic representation of the structure.

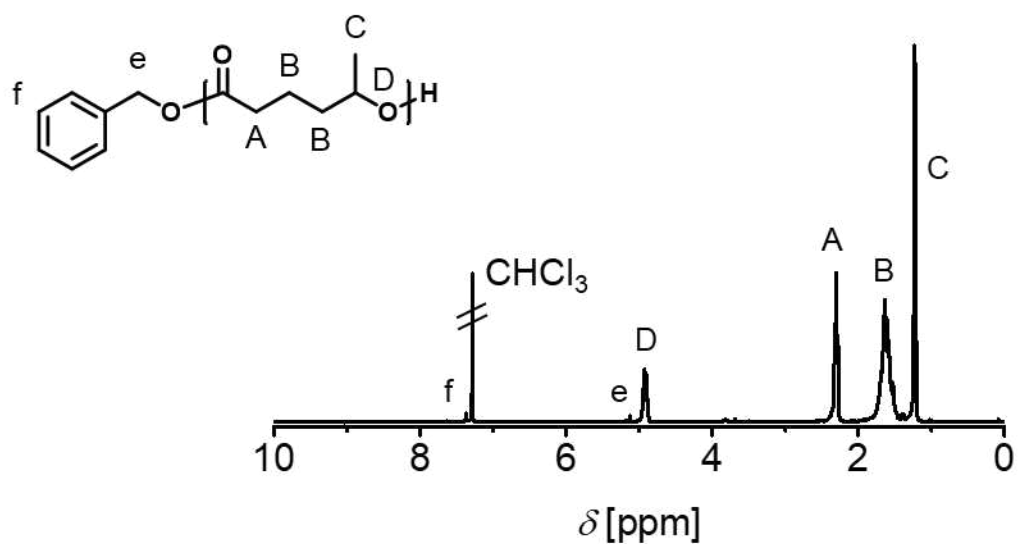


Figure S29: ¹H NMR spectrum (CDCl₃, 300 MHz) of the purified PδCL P7 and assignment of the signals to the schematic representation of the structure.

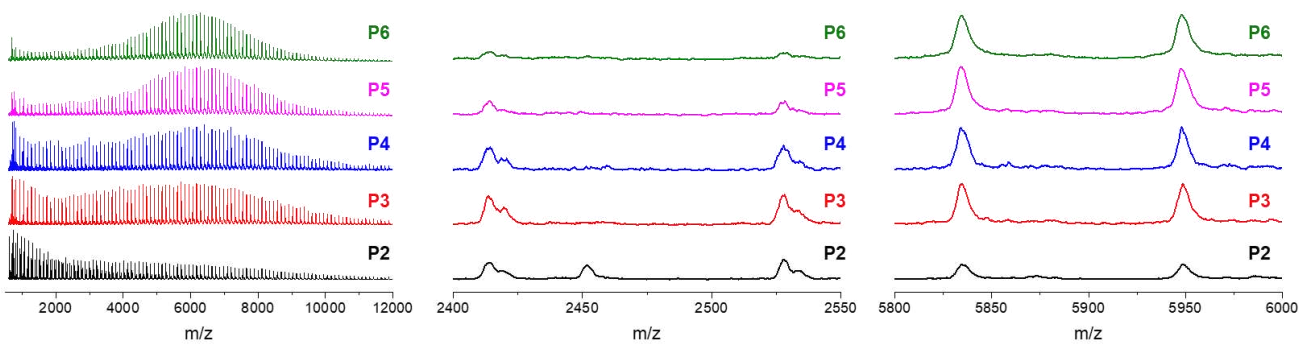


Figure S30: MALDI TOF mass spectra of P(ϵ CL-*ran*- δ CL) (DCTB, NaI, positive linear mode). Left: Full mass spectra. Center: Zoom into the region around $m/z = 2,500$. The zoomed region corresponds to one repeating unit. Peak assignments for **P2** revealing the most prominent side product signals are depicted below. Right: Zoom into the region around $m/z = 5,900$. The zoomed region corresponds to one repeating unit.

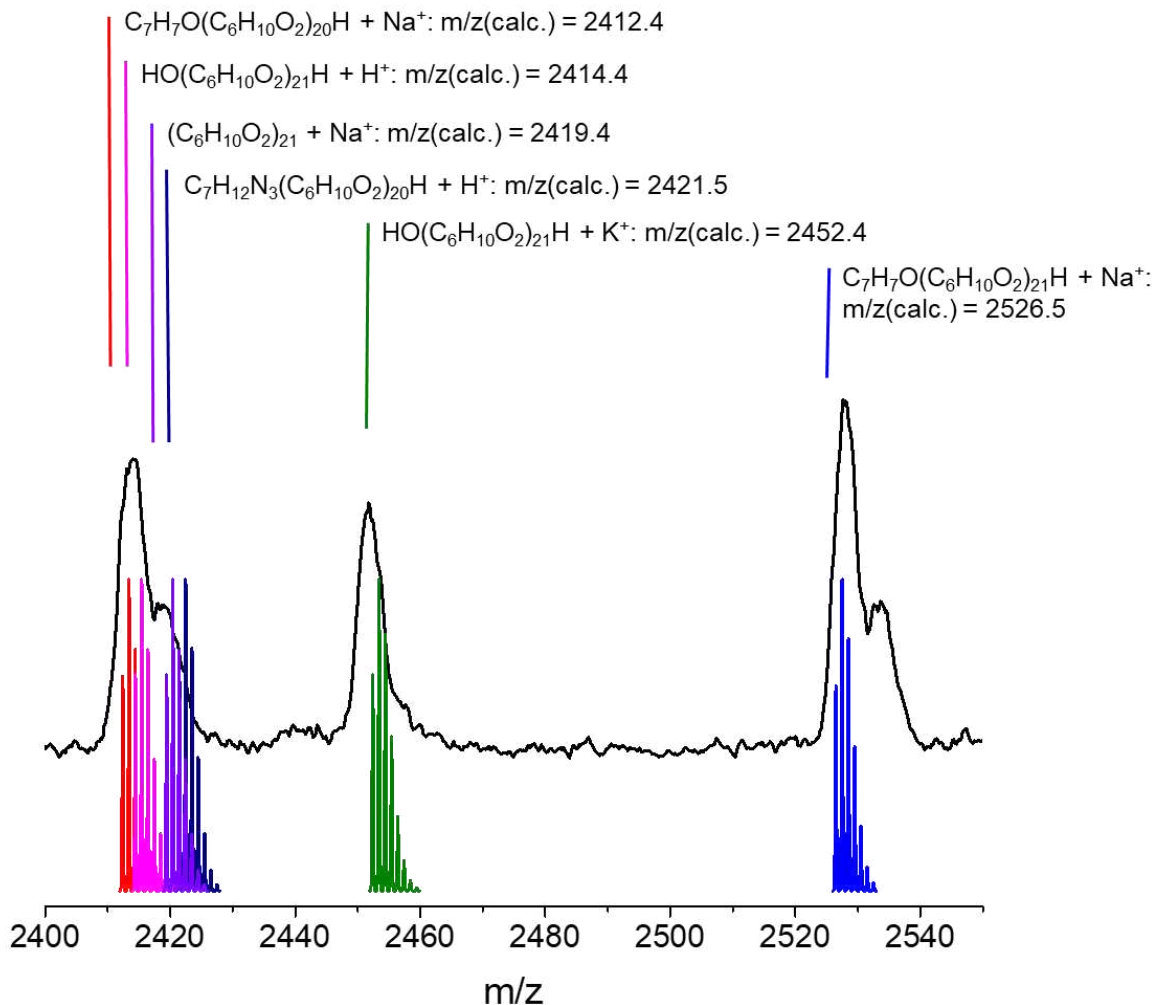


Figure S31: Zoom into the lower m/z region of the MALDI TOF mass spectrum of P(ϵ CL-*ran*- δ CL) **P2** (DCTB, NaI, positive linear mode) and assignment of the detected species *via* the corresponding calculated isotopic patterns. The m/z region corresponds to one repeating unit. The main series was assigned to sodiated PCL initiated by BnOH (red and blue, respectively) and overlaps with potentially present water initiated proton adducts (pink). The assignment of water initiated PCL as potassium adducts (green) confirmed their presence for **P2**, whereas the corresponding m/z signals were absent in the mass spectra of **P3-P6**. Sodiated cyclic PCL (purple) was assigned for all P(ϵ CL-*ran*- δ CL). It remained unclear if proton adducts of additional TBD initiated macromolecules (dark blue) are overlapping due to the resolution as the measurement conditions were optimized for the detection of higher molar mass species in the linear mode.

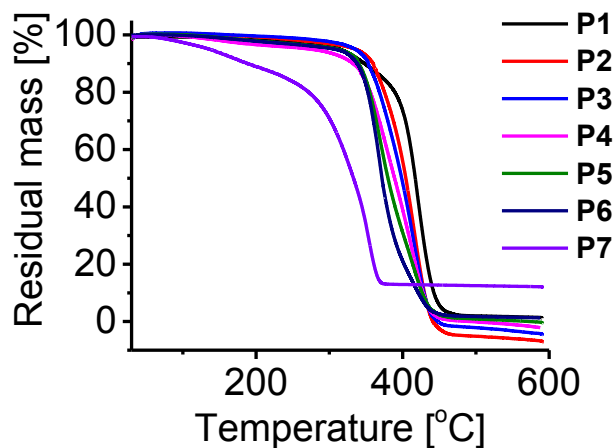


Figure S32: TGA thermograms of the polyester library **P1** to **P7** (N₂, 30 to 590 °C, heating rate 20 °C min⁻¹).

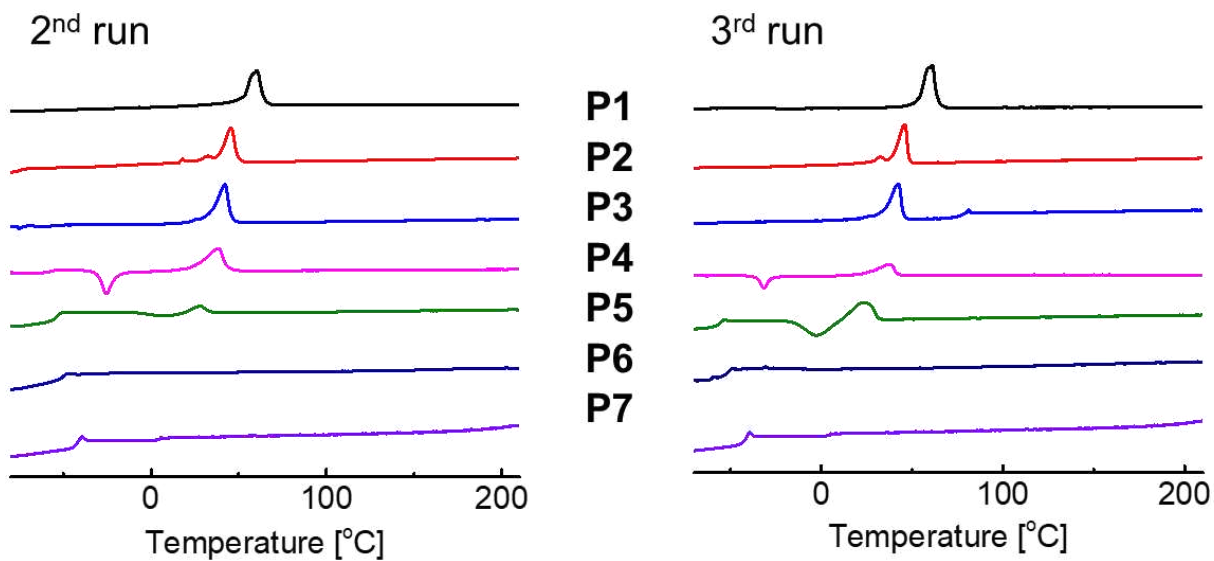


Figure S33: Additional DSC thermograms of the polyester library **P1** to **P7** (-100 to 210 °C). **Left:** Second heating run (heating rate of 20 °C min⁻¹). **Right:** Third heating run (heating rate of 10 °C min⁻¹).

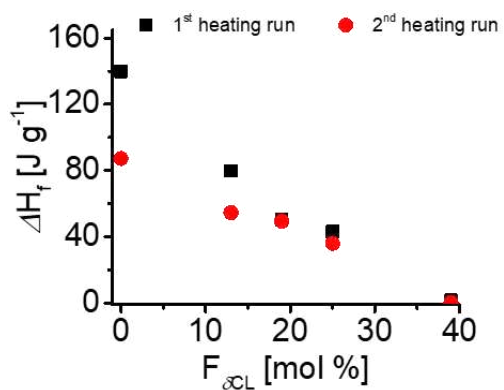


Figure S34: Dependence of the enthalpy of melting on the fraction of δ CL in the copolymer ($F_{\delta\text{CL}}$) during the first and the second heating runs (-100 to 210 °C; heating rate of 20 °C min⁻¹).

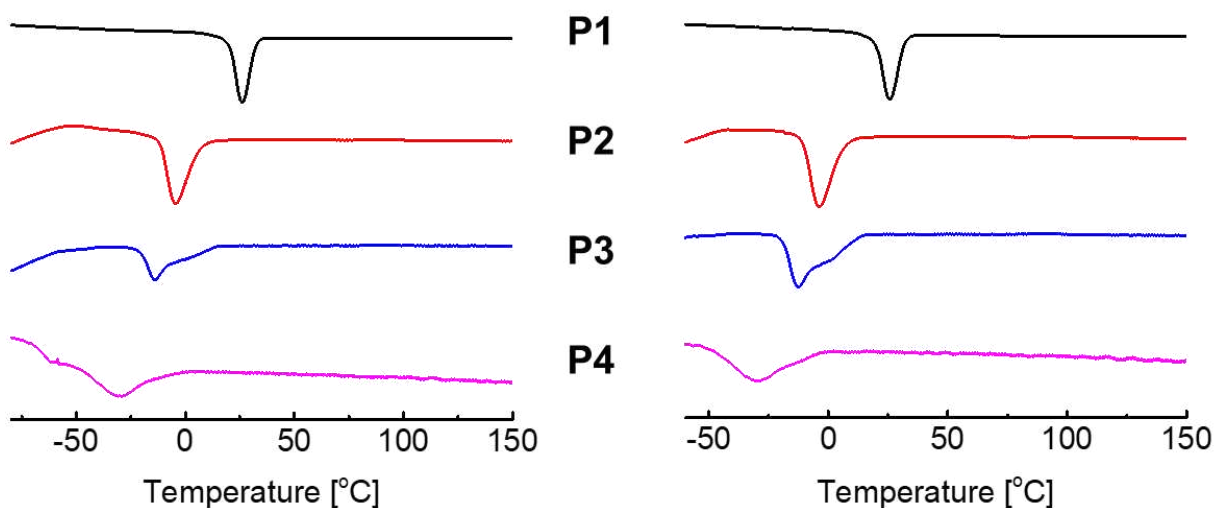


Figure S35: Additional DSC thermograms of the polyesters **P1** to **P4** (210 °C to -100 °C; cooling rate 20 °C min⁻¹). **Left:** First cooling run. **Right:** Second cooling run.

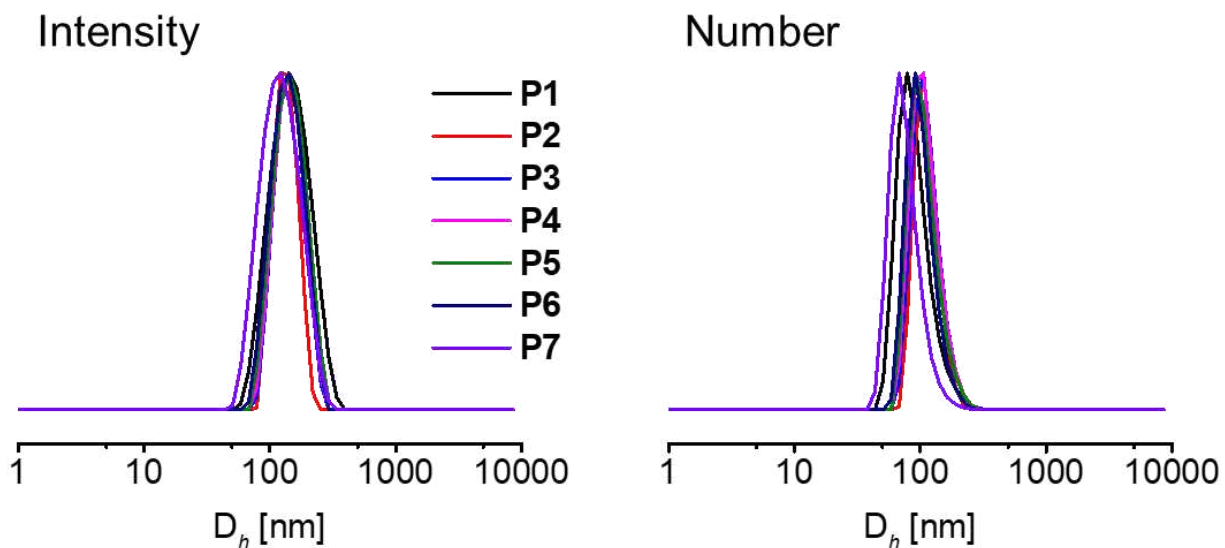


Figure S36: Size distributions of the nanoparticle dispersions of **P1** to **P7** obtained by DLS analysis ($c(\text{polymer}) = 0.1 \text{ mg mL}^{-1}$). **Left:** Intensity-weighted distributions. **Right:** Number-weighted distributions.

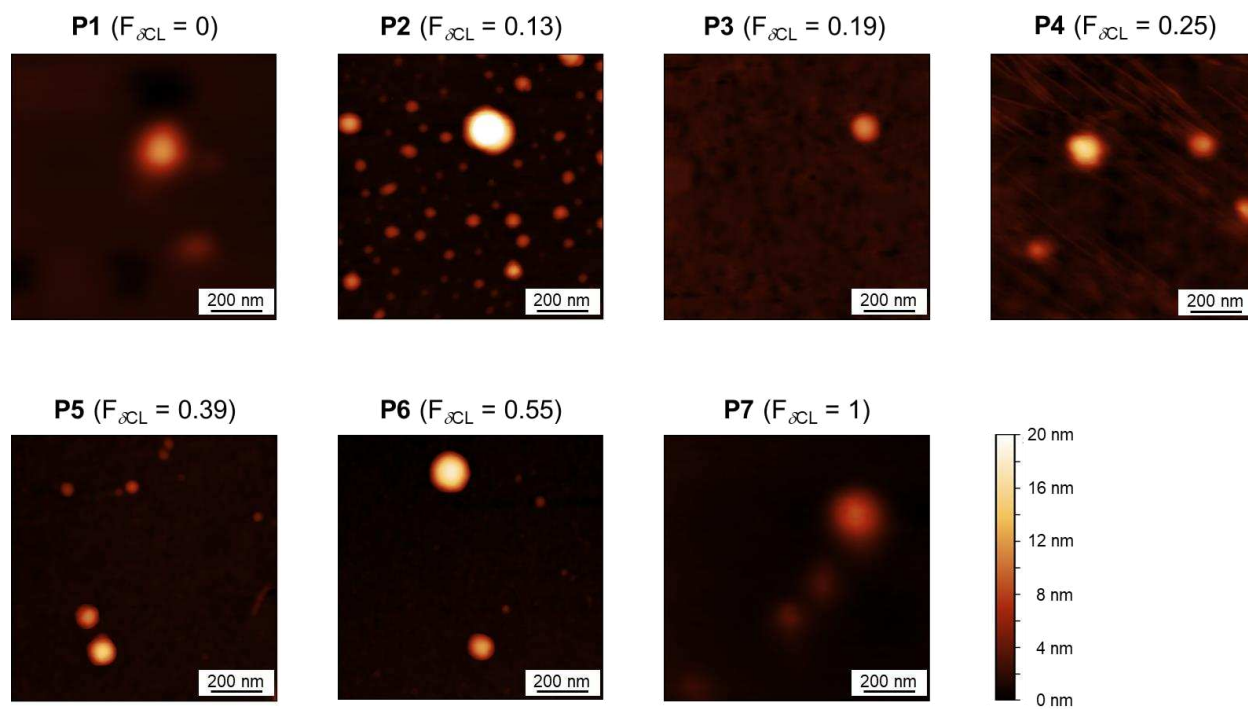


Figure S37: AFM height images of the nanoparticles obtained from **P1** to **P7**.

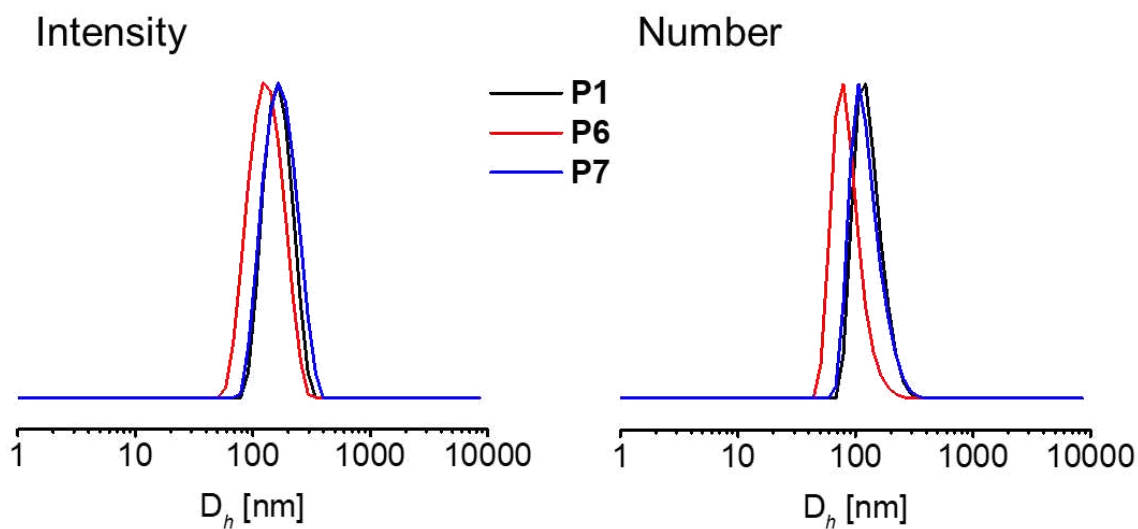


Figure S38: Size distributions of the pyrene encapsulated nanoparticle suspensions of **P1**, **P6** and **P7** obtained by DLS analysis ($c(\text{polymer}) = 0.1 \text{ mg mL}^{-1}$, $c(\text{pyrene}) = 1 \text{ } \mu\text{g mL}^{-1}$). **Left:** Intensity-weighted distributions. **Right:** Number-weighted distributions.

Table S4: DLS data of the pyrene loaded nanoparticles.

Sample	P1	P6	P7
$F_{\&L}$ [mol%]	0	55	100
D_h [nm]	158	120	160
PDI	0.097	0.103	0.103

References

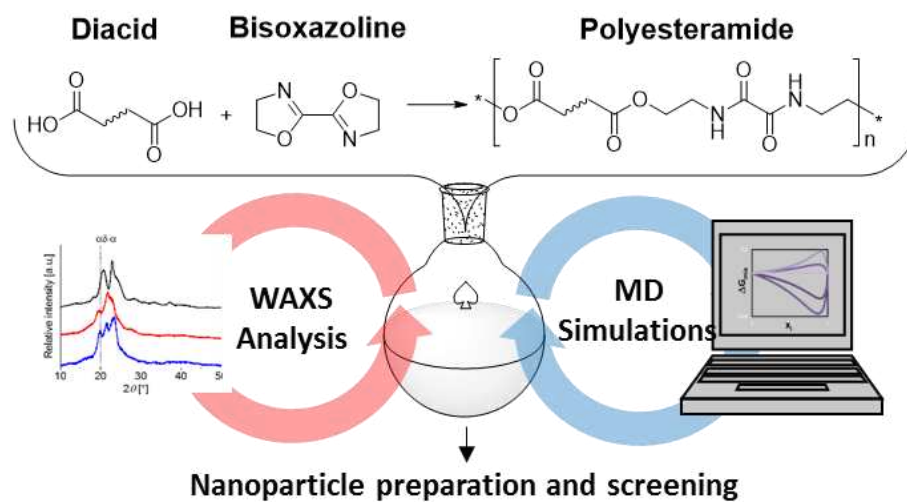
- [1] Schneiderman, D. K.; Hillmyer, M. A., Aliphatic polyester block polymer design. *Macromolecules* **2016**, *49*, 2419-2428.
- [2] Yin, M.; Baker, G. L., Preparation and characterization of substituted polylactides. *Macromolecules* **1999**, *32*, 7711-7718.
- [3] Hillmyer, M. A.; Tolman, W. B., Aliphatic polyester block polymers: Renewable, degradable, and sustainable. *Acc. Chem. Res.* **2014**, *47*, 2390-2396.
- [4] Dubois, P.; Coulembier, O.; Raquez, J.-M. in *Handbook of ring-opening polymerization*. John Wiley & Sons: 2009.
- [5] Lohmeijer, B. G. G.; Pratt, R. C.; Leibfarth, F.; Logan, J. W.; Long, D. A.; Dove, A. P.; Nederberg, F.; Choi, J.; Wade, C.; Waymouth, R. M.; Hedrick, J. L., Guanidine and amidine organocatalysts for ring-opening polymerization of cyclic esters. *Macromolecules* **2006**, *39*, 8574-8583.

Publication 4

A polyesteramide library from dicarboxylic acids and 2,2'-bis(2-oxazoline): Synthesis, characterization, nanoparticle formulation and molecular dynamics simulations

I. Muljajew, A. Erlebach, C. Weber, J. R. Buchheim, M. Sierka, U. S. Schubert

Polym. Chem. **2020**, *11*, 112–124.





Cite this: *Polym. Chem.*, 2020, **11**, 112

A polyesteramide library from dicarboxylic acids and 2,2'-bis(2-oxazoline): synthesis, characterization, nanoparticle formulation and molecular dynamics simulations†

Irina Muljajew,^{a,b} Andreas Erlebach,^{b,c} Christine Weber,^{a,b} Johannes R. Buchheim,^d Marek Sierka^{b,c} and Ulrich S. Schubert^{*a,b}

The step growth polyaddition of a variety of dicarboxylic acids and 2,2'-bis(2-oxazoline) enabled access to a library of polyesteramides (PEA) with different linker lengths or bulkiness. PEA with alkylene spacers represented semicrystalline materials due to hydrogen bond formation between the oxamide moieties, as is evident from dynamic scanning calorimetry and wide-angle X-ray scattering ($145\text{ °C} < T_m < 225\text{ °C}$). In contrast, PEAs comprising substituted spacers resulted in amorphous materials suitable for the preparation of nanoparticle dispersions by means of direct nanoprecipitation from hexafluoroisopropanol into water. Strong intermolecular interactions that were evident from Hildebrand solubility parameters δ resulted in the formation of aggregates for the semi-crystalline materials. Although Hildebrand parameters alone provided less accurate solubility predictions of the PEAs in acetone and THF, the Flory–Huggins parameters χ_{PS} revealed pronounced changes of intermolecular interactions with variation of the polymer structure, clearly demonstrating a tunable hydrophobicity of the synthesized PEAs.

Received 28th August 2019,
Accepted 20th November 2019

DOI: 10.1039/c9py01293a

rsc.li/polymers

Introduction

Polymeric nanoparticles have great potential to increase the bioavailability of hydrophobic drugs.^{1–3} Mainly FDA-approved Resomer® materials, *i.e.* block copolymers composed of poly(ethylene oxide), and a polyester based on lactic acid and glycolic acid, are applied for this purpose. Although the variation of the monomer fractions allows for a certain tailoring of the nanoparticle properties, such as encapsulation efficiency or drug release, these materials are often not suited for specific cargos because of a low thermodynamic compatibility between the host and guest. An optimum carrier material for a given drug would require a targeted tailoring of the compatibility. Intrinsically, this has to be optimized for each individual active pharmaceutical ingredient (API) and requires access to a

multitude of different polymers to match its hydrophilicity. As many drugs contain functional groups, specific interactions with functional groups of the polymer carrier could furthermore be exploited in the development of an optimum carrier material.

Nanoprecipitation represents an easy method for the formulation of aqueous nanoparticle dispersions.⁴ Despite the relatively simple experimental procedure, the process has to be optimized for each polymer with regard to variables such as the concentration, solvent to non-solvent ratio, stirring speed, or addition of surfactants. Encapsulation of an API further increases the complexity of the process.⁵ Combining all these experimental possibilities with a variety of polymers results in a multidimensional parameter space that is difficult to handle by experiment alone, making the optimization of the carrier material, in fact, a trial and error process.

In silico predictions are able to accelerate this process, guiding the design of polymeric nanocarriers with tailored properties. Notably, atomistic simulations can be used to predict the thermodynamic properties of the polymer materials, avoiding nanoformulation trials of thermodynamically incompatible materials. In addition, understanding the underlying intermolecular interactions and structure–property relationships represents the key step towards a targeted development of nanocarriers tailor-made for a specific API.^{6,7} Solubility parameters (SP), which can be obtained from atomistic molecular dynamics (MD) simulations, are useful for rapid ranking of

^aLaboratory of Organic and Macromolecular Chemistry (IOMC), Friedrich Schiller University Jena, Humboldtstr. 10, 07743 Jena, Germany.

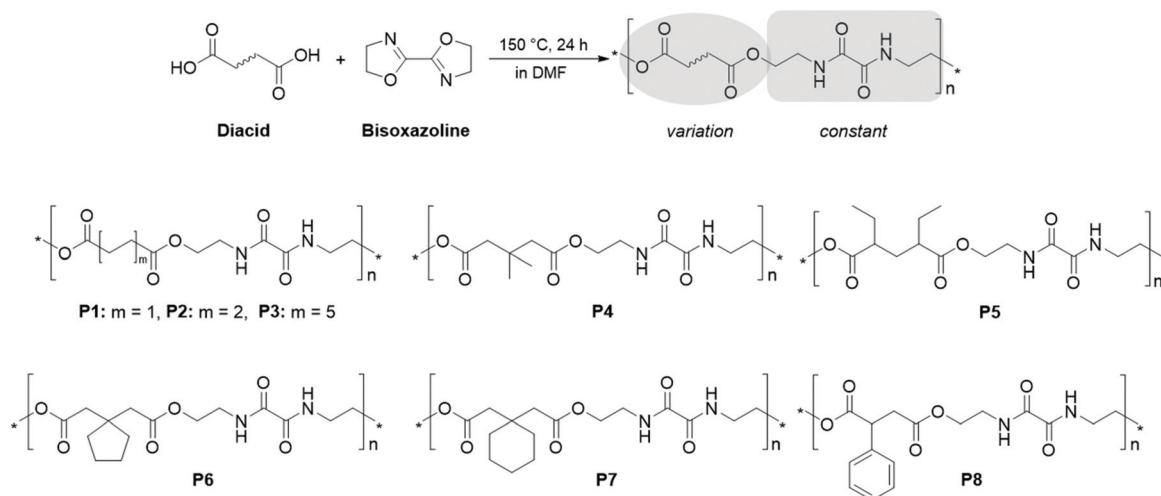
E-mail: ulrich.schubert@uni-jena.de

^bJena Center for Soft Matter (JCSM), Friedrich Schiller University Jena, Philosophenweg 7, 07743 Jena, Germany

^cOtto Schott Institute of Materials Research (OSIM), Friedrich Schiller University Jena, Löbdergraben 32, 07743 Jena, Germany

^dInstitute for Technical Chemistry and Environmental Chemistry, Center for Energy and Environmental Chemistry Jena (CEEC Jena), Friedrich Schiller University Jena, Philosophenweg 7a, 07743 Jena, Germany

† Electronic supplementary information (ESI) available. See DOI: 10.1039/c9py01293a



Scheme 1 Schematic representation of the polymerization approach and the structures of the obtained polyesteramides **P1** to **P8**.

polymers and can be applied to predict solvent compatibility and bulk properties. However, SP do not account for entropic effects, concentration dependence and unique interactions between molecules.⁸ The description can be refined by combination with the Flory–Huggins (FH) theory, which includes enthalpic and entropic factors for the mixing of two components. In addition, specific interactions such as hydrogen bonding can be considered by performing simulations of polymer mixtures.^{8–11}

Aiming towards the development of such a combined experimental and *in silico* approach, we selected polyesteramides (PEA) as a polymer class. Besides enabling the degradation of the polymeric nanoparticle by hydrolysis of the ester moieties,^{12–14} the amide functionalities might induce specific interactions *via* hydrogen bonding. These properties are, *e.g.*, exploited in the commercial BAK® materials based on 1,4-butanediol, adipic acid and ϵ -caprolactam.^{15,16} PEAs can be synthesized by ring opening polymerization (ROP) of cyclic morpholinediones^{17,18} or, traditionally, by polycondensation of diols, dicarboxylic acids and amino acids yielding PEAs with randomly distributed amide and ester functionalities.¹⁹ The laborious monomer synthesis ruled out the ROP as a synthetic strategy for tailoring of the polymer properties *via* high-throughput experimentation (HTE) approaches.

Although bis(2-oxazoline)s are often used as coupling agents for chain extension of, *e.g.*, polyamide^{20,21} or polyester^{20,22–24} prepolymers, comparably little attention has been paid towards their direct application for PEA synthesis. A nucleophilic attack of a carboxylic acid at the 2-oxazoline ring results in its opening and the formation of a diamide structure.^{25,26} Alternating diester and diamide moieties can hence be realized by the AA/BB polyaddition of dicarboxylic acids and bis(2-oxazolines).^{25,27} Benefitting from the experimental simplicity and a wide range of carboxylic acids commercially available to serve as monomers, this synthetic approach fulfills the basic requirements for the adjustment of the hydrophilicity of PEA materials in a HTE fashion.

Mostly, the reaction of aromatic bis(2-oxazoline)s such as 1,3- and 1,4-phenylene bis(2-oxazoline)s with dicarboxylic acids has been studied.^{25,28–31} Further examples include other aromatic bisoxazolines based on 2,5-furandicarboxylic acid,³² 2,6-pyridine dicarboxylic acid,³³ (1,1'-biphenyl)-4,4'-dicarboxylic acid,^{30,34} bis(4-carboxyphenyl)phenylphosphine oxide,³⁵ or phenolphthalein.³⁶ However, simple 2,2'-bis(2-oxazoline) (BisOx) has, to the best of our knowledge, not been utilized so far, and the reported polymers have not been applied for the formulation of nanoparticles. As depicted in Scheme 1, the resulting PEAs feature a diethylene oxamide moiety, whereas the spacer between the alternating ester functionalities is determined by the dicarboxylic acid employed for the polyaddition. It should be noted that two similarly structured oligomers with C₄ and C₈ alkylene spacers have been reported by Yin *et al.*, however *via* a more complicated synthesis route.³⁷

In order to facilitate the integration of a general experimental and *in silico* methodology for polymeric nanoparticles in an aqueous dispersion, we employed a range of dicarboxylic acids, also including substituted aliphatic spacers. This resulted in a broad variation of the hydrophilicity, the solid state properties and nanoprecipitation characteristics within the PEA library. The feasibility of the concept was consistently evaluated throughout the workflow by comparison of experimental results from wide-angle X-ray scattering (WAXS), solubility and nanoprecipitation with *in silico* predictions based on SP and FH theory combined with atomistic MD simulations.

Experimental section

Materials

Succinic acid (99.0%), 2,4-diethylglutaric acid (DL- and *meso*-mixture, 98.0%), 1,1-cyclopentanediacytic acid (98.0%), 1,1-cyclohexanediacytic acid (98.0%), and 2,2'-bis(2-oxazoline)

(BisOx, 97.0%) were obtained from Tokyo Chemical Industry (TCI). Adipic acid (99.0%), dodecanedioic acid (99.0%), 3,3-dimethylglutaric acid (98.0%), (\pm)-phenylsuccinic acid (98.0%), and 1,1,1,3,3,3-hexafluoro-2-propanol (HFIP, 99.0%) were purchased from Sigma Aldrich (now MERCK). *N,N*-Dimethylformamide (DMF, 99.8%, extra dry over molecular sieves) was purchased from ACROS Organics. All other chemicals and solvents were obtained from common commercial sources and used without further purification, unless otherwise stated.

Instruments

Proton nuclear magnetic resonance (^1H NMR) spectra and diffusion ordered NMR spectroscopy (DOSY) spectra were recorded at room temperature in 1,1,1,3,3,3-hexafluoro-2-propanol- d_2 (HFIP- d_2) on a Bruker Avance 400 MHz spectrometer using the residual solvent resonance as an internal standard. The chemical shifts are given in ppm. For infrared spectroscopy, an IRAffinity-1 CE system from Shimadzu, equipped with a quest ATR diamond extended range X - single-reflection-ATR cuvette, was used.

Size exclusion chromatography (SEC) was performed on an Agilent 1200 series system equipped with a PSS degasser, a G1310A pump, a G1329A auto sampler, a Techlab oven, a G1362A RI detector, and a PSS GRAM guard/30/1000 Å (10 μm particle size) column. The system was run with an eluent composed of *N,N*-dimethylacetamide (DMAc) with 0.21 wt% LiCl at a flow rate of 1 mL min^{-1} at 40 °C and was calibrated with polystyrene (PS) standards (400 to 1 000 000 g mol^{-1}) purchased from Polymer Standards Services GmbH (PSS).

For the measurement of the matrix-assisted laser desorption/ionization (MALDI) spectra, an Ultraflex III TOF/TOF from Bruker Daltonics was used. The instrument was equipped with a Nd:YAG laser and a collision cell. All spectra were measured in the positive reflector mode using 2,5-dihydroxybenzoic acid (DHB) as a matrix. Ionization occurred readily from the sodium and potassium ions naturally present. The instrument was calibrated prior to each measurement with an external PMMA standard from PSS. Data were processed *via* Bruker Data Analysis software version 4.2.

Thermogravimetric analysis (TGA) was performed under a N_2 atmosphere on a Netzsch TG 209 F1 Iris from 30 to 600 °C at a heating rate of 20 K min^{-1} . Differential scanning calorimetry (DSC) measurements were performed on a Netzsch DSC 204 F1 Phoenix under a N_2 atmosphere from -50 to 120 °C or 260 °C. Three cycles were recorded for each sample. The first and the second heating runs were conducted at a heating rate of 20 K min^{-1} . For the third heating run, a heating rate of 10 K min^{-1} was applied. A cooling rate of 20 K min^{-1} between the heating runs was applied at all times. The glass transition temperature (T_g , inflection value) and the melting temperature (T_m) values are reported from the second heating run.

The X-ray diffraction studies were performed using a Bruker Phaser D2 diffractometer in reflection mode with Cu-K α radiation ($\lambda = 1.54056$ Å) over a range of 2θ from 5 to 50° with a scanning rate of 0.015° s^{-1} . Structure refinement of **P1** was rea-

lized by the Rietveld method using Maud software.³⁸ The background was determined using a fifth-order polynomial. LaB₆ was used as a standard material to investigate the instrumental broadening. The degree of crystallinity was calculated with the integrated intensities of the amorphous and crystalline scattering curve in a range of 2θ from 15 to 30°.^{39,40}

Dynamic light scattering (DLS) and ζ -potential measurements were performed on a Zetasizer Nano ZS from Malvern Instruments at 25 °C ($\lambda = 633$ nm) at an angle of 173°. Each measurement was performed five times for DLS and thrice for the ζ -potential. The mean particle size was approximated as the effective (*Z*-average) diameter and the width of the distribution as the polydispersity index (PDI) of the particles obtained by the method of cumulants assuming a spherical shape.

Polyesteramide synthesis

The respective diacid (1 mmol) and BisOx (641 mg, 1 mmol) were dissolved or suspended in 0.5 mL DMF. The vial was closed and the solution was degassed by gently bubbling with argon. The polymerization was performed at 150 °C for 24 h, and the reaction solution was cooled to room temperature. Because **P1–P3** precipitated, HFIP was added to the reaction mixtures to dissolve the polyesteramides prior to precipitation into methanol at room temperature. All other PEAs were precipitated into cold (-20 °C) methanol. The obtained polymeric materials were dried at 40 °C in a vacuum oven and characterized by IR spectroscopy, ^1H and DOSY NMR spectroscopy, MALDI-ToF mass spectrometry, SEC, TGA, DSC and wide-angle X-ray scattering experiments.

Poly{succinic acid-*alt*-[bis(2-oxazoline)]} **P1**: ^1H NMR (400 MHz, HFIP- d_2): $\delta/\text{ppm} = 8.05$ ($2 \times \text{NH}$); 4.28 ($2 \times \text{CH}_2$, $-\text{CH}_2\text{-OOCR}$); 3.85 ($2 \times \text{CH}_2$, $-\text{CH}_2\text{-OH}$); 3.66 ($2 \times \text{CH}_2$, $-\text{CH}_2\text{-NHCOR}$); 3.55 ($2 \times \text{CH}_2$, $\text{HO-CH}_2\text{-CH}_2\text{-NHCOR-}$); 2.76 ($2 \times \text{CH}_2$, $-\text{CH}_2\text{-COOR}$).

Poly{adipic acid-*alt*-[bis(2-oxazoline)]} **P2**: ^1H NMR (400 MHz, HFIP- d_2): $\delta/\text{ppm} = 8.04$ ($2 \times \text{NH}$); 4.26 ($2 \times \text{CH}_2$, $-\text{CH}_2\text{-OOCR}$); 3.85 ($2 \times \text{CH}_2$, $-\text{CH}_2\text{-OH}$); 3.65 ($2 \times \text{CH}_2$, $-\text{CH}_2\text{-NHCOR}$); 3.55 ($2 \times \text{CH}_2$, $\text{HO-CH}_2\text{-CH}_2\text{-NHCOR}$); 2.48 ($2 \times \text{CH}_2$, $-\text{CH}_2\text{-COOR}$); 1.71 ($2 \times \text{CH}_2$, $-\text{CH}_2\text{-CH}_2\text{-COOR}$).

Poly{dodecanedioic acid-*alt*-[bis(2-oxazoline)]} **P3**: ^1H NMR (400 MHz, HFIP- d_2): $\delta/\text{ppm} = 8.05$ ($2 \times \text{NH}$); 4.25 ($2 \times \text{CH}_2$, $-\text{CH}_2\text{-OOCR}$); 3.85 ($2 \times \text{CH}_2$, $-\text{CH}_2\text{-OH}$); 3.65 ($2 \times \text{CH}_2$, $-\text{CH}_2\text{-NHCOR}$); 3.55 ($2 \times \text{CH}_2$, $\text{HO-CH}_2\text{-CH}_2\text{-NHCOR}$); 2.43 ($2 \times \text{CH}_2$, $-\text{CH}_2\text{-COOR}$); 1.68 ($2 \times \text{CH}_2$, $-\text{CH}_2\text{-CH}_2\text{-COOR}$); 1.36 ($5 \times \text{CH}_2$, $-(\text{CH}_2)_5\text{-CH}_2\text{-CH}_2\text{-COOR}$).

Poly{dimethylglutaric acid-*alt*-[bis(2-oxazoline)]} **P4**: ^1H NMR (400 MHz, HFIP- d_2): $\delta/\text{ppm} = 8.05$ ($2 \times \text{NH}$); 4.26 ($2 \times \text{CH}_2$, $-\text{CH}_2\text{-OOCR}$); 3.85 ($2 \times \text{CH}_2$, $-\text{CH}_2\text{-OH}$); 3.66 ($2 \times \text{CH}_2$, $-\text{CH}_2\text{-NHCOR}$); 3.54 ($2 \times \text{CH}_2$, $\text{HO-CH}_2\text{-CH}_2\text{-NHCOR}$); 2.53 ($2 \times \text{CH}_2$, $-\text{CH}_2\text{-COOR}$); 1.17 ($2 \times \text{CH}_3$). SEC (DMAc, RI detection, PS calibration): $M_n = 5200$ g mol^{-1} , $D = 1.26$.

Poly{diethylglutaric acid-*alt*-[bis(2-oxazoline)]} **P5**: ^1H NMR (400 MHz, HFIP- d_2): $\delta/\text{ppm} = 8.11\text{--}7.89$ ($2 \times \text{NH}$); 4.36–4.18 ($2 \times \text{CH}_2$, $-\text{CH}_2\text{-OOCR}$); 3.85 ($2 \times \text{CH}_2$, $-\text{CH}_2\text{-OH}$); 3.68 ($2 \times \text{CH}_2$, $-\text{CH}_2\text{-NHCOR}$); 3.54 ($2 \times \text{CH}_2$, $\text{HO-CH}_2\text{-CH}_2\text{-NHCOR}$);

2.55–2.31 ($2 \times \text{CH}$, $-\text{CH}-\text{COOR}$); 2.11–1.54 ($3 \times \text{CH}_2$, $-\text{CH}_2-\text{CHR}-\text{COOR}$); 0.94 ($2 \times \text{CH}_3$). SEC (DMAc, RI detection, PS calibration): $M_n = 6200 \text{ g mol}^{-1}$, $D = 1.26$.

Poly{cyclopentanediacetic acid-*alt*-[bis(2-oxazoline)]} **P6**: ^1H NMR (400 MHz, HFIP- d_2): $\delta/\text{ppm} = 8.05$ ($2 \times \text{NH}$); 4.26 ($2 \times \text{CH}_2$, $-\text{CH}_2-\text{OOCR}$); 3.85 ($2 \times \text{CH}_2$, $-\text{CH}_2-\text{OH}$); 3.67 ($2 \times \text{CH}_2$, $-\text{CH}_2-\text{NHCOR}$); 3.55 ($2 \times \text{CH}_2$, $\text{HO}-\text{CH}_2-\text{CH}_2-\text{NHCOR}$); 2.64 ($2 \times \text{CH}_2$, $-\text{CH}_2-\text{COOR}$); 1.84–1.58 ($4 \times \text{CH}_2$, cyclopentane). SEC (DMAc, RI detection, PS calibration): $M_n = 4200 \text{ g mol}^{-1}$, $D = 1.36$.

Poly{cyclohexanediacetic acid-*alt*-[bis(2-oxazoline)]} **P7**: ^1H NMR (400 MHz, HFIP- d_2): $\delta/\text{ppm} = 8.08$ – 7.94 ($2 \times \text{NH}$); 4.25 ($2 \times \text{CH}_2$, $-\text{CH}_2-\text{OOCR}$); 3.85 ($2 \times \text{CH}_2$, $-\text{CH}_2-\text{OH}$); 3.66 ($2 \times \text{CH}_2$, $-\text{CH}_2-\text{NHCOR}$); 3.55 ($2 \times \text{CH}_2$, $\text{HO}-\text{CH}_2-\text{CH}_2-\text{NHCOR}$); 2.73–2.52 ($2 \times \text{CH}_2$, $-\text{CH}_2-\text{COOR}$); 1.80–1.35 ($5 \times \text{CH}_2$, cyclohexane). SEC (DMAc, RI detection, PS calibration): $M_n = 4400 \text{ g mol}^{-1}$, $D = 1.49$.

Poly{phenylsuccinic acid-*alt*-[bis(2-oxazoline)]} **P8**: ^1H NMR (400 MHz, HFIP- d_2): $\delta/\text{ppm} = 8.10$ – 7.88 ($2 \times \text{NH}$); 7.53–7.00 ($5 \times \text{CH}$, $\text{Ar}-\text{H}$); 4.36–4.09 ($2 \times \text{CH}_2$, $-\text{CH}_2-\text{OOCR}$); 3.90–3.81 ($2 \times \text{CH}_2$, $-\text{CH}_2-\text{OH}$); 3.72–3.44 ($4 \times \text{CH}_2$, $-\text{CH}_2-\text{NHCOR}$, $\text{HO}-\text{CH}_2-\text{CH}_2-\text{NHCOR}$); 3.35–3.18 (CH , $-\text{CHAr}-$); 3.07–2.80 (CH_2 , $-\text{CH}_2-\text{COOR}$). SEC (DMAc, RI detection, PS calibration): $M_n = 2500 \text{ g mol}^{-1}$, $D = 1.85$.

Nanoparticle preparation

Aqueous nanoparticle suspensions were prepared by the nanoprecipitation method. 1 mg of polymer was dissolved in 1 mL of HFIP. 0.5 mL of this solution was slowly injected into 5 mL of MilliQ water under stirring (1000 rpm) at room temperature. The open vial was left stirring overnight in order to evaporate the HFIP. DLS measurements were performed 24 h after preparation.

The Flory–Huggins theory

Solubility predictions using the FH theory^{41–43} are based on a mean-field lattice approach, which divides the mixed state into equally sized segments with a molar volume v_m . Each of these segments represents subunits of a polymer (1) or solvent (2) molecule, which interact with an average energy per segment pair ϵ_{ij} . The FH parameter χ_{FH} is defined as⁴⁴

$$\chi_{\text{FH}} = \frac{z_{\text{FH}}}{RT} (\epsilon_{12} - 0.5(\epsilon_{11} + \epsilon_{22})), \quad (1)$$

where T is the temperature, R the gas constant, and z_{FH} the coordination number of the mean-field lattice. For a binary mixture containing mole fractions x_1 and x_2 of polymer and solvent segments, respectively, the energy of mixing per segment $\Delta e_{\text{m,FH}}$ can be calculated as

$$\Delta e_{\text{m,FH}} = RTx_1x_2\chi_{\text{FH}}. \quad (2)$$

Note that in FH theory every segment occupies the same volume and, therefore, the segment mole fractions x_i are the same as the volume fractions of the components. For small mixing volume changes, the segment molar Gibbs energy of

mixing Δg_{m} for the polymer and solvent molecules consisting of r_1 and r_2 segments, respectively, is given as

$$\Delta g_{\text{m}} = RT \left(\frac{x_1}{r_1} \ln \phi_1 + \frac{x_2}{r_2} \ln \phi_2 + x_1x_2\chi_{\text{FH}} \right). \quad (3)$$

The original definition of the FH parameter does not account for the actual atomic structure of polymer–solvent mixtures.⁴⁴ Here, we derive a modified formula for χ_{FH} , which includes the structural information through the radial distribution functions (RDF) of segment pairs obtained from atomistic simulations. The self-energy per segment pair ϵ_{ii} is calculated from the Hildebrand solubility parameter δ_i of the pure substances ($i = 1, 2$), the molar volume v_i of segment i and the coordination number z_{ii} obtained from the corresponding RDF (see the ESI†)^{45,46}

$$\epsilon_{ii} = \frac{-2v_i\delta_i^2}{z_{ii}}. \quad (4)$$

Similarly, the interaction energy between segments ϵ_{12} is calculated using the solubility parameter of the binary mixture δ_m and the average coordination number \bar{z}_{12} of the polymer and solvent segments (see the ESI†)

$$\epsilon_{12} = \frac{1}{\bar{z}_{12}} (-2v_m\delta_m^2 - x_1z_{11m}\epsilon_{11} - x_2z_{22m}\epsilon_{22}), \quad (5)$$

where x_1 and x_2 as well as z_{11m} and z_{22m} are the mole fractions and coordination numbers of the polymer and solvent segments in the mixture, respectively. v_m is defined as the average molar volume of the mixture per polymer repeating unit and solvent molecule. For the coordination number z_{FH} of the FH mean-field lattice (*cf.* eqn (1)), the total coordination number of the mixed state is used with $z_{\text{FH}} = x_1z_{11m} + x_2z_{22m} + \bar{z}_{12}$.

Further improvement of thermodynamic modeling of polymer mixtures can be achieved employing composition dependent FH interaction parameters.⁴⁷ So far, such parameters have been derived by fitting experimental phase diagrams.⁴⁷ Here, we present an approach which derives the composition dependent FH interaction parameter directly from atomistic simulations. For this purpose, the coordination number z_{FH} in eqn (1) is replaced with linear model functions $F_i(x_i) = A_i(1 - x_i) + B_i$ and a parameter F_{12} that takes into account the structural changes with varying mixture compositions. The resulting FH parameter χ_z is given as (see the ESI†)

$$\chi_z = \frac{1}{RT} (F_{12}\epsilon_{12} + 0.5(F_1(x_1)\epsilon_{11} + F_2(x_2)\epsilon_{22})). \quad (6)$$

The composition independent parameters A_i , B_i and F_{12} are adjusted to yield the coordination numbers of the segments in the mixed state z_{11m} , z_{22m} and \bar{z}_{12} that correspond to the intermolecular structure obtained from atomistic simulations (see the ESI† for details). In contrast to the original definition of χ_{FH} , (eqn (2)), χ_z yields the FH energy of mixing $\Delta e_{\text{m,z}} = RTx_1x_2\chi_z$ that has the same value as the energy of mixing $\Delta e_{\text{m,sim}}$ derived directly from atomistic simulations, *i.e.*

$$\Delta e_{\text{m,z}} = \Delta e_{\text{m,sim}} = x_1v_1\delta_1^2 + x_2v_2\delta_2^2 - v_m\delta_m^2. \quad (7)$$

Computational procedure

Atomistic simulations were performed employing the *Materials Studio* (Version 17.1) program suite⁴⁸ along with the COMPASSII force field.⁴⁹ All materials were modelled as three-dimensional periodic amorphous cells constructed using a configurational bias Monte Carlo procedure⁵⁰ implemented in the *Amorphous Cell* module based on the algorithm of Theodorou and Suter.⁵¹

The unit cells of PEAs **P1** to **P8** (Scheme 1) contained 50 polymer chains with a degree of polymerization (DP) of 10, which is close to the experimentally determined values (cf. Table 1). The same DP was chosen for all models to facilitate a direct comparison and analysis of simulation results for different PEA structures. The unit cells of pure solvents, tetrahydrofuran (THF) and acetone (ACE), contained 800 molecules. In order to test the thermodynamic models described above, structure models for four different polymer–solvent mixtures with an approximate solvent content of 10 wt% were created. **P4** and **P8** were chosen as test cases. For both, the unit cells contained 50 polymer chains (DP = 10) as well as 232 and 258 THF molecules for **P4** and **P8**, respectively. The structure models of the ACE-**P4** and ACE-**P8** mixtures comprised 288 and 320 acetone molecules, respectively.

For each unit cell, three amorphous initial structures were constructed and geometrically optimized. Next, the lowest energy minima were refined employing MD simulations along with a simulated annealing procedure for generation of energetically more stable configurations. For this, the structure models were equilibrated at $T = 300$ K using the canonical (NVT) ensemble followed by a stepwise temperature increase up to 1000 K and a later decrease back to 300 K. In each step, the temperature was increased (decreased) by 100 K and, subsequently, the structure was equilibrated for 5 ps.

Next, MD simulations using the isothermal-isobaric (NPT) ensemble at zero target pressure and $T = 300$ K were performed with an equilibration for 100 ps employing the Berendsen barostat⁵² and a further simulation using the Parrinello–Rahman barostat^{53–55} with a duration of 300 ps. The average cell parameters of the structure models were evaluated for the last 200 ps of the NPT simulations. The unit cells of the final structures of the NPT trajectories were scaled to the average

cell parameters and the structure models were again equilibrated for 250 ps employing the NVT ensemble with a target temperature of 300 K. Average values of properties such as cohesive energy densities C , which are related to the Hildebrand solubility parameters with $C = \delta^2$, were calculated from the last 200 ps of the NVT simulations. All MD simulations employed the module *Forcite* along with a time step of 1 fs and the Nosé–Hoover thermostat.^{56,57}

The total equilibration time in our simulations including the initial annealing procedure and following NPT and NVT MD simulations is 725 ps. This time is certainly not sufficient to describe full relaxation of polymer conformations, which takes place on at least the μ s scale. However, the Monte Carlo algorithm of Theodorou and Suter^{50,51} used to generate initial polymer models was demonstrated⁵¹ to yield already well-relaxed amorphous glassy polymer models. The subsequent MD simulations are used only to sample the local atomic and vibrational motions, which take place at the fs to ps scale. In addition, for each model used in our simulations we have generated three fully independent initial structures, which yield virtually the same cohesive energy densities and RDF, in particular of the first coordination sphere.

Calculations of the RDF used coarse grained models of the final, geometrically optimized structures of the last NVT trajectory. Generation of coarse grained models used the module *Mesostructure Builder* approximating one polymer repeating unit (cf. Scheme 1) and solvent molecule as one coarse grained bead, respectively. The coarse grained models obtained were then used for the calculation of the intermolecular RDFs and coordination numbers z_{ij} used in eqn (3) and (4) (see the ESI†).

For elucidation of the crystal structure of **P1**, 16 initial structures assuming an infinite chain length were constructed similar to previous theoretical studies on the crystal structure of Nylon 6 (see the ESI†).⁵⁸ All initial structures were geometrically optimized under constant (zero) pressure conditions. Subsequently, the X-ray diffraction patterns were calculated employing the module *Reflex* (*Materials Studio*, Version 17.1). Finally, three crystal structures showing diffraction peak positions similar to the experimentally observed X-ray diffracto-

Table 1 Selected characterization data of the polyesteramides **P1** to **P8** obtained from NMR spectroscopy, SEC, DSC and WAXS. 2,2'-Bis(2-oxazoline) was used for the synthesis of all PEAs

PEA	Diacid	$M_{n(\text{NMR})}^a$ [g mol ⁻¹]	DP ^a	$M_{n(\text{SEC})}^b$ [g mol ⁻¹]	D^b	T_g^c [°C]	T_m^c [°C]	X_c^d [%]
P1	Succinic acid	1200	4	n.a.	n.a.	n.a.	152/211/222	50
P2	Adipic acid	5000	17	n.a.	n.a.	n.a.	181/189	18
P3	Dodecanedioic acid	7600	20	n.a.	n.a.	n.a.	149/168	39
P4	Dimethylglutaric acid	4400	14	5200	1.26	21	n.a.	n.a.
P5	Diethylglutaric acid	7100	21	6200	1.26	14	n.a.	n.a.
P6	Cyclopentanediactic acid	3800	11	4200	1.36	25	n.a.	n.a.
P7	Cyclohexanediactic acid	4600	13	4400	1.49	26	n.a.	n.a.
P8	Phenylsuccinic acid	2600	8	2500	1.90	50	n.a.	n.a.

^a Determined by ¹H NMR spectroscopy (400 MHz, HfIP-d₂). ^b Determined by SEC (DMAc, 0.21 wt% LiCl, RI detection, PS calibration).

^c Determined by DSC in the 2nd heating run, inflection values are reported for T_g . ^d The degree of crystallinity determined by WAXS.

gram of **P1** were chosen for the structure refinement (*cf.* Experimental section and Fig. S13†).

Results and discussion

Polymer synthesis and characterization

A PEA library was synthesized by polyaddition of 2,2'-bis(2-oxazoline) as an AA monomer and eight different dicarboxylic acids acting as the BB monomers. The bisoxazoline monomer was kept constant throughout the study to explore the impact of different diacid structures on the properties of the resulting PEAs. The utilized dicarboxylic acids are indicated in the corresponding PEA structures depicted in Scheme 1 and were commercially available, being therefore ideally suitable for a screening approach. The polymerization followed an AA + BB step-growth mechanism, including the opening of the 2-oxazoline rings by a nucleophilic attack of the carboxylic acid.^{25,27,28,59} As both monomers were bifunctional, this yielded a repetitive oxalamide unit and two ester moieties in the main chain of the PEA. For **P1–P3**, unsubstituted aliphatic dicarboxylic acids were used, aiming towards information regarding the influence of the spacer length between the diamide groups on the polymer properties. In addition, a C₃ spacer between the ester moieties was kept constant, whereas the substitution pattern was varied: dimethyl and diethyl residues were introduced to alter the hydrophobicity of **P4** and **P5**, whereas **P6** and **P7** were obtained from diacids with aliphatic cyclic substituents, *i.e.* cyclopentyl and cyclohexyl moieties. It should be noted that the carbon atom number is the same for **P5** and **P6**. **P8** included an aromatic moiety to further investigate the effect of the additional electron density. The syntheses were performed in a straightforward manner by simply adding the monomers in equimolar amounts in DMF and heating the reaction mixture at 150 °C overnight. An overview of the synthesized PEAs and their characterization results is provided in Table 1.

IR spectroscopy provided initial confirmation of the functional groups present in the PEAs (Fig. S1 and S2†). All IR

spectra clearly revealed the presence of ester moieties, as indicated by the ester carbonyl bands around 1730 cm⁻¹. Also the amide I and amide II bands around 1650 cm⁻¹ and 1530 cm⁻¹, respectively, were detected for all PEAs, thereby indicating a successful polyaddition reaction. The spectra also hinted towards the absence of a starting material, as neither ν OH stretching bands of the dicarboxylic acid, nor ether (1110 cm⁻¹) or imine (1621 cm⁻¹) bands deriving from the 2-oxazoline were detected. In particular, the area increase of the ν -CH₂- stretching band was consistent with the increased length of the aliphatic linker between the ester groups in the PEA series **P1** to **P3**. Besides, the IR spectrum of **P8** exhibited the sharp ν (=CH-) aromatic band.

Presumably due to hydrogen bonds forming between the amide moieties, in particular the PEAs containing unsubstituted aliphatic spacers **P1** to **P3** were not readily soluble in a range of common deuterated solvents. However, HFIP is well-known to break such hydrogen bonds. As all synthesized PEAs were soluble in HFIP, the deuterated form of the solvent was applied for ¹H NMR spectroscopy, enabling further structural insight into the new materials. Fig. 1 exemplarily depicts the ¹H NMR spectrum of **P3**. The spectra of all other synthesized PEAs are provided in the ESI (Fig. S3–S9†).

In particular, peaks 4 and 5 in Fig. 1 confirmed the opening of both oxazoline rings forming amide and ester moieties with the dicarboxylic acids. The respective signals labelled 4' and 5' were associated with the polymer end groups functionalized with a -CONH-CH₂-CH₂-OH moiety (see below), as confirmed by additional DOSY experiments (data not shown). As no carboxylic acid protons were detected in the ¹H NMR spectra for any PEA, the peak integrals of these signals were utilized to estimate the DP. The resulting molar masses *M*_{n(NMR)} varied between 1200 and 7100 g mol⁻¹ for **P1** to **P8** and corresponded to DP values between 4 and 21. A clear correlation between the utilized diacid and the DP of the PEA could not be found. It should be noted that all other signals in the spectra of the different PEAs could be unambiguously assigned to the spacers between the ester moieties that result from the use of various dicarboxylic acids for the polyadditions.

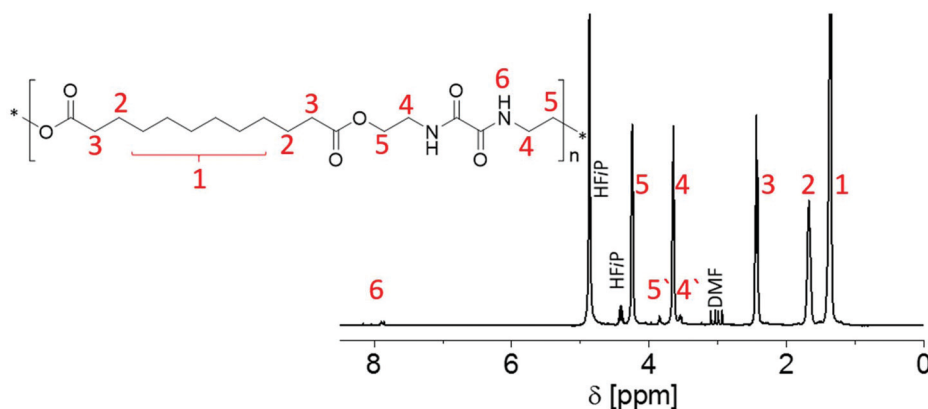


Fig. 1 ¹H NMR spectrum (400 MHz, HFIP-d₂) of **P3** and assignment of the peaks to the schematic representation of the polymer structure. Peaks 5' and 4' correspond to the chemical shift of a polymer end group -CONH-CH₂-CH₂-OH.

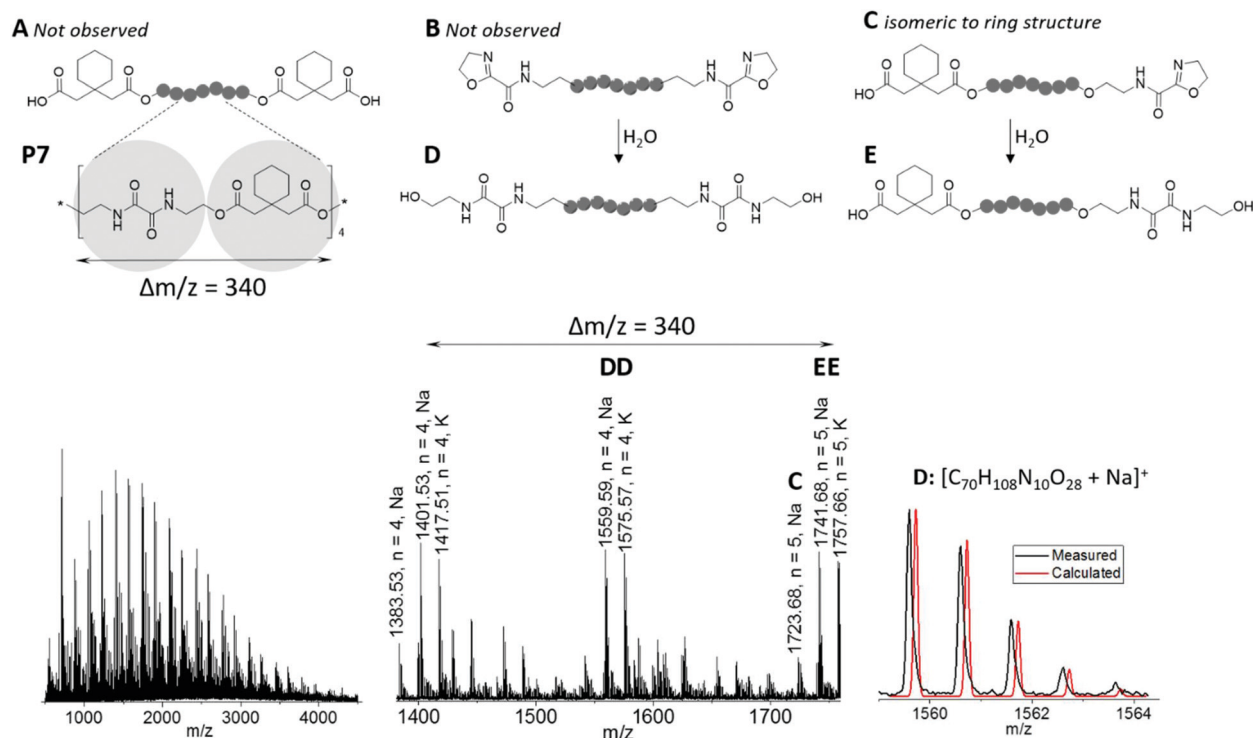


Fig. 2 MALDI-ToF mass spectrum (matrix: DHB) of **P7**. Top row: Species **A**, **B**, and **C** including end groups expected from the polymerization mechanism and formation of end groups yielding species **D** and **E** that were detected in the mass spectrum. Left bottom: Full mass spectrum. Center bottom: Zoom into the most abundant m/z region and peak assignment. Right: Overlay of the calculated and measured isotopic pattern for the exemplary structural assignment of one observed **D** peak.

MALDI-ToF mass spectrometry investigation provided further insight into the polymer end groups present in the samples, as exemplarily shown for **P7** in Fig. 2. In accordance with the repeating unit of the PEA obtained from BisOx and cyclohexanediactic acid, the spectrum featured peaks spaced by regular m/z intervals of $\Delta m/z = 340$. Besides several less abundant m/z series, four main distributions were assigned. Because ionization occurred with both, sodium and potassium cations, these corresponded to two different PEA species. Three species would be expected from the polyaddition mechanism: chains functionalized with two 2-oxazoline end groups, chains comprising two carboxylic acid end groups, and chains carrying one 2-oxazoline and one carboxylic acid end group. It should be noted that the latter are isobaric to cyclic species and, surprisingly, represented the only one of these structures that could be assigned to less intense peaks in the MALDI-ToF mass spectrum (species **C** in Fig. 2). Instead of 2-oxazoline terminated macromolecules, $-\text{CO}-\text{NH}-\text{CH}_2\text{CH}_2-\text{OH}$ end groups were found, either on both chain ends of **P7** (species **D** in Fig. 2), or in combination with a carboxylic acid end group (species **E** in Fig. 2). Exemplarily, an overlay of calculated and measured isotopic patterns is depicted for the sodium adduct of the former. These end groups were presumably formed by opening of the 2-oxazoline rings by a nucleophilic attack of water. In fact, similar structures appeared during attempts to recrystallize BisOx from methanol, or were present in batches of BisOx that were stored for a long time. Although alcohols

can also act as nucleophiles to attack 2-oxazoline moieties,⁶⁰ none of the resulting macromolecules were found in the MALDI-ToF mass spectra.

As **P4** to **P8** were soluble in DMAc, these PEAs were further investigated by SEC to obtain information regarding the molar mass distribution (Fig. S10†). The obtained molar masses $M_{n(\text{SEC})}$ from 2500 to 6200 g mol^{-1} were in reasonable agreement with values obtained from $^1\text{H NMR}$ spectroscopy. The purified polymers featured unimodal molar mass distribution with dispersity values (\mathcal{D}) from 1.3 to 1.9, as expected for a step-growth polymerization with limited control over the DP.

Bulk properties

Despite the rather oligomeric nature of the PEAs, detailed investigations regarding their structures in solid state were performed. Thereby, it was possible to gain access to qualitative information regarding the presence of strong intermolecular interactions between the macromolecules in a straightforward manner. Enabling the formation of crystallites in bulk materials, these interactions might also complicate the formation of nanoparticle dispersions. The PEAs were hence investigated by means of DSC and WAXS. TGA measurements were performed to ensure the thermal stability during the course of the measurements (Fig. S11†).

DSC measurements were performed using the bulk materials in the temperature range from -50 to 260 $^\circ\text{C}$ for **P1**

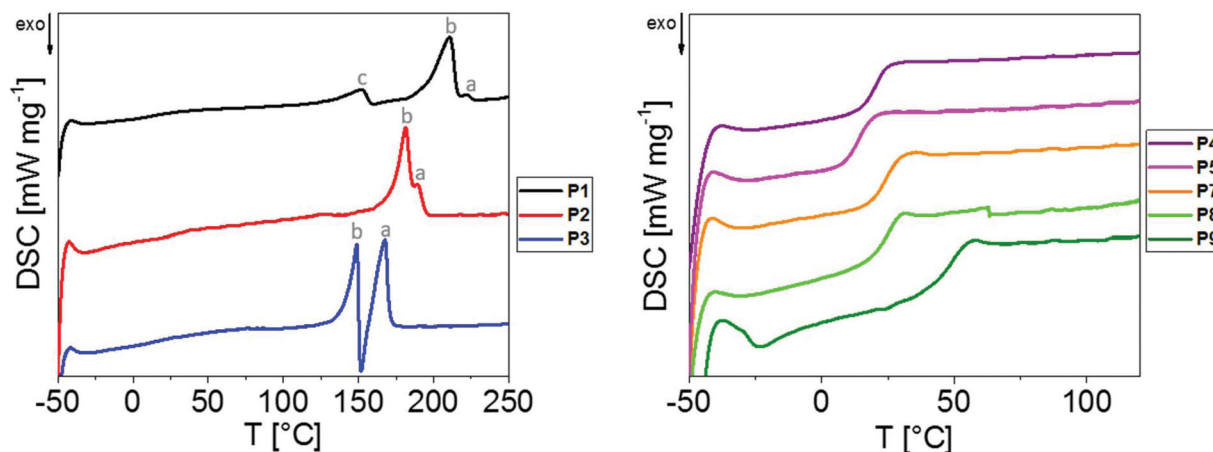


Fig. 3 DSC thermograms (second heating run, heating rate: 20 K min⁻¹). Left: PEAs **P1** to **P3** comprising linear alkylene spacers of various lengths (measurement from -50 to 260 °C). Right: PEAs **P4** to **P8** comprising different substituents (measurement from -50 to 120 °C). The y axes are shifted vertically for clarity.

to **P3** and from -50 to 120 °C for **P4** to **P8** (Table 1 and Fig. 3). For **P1** to **P3** comprising linear aliphatic spacers of various lengths, the DSC thermograms revealed melting peaks ranging from 149 to 222 °C, indicating the presence of semi-crystalline materials.

Exclusively the thermogram of **P1**, *i.e.* the PEA synthesized from the shortest dicarboxylic acid, revealed a third peak (labelled with “c” in Fig. 3) at 152 °C, which might have resulted from less perfect crystals in the form of “bundle chains” due to decreased chain flexibility. Two distinct melting peaks at higher temperatures (labelled as “a” and “b” in Fig. 3) were observed for **P1** to **P3**, which might indi-

cate the presence of two modifications in the bulk materials. The corresponding T_m values decreased with the increase in the length of the alkylene spacer between the ester moieties, which is consistent with observations made for aliphatic/aromatic PEAs by Kronek *et al.*³⁰ In addition, the fraction of crystalline domains melting at higher temperatures (“a” Fig. 3) increased with the increase in the linker length.

To gain deeper insight into their crystalline structures, **P1** to **P3** were hence further analyzed by means of WAXS (Fig. 4). The corresponding lattice parameters for **P1** and **P3** are listed in the ESI.†

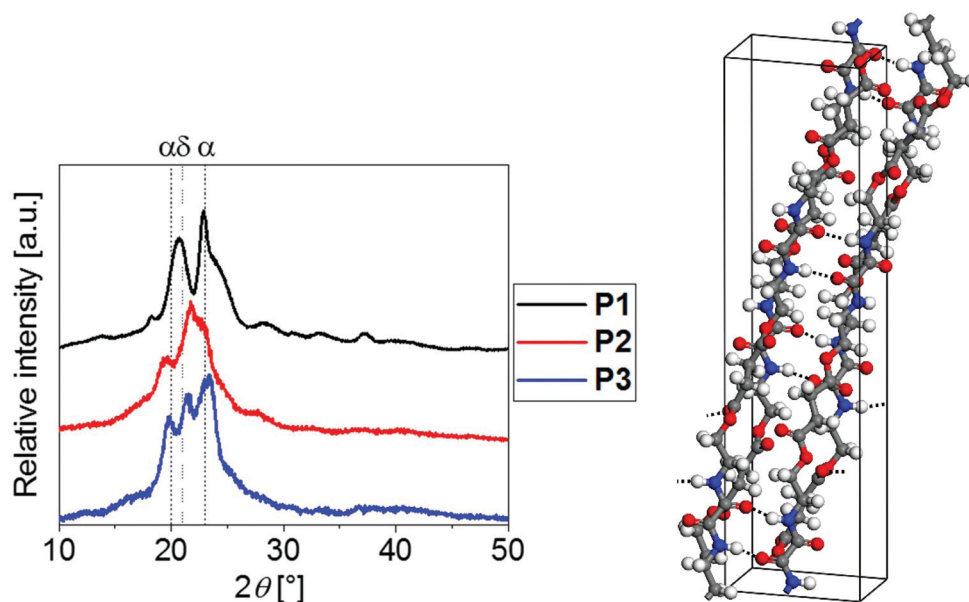


Fig. 4 Left: Wide-angle X-ray diffractograms of PEAs **P1** (synthesized from BisOx and succinic acid), **P2** (synthesized from BisOx and adipic acid) and **P3** (synthesized from BisOx and dodecanedioic acid). Dotted lines indicate the characteristic Bragg reflections of Nylon11 α and δ forms. Right: Structure model of the crystalline structure of **P1** obtained by comparison of measured and calculated diffractograms (C: grey, O: red, H: white, dotted lines: H-bonds).

The similar positions of the diffraction peak maxima for **P1** to **P3** hinted towards the presence of similar crystalline phases. The well-studied polyamides with alkylene spacers between the amide moieties, *i.e.*, Nylon 6 or 11, are known to crystallize in a triclinic α -form ($2\theta \approx 20^\circ$, $2\theta \approx 23^\circ$) and a hexagonal δ -form ($2\theta \approx 21^\circ$), among others.^{61–65} Similar modifications were found for the investigated PEAs. In agreement with the melting peak observed from DSC, **P1** crystallized predominantly in an α -form ($2\theta \approx 21^\circ$, $2\theta \approx 23^\circ$, compare Fig. 4). In contrast, **P3** clearly revealed the additional Bragg reflection at $2\theta \approx 21.4^\circ$ that is associated with the δ modification, which is consistent with the two melting events observed using DSC. Unfortunately, the degree of crystallinity of **P2** was not sufficient for drawing analogous conclusions.

One would expect that the hydrogen bond interactions between the amide moieties of the PEAs represent the major driving force for crystallization. The higher mass fraction of amide moieties for PEAs with shorter alkylene spacers explained the high degree of crystallinity of **P1** ($X_c = 50\%$). This PEA was hence selected for computational studies aiming to elucidate the intermolecular structure and interactions at the atomic level. The structure model depicted in Fig. 4 was successfully employed for Rietveld refinement of the experimentally determined diffractogram. Excellent agreement between the calculated and refined lattice parameters support the reliability of the structure model obtained (see the ESI†). Two hydrogen bonds per repeating unit were formed between the amide groups between neighboring polymer chains. Such directional intermolecular interactions are expected to promote ordering of polymer chains during crystallization rationalizing the comparatively high degree of crystallinity of **P1**.

The PEAs **P4** to **P8** containing substituted spacers were found to be amorphous, as only glass transitions were detected by DSC with T_g values ranging from 14 to 50 °C (Table 1 and Fig. 3). Due to an increase in the free volume induced by the larger ethyl substituents of **P5**, its T_g of 14 °C was lower than that of the methyl substituted **P4** ($T_g = 21$ °C). For the cyclopentyl and cyclohexyl substituted **P6** and **P7**, respectively, similar T_g values of 25 °C and 26 °C were found. The aromatic residue of **P8** led to a significantly increased T_g of 50 °C. It should be noted that neither DSC investigations conducted up to 260 °C nor WAXS studies indicated the presence of any crystalline domains, showing that all substituents effectively prevented the crystallization of the PEAs **P4** to **P8**.

Computational solubility predictions

Having successfully gained access to eight PEAs with various structures based on the dicarboxylic acid utilized, their applicability to form nanoparticles in aqueous dispersions was targeted. Nanoprecipitation represents a straightforward method to obtain these, in the best case avoiding the addition of emulsifiers or harsh formulation conditions.⁴ A volatile and water-miscible solvent that is able to dissolve the polymer is required for this purpose. THF and acetone are the most commonly used ones. Having realized solubility issues with the PEA

series, we employed atomistic simulations to analyze their solubility behavior.

In order to facilitate the analysis, the cohesive energy densities C calculated by MD simulations can be separated into the electrostatic C_{el} and the van der Waals C_{vdw} contributions. The fraction of van der Waals interactions in the total intermolecular energy density is defined as

$$f_{vdw} = \frac{C_{vdw}}{C}. \quad (8)$$

f_{vdw} is used to characterize the intermolecular interactions of the PEAs. In a similar way, the Hildebrand solubility parameter δ can be decomposed into the electrostatic δ_{el} and the van der Waals δ_{vdw} contributions, with $\delta^2 = \delta_{el}^2 + \delta_{vdw}^2$. Fig. 5 and Table 2 compare the total Hildebrand δ and van der Waals interaction parameters δ_{vdw} for **P1** to **P8** as well as THF and acetone. In addition, Table 2 shows the electrostatic interaction parameter δ_{el} , the fraction of the van der Waals interactions f_{vdw} and the calculated mass densities.

For the PEA comprising linear aliphatic spacers of various lengths between the ester moieties, **P1** showed the strongest intermolecular interaction among the investigated PEAs. δ considerably decreased while f_{vdw} continuously increased with the number of backbone carbon atoms in the polymer repeating unit (**P2** and **P3**). This is connected with an increase of the

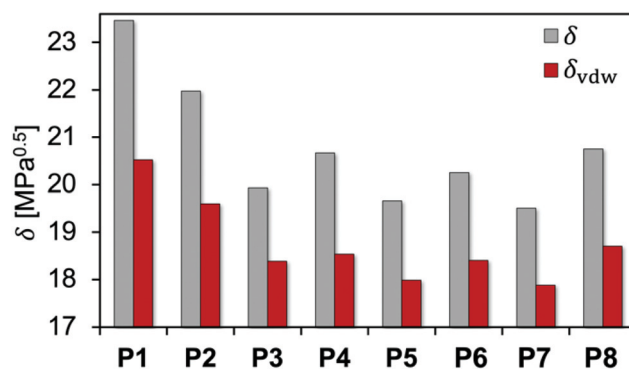


Fig. 5 Total δ and van der Waals δ_{vdw} interaction parameters calculated for all polyestaramides **P1** to **P8**.

Table 2 Interaction parameters δ , fraction of van der Waals interactions f_{vdw} and mass densities ρ calculated for all PEAs as well as THF and acetone (ACE)

PEA	δ [MPa ^{0.5}]	δ_{vdw} [MPa ^{0.5}]	δ_{el} [MPa ^{0.5}]	f_{vdw} [%]	ρ [g cm ⁻³]
P1	23.5	20.5	11.4	76.5	1.296
P2	22.0	19.6	10.0	79.5	1.237
P3	19.9	18.4	7.7	85.1	1.117
P4	20.7	18.5	9.1	80.4	1.214
P5	19.7	18.0	8.0	83.7	1.167
P6	20.3	18.4	8.5	82.6	1.222
P7	19.5	17.9	7.8	84.0	1.200
P8	20.8	18.7	9.0	81.2	1.253
THF	18.3	17.7	4.9	93.0	0.850
ACE	19.3	16.9	9.3	76.7	0.784

hydrophobicity of the PEAs when additional CH₂ groups are incorporated, while larger repeating units favor steric effects leading to weaker intermolecular interactions. The same trend was observed on comparing **P4** and **P5** (methyl vs. ethyl substituents) as well as **P6** and **P7** (cyclopentyl vs. cyclohexyl substituents), respectively. Introducing an aromatic moiety in **P8** leads to a slightly higher δ and lower f_{vdw} compared to **P6** and **P7**. This indicates that the presence of aromatic groups has only minor influence on the polymer–polymer interactions for the investigated PEAs.

The variation of δ and f_{vdw} calculated for the PEAs clearly indicates differences in solubilities. In previous studies, solubility predictions using Hildebrand parameters calculated using MD simulations were successfully correlated with experimental data for several compounds.^{10,11}

However, the general applicability of atomistic simulations combined with the FH theory for reliable predictions of the thermodynamic compatibility between polymers and low molar mass compounds has been questioned recently.^{66–68} In contrast to the previous models, our approach explicitly considers the intermolecular structure obtained from atomistic simulations for calculation of the FH interaction parameter χ_{FH} (eqn (1)) and its composition dependent counterpart χ_z (eqn (6)). In order to test the accuracy of both models for solubility predictions, the solubility of **P4** and **P8** in THF and acetone was tested experimentally. At a polymer concentration of 5 mg mL⁻¹, **P4** was soluble whereas **P8** was insoluble in both solvents. Table 3 compares the corresponding values of the energies of mixing Δe_m at solvent concentrations of about 10 wt% ($x_1 \approx 0.65$) used for the atomistic simulations. In addition, the Gibbs energies of mixing Δg_m for a polymer concentration of 5 mg mL⁻¹ ($x_1 \approx 0.004$) used for the experimental solubility tests are displayed. All calculations are performed at 300 K.

Both solubility predictions using χ_{FH} and χ_z agreed with the experimental observations, since **P4** is predicted to be soluble in THF and acetone ($\Delta g_m < 0$), whereas **P8** is insoluble in both solvents ($\Delta g_m > 0$). However, the energy of mixing obtained from atomistic simulations and $\Delta e_{m,z}$ ($\Delta e_{m,z} = \Delta e_{m,sim}$, eqn (7)) was negative at $x_1 \approx 0.65$ for the mixtures THF-**P8** and ACE-**P8**, but the FH theory along with χ_{FH} predicted strongly endothermic mixtures at this composition. Consequently, considerable deviations between $\Delta g_{m,z}$ and $\Delta g_{m,FH}$ were observed for the mixtures containing **P8**. In contrast, smaller differences between the predictions using χ_{FH} and χ_z were found for the tested **P4** solutions.

For comparison, some previous studies calculated the FH interaction parameter from atomistic simulations without consideration of the actual intermolecular structure, e.g., using the formula⁸

$$\chi_{FH}^* = \frac{\Delta e_{m,sim}}{RTx_1x_2} \quad (9)$$

In the case of the **P8** mixtures for which $\Delta e_{m,sim} < 0$, eqn (9) would yield negative FH parameters and, therefore, incorrectly predict complete solubility of **P8** in THF and acetone. In contrast, our definition of the FH parameters χ_{FH} and χ_z explicitly takes into account the intermolecular structure obtained from atomistic simulations. This leads to correct predictions for dilute polymer solutions. For such low polymer concentrations, $\Delta g_{m,z}$ and $\Delta g_{m,FH}$ differ only slightly indicating that a random mean-field lattice along with a composition independent coordination number z_{FH} reasonably approximates dilute polymer solutions (Fig. S15†). However, for higher polymer concentrations, calculations using χ_{FH} considerably deviated from predictions using the composition dependent χ_z and yielded energies of mixing inconsistent with the simulation results (see the ESI†). This applied in particular to the solutions containing **P8**, which is probably connected with steric effects and specific interactions originating from the phenyl groups. Thus, the use of the composition dependent χ_z was of central importance to achieve satisfactory agreement with both simulations and experimental results in the case of the investigated PEA solutions, since χ_z implicitly includes the deviations of the polymer mixture from the random mean-field lattice. However, directional interactions such as hydrogen bonding are not explicitly considered in FH theory.⁶⁹ As a consequence, more accurate thermodynamic models are required for reliable solubility predictions of polymers showing pronounced specific interactions. This applies in particular to **P1** for which WAXS experiments and the calculated crystal structure showed a strong influence of H-bonds on the polymer properties.

Aqueous nanoparticle dispersions

As the MD simulations indicated that the most commonly used solvents, *i.e.* THF and acetone, were not applicable for the entire series of the PEAs due to solubility restrictions, HFIP was applied as an alternative solvent for nanoprecipitation. HFIP is volatile (boiling temperature of 58 °C at ambient pressure), miscible with water and solubilizes all of the investi-

Table 3 Flory-Huggins parameter χ_{FH} (eqn (1)), χ_z (eqn (6)) and energy of mixing $\Delta e_{m,sim}$ [kJ mol⁻¹] of the tested polymer solutions at compositions used in simulations ($x_1 \approx 0.65$) and Gibbs energies of mixing Δg_m [J mol⁻¹] at the experimental mixture composition ($x_1 \approx 0.004$)

x_1	0.04					0.65		
	Exp.	χ_{FH}	χ_z	$\Delta g_{m,z}$	$\Delta g_{m,FH}$	χ_{FH}	χ_z	$\Delta e_{m,sim}$
THF- P4	Soluble	-13.3	-6.9	-96	-160	-13.3	1.0	0.53
THF- P8	Insoluble	35.5	26.5	235	324	35.5	-6.2	-3.49
ACE- P4	Soluble	-7.4	-3.0	-59	-103	-7.4	-4.0	-2.33
ACE- P8	Insoluble	34.4	25.2	221	312	34.4	-7.6	-4.51

Table 4 DLS data and ζ potentials of polymeric nanoparticles prepared from HFiP. D_h denotes the Z-average

	P1	P2	P3	P4	P5	P6	P7	P8
D_h [nm]	Aggregation			114	143	227	160	76
PDI				0.13	0.05	0.13	0.05	0.18
ζ [mV]				-33	-37	-36	-35	-44

gated PEAs **P1** to **P8**, therefore meeting all the requirements for nanoprecipitation.

Although the nanoparticle formation by means of nanoprecipitation can in general be optimized for individual polymers by variation of, e.g., the polymer concentration or solvent/non-solvent ratios, constant formulation parameters ($c(\mathbf{P1}$ to $\mathbf{P8}) = 1 \text{ mg mL}^{-1}$, volume ratio of HFiP/water = 1/10) were applied in this study to compare the influence of the PEA structure on the capability to easily form nanoparticles in aqueous dispersions. Accordingly, a solution of each polymer in HFiP was slowly injected into water under vigorous stirring, maintaining these concentrations and subsequently letting the organic solvent evaporate under ambient conditions. The obtained dispersions were analyzed by means of DLS (Fig. S11† and Table 4).

Despite the variation of the alkylene spacer length between the ester moieties, all semi-crystalline PEAs (**P1** to **P3**) resulted in aggregation during nanoprecipitation attempts, presumably due to the strong intermolecular interactions that were also evident from the Hildebrand solubility parameters. In particular, **P1** and **P2** formed macroscopic precipitates. In contrast, aqueous nanoparticle dispersions were successfully obtained from HFiP solutions of the amorphous PEAs **P4** to **P8**, irrespective of the increased or decreased number of carbon atoms compared to the semi-crystalline **P1** to **P3** (Fig. S12†). Except for the phenyl substituted **P8** that produced smaller nanoparticles, the nanoparticle sizes varied from 160 to 230 nm, with batch to batch differences of ± 25 nm. All nanoparticles exhibited negative zeta potentials ζ between -33 and -44 mV, indicating the stability of the aqueous dispersions (Table 4). Those PEAs that successfully formed nanoparticles showed lower particle size with the increase in the Hildebrand solubility parameter with the exception of **P6**. Similarly, it has been shown recently that the polymer nanoparticle size decreases with the increase in the FH parameter of the polymer and solvent used for nanoparticle preparation.⁶⁹ However, aggregation of **P1** to **P3** and considerably higher particle size of **P6** demonstrate that accurate modeling of polymer nanoparticle formation requires, as mentioned above, the consideration of specific interactions such as hydrogen bonding and, moreover, precipitation kinetics.

Conclusions

The polyaddition polymerization of 2,2'-bis(2-oxazoline) and dicarboxylic acids with different aliphatic substituents enabled

straightforward access to a PEA library. PEA with linear alkylene spacers between the ester moieties represented semi-crystalline materials, as confirmed by means of WAXS and DSC. Substituents at the spacer prevented the formation of crystallites through hydrogen bonding between the amide moieties of the material. These amorphous PEAs successfully formed aqueous nanoparticle dispersions by simple nanoprecipitation from HFiP into water. In contrast, strong intermolecular interactions that were evident from Hildebrand solubility parameters resulted in the formation of aggregates for the semi-crystalline materials. Although the predictability *via* Hildebrand parameters alone is to be taken into consideration with more than a grain of salt, MD simulations in combination with our improved FH theory provided accurate solubility predictions for the PEAs in THF and acetone.

However, in order to verify the general applicability of this theory along with χ_z for at least qualitative solubility predictions of polymers with low molar mass compounds of interest for nanomedicine, *i.e.* drugs, more test simulations are required, which will be the subject of a future publication. These will guide our future research regarding detailed formulation studies including a variety of solvents, concentrations and anti-inflammatory APIs to be encapsulated into polymeric nanoparticles formed from the developed PEAs.

Conflicts of interest

There are no conflicts to declare.

Acknowledgements

This project forms part of the Collaborative Research Centre PolyTarget (SFB 1278, projects A01 and Z01) funded by the German Research Foundation (DFG).

References

- 1 A. Bhakay, M. Rahman, R. N. Dave and E. Bilgili, *Pharmaceutics*, 2018, **10**, 86.
- 2 E. Lepeltier, C. Bourgaux and P. Couvreur, *Adv. Drug Delivery Rev.*, 2014, **71**, 86–97.
- 3 S. Guo and L. Huang, *Biotechnol. Adv.*, 2014, **32**, 778–788.
- 4 S. Schubert, J. T. Delaney Jr. and U. S. Schubert, *Soft Matter*, 2011, **7**, 1581–1588.
- 5 C. J. M. Rivas, M. Tarhini, W. Badri, K. Miladi, H. Greige-Gerges, Q. A. Nazari, S. A. G. Rodríguez, R. Á. Román, H. Fessi and A. Elaissari, *Int. J. Pharm.*, 2017, **532**, 66–81.
- 6 S. Sen, Y. Han, P. Rehak, L. Vuković and P. Král, *Chem. Soc. Rev.*, 2018, **47**, 3849–3860.
- 7 A. Gooneie, S. Schuschnigg and C. Holzer, *Polymer*, 2017, **9**, 16.
- 8 L. Huynh, C. Neale, R. Pomès and C. Allen, *Nanomedicine*, 2012, **8**, 20–36.

- 9 X. D. Guo, L. J. Zhang and Y. Qian, *Ind. Eng. Chem. Res.*, 2012, **51**, 4719–4730.
- 10 A. Erlebach, T. Ott, C. Otzen, S. Schubert, J. Czaplewska, U. S. Schubert and M. Sierka, *J. Comput. Chem.*, 2016, **37**, 2220–2227.
- 11 A. O. Kasimova, G. M. Pavan, A. Danani, K. Mondon, A. Cristiani, L. Scapozza, R. Gurny and M. Moeller, *J. Phys. Chem. B*, 2012, **116**, 4338–4345.
- 12 K. Herzog, R.-J. Mueller and W.-D. Deckwer, *Polym. Degrad. Stab.*, 2006, **91**, 2486–2498.
- 13 Y. Ikada and H. Tsuji, *Macromol. Rapid. Commun.*, 2000, **21**, 117–132.
- 14 L. N. Woodard and M. A. Grunlan, *ACS Macro Lett.*, 2018, **7**, 976–982.
- 15 S. Mecking, *Angew. Chem., Int. Ed.*, 2004, **43**, 1078–1085.
- 16 E. Grigat, R. Koch and R. Timmermann, *Polym. Degrad. Stab.*, 1998, **59**, 223–226.
- 17 N. Franz and H. A. Klok, *Macromol. Chem. Phys.*, 2010, **211**, 809–820.
- 18 Y. Feng, J. Lu, M. Behl and A. Lendlein, *Macromol. Biosci.*, 2010, **10**, 1008–1021.
- 19 A. Rodriguez-Galan, L. Franco and J. Puiggali, *Polymer*, 2011, **3**, 65–99.
- 20 L. Néry, H. Lefebvre and A. Fradet, *Macromol. Chem. Phys.*, 2004, **205**, 448–455.
- 21 A. Douhi and A. Fradet, *J. Polym. Sci., Part A: Polym. Chem.*, 1995, **33**, 691–699.
- 22 J. V. Seppälä, A. O. Helminen and H. Korhonen, *Macromol. Biosci.*, 2004, **4**, 208–217.
- 23 S. Y. Xu, Y. H. Shi, J. B. Zhao, S. L. Jiang and W. T. Yang, *Polym. Adv. Technol.*, 2011, **22**, 2360–2367.
- 24 C. Q. Huang, S. Y. Luo, S. Y. Xu, J. B. Zhao, S. L. Jiang and W. T. Yang, *J. Appl. Polym. Sci.*, 2010, **115**, 1555–1565.
- 25 B. M. Culbertson, *Prog. Polym. Sci.*, 2002, **27**, 579–626.
- 26 C. Weber, T. Neuwirth, K. Kempe, B. Ozkahraman, E. Tamahkar, H. Mert, C. R. Becer and U. S. Schubert, *Macromolecules*, 2011, **45**, 20–27.
- 27 K. Kempe, *Macromol. Chem. Phys.*, 2017, **218**, 1700021.
- 28 T. Kagiya, S. Narisawa, T. Maeda and K. Fukui, *J. Polym. Sci., Part B: Polym. Lett.*, 1966, **4**, 257–260.
- 29 J. Lustoň, J. Kronek, O. Markus, I. Janigová and F. Böhme, *Polym. Adv. Technol.*, 2007, **18**, 165–172.
- 30 J. Kronek, J. Nedbal, H. Valentová, M. Neubert, I. Janigová, N. Petrenčíková, P. Šrámková, K. Csomorová and L. Petra, *Polym. Test.*, 2018, **68**, 1–7.
- 31 Y. Sano, *J. Polym. Sci., Part A: Polym. Chem.*, 1989, **27**, 2749–2760.
- 32 C. H. Wilsens, N. J. Wullems, E. Gubbels, Y. Yao, S. Rastogi and B. A. Noordover, *Polym. Chem.*, 2015, **6**, 2707–2716.
- 33 P. Chevallier, J.-C. Soutif, J.-C. Brosse and A. Rincón-Guerrero, *Eur. Polym. J.*, 1998, **34**, 767–778.
- 34 J. Lustoň, J. Kronek, A. Kleinová, I. Janigová, H. Valentová and J. Nedbal, *J. Polym. Sci., Part A: Polym. Chem.*, 2012, **50**, 3936–3943.
- 35 I. B. Mansour, K. Alouani, E. Chauveau, V. Martin, F. Schiets and R. Mercier, *Eur. Polym. J.*, 2010, **46**, 814–820.
- 36 S. Li and M. Tao, *J. Therm. Anal. Calorim.*, 2013, **113**, 633–639.
- 37 T. Yin, H. Y. Sun, J. B. Zhao, Z. Y. Zhang and W. T. Yang, *Polym. Eng. Sci.*, 2014, **54**, 756–765.
- 38 P. Scardi, L. Lutterotti and P. Maistrelli, *Powder Diffr.*, 1994, **9**, 180–186.
- 39 J. B. Nichols, *J. Appl. Phys.*, 1954, **25**, 840–847.
- 40 J. E. Johnson, *J. Appl. Polym. Sci.*, 1959, **2**, 205–209.
- 41 P. J. Flory, *J. Chem. Phys.*, 1942, **10**, 51–61.
- 42 M. L. Huggins, *J. Phys. Chem.*, 1942, **46**, 151–158.
- 43 M. L. Huggins, *J. Am. Chem. Soc.*, 1942, **64**, 1712–1719.
- 44 I. Teraoka, in *Polymer Solutions: An Introduction to Physical Properties*, John Wiley & Sons, Inc., New York, 2002.
- 45 G. A. Mansoori, *Fluid Phase Equilib.*, 1993, **87**, 1–22.
- 46 J. H. Hildebrand, in *The Solubility of Nonelectrolytes*, Dover Publications, Inc., New York, 1964.
- 47 B. A. Wolf, in *Making Flory–Huggins Practical: Thermodynamics of Polymer-Containing Mixtures*, Springer-Verlag, Berlin, Heidelberg, 2011.
- 48 Dassault Systèmes BIOVIA, *Materials Studio, 17.1.0.48*, Dassault Systèmes, San Diego, 2017.
- 49 H. Sun, Z. Jin, C. Yang, R. L. C. Akkermans, S. H. Robertson, N. A. Spenley, S. Miller and S. M. Todd, *J. Mol. Model.*, 2016, **22**, 47.
- 50 R. L. C. Akkermans, N. A. Spenley and S. H. Robertson, *Mol. Simul.*, 2013, **39**, 1153–1164.
- 51 D. N. Theodorou and U. W. Suter, *Macromolecules*, 1985, **18**, 1467–1478.
- 52 H. J. C. Berendsen, J. P. M. Postma, W. F. v. Gunsteren, A. DiNola and J. R. Haak, *J. Chem. Phys.*, 1984, **81**, 3684–3690.
- 53 M. Parrinello and A. Rahman, *Phys. Rev. Lett.*, 1980, **45**, 1196–1199.
- 54 M. Parrinello and A. Rahman, *J. Appl. Phys.*, 1981, **52**, 7182–7190.
- 55 G. J. Martyna, D. J. Tobias and M. L. Klein, *J. Chem. Phys.*, 1994, **101**, 4177–4189.
- 56 S. Nosé, *J. Chem. Phys.*, 1984, **81**, 511–519.
- 57 W. G. Hoover, *Phys. Rev. A*, 1985, **31**, 1695–1697.
- 58 Y. Li and W. A. Goddard, *Macromolecules*, 2002, **35**, 8440–8455.
- 59 P. A. Gunatillake, G. Odian and D. A. Tomalia, *Macromolecules*, 1988, **21**, 1556–1562.
- 60 T. Huber, F. Böhme, H. Komber, J. Kronek, J. Lustoň, D. Voigt and B. Voit, *Macromol. Chem. Phys.*, 1999, **200**, 126–133.
- 61 H. Arimoto, M. Ishibashi, M. Hirai and Y. Chatani, *J. Polym. Sci., Part A: Gen. Pap.*, 1965, **3**, 317–326.
- 62 J. P. Parker and P. H. Lindenmeyer, *J. Appl. Polym. Sci.*, 1977, **21**, 821–837.
- 63 Q. Zhang, Z. Mo, H. Zhang, S. Liu and S. Z. Cheng, *Polymer*, 2001, **42**, 5543–5547.
- 64 J. Fernandez, G. Swallowe and S. Lee, *J. Appl. Polym. Sci.*, 2001, **80**, 2031–2038.

- 65 H. Shanak, K.-H. Ehses, W. Götz, P. Leibenguth and R. Pelster, *J. Mater. Sci.*, 2009, **44**, 655–663.
- 66 B. D. Anderson, *J. Pharm. Sci.*, 2018, **107**, 24–33.
- 67 A. D. Glova, S. G. Falkovich, D. I. Dmitrienko, A. V. Lyulin, S. V. Larin, V. M. Nazarychev, M. Karttunen and S. V. Lyulin, *Macromolecules*, 2018, **51**, 552–563.
- 68 E. R. Turpin, V. Taresco, W. A. Al-Hachami, J. Booth, K. Treacher, S. Tomasi, C. Alexander, J. Burley, C. A. Laughton and M. C. Garnett, *Mol. Pharmaceutics*, 2018, **15**, 4654–4667.
- 69 T. Cowen, K. Karim and S. A. Piletsky, *Polym. Chem.*, 2018, **9**, 4566–4573.

Supporting information

Polyesteramide library from dicarboxylic acids and 2,2' bis(2 oxazoline): Synthesis, characterization, nanoparticle formulation and molecular dynamic simulations

Irina Muljajew,^{†,‡} Andreas Erlebach,^{‡,§} Christine Weber,^{†,‡} Johannes R. Buchheim,[&] Marek Sierka,^{‡,§} Ulrich S. Schubert^{†,‡,}*

[†]Laboratory of Organic and Macromolecular Chemistry (IOMC), Friedrich Schiller University Jena, Humboldtstr. 10, 07743 Jena, Germany

[‡]Jena Center for Soft Matter (JCSM), Friedrich Schiller University Jena, Philosophenweg 7, 07743 Jena, Germany

[§]Otto Schott Institute of Materials Research (OSIM), Friedrich Schiller University Jena, Lößdergraben 32, 07743 Jena, Germany

[&]Institute for Technical Chemistry and Environmental Chemistry, Center for Energy and Environmental Chemistry Jena (CEEC Jena), Friedrich Schiller University Jena, Philosophenweg 7a, 07743 Jena, Germany

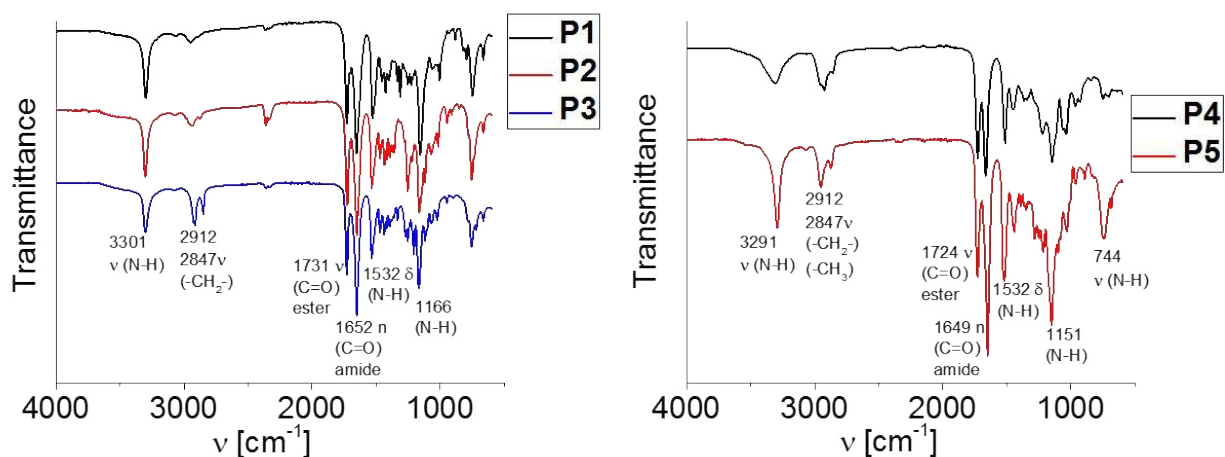


Figure S1: FT-ATR-IR spectra of the polyestaramides **P1** to **P5**.

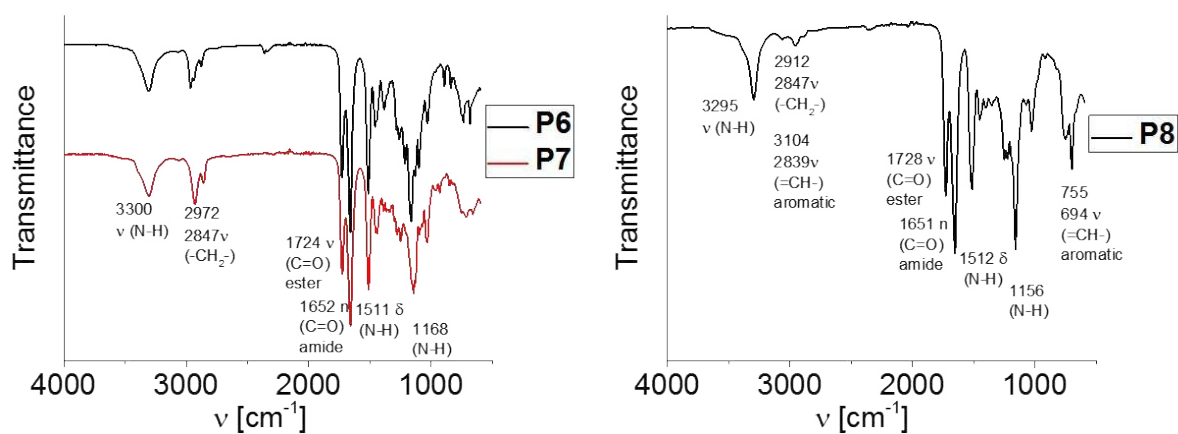


Figure S2: FT-ATR-IR spectra of the polyestaramides **P6** to **P8**.

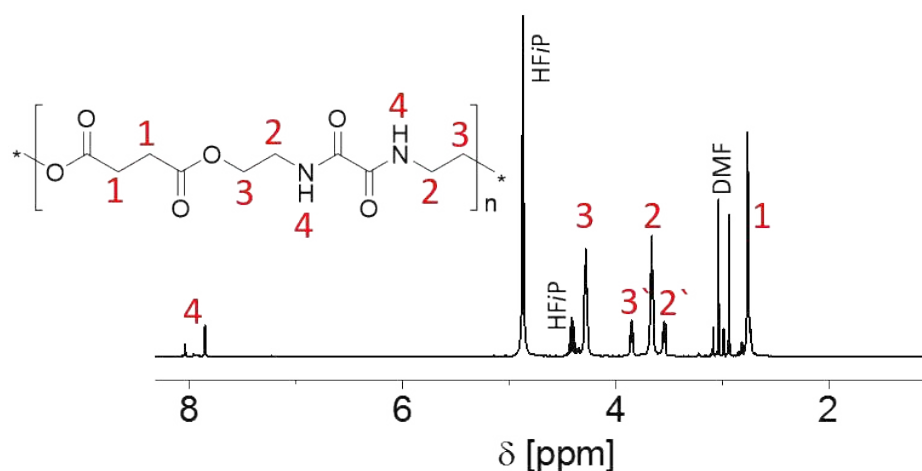


Figure S3: ^1H NMR spectrum (400 MHz, HF*i*P- d_2) of **P1** and assignment of the peaks to the schematic representation of the polymer structure. Peaks 3' and 2' correspond to the chemical shift of a polymer end group $-\text{CONH}-\text{CH}_2-\text{CH}_2-\text{OH}$.

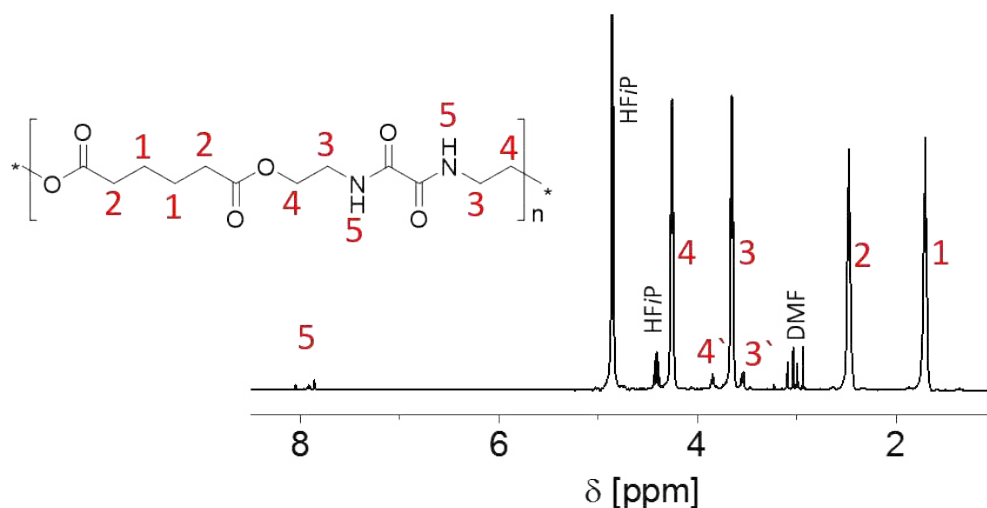


Figure S4: ^1H NMR spectrum (400 MHz, HF*i*P- d_2) of **P2** and assignment of the peaks to the schematic representation of the polymer structure. Peaks 4' and 3' correspond to the chemical shift of a polymer end group $-\text{CONH}-\text{CH}_2-\text{CH}_2-\text{OH}$.

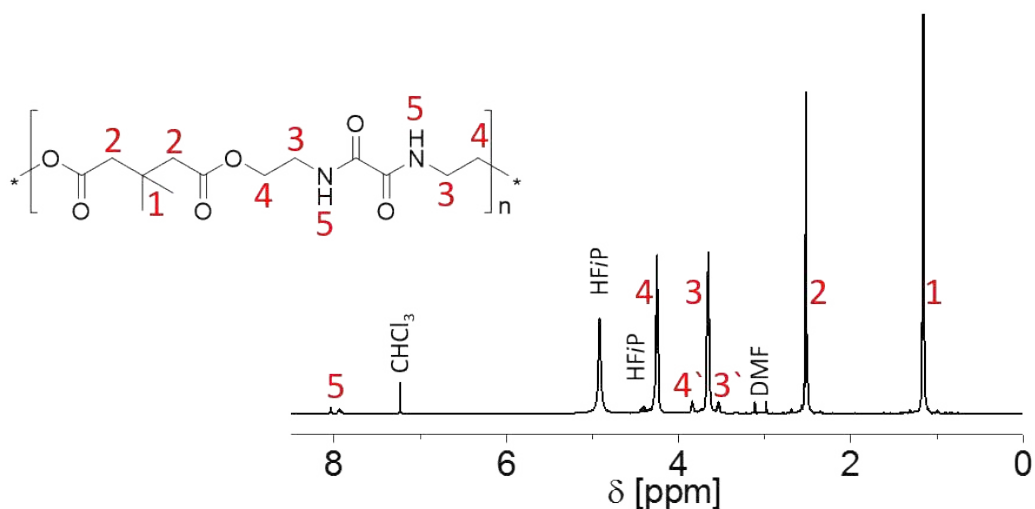


Figure S5: ^1H NMR spectrum (400 MHz, HFIP- d_2) of **P4** and assignment of the peaks to the schematic representation of the polymer structure. Peaks 4' and 3' correspond to the chemical shift of a polymer end group $-\text{CONH}-\text{CH}_2-\text{CH}_2-\text{OH}$.

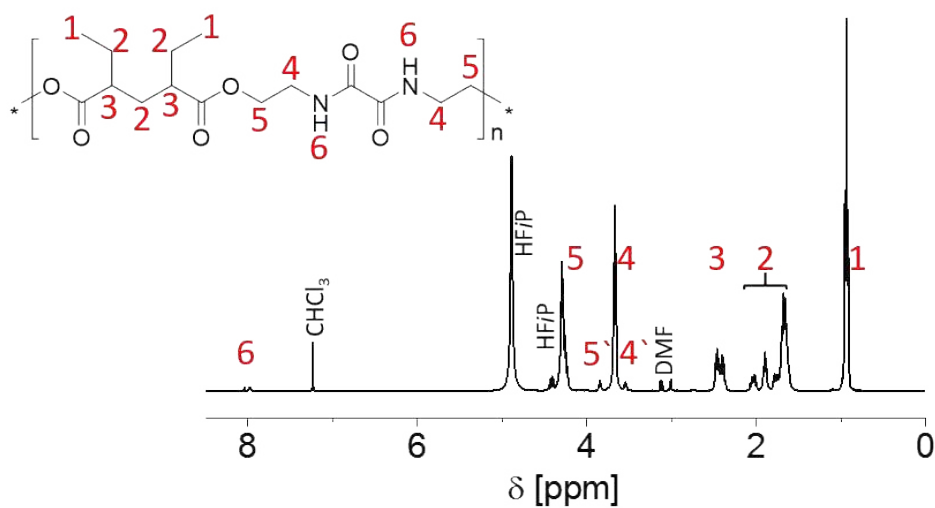


Figure S6: ^1H NMR spectrum (400 MHz, HFIP- d_2) of **P5** and assignment of the peaks to the schematic representation of the polymer structure. Peaks 5' and 4' correspond to the chemical shift of a polymer end group $-\text{CONH}-\text{CH}_2-\text{CH}_2-\text{OH}$.

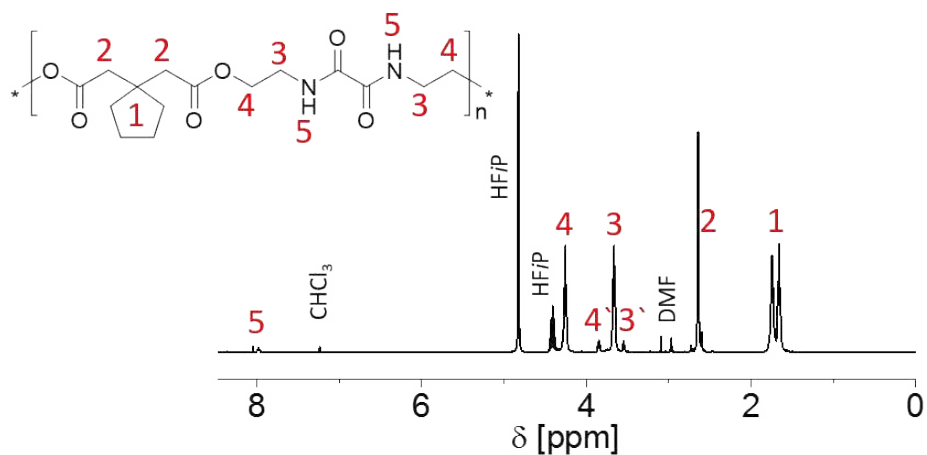


Figure S7: ¹H NMR spectrum (400 MHz, HFIP-d₂) of **P6** and assignment of the peaks to the schematic representation of the polymer structure. Peaks 4' and 3' correspond to the chemical shift of a polymer end group -CONH-CH₂-CH₂-OH.

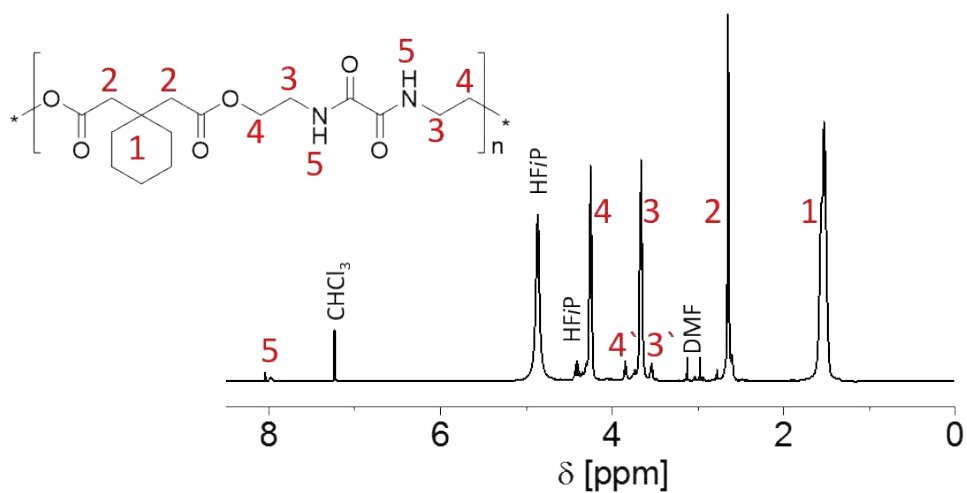


Figure S8: ¹H NMR spectrum (400 MHz, HFIP-d₂) of **P7** and assignment of the peaks to the schematic representation of the polymer structure. Peaks 4' and 3' correspond to the chemical shift of a polymer end group -CONH-CH₂-CH₂-OH.

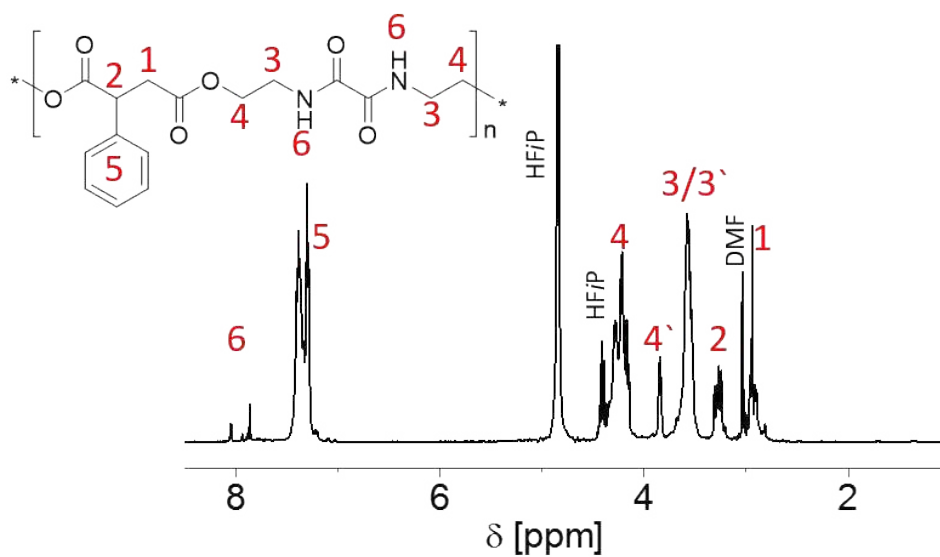


Figure S9: ^1H NMR spectrum (400 MHz, HFIP- d_2) of **P8** and assignment of the peaks to the schematic representation of the polymer structure. Peaks 4' and 3' correspond to the chemical shift of a polymer end group $-\text{CONH}-\text{CH}_2-\text{CH}_2-\text{OH}$.

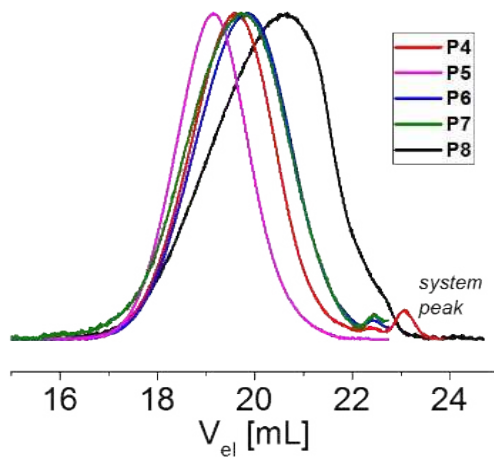


Figure S10: SEC elugrams (DMAc, RI detection) of the polyesters **P4** to **P8**.

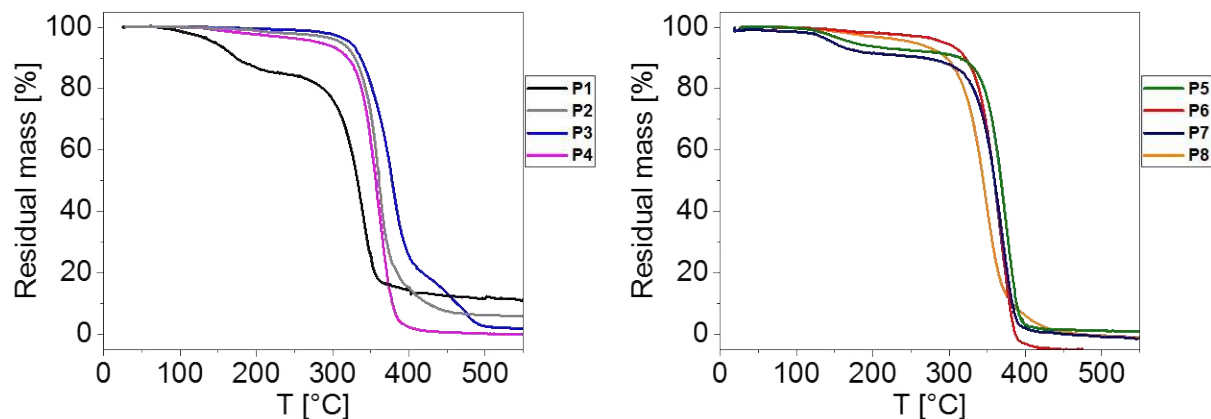


Figure S11: TGA thermograms of **P1** to **P4** (left) and **P5** to **P8** (right) (N_2 atmosphere, heating rate 20 K min^{-1}). The mass loss below $200\text{ }^\circ\text{C}$ was due to residual DMF present in **P1**, **P7** and **P5**.

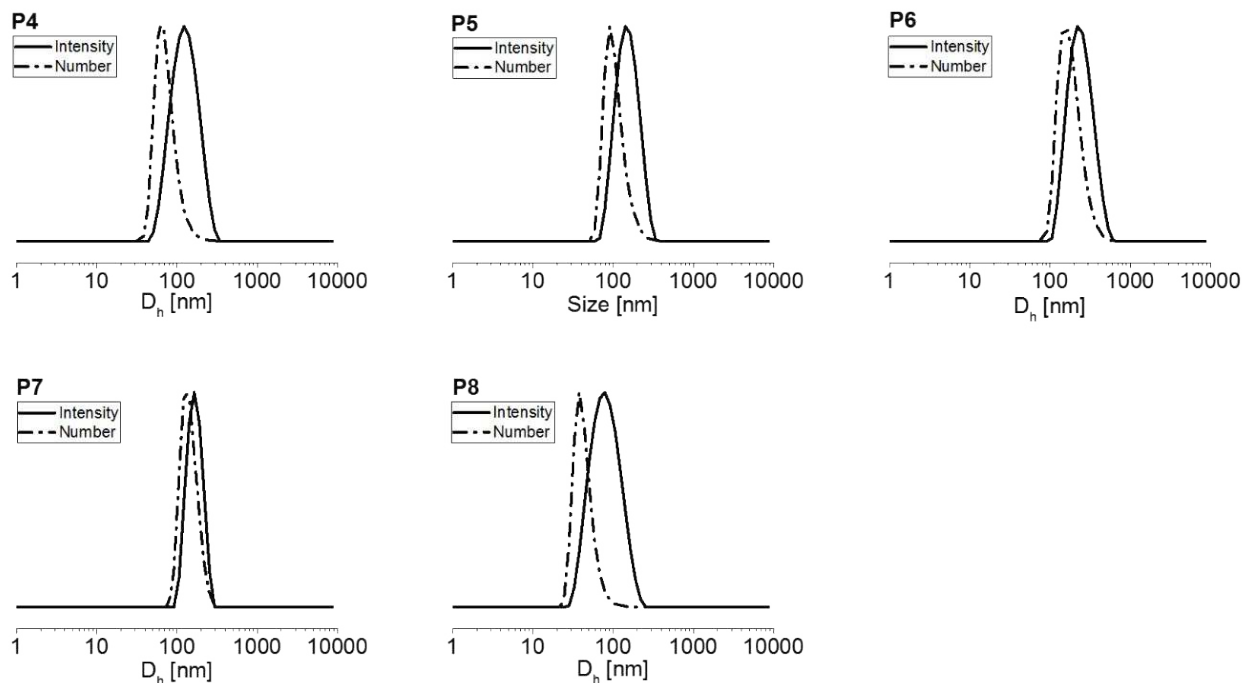


Figure S12: DLS size distributions of the nanoparticles prepared from **P3** to **P8**. The full lines represent the intensity-weighted data, the dotted lines represent the number-weighted data.

Additional information to WAXS investigations:

P1: The material crystallized in the α -form. The reflection positions were $2\theta = 18.3^\circ$ ($d = 4.81 \text{ \AA}$), $2\theta = 20.8^\circ$ ($d = 4.25 \text{ \AA}$), $2\theta = 23.2^\circ$ ($d = 3.85 \text{ \AA}$) and a shoulder with the Bragg-Reflex $2\theta = 24.7^\circ$ ($d = 3.66 \text{ \AA}$). From this, the primitive unit cell was determined with the following parameters:

Lattice parameter	Experimental value	Calculated value structure IIIa	Refined value
a [\AA]	4,96	8.886	8.414
b [\AA]	10,86	9.337	9.952
c [\AA]	22,7	31.272	33.267
α [$^\circ$]	51	89.7	78.6
β [$^\circ$]	77	88.3	84.6
γ [$^\circ$]	60	68.0	60.9

The degree of crystallization was about 50%.

P3: The material included an α - and δ -modification. The Bragg reflections of the α -phase were $2\theta = 19.7^\circ$ ($d = 4.50 \text{ \AA}$) and $2\theta = 23.2^\circ$ ($d = 3.83 \text{ \AA}$). The δ phase was identified by the Bragg angle $2\theta = 21.4^\circ$ ($d = 4.15 \text{ \AA}$). From this, the primitive unit cells were determined with the following parameters:

Lattice parameter	α -Phase	δ -Phase
a	5,17 \AA	4,79 \AA
b	10,8 \AA	4,79 \AA
c	21,7 \AA	112,8 \AA
α	51°	90°
β	77°	90°
γ	61°	90°

The α -phase thus has a preferred (100) orientation and growth of the crystals. The degree of crystallization was about 39%.

Construction of initial crystal structure models for **P1** is shown in **Figure S13**. Three chain conformations were tested using a chain fragment containing two repeating units with every atom in plane (**I**), with rotation of the alkaline spacer and ester groups by 90° in the same (**II**) and opposite direction (**III**). After geometry optimization of **I-III**, 4 chain fragments were placed into an orthorhombic unit cell with lattice parameters of 7.0, 35.1 and 10.5 Å for *a*, *b* and *c* axis, respectively. In addition, a parallel (*e.g.*, **Ip**) and antiparallel (*e.g.*, **Ia**) chain alignment (**Figure S13b** and **S13c**) as well as a shift of the polymer chains along the along *b* axis by about 10 Å (*e.g.*, **Ipb**) and along the *c* axis by about 3.5 Å (*e.g.*, **Ipc**) was tested. As in case of **Iabc**, most of the optimized crystal structures show the diffraction peak with highest intensity at 2θ of 26.3° not present in experimentally determined diffractogram. In contrast, **IIIa** and **IIac** reveal the main diffraction peaks below $2\theta = 25^\circ$. Therefore, these structure models were chosen for Rietveld refinement.

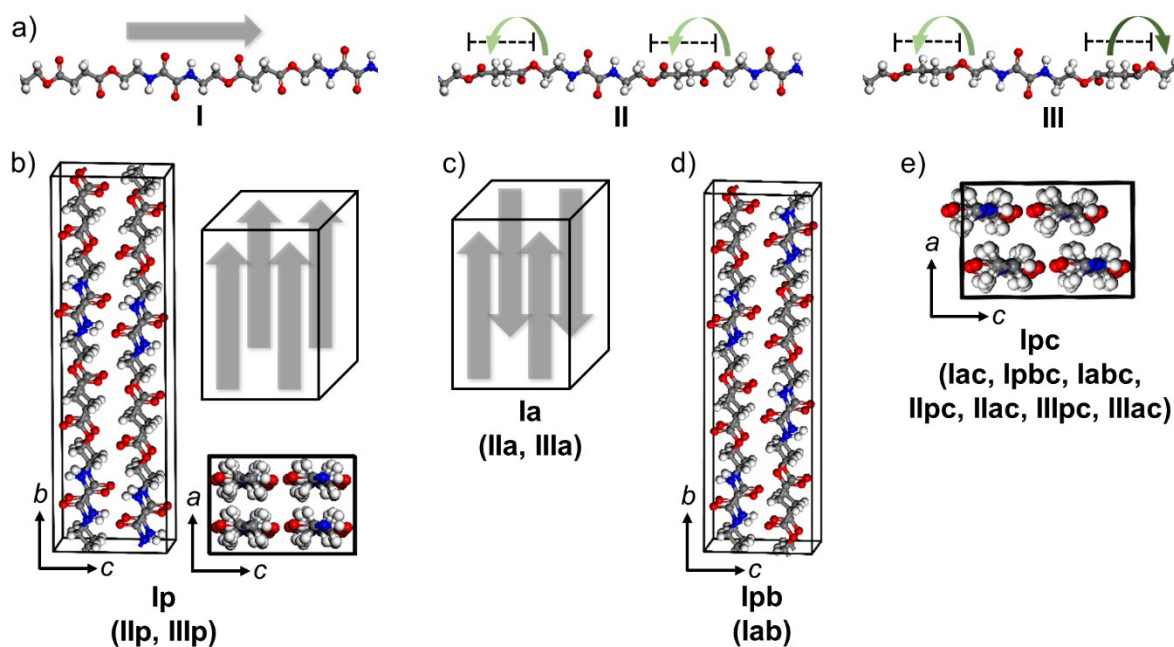


Figure S13: Construction of initial structure models of **P1** using a) different chain conformations (**I**, **II**, **III**), b) parallel (**p**) or c) antiparallel (**a**) alignment in the orthorhombic unit cell as well as d) shifted polymer chains along the *b* (**b**) or e) *c* (**c**) axis. Notations of other initial structure models not shown are given in brackets. C: grey, O: red, H: white.

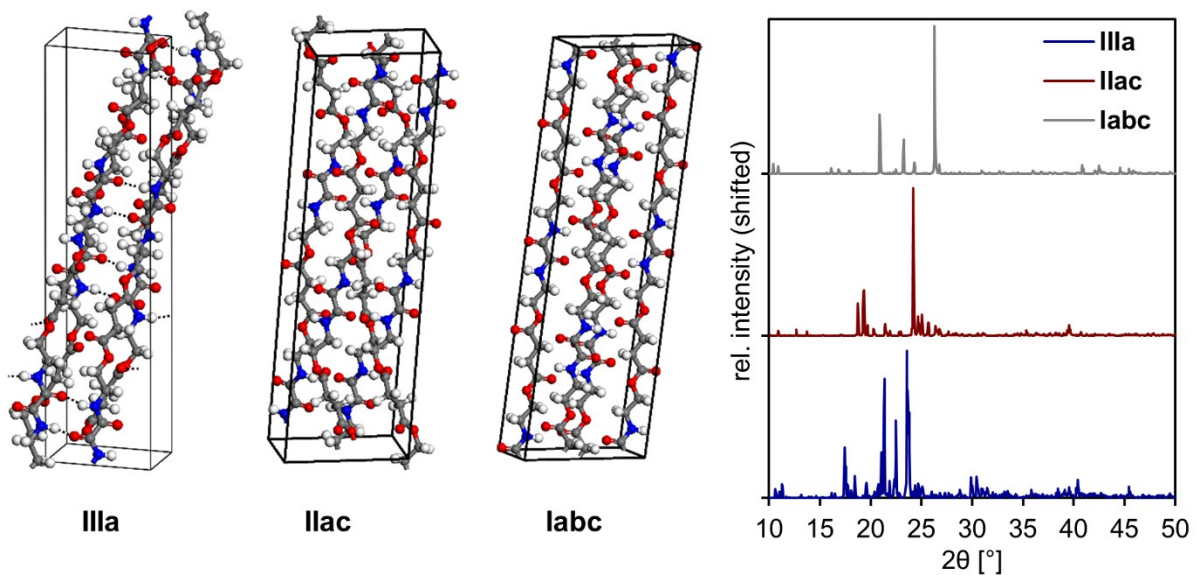


Figure S14: Geometrically optimized crystal structures (a) used for Rietveld refinement of experimentally determined diffractogram and calculated X-ray diffraction patterns (b) of **P1** (C: grey, O: red, H: white).

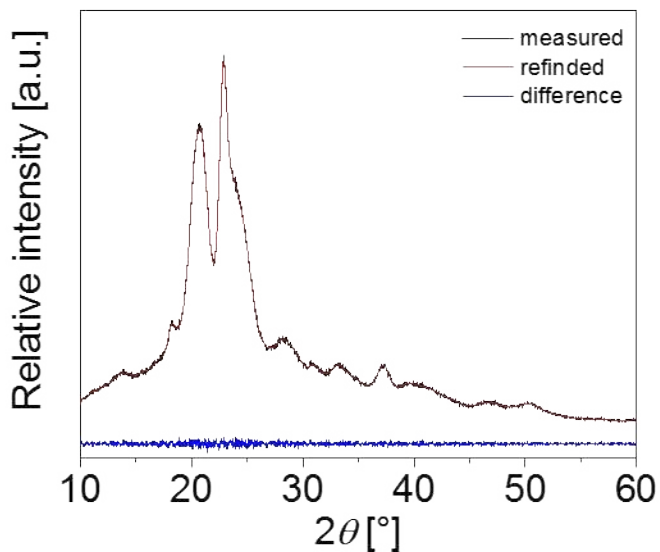


Figure S15: Rietveld structure refinement of the measured diffractogram of **P1** with the calculated diffractogram based on structure **IIIa**.

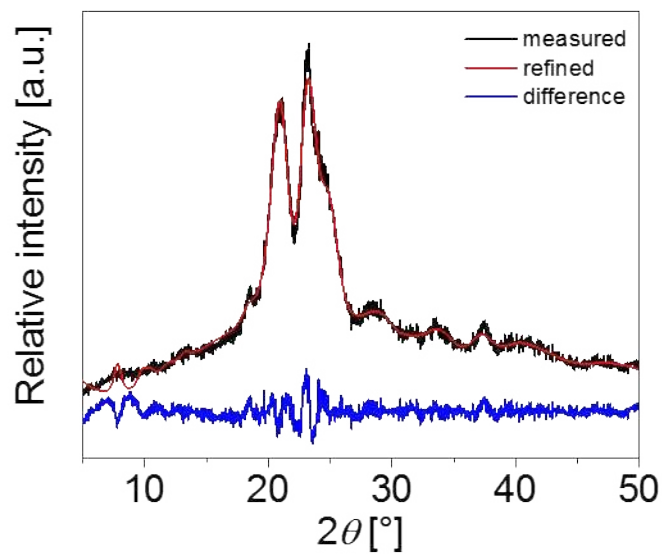


Figure S16: Rietveld structure refinement of the measured diffractogram of **P1** with the calculated diffractogram based on structure **IIac**.

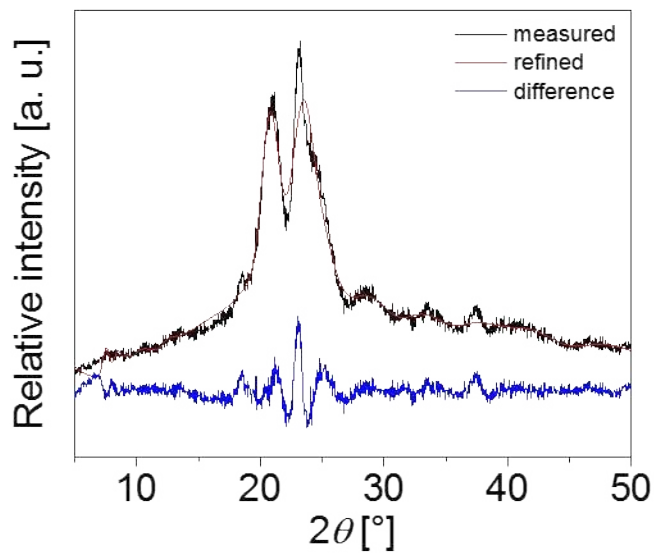


Figure S17: Rietveld structure refinement of the measured diffractogram of **P1** with the calculated diffractogram based on structure **Iabc**.

The average potential energy per segment e for an amorphous solid consisting of segments with a radial distribution function $g_{ij}(r)$ interacting through a pair potential $\phi_{ij}(r)$ is given as¹

$$e = \frac{\rho}{2} \sum_{i=1}^c \sum_{j=1}^c x_i x_j \int_0^{\infty} \phi_{ij}(r) 4\pi r^2 g_{ij}(r) dr, \quad (\text{S1})$$

where c denotes different components with segment fractions x , the segment density ρ and the center-to-center distance r between two segments. Here, one segment is defined as one polymer repeating unit or solvent molecule. $\phi_{ij}(r)$ assumes the functional form of a square well potential, with

$$\phi_{ij}(r) = \begin{cases} \infty, & r < r_0 \\ \varepsilon_{ij}, & r_0 \leq r \leq r_1 \\ 0, & r > r_1. \end{cases} \quad (\text{S2})$$

Figure S18 shows the radial distribution function determined for pure THF along with the corresponding pair potential. Using this form of potential function, the evaluation of the integral in Eqn. S1 can be limited to the interval $[r_0, r_1]$ with the distance independent interaction energy ε_{ij} since $g_{ij}(r) = 0$ for $r < r_0$ and $\phi_{ij}(r) = 0$ for $r > r_1$. Therefore, Eqn. S1 can be rewritten using Eqn. S2 and $\rho_j = x_j \rho$ as

$$e = \frac{1}{2} \sum_{i=1}^c \sum_{j=1}^c x_i \varepsilon_{ij} \rho_j \int_{r_0}^{r_1} 4\pi r^2 g_{ij}(r) dr. \quad (\text{S3})$$

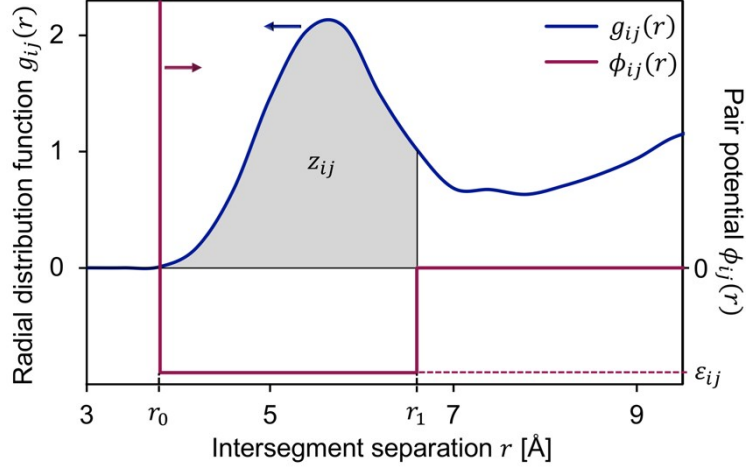


Figure S18: Radial distribution function $g_{ij}(r)$ determined for pure THF along with the corresponding square well potential $\phi_{ij}(r)$ (Eqn. S2). The shaded area represents the integral used for calculation of the coordination number z_{ij} (Eqn. S4).

The coordination number z_{ij} is defined as the average number of segments j surrounding segments i in a spherical shell ranging from r_0 to r_1

$$z_{ij} = \rho_j \int_{r_0}^{r_1} 4\pi r^2 g_{ij}(r) dr, \quad (\text{S4})$$

Using z_{ij} for a pure (p) amorphous solid solely containing segments i Eqn. S3 simplifies to

$$e_{i,p} = \frac{z_{ii,p}}{2} \epsilon_{ii}. \quad (\text{S5})$$

Similarly, defining an average coordination number $\bar{z}_{12} = x_1 z_{12} + x_2 z_{21}$ between unlike segments i - j , Eqn. S3 for a binary mixture (m) simplifies to

$$e_m = \frac{1}{2} (x_1 z_{11,m} \epsilon_{11} + x_2 z_{22,m} \epsilon_{22} + \bar{z}_{12} \epsilon_{12}). \quad (\text{S6})$$

The parameter r_1 used for calculation of z_{ij} (Eqn. S4) corresponds to the diameters of spheres with volumes v_i and v_m , which are the average segment volumes obtained from atomistic simulations of the pure components and the mixture, respectively. Inserting Eqns. S5 and S6 into the general definition of the energy of mixing per segment Δe_m

$$\Delta e_m = e_m - x_1 e_{1,p} - x_2 e_{2,p}, \quad (\text{S7})$$

yields the energy of mixing $\Delta e_{m,z}$ as a function of the coordination number changes of mixing $\Delta z_i = z_{ii,m} - z_{ii,p}$

$$\Delta e_{m,z} = \frac{1}{2}(x_1 \Delta z_1 \varepsilon_{11} + x_2 \Delta z_2 \varepsilon_{22} + \bar{z}_{12} \varepsilon_{12}). \quad (\text{S8})$$

For both Δz_i and \bar{z}_{12} quadratic composition dependency is assumed with the functional forms

$$\Delta z_i = A_i(1 - x_i)^2 + B_i(1 - x_i), \quad (\text{S9a})$$

$$\bar{z}_{12} = 2A_{12}x_1x_2. \quad (\text{S9b})$$

Figure S19 shows the composition dependence of Δz_i and \bar{z}_{12} calculated for the mixture containing **P4** and THF (solid lines). The composition independent parameters A_i and B_i in Eqns. S9a and S9b are obtained using three known values of Δz_i and \bar{z}_{12} at $x_i = 0$, $x_i = 1$ as well as the composition used for the atomistic simulations (squares in Fig. S14). For $x_i \rightarrow 0$, that is infinite dilution of component i , no intermolecular i - i contacts are present in the mixture such that $\Delta z_i \rightarrow -z_{ii,p}$. Similarly, no change of the coordination numbers $\Delta z_i \rightarrow 0$ occurs for mixtures at $x_i \rightarrow 1$. Obviously, \bar{z}_{12} is zero for compositions close to the pure states. In addition, the total coordination number z is shown in Fig. S14, for which applies: $z = x_1 z_{11,m} + x_2 z_{22,m} + \bar{z}_{12}$.

The use of the model functions Eqns. S9a and S9b allows to include the effect of different coordination states of unequal sized segments in the mixture as a function of the composition. In contrast, the Flory-Huggins (FH) theory employs a mean-field approximation with equally sized segments and a composition independent lattice coordination number z_{FH} . Here, z_{FH} is defined as the total coordination number z of the mixture calculated from atomistic simulations. Due to the random occupation of the FH mean-field lattice, the coordination numbers of the mixture are approximated as $\bar{z}_{12} \approx 2x_1x_2z_{FH}$ and $z_{ii,m} \approx x_iz_{FH}$. Since in the FH theory the coordination numbers of the pure states are $z_{ii,p} = z_{FH}$, the coordination number change Δz_i is a linear function of the composition $\Delta z_i \approx z_{FH}(x_i - 1) = -z_{FH}x_j$. Inserting these relations into Eqn. S8 results in the known FH expression for the energy of mixing $\Delta e_{m,FH}$ along with the definition of the FH interaction parameter χ_{FH} (*cf.* Eqns. 1 and 2)²

$$\Delta e_{m,FH} = RTx_1x_2 \frac{z_{FH}}{RT} (\varepsilon_{12} - 0.5(\varepsilon_{11} + \varepsilon_{22})) = RTx_1x_2 \chi_{FH} \quad (S10)$$

Results for the coordination numbers and the energy of mixing for the THF-**P4** mixture using the FH theory are also shown in Fig. S14 (dashed lines).

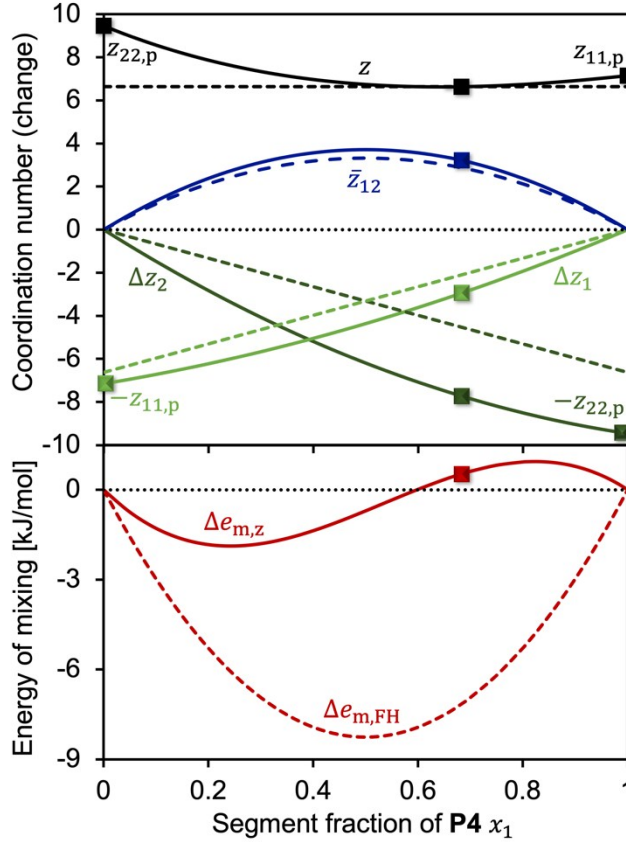


Figure S19: Total coordination number z , coordination number of unlike segments \bar{z}_{12} and the coordination number change of like segments Δz_i (upper part) as well as the energy of mixing Δe_m (lower part) as a function of composition for the mixture THF-**P4**. Solid lines: Model using Eqns. S5-S9, dashed lines: FH theory (Eqn. S10), squares: Values calculated from atomistic simulations.

In order to keep consistency with the FH expression for the entropy of mixing (*cf.* Eqn. 3), equally sized segments are assumed for the mixed state showing the average segment volume of the mixture v_m . However, the effects of unequally sized particles on the lattice coordination number as a function the composition can be considered with a composition dependent FH parameter χ_z . The actual intermolecular structure of the mixture is implicitly included in the mean-field approach

of the FH theory taking a ‘non-randomness’ of the lattice into account. For this, Eqn. S8 is used for calculation χ_z , such that $\Delta e_{m,z} = RTx_1x_2\chi_z$, yielding

$$\chi_z = \frac{1}{RT} \left(\frac{\bar{z}_{12}}{2x_1x_2} \varepsilon_{12} + 0.5 \left(\frac{\Delta z_1}{x_2} \varepsilon_{11} + \frac{\Delta z_2}{x_1} \varepsilon_{22} \right) \right). \quad (\text{S11})$$

Finally, inserting Eqns. S9a and S9b into S11, using $x_1 + x_2 = 1$ and defining the functions $F_i(x_i)$ as well as F_{12}

$$F_i(x_i) = \frac{\Delta z_i}{1 - x_i} = A_i(1 - x_i) + B_i, \quad (\text{S12a})$$

$$F_{12} = \frac{\bar{z}_{12}}{2x_1x_2} = A_{12}, \quad (\text{S12b})$$

results in a linear dependency of the FH parameter χ_z on the composition (*cf.* Eqn. 6)

$$\chi_z = \frac{1}{RT} (F_{12} \varepsilon_{12} + 0.5 (F_1(x_1) \varepsilon_{11} + F_2(x_2) \varepsilon_{22})). \quad (\text{S13})$$

In this work, the calculation of the model parameters required in Eqns. S4-S13 used atomistic simulations providing two central quantities, (*i*) the intermolecular RDF $g_{ij}(r)$ characterizing the amorphous structure and (*ii*) the cohesive energy densities C as measure for the intermolecular interactions. The latter are related to the Hildebrand solubility parameter *via* $\delta = \sqrt{C}$. The RDF $g_{ij}(r)$ required for calculation of z_{ij} (Eqn. S4) are obtained using coarse-grained models of the equilibrated and geometrically optimized (atomistic) structures. The parameter r_0 is defined as intersegment distance at which $g_{ij}(r) > 0$ for $r > r_0$. As mentioned above, for calculation of the coordination numbers between like segments, the diameter of a sphere with volume v_i was chosen for r_1 , which corresponds to the center-to-center distance of two segments in contact. For calculation of \bar{z}_{12} , the average molar volume of the mixture v_m was used.

In addition, δ (or C) is connected with the potential energy (Eqns. S5 and S6) and the molar volumes of the pure states (per segment) v_i^3 by the relation $e_i = -v_i \delta_i^2$. The same relation holds for the potential energy of the mixture $e_m = -v_m \delta_m^2$. Inserting these relations in Eqns. S5-S7 yields Eqns. 4, 5 and 7.

Figure S20 shows the dependence of Δg_m on the polymer segment fraction x_1 for the tested PEA solutions calculated using χ_{FH} and χ_z .

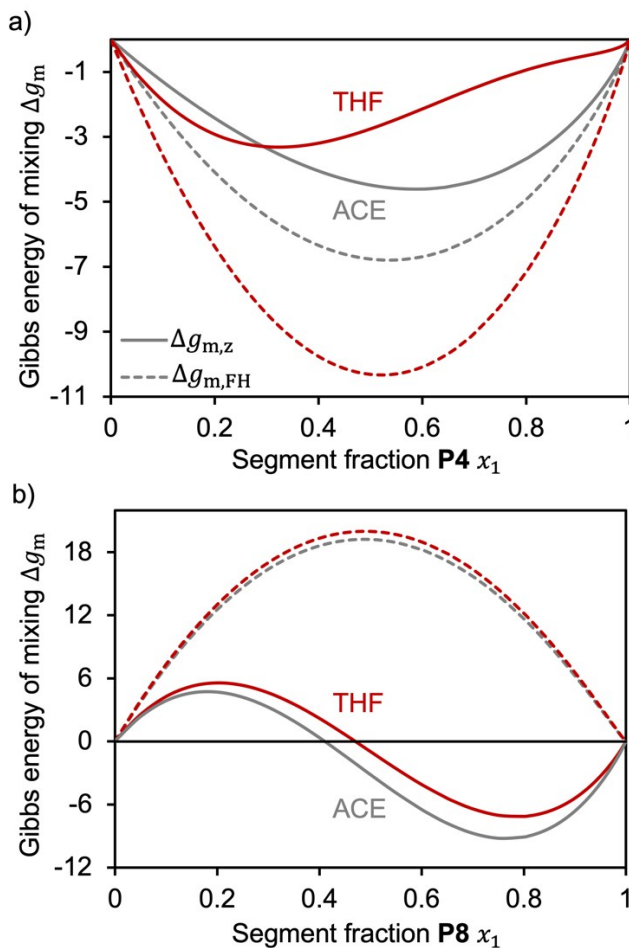


Figure S20: Gibbs energies of mixing Δg_m (Eqn. 3) as a function of the polymer segment fraction x_1 of binary mixtures containing THF (red) and acetone (ACE, gray) as well as (a) **P4** and (b) **P8**, calculated using χ_{FH} (Eqn. 1, dashed lines) and χ_z (Eqn. 6, solid lines).

All model parameters for the pure polymers (**P4**, **P8**) and solvents (THF, ACE) are summarized in **Table S1**. The parameter characterizing the corresponding mixtures are shown in **Table S2**.

Table S1. Hildebrandt solubility parameters δ_i , molar volumes (per segment) v_i , coordination number $z_{ii,p}$ and pair interaction parameter ϵ_{ii} of the pure components.

	P4	P8	THF	ACE
δ_i [MPa ^{0.5}]	20.67	20.75	18.33	19.26
v_i [cm ³ /mol]	247.50	267.06	84.83	74.46

$z_{ii,p}$	7.15	5.09	9.46	8.42
ε_{ii} [kJ/mol]	-29.58	-45.21	-6.03	-6.56

Table S2. Hildebrandt solubility parameters δ_m [MPa^{0.5}], average molar volumes (per segment) v_m [cm³ mol⁻¹], polymer segment fraction x_1 used for atomistic simulations (sim), model parameters for coordination numbers Δz_i and \bar{z}_{12} (Eqn. S9), pair interaction parameters ε_{ij} [kJ mol⁻¹], coordination numbers of the Flory-Huggins (FH) lattice z_{FH} , FH parameters χ_{FH} (Eqns. S10), as well as the energies of mixing Δe_m (Eqns. S8 and S10) [kJ mol⁻¹] obtained for compositions x_1 used in experiments (exp) of about 0.004.

	THF-P4	THF-P8	ACE-P4	ACE-P8
δ_m [MPa ^{0.5}]	20.46	20.99	20.98	21.33
v_m [cm ³ mol ⁻¹]	192.85	202.16	180.45	187.67
x_1 (sim)	0.68	0.66	0.63	0.61
A_1	3.13	-4.67	1.14	-5.03
B_1	-10.28	-0.42	-8.28	-0.06
A_2	5.85	6.26	6.44	6.48
B_2	-15.31	-15.72	-14.86	-14.90
A_{12}	7.42	7.51	7.79	7.50
ε_{ij} [kJ mol ⁻¹]	-22.79	-12.77	-20.74	-13.39
z_{FH}	6.63	6.89	6.90	6.87
χ_{FH}	-13.3	35.5	-7.42	34.37
$\Delta e_{m,z}$ (exp) [kJ mol ⁻¹]	-0.07	0.26	-0.03	0.25
$\Delta e_{m,FH}$ (exp) [kJ mol ⁻¹]	-0.13	0.35	-0.07	0.34

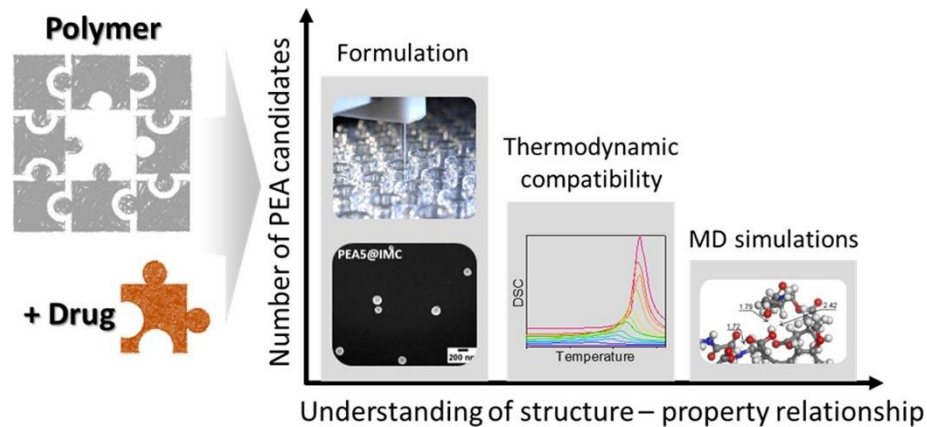
- 1 G. A. Mansoori, *Fluid Ph. Equilibria* 1993, **87**, 1-22.
- 2 I. Teraoka, in *Polymer Solutions: An Introduction to Physical Properties*, John Wiley & Sons, Inc., New York, 2002.
- 3 J. H. Hildebrand, in *The Solubility of Nonelectrolytes*, Dover Publications, Inc., New York, 1964.

Publication 5

A combined experimental and *in silico* approach to determine the compatibility of poly(ester amide)s and indomethacin in polymer nanoparticles

I. Muljajew, M. Chi, A. Vollrath, C. Weber, B. Beringer–Siemers, S. Stumpf, S. Hoepfner, M. Sierka, U. S. Schubert

Eur. Polym. J. **2021**, *156*, 110606.





A combined experimental and *in silico* approach to determine the compatibility of poly(ester amide)s and indomethacin in polymer nanoparticles

Irina Muljajew^{a,b}, Mingzhe Chi^c, Antje Vollrath^{a,b}, Christine Weber^{a,b},
Baerbel Beringer-Siemers^{a,b}, Steffi Stumpf^{a,b}, Stephanie Hoepfner^{a,b}, Marek Sierka^c,
Ulrich S. Schubert^{a,b,*}

^a Laboratory of Organic and Macromolecular Chemistry (IOMC), Friedrich Schiller University Jena, Humboldtstrasse 10, 07743 Jena, Germany

^b Jena Center for Soft Matter (JCSM), Friedrich Schiller University Jena, Philosophenweg 7, 07743 Jena, Germany

^c Otto Schott Institute of Materials Research (OSIM), Friedrich Schiller University Jena, Loebdergraben 32, Jena 07743, Germany

ARTICLE INFO

Keywords:

Poly(ester amide)s
Indomethacin
Nanoparticles
Flory-Huggins parameter
Encapsulation efficiency
Dynamic scanning calorimetry

ABSTRACT

The development of optimized carrier materials for the encapsulation of new high-potency drugs is frequently hampered by the need for trial-and-error experiments. Combining experimental and *in silico* approaches with a feedback loop is a promising way to overcome this drawback. Here, such a combined study is conducted to investigate the compatibility and the underlying interactions of the anti-inflammatory drug indomethacin (IMC) and six poly(ester amide)s (PEA). Optimization of nanoparticle formulation conditions via a high-throughput nanoprecipitation screening yielded particles in the desired size range of 100 to 400 nm. Formulation of IMC loaded PEA nanoparticles with reduced surfactant impact indicated strong influence of the polymer structure and density on the polymer performance. Differential scanning calorimetry of PEA and IMC blends enabled access to saturation conditions (7 to 18% at 111 °C) and pointed towards thermodynamic compatibility (Flory-Huggins (FH) interaction parameters -0.20 to -0.52). FH parameters from atomistic molecular dynamics simulations were found to be in agreement with the experimental values, additionally rationalizing the PEA-drug compatibilities through hydrogen bonding interactions. Cross comparison of all elements of the study showed that both compatibility and nanoparticle formation ability contribute to the encapsulation efficiency.

1. Introduction

Polymer-assisted drug delivery represents a powerful tool to increase bioavailability of highly potent active pharmaceutical ingredients (API), which are either too hydrophobic [1] or too sensitive towards biodegradation alone. [2,3] In particular, nanoparticulate carriers with hydrophobic character seem feasible to circumvent these challenges, as demonstrated by the multitude of API encapsulated in mostly poly(lactic-co-glycolic acid) (PLGA) as an approved material. [4–8] However, the limited adaptability of approved carrier materials to a given API represents a current challenge within the scientific field, demanding sophisticated answers to problems such as improvement of the encapsulation efficiency (EE). These major challenges can be overcome by engineering and optimizing the properties of nanoparticles (NP), which are determined by the tailored polymeric materials from which

they are made. Poly(ester amide)s (PEA) are considered promising candidates for biomedical applications as they exhibit several promising features. [9] They can be synthesized from biogenic monomers [10] and are potentially degradable by hydrolysis of the ester bonds or enzymatic cleavage of the amide bonds. [11] Furthermore, their ability to form hydrogen bonds through the amide moieties results in different thermal as well as mechanical properties compared to polyesters such as PLGA. [12] More importantly, such hydrogen bonding can promote directional interaction with an API, thereby increasing the drug loading capacity. [13]

In addition, formulation methods represent a major factor with respect to the establishment of structure-properties relationships. [14,15] The solvent displacement method, also called nanoprecipitation, is a one-step procedure for the formulation of aqueous NP dispersions that stands out due to its experimental simplicity. [16,17] NP

* Corresponding author.

E-mail address: ulrich.schubert@uni-jena.de (U.S. Schubert).

dispersions can be obtained by direct combination of the continuous, aqueous phase with a miscible organic phase containing the polymer alone or together with the hydrophobic API. However, the resulting product is easily altered by various parameters, such as settings of addition, presence of surfactants, concentration, or the type of organic solvent.[7,17] All these factors need to be optimized, which may be time consuming and cumbersome. Despite these drawbacks, the method enables tailoring of NP properties and is perfectly suited for an automated high-throughput screening. This straightforward method is hence especially favorable in an early development stage if the compounds of interest are not yet established in the field.

The EE of API in polymer nanocarriers is of fundamental importance and is related to the thermodynamic compatibility of the materials.[18] However, NPs alone represent metastable materials, additionally relying on factors such as the kinetic entrapment of the API within the particle.[19] In this light, the investigation of thermodynamic compatibility of the bulk materials, *i.e.* carrier material and API, is much more informative and limits the impacts of the multidimensional parameter space present in the nanoformulation process.

Many methods are known for the determination of compound-solvent interactions and solubility parameters.[20,21] They vary from simple group contribution methods to more experimentally demanding procedures such as gas chromatography with the polymer of interest as the stationary phase. However, the implementation of specific interaction contributions including hydrogen bonding leads often to erroneous results if simple solubility parameters are considered as these directional interactions are harder to determine and therefore to take into account.

On the other hand, the investigation of polymer-drug blends by differential scanning calorimetry (DSC) is perfectly suited as the analytical technique is commonly available in research labs, the sample preparation is straightforward and the required amount of compounds is reasonable.[22,23] Based in the research field of polymeric amorphous solid dispersions, experimental methods were previously introduced for the rational selection of polymer-drug combinations based on the correlation of their physicochemical and thermal properties,[24] *e.g.* the determination of experimental miscibility *via* the melting enthalpy method. Here, the melting enthalpy of the crystalline API in a drug-polymer system is measured in dependence of its mass fraction within the blend. The dissolved amount of the API in the polymer matrix does not contribute to the melting endotherm and, therefore, can be determined by extrapolating the plot to zero enthalpy.[25]

Additionally, the change of melting temperature of the crystalline API in dependence of its mass fraction within the blend can be implemented to calculate the thermodynamic compatibility through miscibility and the resulting melting point depression.[26]

The Flory-Huggins (FH) theory is a lattice based theory, which takes into account enthalpic as well as entropic contributions resulting from mixing polymer and solvent and has been also applied to drug-polymer blends.[26] It was specifically developed for polymer-based systems and enables the estimation of the molar Gibbs energy of mixing, ΔG_{mix} . This is done *via* a simplified description of (combinatorial) entropy contributions. The enthalpy contribution of the drug-polymer interactions to ΔG_{mix} is included in the FH interaction parameter, χ . Two components are predicted to be miscible if $\chi < 0.5$. [27] A negative value of χ indicates drug-polymer miscibility as it predicts stronger drug-polymer interaction compared to individual drug-drug or polymer-polymer interactions. In contrast, a value of $\chi > 0.5$ indicates that homomolecular interactions are preferred over heteromolecular ones which, as a result, may lead to phase separation.

Besides accessibility through DSC studies, the FH parameter can also be obtained from atomistic molecular dynamics (MD) simulations with reliable representation of the polymer structure. Its analysis enables access to a plethora of additional insights into the mixture on a molecular level as specific interactions can be analysed and quantified. Examples include hydrogen bonding or a special arrangement of drug molecules within the carrier material. FH theory combined with MD

simulations has been successfully applied to evaluate and predict the efficiency of API incorporation into various polymer carriers.[27–29]

In our previous work we established the synthesis of poly(ester amide)s based on a step growth polyaddition of 2,2'-bis(2-oxazoline) and commercially available dicarboxylic acids.[12] After the characterization of the polymeric materials, experimental solubility results were correlated with predictions obtained by atomistic MD simulations. First evaluation of the PEAs as potential NP candidates was performed by non-optimized nanoprecipitation processes and simple Hildebrand parameters. However, the miscibility with API and the ability to encapsulate it has not yet been investigated. We approached this issue by a systematic study to identify the flagship combination focusing on elucidation of the underlying structural and molecular reasons. In the first step the NP formulation ability was screened by nanoprecipitation in a high-throughput manner including the variation of concentration, organic solvent and continuous phase. Secondly, the compatibility of polymer and the nonsteroidal anti-inflammatory drug indomethacin (IMC) was tested by encapsulation into NPs and correlated to its miscibility with the PEA bulk materials as assessed by DSC. In the third step, the best and the worst performing combinations were subjected to detailed atomistic MD simulations to elucidate whether the thermodynamic compatibility between the PEA and IMC was influenced by specific interactions such as hydrogen bonding. This combined experimental and *in silico* approach sets the basis for a validation feedback loop to enable the prediction of optimum polymer structures for a given drug. As such method circumvents trial and error experiments to identify an optimum carrier material, it will be particularly beneficial for new highly potent APIs that are difficult to encapsulate and suffer from lack of available data.

The following nomenclature will be used throughout the manuscript: **PEA@IMC** for encapsulated indomethacin in NP with **PEA@empty** for unloaded NP, **PEA [IMC]** for blends of API and polymer and **PEA+IMC** for MD simulations results of polymer cells with one indomethacin molecule.

2. Materials

Poly(vinyl alcohol) (PVA, Mowiol® 4–88), 1,1,1,3,3,3-hexafluoroisopropanol (HFIP, ≥99%), and dimethyl sulfoxide (DMSO, >99%, spectroscopic grade), *N,N*-dimethylformamide (DMF, >99%) as well as *N,N*-dimethylacetamide (DMA, >99%) were purchased from Sigma-Aldrich. Tetrahydrofuran (THF) and acetonitrile were obtained from a solvent purification system (SPS; Pure solv EN, InnovativeTechnology). Indomethacin (IMC, >98.0%) was purchased from Tokyo Chemical Industry.

The PEA synthesis was previously reported.[12] Briefly, the respective diacid (1 eq) and 2,2'-bis(2-oxazoline) (1 eq) were dissolved in DMF to yield a 4 M solution and subsequently degassed by gently bubbling with argon. The polymerization was carried out at 150 °C for 24 h. The crude product was purified by precipitation into cold (–20 °C) methanol. The polymers were dried utilizing a high vacuum pump resulting in a voluminous, fluffy product and which was subsequently stored at –20 °C. This procedure enabled precise handling of the polymers with low T_g . Relevant characterization data of the polymers used in the study at hand as well as the structures of the polymers are summarized in Table 1. A full characterization of the PEAs can be found in our previous publication.[12]

3. Methods

3.1. Automated nanoparticle screening with the pipetting robot

High-throughput nanoprecipitation was performed using a FasTrans liquid handling robot (Analytik Jena AG) using 96 well plates (Greiner Bio-One GmbH). Automated nanoprecipitation of all PEAs was carried out from up to three suitable solvents (Fig. 1). For each combination of

Table 1
Materials used in this study with selected properties for calculation of saturation values and Flory-Huggins interaction parameter.

Material	Structure	M_n in g mol^{-1a}	ρ in g cm^{-3b}	Thermal properties ^d
PEA1		7,600	1.117	$T_m = 149.7\text{ }^\circ\text{C}$ and $176.0\text{ }^\circ\text{C}$
PEA2		4,400	1.214	$T_g = 35.9\text{ }^\circ\text{C}$
PEA3		7,100	1.167	$T_g = 19.6\text{ }^\circ\text{C}$
PEA4		3,800	1.222	$T_g = 21.7\text{ }^\circ\text{C}$
PEA5		4,600	1.200	$T_g = 50.8\text{ }^\circ\text{C}$
PEA6		2,600	1.253	$T_g = 50.4\text{ }^\circ\text{C}$ $T_m = 132.4\text{ }^\circ\text{C}$
Indomethacin (IMC)		357	1.34 ^c	$T_m = 164.9\text{ }^\circ\text{C}$ $\Delta H = 78.66\text{ J g}^{-1}$

^a Determined by ^1H NMR spectroscopy (400 MHz, HFIP- d_2) [12].

^b Calculated values from molecular dynamics simulations [12].

^c From Taylor and coworkers [30].

^d Determined by DSC in the 1st heating run (20 K min^{-1}), inflection values are reported for T_g . PEAs annealed at $111\text{ }^\circ\text{C}$ for 24 h.

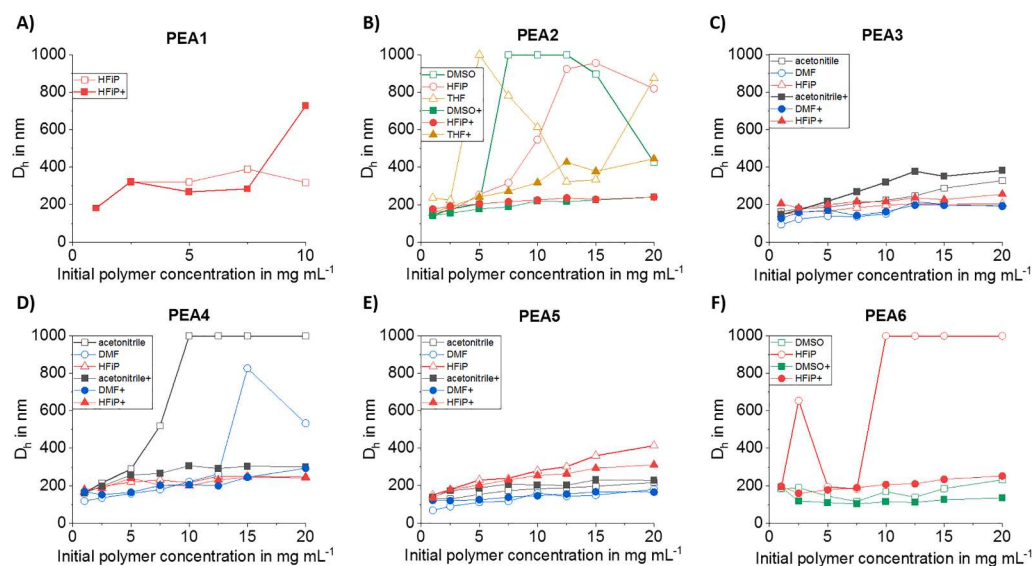


Fig. 1. Nanoparticle formulation of different PEAs from various solvents performed via high-throughput nanoprecipitation using a liquid handling robot. Solvent (solid symbol) or Solvent+ (empty symbol) indicates formulation from the organic solvent into pure water or a 0.3% aqueous PVA solution, respectively. Hydrodynamic diameters given from dynamic light scattering (DLS) measurements. Individual values are additionally listed in Table SI 1.

PEA and solvent, a polymer stock solution was prepared ($c = 20\text{ mg mL}^{-1}$) from which a dilution series yielded solutions of varying concentration ($c = 1, 2.5, 5, 7.5, 10, 12.5$ and 15 mg mL^{-1}). Nanoprecipitation was carried out by pipetting $25\text{ }\mu\text{L}$ of these polymer solutions into $190\text{ }\mu\text{L}$ of either purified water (Thermo Scientific, GenPure ultrapure water system) or 0.3% (w/v) PVA solution. After the

organic polymer solution was dropped into the aqueous phase, the suspension was mixed by pipetting up and down. Each formulation was prepared twice. The 96 well plate was left uncovered at least for 2 h to allow volatile solvent evaporation. Afterwards, $15\text{ }\mu\text{L}$ of the final NP suspension were diluted with $185\text{ }\mu\text{L}$ of pure water, thereby ensuring that the solvent residue of the non-volatile solvents, such as DMSO, DMF

or DMA, was reduced to <1%. Subsequent DLS measurements were carried out in a ZEN cuvette using 100 μL of the diluted sample without further treatment.

3.2. Indomethacin encapsulation into PEA

For the encapsulation of IMC into the PEA NP, nanoprecipitation was performed by injection using a syringe pump (Aladdin AL1000-220, World Precision Instruments). First, a polymer solution with $c = 5 \text{ mg mL}^{-1}$ and $V = 5 \text{ mL}$ was prepared in HFIP. In addition, a stock solution in DMSO of the active ingredient IMC with $c = 10 \text{ mg mL}^{-1}$ was prepared. 75 μL of the IMC stock solution were added to the polymer solution and vortexed to result in 5.075 mL of a PEA/IMC solution containing 25 mg of PEA and 0.075 mg of IMC. The polymer-IMC solution was injected with a flow rate of 2 mL min^{-1} into 40 mL of pure water while stirring continuously at 800 rpm. Subsequently, 4 mL of a 3% (w/v) PVA solution were immediately added to stabilize the particles. The final PVA concentration was 0.3% (w/v). HFIP evaporated overnight and the suspensions were checked the next day with respect to aggregates. In the case of visible aggregates, the sample was centrifuged for 2 min at $16,233 \times g$ with a Rotina 5804 R centrifuge (Eppendorf) and the pellet was removed, whereas the supernatant was kept. For particle purification and collection, the suspension was centrifuged at $12,851 \times g$ for 60 min at 20°C . The particles were resuspended in 2.5 mL of pure water. To improve the resuspension, the sample was vortexed for 10 sec and then treated in an ultrasonic bath for additional 30 min. The samples were left overnight in the refrigerator at 4°C and analyzed the next day. Subsequently, freeze drying of the suspensions was carried out on an Alpha 1-2 LD plus freeze dryer (Martin Christ Gefriertrocknungsanlagen GmbH) for 24 h. Subsequently, the particle yield was determined via precise weighing using a fine-balance (Radwag, MYA-4Y microbalance).

3.3. Light scattering measurements

The Zetasizer Nano ZS with a laser wavelength of $\lambda = 633 \text{ nm}$ measuring the counts backscattered at 173° (Malvern Instruments) was used for dynamic light scattering (DLS) measurements as well as for the determination of the ζ -potential by electrophoretic light scattering (ELS). For DLS after 30 s equilibration time, five repeated measurements at 25°C with five runs \dot{a} 30 s were performed. The ζ -potential was determined at 25°C with 3 repeated measurements. Particle dispersions were characterized before (undiluted, $c \approx 0.625 \text{ mg mL}^{-1}$) and after purification (diluted, $c \approx 0.006$ to 0.020 mg mL^{-1}) as well as after lyophilization and resuspension (diluted $c \approx 0.006$ to 0.020 mg mL^{-1}). The mean particle diameter (Z-average value, D_h) and the width of the size distribution – given as polydispersity index (PDI) – were obtained utilizing the cumulant analysis method.

3.4. UV Vis spectroscopy

Absorbance measurements for the determination of EE and loading capacity (LC) of the drug in the NPs were performed in a Hellma Quartz flat-transparent plate with 96 wells using a TECAN Infinite M200 PRO plate reader. 200 μL of the final NP dispersion were lyophilized and the residue was dissolved in 200 μL of DMA. The absorbance of the solution was measured in a 96 quartz well-plate at $\lambda = 318 \text{ nm}$ with 3×3 multiple reads per well and 2000 μm well border. The calibration curve of IMC was obtained in DMA under the same measurement conditions (Supporting Information). The EE and LC values were calculated using the following definitions:

$$EE = \frac{m_{drug}}{m_{drug,added}} \quad (1)$$

$$LC = \frac{m_{drug}}{m_{drug} + m_{polymer}} \quad (2)$$

where m_{drug} and $m_{polymer}$ are the respective masses of recovered drug and polymer while $m_{drug,added}$ is the drug amount initially injected to the formulation.

3.5. Scanning electron microscopy

Scanning electron microscopy (SEM) measurements were carried out with a Sigma VP Field Emission Scanning Electron Microscope (Carl-Zeiss AG). The NP suspensions were diluted to 0.2 mg mL^{-1} and one droplet was placed on mica surface and lyophilized for 2 h. The NPs were coated with platinum (4 nm) using a sputter coating device (CCU-010 HV, Safematic) and SEM images were obtained using the InLens detector with an accelerat on voltage of 6 kV.

3.6. Thermal analyses

Thermogravimetric analysis (TGA) was performed under a N_2 atmosphere on a Netzsch TG 209 F1 Iris from 30 to 600°C at a heating rate of 20 K min^{-1} . Differential scanning calorimetry (DSC) measurements were performed on a Netzsch DSC 204 F1 Phoenix device equipped with a Netzsch DSC 204 F1 t-sensor under a N_2 atmosphere in the temperature range from -50 to 190°C . Two cycles were recorded for each sample while both heating and cooling rates of 20 K min^{-1} were applied. The glass transition temperature (T_g , inflection value) and the melting temperature (T_m) values were reported from the first heating run. Aluminum oxide crucibles with a volume of 85 μL and lid having a hole were used. Additional correction measurements of empty aluminum oxide crucibles both as reference and sample were applied for each subsequent sample measurement to account for calibration differences as the instrument calibration was set up for aluminum pans. The data were evaluated with Netzsch Proteus – Thermal Analysis version 4.6.1.

Sample preparation for DSC. Physical mixtures of the PEA and IMC were prepared by weighing in the compounds together in the desired ratio to give a total mass of 100 mg and subsequent milling by hand with a pestle and mortar for 10 min. Approximately 15 mg of the resulting blend were transferred into an aluminum oxide crucible, annealed for 24 h at 111°C in an oven (BINDER™ drying oven ED53) and subsequently measured by DSC as described above.

3.7. Computational details

3.7.1. Flory-Huggins interaction parameter

Based on the lattice model, FH theory comprises the mixing of binary systems as a process determined by a combination of enthalpic and entropic contributions.[27,31] The change of Gibbs free energy of mixing is defined as

$$\Delta G_{mix} = \Delta H_{mix} - T\Delta S_{mix} \quad (3)$$

$$\Delta G_{mix} = RT \left(\frac{x_1}{r_1} \ln \varphi_1 + \frac{x_2}{r_2} \ln \varphi_2 + x_1 x_2 \chi \right) \quad (4)$$

where R is gas constant, T is temperature, x_i , r_i and φ_i are mole fraction, degree of polymerization and volume fraction, respectively (for a drug molecule $r_i = 1$), and χ is the FH interaction parameter. This parameter can be calculated using two methods, denoted here as methods I and II.[12,32] The method I is the simplest one and expresses the FH parameter in terms of Hildebrand solubility parameters δ of pure components 1 and 2,

$$\chi_{Sim} = \frac{V_m}{RT} (\delta_1 - \delta_2)^2 \quad (5)$$

where V_m is the molar volume of one lattice segment and δ_1 and δ_2 are Hildebrand solubility parameters of pure components 1 and 2, respectively. δ is defined as the square root of cohesive energy density (CED), which can be obtained from MD simulations of pure components. The more accurate method II employs atomistic MD simulations of

actual binary mixtures with χ_{Sim} defined as [27,31]

$$\chi_{Sim} = \frac{V_m}{RT} \Delta E_{mix} = \frac{V_m}{RT} (\varphi_1 CED_1 + \varphi_2 CED_2 - CED_{1-2}) \quad (6)$$

where ΔE_{mix} is the energy of mixing, φ_1 and φ_2 are the volume fractions of components 1 and 2, respectively. CED_1 and CED_2 are the cohesive energy densities of pure components 1 and 2, respectively, and CED_{1-2} is the cohesive energy density of the mixture. Unlike the method I, in method II explicit MD simulations of mixtures allow to capture specific interactions between components. In this study, FH parameters of PEA+IMC mixtures were calculated with both methods at 300 K.

3.7.2. Computational procedure

MD simulations were performed employing the simulation platform *Materials Studio* (Version 2019)[33] along with the COMPASS II force field [34]. The *Forcite* module of *Materials Studio* was applied for all MD simulations along with a time step of 1 fs and Nosé–Hoover thermostat. [35,36] All compounds were modelled as three-dimensional periodic amorphous cells constructed using a configurational bias Monte Carlo procedure implanted in the *Amorphous Cell* module based on algorithms of Theodorou and Suter.[37]

All unit cells of pure PEA2 and PEA5 contained 50 polymer chains and each chain consisted of 10 repeating units. The unit cell of IMC contained 50 molecules. Unit cells of mixture models comprised 15 PEA chains and one IMC molecule.

Four initial configurations for each pure PEA2 and PEA5 model and ten configurations for each IMC and mixture models were constructed and geometrically optimized. Next, the structures with lowest energy were refined employing MD simulations along with a simulated annealing procedure for generation of energetically more stable configurations.[12,32] During simulated annealing, structure models were equilibrated at 300 K using the canonical (NVT) ensemble followed by a stepwise temperature increase up to 1000 K and a later decrease back to 300 K. In each step, temperature was changed by 100 K and then the structure was equilibrated for 5 ps.

Next, MD simulations using isothermal-isobaric (NPT) ensemble at zero target pressure and 300 K were performed with a 100 ps equilibration using Berendsen barostat[38] followed by Parrinello-Rahman barostat[39] with a duration of 300 ps. Average cell parameters of structure models were evaluated for the last 200 ps of the NPT simulations. The unit cells of the final structures of the NPT trajectories were scaled to the average cell parameters and equilibrated for 250 ps using NVT ensemble with a target temperature of 300 K. Average values of properties such as CED were calculated from the last 200 ps of NVT simulations. Similar to our previous work,[12] MD simulations were applied only to sample the local atomic and vibrational motions. To sample different polymer conformations for each polymer we constructed four fully independent initial structures, which yielded virtually the same CED values. Averaged intermolecular radial distribution function (RDF) plots for selected atom pairs were calculated from equilibrated MD trajectories of the lowest energy structures.

4. Results and discussion

Atomistic MD simulations are a very powerful tool to understand molecular interactions between a polymer and a particular drug. However, they are computationally very challenging for nanoparticle dispersions due to the complexity of the systems, which usually consist of at least four compounds such as water, surfactant, polymer and active ingredient. Nevertheless, simulating the model consisting of the two main components, *i.e.*, polymer and active ingredient, are computationally feasible. The formulation setup was hence designed to most closely match the model, avoiding the use of surfactants as far as possible, although this may come to the cost of encapsulation efficiency.

4.1. Formulation screening via high-throughput nanoprecipitation

To investigate whether the PEAs form nanoscale particles, and if so, in which size ranges, a NP formation screening was performed with a liquid handling robot using different solvents, various polymer concentrations as well as two different continuous phases, *i.e.* water and a 0.3% (w/v) PVA solution. All PEAs were soluble in HFIP and therefore formulated from this solvent. PEA2 and PEA6 were additionally soluble in THF and DMSO and were therefore also formulated using these solvents. For PEA6, however, the polymer solubility in THF was limited to 5 mg mL⁻¹ at room temperature and the particle formulation was not successful for concentrations above 1 mg mL⁻¹. For PEA3, PEA4 and PEA5 also acetonitrile and DMF were used for the formulation due to the good solubility of the polymers in these solvents. Different initial PEA concentrations ranging from 1 to 20 mg mL⁻¹ were tested in a high-throughput screening using a liquid handling robot that dropped the polymer solution into the continuous phase (Fig. 1 and Figure SI 1). After completed formulation, a dilution step reduced the amount of the non-volatile solvents to <1% in order to avoid an influence on the NP properties as well as DLS measurements due to substantial changes of the viscosity.

PEA1 exhibited a narrow condition range where the polymer formed particles with $D_h \approx 300$ nm (Fig. 1A). Outside of this window, the performance of PEA1 was not satisfactory due to broad polydispersity and low stability. When PEA2 was formulated into a 0.3% (w/v) aqueous PVA solution the polymer formed NPs for all concentrations and from all organic solvents with sizes ranging from 150 to 400 nm, with slightly higher sizes for THF (Fig. 1B). Without surfactant, however, aggregation occurred, resulting in higher D_h . Similar formulation results were obtained for PEA4 (Fig. 1D). With surfactant the PEA4 formed NPs over the tested range with sizes from 120 to 260 nm. But without surfactant only formulations from HFIP remained stable without aggregation. PEA3 and PEA5 featured similar solubility properties and potentially could behave similarly in particle formation. Indeed, nanoprecipitation from all organic solvents and concentrations resulted in defined particles with D_h values between 90 and 400 nm for both polymers. Formulations in water and in aqueous PVA solution were straightforward. The formulation of PEA6 into a 0.3% (w/v) PVA solution resulted in NPs with $D_h \approx 200$ nm, but without surfactant aggregation occurred as represented by an overall higher D_h in particular for HFIP. Additional details can be found in the Supporting Information.

After optimization, the high-throughput screening was suitable to produce NP from all PEAs (except PEA1). However, the stability of the particles and the resulting size were crucially dependent on the solvent character and the presence of the surfactant. Small particles below 100 nm could be prepared of PEA3 and PEA5 from DMF. Medium-sized particles (100 to 200 nm) could be formulated of all polymers PEA2-PEA6 within the low concentration range (1 to 10 mg mL⁻¹). The largest particles ($D_h \approx 400$ nm) with moderate dispersity ($PDI \approx 0.2$) were obtained from highly concentrated polymer solution of PEA2 (in THF), PEA3 (in acetonitrile) and PEA5 (in HFIP). The overall hydrophobicity, which is commonly related to the total number of carbon atoms, did not seem to correlate with the NP formation ability. Both PEA3 and PEA4 feature seven carbon atoms between the ester groups resulting from the utilized acid during the synthesis. However, their NP forming behavior differed significantly. Also, PEA1 with ten carbon atoms performed worse than PEA5 with eight carbon atoms between the ester units. As a consequence, the hydrophobicity of the materials does not represent the only factor influencing the ability of the PEA to form stable nano-dispersions. However, other influencing parameters were observed. Close proximity of polymer chains causing partial crystallinity had an unfavorable effect on NP formation as both PEA1 and PEA6 performed poorly during the high throughput screening and exhibited melting events during thermal analysis (Table 1). This finding is in agreement with initial PEA studies.[12] In this light, substituted PEAs with higher density (Table 1) formed less defined NPs as for both properties the

trend was **PEA6** > **PEA2/PEA4** > **PEA3/PEA5**. Overall, it was shown that HFIP presented an excellent solvent for the nanoprecipitation of all PEAs as stable NPs could be formulated from the respective polymer solutions. It was even possible to formulate particles in the nanoscale size range without the utilization of the surfactant PVA. This was of great importance for the subsequent formulations with IMC for which the presence of the surfactant had to be avoided during the nanoprecipitation step in order to allow a reliable evaluation of the polymer influence on the API loading eliminating possible effects arising from surfactant.

4.2. Indomethacin loaded poly(ester amide) nanoparticles

For the loading of the PEAs with IMC, HFIP was hence selected as the polymer solvent. According to a solvent to non-solvent ratio of 1:8, the polymer-IMC solution was injected into pure water using a syringe pump. Directly after the formulation step PVA was added to stabilize the particles and to avoid aggregation or adherence of the PEAs to the wall of the falcon that was otherwise observed during purification. Nevertheless, this approach reduced the surfactant effect on the overall polymer performance and provided access to experimental formulation data that are independent of surfactant-polymer and surfactant-IMC interactions. All IMC-loaded and empty (*i.e.* control) PEA NPs were examined by DLS after each preparation and purification step to obtain insights into the dispersion stability (Fig. 2). The resulting sizes and PDI values of the IMC-loaded particles and the empty particles as well as the respective size distribution curves after each step, *i.e.* purification, lyophilization and resuspension are shown in the Supporting Information (Table SI 2 to Table SI 5, Figure SI 1).

The DLS measurements directly after formulation with IMC revealed a stable particle formation for all PEA except for **PEA1**, whose formulation resulted in significant amounts microparticles present. For all other polymers, the particle sizes ranged from 120 to 167 nm – a size range described as beneficial for particle uptake in cells.[40,41] The PDI values ranged from 0.07 for **PEA5@IMC** to 0.46 for **PEA2@IMC**. In general, empty particles were larger than loaded particles with equal or smaller PDI values, pointing towards a potential presence of attractive PEA-IMC interactions.[42,43] The measured ζ -potentials ranged from -9.8 to -17.3 mV (Fig. 2B) and indicate sufficient stability of the suspensions. The observation is common for many kinds of polymeric NPs and is attributed to preferred association of hydroxide ions from neat water on the surface leading to a negative ζ -potential.[44]

The final particle yields revealed a material loss during formulation and purification, *i.e.* due to large aggregate formation. Particle yields between 5% (**PEA2@IMC**) and 23% (**PEA5@IMC**) were obtained indicating low NP stability of **PEA2**-based formulations and increased stability for **PEA5**. For **PEA3@IMC**, **PEA4@IMC** and **PEA6@IMC** particle yields of 11 to 13% were recovered. Based on the DLS results and the NP yields it can be clearly stated that the polymer **PEA5** formed the most stable IMC loaded particles, followed by the polymers **PEA3**, **PEA4**, **PEA6**. Contrary, the polymer **PEA2** was only conditionally suitable and the polymer **PEA1** was not suitable.

The imaging of **PEA@IMC** and **PEA@empty** NPs by SEM measurements was difficult due to drying artifacts and particle images were obtained only to a limited extent, wherein the **PEA5@IMC** particles performed best (Fig. 3 and Figure SI 2). In the images of **PEA1@IMC**, **PEA2@IMC** and **PEA3@IMC** particle aggregation is visible. Rather large sizes between 200 and 500 nm for **PEA2@IMC** and particles agglomerates within 500 nm to micrometer range for **PEA3@IMC** were detected with a few single particles around 100 nm. Such small particles were also visible for **PEA1@IMC**, however, so were also larger agglomerates and elongated structures. For **PEA4@IMC**, **PEA5@IMC** and **PEA6@IMC** size ranges of 100 to 200 nm were imaged, which is in good agreement to the DLS findings, although particle density was very low for **PEA4@IMC** and only occasionally particles were found.

The EE of IMC in the **PEA2-6** NPs was determined by UV Vis spectroscopy (Fig. 2C). The lyophilized particles were dissolved in DMA and the absorbance was recorded at $\lambda = 318$ nm. The EE of **PEA1@IMC** was not determined due to initial aggregation and lack of solubility in DMA. **PEA5** achieved the highest EE with 53% as well as the highest LC of 1.54% (Fig. 2C). The second highest loading was achieved for **PEA3** with a resulting EE of 43% (LC = 1.34%) followed by polymer **PEA4** with an EE of 39% (LC = 1.15%). **PEA6** and **PEA2** only achieved an EE of 31 to 32% (LC up to 0.93%). The obtained EE values confirmed the expectations from the DLS measurements that **PEA5** and also **PEA3** formed the most stable particles and therefore reached the highest IMC loading.

4.3. Bulk miscibility of IMC with PEA

The formulation study consisting of the NP-solvent-screening and the subsequent API encapsulation both indicated the same best performers. However, due to the matching trends it was not clear if the beneficial properties arose from the NP stability or from favorable drug-polymer-interactions. To elucidate this aspect, blends of the polymer-drug pairs were further investigated by thermal analysis in bulk to reduce the number of influencing factors. Two methods were chosen to investigate the thermodynamic compatibility experimentally: i) Determination of saturation of amorphous polymer matrices by IMC from zero-enthalpy extrapolation[25] and ii) the determination of the Flory-Huggins interaction parameter of PEA-IMC from melting point depression.[26] Many methods are published for the investigation of drug-polymer compatibility, however the chosen methods stand out as particularly fast, cost-effective and straightforward.[20,23,45] Nonetheless, the DSC-based methods were complicated due to the partial crystallinity of **PEA1** and **PEA6**. Because melting events of these PEAs occurred in a similar temperature range as that of the drug in the relevant first heating run, **PEA1** and **PEA6** were excluded from the investigation.

For the other polymers **PEA2-PEA5**, samples for DSC were prepared by gently hand milling the materials for 10 min in the desired ratio and subsequent annealing at 111 °C for 24 h. This temperature was set intentionally between the T_g of the polymers and T_m of IMC, additionally removing possible moisture residue. The milling step was reported to have a favorable effect on the mixing due to particle size reduction as well as acceleration of the homogenization process.[46,47] The limited

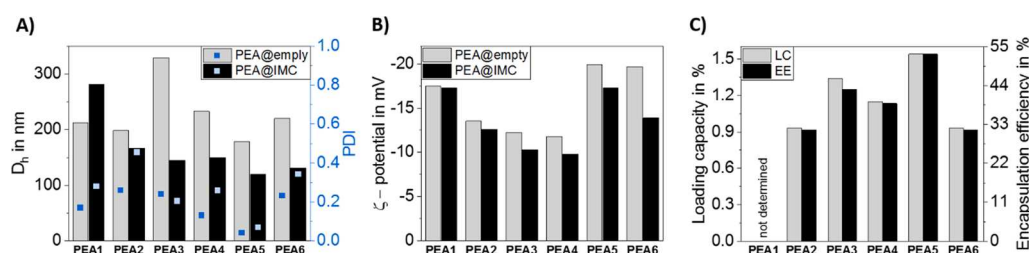


Fig. 2. Characterization results of unloaded PEA particles (PEA@empty) and indomethacin loaded PEA particles (PEA@IMC NPs): A) D_h and PDI from DLS, B) ζ -potential in water from electrophoretic light scattering, C) Loading capacity (LC) and encapsulation efficiency (EE) of PEA@IMC NP. The IMC amount was quantified via UV Vis spectroscopy and calculated in relation to the polymer mass.

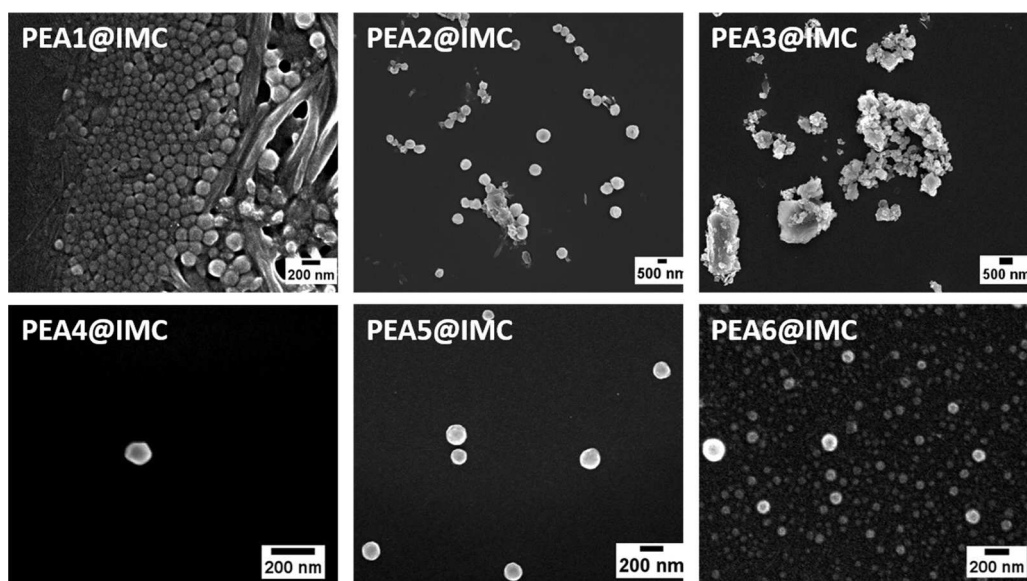


Fig. 3. Scanning electron microscopy images of indomethacin loaded poly(ester amide) nanoparticles (PEA@IMC) coated with platinum. Micrographs of unloaded particles are depicted in the supporting information.

amount of amorphous IMC produced by milling was previously reported to recrystallize during the annealing step above 60 °C.[48] As a result, the sample obtained after preparation was considered as a biphasic system composed of a saturated amorphous molecular dispersion in equilibrium with the undissolved excess of crystalline IMC. In agreement with previous studies, heating and cooling rates were set to 20 K min⁻¹. [25,49] The relatively fast heating rate suppresses undesired dissolution that might occur during slow heating as the drug might further dissolve into the matrix and thereby cause overestimation of saturation. The DSC experiments were conducted from -50 to 190 °C. This temperature window was set due to TGA analysis of the polymers to avoid mass loss at higher temperatures (Figure SI 4). Therefore, to ensure the polymer integrity and to avoid event overlapping in the DSC thermograms, the measurements were performed up to 190 °C. However, this complicated the setting of an accurate baseline for integration of the melting peak.

We hence refrained from usage of melting enthalpies of blends containing >90% IMC during our calculations. In contrast, the melting point depression within blends containing lower amounts of IMC enabled a straightforward baseline setting and peak integration. IMC mass fractions above 40 wt% were used to ensure a significant and, therefore, detectable amount of crystals within the matrix. The presence of the original morphology of IMC after the sample preparation has been already abundantly described in literature.[47] In addition, the chemical integrity of the individual compounds IMC and PEA2-PEA5 after exposure to sample preparation was confirmed by DSC, TGA, size exclusion chromatography (SEC), as well as ¹H nuclear magnetic resonance (NMR) spectroscopy (data not shown).

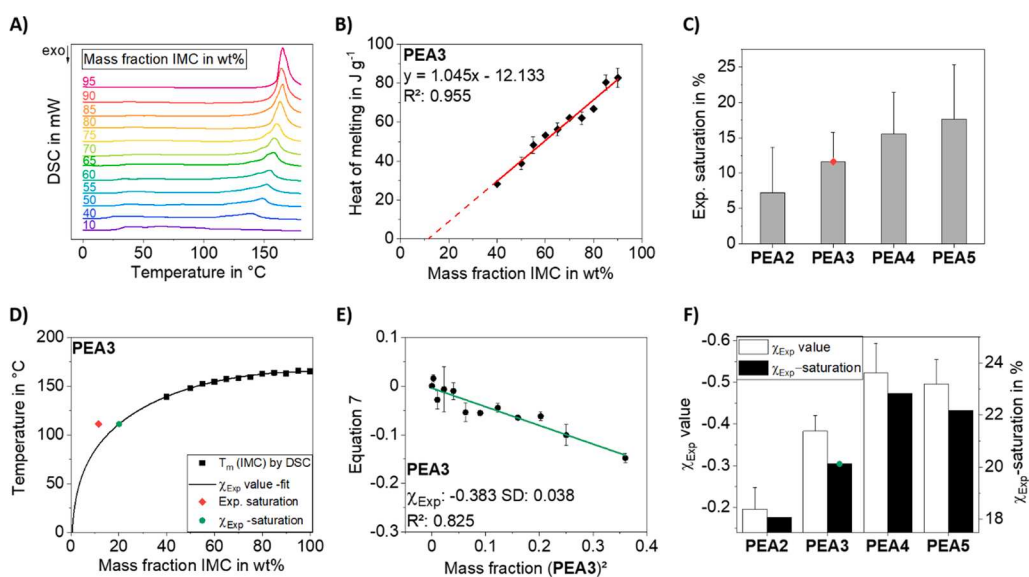


Fig. 4. A) Differential scanning calorimetry (DSC) thermograms of PEA3 [IMC] blends at different mass fractions annealed prior at 111 °C. B) Melting enthalpy from (A) plotted against the IMC mass fraction for PEA3 [IMC] blends with linear extrapolation towards zero enthalpy / experimental saturation. C) Experimental saturation values from zero enthalpy extrapolation for the polymers PEA2/3/4/5 [IMC] annealed prior at 111 °C. D) Representative melting point depression curve of PEA3 [IMC]: (Square) measured melting temperatures by DSC, (solid line) predicted behavior of melting point depression for the experimentally determined χ_{Exp} interaction parameter of -0.40, (diamond) experimentally determined saturation from zero enthalpy extrapolation from (C) at 111 °C, (circle) predicted saturation for χ_{Exp} interaction parameter of -0.40. E) Plot used to calculate the Flory-Huggins interaction parameter χ_{Exp} based on Equation (7). F) Flory-Huggins interaction parameters

for PEA2/3/4/5 [IMC] and the predicted saturation values at 111 °C.

4.4. Experimental miscibility via the melting enthalpy method

DSC thermograms of **PEA3 [IMC]** blends at different mass fractions are shown in Fig. 4A. For all analyzed mass fractions, an endothermic peak was evident, caused by the crystalline IMC still present in the blend. It was hence concluded that the saturation of **PEA3** with IMC should be below 40 wt%. The plot of the heat of melting ΔH_m against the corresponding mass fractions of the blend allowed the calculation of experimental saturation values because the decrease of the heat of melting was not only caused by the decreasing IMC content but also by the dissolution of the crystalline IMC into the polymeric matrix. The latter amount corresponded to the intercept value with the x-axis from the extrapolation towards zero enthalpy. In the case of **PEA3**, the miscible polymer-IMC phase was saturated by 12% of IMC (Fig. 4B). The same experimental procedure was performed with the other PEAs and increased saturation values resulted from **PEA2** and 7% to **PEA5** and 17% (Fig. 4C). Detailed information and respective graphs for the polymer blends of **PEA2**, **PEA4** and **PEA5** with IMC are available in the Supporting Information (Figure SI 5 and Figure SI 6). All blends were prepared twice and the resulting averages as well as standard deviations are shown (Fig. 4B and Figure SI 5). The linear regression was applied to the obtained data cloud of all individual measurement values leading to sufficient correlation coefficients ($R^2 \geq 0.88$) and, subsequently, also to the variance in the saturation values (Fig. 4C). The low T_g values of the PEAs (Table 1) complicated the sample handling and thereby somewhat affected the reproducibility. Also variance in the heat of melting values for higher mass fractions had a strong impact as they were easily falsified by the baseline error discussed above. Blends with 10 wt% and 25 wt% did not reveal any melting peaks. However, this did not necessarily implicate a complete dissolution of IMC in the PEA matrix as low amounts of crystalline IMC might not have been detected due to the sensitivity of the instrument.

4.5. Experimental Flory-Huggins interaction parameters

More information was extracted from the stack of DSC thermograms as depicted in Fig. 4A and Figure SI 5. A shift of the melting peaks towards lower temperatures was observed with decreasing IMC content, i. e. melting point depression was detected for all analyzed PEA[IMC] pairs. The T_m values indicated as black squares for **PEA3 [IMC]** are shown in Fig. 4D, representing average values of two measurements. The data sets were used to calculate the extrapolation (solid line, χ_{Exp} -fit) by the Flory-Huggins model applying the following equation:

$$-\left(\frac{1}{T_m} - \frac{1}{T_m^0}\right) \times \frac{\Delta H_f}{R} - \ln \Phi_d - \left(1 - \frac{1}{m}\right) \Phi_p = \chi_{Exp} \Phi_p^2 \quad (7)$$

where T_m is the temperature of melting of the drug in the blend, T_m^0 and ΔH_f are the melting temperature and enthalpy of fusion of the pure drug, respectively, R is the gas constant, Φ_d and Φ_p are the mass fractions of the drug and polymer, respectively, m is the molar volume ratio of the polymer and drug and χ_{Exp} is the Flory-Huggins interaction parameter. The plot of the left-hand side of the Equation (7) against the Φ_p^2 provides ideally a linear correlation and its slope equals the FH interaction parameter χ_{Exp} . This correlation is shown in Fig. 4E for **PEA3 [IMC]** and in Figure SI 8 for other PEA[IMC] combinations. Again, linear regression was applied to the obtained data cloud of all individual measurement values leading to sufficient correlation coefficients. The resulting FH interaction parameters χ_{Exp} are summarized in Fig. 4F. The FH values were used to calculate the χ_{Exp} -fit, which itself was subsequently used to determine an extrapolated saturation values (χ_{Exp} -saturation) at 111 °C (Fig. 4F). The trends for the χ_{Exp} values and for χ_{Exp} -saturation agreed because the values are interconnected. The critical value of 0.5 for the FH parameters was surpassed for all PEA[IMC] combinations indicating favorable interactions between API and polymer leading to their

miscibility. The compatibility increased from **PEA2 [IMC]** ($\chi_{Exp} = -0.20$, 18.07%) to **PEA4 [IMC]** ($\chi_{Exp} = -0.52$, 22.82%) and then only slightly decreased for **PEA5 [IMC]** ($\chi_{Exp} = -0.50$, 22.17%).

In general, the compatibility trends indicated by saturation values were coherent with those determined either by zero enthalpy extrapolation or from melting point depression. The method-to-method differences of saturation decreased from 11% for **PEA1 [IMC]** to 5% for **PEA5 [IMC]** with overall higher χ_{Exp} -saturation values (Fig. 4D and Figure SI 7). In summary, the solubilization increased with increasing bulkiness of the residue on the PEA main chain. The only mismatch of **PEA4 [IMC]** vs. **PEA5 [IMC]** could be possibly attributed to the difficult handling due to low T_g and the baseline error as discussed above.

In comparison to the PEA@IMC encapsulation study, especially the results of **PEA4** with IMC indicate a different behavior of the nanoparticle dispersions in comparison to bulk material. **PEA4@IMC** encapsulated less drug than **PEA3@IMC** but simultaneously **PEA4 [IMC]** exhibited better compatibility in bulk than **PEA3 [IMC]**. This hints towards a pronounced effect of the NP formulation ability on the encapsulation efficiency.

To obtain deeper insights into the compatibility of IMC with the PEA on a molecular level, two candidates were investigated in detail to enlighten the solubility differences. For this purpose, **PEA2 [IMC]**, exhibiting the lowest compatibility in the DSC study, and **PEA5 [IMC]** as the best performer from the NP study and exhibiting very good thermodynamic compatibility were subject to MD simulations.

4.6. Flory-Huggins interaction parameters from MD simulations

The FH parameters χ_{Sim} and changes of Gibbs free energy of mixing ΔG_{mix} were calculated using two methods. The simpler and less time-consuming method I relied on simulation of cohesive energy densities of the individual compounds. In contrast, the computationally demanding method II accounted for heteromolecular interactions of drug/polymer pairs. The obtained values are shown in Table 2. Method I yielded χ_{Sim} that differ significantly from the experimental values and indicate only poor miscibility of IMC with **PEA2** as well as **PEA5**. In contrast, χ_{Sim} obtained using method II were in very good agreement with the experimental results, in particular for the **PEA5+IMC** mixture (**PEA2 [IMC]**: $\chi_{Exp} = -0.20$, **PEA5 [IMC]**: $\chi_{Exp} = -0.50$).

The values of ΔG_{mix} calculated for **PEA2+IMC** and **PEA5+IMC** were negative for both method I and II, which indicated miscibility of IMC with **PEA2** as well as **PEA5**. However, the values from the two methods showed opposite trends. The values of ΔG_{mix} obtained with method I indicated better solubility of IMC in **PEA2** than in **PEA5**, in disagreement with experimental observations. In contrast, method II correctly predicted higher solubility of IMC in **PEA5** as compared to **PEA2**. The poor performance of the method I for miscibility predictions followed from the heuristic nature of Hildebrand solubility parameters used to obtain χ_{Sim} , which did not account for specific molecular interactions, such as hydrogen bonding. [32]

Fig. 5 shows that multiple hydrogen bonds [50] were formed between the IMC molecule and the surrounding polymer chains with bond distances from 1.72 to 2.48 Å. More pronounced hydrogen bonding in **PEA5+IMC** compared to **PEA2+IMC** was evident from the RDF plots (Fig. 5 C). In the case of the intermolecular atomic $NH_{PEA} - Cl_{IMC}$ pairs the maximum was 2.45 and 2.75 Å for **PEA5+IMC** and **PEA2+IMC**, respectively. Therefore, the chlorine atom of IMC was closer to hydrogen atoms of **PEA5** compared to **PEA2** (Fig. 5C) contributing stronger to the attractive heteromolecular forces. The same trend was found for $N_{PEA} - OH_{IMC}$.

Overall, stronger hydrogen bonds were found in the **PEA5+IMC** as compared to **PEA2+IMC**, which rationalizes the better solubility of IMC in **PEA5**. Intermolecular RDF plots for other types of hydrogen bonds found in simulated structures show similar trend (Figure SI 9).

Table 2

Results of atomistic MD simulations: Cohesive energy density, CED , Hildebrand solubility parameters, δ , energy of mixing, ΔE_{mix} , Flory-Huggins parameters, χ_{Sim} , and Gibbs free energy change of mixing, ΔG_{mix} . χ_{Sim} and ΔG_{mix} were calculated with methods I and II as described in the text.

	CED in J cm^{-3}	δ in $\sqrt{\text{MPa}}$	ΔE_{mix} in J cm^{-3}	χ_{Sim}		ΔG_{mix} in J mol^{-1}	
				I	II	I	II
PEA2+IMC	420.58	20.51	1.46	1.13	0.15	-65.95	-82.15
PEA5+IMC	389.24	19.73	-4.05	2.10	-0.46	-50.06	-92.08
PEA2	421.05	20.52	-	-	-	-	-
PEA5	383.94	19.59	-	-	-	-	-
IMC	570.95	23.89	-	-	-	-	-

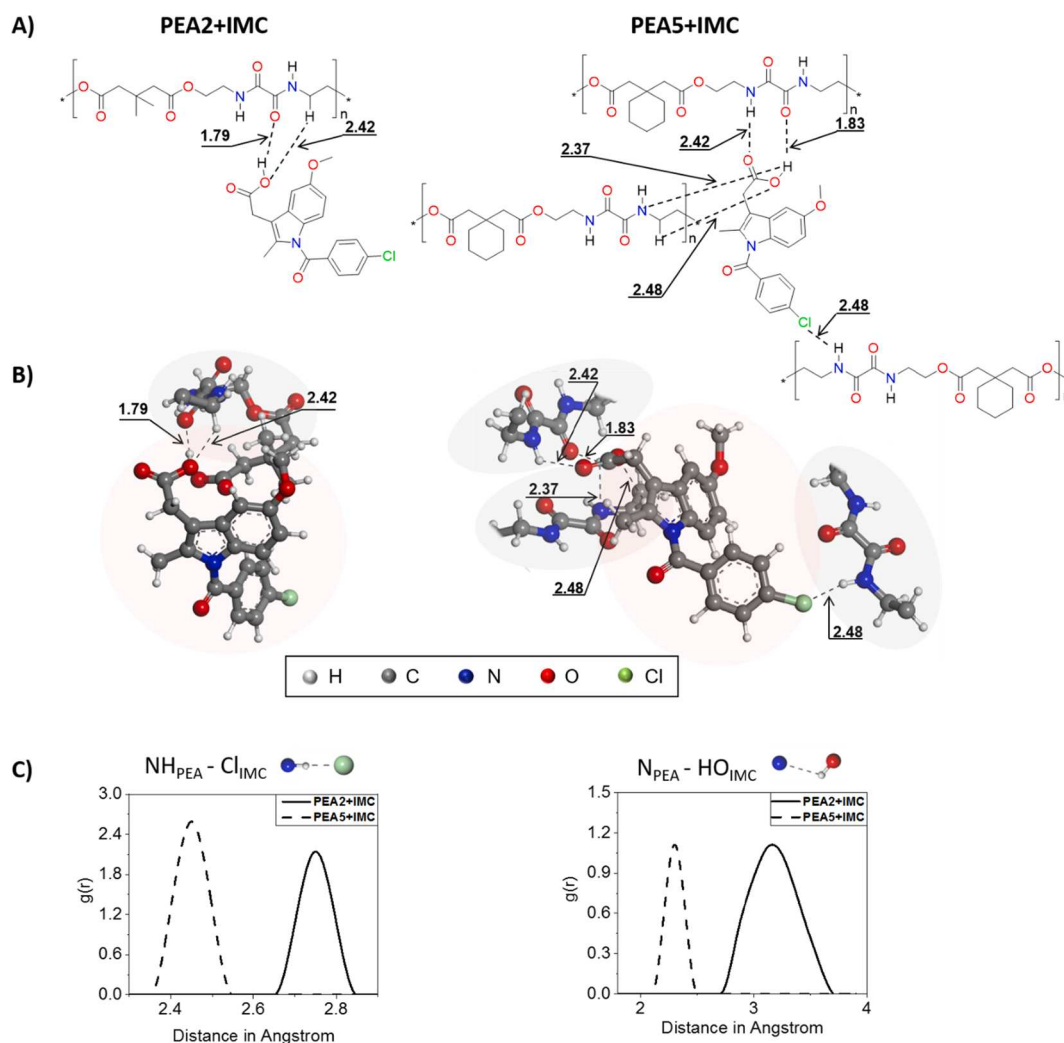


Fig. 5. Snapshots of MD simulation trajectories showing examples of hydrogen bonds between the indomethacin molecule and PEA chains **PEA2+IMC** and **PEA5+IMC**: A) chemical structure representation B) ball-and-stick representation (grey background for PEA, red background IMC). C) Intermolecular radial distribution function (RDF) plots of the two hydrogen bonding types possibly responsible the different solubility behavior.

5. Conclusions

Aiming towards rationalizing the performance of six PEAs with different spacers between the ester moieties for encapsulation of the anti-inflammatory drug IMC, a detailed and systematic investigation of the compatibility was performed covering a sequence of methods based on formulation, DSC studies and MD simulations. A broad nanoprecipitation screening identified suitable formulation conditions and **PEA5** as the optimum polymer for API encapsulation, inversely relating the LC with the polymer density. To exclude additional effects arising through the formulation, the miscibility range and thermodynamic compatibility of PEA-IMC blends were assessed through DSC studies.

Zero melting enthalpy extrapolation and melting point depression consistently confirmed the best and worst performers of the encapsulation study. The Flory-Huggins parameters χ_{Exp} ranging from -0.20 to -0.50 indicated favorable drug-polymer interactions, which were further investigated by MD simulations of the actual binary mixtures. Besides providing χ_{Sim} that were in agreement with experimental values, specific interactions through hydrogen bonding were found, rationalizing the best and worst performers through the number of hydrogen bonds formed between the components, *i.e.* PEA and IMC.

With the powerful tools and deep understanding at hand we now aim at formulation of more complex drugs and plan to exploit the specific

interactions found during our research for *in silico* design of the ultimate carrier material, not only for IMC but also for highly potent new drugs that are not as readily available.

Declaration of Competing Interest

The authors declare that they have no known competing financial interests or personal relationships that could have appeared to influence the work reported in this paper.

Acknowledgments

This work was funded by the Deutsche Forschungsgemeinschaft (DFG, German Research Foundation) – number 316213987 – SFB 1278 “PolyTarget” (projects A01, A04, Z01). The SEM facilities of the Jena Center for Soft Matter (JCSM) were established with a grant from the DFG (INST 275/307-1 FUGG). The authors thank Blerina Shkodra Pula for discussion and Johannes Schenk as well as Renzo Paulus for technical support.

Appendix A. Supplementary data

Supplementary data to this article can be found online at <https://doi.org/10.1016/j.eurpolymj.2021.110606>.

References

- J.A. Zuegg, M. Cooper, Drug-likeness and increased hydrophobicity of commercially available compound libraries for drug screening, *Curr. Top. Med. Chem.* 12 (2012) 1500–1513.
- B. Begines, T. Ortiz, M. Pérez-Aranda, G. Martínez, M. Merinero, F. Argüelles-Arias, A. Alcudia, Polymeric nanoparticles for drug delivery: Recent developments and future prospects, *Nanomaterials* 10 (2020) 1403.
- C. Ye, H. Chi, A review of recent progress in drug and protein encapsulation: Approaches, applications and challenges, *Mater. Sci. Eng., C* 83 (2018) 233–246.
- F. Danhier, E. Ansorena, J.M. Silva, R. Coco, A. Le Breton, V. Préat, PLGA-based nanoparticles: An overview of biomedical applications, *J. Control. Release* 161 (2012) 505–522.
- H. Danafar, Applications of copolymeric nanoparticles in drug delivery systems, *Drug Res.* 66 (2016) 506–519.
- A. Kumari, S.K. Yadav, S.C. Yadav, Biodegradable polymeric nanoparticles based drug delivery systems, *Colloids Surf. B* 75 (2010) 1–18.
- B. Shkodra-Pula, C. Grune, A. Traeger, A. Vollrath, S. Schubert, D. Fischer, U. Schubert, Effect of surfactant on the size and stability of PLGA nanoparticles encapsulating a protein kinase C inhibitor, *Int. J. Pharm.* 566 (2019) 756–764.
- C. Englert, J.C. Brendel, T.C. Majdanski, T. Yildirim, S. Schubert, M. Gottschaldt, N. Windhab, U.S. Schubert, Pharmopolymers in the 21st century: Synthetic polymers in drug delivery applications, *Prog. Polym. Sci.* 87 (2018) 107–164.
- M. Winnacker, B. Rieger, Poly(ester amide)s: Recent insights into synthesis, stability and biomedical applications, *Polym. Chem.* 7 (2016) 7039–7046.
- M. Dirauf, D. Bandelli, C. Weber, H. Görls, M. Gottschaldt, U.S. Schubert, TBD-catalyzed ring-opening polymerization of alkyl-substituted morpholine-2, 5-dione derivatives, *Macromol. Rapid Commun.* 39 (2018) 1800433.
- A. Ghaffar, G. Draaisma, G. Mihov, A. Dias, P. Schoenmakers, S. Van Der Wal, Monitoring the *in vitro* enzyme-mediated degradation of degradable poly(ester amide) for controlled drug delivery by LC-ToF-MS, *Biomacromolecules* 12 (2011) 3243–3251.
- I. Muljajew, A. Erlebach, C. Weber, J.R. Buchheim, M. Sierka, U.S. Schubert, A polyesteramide library from dicarboxylic acids and 2,2'-bis(2-oxazoline): Synthesis, characterization, nanoparticle formulation and molecular dynamics simulations, *Polym. Chem.* 11 (2020) 112–124.
- N. Brunacci, A.T. Neffe, C. Wischke, T. Naoilou, U. Nöchel, A. Lendlein, Oligodepsipeptide (nano) carriers: Computational design and analysis of enhanced drug loading, *J. Control. Release* 301 (2019) 146–156.
- C.I.C. Crucho, M.T. Barros, Polymeric nanoparticles: A study on the preparation variables and characterization methods, *Mater. Sci. Eng., C* 80 (2017) 771–784.
- P. Abasian, S. Ghanavati, S. Rahebi, S. Nouri Khorasani, S. Khalili, Polymeric nanocarriers in targeted drug delivery systems: A review, *Polym. Adv. Technol.* 31 (2020) 2939–2954.
- C.J. Martínez Rivas, M. Tarhini, W. Badri, K. Miladi, H. Greige-Gerges, Q.A. Nazari, S.A. Galindo Rodríguez, R.Á. Román, H. Fessi, A. Elaissari, Nanoprecipitation process: From encapsulation to drug delivery, *Int. J. Pharm.* 532 (2017) 66–81.
- S. Schubert, J.T. Delaney Jr, U.S. Schubert, Nanoprecipitation and nanoformulation of polymers: From history to powerful possibilities beyond poly(lactic acid), *Soft Matter* 7 (2011) 1581–1588.
- D. Hwang, J.D. Ramsey, A.V. Kabanov, Polymeric micelles for the delivery of poorly soluble drugs: From nanoformulation to clinical approval, *Adv. Drug Deliv. Rev.*, 2020.
- A. Budhian, S.J. Siegel, K.I. Winey, Haloperidol-loaded PLGA nanoparticles: Systematic study of particle size and drug content, *Int. J. Pharm.* 336 (2007) 367–375.
- S. Jankovic, G. Tsakiridou, F. Ditzinger, N.J. Koehl, D.J. Price, A.-R. Ilie, L. Kalantzi, K. Kimpe, R. Holm, A. Nair, B. Griffin, C. Saal, M. Kuentz, Application of the solubility parameter concept to assist with oral delivery of poorly water-soluble drugs – a PEARRL review, *J. Pharm. Pharmacol.* 71 (2019) 441–463.
- M.M. Lübtow, M.S. Haider, M. Kirsch, S. Klisch, R. Luxenhofer, Like dissolves like? A comprehensive evaluation of partial solubility parameters to predict polymer–drug compatibility in ultrahigh drug-loaded polymer micelles, *Biomacromolecules* 20 (2019) 3041–3056.
- J.A. Baird, L.S. Taylor, Evaluation of amorphous solid dispersion properties using thermal analysis techniques, *Adv. Drug Deliv. Rev.* 64 (2012) 396–421.
- P. Pandi, R. Bulusu, N. Kommineni, W. Khan, M. Singh, Amorphous solid dispersions: An update for preparation, characterization, mechanism on bioavailability, stability, regulatory considerations and marketed products, *Int. J. Pharm.* 586 (2020), 119560.
- S. Baghel, H. Cathcart, N.J. O'Reilly, Polymeric amorphous solid dispersions: A review of amorphization, crystallization, stabilization, solid-state characterization, and aqueous solubilization of biopharmaceutical classification system class II drugs, *J. Pharm. Sci.* 105 (2016) 2527–2544.
- Y. Amharar, V. Curtin, K.H. Gallagher, A.M. Healy, Solubility of crystalline organic compounds in high and low molecular weight amorphous matrices above and below the glass transition by zero enthalpy extrapolation, *Int. J. Pharm.* 472 (2014) 241–247.
- P.J. Marsac, S.L. Shamblin, L.S. Taylor, Theoretical and practical approaches for prediction of drug–polymer miscibility and solubility, *Pharm. Res.* 23 (2006) 2417–2426.
- A.O. Kasimova, G.M. Pavan, A. Danani, K. Mondon, A. Cristiani, L. Scapozza, R. Gurny, M. Möller, Validation of a novel molecular dynamics simulation approach for lipophilic drug incorporation into polymer micelles, *J. Phys. Chem. B* 116 (2012) 4338–4345.
- X.D. Guo, L.J. Zhang, Y. Qian, Systematic multiscale method for studying the structure–performance relationship of drug–delivery systems, *Ind. Eng. Chem. Res.* 51 (2012) 4719–4730.
- L. Huynh, C. Neale, R. Pomès, C. Allen, Computational approaches to the rational design of nanoemulsions, polymeric micelles, and dendrimers for drug delivery, *Nanomed. Nanotechn. Biol. Med.* 8 (2012) 20–36.
- P.J. Marsac, T. Li, L.S. Taylor, Estimation of drug–polymer miscibility and solubility in amorphous solid dispersions using experimentally determined interaction parameters, *Pharm. Res.* 26 (2008) 139–151.
- L. Huynh, J. Grant, J.-C. Leroux, P. Delmas, C. Allen, Predicting the solubility of the anti-cancer agent docetaxel in small molecule excipients using computational methods, *Pharm. Res.* 25 (2008) 147–157.
- A. Erlebach, I. Muljajew, M. Chi, C. Bückmann, C. Weber, U.S. Schubert, M. Sierka, Predicting solubility of small molecules in macromolecular compounds for nanomedicine application from atomistic simulations, *Adv. Theory Simul.* 3 (2020) 2000001.
- Materials Studio, version 19.1.0.219, Dassault Systèmes BIOVIA: San Diego, 2020.
- H. Sun, Z. Jin, C. Yang, R.L. Akkermans, S.H. Robertson, N.A. Spenley, S. Miller, S. M. Todd, COMPASS II: Extended coverage for polymer and drug-like molecule databases, *J. Mol. Model.* 22 (2016) 47.
- W.G. Hoover, Canonical dynamics: Equilibrium phase-space distributions, *Phys. Rev. A* 31 (1985) 1695–1697.
- S. Nosé, A unified formulation of the constant temperature molecular dynamics methods, *J. Chem. Phys.* 81 (1984) 511–519.
- D.N. Theodorou, U.W. Suter, Detailed molecular structure of a vinyl polymer glass, *Macromolecules* 18 (1985) 1467–1478.
- H.J. Berendsen, J.V. Postma, W.F. van Gunsteren, A. DiNola, J.R. Haak, Molecular dynamics with coupling to an external bath, *J. Chem. Phys.* 81 (1984) 3684–3690.
- M. Parrinello, A. Rahman, Crystal structure and pair potentials: A molecular-dynamics study, *Phys. Rev. Lett.* 45 (1980) 1196–1199.
- P. Forozaandeh, A.A. Aziz, Insight into cellular uptake and intracellular trafficking of nanoparticles, *Nanoscale Res. Lett.* 13 (2018) 339.
- C. He, Y. Hu, L. Yin, C. Tang, C. Yin, Effects of particle size and surface charge on cellular uptake and biodistribution of polymeric nanoparticles, *Biomaterials* 31 (2010) 3657–3666.
- B. Shkodra, A.T. Press, A. Vollrath, I. Nischang, S. Schubert, S. Hoepfner, D. Haas, C. Enzensperger, M. Lehmann, P. Babic, Formulation of liver-specific PLGA-DY-635 nanoparticles loaded with the protein kinase C inhibitor bisindolylmaleimide I, *Pharmaceutics* 12 (2020) 1110.
- A. Reisch, A. Runser, Y. Arntz, Y. Mely, A.S. Klymchenko, Charge-controlled nanoprecipitation as a modular approach to ultrasmall polymer nanocarriers: Making bright and stable nanoparticles, *ACS Nano* 9 (2015) 5104–5116.
- A.V. Delgado, F. González-Caballero, R. Hunter, L.K. Koopal, J. Lyklema, Measurement and interpretation of electrokinetic phenomena (IUPAC technical report), *Pure Appl. Chem.* 77 (2005) 1753–1805.
- M.M. Knopp, L. Tajber, Y. Tian, N.E. Olesen, D.S. Jones, A. Kozyra, K. Löbmann, K. Paluch, C.M. Brennan, R. Holm, A.M. Healy, G.P. Andrews, T. Rades, Comparative study of different methods for the prediction of drug–polymer solubility, *Mol. Pharm.* 12 (2015) 3408–3419.
- A.I. Mahieu, J.-F.O. Willart, E. Dudogon, F. Danède, M. Descamps, A new protocol to determine the solubility of drugs into polymer matrixes, *Mol. Pharm.* 10 (2013) 560–566.

- [47] J. Tao, Y. Sun, G.G. Zhang, L. Yu, Solubility of small-molecule crystals in polymers: D-mannitol in PVP, indomethacin in PVP/VA, and nifedipine in PVP/VA, *Pharm. Res.* 26 (2009) 855–864.
- [48] O. Planinsek, J. Zadnik, M. Kunaver, S. Srcic, A. Godec, Structural evolution of indomethacin particles upon milling: Time-resolved quantification and localization of disordered structure studied by IGC and DSC, *J. Pharm. Sci.* 99 (2010) 1968–1981.
- [49] D. Gramaglia, B.R. Conway, V.L. Kett, R.K. Malcolm, H.K. Batchelor, High speed DSC (hyper-DSC) as a tool to measure the solubility of a drug within a solid or semi-solid matrix, *Int. J. Pharm.* 301 (2005) 1–5.
- [50] T. Steiner, The hydrogen bond in the solid state, *Angew. Chem. Int. Ed.* 41 (2002) 48–76.

Supporting Information

A combined experimental and *in silico* approach to determine the compatibility of poly(ester amide)s and indomethacin in polymer nanoparticles

*Irina Muljajew, ^{a, b} Mingzhe Chi, ^c Antje Vollrath, ^{a, b} Christine Weber, ^{a, b} Baerbel Beringer-Siemers, ^{a, b} Steffi Stumpf, ^{a, b} Stephanie Hoepfener, ^{a, b} Marek Sierka, ^c Ulrich S. Schubert ^{a, b, *}*

^a Laboratory of Organic and Macromolecular Chemistry (IOMC), Friedrich Schiller University Jena, Humboldtstrasse 10, 07743 Jena, Germany

^b Jena Center for Soft Matter (JCSM), Friedrich Schiller University Jena, Philosophenweg 7, 07743 Jena, Germany

^c Otto Schott Institute of Materials Research (OSIM), Friedrich Schiller University Jena, Löbdergraben 32, Jena 07743, Germany.

Detailed discussion of nanoparticle (NP) formation *via* high-throughput screening

Nanoprecipitation was performed in a high-throughput manner using a pipetting robot that dropped the polymer solution into the continuous phase. In detail, 25 μL of the respective, initial polymer solution were dosed into a well containing 190 μL of either pure water or 0.3% (w/v) polyvinyl alcohol (PVA) solution. After mixing by pipetting up and down once, the formulations were allowed to equilibrate for a minimum of two hours. Afterwards, 15 μL of the final NP suspension were taken and diluted with 185 μL of pure water prior to DLS analysis. The dilution step reduced the solvent residue of the non-volatile solvents such as DMSO, DMF or DMAc to $<1\%$ which was important for the subsequent particle size analysis in order to minimize the influence on the viscosity change.

DLS measurements revealed that **PEA1** was not forming NPs above an initial polymer concentration of 10 mg mL^{-1} (**Figure 1A**). Below $c = 10 \text{ mg mL}^{-1}$ particles with D_h of 300 nm and PDI values from 0.3 to 0.5 were obtained in water. However, the overall high NP dispersity indicated that particle formation was not stable. Slight improvement of the NP formulation was achieved in the continuous phase containing the PVA surfactant. Nevertheless, the **PEA1** NP properties were still not satisfactory. **PEA2** formed nanoparticles in water up to an initial polymer concentration of 2.5 mg mL^{-1} in THF, 5 mg mL^{-1} in DMSO and 10 mg mL^{-1} in HFiP (**Figure 1B**). Above these concentrations aggregation occurred. In a 0.3% (w/v) PVA solution, particles with a size range from 150 to 240 nm from DMSO or up to 400 nm from THF as well as HFiP were obtained with PDI values between 0.06 and 0.35. **PEA4** formed NPs in water with hydrodynamic diameters (D_h) from 120 to 260 nm for initial polymer concentrations up to 5 mg mL^{-1} in acetonitrile, 15.5 mg mL^{-1} in DMF and 20 mg mL^{-1} in HFiP (**Figure 1D**). For higher concentrations, aggregation occurred when no surfactant was present. With the application of

PVA, defined NPs were obtained for all concentrations from all three solvents, resulting in particle sizes between 160 nm (PDI 0.2) for 1 mg mL⁻¹ and 301 nm (PDI 0.16) for 20 mg mL⁻¹. **PEA3** and **PEA5** featured similar solubility properties and therefore might be expected to perform similarly in particle formation. Indeed, nanoprecipitation from HFiP, acetonitrile and DMF resulted in defined particles in the size range from 90 nm to 400 nm for both polymers, which formulated well in water and in PVA solution. DMF led to the smallest particles (90 to 200 nm). The particle sizes increased when HFiP or acetonitrile was used, with the largest particles for **PEA3** obtained from an acetonitrile polymer solution ($D_h = 380$ nm, PDI 0.26 in PVA solution) and for **PEA5** with HFiP ($D_h = 412$ nm, PDI 0.12 in water). Nanoprecipitation of **PEA6** from DMSO and HFiP in water led to unstable formulations and strong aggregation, as indicated by high PDI values of 0.5. With the PVA surfactant, particle sizes between 100 and 250 nm were obtained with low PDI values of 0.08 to 0.13.

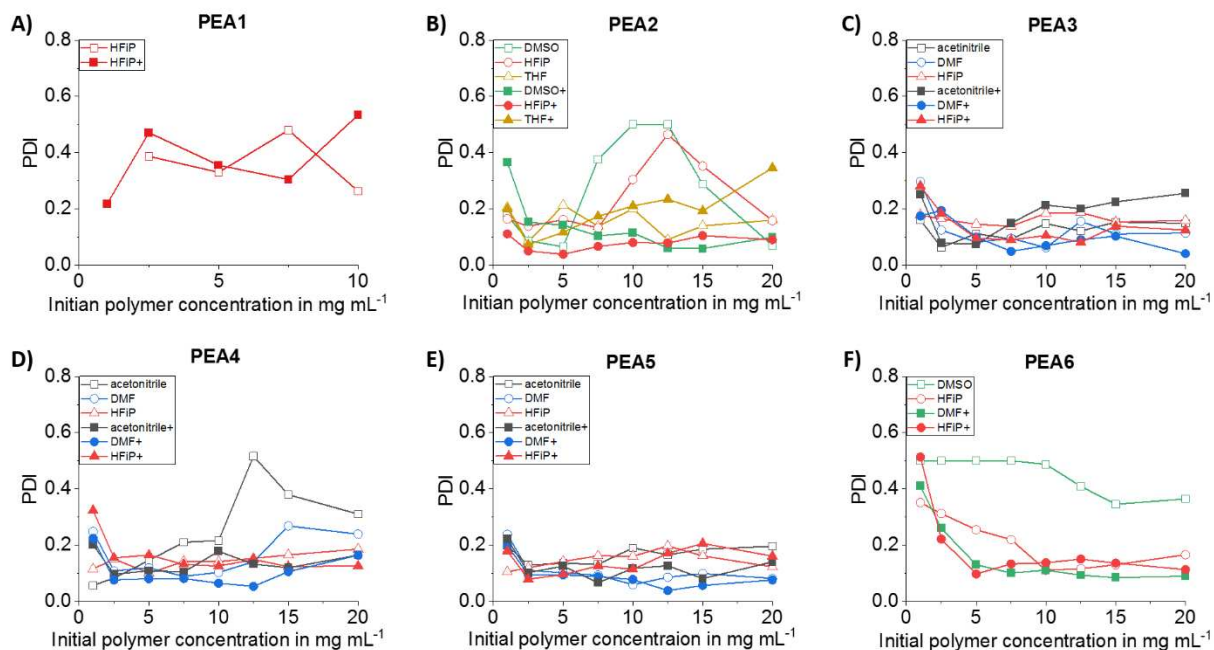


Figure SI 1. Polydispersity index (PDI) values for nanoparticle formulation of different PEAs from various solvents performed on a liquid handling robot. *Solvent (solid symbol)* or *Solvent+* (*empty symbol*) indicates formulation from the organic solvent into pure water or a 0.3% aqueous PVA solution, respectively.

Table SI 1. Nanoparticle formulation of different PEAs from various organic solvents in two continuous phases (pure water or a 0.3% aqueous PVA solution) performed *via* high-throughput nanoprecipitation using a liquid handling robot. Hydrodynamic diameter values given in nm of two independent formulations (indicated by I or II) as well as the plotted average ($\bar{\text{O}}$, Figure 1) determined by dynamic light scattering (DLS).

PEA1 in water			
c (mg mL⁻¹)	HFiP I	HFiP II	HFiP $\bar{\text{O}}$
1.00			
2.50	313	331	322
5.00	340	301	321
7.50	381	398	390
10.00	294	343	318
PEA1 in PVA			
c (mg mL⁻¹)	HFiP I	HFiP II	HFiP $\bar{\text{O}}$
1.00	184	180	182
2.50	429	219	324
5.00	256	280	268
7.50	323	246	284
10.00	233	1220	726

PEA2 in water									
c (mg mL⁻¹)	THF I	THF II	THF $\bar{\text{O}}$	DMSO I	DMSO II	DMSO $\bar{\text{O}}$	HFiP I	HFiP II	HFiP $\bar{\text{O}}$
1.00	168	305	236	145	140	142	163	159	161
2.50	202	246	224	176	177	177	162	169	166
5.00	1134	1106	1120	209	202	205	270	237	254
7.50	906	657	781	1769	401	1085	434	199	316
10.00	662	564	613	2403	1838	2121	849	244	547
12.50	336	309	322	1555	2932	2244	1563	286	924
15.00	407	260	333	750	1047	898	1339	574	956
20.00	819	933	876	416	434	425	1192	448	820
PEA2 in PVA									
c (mg mL⁻¹)	THF I	THF II	THF $\bar{\text{O}}$	DMSO I	DMSO II	DMSO $\bar{\text{O}}$	HFiP I	HFiP II	HFiP $\bar{\text{O}}$
1.00	160	151	155	162	124	143	195	159	177
2.50	195	187	191	170	139	154	193	191	192
5.00	244	238	241	174	181	178	215	194	204
7.50	273	270	272	187	189	188	221	211	216
10.00	296	341	318	223	217	220	231	219	225
12.50	398	456	427	220	212	216	241	231	236
15.00	371	385	378	228	222	225	230	228	229
20.00	470	420	445	243	238	240	246	236	241

Table SI 1. Continued.

PEA3 in water									
c (mg mL ⁻¹)	THF I	THF II	THF Ø	DMSO I	DMSO II	DMSO Ø	DMA I	DMA II	DMA Ø
1.00	169	157	163	98	89	94	153	141	147
2.50	176	180	178	122	124	123	166	154	160
5.00	186	186	186	128	151	139	175	158	166
7.50	205	208	207	141	131	136	170	199	184
10.00	226	221	223	153	150	151	202	193	197
12.50	260	234	247	273	158	216	205	204	205
15.00	280	296	288	228	177	202	199	206	202
20.00	323	334	329	188	195	191	199	212	205
PEA3 in PVA									
c (mg mL ⁻¹)	THF I	THF II	THF Ø	DMSO I	DMSO II	DMSO Ø	DMA I	DMA II	DMA Ø
1.00	134	159	146	127	128	127	238	174	206
2.50	171	173	172	134	184	159	184	179	182
5.00	217	220	219	180	161	171	199	200	200
7.50	270	266	268	143	142	142	226	208	217
10.00	333	307	320	169	157	163	218	216	217
12.50	361	395	378	181	214	198	235	238	236
15.00	365	338	352	212	183	197	223	230	227
20.00	385	380	382	191	197	194	258	254	256

PEA4 in water									
c (mg mL ⁻¹)	HFiP I	HFiP II	HFiP Ø	ACN I	ACN II	ACN Ø	DMF I	DMF II	DMF Ø
1.00	166	167	167	177	148	162	114	123	119
2.50	196	197	197	221	209	215	145	126	135
5.00	224	216	220	334	245	289	155	161	158
7.50	230	231	231	618	422	520	183	175	179
10.00	215	219	217	1262	768	1000	235	208	222
12.50	259	243	251	1332	2084	1000	297	229	263
15.00	253	248	251	2653	3196	1000	1318	336	827
20.00	251	241	246	533	1988	1000	308	758	533
PEA4 in PVA									
c (mg mL ⁻¹)	HFiP I	HFiP II	HFiP Ø	ACN I	ACN II	ACN Ø	DMF I	DMF II	DMF Ø
1.00	153	206	179	165	154	160	209	128	168
2.50	184	188	186	187	208	197	145	160	153
5.00	276	207	241	240	275	257	165	165	165
7.50	214	192	203	276	256	266	189	215	202
10.00	188	211	200	301	313	307	186	226	206
12.50	228	234	231	296	288	292	196	204	200
15.00	256	235	245	296	312	304	251	241	246
20.00	246	238	242	304	298	301	259	327	293

Table SI 1. Continued.

PEA5 in water									
c (mg mL ⁻¹)	THF I	THF II	THF Ø	DMSO I	DMSO II	DMSO Ø	DMA I	DMA II	DMA Ø
1.00	83	55	69	129	132	131	163	137	150
2.50	107	72	90	129	130	129	169	191	180
5.00	125	98	112	156	152	154	210	251	231
7.50	133	102	118	175	173	174	238	241	239
10.00	160	162	161	186	183	184	276	284	280
12.50	165	120	143	192	186	189	298	305	302
15.00	173	126	150	198	195	197	340	380	360
20.00	182	180	181	216	219	218	414	413	413
PEA5 in PVA									
c (mg mL ⁻¹)	THF I	THF II	THF Ø	DMSO I	DMSO II	DMSO Ø	DMA I	DMA II	DMA Ø
1.00	115	129	122	139	138	138	140	131	136
2.50	131	110	120	182	165	174	174	184	179
5.00	127	124	125	186	191	188	205	202	204
7.50	141	137	139	209	209	209	230	232	231
10.00	145	148	147	213	194	204	258	252	255
12.50	153	158	156	217	188	203	269	260	264
15.00	167	168	168	237	226	231	286	301	293
20.00	154	178	166	230	226	228	287	336	312

PEA6 in water									
c (mg mL ⁻¹)	DMSO I	DMSO II	DMSO Ø	HFIP I	HFIP II	HFIP Ø	THF I	THF II	THF Ø
1.00	181	184	183	196	181	188	262	227	244
2.50	123	256	190	470	839	654	639	401	520
5.00	136	155	145	188	201	194	339	11267	1000
7.50	108	124	116	164	202	183	1000	1000	1000
10.00	181	156	168	146	158	152	1000	1000	1000
12.50	110	168	139	154	158	156	1000	1000	1000
15.00	180	190	185	172	166	169	1000	1000	1000
20.00	270	193	232	206	198	202	1000	1000	1000
PEA6 in PVA									
c (mg mL ⁻¹)	DMSO I	DMSO II	DMSO Ø	HFIP I	HFIP II	HFIP Ø	THF I	THF II	THF Ø
1.00	204	183	193	261	134	197	171	362	266
2.50	103	134	118	165	154	160	915	646	781
5.00	118	102	110	176	181	178	333	828	580
7.50	102	105	103	187	193	190	1000	1000	1000
10.00	114	115	114	207	207	207	1000	1000	1000
12.50	111	111	111	214	207	211	1000	1000	1000
15.00	135	116	125	244	225	235	1000	1000	1000
20.00	140	131	135	258	246	252	1000	1000	1000

Table SI 2. Characteristics of indomethacin loaded PEA NP (**PEA@IMC**) after different steps.

Sample	D_h		D_h		D_h		ζ	NP yield	NP yield	LC	EE
	(Z_{av} , nm)	PDI	(Z_{av} , nm)	PDI	(Z_{av} , nm)	PDI					
	After formulation (A)		After purification (B)		After lyophilization (C)						
PEA1@IMC	1441	0.28	322	0.49	281	0.28	-17.3	1.31	5.24	-	-
PEA2@IMC	217	0.20	104	0.17	167	0.46	-12.6	1.24	4.96	0.90	31
PEA3@IMC	199	0.15	140	0.22	145	0.20	-10.3	2.86	11.44	1.34	43
PEA4@IMC	199	0.13	142	0.21	150	0.26	-9.8	2.85	11.40	1.15	39
PEA5@IMC	167	0.06	113	0.05	120	0.07	-17.3	5.84	23.36	1.54	53
PEA6@IMC	194	0.32	109	0.12	131	0.34	-13.9	3.29	13.16	0.93	32

Table SI 3. Characteristics of unloaded PEA NP (**PEA@empty**) after different steps.

Sample	D_h		D_h		D_h		ζ	NP yield	NP yield
	(Z_{av} , nm)	PDI	(Z_{av} , nm)	PDI	(Z_{av} , nm)	PDI			
	After formulation (A)		After centrifugation (B)		After lyophilization (C)				
PEA1@empty	499	0.32	212	0.17	212	0.17	-17.5	6.45	25.8
PEA2@empty	278	0.21	198	0.10	198	0.26	-13.5	0.63	1.26
PEA3@empty	600	0.34	339	0.22	329	0.24	-12.2	0.98	3.92
PEA4@empty	1095	0.5	234	0.14	233	0.13	-11.8	1.33	5.32
PEA5@empty	272	0.13	176	0.10	178	0.04	-19.9	2.63	10.52
PEA6@empty	410	0.58	212	0.29	220	0.23	-19.7	2.35	9.40

Table SI 4. Indomethacin loaded PEA NPs (**PEA@IMC**): Size distributions after formulation, purification and lyophilization with subsequent resuspension.

After formulation		
NP	Intensity distribution	Number distribution
PEA1@IMC		
PEA2@IMC		
PEA3@IMC		
PEA4@IMC		
PEA5@IMC		
PEA6@IMC		

Table SI 4 (continued). Indomethacin loaded PEA NPs (PEA@IMC): Size distributions after formulation, purification and lyophilization with subsequent resuspension.

After purification		
NP	Intensity distribution	Number distribution
PEA1@IMC		
PEA2@IMC		
PEA3@IMC		
PEA4@IMC		
PEA5@IMC		
PEA6@IMC		

Table SI 4 (continued). Indomethacin loaded PEA NPs (PEA@IMC): Size distributions after formulation, purification and lyophilization with subsequent resuspension.

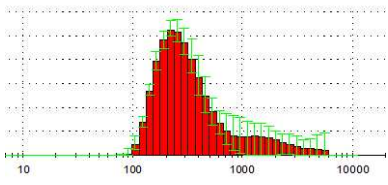
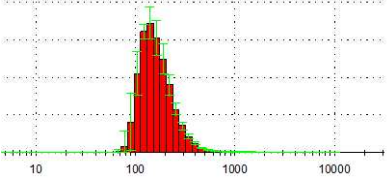
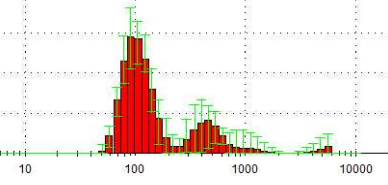
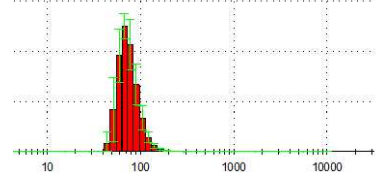
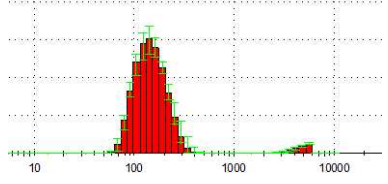
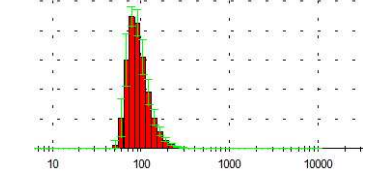
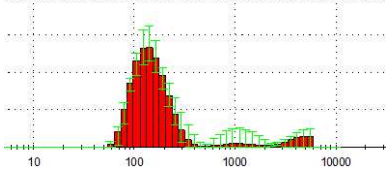
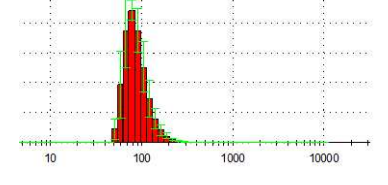
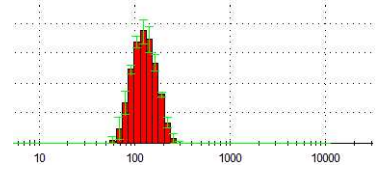
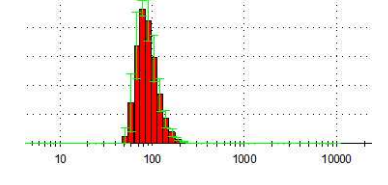
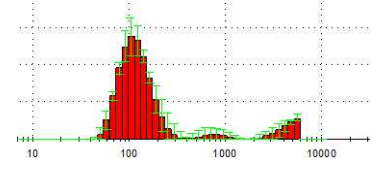
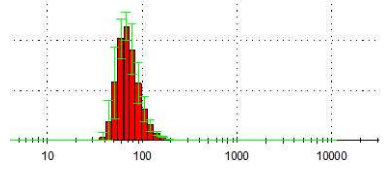
After lyophilization		
NP	Intensity distribution	Number distribution
PEA1@IMC		
PEA2@IMC		
PEA3@IMC		
PEA4@IMC		
PEA5@IMC		
PEA6@IMC		

Table SI 5. Unloaded PEA NPs (PEA@empty): Size distributions after formulation and lyophilization with subsequent resuspension.

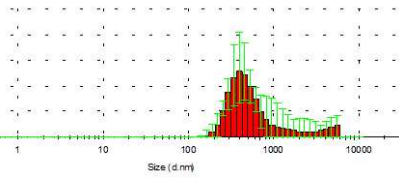
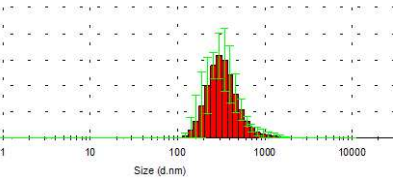
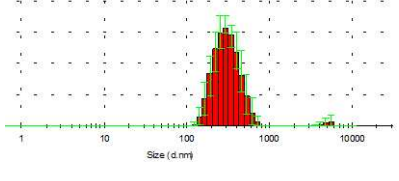
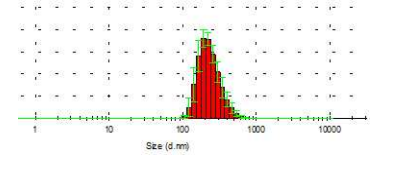
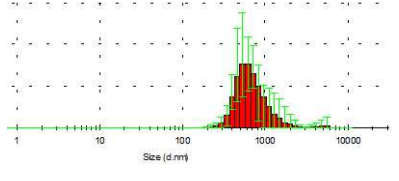
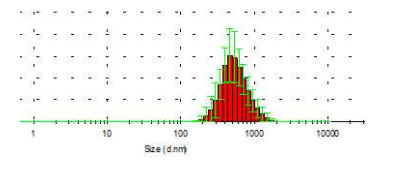
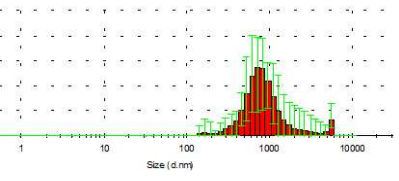
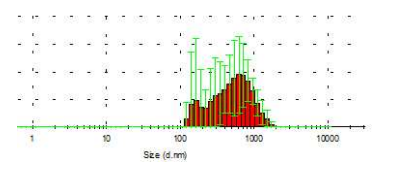
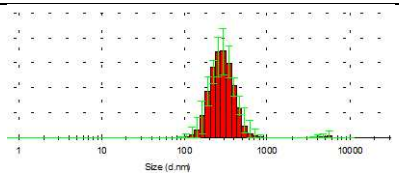
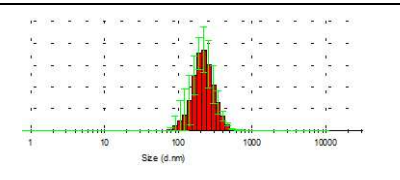
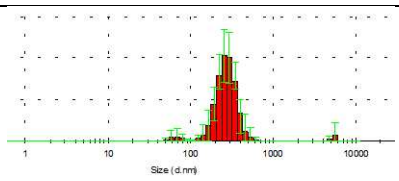
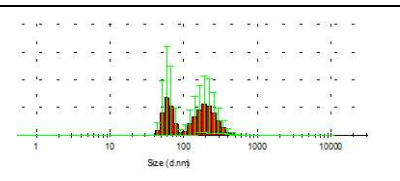
After formulation		
NP	Intensity distribution	Number distribution
PEA1@empty		
PEA2@empty		
PEA3@empty		
PEA4@empty		
PEA5@empty		
PEA6@empty		

Table SI 5 (continued). Unloaded PEA NPs (**PEA@empty**): Size distributions after formulation, and lyophilization with subsequent resuspension.

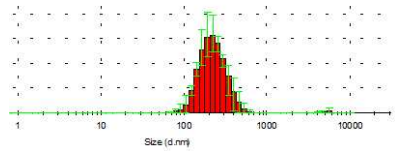
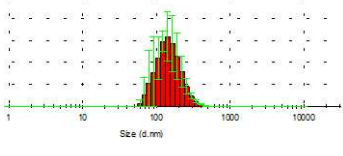
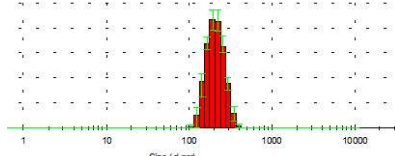
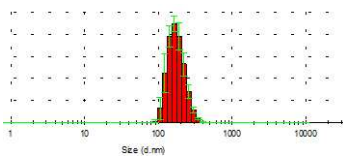
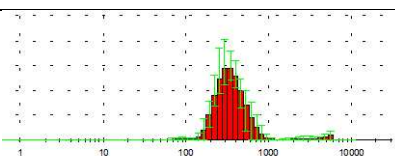
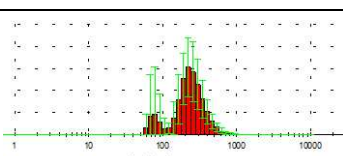
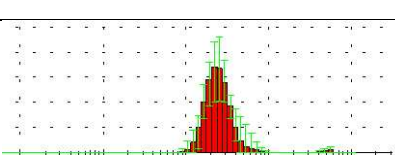
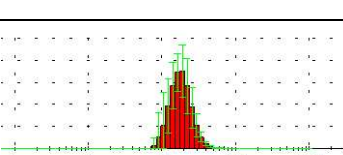
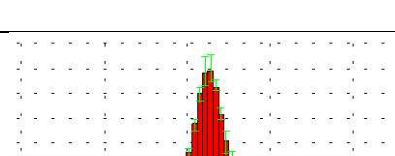
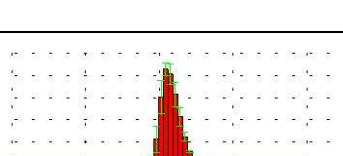
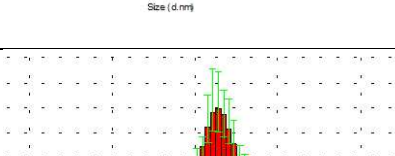
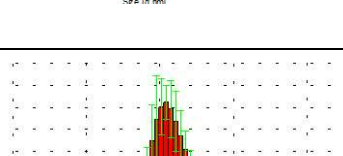
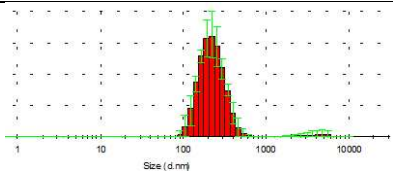
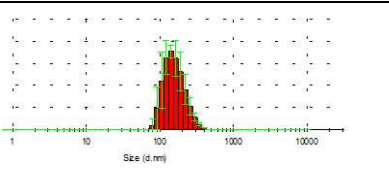
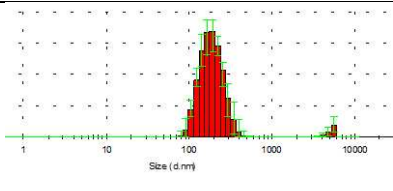
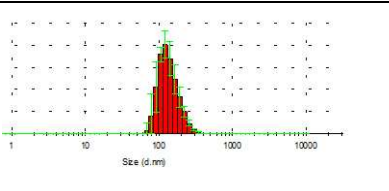
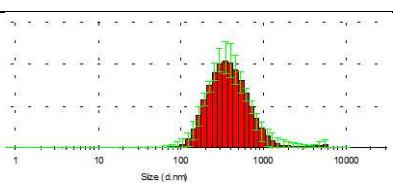
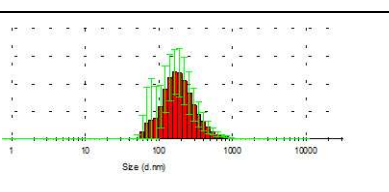
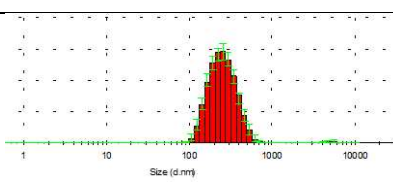
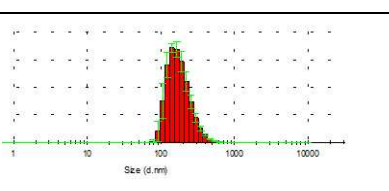
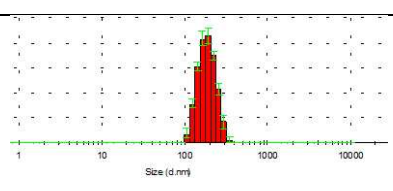
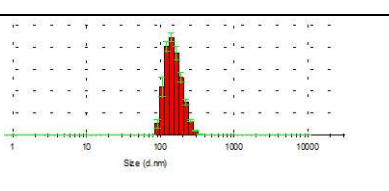
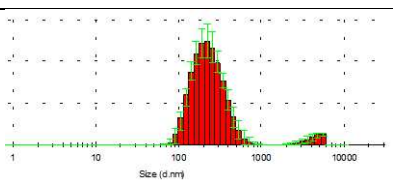
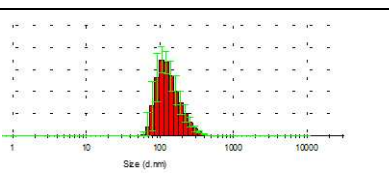
After centrifugation		
NP	Intensity distribution	Number distribution
PEA1@empty		
PEA2@empty		
PEA3@empty		
PEA4@empty		
PEA5@empty		
PEA6@empty		

Table SI 5 (continued). Unloaded PEA NPs (**PEA@empty**): Size distributions after formulation and lyophilization with subsequent resuspension.

After lyophilization and resuspension		
NP	Intensity distribution	Number distribution
PEA1@empty		
PEA2@empty		
PEA3@empty		
PEA4@empty		
PEA5@empty		
PEA6@empty		

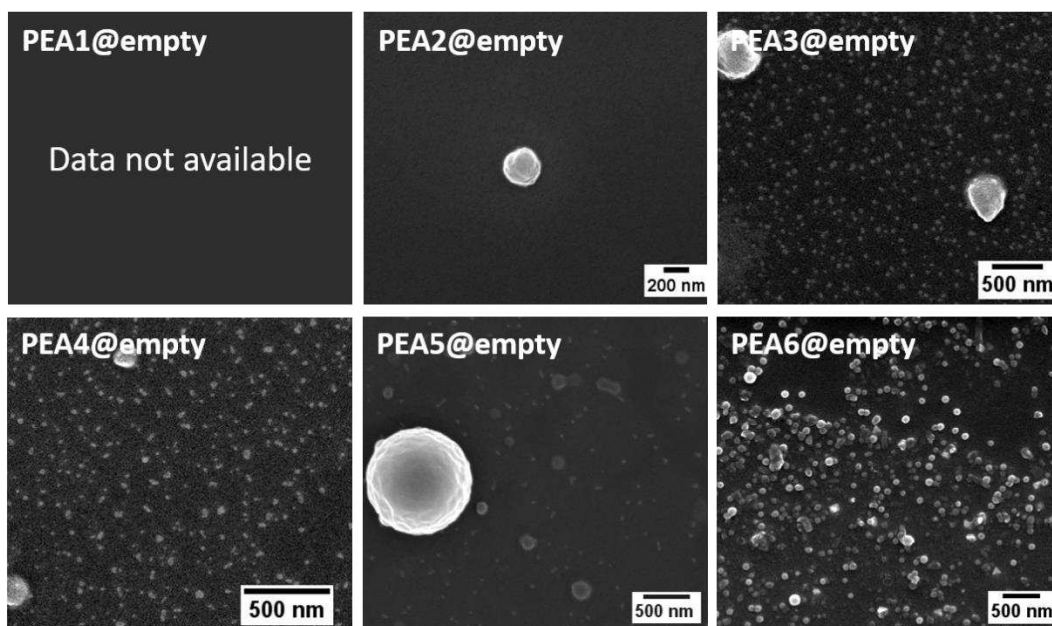


Figure SI 2. SEM images of unloaded PEA NPs (PEA@empty).

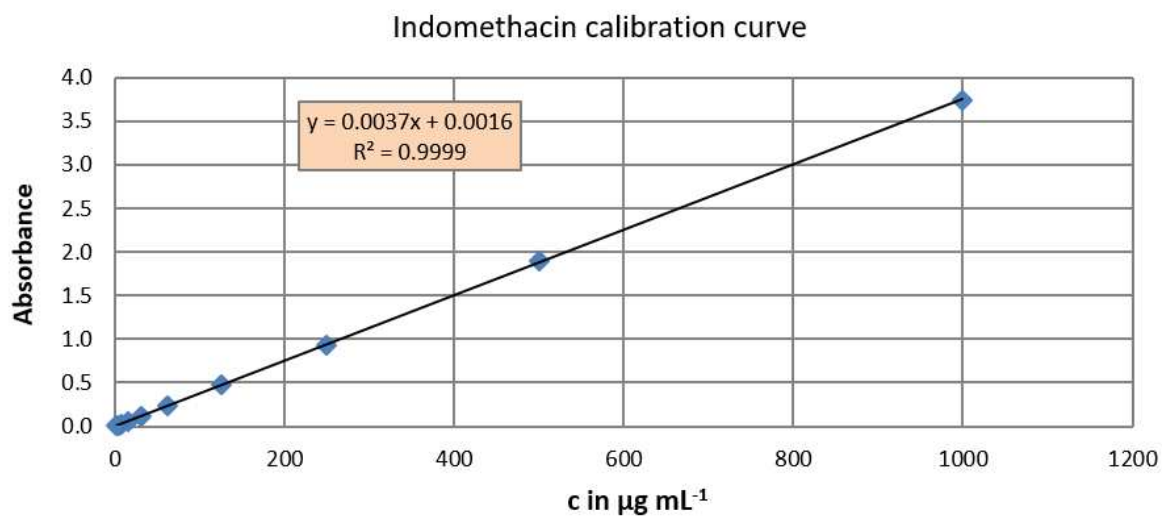


Figure SI 3. Calibration curve of indomethacin in *N,N*-dimethylacetamide (DMA). Absorbance measured at $\lambda = 318$ nm with 3×3 multiple reads per well and $2000 \mu\text{m}$ well border ($T = 25$ °C).

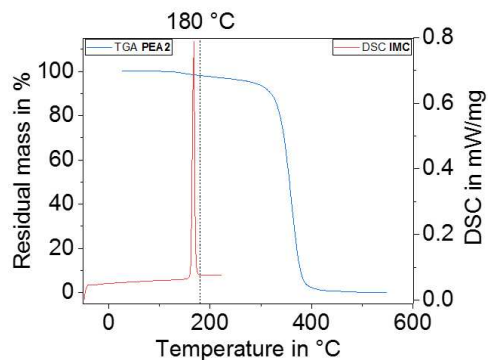


Figure SI 4. Overlay of differential scanning calorimetry thermogram of indomethacin (1st heating run, heating rate 20 K min⁻¹) and thermogravimetric analysis thermogram of **PEA2** (heating rate 20 K min⁻¹).

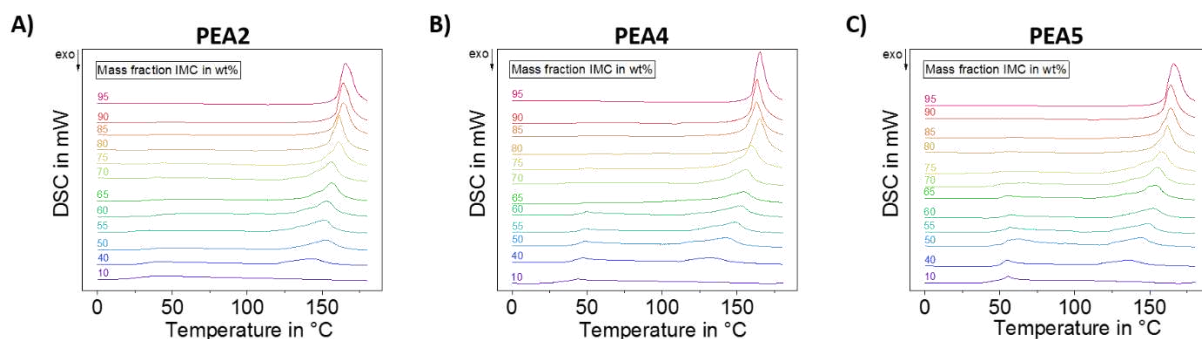


Figure SI 5. Differential scanning calorimetry thermograms of **PEA[IMC]** blends at different mass fractions after annealing at 111 °C (1st heating run, heating rate 20 K min⁻¹).

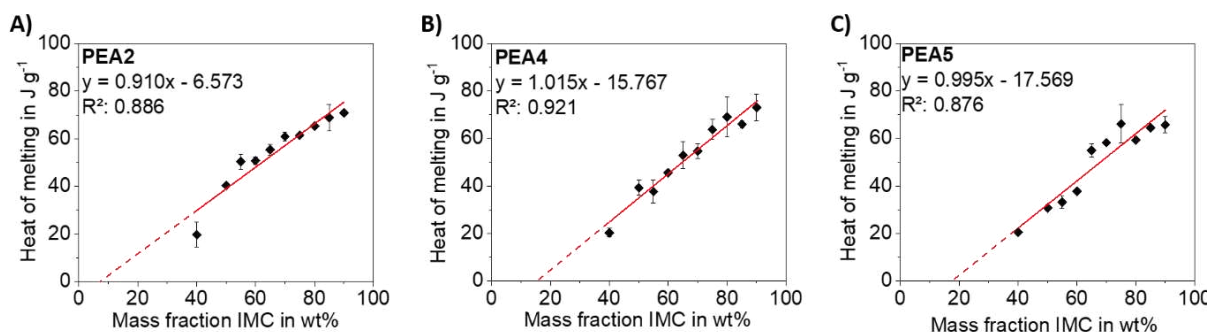


Figure SI 6. Melting enthalpies plotted against the IMC mass fraction for **PEA[IMC]** blends with linear extrapolation towards zero enthalpy / experimental saturation.

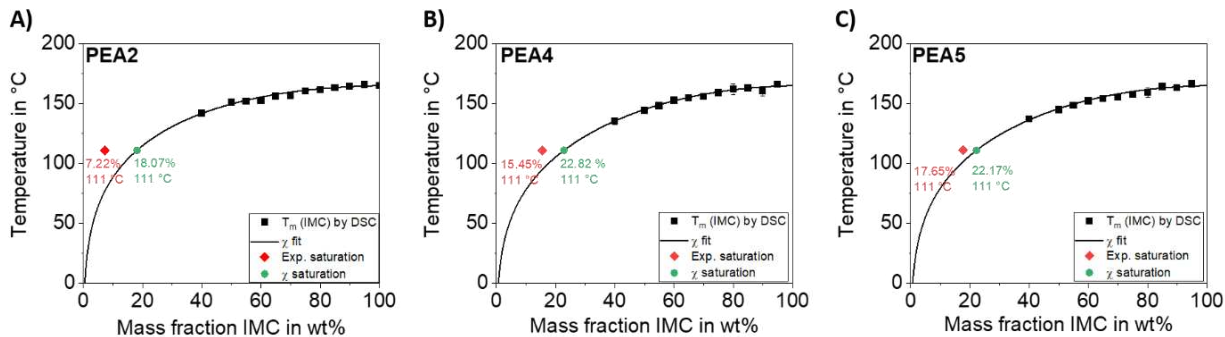


Figure SI 7. Melting point depression curves of PEA[IMC] blends: (square) measured melting temperatures by DSC, (solid line) predicted behavior of melting point depression for the experimentally determined χ interaction parameter, (red diamond) experimentally determined saturation from zero enthalpy extrapolation, (green circle) predicted saturation for χ interaction parameter.

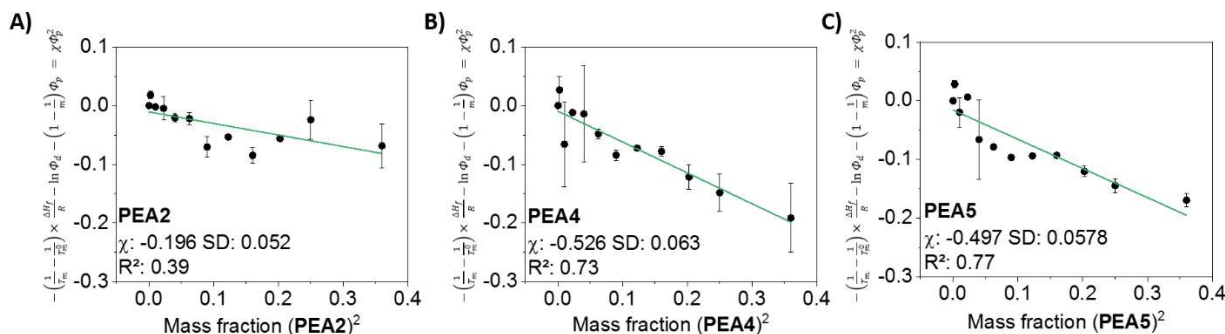


Figure SI 8. Plots used to calculate the Flory-Huggins interaction parameter χ applying Equation (7).

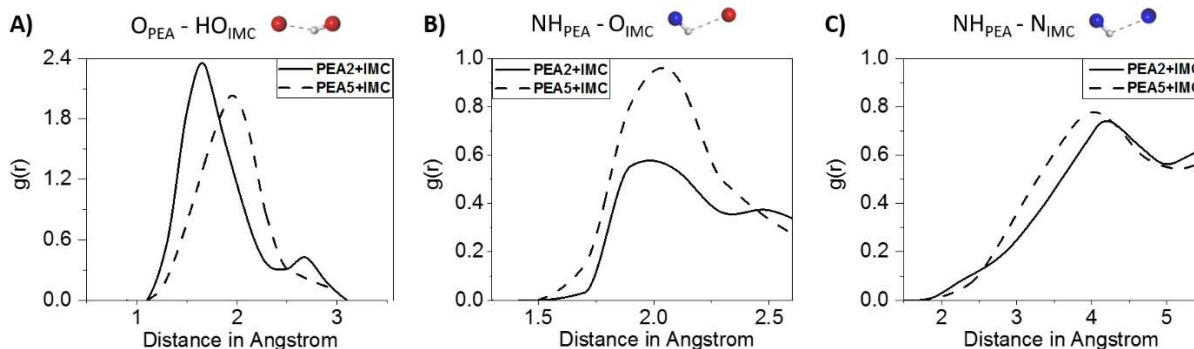


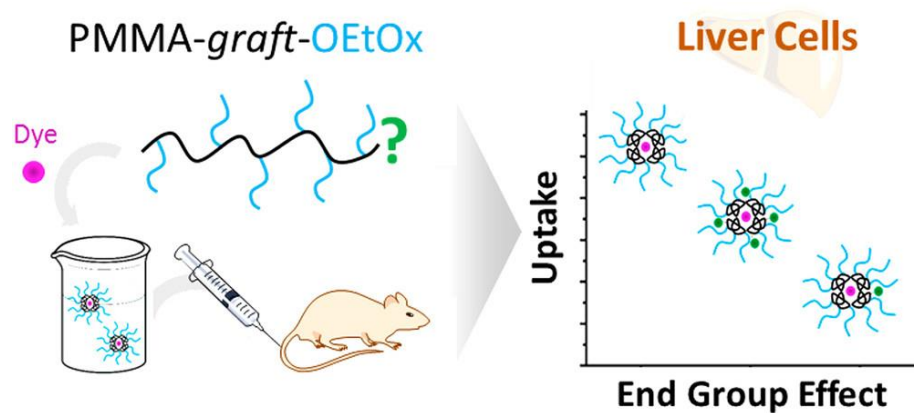
Figure SI 9. Intermolecular radial distribution function (RDF) plots of different hydrogen bonds between the indomethacin molecule and PEA2 or PEA5 polymer chains obtained from atomistic MD simulations.

Publication 6

Stealth effect of short polyoxazolines in graft copolymers: Minor changes of backbone end group determine liver cell-type specificity

I. Muljajew, S. Huschke, A. Ramoji, Z. Cseresnyés, S. Hoepfner, I. Nischang, W. Foo, J. Popp, M. T. Figge, C. Weber, M. Bauer, U. S. Schubert, A. T. Press

ACS Nano **2021**, *15*, 12298–12313.



Stealth Effect of Short Polyoxazolines in Graft Copolymers: Minor Changes of Backbone End Group Determine Liver Cell-Type Specificity

Irina Muljajew, Sophie Huschke, Anuradha Ramoji, Zoltán Cseresnyés, Stephanie Hoepfner, Ivo Nischang, Wanling Foo, Jürgen Popp, Marc Thilo Figge, Christine Weber, Michael Bauer, Ulrich S. Schubert,* and Adrian T. Press*



Cite This: *ACS Nano* 2021, 15, 12298–12313



Read Online

ACCESS |



Metrics & More



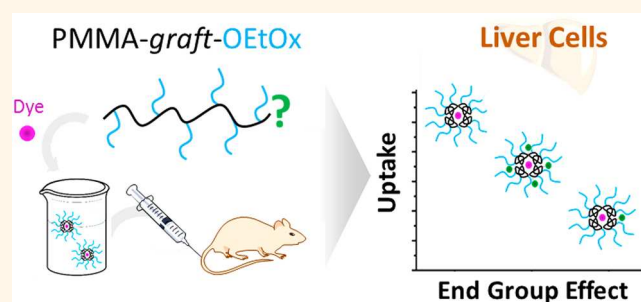
Article Recommendations



Supporting Information

ABSTRACT: Dye-loaded micelles of 10 nm diameter formed from amphiphilic graft copolymers composed of a hydrophobic poly(methyl methacrylate) backbone and hydrophilic poly(2-ethyl-2-oxazoline) side chains with a degree of polymerization of 15 were investigated concerning their cellular interaction and uptake *in vitro* as well as their interaction with local and circulating cells of the reticuloendothelial system in the liver by intravital microscopy. Despite the high molar mass of the individual macromolecules ($M_n \approx 20 \text{ kg mol}^{-1}$), backbone end group modification by attachment of a hydrophilic anionic fluorescent probe strongly affected the *in vivo* performance. To understand these effects, the end group was additionally modified by the attachment of four methacrylic acid repeating units. Although various micelles appeared similar in dynamic light scattering and cryo-transmission electron microscopy, changes in the micelles were evident from principal component analysis of the Raman spectra. Whereas an efficient stealth effect was found for micelles formed from polymers with anionically charged or thiol end groups, a hydrophobic end group altered the micelles' structure sufficiently to adapt cell-type specificity and stealth properties in the liver.

KEYWORDS: polyoxazoline, graft copolymer, micelle, drug delivery, liver, reticuloendothelial system, intravital microscopy



INTRODUCTION

Targeting drugs to a desired tissue or cell-type is a common goal of modern pharmaceutical approaches. Often, carriers are used which employ active, passive, or a combination of both targeting strategies to enrich their payload in the desired environment.¹ For the encapsulation and the controlled release of numerous small molecules, polymeric drug carrier systems represent attractive vehicles for tissue-specific drug delivery.² Nanocarriers such as micelles below 50 nm in diameter were reported to be preferable in the use of tumor treatment.³ Their small size leads to favorable tissue penetration properties, which allows them to reach even poorly perfused tissue, e.g., hypoxic tumor areas. Their small size further leads to rapid renal filtration and elimination. The resulting short circulation time decreases the risk for nonspecific uptake and detrimental side effects. Since polymer-based nanoparticles are foreign bodies for the host, the reticuloendothelial system (RES) recognizes, engulfs, and destroys them.⁴ In the worst case, the RES additionally triggers an inflammatory response which decreases the effectiveness of further nanoparticle-based drug

applications due to the generation of specific antibodies against these carriers.⁵

The coupling of stealth polymers to polymeric drug carriers can prevent their recognition by the RES and thereby decreases unspecific side effects and also the necessary amount of polymer-encapsulated drug to be administered.⁶ The current clinical standard for stealth polymers used in many drug formulations is poly(ethylene glycol) (PEG).^{7–9} It is successfully applied in various drug formulations to solubilize hydrophobic compounds for systemic administration or as stealth polymer for nanoparticles.¹⁰ Moreover, it is also commonly used in food and daily cosmetic products. The consequences of such often long-term exposures are subclinical

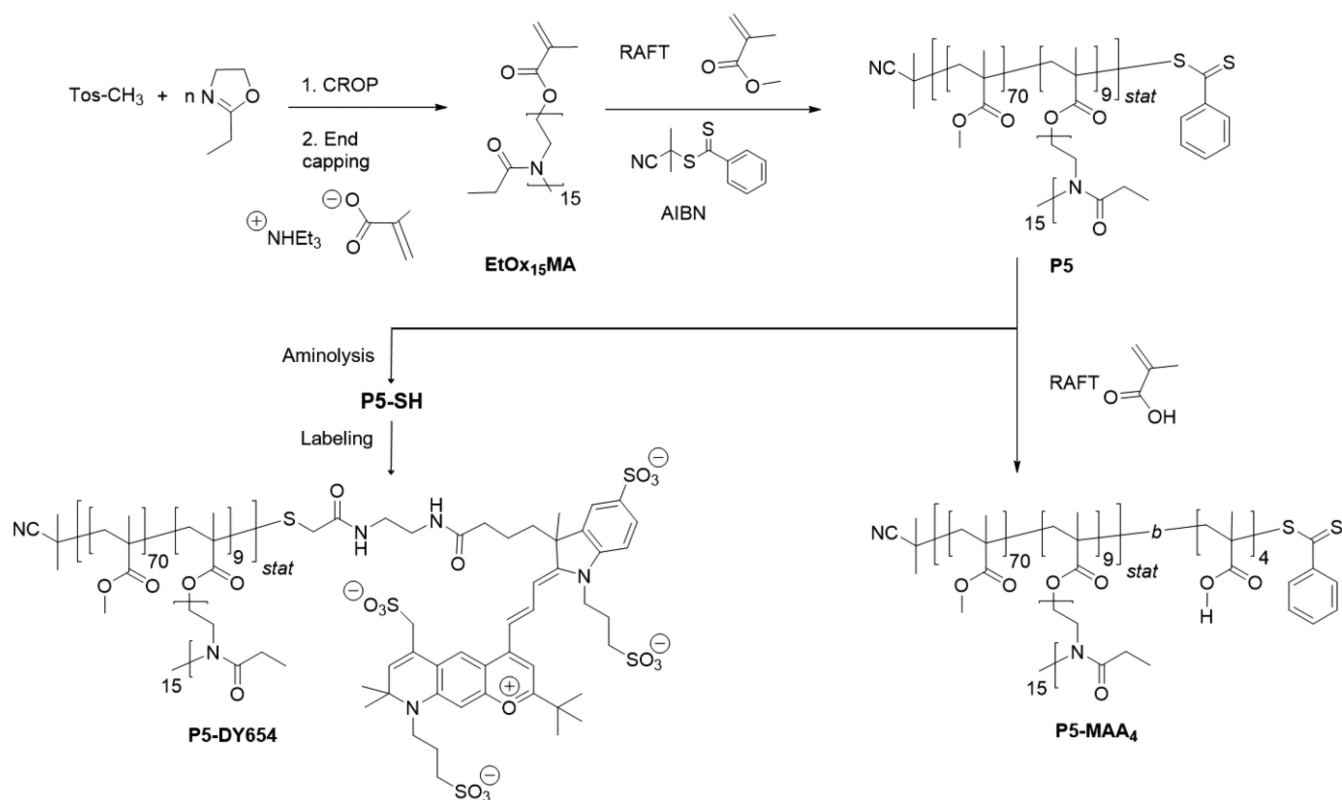
Received: May 18, 2021

Accepted: June 28, 2021

Published: July 16, 2021



Scheme 1. Schematic Representation of the Synthesis Route toward the PMMA-graft-OEtOx₁₅ Graft Copolymers P5, P5-SH, P5-DY654, and P5-MAA₄^a



^aCROP: Cationic ring-opening polymerization. RAFT: Reversible addition–fragmentation chain transfer polymerization. AIBN: 2,2'-Azobis(2-methylpropanitrile).

immune reactions, resulting in the production of anti-PEG antibodies in individuals. Studies on healthy individuals from 2016 confirmed detectable levels of anti-PEG antibodies in up to 72% of the tested individuals, which had not been in contact with PEG-containing clinical drugs.^{11–13} These antibodies can render PEG-mediated stealth effects of drug carriers ineffective by recognizing and binding PEG on the surface of these drug carriers, marking them for immune cells. The induction of the immune system further may trigger mild to severe side effects, resulting in intolerance reactions as severe as anaphylaxis.¹³ Therefore, alternative stealth polymers were introduced in the past few years.

A promising candidate to overcome bottlenecks of clinical translation is poly(2-ethyl-2-oxazoline) (PEtOx).¹⁴ Kierstead *et al.* investigated the induction of accelerated blood clearance with liposomes modified with various potential stealth polymers, including poly(2-methyl-2-oxazoline) (PMeOx).¹⁵ In this mentioned study, PEG and PMeOx were both rapidly cleared, whereas poly(*N*-vinyl-2-pyrrolidone), poly(*N,N*-dimethylacrylamide), poly{*N*-(2-hydroxypropyl)methacrylamide}, and poly(*N*-acryloylmorpholine) modifications did not cause accelerated blood clearance in rats. However, in the same species, Woodle *et al.* investigated PMeOx- and PEtOx-based lipid conjugates and found a long circulation time.¹⁶ In line with these findings, Moreadith *et al.* did not observe antibody formation against PEtOx in rabbits, suggesting stealth properties of PEtOx.¹⁷ In fact, PEtOx–drug conjugates directed against Parkinson's disease and restless leg syndrome have reached Phase 2 clinical trials.¹⁸ In addition to the covalent attachment of PEtOx to active pharmaceutical

ingredients, hydrophilic poly(2-oxazoline)s (POx), such as PEtOx, form part of various drug delivery vehicles such as micelles, polyplexes, or nanoparticles in academic research.^{19,20} In particular for micellar drug carriers, PEtOx is mostly introduced as part of linear block copolymers in combination with hydrophobic blocks. Although the variation of the amphiphilic di- or triblock copolymer architecture may lead to differently assembled structures depending on the length of the hydrophilic block,²¹ the use of branched structures may contribute to overcoming dissociation issues.²² Exploiting other polymer architectures, such as amphiphilic graft copolymers, can hence be attractive for the design of drug delivery systems. For instance, graft copolymers composed of polyesters and PEG reduced the protein adsorption compared to their linear block copolymer analogues, thereby demonstrating improved stealth properties.^{23,24}

Graft copolymers with hydrophobic polytyrosine²⁵ or polycaprolactone²⁶ backbones and hydrophilic POx side chains and heterografted comb polymers comprising PLA and PEtOx side chains²⁷ are capable of self-assembly and of encapsulating hydrophobic dyes. For instance, the micellization of poly(2-nitrobenzyl acrylate) as a hydrophobic building block and PEtOx was more straightforward in a graft copolymer architecture than that of the linear block copolymer.^{28,29} Also, more complex systems comprising coumarin moieties revealed micellization and enabled the encapsulation of a hydrophobic photosensitizer.^{30,31} However, to the best of our knowledge, the *in vivo* performance of POx-based graft copolymer micelles has not been reported so far.

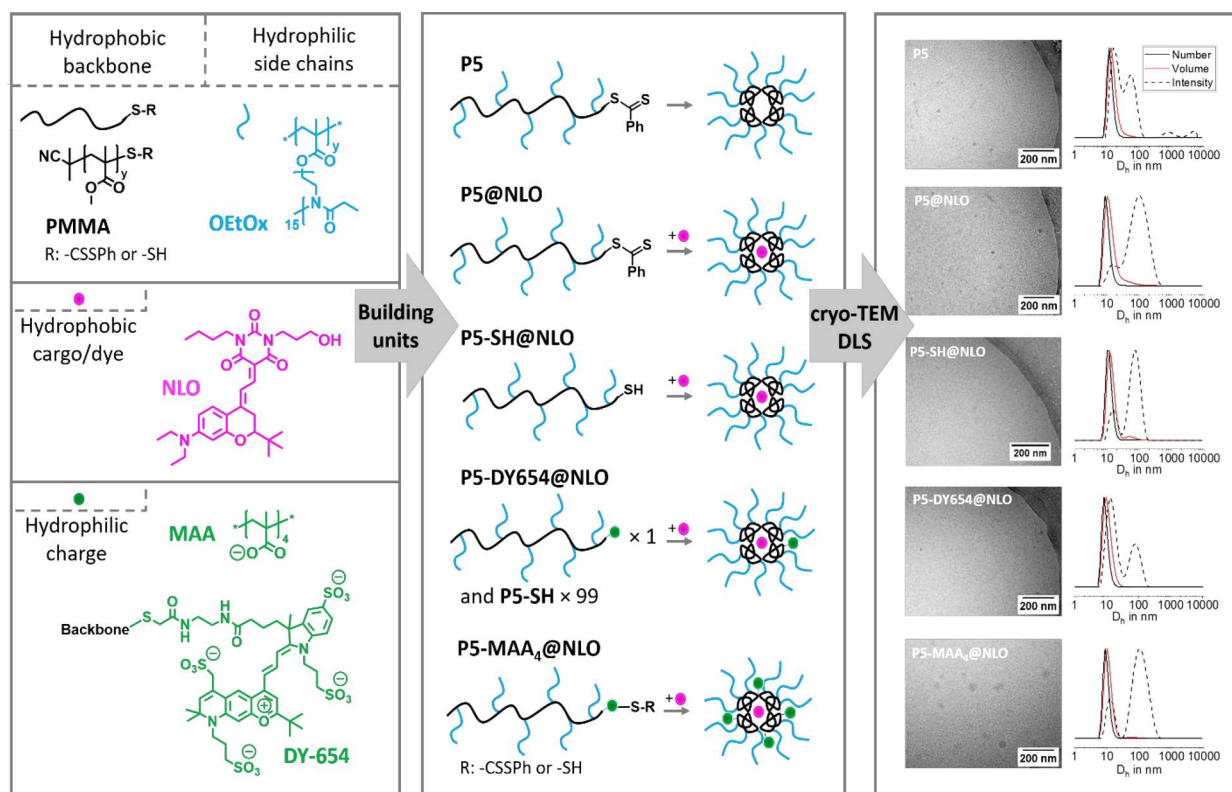


Figure 1. Left: Schematic representation of the building units used to form micelles with different moieties situated between core and shell. PMMA: Poly(methyl methacrylate). OEtOx₁₅: Oligo(2-ethyl-2-oxazoline). NLO: Neutral lipid orange. MAA: Methacrylic acid. Middle: Simplified schematic overview of the polymer structures and the proposed micelles formed in aqueous solutions. Right: Aqueous cryo-TEM of micelles of P5 and dye-loaded micelles (concentration of polymer $c = 10 \text{ mg mL}^{-1}$ in aqueous solution). Dynamic light scattering (DLS) plots of micelles of P5 and dye-loaded micelles with the number (solid black line), volume (red line), and intensity (dashed line) distributions (concentration of polymer $c = 1 \text{ mg mL}^{-1}$ in aqueous solution).

Graft copolymers enable a more flexible design than linear block copolymers. In addition to obvious parameters such as the grafting degree and side chain length, additional functional moieties can be introduced³² at the backbone end groups. Such changes might alter the micellar structures formed and, hence, also influence the stealth effect. Such end group effects are well-known and exploited for micellar carriers composed of end group modified block copolymers. For instance, reduced protein adsorption can be achieved by neutral and slightly negatively charged nanocarriers, while the latter further exhibit lower rates of nonspecific organ uptake.^{33,34} However, they have not yet been investigated for graft copolymers, to the best of our knowledge.

Based on these considerations, we synthesized amphiphilic graft copolymers based on poly(methyl methacrylate)-graft-oligo(2-ethyl-2-oxazoline) (PMMA-graft-OEtOx) and slightly varied their backbone end group to understand their influence on the *in vivo* fate of the loaded nanocarriers. The hydrophilic oligo(2-ethyl-2-oxazoline) (OEtOx)-based macromonomer was copolymerized with the hydrophobic comonomer methyl methacrylate (MMA), thereby ensuring the formation of a comparable hydrophilic OEtOx layer. Subsequently, anionic moieties were introduced at the ω -chain end of the hydrophobic backbone to challenge standard labeling protocols critically. As expected from the known micellization of their PMMA-graft-PEG analogues,³⁵ the polymers self-assembled into core-shell micelles and enabled encapsulation of a hydrophobic dye, which served as a label for the

investigation of the uptake and distribution in murine liver cells utilizing intravital fluorescence microscopy.

RESULTS AND DISCUSSION

Oligo(EtOx) was synthesized by cationic ring-opening polymerization (CROP) and end functionalization of the living chain end with triethylammonium methacrylate to result in the macromonomer EtOx₁₅MA. Subsequently, the macromonomer method was applied through reversible addition-fragmentation chain transfer (RAFT) copolymerization of MMA and EtOx₁₅MA, yielding PMMA-graft-OEtOx₁₅ graft copolymers comprising a hydrophobic PMMA backbone and hydrophilic OEtOx side chains (Scheme 1). Previously, we identified a graft copolymer composed of 90 mol % of MMA and 10 mol % of EtOx₁₅MA (P5) as an optimum for micellar encapsulation of the hydrophobic dye Disperse Orange 3.³⁷ This statistical copolymer was hence selected as a potential micellar drug carrier to investigate their cell-type specificity in the liver.

P5 was modified by two methods that introduced a small amount of negative charges by modifying their backbone end group. In the first approach, similar to common practice for introducing fluorescent probes, the remaining dithioester end group, resulting from the chain transfer agent (CTA) used during RAFT polymerization was removed quantitatively by aminolysis with hexylamine (Figure S11). The resulting thiol P5-SH was further coupled to the hydrophilic dye DY654 via nucleophilic substitution using an iodoacetamide derivative. The successful attachment of the dye P5-DY654 was validated

Table 1. Key Properties of the PMMA-graft-OEtOx₁₅-Based Polymers and Micelles

polymer	M_n in g mol ^{-1a}	D^a	D_h empty micelle ^c (nm)	D_h NLO loaded micelle ^c (nm)	zeta-potential (mV) ^d
P5 ^b	22,900	1.10	number av.: 12 volume av.: 18 intensity av.: 26	number av.: 11 volume av.: 16 intensity av.: 61	-27
P5-MAA ₄	22,100	1.15	number av.: 7 volume av.: 9 intensity av.: 20	number av.: 9 volume av.: 12 intensity av.: 50	-33
P5-DY654	22,700	1.11	number av.: 9 volume av.: 11 intensity av.: 13	number av.: 11 volume av.: 12 intensity av.: 21	nd ^f
P5-SH	22,700	1.11	number av.: 11 volume av.: 13 intensity av.: 20	number av.: 11 volume av.: 15 intensity av.: 44	-20
P5 + P5-MAA ₄ ^e			number av.: 12 volume av.: 16 intensity av.: 25	number av.: 10 volume av.: 12 intensity av.: 24	-20

^aDetermined by SEC (DMAc, 0.21 wt % LiCl, RI detection, PMMA calibration). ^bAbsolute molar mass determined by analytical ultracentrifugation for P5 in acetone, *i.e.*, single macromolecule $M_n = 24,700$ g mol⁻¹, micellar form in water $M_n = 231,800$ g mol⁻¹, resulting in an aggregation number $N_{agg} = 9.4$.³⁴ ^cDetermined by dynamic light scattering. Concentration of polymer $c \approx 1$ mg mL⁻¹ in aqueous solution at 25 °C, filtered samples with 0.45 μm NY. Loaded micelles contained on average 10 NLO molecules per micelle. ^dConcentration of polymer $c = 5$ mg mL⁻¹ in 0.1 mmol L⁻¹ NaCl aqueous solution at 25 °C, filtered samples with 0.45 μm NY. ^eP5 + P5-MAA₄ represents mixed micelles composed of 1% P5-MAA₄ and 99% of P5. ^fNot detectable.

by size exclusion chromatography (SEC) measurements utilizing refractive index and diode array detection (Figure S12), both revealing a polymer signal at the same elution volume. Also, the absorption and emission spectrum of the dye remained unaffected by the coupling approach, which yielded 99% of polymer chains with thiol end group (*i.e.*, P5-SH) and 1% of polymer chains with one dye attached at the backbone end. Attachment of multiple dyes per macromolecule was circumvented by utilizing the end functionalization strategy.

To introduce additional anionic moieties at the same position that would mimic the sulfonate moieties of DY654, the second modification approach relied on the application of P5 as a macro-CTA in a RAFT polymerization of methacrylic acid (MAA). For this purpose, a short block comprising only four repeating units of MAA was introduced at the end of the graft copolymer backbone, yielding P5-MAA₄. Consistent with the polymerization mechanism, all polymer chains were modified, while the dithioester end group remained partially present. As targeted, the degree of polymerization (DP) value of the short PMAA block was 4 according to M/CTA \times conversion, which was further confirmed by means of acid–base titration of the purified P5-MAA₄ (Figure S13).

All four P5-based polymers spontaneously self-assembled into spherical micelles upon dissolution in water, as determined by means of cryo-transmission electron microscopy (cryo-TEM) and dynamic light scattering (DLS) (Figure 1 and Figures S14 and S15). The average P5 micelles in aqueous solution were formed by 9.4 single polymer chains, as demonstrated previously by analytical ultracentrifugation.³⁶ The high structural similarity between the polymers suggests similar aggregation numbers for P5-SH, P5-DY654, and P5-MAA₄. In accordance with the negative charges introduced at the end of the graft copolymer backbone in P5-MAA₄, the zeta-potential slightly decreased compared to that of the P5 and P5-SH micelles without anionically charged end groups, although the difference should not be overrated (Table 1). The micelle structure consisting of a hydrophobic PMMA core and a hydrophilic OEtOx₁₅ shell allowed the solubilization of the

hydrophobic cargo neutral lipid orange (NLO) *via* the thin film method, *i.e.*, the redissolution of a dried polymer–cargo blend in type-1 water followed by purification *via* centrifugation (Figure S16).²⁰ Most micelles were able to solubilize at least two NLO molecules per macromolecule (Figures S17 and S18). To enable a more straightforward characterization by means of Raman spectroscopy, the NLO content was adjusted to one molecule NLO per polymer chain, *i.e.*, 10 NLO molecules per micelle.

DLS studies suggested the presence of a few larger aggregated structures, which were only observable in the intensity size distribution (Table 1, Figure 1, and Figure S15). The more representative number distribution indicated hydrodynamic diameters around 10 nm for loaded as well as unloaded micelles. It should, however, be noted that the DLS laser wavelength ($\lambda = 633$ nm) limited the characterization of P5-DY654 micelles due to the absorption range of the DY654.

Cryo-TEM confirmed the presence of spherical micelles with diameters mostly around 10 nm in all samples, regardless if loaded or unloaded (Figure 1 and Figure S15). The small size is consistent with the micelle composition of only 10 graft copolymer macromolecules and the low DP of the hydrophilic building blocks. Apparently, the small hydrophilicity change of the varied graft copolymer backbone end groups did not affect the micellization in a significant manner.

Raman spectroscopy was performed on the micelles to investigate the effect of these modifications on the structures of otherwise similar micelles.³⁷ The Raman spectrum of a given molecule captures vibrational frequencies specific to the molecular bonds and the molecule's symmetry. Here, Raman spectroscopy was applied due to its sensitivity to conformational changes. The molecular arrangement of the polymer leading to conformational changes exhibits vibrational signatures in the Raman spectrum. Thus, conformational changes in the micelles will alter the resulting molecular fingerprint, and the Raman peak positions allow one to pinpoint the contributing molecular vibrations. For the analysis, the micelle solutions were preconcentrated by

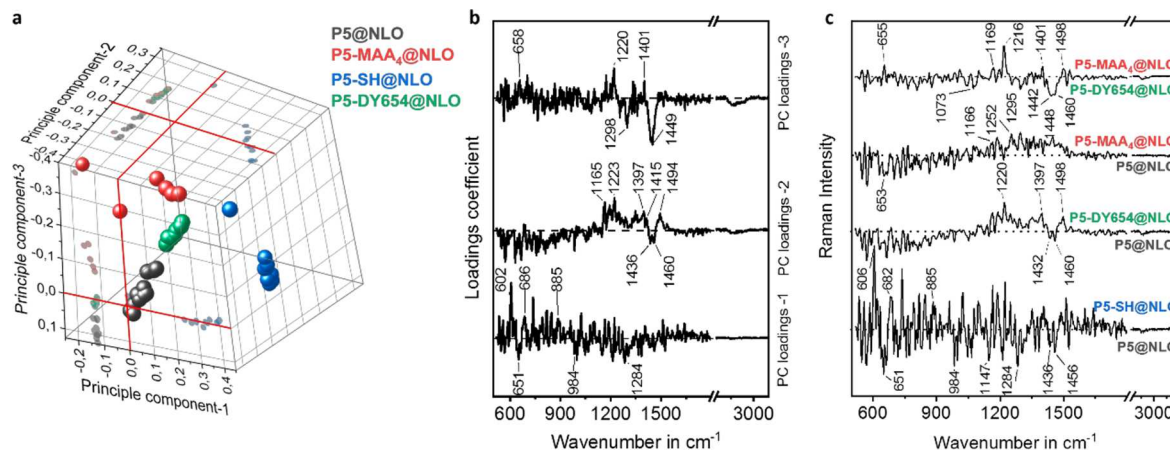


Figure 2. Hydrophilicity induces changes in the micellar confirmation. Raman spectra from micelles were obtained in liquid-state. (a) Principal component analysis of the Raman spectra of P5@NLO and the more hydrophilic micelles P5-DY654@NLO, P5-MAA₄@NLO, and P5-SH@NLO. The spectral differences in the micelles can be visualized in the 3D-PC score plot obtained using PC-1, PC-2, and PC-3. 2D PC score plots are provided in Figure S19. (b) Loading coefficients PC-1, PC-2, and PC-3 and (c) difference Raman spectra display the relative Raman spectral changes between the micelles.

evaporation due to exposure to the laser while recording Raman spectra. After the measurements, the micelle solutions were visually inspected under the microscope and exhibited no change in their physical state.

Furthermore, to understand the spectral differences observed in the Raman spectra of the micelles and trace vibrations to their molecular origin, Raman spectra of the pure substances, *i.e.*, the dyes NLO and DY654, P5, PMAA, PMMA, and PEOx were also recorded (Figure S19). The Raman fingerprints of micelles loaded with NLO (P5@NLO, P5-DY654@NLO, P5-MAA₄@NLO, and P5-SH@NLO) in solution were compared with the reference substances, revealing that the micelles' Raman spectra are dominated by strong NLO signals accompanied by a high spectral noise due to strong fluorescence background from the NLO. To investigate the fine differences present in the Raman spectra of the micelles, principal component analysis (PCA) was performed. PCA is an unsupervised analysis method, which does not require manual classifications. PCA utilizes the Raman spectral features such as Raman band position, intensity, band shape, or noise to cluster Raman spectra according to similarity. Furthermore, the PCA loadings provide information about the contributing Raman peaks, allowing one to visualize the separation of respective groups in the PCA score plot (Figure 2a and Figure S110). These spectral differences can be visualized from the PC loading coefficients shown in Figure 2b. The performed PCA led to a clear differentiation of P5-MAA₄@NLO from P5@NLO and P5-DY654@NLO by the principal component PC-3. The Raman peaks at 658, 1220, and 1401 cm^{-1} belong to P5-MAA₄@NLO with positive PC-3 scores. The Raman peaks at 1298 and 1449 cm^{-1} belong to P5-DY654@NLO and P5@NLO with negative PC-3 scores. PC-2 distinguished P5@NLO (1436 and 1460 cm^{-1}) from the other micelles, whereas PC-1 separated P5-SH@NLO. The negative Raman peak visible in the PC-1 at 651 cm^{-1} belongs to NLO in all micelles except P5-SH@NLO. The positive peaks at 602 and 686 cm^{-1} correspond to P5-SH@NLO.

The changes in the micelles captured by the loadings were also observed in the difference Raman spectra displayed in Figure 2c. As can be seen from the 3D score plot, all four

micelles formed distinct clusters and were well-separated from each other. Hence, Raman spectroscopy provided experimental evidence of different molecular arrangements within the micelles due to the different end groups, altering the environment of the NLO dye within the carriers.

Before the fate of the micellar assemblies were tested in *in vitro* and *in vivo* experiments, their integrity was in focus, as dilution and the presence of biological media might affect their structure. The blood volume of mice is generally calculated with 58.5 mL of blood/kg body weight. Considering the amounts injected *in vivo* in this study (150 μg per animal), an initial blood concentration of 103 $\mu\text{g mL}^{-1}$ is expected in a 25 g mouse (average body weight of mice used in the study). Analytical ultracentrifugation measurements of diluted samples were hence performed at such concentrations and even below (40 $\mu\text{g mL}^{-1}$). Results confirmed the integrity of the loaded micelles in water with assemblies containing cargo even at the lowest concentration investigated and with hydrodynamic sizes consistent to DLS and cryo-TEM (see Supporting Information for details, Figure S111). In addition, DLS indicated the stability of the loaded micelles in physiologically relevant buffers (KHB and PBS) at 37 °C (see Supporting Information, Figure S112). In fact, loaded micelles were directly formed in these buffers *via* the thin film method. These findings are supported by free-flow electrophoresis (FFE) performed in the presence of albumin, the most abundant plasma protein, indicating the stability of the micelles and successful shielding of the NLO cargo from interaction with albumin (see Supporting Information, Figure S113).

Primary mouse embryonic fibroblasts (MEFs) are a valuable source for primary cells to study the uptake route of the various micelles in model cells. MEFs do not exhibit classical tumor mutations that are known to impact endocytosis and pinocytosis rates.³⁸ Their embryonic origin results in delayed senescence and stable metabolic activity while also exhibiting fully functional endocytic and pinocytotic pathways over multiple passages.³⁹ In *in vitro* studies, none of the micelles showed toxicity after 24 h in MEFs (Figure S114). A rapid cellular uptake (after 10 min) and similar intracellular distribution of the cargo NLO (in DMSO) and the NLO-loaded micelles were observed *in vitro*. Incubating cells with

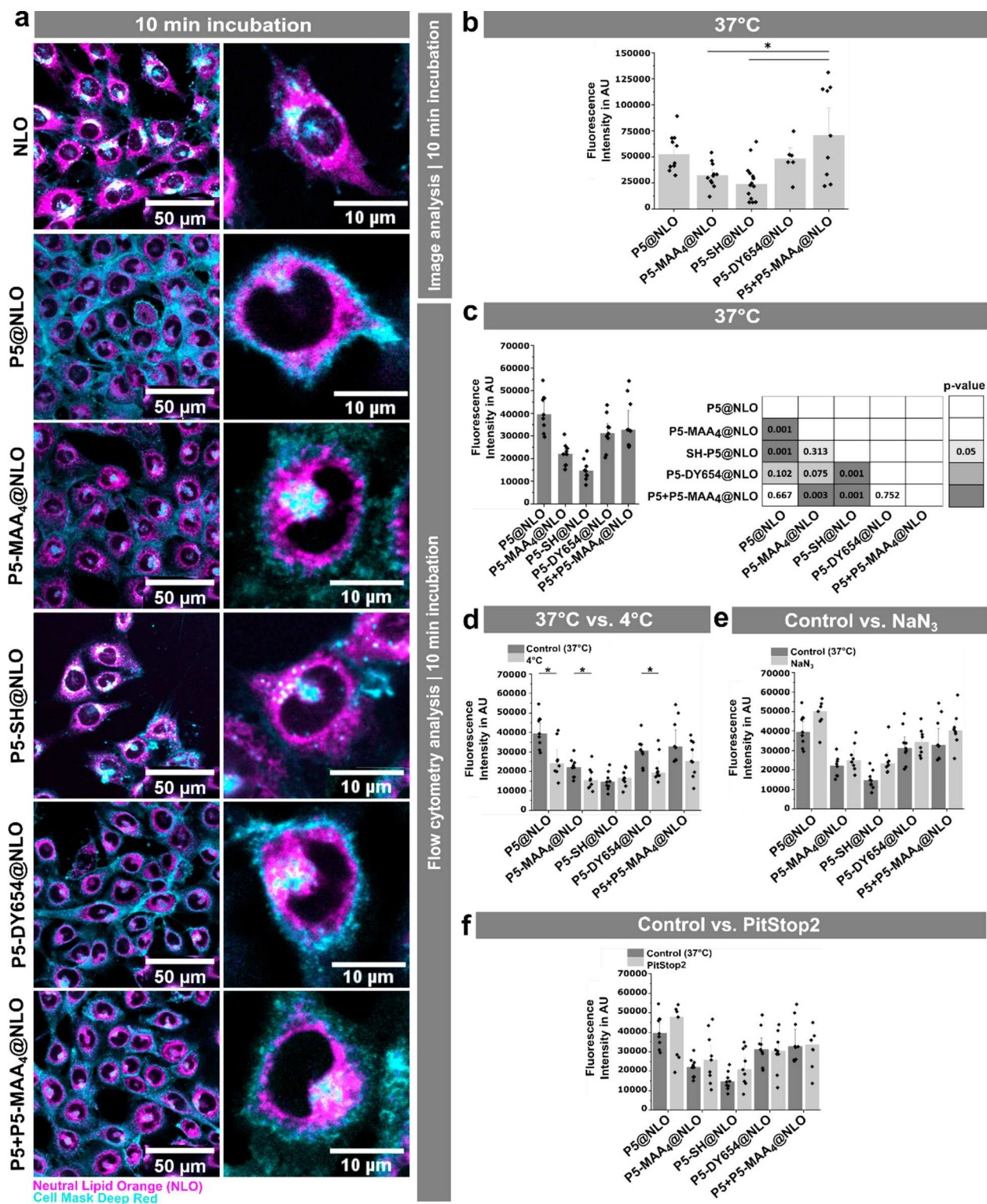


Figure 3. Influence of end group modifications of graft copolymer micelles on endocytosis-independent uptake *in vitro*. (a) Live cell imaging of cell masks deep red (cyan)-stained MEFs, incubated 10 min with 20 nmol L⁻¹ NLO (magenta) or 50 μg mL⁻¹ NLO-loaded micelle. (b) Quantification of fluorescence intensities from fluorescent images. One-way ANOVA between groups, **p* < 0.05. (c) Flow cytometry analysis of MEFs, incubated 10 min with 50 μg mL⁻¹ NLO-loaded micelles. Heatmap of *p* values from a parametric one-way ANOVA between groups with a Tukey posthoc test for pairwise differences, *n* = 3. (d–f) Uptake of various micelles in the presence of different inhibitors determined by flow cytometry, unpaired *t* test control vs treatment, **p* < 0.05. (d) Uptake of various micelles at 4 or 37 °C. (e) Uptake of various micelles in the presence of 10 mmol L⁻¹ NaN₃. (f) Uptake of various micelles in the presence of 30 μmol L⁻¹ Pitstop-2. By unpaired *t* test control vs treatment, **p* < 0.05, no statistical difference between control and treatment for (e) and (f) was found. (b–f) Intensities were corrected for intrinsic intensity and NLO loading differences. Data are shown as median + standard deviation, and individual values are depicted as dots.

Table 2. Qualitative Assessment of the *In Vivo* Uptake in Different Cell Types^a

micelle	anionic charge	DTB (hydrophobic)	Kupffer cells	hepatocytes	LSEC	calculated $t_{1/2}$
P5-SH@NLO	none	none	+	+	nd ^b	++++
P5-DY654@NLO	+	none	++	++++	nd ^b	+++
P5-MAA ₄ @NLO	++++	+	+++	++	+	+++++
P5@NLO	none	+++	++++	+++	nd ^b	+
P5 + P5-MAA ₄ @NLO	+	+++	+++++	+++++	++	++

^aData were sorted according to uptake in Kupffer cells. The signal intensity for the observation was compared for the micelles (from + (lowest) to +++++ (highest) signal) ^bNot detected.

NLO led to staining of perinuclear, elongated organelles, *e.g.*, mitochondria or endoplasmic reticulum. NLO-loaded micelles preferentially accumulated in similarly shaped perinuclear compartments (Figure 3a). NLO fluorescence intensity in cells was highest when incubated with the micelles composed of graft copolymers featuring hydrophobic dithiobenzoate end groups, P5@NLO. The negative charges introduced at the interface of the micellar core and shell achieved by the terminal modification of P5 with four units of methacrylic acid or DY654 (which possess four sulfonic residues) gradually decreased the uptake efficiency, indicating an improved shielding of these micelles (Figure 3b). Since chain extension of P5 with MAA was quantitative but labeling with DY654 was only 1% while remaining polymer chains were left with a terminal -SH group, the question occurred whether the differences can be attributed to charge or hydrophilicity. To mimic the P5-DY654 micelle, P5, comprising a hydrophobic end group, was combined with the MAA-modified P5-MAA₄ to yield a mixture where 1% of the molecules carried the terminal charge. The resulting NLO-loaded micelle (P5 + P5-MAA₄@NLO) accumulated in MEFs as efficiently as P5@NLO, highlighting the importance of the presence or absence of the dithiobenzoate end group for the performance of these micelles. As 99% of P5-DY654 comprised graft copolymers with a terminal thiol moiety, micelles exclusively formed from P5-SH were compared. P5-SH@NLO revealed the lowest cellular uptake under serum-free incubation conditions in this study using microscopy and flow cytometry analysis (Figure 3b,c). That hints toward a more pronounced effect of the hydrophobicity of the end group (P5 vs P5-SH) compared to that of negative charges (P5 vs P5-MAA₄).

Performing the experiments at 4 °C decreased the uptake of P5@NLO, P5-MAA₄@NLO, and P5-DY654@NLO in MEFs significantly in comparison to the control experiments performed at 37 °C (Figure 3d). Protein absorption can be a confounder of uptake processes and impact the uptake route. The uptake rates at 37 and 4 °C were similar when those experiments were performed in the presence of 10% fetal bovine serum to the medium for the micelles investigated here (Figure S114c), thereby indicating the independence of the uptake from the interaction with serum proteins *in vitro*. Further experiments were carried out to exclude the endocytic uptake of those micelles under serum-free conditions. Before the incubation with micelles, we treated cells with the ATPase inhibitor sodium azide, which inhibits various active uptake mechanisms in cells but did not affect the uptake of the micelles (Figure 3e). Pitstop-2, a known inhibitor for preferentially clathrin-mediated endocytosis,^{40,41} did not reduce micellar uptake (Figure 3f). We further validated these findings using MEFs expressing a marker for clathrin-mediated endocytosis, early endosome antigen (EEA) 1, fused to the green fluorescent protein (GFP). Analyzing EEA1-GFP-

positive vesicles in the perinuclear and peripheral regions of the cells, we did not find any specific NLO accumulation in these vesicles (Figure S116). These results indicate that the uptake of micelles is independent of the cellular energy level and does not require clathrin-mediated endocytosis. The filamentous perinuclear staining pattern was visible as early as 10 min after adding the micelles. Together with the temperature sensitivity of the uptake, our data suggest a direct translocation through the cell membrane, *e.g.*, by penetration, without a rate limitation by active, energy-dependent endocytosis.⁴²

The effects seen in the cell culture translate to the *in vivo* situation. Intravital microscopy (IVM) of the liver was applied to study pharmacokinetics. The liver is a significant clearance organ and allows the assessment of the nanocarrier interaction with parenchymal cells (hepatocytes) and a majority of cell types commonly summarized as the reticuloendothelial system. Cells of the RES are specialized to recognize different foreign bodies and thus also nanocarriers.⁴³ In the liver, circulating immune cells (lymphocytes),^{37,44,45} Kupffer cells (livers' local macrophages),^{46–50} liver sinusoidal endothelial cells (LSECs, livers' specialized endothelial cells),^{46–50} and hepatocytes come together, forming a powerful barrier able to clear a large variety of nanocarriers.^{37,44,45,51} After cells of the RES engulf nanocarriers, they signal to their environment, which in many cases triggers an immune response, potentially causing hypersensitivity or, in rare cases, even anaphylactic reactions.^{13,52} Their distinct morphology and tissue distribution allow their (automated) identification without additional staining once they take up the fluorescent cargo and appear in the images. Circulating immune cells are recognized by IVM due to their specific location in the sinusoids and their mobility, *i.e.*, their movement in time-lapse microscopy. Lymphocytes become only visible in fluorescence IVM through staining by the used payload NLO. No NLO-positive circulating cells were observed in the capillaries (Video S6). These results suggest that the uptake by circulating immune cells has little impact on the clearance of the investigated micelles. The clearance of the different micelles by hepatocytes, LSECs, and Kupffer cells varied (Table 2). Their strong NADPH autofluorescence enables one to identify hepatocytes without further staining. The discrimination of LSECs and Kupffer cells was confirmed by antibody-based *in vivo* F4/80 staining at the end of each experiment to circumvent interference with carrier-cell interaction (Figure 4a,b). Their unique location along the sinusoids discriminates LSECs at the interphase between NADPH-negative and -positive structures (Figure 4b). Hepatocytes are parenchymal cells located behind the fenestrated capillaries formed by LSECs. Kupffer cells are located in those capillaries, exposing large surfaces into the capillary lumen and interacting with molecules passing by. The amount of the micelles passing

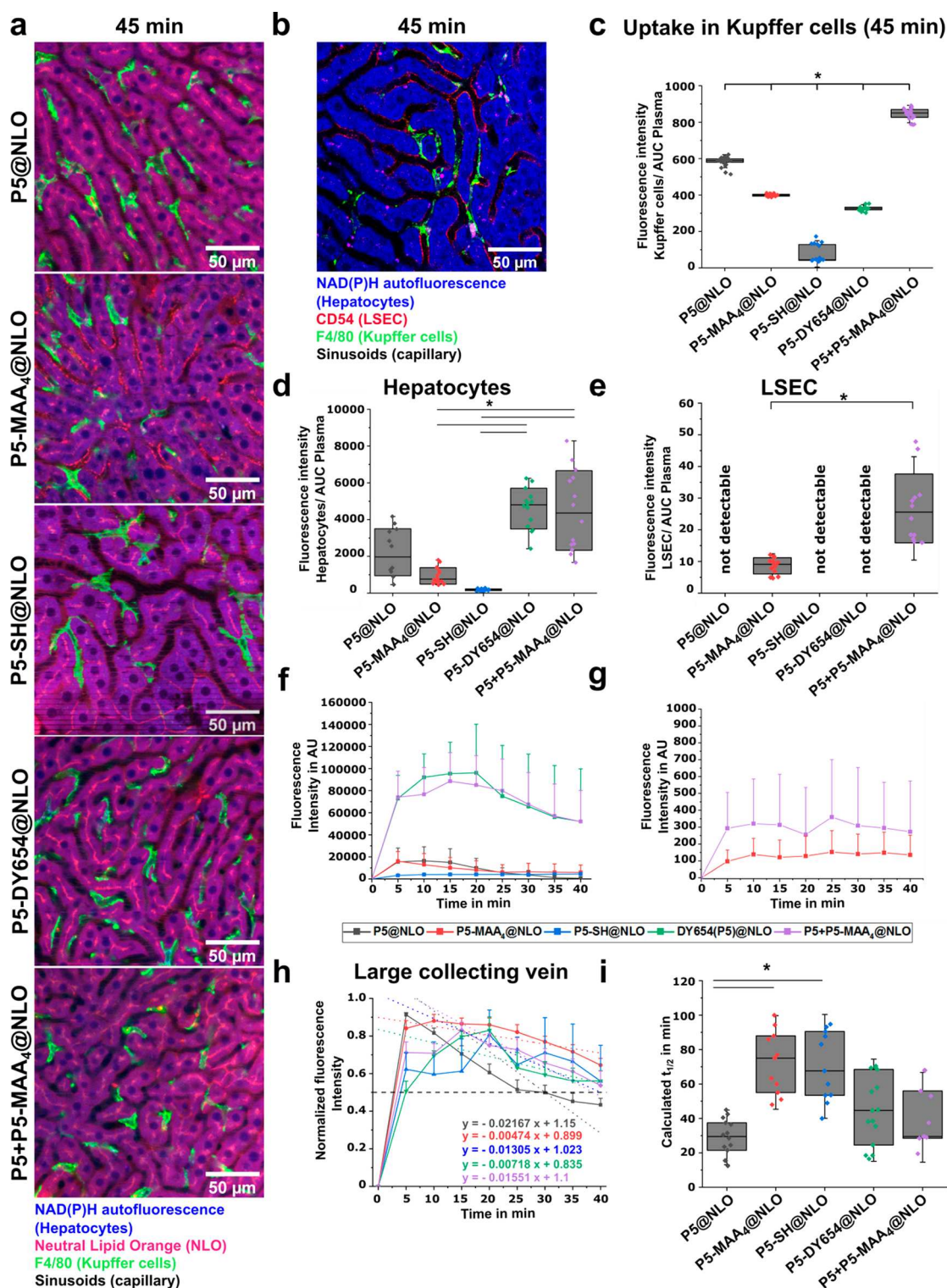


Figure 4. End group modifications of graft copolymer micelles influence cell-type-specific uptake in the liver and mediates stealth effects. (a) Intravital microscopy of murine liver 45 min after injection of NLO-loaded micelles. Their NADPH autofluorescence visualizes hepatocytes. Kupffer cells were counterstained with an F4/80-FITC (green) antibody, injected at the end of the experiment. (b) (Co)localization of sinusoids (black) and liver cells commonly contributing to nanocarrier clearance: Hepatocytes are identified by their high NADPH autofluorescence (blue). LSECs stained with anti-CD54 APC (red) and Kupffer cells with anti-F4/80 FITC (green). (c–e) All data were normalized by the AUC to account for differences in the absolute accumulation of the various micelles in the liver. (c) Mean NLO fluorescence intensity in Kupffer cells. (d,e) Maximal NLO fluorescence intensity in hepatocytes and LSECs. (f,g) Uptake and elimination kinetics of NLO by hepatocytes and LSECs. (h) Normalized fluorescence intensity of circulatory half-life quantified from intravital microscopy time series of large portal vein branches in the liver. (i) Calculated circulatory half-life ($t_{1/2}$). (c,d,e,i) Data are depicted as median (line), box plots indicate 25, 75 percentile, whiskers reflect standard deviation, one-way ANOVA between groups, Tukey test, $*p < 0.05$. Five areas ($425 \mu\text{m}^2$ each) of each liver were analyzed from 3 to 4 mice per group.

through the liver during the imaging period may bias the amount that is taken up by the different cell types. To obtain comparable data on the uptake of the individual micelles in the different liver cells, we analyzed the plasma disappearance from large veins in the liver and calculated the area under the curve (AUC) (Figure S120). This enabled us to estimate the amount of NLO that passed through the liver and normalize to the accumulation of NLO signals in the different cells. P5@NLO composed of graft copolymers with the hydrophobic dithiobenzoate end group was cleared by hepatocytes (Figure 4d,f), accumulated rapidly in Kupffer cells (Figure 4c), but was not detected in LSECs (Figure 4e,g). It also had the lowest plasma half-life among the various micelles studied (Figure 4i), indicating an overall rapid uptake and clearance by the liver. The micelle without dithiobenzoate moieties and charges (P5-SH@NLO) differed substantially from P5@NLO. P5-SH@NLO micelles were characterized by one of the most extended circulation times of all micelles investigated (Figure 4i) and were poorly taken up by hepatocytes and Kupffer cells (Figure 4d,c). Similar to P5@NLO, they did not accumulate in LSEC (Figure 4e). The addition of a charged end group in P5-MAA₄@NLO only slightly reduced the uptake in Kupffer cells and hepatocytes compared to P5@NLO (Figure 4c,d) but led to recognition and uptake by LSEC (Figure 4g,e). While the cell-type-specific clearance pattern in the liver was altered, the overall half-life increased to the level of P5-SH@NLO (Figure 4i), indicating that the end group modification affects the uptake in other tissues as well. Reducing the density of MAA₄-labeled chains to 1% in P5 + P5-MAA₄@NLO increased the uptake of the micelles in hepatocytes, Kupffer cells, and LSEC to a level above that of P5@NLO (Figure 4c–e). The substantial clearance in the liver might result from a better cell interaction of the micelles with surfaces and surface receptors,^{53,54} likely due to rearrangement of the micellar shell exposing anionic methacrylate moieties on the micelles. The labeling of the graft copolymers by DY654 increased accumulation in hepatocytes (Figure 4d) and to a lesser extent in Kupffer cells (Figure 4c) but did not result in uptake by LSECs (Figure 4e).

Overall, the micelles without or with only a small amount of hydrophobic dithiobenzoate showed increased stealth properties, *i.e.*, reduced uptake in Kupffer cells and increased plasma half-life time (Table 2). However, the exemption was the mixed micelle P5 + P5-MAA₄@NLO that stimulated the uptake by Kupffer cells (Figure 4c) and minimally increased the circulation time (Figure 4i). The use of charged terminal groups (MAA₄, DY654) resulted in increased recognition by hepatocytes compared to the uncharged, more hydrophilic micelle P5-SH, possibly due to recognition as anionic moieties that can interact with anionic transporters on the hepatocyte surface.⁵⁵ In contrast to the similarly charged DY654, the MAA₄ moiety resulted in recognition and uptake by LSECs in the liver. Previous studies have already observed a methacrylic acid content-dependent recognition of polymethacrylate-based nanoparticles by LSECs in the liver,⁵⁶ giving rise to the question of whether methacrylic acid-based anionic charges may serve as a basis of targeting moieties in nanocarriers. These effects occurred even though the charges were located at the interface of the micellar core and shell, *i.e.*, without being directly exposed as end groups of the OEtOx building blocks forming the shell.

These different uptake kinetics and cellular distributions in the liver might be a consequence of direct and indirect effects,

such as differences in the interaction with cell surface factors such as sugars or, *e.g.*, organic anion receptors, or changes in the quality and quantity of adsorbed proteins.^{57,58}

CONCLUSION

Micelles formed from graft copolymers comprising the PEG alternative OEtOx have a high potential as polymeric drug carriers. An efficient stealth effect introduced by a dense layer of multiple short OEtOx chains around a hydrophobic PMMA core was evident from a strongly reduced uptake of very small micelles in Kupffer cells. Despite the high molar mass of the graft copolymers of 20 kg mol⁻¹, the hydrophobic backbone end group strongly affected the micelles' liver clearance and stealth effect. The hydrophobic dithiobenzoate end group resulted in a considerable increase in uptake of the micelles by Kupffer cells, *i.e.*, loss of stealth properties, an effect that was avoided by cleavage of the end group or introduction of a few anionic charges per macromolecule.

It was hence evident that minimal alterations of the macromolecule, similar or equal to those made by labeling with fluorescent probes, strongly altered the micelles' stealth properties and liver clearance. The direct and tailored end group modification approach presented here enabled us to unravel hydrophobicity and charge effects systematically. This implies that the design of macromolecular carriers remains a delicate matter. Aside from obvious parameters, such as block ratio and chain length of linear amphiphilic polymers, significant effects can arise from minor end group modifications introduced at the interface between core and shell of the micelles composed of amphiphilic graft copolymers.

METHODS

Materials Used for the Synthesis. All chemicals and solvents were obtained from standard commercial sources and used without further purification unless otherwise stated. 2-Ethyl-2-oxazoline (EtOx) was dried over barium oxide and distilled under argon atmosphere before use. Methyl *p*-toluenesulfonate (MeTos) was distilled and stored under argon. 2,2'-Azobis(2-methylpropionitrile) (AIBN, 98%) was purchased from Acros and recrystallized from methanol. The CTA 2-cyanopropyl dithiobenzoate (CPDB, 97%) was obtained from Strem Chemicals. Methyl methacrylate and methacrylic acid were flushed through a short column filled with an inhibitor remover prior to use. Dyomics GmbH kindly provided DY654-iodoacetamide and neutral lipid orange (NLO). The albumin protein was purchased from SERVA (bovine albumin fraction V, protease and fatty acid-free, diagnostic grade lyophilic, $M_r = 67,000.00$ g mol⁻¹). The Krebs–Henseleit buffer (modified with 2 g L⁻¹ glucose) and phosphate-buffered saline (pH 7.4) were purchased from Sigma-Aldrich. PMMA and PMAA used as reference materials for Raman spectroscopy were synthesized by RAFT polymerization as previously described.⁵⁹

Synthesis. EtOx₁₅MA. The oligo(2-ethyl-2-oxazoline) methacrylate (EtOx₁₅MA) was synthesized as previously published.³⁶ Briefly, 0.74 g (4 mmol) of MeTos, 5.95 g (60 mmol) of EtOx, and 8.97 mL of acetonitrile were transferred into a preheated vial under inert conditions. The polymerization was performed in the microwave synthesizer (Biotage Initiator+) at 140 °C for 60 s. Subsequently, 0.52 g (6 mmol) of methacrylic acid (MAA) and 0.81 g (8 mmol) of triethylamine (NEt₃) were added, and the reaction solution was kept at 50 °C overnight. The reaction mixture was dissolved in chloroform, washed with aqueous sodium bicarbonate solution and brine, dried over sodium sulfate, and concentrated under reduced pressure. DP = 15.5, DF = 0.90.

P5. The PMMA-*graft*-OEtOx₁₅ was synthesized as previously published.³⁵ Briefly, 1.0 g (0.6 mmol) of EtOx₁₅MA, 252.4 mg (2.5 mmol) of MMA, 1.4 mg (8.8 μmol) of AIBN, and 7.7 mg (35 μmol)

of CPDB were dissolved in ethanol at an overall monomer concentration $[M]_0$ of 1 mol L⁻¹ ($[M]/[CPDB]/[AIBN]$ ratio of 90:1:0.25). The reaction solution was gently degassed by argon bubbling and subsequently heated at 70 °C overnight. The raw product was purified by preparative SEC (BioBeads SX-1 from Bio-Rad in THF) and characterized by means of SEC and ¹H NMR spectroscopy. Conversion: 88%. Composition: 89 mol % of MMA. SEC (LiCl in DMAc, RI detection, PMMA calibration): $M_n = 22,900$ g mol⁻¹, $\bar{D} = 1.10$.

P5-SH. First, 0.3 g (14 μmol) of P5 and 0.1 g (0.9 mmol) of hexylamine were dissolved in CH₂Cl₂ (2 mL each), degassed by argon bubbling, subsequently combined, and stirred overnight at room temperature. The raw product was purified by precipitation in cold diethyl ether. SEC (LiCl in DMAc, RI detection, PMMA calibration): $M_n = 22,700$ g mol⁻¹, $\bar{D} = 1.11$. SEC (LiCl in DMAc, DA detection at 311 nm, PMMA calibration): no polymer signal.

P5-DY654. For this compound, 0.17 g (8.2 μmol) of P5-SH and 1 mg (0.82 μmol) of DY654-iodoacetamide were dissolved in 4 mL of DMF, degassed by argon bubbling, and stirred in the dark at room temperature for 72 h. The raw product was purified by column chromatography (Sephadex G-25 Medium from Sigma-Aldrich in water). The successful coupling of the dye and the polymer purity were verified by SEC measurements with simultaneous RI and DA detection at 656–658 nm. Labeling efficiency of 8% was determined by UV–VIS absorption spectroscopy (Analytik Jena SPECORD 250) using a calibration curve generated from a serial dilution of the dye at the absorption maximum in water ($\lambda = 566$ nm). SEC (LiCl in DMAc, RI and DA detection, PMMA calibration): $M_n = 22,700$ g mol⁻¹, $\bar{D} = 1.11$.

P5-MAA₄. First, 0.2 g (9.1 μmol) of P5, 0.37 mg (2.3 μmol) of AIBN, and 7.9 mg (91.3 μmol) of MAA were dissolved in ethanol, degassed by argon bubbling, and heated at 70 °C for 72 h. To determine the MAA conversion (40%, corresponding to a DP value of 4), aliquots were taken before and after heating and analyzed by means of ¹H NMR spectroscopy. The reaction mixture was dissolved in CHCl₃ (50 mL), washed with water (3 × 50 mL), dried over sodium sulfate, concentrated, and dried under reduced pressure at 40 °C. The DP of 4 for the MAA block was additionally determined by acid/base titration. For this purpose, the polymer was dissolved in deionized water, and 1 mL of 0.1 M hydrochloric acid solution was added. The titration was performed against 0.1 M aqueous sodium hydroxide solution using a 765 Dosimat from Metrohm, a digital pH/mV thermometer GMH 3530 from Greisinger Electronic, and the EBS 20M Recorder software. SEC (LiCl in DMAc, RI detection, PMMA calibration): $M_n = 22,100$ g mol⁻¹, $\bar{D} = 1.15$.

NMR Spectroscopy. Proton nuclear magnetic resonance (¹H NMR) spectra were recorded at room temperature in CDCl₃ on a Bruker Avance 300 MHz using the residual solvent resonance as an internal standard. The chemical shifts are given in parts per million.

Size Exclusion Chromatography. A Shimadzu system with a PSS degasser, a G1362A RI detector, a G1315D DA detector, a G1310A pump, a G1329A autosampler, a Techlab oven, and a PSS GRAM guard/30/1000 Å column with a 5 μm particle size was used. The system was run with an eluent composed of *N,N*-dimethylacetamide with 0.21% LiCl at a flow rate of 1 mL min⁻¹ at 40 °C and was calibrated with PMMA standards (~400 to 1,000,000 g mol⁻¹).

Neutral Lipid Orange Encapsulation. The encapsulation experiments were performed according to a procedure established previously for Disperse Orange 3.³⁶ Polymer and dye solutions in acetone were prepared to yield molar ratios of [P] to [NLO] of 1:1, 1:2, 1:3, 1:4, and 1:5. Subsequently, the solvent was removed to complete dryness. Water was added, and the mixture was stirred overnight. The non-encapsulated dye was removed by centrifugation (ROTINA 380 R from Andreas Hettich GmbH & Co. KG D-78532 Tuttlingen equipped with a fixed-angle rotor), and supernatant was freeze-dried (Alpha 2-4 LDplus from Martin Christ Gefriertrocknungsanlagen GmbH). The solid material obtained was dissolved in acetone, and the dye uptake was determined by means of UV–vis absorption spectroscopy at room temperature (Analytik Jena

SPECORD 250 spectrometer) using a calibration curve generated from a serial dilution of the dye at the absorption maximum in acetone ($\lambda = 556$ nm).

For the formulation of P5@NLO in PBS and KHB, the respective buffers were simply added to the thoroughly dried thin film (here, the same ratio of P5 to NLO was used as for the animal experiments), purified by centrifugation, and measured by DLS at 37 °C.

Dynamic Light Scattering and Zeta-Potential. For unloaded micelle solutions, the respective polymer was directly dissolved in Milli-Q water. For the NLO-loaded micelles, the supernatant after centrifugation was used. DLS measurements were performed using a Zetasizer Nano ZS (Malvern Instruments, Herrenberg, Germany). After an equilibration time of 180 s, 3 × 30 runs were carried out at 25 °C ($\lambda = 633$ nm). The counts were detected at an angle of 173°, and mean particle size was approximated as the effective (*Z*-average) diameter obtained by the cumulants method assuming a spherical shape. Each measurement was performed in triplicate.

DLS measurements of P5-DY654 and P5-DY654@NLO as well as zeta-potential measurements of unloaded micelles were performed using a Zetasizer Ultra (Malvern Instruments, Herrenberg, Germany). The detection angles were fixed by the manufacturer at an angle of 173° for DLS and at an angle of 17° for zeta-potential. For DLS measurements of DY654-containing samples, an optical fluorescence filter was used. After an equilibration time of 30 s, three measurements with up to 30 runs were carried out at 25 °C ($\lambda = 633$ nm). Zetasizer Nano Series disposable folded capillary cells (DTS1070, Malvern) were used for zeta-potential measurement, and low volume disposable cuvettes (ZEN0040, Malvern) were used for DLS. The mean particle size was approximated as the effective (*Z*-average) diameter obtained by the cumulants method assuming a spherical shape. Sample preparation for zeta-potential measurements of unloaded micelles included the direct dissolution of the respective polymer in 0.1 mmol L⁻¹ aqueous NaCl and subsequent filtration with a prewetted 0.45 μm Nylon 66 13 mm syringe filter. The data were evaluated with the ZS XPLORER 1.5.0.163 software.

Cryo-Transmission Electron Microscopy. The sample preparation was performed as described above (DLS section). Cryo-TEM investigations were conducted on an FEI Tecnai G² 20 with an acceleration voltage of 200 kV. Samples (8.5 μL) were applied onto Quantifoil grids (Quantifoil, Germany, R2/2) utilizing a Vitrobot Mark IV vitrification system and were transferred to the cryo-TEM holder (Gatan, USA) utilizing a cryo stage. Images were acquired on a 1 × 1 k or a 4 × 4 k CCD camera.

Raman Spectroscopy. The Raman spectra of polymer micelles were recorded using an upright micro-Raman spectrometer (CRM 300, WITec GmbH, Germany) benchtop system equipped with 785 nm laser (laser power 70 mW at the sample plane), a 300 g mm⁻¹ grating, and a deep depletion CCD camera. The liquid suspension of the samples of ~5 μL was placed on the CaF₂ slide, and 10 single spectra were acquired using a 100× objective (NA 0.75, Zeiss) at different positions with 1 s laser exposure time per spectrum. The reference substances (PMMA, EtOx₁₅MA, PMAA) were recorded using an upright micro-Raman spectrometer (InVia-Qontor Renishaw, UK) benchtop system equipped with a 785 nm laser (laser power 23 mW at the sample plane), a 1200 g/mm grating, and a CCD camera. The liquid suspension of the samples of ~5 μL was placed on the CaF₂ slide, and 10 single spectra were acquired using a 50× objective (NA 0.75, Leica) at different positions with 10 s exposure time per spectrum. During Raman spectral recording, white light images were acquired to control the liquid state of the polymer samples. The Raman spectra of NLO and DY654 were recorded in the solid state using a hand-held Raman spectrometer (Progeny, Rigaku Analytical Devices, USA) equipped with a 1064 nm laser (laser power 100 mW at the sample plane). Raman spectra of the powder dye sample were collected from three different positions. Each spectrum was collected with 0.5 s laser exposure time per spectrum. The Raman spectra of the dyes were collected with 1064 nm because, with the 785 nm excitation wavelength, both NLO and DY654 displayed a high fluorescence background. The raw Raman spectra acquired using the benchtop system were preprocessed in GNU R

using in-house built algorithms. The Raman spectra containing cosmic spike and artifact, e.g., high noise, were removed before analysis. The Raman spectra were background corrected by applying the SNIP algorithm (1) and vector normalized. An average spectrum along with a standard deviation was generated for the display. Principal component analysis was performed using preprocessed Raman spectra of P5@NLO, P5-DY654@NLO, and P5-MAA₄@NLO. The analysis was done on GNU R platform. PCA scores and loadings coefficients were generated. For displaying Raman spectroscopy data, OriginPro 2016 (Sr2 b9.3.2.303, OriginLab Corporation) was used.

Analytical Ultracentrifugation. Multidetector sedimentation velocity experiments were performed as described recently.³⁶ They were conducted using an Optima Analytical Ultracentrifuge (Beckmann Coulter Instruments, Brea, CA) with an An-50 Ti eight-hole rotor spun at 42,000 rpm at a temperature of 20 °C. The cells contained double sector Epon centerpieces with a 12 mm solution optical path length and sapphire windows. Those were filled with approximately 440 μL water as a reference and approximately 420 μL of sample solutions diluted in water. Scans were acquired in 3 min intervals using the interference optics and absorbance optical detection system. The radially resolved interference fringes and optical density at a wavelength of 550 nm that is representative of NLO were recorded. The recorded sedimentation velocity data were numerically analyzed with SEDFIT and the $1s-g^*(s)$ model considering nondiffusing species.⁶⁰ For molar mass and hydrodynamic diameter estimations, established routines were used.^{61,62}

Free-Flow Electrophoresis. Free-flow electrophoresis (FFE) was measured on a system kindly made available to us by FFE Service GmbH (Feldkirchen, Germany). The device was equipped with a separating chamber front piece of $500 \times 100 \times 0.2$ mm and a chamber volume of 10.9 mL, an S5 inlet, a cooler with the temperature set to 10 °C, a tube diameter of 0.51 mm, a PP60 membrane, a spacer with a thickness of 0.2 mm and paper filter of 0.3 mm. The anode and the cathode solution contained 150 mmol L^{-1} isobutyric acid (IBA), 150 mmol L^{-1} Tris + Tris, resulting in a pH value of 7.46 and a conductivity of 5810 μS . P5@NLO and albumin solution were incubated for 24 h at room temperature prior to FFE studies.

Fluorescence Spectroscopy. Spectra were measured on a multiplate reader (EnSpire Multimode Plate Reader, PerkinElmer, USA). Micelles were analyzed in deionized water. For excitation scans, the emission wavelength was set to 640 nm (P5-DY654@NLO and P5-SH@NLO), 690 nm (P5@NLO), and 700 nm (P5-MAA₄@NLO and P5 + P5-MAA₄@NLO). The emission scans were performed by exciting the dye at 480 nm (bandwidth 5 nm). A correction factor was calculated from serial dilutions of the micelles, correcting for differences in NLO loading between micelles. Therefore, the micelles were excited at $\lambda_{\text{Ex}} = 488$ nm (bandwidth 5 nm), and the emission was measured at $\lambda_{\text{Em}} = 575$ nm (bandwidth 5 nm). The correction factor represents the relative values of the slope of the fluorescence intensity against the micelle concentration.⁶³

Cell Culture. Mouse embryonic fibroblasts were cultured in cell culture flasks at 37 °C, 5% CO_2 (HeraCell CO_2 Incubator, Heraeus, Germany) and water vapor supplemented atmosphere. For the cultivation, Dulbecco's modified Eagle's medium (Gibco, Thermo Fisher Scientific, Germany) supplemented with 10% fetal bovine serum (Thermo Fisher Scientific, Germany), 100 IU streptomycin, 100 IU penicillin (Gibco, Thermo Fisher Scientific, Germany), and 1% stable glutamine (GlutaMax, Gibco, Thermo Fisher Scientific, Germany) was used. Cells were detached and passaged every 3 to 4 days by pipetting.

Cytotoxicity. MEFs were incubated with different micelles in growth media without fetal bovine serum and antibiotics for 24 h. Supernatants were taken, and lactate dehydrogenase (LDH) activity was assessed as a surrogate for membrane damage and toxicity using the CytoTox96 nonradioactive cytotoxicity assay (Promega, Germany). The absorbance of the red formazan product from the conversion of the tetrazolium salt was quantified on a multiplate reader (EnSpire Multimode Plate Reader, PerkinElmer, USA) at 490 nm (bandwidth 5 nm). A 100% cell lysis positive control was used to

determine the maximum amount of LDH present. The lysis rate was calculated by subtracting the medium background from each value and relativizing the absorbance values of the treated cells to that of the positive control. Experiments were performed in nine replicates on three individual days.

Micellar Uptake in Murine Embryonic Fibroblasts. Murine embryonic fibroblasts cultivated in 24-well plates as stated above were incubated with various micelles (diluted to a concentration of 10, 100, and 250 $\mu\text{g mL}^{-1}$) in serum-free medium at 37 °C in a humidified atmosphere. After 24 h, MEFs were detached in PBS (Lonza, Switzerland) containing 5 mmol L^{-1} EDTA (Thermo Fisher Scientific, Germany). The uptake was then quantified using the NLO fluorescence using flow cytometry (BD Accuri C6 Plus, BD Bioscience, Germany) (approximately 10,000 cells per sample). The correction factor was applied to the raw data correcting for the differences in NLO loading, i.e., endogenous brightness between micelles. Experiments were performed in nine replicates on three individual days.

Micellar Uptake Mechanism. MEF cells (4.5×10^4 per well) were seeded in 96-well plates and incubated at 37 °C 24 h before the experiment. The medium was then replaced with a serum-free medium containing 30 $\mu\text{mol L}^{-1}$ Pitstop-2 (Sigma-Aldrich, Germany, dissolved in DMSO) or 0.08% DMSO alone and left with cells for 15 min at 37 °C. To check for the energy dependency of the micellar uptake, the cells were incubated with 10 mmol L^{-1} NaN_3 (ATPase-inhibitor)⁶⁴ at 37 °C for 1 h or at 4 °C⁶⁵ for 1 h before incubation with the micelles, respectively. After incubation, the medium was replaced again with 150 μL of fresh serum-free medium to remove excess Pitstop-2 or NaN_3 . To validate the effectiveness of Pitstop-2 in this experiment, we used in parallel Nile red (NR)-loaded nanoparticles P(MMA-co-MAA)@NR (Figure S115). In a subset of experiments, MEFs were incubated with micelles at 37 and 4 °C for 10 min in DMEM supplemented with 10% fetal bovine serum. These nanoparticles are composed of a statistical copolymer of MMA with 10 mol % of MAA, representing the chemical composition of the micellar core without an OEtOx corona ($D_h = 167$ nm, PDI 0.08, zeta-potential = -27 mV) and are known for their endocytotic uptake.⁵⁶ Micelles (50 $\mu\text{g mL}^{-1}$ in 50 μL of ddH₂O) or polymethacrylate nanoparticle (P(MMA-co-MAA)@NR), which are known for their endocytosis-dependent uptake, were added for 10 min to the cells. For the temperature-dependent experiment at 4 °C, this step was still at 4 °C. Afterward, cells were detached with PBS (Lonza, Switzerland), 5 mmol L^{-1} EDTA (Thermo Fisher Scientific, Germany) for 30 min at 37 °C in test tubes. The micellar uptake was then quantified utilizing the NLO fluorescence using flow cytometry (BD Accuri C6 Plus, BD Bioscience, Germany). Analysis was performed on 10,000 events per sample. For comparison of the fluorescence intensities, a correction factor was applied. The experiment was performed at least independently three times in duplicates.

Live Cell Imaging. Images were acquired using an LSM-780 microscope (Zeiss AG, Jena, Germany) using a 40 \times plan-apochromatic air objective (numeric aperture (NA) 0.95) or a plan-apochromatic 63 \times oil immersion objective (NA 1.40) (both Zeiss AG, Jena, Germany). The plasma membrane of the cells was stained before imaging by incubation of the cells with 5 $\mu\text{g mL}^{-1}$ CellMask Deep Red (Thermo Fisher Scientific, Germany). After 8 min under normal growth conditions, cells were washed twice with prewarmed Hanks' balanced salt solution (HBSS) (Thermo Fisher Scientific, Germany), and FluoroBrite DMEM (Gibco, Thermo Fisher Scientific, Germany) was added. CellMask Deep Red was excited at 633 nm (helium–neon laser) and detected through a 648–744 nm band-pass filter on a photomultiplier tube. Neutral lipid orange (20 nmol L^{-1}) and the different micelles containing NLO at a concentration of 50 $\mu\text{g mL}^{-1}$ were imaged (without additional washing steps) through excitation at 561 nm (helium–neon laser), and fluorescence was detected using a photomultiplier tube through a 571–633 nm band-pass filter for 10 min. The cellular uptake of micelles containing NLO was analyzed using ImageJ 1.51 (Freeware, NIH, USA).^{66,67} In brief, the same threshold was applied to all images. The fluorescence

intensity in 15 regions of interest was determined for all images for three independent replicates.

Early Endosome Staining and Micellar Uptake. 7.5×10^4 MEFs per cm^2 were seeded in 4-well chamber slides (μ -slides, ibidi, Munich, Germany). Cells were cultivated for 24 h at 37°C , 5% CO_2 in DMEM (Gibco, Thermo Fisher Scientific, Germany) supplemented with 10% fetal bovine serum (Thermo Fisher Scientific, Germany), 100 IU streptomycin, 100 IU penicillin (Gibco, Thermo Fisher Scientific, Germany), and 1% stable glutamine (GlutaMaxx, Gibco, Thermo Fisher Scientific, Germany). Afterward, the medium was changed to Opti-MEM (Gibco, Thermo Fisher Scientific, Germany), and 20 particles of Molecular Probes CellLight Early Endosome GFP, BacMam 2.0 (ThermoFischer Scientific, Germany) (Gibco, Thermo Fisher Scientific, Germany) per cell were added and incubated another 18 h at 37°C , 5% CO_2 . Before imaging, cells were washed twice with prewarmed HBSS (Thermo Fisher Scientific, Germany), and FluoroBrite DMEM (Gibco, Thermo Fisher Scientific, Germany) was added. Live cell imaging was then carried out on an LSM-780 (Carl Zeiss AG, Jena, Germany) equipped with a tempered incubation chamber (37°C) and CO_2 control (5% CO_2). EEAI-GFP was excited at 488 nm (argon laser) and detected through a 493–556 nm band-pass filter on a photomultiplier tube. The different micelles containing NLO were added at a concentration of $50 \mu\text{g mL}^{-1}$ and imaged after ~ 10 min of incubation (without additional washing steps). NLO was excited at 561 nm (helium–neon laser), and fluorescence was detected using a photomultiplier tube through a 570–753 nm band-pass filter. Images were acquired using a $40\times$ objective and 1.6-fold digital zoom. The pixel size was optimized with respect to the Nyquist criterion for each image. At each position, five z -planes were recorded around the brightest focal plane (step size of $0.65 \mu\text{m}$). The images were analyzed using the Fiji distribution of ImageJ 1.51 (NIH, USA).^{66,67} The z -positions were averaged, improving the signal-to-noise ratio and ensuring endosomal structures are fully sampled in all dimensions. Intensities were measured along with line profiles (region of interest, ROI), with each line crossing the center of a GFP-stained endosome. The mean GFP and NLO fluorescence intensity were measured along with the line profile. Five to 10 ROIs were analyzed in each cell. Further, three cells were analyzed per micelle, and the fluorescence intensity was corrected to the cellular background. The plots depict the mean gray value for each channel.

Animals. FVB/N mice (male and female) were used in this study. Animals were maintained at the animal facility of the Jena University Hospital under artificial day–night cycles (12 h light–dark cycles; 23°C room temperature; 30–60% environment humidity) in a specific pathogen-free environment. Animal studies were conducted following German legislation on the protection of animals and with permission of the Thuringian state administrative office.

In Vivo Confocal Laser Scanning Microscopy. During all procedures and imaging methods, animals remained under deep general anesthesia using 1–2% isoflurane (CP-Pharma, Germany) and 5 mg kg^{-1} bodyweight p.o. Meloxicam (0.5 mg mL^{-1} suspension, CP-Pharma, Germany) for additional pain relief. Pain reflexes were assessed to gauge the depth of anesthesia. While still under anesthesia, the animals were sacrificed at the end of the experiments. For *in vivo* confocal laser scanning microscopy, first, a tail-vein catheter (30 G) was placed. The liver was exposed by an abdominal incision and carefully placed on a coverslip. Images were acquired using a LSM-780 (Zeiss AG, Jena, Germany) with air-corrected $20\times$ plan-apochromatic (NA 1.15) or $40\times$ plan-apochromatic objective (NA 0.95). Different micelles ($\sim 150 \mu\text{g}$) in 5% glucose solution were injected through the tail vein. The NLO cargo fluorescence was illuminated with similar excitation and emission settings as in the *in vitro* experiments. NADPH autofluorescence was employed for hepatocyte detection, as described before.⁵² After five areas of interest of each liver were localized, different micelles containing NLO were administered *via* the tail-vein catheter. Then, images were taken every minute to monitor kinetics. Five areas of interest per mouse and ≥ 3 mice were analyzed. The analysis was done at the time when kinetic analysis showed the highest value in the fluorescence intensity. Image

analysis was performed by custom image processing, and the analysis algorithm is described in the next section. Kupffer cells and LSEC staining were performed at the end of the experiment, not to affect the distribution pattern of the micelles. Kupffer cells and LSECs were stained by injection of approximately $10 \mu\text{g}$ of FITC-labeled F4/80 (clone: BM8) antibody and $6 \mu\text{g}$ of APC-labeled CD54 (clone: YN1/1.7.4) antibody (Biolegend, USA), respectively. FITC fluorescence illuminated at 488 nm (argon laser) and was detected through a 499–535 nm band-pass filter on a photomultiplier tube.

Image Analysis. Images of labeled and unlabeled liver tissue acquired *via* intravital microscopy were utilized to identify, segment, and quantify various components of the liver using the analysis workflow in Figure S117. The hepatocytes were identified using label-free techniques⁶⁸ based on the autofluorescence images, where their NADPH signal provided proper contrast for a reliable segmentation. In other cases, the end point image of the nanocarrier cargo delivery (cargo: NLO) was used to identify the hepatocytes and to confirm the label-free method (Figures S117 and S118A). In the latter case, the precise time sequence tracking of the hepatic cell content of the delivered cargo was only possible with proper precision if the tissue movement during the time sequence imaging was negligible. The canaliculi locations were approximated as the midline between two rows of hepatocytes (Figure S118A). This approach worked well with autofluorescence-based hepatocyte identification when studying the time dependence of the cargo delivery (supplementary Video S11). In contrast, the NLO-based approach was able to provide end point information about the final cargo accumulation in the canaliculi, as well as to confirm the label-free localization technique (Figure S118Ab,Ac). The sinusoids were identified based on the first few frames of the time sequence experiments using the autofluorescence signal. The vessel wall location was later utilized to identify the LSEC, as these cells align themselves with the vessel walls, forming a linear array of bead-shaped small structures. Due to their very characteristic morphology, LSECs were successfully identified throughout the entire time sequence of images by calculating the population-based morphometric and intensity measures (Figure S118B and supplementary Video S12). This method provided precise tissue-wide information about the nanocarrier cargo delivery to the LSECs, even though these small cells quickly went in and out of focus during the 2D laser scanning imaging experiments. The resident macrophages of the liver (Kupffer cells) were identified and segmented with high precision based on specific fluorescence labeling applied after the cargo delivery experiments. The Kupffer cells were identified *via* a template-matching algorithm⁶⁹ (Figure S119), where the templates were acquired manually from end point images (Figure S119A). The template-matched image segments of the Kupffer cells (Figure S119B) were then preprocessed, binarized using automated thresholding using Otsu's algorithm,⁷⁰ and postprocessed to arrive at the close approximation of individual Kupffer cells (Figure S119C–E). The binary masks were used to calculate the mean fluorescence of the NLO channel (Figure S119F) in the regions of interest corresponding to each Kupffer cell identified by the binary image segments (Figure S119G). Finally, the location of the nuclei and the intercellular space was determined based on the low signal regions of the autofluorescence images (supplementary Video S13). All image analysis tasks were carried out by two custom-written macros (supplementary Video S14 and Video S15) using the Fiji distribution of ImageJ 1.52p.^{66,67}

Quantitative data were normalized to differences in the intrinsic brightness of the micelles using the correction factor⁶³ and by the area under the curve calculated from the plasma disappearance rate in large veins (portal veins) of the liver, accounting for differences in the absolute accumulation of the various micelles in the liver. Data were processed with the R open source version 3.5.2 (2018-12-20, "Eggshell Igloo") and R-Studio open source, version 1.1.463. The packages and functions used were the following: *tidyverse*, *stringr*, *purrr*, *dplyr*, *concatenate*, *RMisc*, *readr*, *readxl*. Data are plotted with OriginPro 2019 (OriginLab Corporation).

ASSOCIATED CONTENT

Supporting Information

The Supporting Information is available free of charge at <https://pubs.acs.org/doi/10.1021/acsnano.1c04213>.

Schematic representation of the detailed synthesis route toward the PMMA-graft-OEtOx₁₅ graft copolymers; overlay of SEC elugrams for P5 and P5-SH and P5-SH with RI and DA detection; SEC elugram, absorption spectrum, emission spectrum, and 3D-SEC elugram of P5-DY654; overlay of SEC elugrams of P5 and P5-MAA₄; titration investigation of P5-MAA₄; DLS correlograms; cryo-TEM images and DLS of P5-MAA₄, P5-DY654, and P5-SH; general workflow for the determination of the dye uptake; dye uptake results for P5@NLO and P5-MAA₄@NLO and corresponding calibration data; fluorescence excitation and emission of different micelles; Raman mean intensity spectra of different micelles, the neat material, and pure dyes NLO and DY654; principal component (PC-1, PC-2, PC-3) analysis of the Raman spectra; additional discussion of micelle stability; stability of P5@NLO investigated by analytical ultracentrifugation; stability of P5@NLO in physiologically relevant buffers determined by DLS; stability of P5@NLO against albumin determined by FFE; toxicity and uptake in MEF (24 h); uptake of P(MMA-co-MAA)@NR in the presence of different inhibitors determined by flow cytometry after 10 min incubation; early endosome staining and micellar uptake *in vitro*; flowchart of the automated image processing; identification of canaliculi and LSECs in live liver tissue; identification of the Kupffer cells in live liver tissue; AUC calculated from plasma disappearance; complete description of 6 supporting videos (PDF)

Video S1: Identification of canaliculi (MP4)

Video S2: Segmentation of LSECs via population sampling (MP4)

Video S3: Location of hepatocyte nuclei and intercellular space (MP4)

Video S4: Real-time screen capture of the leading image analysis (MP4)

Video S5: Real-time screen capture of the second image analysis program (MP4)

Video S6: Representation time series (MP4)

AUTHOR INFORMATION

Corresponding Authors

Ulrich S. Schubert – Laboratory of Organic and Macromolecular Chemistry (IOMC), Friedrich Schiller University Jena, 07743 Jena, Germany; Jena Center for Soft Matter (JCSM), Friedrich Schiller University Jena, 07743 Jena, Germany; orcid.org/0000-0003-4978-4670; Email: ulrich.schubert@uni-jena.de

Adrian T. Press – Department of Anesthesiology and Intensive Care Medicine, Jena University Hospital, 07747 Jena, Germany; Medical Faculty, Friedrich Schiller University Jena, 07743 Jena, Germany; orcid.org/0000-0002-6089-6764; Email: adrian.press@med.uni-jena.de

Authors

Irina Muljajew – Laboratory of Organic and Macromolecular Chemistry (IOMC), Friedrich Schiller University Jena, 07743 Jena, Germany; Jena Center for Soft

Matter (JCSM), Friedrich Schiller University Jena, 07743 Jena, Germany

Sophie Huschke – Department of Anesthesiology and Intensive Care Medicine, Jena University Hospital, 07747 Jena, Germany

Anuradha Ramoji – Institute for Physical Chemistry (IPC) and Abbe Center of Photonics (ACP), Friedrich Schiller University Jena, 07745 Jena, Germany; Leibniz Institute of Photonic Technology (IPHT) Jena, Member of the Leibniz Research Alliance - Leibniz Health Technologies, 07745 Jena, Germany; orcid.org/0000-0003-2723-6614

Zoltán Cserenyés – Research Group Applied Systems Biology, Leibniz Institute for Natural Product Research and Infection Biology, Hans Knoell Institute Jena, 07745 Jena, Germany

Stephanie Hoepfner – Laboratory of Organic and Macromolecular Chemistry (IOMC), Friedrich Schiller University Jena, 07743 Jena, Germany; Jena Center for Soft Matter (JCSM), Friedrich Schiller University Jena, 07743 Jena, Germany; orcid.org/0000-0002-5770-5197

Ivo Nischang – Laboratory of Organic and Macromolecular Chemistry (IOMC), Friedrich Schiller University Jena, 07743 Jena, Germany; Jena Center for Soft Matter (JCSM), Friedrich Schiller University Jena, 07743 Jena, Germany; orcid.org/0000-0001-6182-5215

Wanling Foo – Department of Anesthesiology and Intensive Care Medicine, Jena University Hospital, 07747 Jena, Germany

Jürgen Popp – Institute for Physical Chemistry (IPC) and Abbe Center of Photonics (ACP), Friedrich Schiller University Jena, 07745 Jena, Germany; Leibniz Institute of Photonic Technology (IPHT) Jena, Member of the Leibniz Research Alliance - Leibniz Health Technologies, 07745 Jena, Germany; orcid.org/0000-0003-4257-593X

Marc Thilo Figge – Research Group Applied Systems Biology, Leibniz Institute for Natural Product Research and Infection Biology, Hans Knoell Institute Jena, 07745 Jena, Germany; Institute of Microbiology, Faculty of Biological Sciences, Friedrich Schiller University Jena, 07743 Jena, Germany

Christine Weber – Laboratory of Organic and Macromolecular Chemistry (IOMC), Friedrich Schiller University Jena, 07743 Jena, Germany; Jena Center for Soft Matter (JCSM), Friedrich Schiller University Jena, 07743 Jena, Germany; orcid.org/0000-0003-0712-5255

Michael Bauer – Department of Anesthesiology and Intensive Care Medicine, Jena University Hospital, 07747 Jena, Germany

Complete contact information is available at:

<https://pubs.acs.org/doi/10.1021/acsnano.1c04213>

Author Contributions

I.M. planned, synthesized, formulated, and analyzed polymers and micelles. S.Hu. planned, performed, and analyzed *in vitro* and *in vivo* experiments. A.R. planned, performed, and analyzed Raman microspectroscopic analysis. Z.C. planned and conducted image analysis. S.Ho. performed and analyzed cryo-TEM. I.N. planned and performed analytical ultracentrifugation analysis. W.F. established, performed, and analyzed intravitral co-staining. M.T.F. supervised the image analysis. J.P. supervised Raman microspectroscopy. C.W. planned the study and supervised the synthesis and analysis. M.B. guided the study and supervised animal experiments.

U.S.S. guided the study and supervised the polymer synthesis and micelle preparation. A.T.P. planned and guided the study, performed animal experiments, and supervised cell experiments and analysis. All authors contributed to writing the manuscript.

Notes

The authors declare no competing financial interest.
©I.M. and S.H. contributed equally.

ACKNOWLEDGMENTS

This work was funded by the Deutsche Forschungsgemeinschaft (DFG, German Research Foundation), Project No. 316213987 – SFB 1278 (Projects A01, C01, C03, Z01). The cryo-TEM facilities of the Jena Center for Soft Matter (JCSM) were established with a grant from the DFG and the European Funds for Regional Development (EFRE). This work was as well supported by the “Thüringer Aufbaubank (TAB)” and the “Europäischer Fond für regionale Entwicklung (EFRE)” (2018FGI0025) for funding of analytical ultracentrifugation facilities at the JCSM. The authors thank Pelin Sungur (Friedrich Schiller University, Jena) for her technical support on the cryo-TEM. Mouse embryonic fibroblasts were a gift of the Institute of Human Genetics, Jena University Hospital. Dyomics GmbH Jena provided DY654 and neutral lipid orange. The authors would also like to thank Jens Ulbrich for providing the poly(methyl methacrylate), and Dr. Robert Wildgruber and Markart Meckel from the FFE Service GmbH for free flow electrophoresis measurements.

REFERENCES

- (1) Villaverde, G.; Baeza, A. Targeting Strategies for Improving the Efficacy of Nanomedicine in Oncology. *Beilstein J. Nanotechnol.* **2019**, *10*, 168–181.
- (2) Morachis, J. M.; Mahmoud, E. A.; Almutairi, A. Physical and Chemical Strategies for Therapeutic Delivery by Using Polymeric Nanoparticles. *Pharmacol. Rev.* **2012**, *64*, 505–519.
- (3) Cabral, H.; Matsumoto, Y.; Mizuno, K.; Chen, Q.; Murakami, M.; Kimura, M.; Terada, Y.; Kano, M. R.; Miyazono, K.; Uesaka, M.; Nishiyama, N.; Kataoka, K. Accumulation of Sub-100 Nm Polymeric Micelles in Poorly Permeable Tumours Depends on Size. *Nat. Nanotechnol.* **2011**, *6*, 815–823.
- (4) Kao, Y. J.; Juliano, R. L. Interactions of Liposomes with the Reticuloendothelial System. Effects of Reticuloendothelial Blockade on the Clearance of Large Unilamellar Vesicles. *Biochim. Biophys. Acta, Gen. Subj.* **1981**, *677*, 453–461.
- (5) Zolnik, B. S.; González-Fernández, A.; Sadrieh, N.; Dobrovolskaia, M. A. Nanoparticles and the Immune System. *Endocrinology* **2010**, *151*, 458–465.
- (6) Papahadjopoulos, D.; Allen, T. M.; Gabizon, A.; Mayhew, E.; Matthay, K.; Huang, S. K.; Lee, K. D.; Woodle, M. C.; Lasic, D. D.; Redemann, C. Sterically Stabilized Liposomes: Improvements in Pharmacokinetics and Antitumor Therapeutic Efficacy. *Proc. Natl. Acad. Sci. U. S. A.* **1991**, *88*, 11460–11464.
- (7) Storm, G.; Belliot, S. O.; Daemen, T.; Lasic, D. D. Surface Modification of Nanoparticles to Oppose Uptake by the Mononuclear Phagocyte System. *Adv. Drug Deliv. Rev.* **1995**, *17*, 31–48.
- (8) D’souza, A. A.; Shegokar, R. Polyethylene Glycol (PEG): A Versatile Polymer for Pharmaceutical Applications. *Expert Opin. Drug Deliv.* **2016**, *13*, 1257–1275.
- (9) Torchilin, V. P. Polymer-Coated Long-Circulating Micro-particulate Pharmaceuticals. *J. Microencapsulation* **1998**, *15*, 1–19.
- (10) Veronese, F. M.; Pasut, G. PEGylation, Successful Approach to Drug Delivery. *Drug Discov. Today* **2005**, *10*, 1451–1458.
- (11) Yang, Q.; Jacobs, T. M.; McCallen, J. D.; Moore, D. T.; Huckaby, J. T.; Edelman, J. N.; Lai, S. K. Analysis of Pre-Existing IgG and IgM Antibodies against Polyethylene Glycol (PEG) in the General Population. *Anal. Chem.* **2016**, *88*, 11804–11812.
- (12) Chen, B.-M.; Su, Y.-C.; Chang, C.-J.; Burnouf, P.-A.; Chuang, K.-H.; Chen, C.-H.; Cheng, T.-L.; Chen, Y.-T.; Wu, J.-Y.; Roffler, S. R. Measurement of Pre-Existing IgG and IgM Antibodies against Polyethylene Glycol in Healthy Individuals. *Anal. Chem.* **2016**, *88*, 10661–10666.
- (13) Kozma, G. T.; Mészáros, T.; Vashegyi, I.; Fülöp, T.; Örfi, E.; Dézsi, L.; Rosivall, L.; Bavli, Y.; Urbanics, R.; Mollnes, T. E.; Barenholz, Y.; Szebeni, J. Pseudo-Anaphylaxis to Polyethylene Glycol (PEG)-Coated Liposomes: Roles of Anti-PEG IgM and Complement Activation in a Porcine Model of Human Infusion Reactions. *ACS Nano* **2019**, *13*, 9315–9324.
- (14) Guidolin, K.; Zheng, G. Nanomedicines Lost in Translation. *ACS Nano* **2019**, *13*, 13620–13626.
- (15) Kierstead, P. H.; Okochi, H.; Venditto, V. J.; Chuong, T. C.; Kivimae, S.; Fréchet, J. M. J.; Szoka, F. C. The Effect of Polymer Backbone Chemistry on the Induction of the Accelerated Blood Clearance in Polymer Modified Liposomes. *J. Control. Release* **2015**, *213*, 1–9.
- (16) Woodle, M. C.; Engbers, C. M.; Zalipsky, S. New Amphipatic Polymer-Lipid Conjugates Forming Long-Circulating Reticuloendothelial System-Evading Liposomes. *Bioconjugate Chem.* **1994**, *5*, 493–496.
- (17) Moreadith, R. W.; Viegas, T. X. Poly(2-oxazoline) Polymers – Synthesis, Characterization, and Applications in Development of POZ Therapeutics. In *Polymers for Biomedicine: Synthesis, Characterization, and Applications*, 1st ed.; Scholz, C., Eds.; John Wiley & Sons, Inc.: Hoboken, NJ, 2017; pp 51–76.
- (18) Danish, 100. Pipeline - Serina Therapeutics; <https://serinatherapeutics.com/pipeline/> (accessed June 8, 2020).
- (19) Sedlacek, O.; Hoogenboom, R. Drug Delivery Systems Based on Poly(2-Oxazoline)s and Poly(2-Oxazine)s. *Adv. Therap.* **2020**, *3*, 1900168.
- (20) Luxenhofer, R.; Han, Y.; Schulz, A.; Tong, J.; He, Z.; Kabanov, A. V.; Jordan, R. Poly(2-Oxazoline)s as Polymer Therapeutics. *Macromol. Rapid Commun.* **2012**, *33*, 1613–1631.
- (21) Lu, Y.; Lin, J.; Wang, L.; Zhang, L.; Cai, C. Self-Assembly of Copolymer Micelles: Higher-Level Assembly for Constructing Hierarchical Structure. *Chem. Rev.* **2020**, *120*, 4111–4140.
- (22) Maksym-Bebenek, P.; Neugebauer, D. Study on Self-Assembled Well-Defined PEG Graft Copolymers as Efficient Drug-Loaded Nanoparticles for Anti-Inflammatory Therapy. *Macromol. Biosci.* **2015**, *15*, 1616–1624.
- (23) Sant, S.; Poulin, S.; Hildgen, P. Effect of Polymer Architecture on Surface Properties, Plasma Protein Adsorption, and Cellular Interactions of Pegylated Nanoparticles. *J. Biomed. Mater. Res., Part A* **2008**, *87*, 885–895.
- (24) Rieger, J.; Passirani, C.-P.; Benoit, J.; Van Butsele, K.; Jérôme, R.; Jérôme, C. Synthesis of Amphiphilic Copolymers of Poly(ethylene Oxide) and Poly(ϵ -Caprolactone) with Different Architectures, and Their Role in the Preparation of Stealthy Nanoparticles. *Adv. Funct. Mater.* **2006**, *16*, 1506–1514.
- (25) Bose, A.; Jana, S.; Saha, A.; Mandal, T. K. Amphiphilic Polypeptide-Polyoxazoline Graft Copolymer Conjugate with Tunable Thermoresponsiveness: Synthesis and Self-Assembly into Various Micellar Structures in Aqueous and Nonaqueous Media. *Polymer* **2017**, *110*, 12–24.
- (26) Guillerm, B.; Darcos, V.; Lapinte, V.; Monge, S.; Coudane, J.; Robin, J.-J. Synthesis and Evaluation of Triazole-Linked Poly(ϵ -Caprolactone)-Graft-Poly(2-Methyl-2-Oxazoline) Copolymers as Potential Drug Carriers. *Chem. Commun.* **2012**, *48*, 2879–2881.
- (27) Yildirim, I.; Bus, T.; Sahn, M.; Yildirim, T.; Kalden, D.; Hoepfner, S.; Traeger, A.; Westerhausen, M.; Weber, C.; Schubert, U. S. Fluorescent Amphiphilic Heterografted Comb Polymers Comprising Biocompatible PLA and PETox Side Chains. *Polym. Chem.* **2016**, *7*, 6064–6074.
- (28) Jana, S.; Bose, A.; Saha, A.; Mandal, T. K. Photocleavable and Tunable Thermoresponsive Amphiphilic Random Copolymer: Self-

- Assembly into Micelles, Dye Encapsulation, and Triggered Release. *J. Polym. Sci., Part A: Polym. Chem.* **2017**, *55*, 1714–1729.
- (29) Jana, S.; Saha, A.; Paira, T. K.; Mandal, T. K. Synthesis and Self-Aggregation of Poly(2-Ethyl-2-Oxazoline)-Based Photocleavable Block Copolymer: Micelle, Compound Micelle, Reverse Micelle, and Dye Encapsulation/Release. *J. Phys. Chem. B* **2016**, *120*, 813–824.
- (30) Korchia, L.; Lapinte, V.; Travelet, C.; Borsali, R.; Robin, J.-J.; Bouilhac, C. UV-Responsive Amphiphilic Graft Copolymers Based on Coumarin and Polyoxazoline. *Soft Matter* **2017**, *13*, 4507–4519.
- (31) Oudin, A.; Chauvin, J.; Gibot, L.; Rols, M.-P.; Balor, S.; Goudounèche, D.; Payré, B.; Lonetti, B.; Vicendo, P.; Mingotaud, A.-F.; Lapinte, V. Amphiphilic Polymers Based on Polyoxazoline as Relevant Nanovectors for Photodynamic Therapy. *J. Mater. Chem. B* **2019**, *7*, 4973–4982.
- (32) Alvarado, G. G.; Nguyen, H. V.-T.; Harvey, P.; Gallagher, N. M.; Le, D.; Ottaviani, M. F.; Jasanoff, A.; Delaittre, G.; Johnson, J. A. Polyoxazoline-Based Bottlebrush and Brush-Arm Star Polymers *via* ROMP: Syntheses and Applications as Organic Radical Contrast Agents. *ACS Macro Lett.* **2019**, *8*, 473–478.
- (33) Yamamoto, Y.; Nagasaki, Y.; Kato, Y.; Sugiyama, Y.; Kataoka, K. Long-Circulating Poly(ethylene Glycol)-poly(D,L-Lactide) Block Copolymer Micelles with Modulated Surface Charge. *J. Control. Release* **2001**, *77*, 27–38.
- (34) Xiao, K.; Li, Y.; Luo, J.; Lee, J. S.; Xiao, W.; Gonik, A. M.; Agarwal, R. G.; Lam, K. S. The Effect of Surface Charge on *in Vivo* Biodistribution of PEG-Oligocholic Acid Based Micellar Nanoparticles. *Biomaterials* **2011**, *32*, 3435–3446.
- (35) Maksym, P.; Neugebauer, D. Synthesis of Amphiphilic Semigrafted Pseudo-Pluronics for Self-Assemblies Carrying Indomethacin. *RSC Adv.* **2016**, *6*, 88444–88452.
- (36) Muljajew, I.; Weber, C.; Nischang, I.; Schubert, U. PMMA-G-OEtOx Graft Copolymers: Influence of Grafting Degree and Side Chain Length on the Conformation in Aqueous Solution. *Materials* **2018**, *11*, 528.
- (37) Press, A. T.; Ramoji, A.; vd Luhe, M.; Rinkenauer, A. C.; Hoff, J.; Butans, M.; Rossel, C.; Pietsch, C.; Neugebauer, U.; Schacher, F. H.; Bauer, M. Cargo–Carrier Interactions Significantly Contribute to Micellar Conformation and Biodistribution. *NPG Asia Mater.* **2017**, *9*, e444.
- (38) Recouvreux, M. V.; Commisso, C. Macropinocytosis: A Metabolic Adaptation to Nutrient Stress in Cancer. *Front. Endocrinol. (Lausanne, Switz.)* **2017**, *8*, 261.
- (39) Qiu, L. Q.; Lai, W. S.; Stumpo, D. J.; Blackshear, P. J. Mouse Embryonic Fibroblast Cell Culture and Stimulation. *Bio-protocol* **2016**, *6*, No. e1859.
- (40) Dutta, D.; Williamson, C. D.; Cole, N. B.; Donaldson, J. G. Pitstop 2 Is a Potent Inhibitor of Clathrin-Independent Endocytosis. *PLoS One* **2012**, *7*, No. e45799.
- (41) Liashkovich, I.; Pasrednik, D.; Prystopiuk, V.; Rosso, G.; Oberleithner, H.; Shahin, V. Clathrin Inhibitor Pitstop-2 Disrupts the Nuclear Pore Complex Permeability Barrier. *Sci. Rep.* **2015**, *5*, 9994.
- (42) Sahay, G.; Querbes, W.; Alabi, C.; Eltoukhy, A.; Sarkar, S.; Zurenko, C.; Karagiannis, E.; Love, K.; Chen, D.; Zoncu, R.; Buganim, Y.; Schroeder, A.; Langer, R.; Anderson, D. G. Efficiency of siRNA Delivery by Lipid Nanoparticles Is Limited by Endocytic Recycling. *Nat. Biotechnol.* **2013**, *31*, 653–658.
- (43) Zhang, Y.-N.; Poon, W.; Tavares, A. J.; McGilvray, I. D.; Chan, W. C. W. Nanoparticle-Liver Interactions: Cellular Uptake and Hepatobiliary Elimination. *J. Control. Release* **2016**, *240*, 332–348.
- (44) Alexis, F.; Pridgen, E.; Molnar, L. K.; Farokhzad, O. C. Factors Affecting the Clearance and Biodistribution of Polymeric Nanoparticles. *Mol. Pharmaceutics* **2008**, *5*, 505–515.
- (45) Poon, W.; Zhang, Y.-N.; Ouyang, B.; Kingston, B. R.; Wu, J. L. Y.; Wilhelm, S.; Chan, W. C. W. Elimination Pathways of Nanoparticles. *ACS Nano* **2019**, *13*, 5785–5798.
- (46) Rogoff, T. M.; Lipsky, P. E. Role of the Kupffer Cells in Local and Systemic Immune Responses. *Gastroenterology* **1981**, *80*, 854–860.
- (47) Sadauskas, E.; Wallin, H.; Stoltenberg, M.; Vogel, U.; Doering, P.; Larsen, A.; Danscher, G. Kupffer Cells Are Central in the Removal of Nanoparticles from the Organism. Part. *Part. Fibre Toxicol.* **2007**, *4*, 10.
- (48) Walkey, C. D.; Olsen, J. B.; Guo, H.; Emili, A.; Chan, W. C. W. Nanoparticle Size and Surface Chemistry Determine Serum Protein Adsorption and Macrophage Uptake. *J. Am. Chem. Soc.* **2012**, *134*, 2139–2147.
- (49) Poisson, J.; Lemoine, S.; Boulanger, C.; Durand, F.; Moreau, R.; Valla, D.; Rautou, P.-E. Liver Sinusoidal Endothelial Cells: Physiology and Role in Liver Diseases. *J. Hepatol.* **2017**, *66*, 212–227.
- (50) Sørensen, K. K.; McCourt, P.; Berg, T.; Crossley, C.; Le Couteur, D.; Wake, K.; Smedsrød, B. The Scavenger Endothelial Cell: A New Player in Homeostasis and Immunity. *Am. J. Physiol.* **2012**, *303*, R1217–R1230.
- (51) Press, A. T.; Traeger, A.; Pietsch, C.; Mosig, A.; Wagner, M.; Clemens, M. G.; Jbeily, N.; Koch, N.; Gottschaldt, M.; Bézière, N.; Ermolayev, V.; Ntziachristos, V.; Popp, J.; Kessels, M. M.; Qualmann, B.; Schubert, U. S.; Bauer, M. Cell Type-Specific Delivery of Short Interfering RNAs by Dye-Functionalised Theranostic Nanoparticles. *Nat. Commun.* **2014**, *5*, 5565.
- (52) Halamoda-Kenzaoui, B.; Bremer-Hoffmann, S. Main Trends of Immune Effects Triggered by Nanomedicines in Preclinical Studies. *Int. J. Nanomed.* **2018**, *13*, 5419–5431.
- (53) Campbell, F.; Bos, F. L.; Sieber, S.; Arias-Alpizar, G.; Koch, B. E.; Huwyler, J.; Kros, A.; Bussmann, J. Directing Nanoparticle Biodistribution through Evasion and Exploitation of Stab2-Dependent Nanoparticle Uptake. *ACS Nano* **2018**, *12*, 2138–2150.
- (54) Vácha, R.; Martínez-Veracoechea, F. J.; Frenkel, D. Intracellular Release of Endocytosed Nanoparticles upon a Change of Ligand-Receptor Interaction. *ACS Nano* **2012**, *6*, 10598–10605.
- (55) Fleischer, C. C.; Payne, C. K. Nanoparticle Surface Charge Mediates the Cellular Receptors Used by Protein-Nanoparticle Complexes. *J. Phys. Chem. B* **2012**, *116*, 8901–8907.
- (56) Rinkenauer, A. C.; Press, A. T.; Raasch, M.; Pietsch, C.; Schweizer, S.; Schwörer, S.; Rudolph, K. L.; Mosig, A.; Bauer, M.; Traeger, A.; Schubert, U. S. Comparison of the Uptake of Methacrylate-Based Nanoparticles in Static and Dynamic *in Vitro* Systems as Well as *in Vivo*. *J. Control. Release* **2015**, *216*, 158–168.
- (57) Schrottenegger, M.; Leitner, N. S.; Morgese, G.; Ramakrishna, S. N.; Willinger, M.; Benetti, E. M.; Reimhult, E. Polymer Topology Determines the Formation of Protein Corona on Core-Shell Nanoparticles. *ACS Nano* **2020**, *14*, 12708–12718.
- (58) Corbo, C.; Molinaro, R.; Parodi, A.; Toledano Furman, N. E.; Salvatore, F.; Tasciotti, E. The Impact of Nanoparticle Protein Corona on Cytotoxicity, Immunotoxicity and Target Drug Delivery. *Nanomedicine* **2016**, *11*, 81–100.
- (59) Weber, C.; Remzi Becer, C.; Guenther, W.; Hoogenboom, R.; Schubert, U. S. Dual Responsive Methacrylic Acid and Oligo(2-Ethyl-2-Oxazoline) Containing Graft Copolymers. *Macromolecules* **2010**, *43*, 160–167.
- (60) Schuck, P.; Rossmann, P. Determination of the Sedimentation Coefficient Distribution by Least-Squares Boundary Modeling. *Biopolymers* **2000**, *54*, 328–341.
- (61) Grube, M.; Leiske, M. N.; Schubert, U. S.; Nischang, I. POx as an Alternative to PEG? A Hydrodynamic and Light Scattering Study. *Macromolecules* **2018**, *51*, 1905–1916.
- (62) Nischang, I.; Perevyazko, I.; Majdanski, T.; Vitz, J.; Festag, G.; Schubert, U. S. Hydrodynamic Analysis Resolves the Pharmaceutically-Relevant Absolute Molar Mass and Solution Properties of Synthetic Poly(ethylene Glycol)s Created by Varying Initiation Sites. *Anal. Chem.* **2017**, *89*, 1185–1193.
- (63) Lerch, S.; Dass, M.; Musyanovych, A.; Landfester, K.; Mailänder, V. Polymeric Nanoparticles of Different Sizes Overcome the Cell Membrane Barrier. *Eur. J. Pharm. Biopharm.* **2013**, *84*, 265–274.
- (64) Lee, K. D.; Nir, S.; Papahadjopoulos, D. Quantitative Analysis of Liposome-Cell Interactions *In Vitro*: Rate Constants of Binding

and Endocytosis with Suspension and Adherent J774 Cells and Human Monocytes. *Biochemistry* **1993**, *32*, 889–899.

(65) Simões, S.; Slepishkin, V.; Düzgünes, N.; Pedroso de Lima, M. C. On the Mechanisms of Internalization and Intracellular Delivery Mediated by pH-Sensitive Liposomes. *Biochim. Biophys. Acta, Biomembr.* **2001**, *1515*, 23–37.

(66) Rueden, C. T.; Schindelin, J.; Hiner, M. C.; DeZonia, B. E.; Walter, A. E.; Arena, E. T.; Eliceiri, K. W. ImageJ2: ImageJ for the Next Generation of Scientific Image Data. *BMC Bioinf.* **2017**, *18*, 529.

(67) Schindelin, J.; Arganda-Carreras, I.; Frise, E.; Kaynig, V.; Longair, M.; Pietzsch, T.; Preibisch, S.; Rueden, C.; Saalfeld, S.; Schmid, B.; Tinevez, J.-Y.; White, D. J.; Hartenstein, V.; Eliceiri, K.; Tomancak, P.; Cardona, A. Fiji: An Open-Source Platform for Biological-Image Analysis. *Nat. Methods* **2012**, *9*, 676–682.

(68) Cseresnyes, Z.; Kraibooj, K.; Figge, M. T. Hessian-Based Quantitative Image Analysis of Host-Pathogen Confrontation Assays. *Cytometry, Part A* **2018**, *93*, 346–356.

(69) Thomas, L. S. V.; Gehrig, J. Multi-Template Matching: A Versatile Tool for Object-Localization in Microscopy Images. *BMC Bioinf.* **2020**, *21*, 44.

(70) Otsu, N. A Threshold Selection Method from Gray-Level Histograms. *IEEE Trans. Syst. Man Cybern. Syst.* **1979**, *9*, 62–66.

Supporting information

Stealth Effect of Short Polyoxazolines in Graft Copolymers: Minor Changes of Backbone End Group Determine Liver Cell-Type Specificity

Irina Muljajew^{1,2,#}, Sophie Huschke^{3,#}, Anuradha Ramoji^{4,5}, Zoltán Cseresnyés⁶, Stephanie Hoeppener^{1,2}, Ivo Nischang^{1,2}, Wanling Foo³, Jürgen Popp^{4,5}, Marc Thilo Figge^{6,7}, Christine Weber^{1,2}, Michael Bauer³, Ulrich S. Schubert^{1,2,*}, Adrian T. Press^{3,8,*}

Authors contributed equally

¹ Laboratory of Organic and Macromolecular Chemistry (IOMC), Friedrich Schiller University Jena, Humboldtstraße 10, 07743 Jena, Germany

² Jena Center for Soft Matter (JCSM), Friedrich Schiller University Jena, Philosophenweg 7, 07743 Jena, Germany

³ Department of Anesthesiology and Intensive Care Medicine, Jena University Hospital, Am Klinikum 1, 07747 Jena, Germany

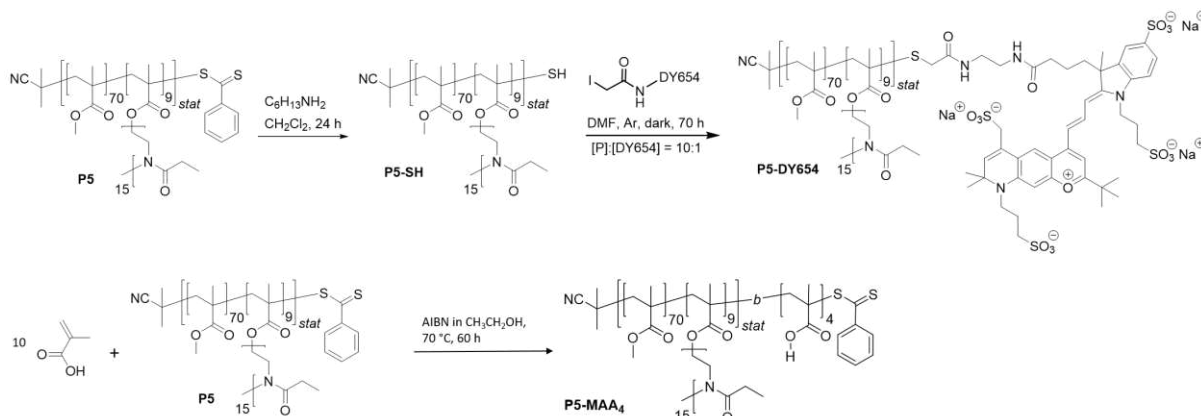
⁴ Institute for Physical Chemistry (IPC) and Abbe Center of Photonics (ACP), Friedrich Schiller University, Jena, Helmholtzweg 4, 07745 Jena, Germany

⁵ Leibniz Institute of Photonic Technology (IPHT) Jena, Member of the Leibniz Research Alliance - Leibniz Health Technologies, Albert-Einstein-Straße 9, 07745 Jena, Germany

⁶ Research Group Applied Systems Biology, Leibniz Institute for Natural Product Research and Infection Biology – Hans Knoell Institute Jena, Adolf-Reichwein-Strasse 23, 07745 Jena, Germany

⁷ Institute of Microbiology, Faculty of Biological Sciences, Friedrich Schiller University Jena, Neugasse 24, 07743 Jena, Germany

⁸ Medical Faculty, Friedrich Schiller University Jena, Bachstraße 18, 07743 Jena, Germany



Scheme SI 1: Schematic representation of the detailed synthesis route towards the PMMA-*graft*-OEtOx₁₅ graft copolymers. Top: **P5-DY654**. DMF: *N,N*-dimethylformamide. Bottom: **P5-MAA₄**. AIBN: Azobisisobutyronitrile.

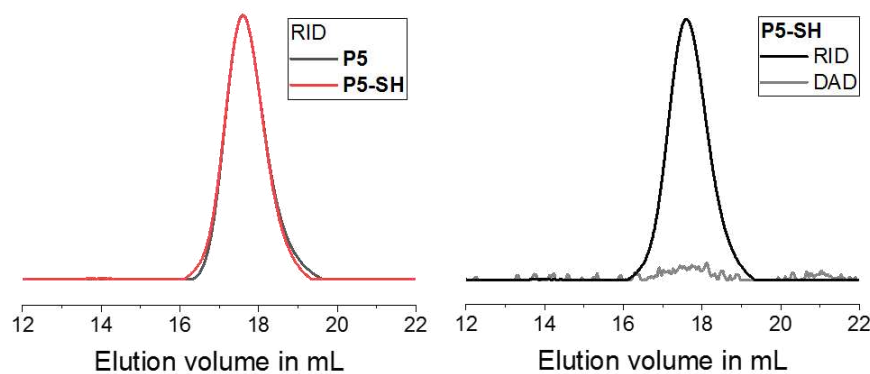


Figure SI 1: Left: SEC elugrams for **P5** and **P5-SH**. Right: SEC elugrams for **P5-SH** with different detectors. (DMAc, LiCl, RID, DAD at 310 to 312 nm). RID: Refractive index detection. DAD: Diode array detection.

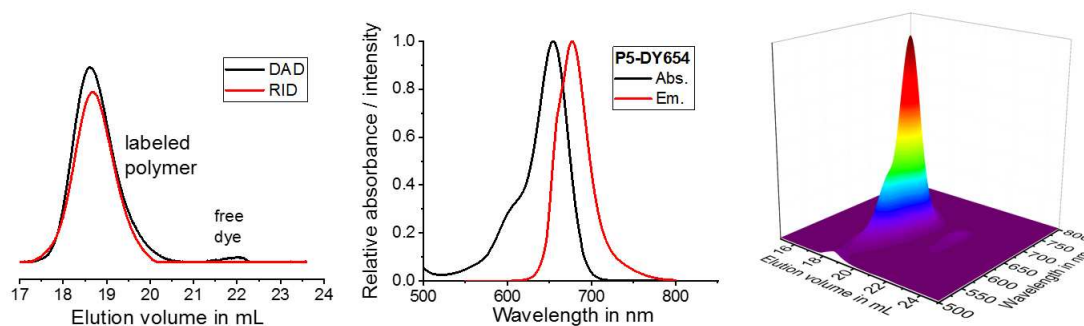


Figure SI 2: Left: SEC elugram of the purified **P5-DY654** (DMAc, LiCl, RID, DAD at 654 to 658 nm). Middle: Absorption and emission spectrum for **P5-DY654** ($c = 2 \text{ mg mL}^{-1}$ in H₂O, $\lambda_{\text{EX}} = 655 \text{ nm}$). Right: 3D-SEC elugram for **P5-DY654** (DAD, DMAc, LiCl). RID: Refractive index detection. DAD: Diode array detection.

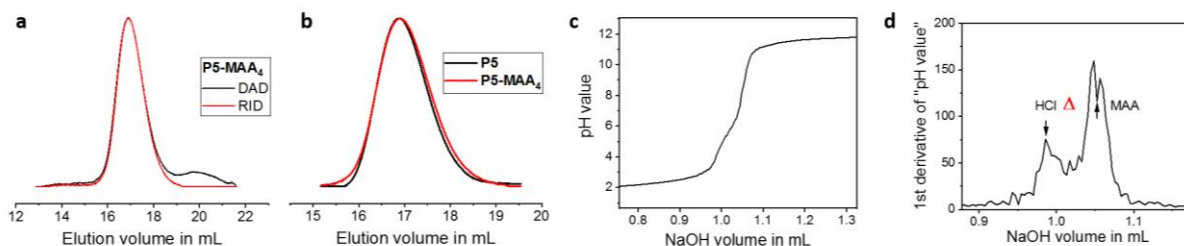


Figure SI 3: (a) SEC elugram of the purified **P5-MAA₄** (DMAc, LiCl, RID, DAD at 310 to 312 nm). (b) Overlay of SEC elugrams of PMMA-*graft*-OEtOx₁₅ **P5** and the chain extended **P5-MAA₄** comprising four methacrylic acid repeating units (DMAc, LiCl, RID). (c) Titration curve of **P5-MAA₄** for determining the degree of polymerization of methacrylic acid (**P5-MAA₄** in aqueous solution and 1 mL of 0.1 M hydrochloric acid against 0.1 M of sodium hydroxide solution). (d) Zoom into the first derivative of the titration curve. Arrows mark the NaOH volume used for the calculation of the **P5-MAA₄** composition.

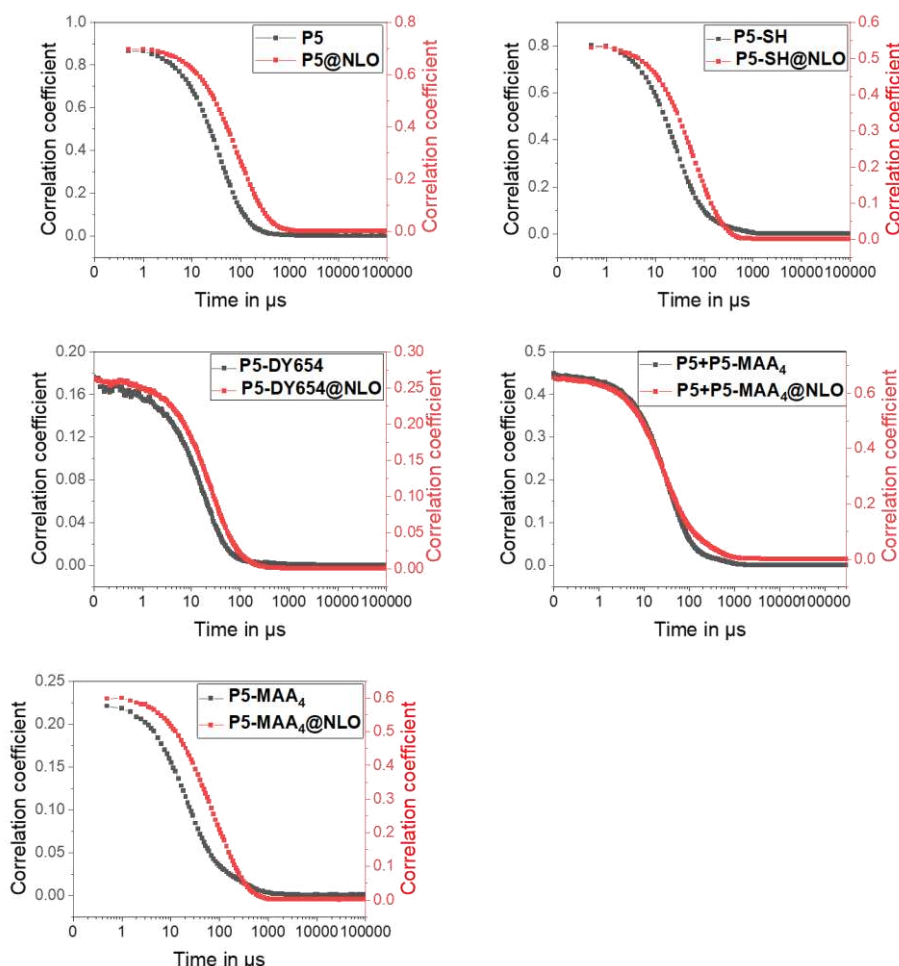


Figure SI 4: Correlation functions of dynamic light scattering measurements of the micelles ($c \approx 1 \text{ mg mL}^{-1}$ in water) Note: DLS measurements of **P5-DY654** were performed applying an optical fluorescence filter.

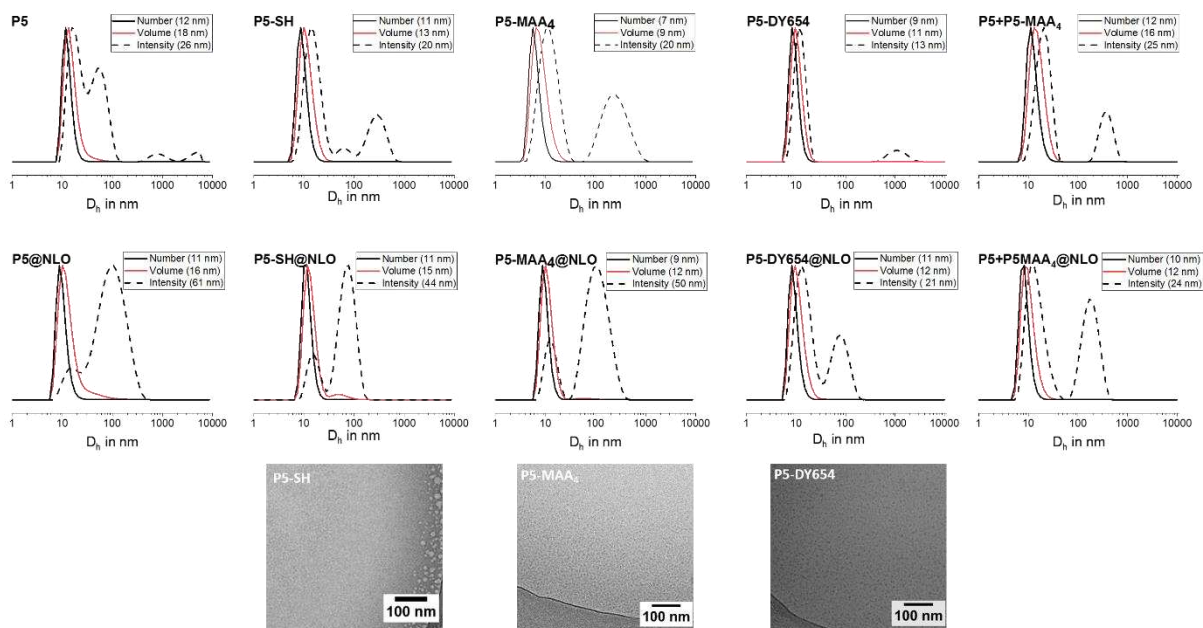


Figure SI 5: Dynamic light scattering plots of the number (solid black line), volume (red line), and intensity (dashed line) distributions ($c \approx 1 \text{ mg mL}^{-1}$ in water) and cryo-TEM image of the unloaded micelles ($c = 10 \text{ mg mL}^{-1}$ in water). Note: DLS measurements of **P5-DY654** were performed applying an optical fluorescence filter.

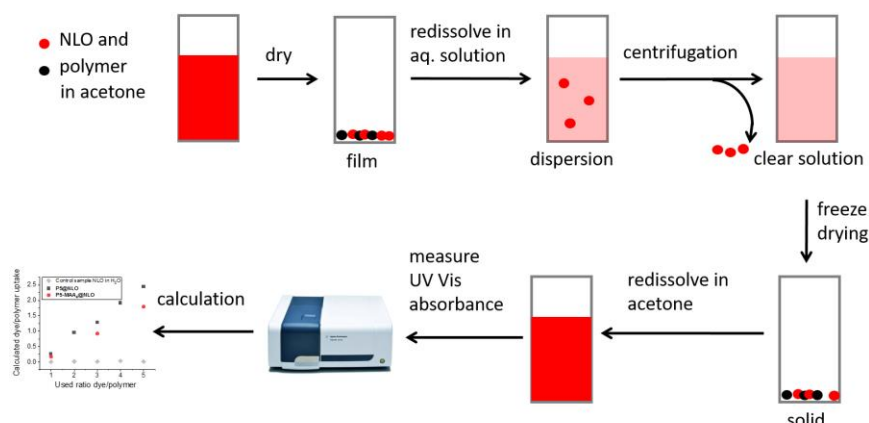


Figure SI 6: General workflow for the determination of the dye uptake.

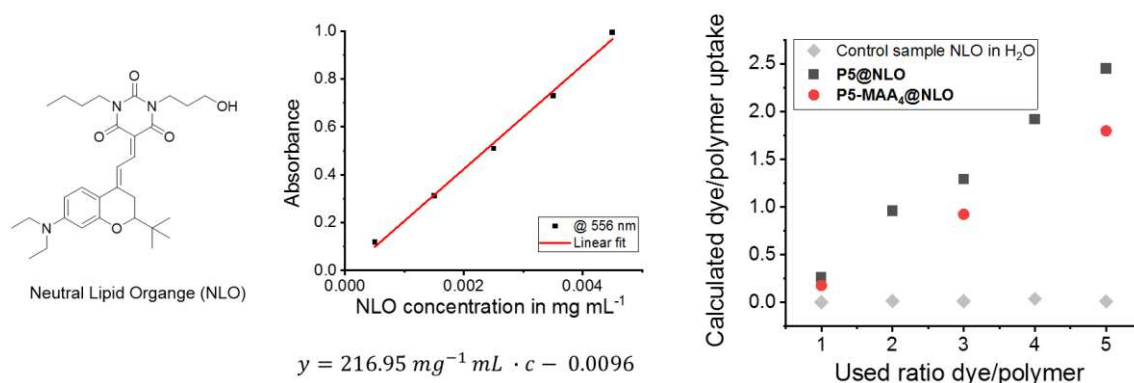


Figure SI 7: Left: Schematic representation of the dye Neutral Lipid Orange (NLO). Middle: Calibration data for the quantification of NLO by UV Vis absorption spectroscopy in acetone at 556 nm. (Graph and linear fit equation). Right: Dye uptake results for **P5@NLO** and **P5-MAA₄@NLO**.

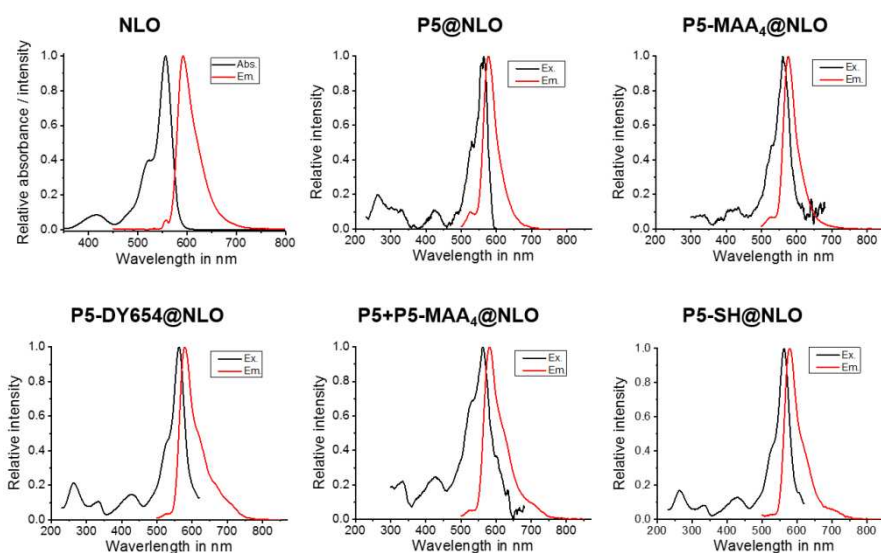


Figure SI 8: Absorption and emission spectra of Neutral Lipid Orange (NLO) in acetone ($c = 10 \mu\text{g mL}^{-1}$) and excitation and emission spectra of NLO containing micelles in deionized water ($c = 50 \mu\text{g mL}^{-1}$). For excitation scans, the emission wavelength was set to 640 nm (**P5-DY654@NLO** and **P5-SH@NLO**), 690 nm (**P5@NLO**), and 700 nm (**P5-MAA₄@NLO** and **P5+P5-MAA₄@NLO**). The emission scans were performed by exciting the dye at 480 nm (bandwidth 5 nm).

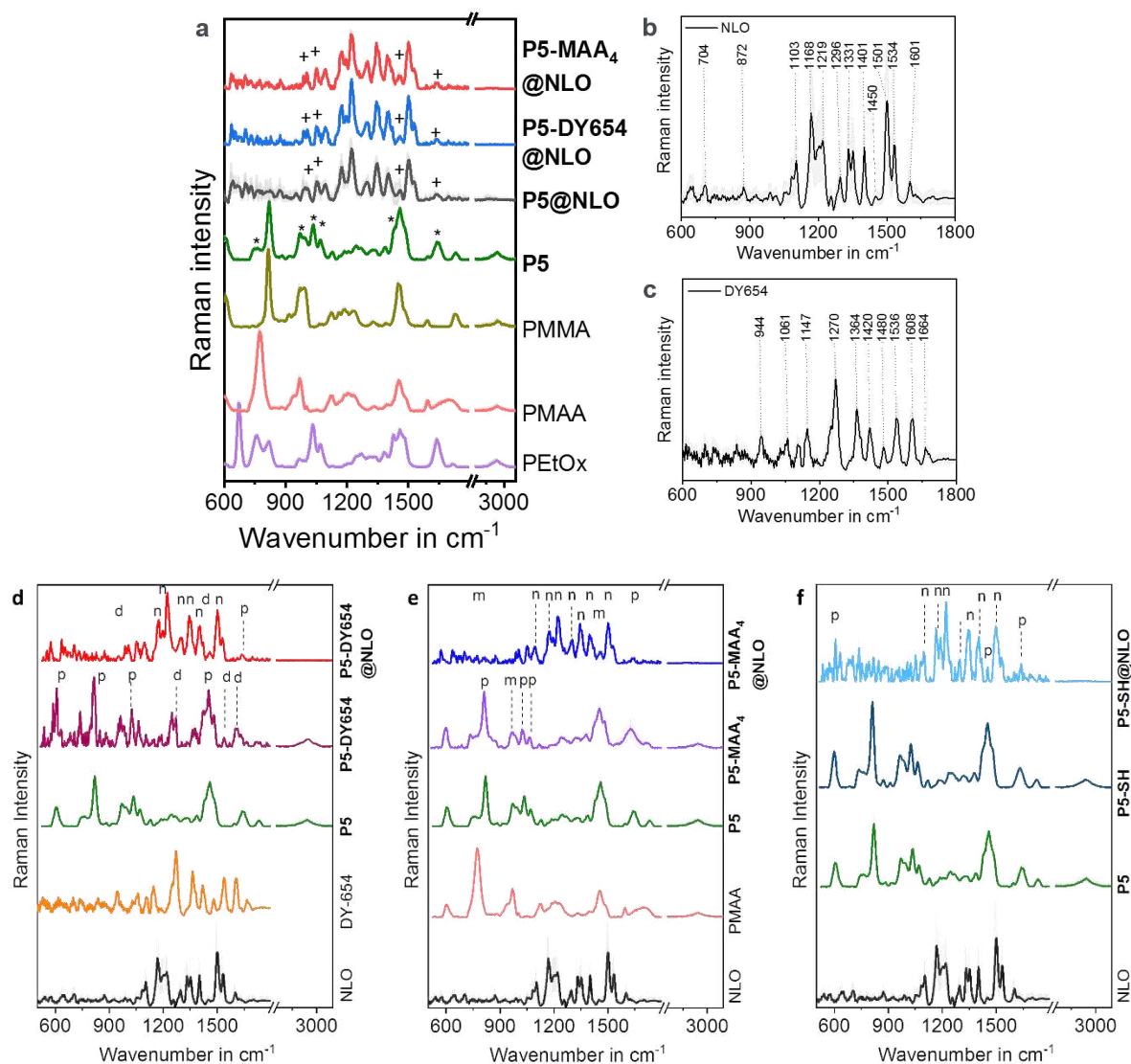


Figure SI 9: Comparison of Raman spectra of the loaded and unloaded micelles with reference samples representing the structural moieties present. Average Raman spectra along with standard deviation (grey shade) are displayed. (a) Raman mean spectra along with standard deviation of different micelles and the neat material. (*) Marks EtOx peaks and (+) marks polymer peaks. (b) & (c) Mean Raman spectra of pure dye NLO and DY654 with standard deviation, respectively. (d) **P5-DY654@NLO**. (e) **P5-MAA₄@NLO**. (f) **P5-SH@NLO**. In the Raman spectra the Raman peaks are labelled as contributions from p = P5, n = NLO, d = DY-654, m = PMAA. The Raman spectra of DY654 were scaled $\times 5$ and the Raman spectra of **P5** are reduced by five times for visualization. All Raman spectra are shifted in the y-axis for the sake of clarity.

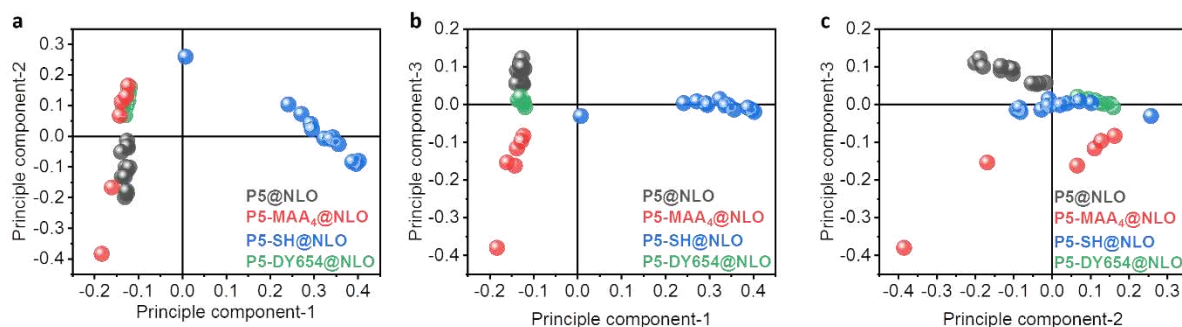


Figure SI 10: Principal component (PC) analysis of the Raman spectra of **P5@NLO**, **P5-DY654@NLO**, **P5-MAA₄@NLO**, and **P5-SH@NLO**. The micelles separation can be visualized in the PC score plot obtained using PC-1, PC-2, and PC-3. (a) PC-1 separates **P5-SH@NLO** from other micelles. (b) PC-1 separates **P5-SH@NLO** from other micelles. PC-3 separates **P5-MAA₄@NLO** from **P5-DY654@NLO** and **P5@NLO**. (c) PC-2 separates **P5@NLO** and **P5-DY654@NLO**. PC-3 separates **P5@NLO** from **P5-MAA₄@NLO**.

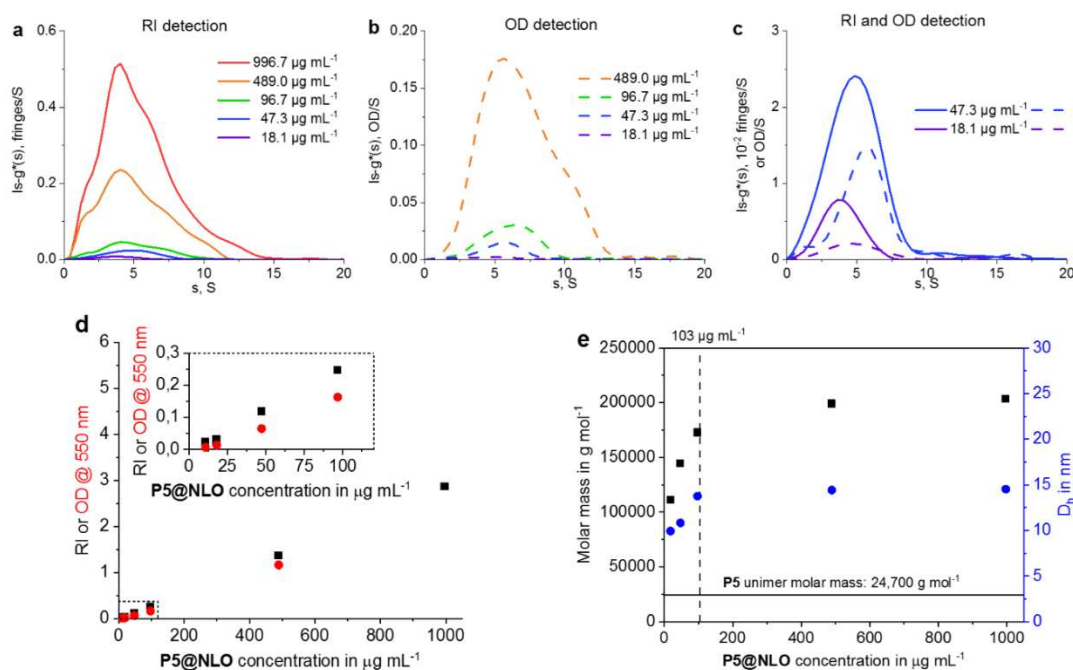


Figure SI 11: Investigation of **P5@NLO** by analytical ultracentrifugation in deionized water at different concentrations. (a-c) Differential distributions of sedimentation coefficients, $Is-g^*(s)$, of **P5@NLO** obtained by sedimentation velocity experiments with different detection modules: (a) Refractive index (RI) detection in terms of interference fringes, (b) absorbance detection in terms of optical density (OD) at $\lambda = 550$ nm, (c) magnified view on the low concentrations. (d) Integrated area of differential distributions of sedimentation coefficients representing the loading concentration of **P5@NLO** shown in (a-c) with an additional zoom into the lower concentration range as inset. (Note: OD at $\lambda = 550$ nm and $c \approx 1$ mg mL⁻¹ led to detector saturation, and the data point was therefore not available). (e) Molar masses and hydrodynamic diameters D_h of **P5@NLO** micelles estimated from the analytical ultracentrifugation data at various concentrations by sedimentation-diffusion analysis and the $c(s)$ model considering effects of diffusion. The horizontal line indicates the determined unimer molar mass.^[1]

Detailed discussion of analytical ultracentrifugation data:

During the *in vivo* experiments, the initial micelle solutions are strongly diluted. 150 μg of loaded micelle were injected per mouse. The average blood volume of the 25 g mouse is 1.46 mL (58.5 mL per kg body weight). This yields an *in vivo* concentration of roughly 103 μg loaded micelle per mL of blood. We hence investigated the stability of the micelles at such concentrations and even below.

A standard method to investigate micellar stability is the encapsulation of fluorescent probes. *E.g.*, the solvatochromic dye pyrene changes its fluorescence spectrum upon encapsulation or release from a micelle and is, therefore, frequently used to determine critical micellization concentrations. However, it is not applicable for micelles that are already loaded with another fluorescent guest, such as NLO. To investigate the integrity of the micelles actually used *in vivo*, *i.e.* **P5@NLO**, analytical ultracentrifugation was applied throughout serial dilution.

Analytical ultracentrifugation allows sedimentation-diffusion analysis and is a powerful method for the determination of absolute molar masses of macromolecular systems. **Figure SI 10** shows differential distributions of sedimentation coefficients, $Is - g^*(s)$, from analytical ultracentrifugation sedimentation velocity data for the **P5@NLO** solutions at different concentrations. Two detection modes were utilized during the experiment, firstly, the universal refractive index (RI) detection in terms of interference fringes (**Figure SI 10a**) as well as the absorbance detection in terms of optical density (OD) at a wavelength of 550 nm (**Figure SI 10b**). While the RI detector could arguably detect both polymeric micelle and cargo, the OD detection allowed the tracing of the NLO dye exclusively and therefore provided evidence for the existence of the dye in the loaded micelle. In both detection modes, relatively broad differential distributions of sedimentation coefficients were monitored. This observation can be considered typical in light of previous analytical ultracentrifugation studies on the P5-based micellar species and further demonstrated that the NLO was an integral component of the micelles throughout the entire concentration range studied.^[1-3] Serial dilution with water demonstrated persistence of the **P5@NLO** micellar structures with an overall decreased abundance down to concentrations between 20 and 50 $\mu\text{g mL}^{-1}$. This range also represented the lower detection limit of **P5@NLO** in the utilized analytical ultracentrifugation setup for both detection modes (**Figure SI 11c**). However, the remaining micellar species still contained the NLO cargo down to the lowest traceable concentration (**Figure SI 11d**). Furthermore,

more detailed modeling of sedimentation velocity data in terms of a sedimentation-diffusion analysis enabled to estimate molar masses and hydrodynamic diameter of the **P5@NLO** micelles. For this purpose, we utilized the modified Svedberg equation for the calculation of molar masses and the corresponding equation for the hydrodynamic diameters, both making use of the translational frictional properties of the micelles.^[4,5] For concentrations above 50 $\mu\text{g mL}^{-1}$, the molar masses were in good agreement with previous studies of unloaded **P5** micelles^[1], and the calculated hydrodynamic diameter D_h of 15 nm was in a similar range as those with DLS and cryo-TEM studies (**Figure 1**). For lower concentrations, calculated molar masses and D_h decreased but remained well above the observed unimer molar mass. Although the accuracy of estimates from experiments at low concentrations is expected to be compromised due to the detection limit and signal-to-noise ratio of the setup available to us, analytical ultracentrifugation data confirmed the persistence of NLO inside the assembled structures at concentrations used *in vivo* and below.

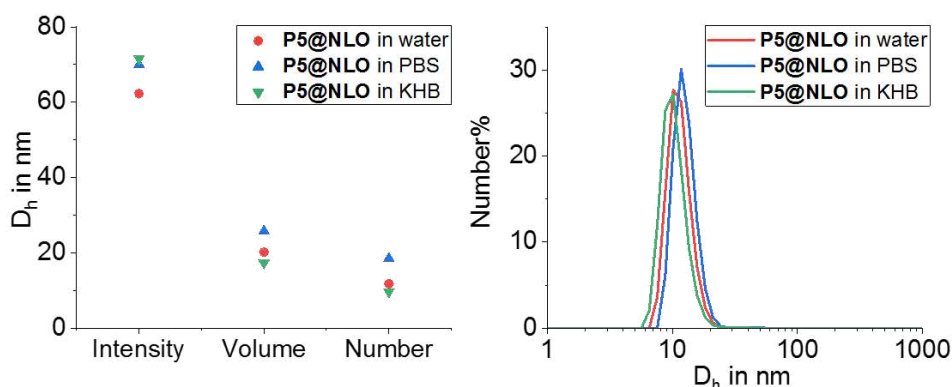


Figure SI 12: Characterization of **P5@NLO** in deionized H₂O, PBS, and KHB (T = 37 °C, c = 1 mg mL⁻¹) by DLS. Left: Resulting average hydrodynamic diameters for intensity, volume and number weighted distributions. Right: Number-weighted hydrodynamic diameter distribution.

A detailed discussion of P5@NLO micelles in two physiological buffers at 37 °C

The dye encapsulation of NLO into **P5** was additionally performed by the thin film method in commonly used buffers such as phosphate-buffered saline (PBS, pH 7.4) and Krebs-Henseleit buffer (KHB, modified with 2 g L⁻¹ glucose). The latter one resembles a composition of ions which is close to the one found in the blood. The summarized results are shown in **Figure SI 11**. The intensity-based DLS results obtained at 37 °C are coherent with the initial data presented in the main manuscript (**Figure 1**), as that the formation of second aggregated species was observed with a D_h of \approx 100 nm, irrespective of the media (or polymer) used. However, the number weighted distribution is more relevant to the *in vivo* data as the intensity of scattered light scales with the radius (or the diameter) to the power of six. Hence, it was concluded that similar micelles with $D_h \leq 14$ nm were predominantly present irrespective of the medium, confirming the stability of the micelles in physiologically relevant buffers.

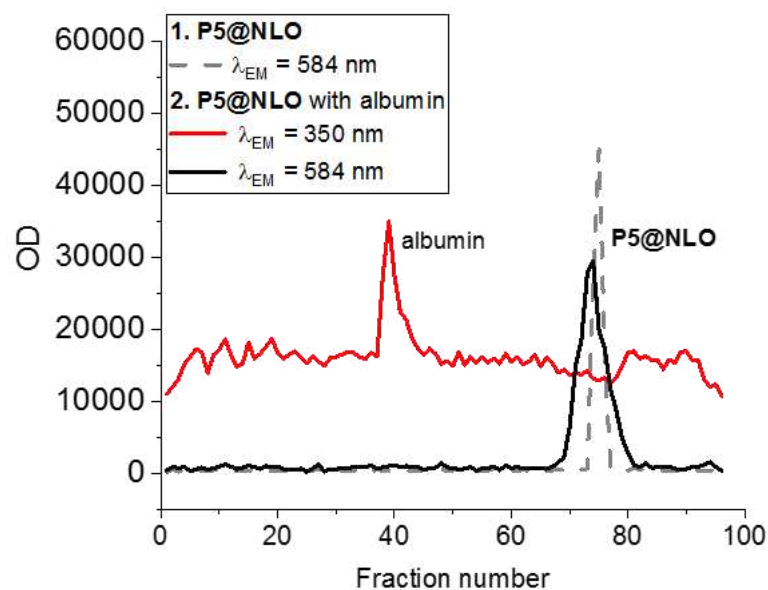


Figure SI 13: Results of the free-flow electrophoresis in optical density values (OD). First sample: **P5@NLO** (0 V, dotted line $\lambda_{EM} = 584$ nm). Second sample: **P5@NLO** with albumin (1000 V, 5 min, red line: $\lambda_{EM} = 350$ nm representative of albumin, black line: $\lambda_{EM} = 584$ nm representative of NLO).

A detailed discussion of Free Flow Electrophoresis (FFE)

To evaluate the persistence of NLO inside the micelles in the presence of proteins, FFE was applied. FFE is a matrix-free electrophoretic technique based on the separation in a lateral electrical field toward a continuous laminar flow of an aqueous medium. At the end of the separation chamber, the separated sample is collected by fractionation outlet tubes and transferred to microtiter plates, subsequently analyzed with a plate reader. FFE was performed with **P5@NLO** micelles and albumin as well as with a mixture of both components at a pH value of 7.5. The fractions were collected in a 96-well plate for all samples and subsequently analyzed with a Tecan reader in a fluorescence top reading mode at two emission wavelengths (350 nm corresponding to albumin and 584 nm corresponding to the NLO, respectively). The results are summarized in **Figure SI 13**. First, the **P5@NLO** was measured to set a reference point as no electric field was applied.

Further, the mixture of **P5@NLO** with albumin was measured with an electric field of 1000 V. A separation was observed for albumin. The uncharged **P5@NLO** showed a slight broadening but no significant motion in comparison to the reference sample. However, albumin moved toward the anode as it is negatively charged at a pH value of 7.5 and was collected at lateral fraction numbers around 40.

Further, these fractions showed no NLO emission at $\lambda_{EM} = 584$. When albumin and **P5@NLO** were measured individually at the same measurement conditions, the same separation behavior was observed (data not shown). The fluorescence signals of albumin and NLO were not detectable together in any of the collected fractions. The overall results hence clearly confirmed a) the retention of NLO within the **P5** micelle and b) the fact that albumin did not interact with the loaded **P5@NLO** micelle at the measurement conditions.

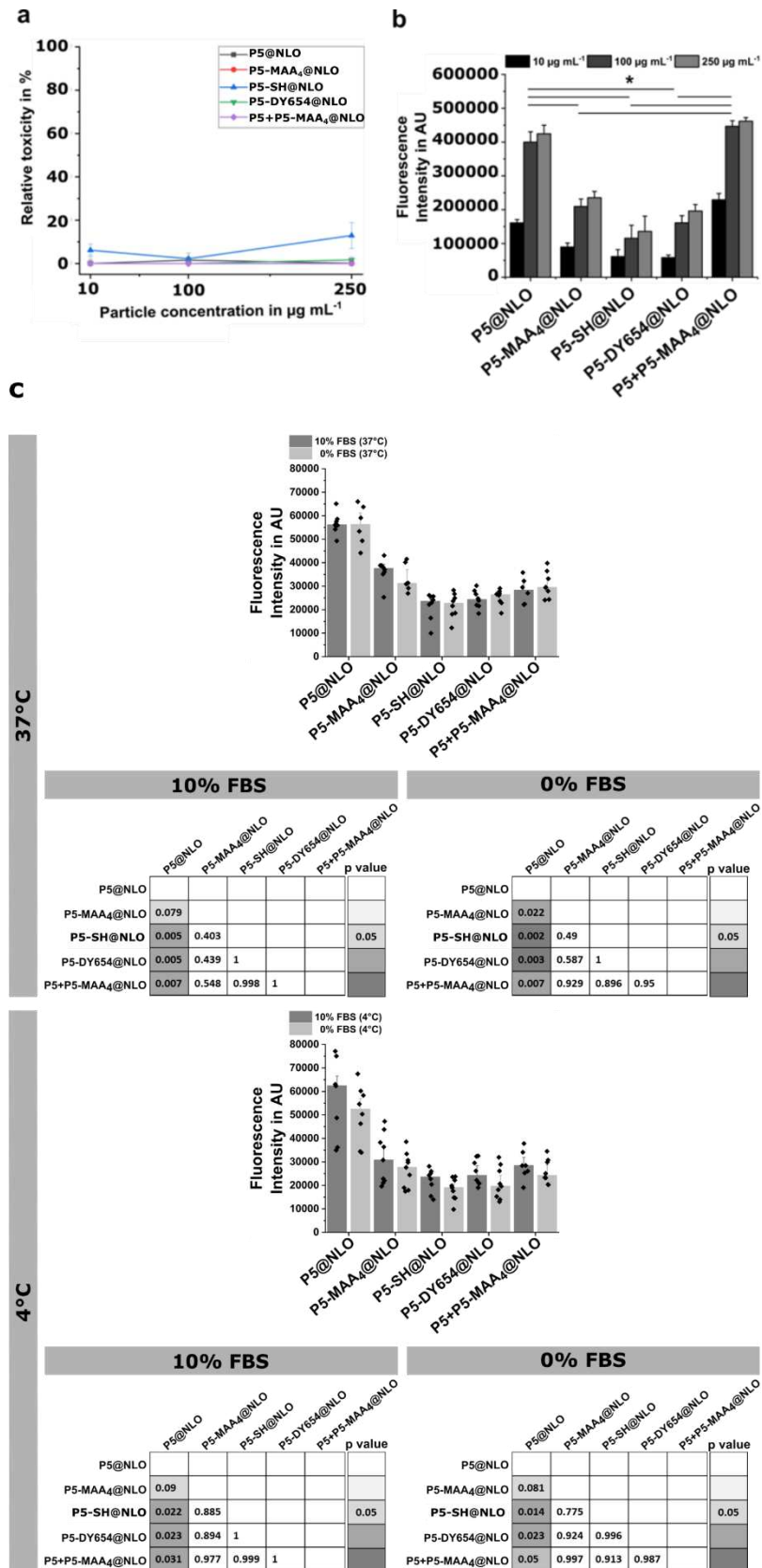


Figure SI 14: (a) Toxicity was assessed in mouse embryonic fibroblasts (MEFs) by quantifying lactate dehydrogenase activity from the supernatant 24 h after the addition of various micelles. This assay indicates toxicity utilizing membrane damage. The experiment was performed at least three times independently in triplicates; data are depicted as mean + SD, one-way ANOVA between groups, * $p < 0.05$. **(b)** Uptake of various concentrations of NLO-loaded micelles in MEF cells after 24 h

incubation. Uptake was quantified by flow cytometry. The experiment was performed at least three times independently in triplicates; data are depicted as mean + SD, one-way ANOVA between groups, * $p < 0.05$. (c) Flow cytometry analysis of MEFs, incubated 10 minutes with $50 \mu\text{g mL}^{-1}$ NLO loaded micelles, at 4°C or 37°C , under serum-free conditions and in media supplemented with 10% FBS. Heatmap of p-values from a parametric one-way ANOVA between groups with a Tukey post-hoc test for pairwise differences, $n=3$.

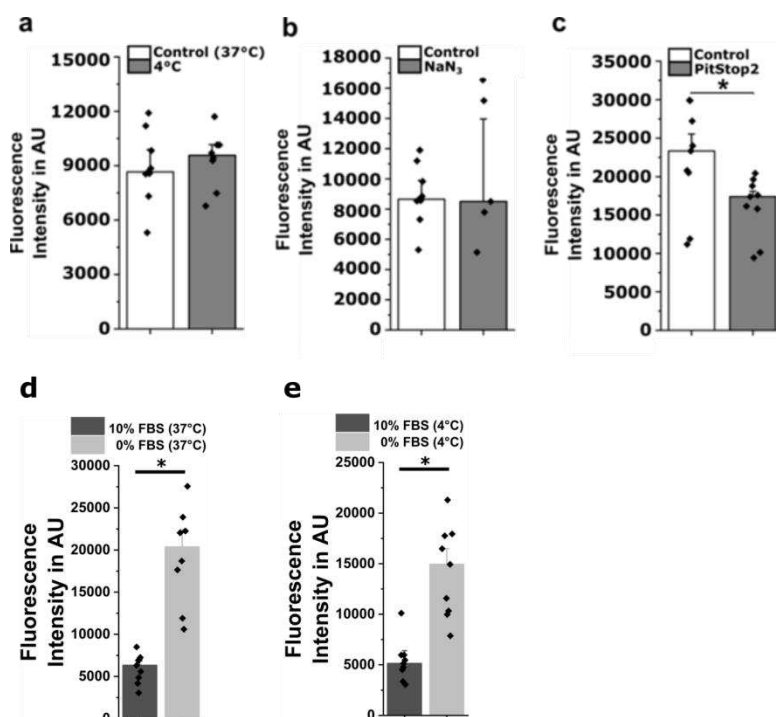


Figure SI 15: (a-c) Uptake of **P(MMA-co-MAA)@NR** in the presence of different inhibitors determined by flow cytometry. The experiments were performed at least three times independently in triplicates; data are depicted as median + SD, individual values are depicted as dots, unpaired t-test control vs. treatment, * $p < 0.05$. (a) Uptake of **P(MMA-co-MAA)@NR** at 4°C . (b) Uptake of **P(MMA-co-MAA)@NR** in the presence of $10 \text{ mmol L}^{-1} \text{NaN}_3$. (c) Uptake of **P(MMA-co-MAA)@NR** in the presence of $30 \mu\text{mol L}^{-1}$ Pitstop 2. (d) Uptake of **P(MMA-co-MAA)@NR** at 37°C in media containing 10% FBS or 0% FBS. (e) Uptake of **P(MMA-co-MAA)@NR** at 4°C in media containing 10% FBS or 0% FBS. No statistical difference between control and treatment for a and b.

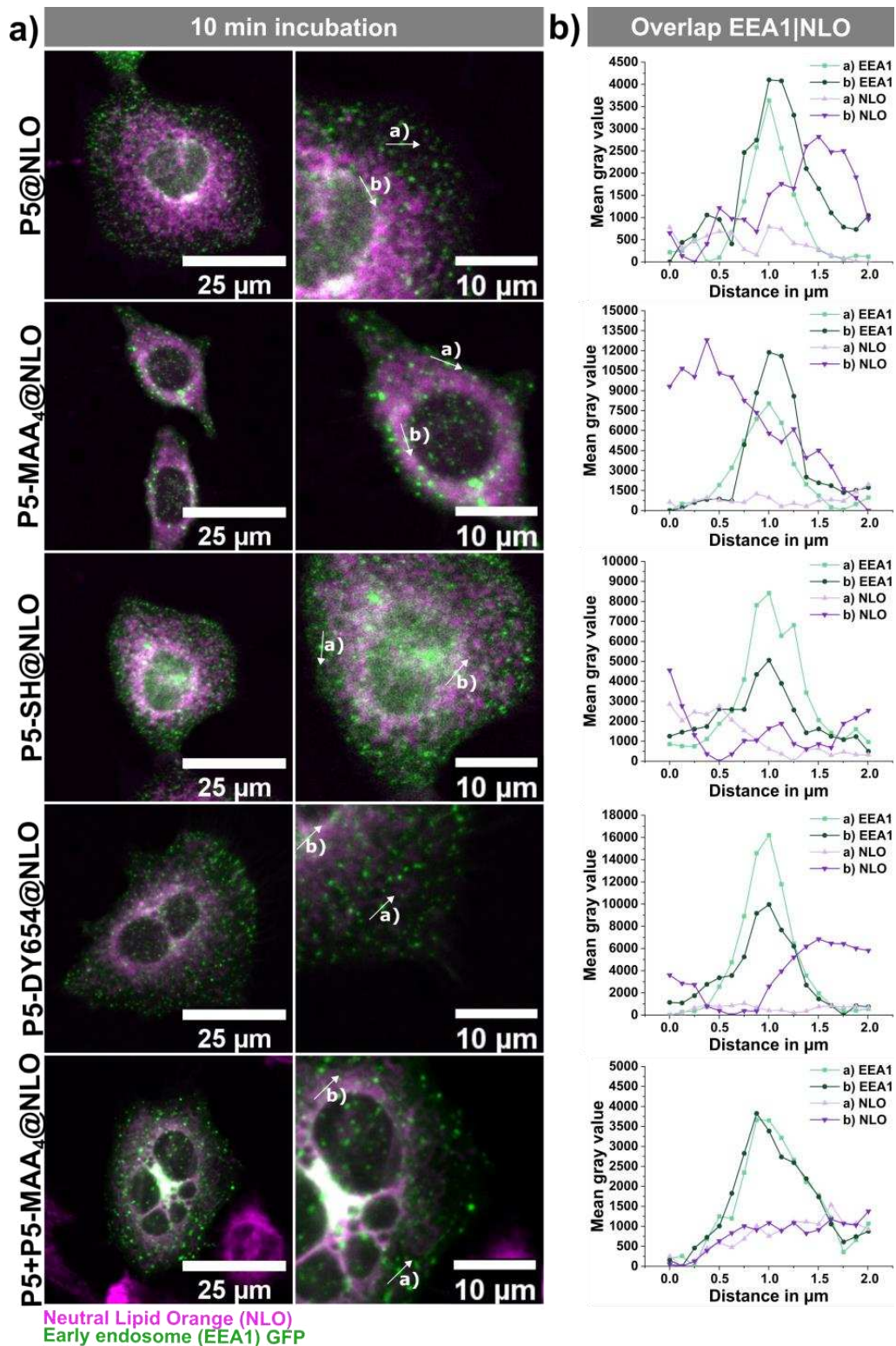


Figure SI 16: Early endosome staining and micellar uptake *in vitro*. (a) Live cell imaging of early endosome (green) stained MEFs, incubated 10 minutes with 50 $\mu\text{g mL}^{-1}$ NLO loaded micelles NLO (magenta), (b) EEA1-GFP, and NLO intensity profiles (region of interest, ROI) with each line profile crossing the center of GFP-stained endosomes. Representative line-profiles for EEA1 positive endosomes distant (a) or close (b) to the nuclei are depicted. NLO accumulation does not specifically accumulate in EEA1 favorable structures. The conclusion is based on 5 to 10 endosomes analyzed per micelle leading to similar results.

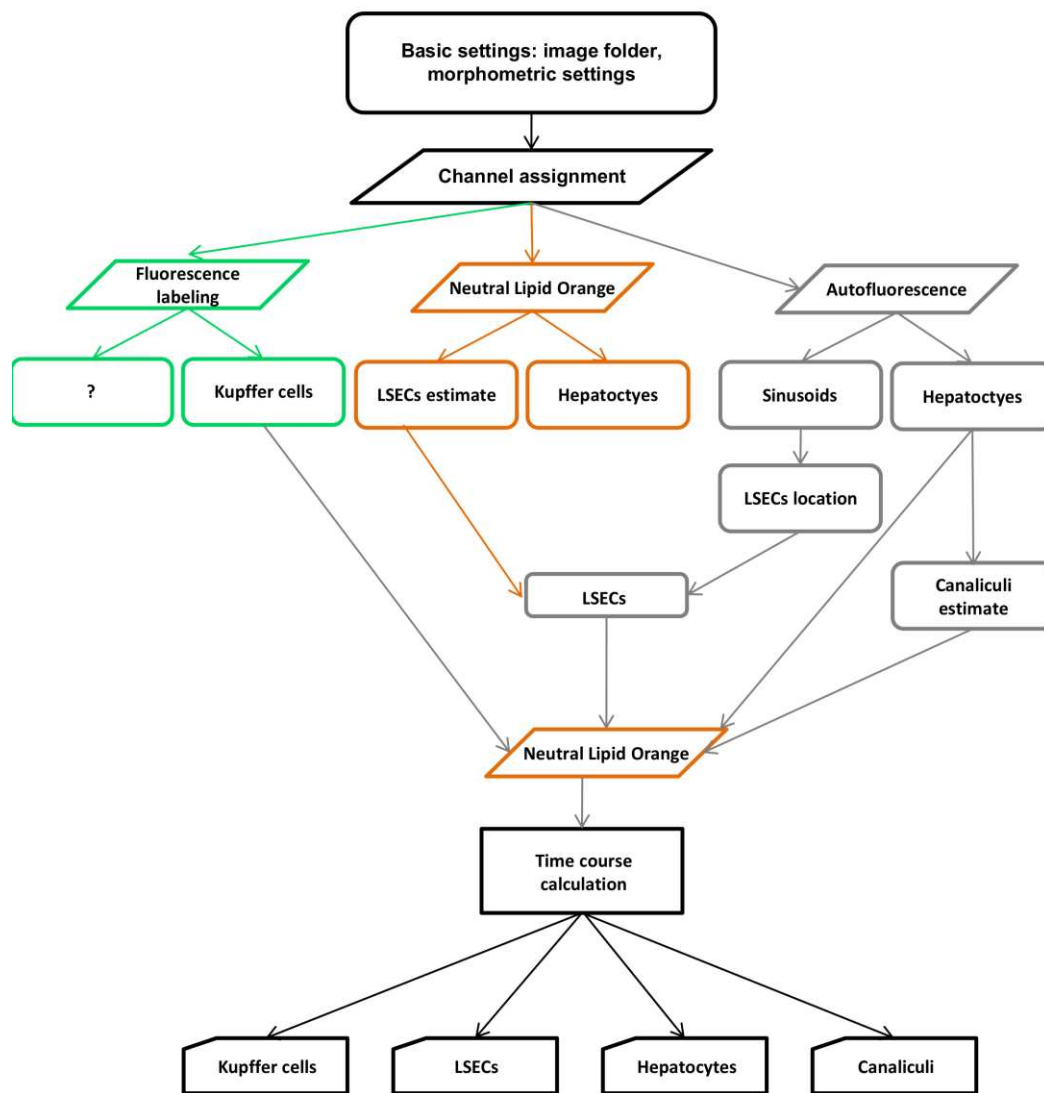


Figure SI 17: Flowchart of the automated image processing algorithm. The workflow begins with gathering basic information, including the location of the images, the targeted size range of the various components (hepatocytes, LSECs, Kupffer cells, possible other cell types with fluorescence labeling), and the standard width of the canaliculi. The images were read into memory from the microscope's native CZI image format, which contained all necessary information about spatial and temporal resolution, as well as the channel layout. The channels were then separated to identify fluorescently labeled (green block; e.g., Kupffer cells, but also any other cell type, marked with “?” in the alternative output from the fluorescence labeling block), NLO-marked (orange block; LSECs, hepatocytes) and autofluorescent (dark grey block; sinusoids, hepatocytes) objects in the images. The localization of the LSECs was confirmed by using the autofluorescence signal from the sinusoid walls (arrow from autofluorescent sinusoids to LSECs location and then LSECs). All identified objects were then measured in the NLO channel, providing the mean fluorescence intensity for each segmented cell of all types. This information was acquired from the time sequence of the NLO channel data, thus providing the kinetics of the cargo uptake by all identified objects (bottom row of cards). See the entire workflow in real-time in **Supplementary Videos SI 4 and SI 5**.

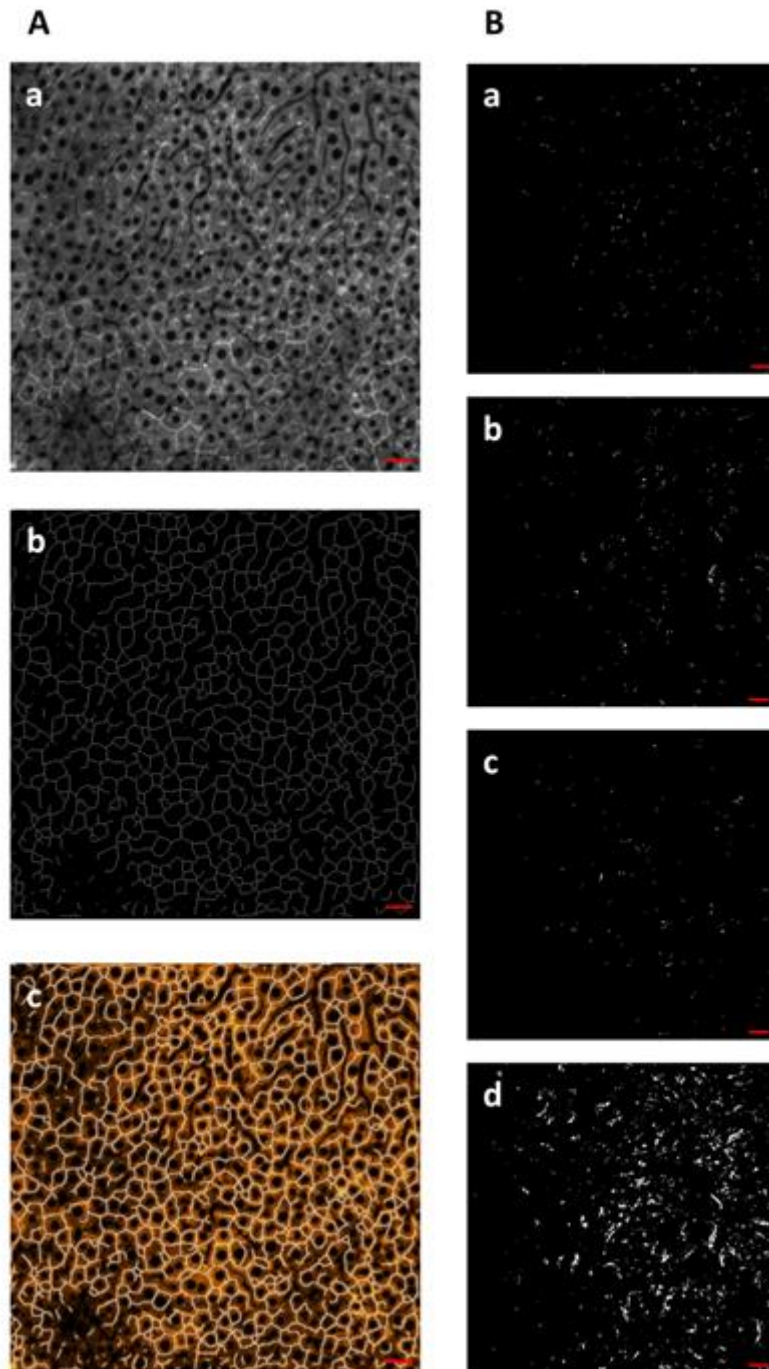


Figure SI 18: Identification of canaliculi and LSECs in live liver tissue. **(A)** The canaliculi location was approximated as the midline between two rows of hepatocytes in the autofluorescence image. This approach was validated by overlapping the NLO channel signal near the end of the time series experiment **(Aa)** with the midline-based canaliculi location **(Ab)**, revealing good agreement with the NLO-highlighted lines **(Ac)**. In order to identify LSECs, images were collected at each time point using the NLO channel, and bright objects corresponding to the LSECs morphometry were segmented. Here the images from an experiment acquired at frame numbers 14, 24, and 34 are shown in **(Ba)**, **(Bb)**, and **(Bc)**, respectively. **(Bd)** shows the maximum intensity projection of all time points, which draws the actual distribution of all LSECs. See the actual time series of this experiment in **Supplementary Video SI 2**. Scale bars 30 μm .

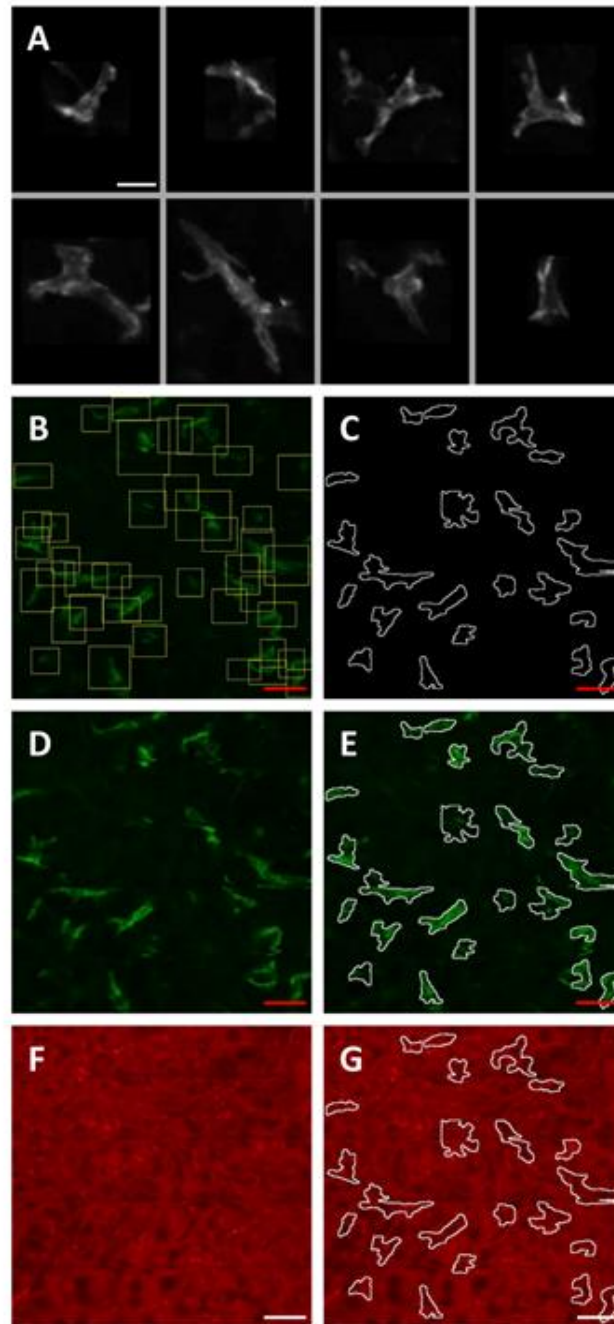


Figure SI 19: Identification of the Kupffer cells in live liver tissue. Rectangular sub-areas occupied by Kupffer cells were first identified by template matching based on the green fluorescence labeling signal (see Methods). **(A)** Eight examples of the 35 templates were extracted manually from a random set of images showing labeled Kupffer cells. **(B)** Example of an image of labeled Kupffer cells with the matching templates marked with yellow rectangular regions. **(C)** The Kupffer cells in each of these rectangles were identified *via* preprocessing, auto thresholding and postprocessing, resulting in the outlines of individual cells. Drawing the final cell regions over the green channel **(D, E)**, as well as the NLO channel **(F)**, produced the fluorescence measures of the NLO cargo in the individual Kupffer cells within each Kupffer cell region **(G)**. See the workflow in real-time in **Supplementary Video SI 5**. Scale bars: **(A)**: 10 μm , **(B)**-**(G)**: 30 μm .

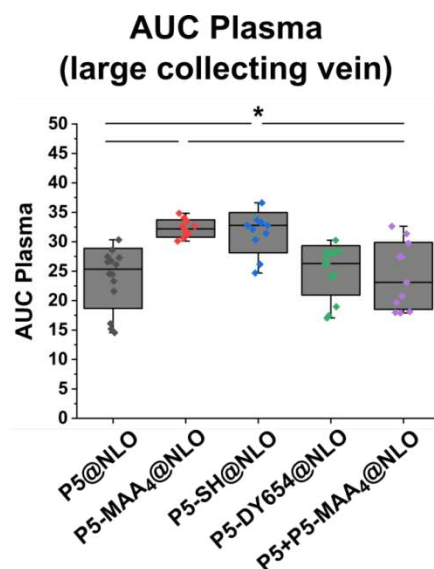


Figure SI 20: The area under the curve (AUC) was calculated from the plasma disappearance rate measured in the large collecting vein in the liver. Data are depicted as median (line), box plots indicate 25, 75 percentile, whiskers reflect standard deviation, one-way ANOVA between groups, Tukey test, * $p < 0.05$. 5 areas ($425 \mu\text{m}^2$ each) of each liver were analyzed from 3 to 4 mice per group.

Supplementary Videos

Supplementary Video SI 1: The identification of canaliculi as midlines between rows of hepatocytes. The first half of the video shows a time series experiment with the estimated location of the canaliculi marked with black lines in the NLO image. In the second half of the video, only the canaliculi area is shown during the same time series.

Supplementary Video SI 2: The segmentation of LSECs *via* population sampling. The video shows the NLO channel signal after having been processed by our Fiji-based custom-written image analysis software. The objects that remain in these time series images are selected based on their similarity to the morphometric characteristics of LSECs and their location by the walls of the sinusoids. LSECs are identified at each time point, and the binary masks corresponding to the individual cells are shown in a time series. At the end of the video, the result of the maximum intensity projection (MIP) calculation is shown to signify the entire population of segmented LSECs in this experiment. The formation of tubular structures can be observed in the MIP image, corresponding to the specific localization of the LSECs near the sinusoid walls.

Supplementary Video SI 3: The location of hepatocyte nuclei and intercellular space. The video shows the time series of the segmentation results targeting the dark areas of the autofluorescence images. These dark regions underwent morphological filtering to identify the typical shapes of the nuclei and the intercellular space (mostly sinusoids).

Supplementary Video SI 4: Real-time screen capture video of the leading image analysis software in action. The program is a Fiji macro written in ImageJ 1.52p. The video shows all steps mentioned in the Methods section "Image analysis" and shown in **Supplementary Videos SI 1 to SI 3**. The workflow corresponds to the graph in **Supplementary Figure SI 17**.

Supplementary Video SI 5: Real-time screen capture of the second image analysis program. This software is designed to segment Kupffer cells in the specific labeling (green) channel and to measure the NLO fluorescence in the orange channel within the segmented areas corresponding to individual macrophages. The workflow depicted here corresponds to **Supplementary Figure SI 17**.

Supplementary Video SI 6: The video depicts representative time series (1 frame per minute beginning at 1 min before injection) from the imaging of different micelles (indicated in the video). Circulating immune cells, *i.e.*, lymphocytes (T-cells, B-cells, Natural Killer (NK) cells) and leukocytes (Monocytes, Granulocytes, Mast cells), are recognized by intravital microscopy due to their specific location in the sinusoids and their mobility, *i.e.*, their movement in time-lapse microscopy. Lymphocytes become only visible in fluorescence intravital microscopy through staining *e.g.* by the encapsulated NLO cargo.

Supporting References

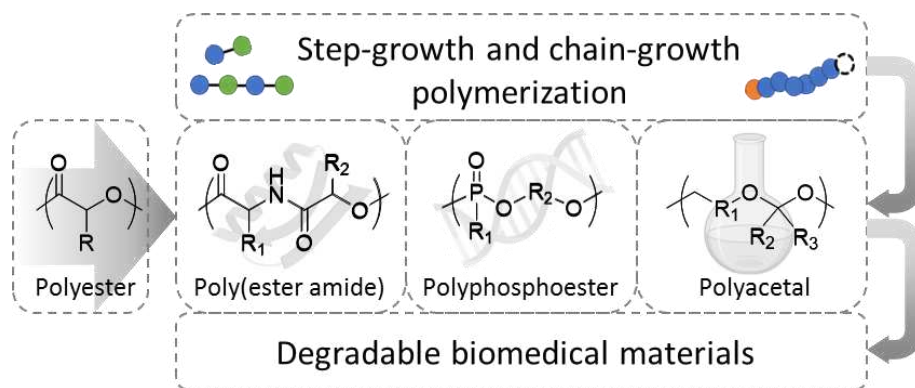
- [1] Muljajew, I.; Weber, C.; Nischang, I.; Schubert, U. PMMA-g-OEtOx Graft Copolymers: Influence of Grafting Degree and Side Chain Length on the Conformation in Aqueous Solution. *Materials* **2018**, *11*, 528.
- [2] Cinar, G.; Englert, C.; Lehmann, M.; Nischang, I. *In Situ*, Quantitative Assessment of Multifunctional Nanoscale Drug Delivery Systems in Human Serum. *Anal. Chem.* **2020**, *92*, 7932-7939.
- [3] Cinar, G.; Englert, C.; Schubert, U. S.; Nischang, I. Salient Features of Medical Nanoparticles in Biological Fluids from an Analytical Ultracentrifuge. *Nanoscale* **2020**, *12*, 22462-22466.
- [4] Grube, M.; Leiske, M. N.; Schubert, U.S.; Nischang, I. POx as an Alternative to PEG? A Hydrodynamic and Light Scattering Study. *Macromolecules* **2018**, *51*, 1905-1916.
- [5] Nischang, I.; Perevyazko, I.; Majdanski, T.; Vitz, J.; Festag, G.; Schubert, U. S. Hydrodynamic Analysis Resolves the Pharmaceutically-Relevant Absolute Molar Mass and Solution Properties of Synthetic Poly(ethylene Glycol)s Created by Varying Initiation Sites. *Anal. Chem.* **2017**, *89*, 1185-1193.

Appendix - Publication 1

Recent advances in degradable synthetic polymers for biomedical applications
- Beyond polyesters

M. Dirauf, I. Muljajew, C. Weber, U. S. Schubert

Prog. Polym. Sci. **2022**, *129*, 101547.



Note: The status of this publication was “*under revision*” at the time of thesis submission.

The paper was published in the meantime, hence, the updated version is attached in the following.



Recent advances in degradable synthetic polymers for biomedical applications - Beyond polyesters



Michael Dirauf^{a,b}, Irina Muljajew^{a,b}, Christine Weber^{a,b}, Ulrich S. Schubert^{a,b,*}

^aLaboratory of Organic and Macromolecular Chemistry (IOMC) Friedrich Schiller University Jena, Humboldtstr. 10, 07743 Jena, Germany

^bJena Center for Soft Matter (JCSM), Friedrich Schiller University Jena, Philosophenweg 7, 07743 Jena, Germany

ARTICLE INFO

Article history:

Received 13 December 2021

Revised 1 April 2022

Accepted 6 April 2022

Available online 11 April 2022

Keywords:

Poly(ester amide)s

Polyphosphoesters

Polyacetals

Polyketals

Step-growth polymerization

Ring-opening polymerization

Degradable polymers

ABSTRACT

Polyesters have been studied intensely over the last few decades and proved to be suitable for a wide range of applications. Despite all benefits, drawbacks such as e.g. the acidification of the microenvironment during degradation, represent ongoing issues. Therefore, the necessity of developing alternative materials in e.g. drug delivery systems represents an emerging field in polymer science. In that regard, this review covers the latest developments of (bio)degradable synthetic polymers beyond polyesters. In spite of seemingly different on first glance, poly(ester amide)s, polyphosphoesters as well as polyacetals have recently experienced a boost with respect to the development of new synthetic routes that enable access to more tailored materials. The successful synthesis and characterization of the new materials represent fundamental premises for the understanding of structure-property relationships which, in turn, form the basis for the development of reasonable tailored pharmacopolymers. The review hence scrutinizes the recent synthetic developments of these polymer classes throughout the last 10 years, putting them into the context of applications that have arisen for less novel materials.

© 2022 The Authors. Published by Elsevier B.V.

This is an open access article under the CC BY license (<http://creativecommons.org/licenses/by/4.0/>)

Abbreviations

¹H NMR Proton nuclear magnetic resonance

ADMET Acyclic diene metathesis

AL Aldehyde

API Active pharmaceutical ingredient

ATRP Atom-transfer radical polymerization

Boc *tert*-Butyloxycarbonyl protective group

*b*PEI Branched poly(ethylene imine)

CA Cyclic acetal

CAGW Cys-Ala-Gly-Trp

Cbz Benzyloxycarbonyl protection group

CE Cyclic ether

CIM Cyclic imidate mechanism

CM Comonomer

cPE Cyclic phosphoester monomer

CREDV Cys-Arg-Glu-Asp-Val

CROP Cationic ring-opening polymerization

Cryo-TEM Cryo-transmission electron microscopy

CTA Chain transfer agent

DBU 1,8-Diazabicyclo(5.4.0)undec-7-ene

D_h Hydrodynamic diameter

DLS Dynamic light scattering

DMAEMA 2-*N,N*-Dimethylaminoethyl methacrylate

DMP 2,2-Dimethoxy propane

DO Diol

DOTAP *N*-[1-(2,3-Dioleoyloxy)propyl]-*N,N,N*-trimethylammonium methylsulfate

DOX Doxorubicin

DP Degree of polymerization

DPP Diphenylphosphoric acid

DTBP 2,6-Di-*tert*-butylpyridine

ECS Endothelial cells

ESI MS Electrospray ionization mass spectrometry

EtAlCl₂ Ethylaluminum dichloride

EtSO₃H Ethanesulfonic acid

Fmoc Fluorenylmethoxycarbonyl

GlcNAc *N*-Acetylglucosamine

HAE Hemiacetal ester

HCPT 10-Hydroxycamptothecin

HPLC High performance liquid chromatography

HSAB Hard and soft acids and bases

HUVEC Human vascular endothelial cells

IBEA 1-(Isobutoxy)ethyl acetate

IBU Ibuprofen

IBVE Isobutyl vinyl ether

* Corresponding author.

E-mail address: ulrich.schubert@uni-jena.de (U.S. Schubert).

IUPAC	International union of pure and applied chemistry
KE	Ketone
LCST	Lower critical solution temperature
LNCaP	Lymph node carcinoma of the prostate
IPE	Linear phosphoester monomer
IPEI	Linear poly(ethylene imine)
M/cat.	Monomer to catalyst ratio
M/I	Monomer to initiator ratio
MALDI MS	Matrix-assisted laser-desorption mass spectrometry
MD	Morpholine-2,5-dione
mPEG	α -Methoxy-poly(ethylene glycol)
N/P	Nitrogen to phosphorous ratio
NADPH	Nicotinamide adenine denucleotide phosphate
NHS	<i>N</i> -Hydroxyl succinimide
OTf	Triflate
PBS	Phosphate-buffered saline
PCL	Poly(ϵ -caprolactone)
PDLA	Poly(D-lactide)
pDNA	Plasmid DNA
PDO	<i>p</i> -Dioxanone
PEA	Poly(ester amide)
PEG	Poly(ethylene glycol)
PEGMA	Poly(ethylene glycol) methacrylate
PEI	Poly(ethylene imine)
PEO	Poly(ethylene oxide)
PETox	Poly(2-ethyl-2-oxazoline)
PLA	Poly(lactide)
PLGA	Poly(lactide-co-glycolide)
PLLA	Poly(L-lactide)
PMD	Poly(morpholine-2,5-dione)
PMDETA	N^1 -[2-(Dimethylamino)ethyl]- N^1,N^3,N^3 -trimethylethane-1,2-diamine
PNVP	Poly(<i>N</i> -vinyl pyrrolidone)
POx	Poly(2-oxazoline)
PPDO	Poly(<i>p</i> -dioxanone)
PPE	Polyphosphoester
PPEGMA	Poly(poly(ethylene glycol) methacrylate)
PTX	Paclitaxel
REDV	Arg-Glu-Asp-Val
RGD	Arg-Gly-Asp
RGDS	Arg-Gly-Asp-Ser
ROMP	Ring-opening metathesis polymerization
ROP	Ring-opening polymerization
SEC	Size-exclusion chromatography
SEM	Scanning electron microscopy
siRNA	Small interfering ribonucleic acid
Sn(Oct) ₂	Tin(II)-ethyl hexanoate
TBD	1,5,7-Triazabicyclo(4.4.0)dec-5-ene
T _{cp}	Cloud point temperature
TEM	Transmission electron microscopy
TFA	Trifluoroacetic acid
T _g	Glass-transition temperature
THF	Tetrahydrofuran
TIM	Thioimide mechanism
T _m	Melting point
TMEDA	<i>N,N,N',N'</i> -Tetramethylethane-1,2-diamine
TU	Thiourea
UCST	Upper critical solution temperature
UV	Ultra violet
VE	Vinyl ether
ZnEt ₂	Diethyl zinc

1. Introduction

Nowadays, the global production of plastic based devices is of excessive growth [1]. This is due to the availability of a broad

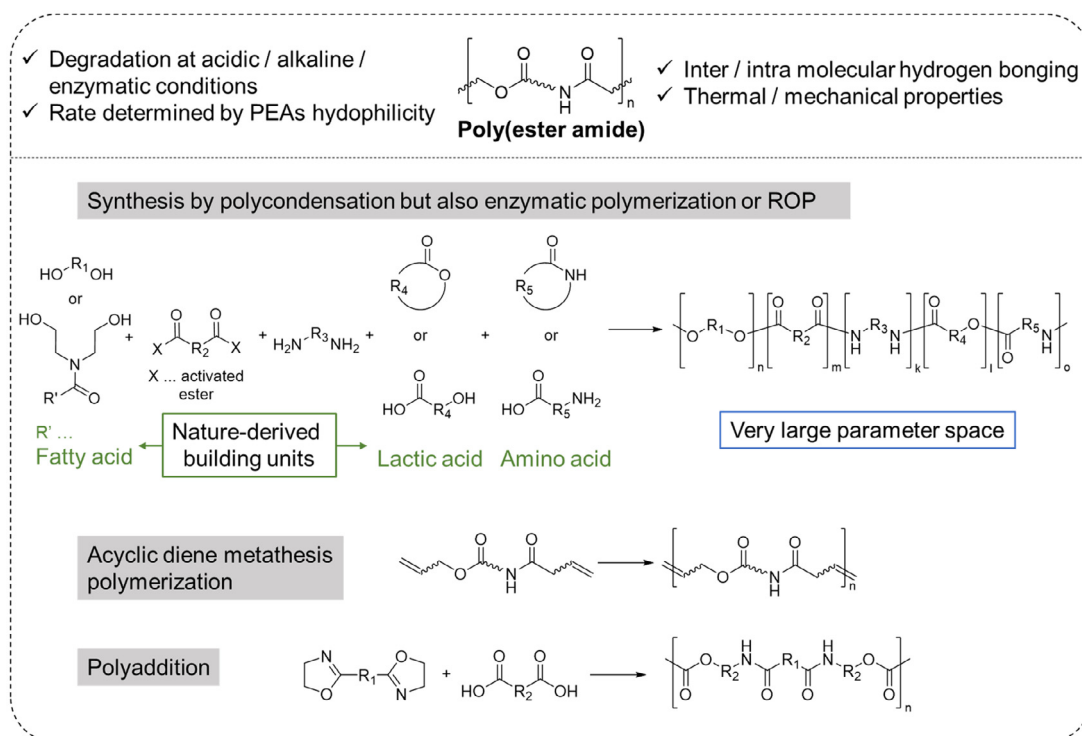
variety of (functional) polymers featuring different mechanical or chemical properties [2–4]. However, most of these materials are not (bio)degradable. In consequence, plastic waste production also increases which, in return, contributes to the pollution of the environment [5, 6]. The logical prerequisite to tackle this issue is the utilization of degradable plastics, ideally derived from renewable resources. In this regard, the class of polyesters is dominating the different application fields with (bio)degradable properties [7]. Considering commodity materials [8], a range of polyesters are produced on industrial scale, including poly(ethylene terephthalate) (PET), poly(lactic acid) (PLA), poly(butylene succinate), poly(butylene adipate terephthalate) (PBAT, Ecoflex) and polyhydroxyalkonates (PHAs). Such materials are already serving in numerous applications in textiles or food packaging [9].

In particular when used in medical or pharmaceutical applications, degradability of polymeric materials represents a crucial factor to avoid accumulation in the organism [11]. Poly(ethylene glycol) (PEG) vacuole formation in the liver represents one example [10]. Potentially, the non-degradable nature of some pharmacopolymers hampers their successful transition to pharmaceutical products [11]. Also considering degradable, synthetic polymers for tissue engineering or nanoscaled drug delivery systems, mainly polyesters are on the market or in clinical trials [11–13]. The variety of approved materials includes PLA, poly(glycolic acid) (PGA), poly(ϵ -caprolactone) (PCL), their copolymers, as well as less prominent polyesters such as polyoxalate, poly(butylene terephthalate) or poly(bis-(*p*-carboxyphenoxy)propane-co-sebacic acid) [14]. The strong research focus on polyesters is possibly due to a faster “bench to bedside” translation as it is more cost and time efficient if the polymeric materials are already used in other pharmaceutical products.

However, there is a clear need for improved approaches and materials. For example, acidification of the microenvironment upon ester degradation can lead to protein destabilization [15, 16] as well as autocatalytic degradation [17] for some polyesters [18]. Pronounced control of degradation pathways is required to avoid short service life times of pharmaceutical products [19]. When poorly water-soluble active pharmaceutical ingredients (API) are encapsulated into hydrophobic polyesters, uncontrolled or unspecific polymer-API interactions can result in API leakage or burst release [20, 21]. In addition, the occurrence of acidic degradation products limits the applicability of such systems to API tolerating decreased pH values in the microenvironment [18].

Whereas several properties such as crystallinity or hydrophilic-hydrophobic balance (HHB) can be adjusted for polyesters [22, 23], additional functional moieties can only be introduced as α - or ω -end groups. In view of pharmacopolymers with tailor-made adjustments for “personalized” applications, current literature frequently reports alternative (bio)degradable polymer classes that could serve as substitute materials [24–26]. Among a variety of such candidates, poly(ester amide)s (PEA) or poly(hemiacetal ester)s maintain the advantages of polyesters and approach such disadvantages through incorporation of additional functional groups in the polymer backbone. The latter may either tailor the degradation behavior or broaden the range of applicable API through possibilities of specific interactions such as, e.g., hydrogen bonding. Other new degradable materials such as poly(2,5-morpholinedione)s, or polyphosphoesters (PPE) are inspired by natural building units such as amino acids or DNA, which seems promising in terms of bioresorbability.

In fact, such advantages of polyester alternatives have been exploited for several years, often with strong focus on exploiting their use as pharmacopolymers [27]. In spite of seemingly different on first glance, PEA, polyacetals as well as PPE have recently experienced a boost with respect to the development of new synthetic routes that enable access to more tailored materials. The success-



Scheme 1. Advantages of poly(ester amide)s and schematic representation of an overview step-growth polymerizations yielding poly(ester amide)s.

ful synthesis and characterization of the new materials represent fundamental premises for the understanding of structure-property relationships which, in turn, form the basis for the development of reasonable tailored pharmapolymer. A considerable variety of polymer architectures exists within the polymer classes, which is due to the necessity to attach stealth polymers or biologically active molecules in materials applicable in drug delivery. The review hence scrutinizes the recent synthetic developments of these polymer classes throughout the last 10 years, putting them into the context of applications that have arisen for less novel materials.

2. Poly(ester amide)s

2.1. Step-growth polymerization

Step-growth polymerization represents a versatile approach to yield a manifold of PEAs via a variety of methods. The polycondensation of mixtures of commonly used monomers that yield polyesters or polyamides in homopolymerizations represents the simplest approach. AB or AA / BB monomers include diols, diamines, dicarboxylic acids, hydroxy acids or amino acids and their derivatives, which enables an immense parameter space (Scheme 1) [28–30]. The resulting PEAs are frequently used as prepolymers for, e.g. polyurethane [31] synthesis or other coupling methods to increase the molar masses [32]. Whereas typical polycondensation procedures involve harsh reaction conditions, in particular when carboxylic acids are applied as monomers, mild enzymatic polymerization approaches offer several advantages, as has recently been reviewed [33].

Facilitating intra- and intermolecular hydrogen bonding, amide moieties are incorporated into polyester-based materials to alter the mechanical properties [34]. In turn, polyamides are often modified with ester moieties to accelerate their degradation behavior. The latter is particularly important with respect to avoiding long-term contamination of the environment with commodity plastics.

In view of sustainability, current efforts are directed towards development of recyclable materials, at best through depolymerization or hydrolysis yielding the monomers.

Nature provides a range of building blocks that enables the production of PEA from renewable materials. In addition to bifunctional monomers that can be directly used for PEA synthesis, a steadily increasing amount of promising materials based on vegetable oils is currently developed [35–37]. Most approaches rely on a fatty acid amide with diethanolamine, which subsequently acts as a diol monomer to produce ester functionalities with varying dicarboxylic acid derivatives. The biocompatibility and mechanical properties of such materials have led to biomedical applications, e.g. for wound healing when loaded with antifungals [36]. Thereby, hydrogen bonding to drugs such as lovastatin or the use of branched materials with decreased glass transition temperature were beneficial for the formulation characteristics [38].

Besides several hydroxy acids obtained from renewable resources, as e.g., lactic acid, natural amino acids represent obvious biocompatible monomers and have long been applied in several copolymerizations to yield PEA via step-growth polymerizations [39, 40]. An adjustment of material properties such as hydrophilicity or hydrolysis rate is possible via the dicarboxylic acid (derivatives) and diol used as comonomers [41]. Degraded via surface erosion mechanism into less acidic products compared to the standard PLGA, such materials are becoming widely used in various forms for drug delivery. Examples include matrix tablets loaded with ketoprofen [42], or microspheres for intravitreal drug delivery [43, 44] as well as treatment of arthritis [45–47].

Replacement of the dicarboxylic acid and diol by ϵ -caprolactone as an AB monomer yielded PEA with the accordingly altered structures as random copolymers with a tendency to alternate. Harsh polymerization conditions ($T > 200$ °C) were required, in particular when the neat amino acids β -alanine [48] and alanine [49] were used. Use of the glycine and alanine ethyl esters and 1,5,7-triazabicyclo(4.4.0)dec-5-ene (TBD) as catalyst reduced reac-

tion temperatures to 120 °C but racemization could not be fully circumvented [50]. When also the amino acid monomer is replaced by a cyclic monomer, the PEA are in fact obtained via a chain-growth polymerization, as e.g. reported for the copolymerizations of ϵ -caprolactam / lactide [51] or ϵ -caprolactam / ϵ -caprolactone [34]. Such approaches enabled access to PEA block copolymer architectures through the use of Jeffamines®, an amino endfunctionalized polyether, as macroinitiators and sequential monomer addition [52, 53].

Other less common functional moieties also enable access to PEA via step growth polymerizations. Often used for coupling of precursors to achieve high molar mass polymers [54–58], the AA+BB polyaddition of bisoxazolines and dicarboxylic acids facilitates access to PEAs without the need to remove condensation products [59–62]. The advantage holds true also for the polyaddition using analogous AB [63] or AB₂ monomers [64, 65]. Mainly, the polymerization of aromatic bis(2-oxazolines) is exploited focusing on the thermal properties of the resulting polymers [66–71]. In contrast, the application of the simple 2,2'-bis(2-oxazoline) as monomer resulted in PEAs with an oxamide repeating unit. These polymers were investigated as nanocarriers for the hydrophobic drug indomethacin [61, 62, 72].

Another alternative approach towards PEA is the polymerization of monomers containing the respective esters and amides via reaction of other functional groups, as reported in the acyclic diene metathesis (ADMET) polymerization of a diglycine diene derivative with ethyleneglycol dimethacrylate [73]. Also a hyperbranched PEA featuring hydroxyl moieties is commercially available and opens avenues for the straightforward introduction of other functional groups via post-polymerization reactions [74].

2.2. ROP of cyclic depsipeptides – poly(morpholine-2,5-dione)s

Chain-growth polymerization represents a powerful tool to synthesize high molar mass polymers. Regarding the PEA synthesis, particularly the ring-opening polymerization (ROP) of cyclic monomers, the morpholine-2,5-diones (MD), represents the most commonly applied polymerization procedure. The resulting materials feature strictly alternating ester and amide moieties along the polymer backbone. Their degradation products are based on α -hydroxy and α -amino acids. Since Helder et al. reported the first successful homopolymerization of 6-methyl-morpholine-2,5-dione in 1985 [75], this synthesis approach has become the most commonly applied strategy to obtain PEA from MD. This review covers the latest developments of this research aspect. Further information can be found in other reviews [76–78]. In particular, the review by Feng et al. presents a comprehensive summary of the literature until 2010 [77]. Due to the rapidly growing interest and latest developments in PEA research, we aim for closing this gap and provide a summary of the recent reports.

2.2.1. Monomer synthesis

Different strategies towards the synthesis of MD monomers have been developed, as detailed in the review article by Basu et al. [76]. Generally, MD are synthesized from α -amino acids as starting materials. In a first step, a linear precursor is generated through covalent attachment of an α -hydroxy acid derivative. This can be either done via the carboxylic acid moiety of the α -amino acid to result in an ester precursor, or via the carboxylic acid moiety of the α -hydroxy acid leading to an amide moiety. The latter approach is frequently performed in recent literature reports and will therefore be highlighted in the following (Scheme 2, top). The amino acid is reacted with chloroacyl chlorides or bromoacyl bromides, yielding the respective *N*-(α -haloacyl)- α -amino acid precursor. The subsequent cyclization is performed in highly diluted solution at moderate temperatures in order to avoid the formation of

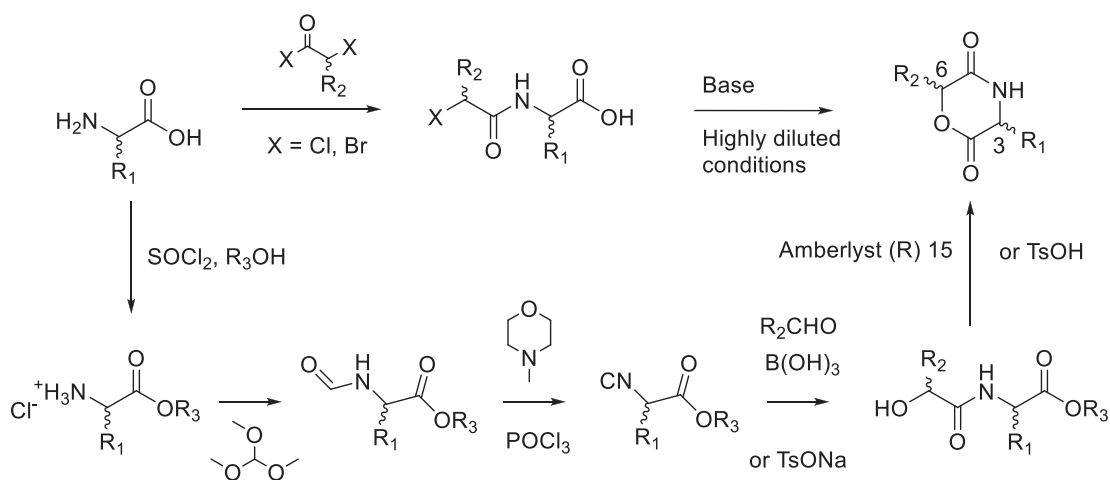
oligomers. The purified monomers are typically obtained after column chromatography, recrystallization, or a combination of both. However, the comparably low final yields of the MD monomers represent a drawback of this established synthesis procedure. Although varying significantly from report to report, rather poor to moderate yields ranging from 7% for highly sterically hindered MD (*vide infra*, MD15) [79], up to about 50% for the mostly utilized 3-methyl-morpholine-2,5-dione (*vide infra*, MD8) were reported [80–83].

Aiming at overcoming this limitation, Zi-Chen and coworkers demonstrated a new approach providing MD monomers in excellent yields (Scheme 2, bottom) [84]. Instead of utilizing the α -amino acids directly for the precursor synthesis, the amino moieties are converted to their corresponding isocyanides and subsequently reacted with aldehydes in a Passerini type reaction, yielding the *N*-(α -hydroxyacyl)- α -amino acid precursors in yields from 82 to 91%. Different substituents in 3- and 6-position were introduced by choice of the amino acid and the aldehyde, whereby the stereocenter in 3-position was retained and therefore predetermined by the α -amino acid. The subsequent cyclization of the precursor was achieved under reflux conditions in toluene utilizing catalytic amounts of Amberlyst (R) 15 ion-exchange resin or *p*-toluenesulfonic acid (TsOH). Nine MD monomers, ultimately derived from glycine, L-leucine or L-phenylalanine were obtained with respective cyclization yields varying between 71 and 90%. The respective overall yields from 60 to 77% thus emphasize the great potential and variability of this new approach. It should be noted that the stereocenter in 6-position cannot be pre-determined because this carbon atom generates a prochiral center throughout the reaction, resulting in a mixture of diastereomers.

MD can generally be categorized in monomers with hydrocarbon substituents (Fig. 1, MD1 to MD16), and heterocycles comprising substituents with additional functional moieties (Table 1, MD17 to MD30). For clarity, each MD is assigned to a specific number herein, which is defined in Fig. 1 or Table 1. The individual numbers will be referred to in the following text.

As shown in Fig. 1, a broad variety of MD with varying hydrophilicity or hydrophobicity has been reported and polymerized via ROP throughout the last decade. Interestingly, at least one site of the heterocyclic monomer comprises a non-sterically demanding moiety (such as hydrogen or methyl), whereas the other substituent can be of higher steric demand. However, no reports on monomers with two sterically demanding groups were published. This might be due to a low reactivity caused by the steric hindrance of such monomers potentially hampering the ROP process. In addition, already MD10 and MD15 featuring only one highly sterically demanding substituent were accessible in low yields of 7 and 15%, respectively [79].

Aiming at materials that can be readily functionalized in post-polymerization modification approaches, thioethers (MD27 to MD30) as well as allyl groups (MD25 and MD26) have been incorporated into MD monomers. The latter was used to functionalize PEA by radical thiol-ene additions using various thiols featuring additional reactive groups, including amines, carboxylic acids and alcohols [85]. However, the conversions varied significantly dependent on the applied thiol (quantitative for the carboxylic acid and alcohol decorated thiols, < 25% for sterically hindered non-functional thiols). Most PEA retained an intact backbone structure during the post-polymerization functionalizations. However, the amino moiety at the respective thiol induced backbone degradation. In contrast, the PEA chains of the methionine based PMD26 remained intact during oxidation utilizing hydrogen peroxide in formic acid [86]. The nucleophilic character of methionine's sulfur atom was furthermore exploited in nucleophilic substitutions using propargyl bromide or propylene oxide resulting in polymers featuring positively charged sulfonium sidechains [86].



Scheme 2. Schematic representation of the different synthesis routes towards MD monomers.

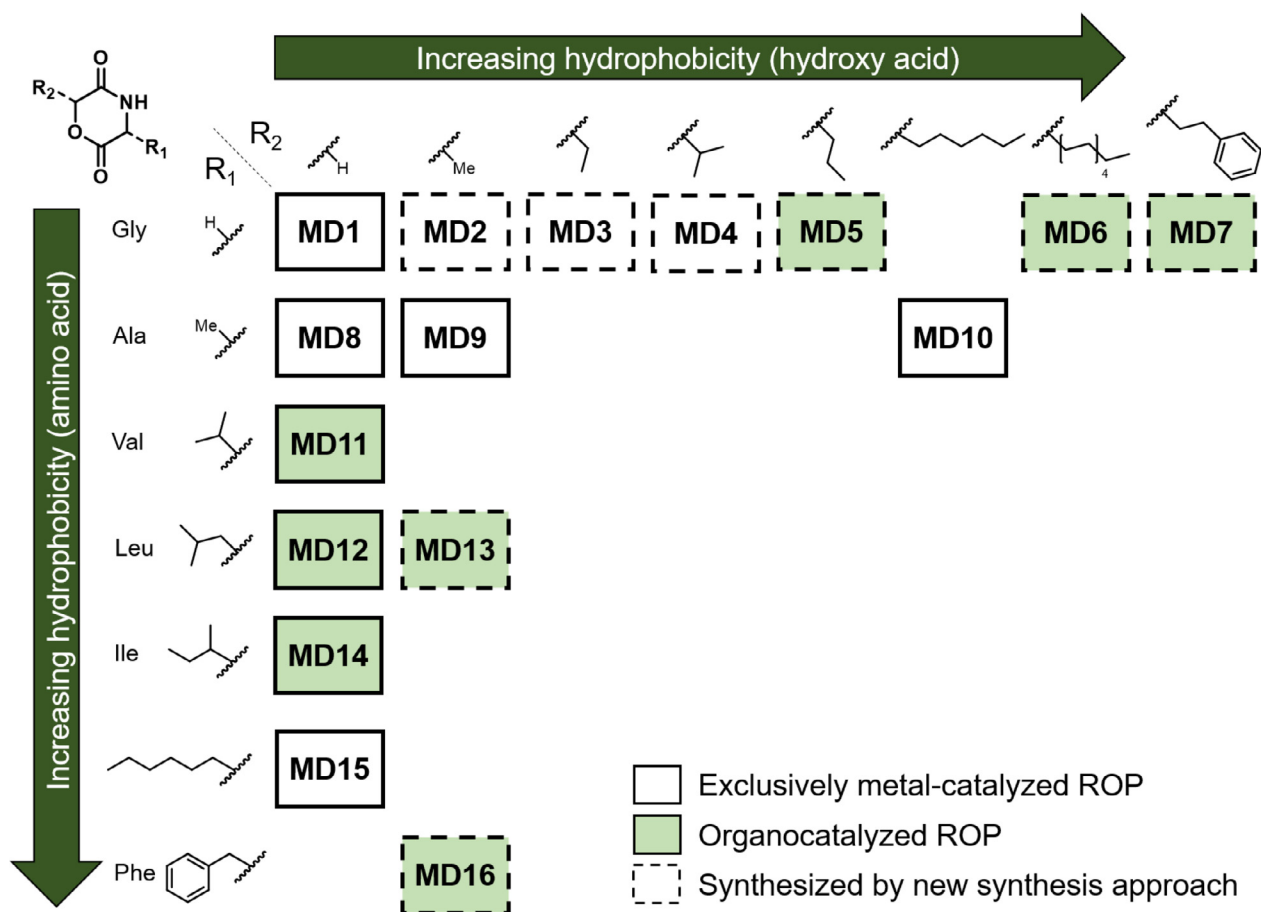


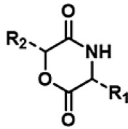
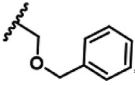
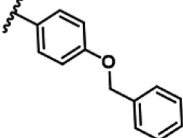
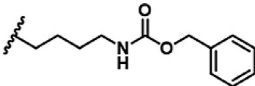
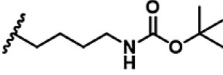
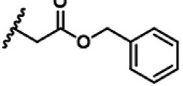
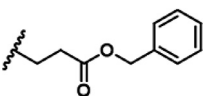
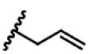
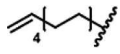
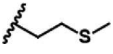
Fig. 1. General schematic overview of MD monomers with hydrocarbon substituents reported in the last decade. The color indicates the application of the individual MD in organo- or metal-catalyzed ROP. MD with dashed frames were obtained via the monomer synthesis pathway as reported by Zi-Chen and coworkers [84].

On the other hand, functional groups such as amines, alcohols or carboxylic acids can also be present in MD monomers by choice of the amino acid used for the monomer synthesis. However, neither the ROP of MD, nor the monomer synthesis tolerate these functional groups. As a consequence, protection prior to monomer synthesis, and deprotection subsequent to polymerization is mandatory. However, synthetic methods benefit

from protection group chemistry that has been well-established within peptide research. The commercial availability of various *tert*-butyloxycarbonyl (Boc), benzyl- or benzyloxycarbonyl (Cbz)-protected α -amino acids has thus promoted the frequent introduction of functional moieties in 3-position of the MD monomer (R₁ in Table 1).

Table 1

Overview of functional MD monomers including protective groups, deprotection strategies as well as possible post-polymerization modification reactions.

		R ₁ (Amino acid)	R ₂ (Hydroxy acid)	Deprotection	Function	Possible modifications	Homopolymer	Copolymer (mol% feed)	Refs.
L-Ser			H (MD17)	Hydrogenation	-OH	Esterification	x	/	[90]
			Me (MD18)				/	x (up to 10%)	[87]
L-Tyr			H (MD19)				x	/	[90]
L-Lys			H (MD20)	HBr/AcOH	-NH ₂	Amidation	x	x (5%)	[85, 88]
			Me (MD21)	Hydrogenation			/	x	[91]
L-Lys			H (MD22)	TFA			x	/	[85]
L-Asp			H (MD23)	TFA/ thioanisole	-COOH	Amidation, esterification	/	x (5%)	[88, 89, 92, 93]
L-Glu			H (MD24)	Hydrogenation			/	x (up to 30%)	[88,89, 92,93]
allyl-Gly			H (MD25)	Not necessary	Allyl	Radical thiol-ene addition	x	/	[85]
Gly	H		 (MD26)				x	/	[84]
D,L-Met			H (MD27)	Not necessary	Thio- ether	Oxidation, addition	x	/	[86]
			Me (MD28)				x	/	[86]
			Et (MD29)				x	/	[86]
			nBu (MD30)				x	/	[86]

For instance, a copolymer composed of the benzyl protected serine-based **MD18** and lactide was deprotected in a hydrogenation approach without notable main chain degradation at degrees of deprotection of about 90%, yielding a PEA with pendant hydroxyl moieties [87]. The deprotection strategies for Cbz-protected lysine containing PEA was accomplished either by treatment with HBr/HOAc, or by hydrogenations. Klok et al. utilized both methodologies aiming to gain access to a quantitatively deprotected **PMD20** homopolymer, however, either resulting in incomplete deprotection or in backbone degradation [85]. Similar difficulties occurred during deprotection of the Boc-protected **PMD22** homopolymer. In contrast, Ohya and coworkers reported successful deprotection of copolymers composed of lactide and either the Cbz-protected lysine-based **MD20** or the benzyl protected asparagine-based **MD23** (5 mol%, respectively) with degrees of deprotection of 70 to 85% [88]. Copolymers featuring the glutamic acid-derived benzyl-protected **MD24** (up to 30% **MD24**) were deprotected by hydrogenation in a quantitative manner without degradation [89]. Apparently, high degrees of deprotection without main chain degradation can be achieved for statistical copolymers featuring a comparably low molar fraction of MD, whereas the deprotection of PEA homopolymers derived from MD based on functional amino acids is not straightforward.

2.2.2. Recent developments regarding the catalysis of the ROP of MD

In general, the ROP of MD proceeds in a similar fashion as that of cyclic ester monomers such as, e.g., lactide or glycolide. Besides early enzyme-mediated polymerizations as detailed by Feng [77], recently applied ROP catalysts can be categorized into metal- or organo-based systems. Nowadays, in particular the utilization of organocatalysts represents an emerging field. On the other hand, a significant push towards the optimization of the metal-catalyzed ROP is clearly evident from current reports. The following section highlights the individual approaches and details the achieved developments. **Fig. 2** illustrates recently applied catalysts and **Table 2** summarizes characterization data as well as reaction conditions.

2.2.2.1. Recent developments in the metal-catalyzed ROP of MD.

Tin(II)-ethylhexanoate (Sn(Oct)₂) still represents the most common catalyst in a broad variety of ROPs, also for the preparation of PEA derived from MD. This is due to its robustness, commercial availability as well as ease of handling. For instance, Lendlein and coworkers utilized this catalyst to gain access to PEA with varying aliphatic sidechains ranging from low (**MD8**) up to higher sterical demand (**MD14**, **MD10** and **MD15**) by applying typically used bulk polymerization conditions [79, 94]. Noteworthy, the authors additionally tested a polymerization in toluene but conversions and fi-

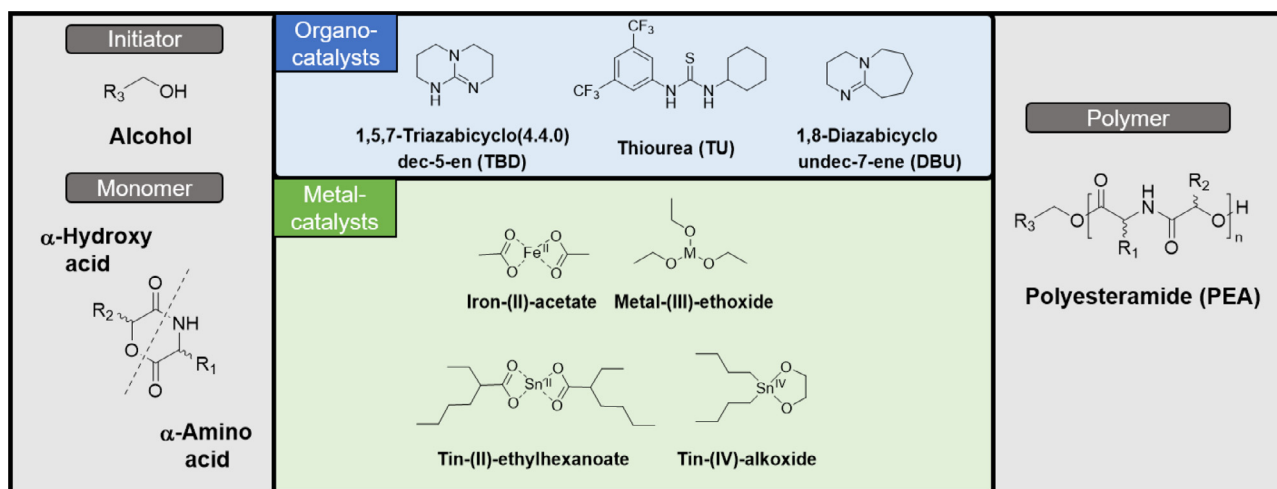


Fig. 2. Left: Schematic representation of applicable initiators and MD monomers. Middle top: Schematic representation of utilized organo-catalysts. Middle bottom: Schematic representation of recently applied metal-based catalysts. Right: Schematic representation of PEA structures derived from ROP of MDs.

nal yields were rather poor. This observation demonstrates one key restriction of this catalyst, which is the necessity of high reaction temperatures to actively catalyze the ROP, limiting potential solvents to those featuring high boiling points. Apart from this, severe drawbacks such as the broadening of the molar mass distributions and rather long reaction times (up to days) intrinsically hamper the preparation of tailor-made well-defined polymeric materials. Therefore, recent metal-catalyzed ROPs aim to overcome these issues.

The $\text{Sn}(\text{Oct})_2$ catalyzed ROP of MD featuring functional groups in 3-position was optimized for the Cbz protected lysine-based **MD20** in bulk [85]. In a broad screening of the monomer to catalyst (M/cat.) ratio without additional initiator, the highest molar masses were achieved by applying a low M/cat. ratio of 40. Although this came to the cost of limited molar masses ($DP \approx 60$) and broad dispersity ($D \approx 2$) values due to chain-transfer reactions occurring at higher conversions, this ROP represents one of the few homopolymerizations reported for functional MD monomers. It was further applied using the Boc-protected lysine based monomer **MD22** and **MD25** comprising a double bond.

In another approach, the HSAB principle was considered as a key factor for the catalytic activity of metal-based catalysts in the ROP of MD [90]. In a screening of different metal complexes (see Table 2), the authors observed that $\text{Fe}(\text{OAc})_2$, featuring a softer metal center than $\text{Sn}(\text{Oct})_2$, was more efficient in the 1,8-octanediol initiated ROP of **MD14** and **MD17** (based on isoleucine and benzyl-protected serine, respectively). This behavior was explained by a weaker metal-oxygen bonding promoting the propagation. However, $\text{Sn}(\text{Oct})_2$ was superior for the ROP of **MD19** based on benzyl-protected tyrosine, most likely due to the larger ion radius of Sn^{2+} enhancing the interaction of the catalyst center with the ester moiety of the more sterically hindered monomer. In addition, various metal-ethoxides (In^{II} , Fe^{III} , Mg^{II} and Al^{III}) were tested, however, without sufficiently catalyzing the ROP. In contrast, a Sn^{IV} alkoxide prepared from ethylene glycol acted as efficient catalyst / initiator in the ROP of **MD14** [95]. Even at high temperatures, PEA with two defined hydroxyl ω -end groups were produced via this bifunctional initiator, as confirmed by matrix-assisted laser-desorption mass spectrometry (MALDI MS). The catalytic system was furthermore applied for various copolymers comprising **MD8**, **MD14** and **MD12**.

These studies clearly demonstrate the achieved progress in the development of optimized metal-based ROP of MD, however also showing that the replacement of $\text{Sn}(\text{Oct})_2$ can be cum-

bersome due to its versatility being able to polymerize most MD.

2.2.2.2. The emerging field of the organo-catalyzed ROP of MD. On the other hand, highly active organocatalysts have gained considerable attention among the community opening a novel synthesis procedure that circumvents problems affiliated with the usage of $\text{Sn}(\text{Oct})_2$.

Pioneering this strategy back in 2005, Hedrick and coworkers utilized *N*-heterocyclic carbenes and a combination of (-)-sparteine with a thiourea (TU) cocatalyst for the polymerization of **MD9** or **MD13** [96, 97]. Interestingly, this approach was only revisited recently applying the “super-base” catalyst TBD [98]. Five MD based on glycolic acid and aliphatic α -amino acids were polymerized at room temperature in solution. Narrowly dispersed PEA were obtained from the soluble **MD11**, **MD12** and **MD14**, respectively. Although hampered by inter- and intramolecular transesterification processes at higher conversions, precise molar mass, α - and ω -end group control was possible through choice of the initiating alcohol BnOH up to moderate monomer conversions. Shortly after, Zi-Chen and coworkers found that the loss of control was avoided when a TU based co-catalyst was added, enabling access towards various high molar mass PEA with low dispersity values ($D < 1.1$) even at quantitative conversions. In addition, a block copolymer was obtained by sequential monomer addition [84]. Similar findings were reported for the 1,8-diazabicyclo(5.4.0)undec-7-ene (DBU) catalyzed ROP of **MD12** [99]. In detail, a dispersity drop from 3.06 to 1.15 was achieved when 10 eq. TU were applied. In terms of the homopolymerization kinetics, an increased amount of TU led to a decrease of the polymerization rate because it promoted a thioimide mediated (TIM) polymerization mechanism. Whereas TIM is somewhat slower compared to the cyclic imide mechanism (CIM) mainly occurring without TU, it grants good control over the polymerization. Additionally, the authors demonstrated that the use of primary alcohols as initiators resulted in a faster initiation when compared to secondary ones.

Also the organocatalytic polymerization of methionine based MD (**MD27** - **MD30**) was investigated in detail [86]. Firstly, **MD27** was polymerized in different chain lengths using a DBU/TU binary catalyst system, yielding well defined materials ($D \leq 1.11$). When the more sterically demanding and less reactive monomers **MD28** and **MD29** were used, a weaker TU needed to be applied to promote the polymerization. The bulkiest **MD30** could, however, not be polymerized.

Table 2
Reaction conditions and selected characterization data of the PEA homopolymers.

Monomer	Initiator	Catalyst	Solvent	T (°C)	t (h)	M/I	M _n ^a (g mol ⁻¹)	D ^a	Refs.
MD15	Ethylene glycol	Sn(Oct) ₂	Bulk	140	18	30	5600	1.2	[79]
MD10	Ethylene glycol	Sn(Oct) ₂	Bulk/toluene ^c	140	12	28	5400	1.2	[79]
MD8	Ethylene glycol	Sn(Oct) ₂	Bulk/toluene ^c	140	16	46	5700	1.4	[79]
MD20	None	Sn(Oct) ₂	Bulk	110	20	40 ^b	24,400	2.5	[85]
MD22	None	Sn(Oct) ₂	Bulk	110	20	40 ^b	21,700	2.0	[85]
MD25	None	Sn(Oct) ₂	Bulk	110	20	40 ^b	13,300	1.8	[85]
MD14	1,8-Octane diol	Fe(OAc) ₂ Sn(Oct) ₂ In(OEt) ₃ Mg(OEt) ₂ Al(OEt) ₃ Fe(OEt) ₃	Bulk	135 to 160	3.5 to 24	29	3100 to 5800	1.13 to 1.19	[90]
MD18	1,8-Octane diol	Fe(OAc) ₂ Sn(Oct) ₂	Bulk	135	5 to 24	29	4700 to 7800	1.26 to 1.45	[90]
MD19	1,8-Octane diol	Fe(OAc) ₂ Sn(Oct) ₂	Bulk	150	5 to 24	29	6000 to 8040	1.27 to 1.41	[90]
MD8	Ethylene glycol	Sn ^{IV} salt	Bulk	140	24	n.a.	13,000	1.7	[95]
MD14	Ethylene glycol	Sn ^{IV} salt	Bulk	140	24	n.a.	14,000	1.5	[95]
MD12	Ethylene glycol	Sn ^{IV} salt	Bulk/toluene ^d	140	24	n.a.	11,000	1.5	[95]
MD1	Benzyl alcohol	TBD	THF ^c	RT	1	100	4500	1.41	[98]
MD8	Benzyl alcohol	TBD	THF ^c	RT	1	100	6500	1.27	[98]
MD11	Benzyl alcohol	TBD	THF	RT	0 to 1	100	9500 to 16,600	1.12 to 1.27	[98]
MD12	Benzyl alcohol	TBD	THF	RT	0 to 1	100	7600 to 16,300	1.10 to 1.17	[98]
MD14	Benzyl alcohol	TBD	THF	RT	0 to 1	100	10,200 to 21,000	1.13 to 1.34	[98]
MD5	Benzyl alcohol	DBU/TU	CH ₂ Cl ₂	25	0 to 5	100	5000 to 12,500	1.06 to 1.12	Selected examples from [84]
MD26	Benzyl alcohol	DBU/TU	CH ₂ Cl ₂	25	0 to 5	100	5000 to 22,500	1.06 to 1.10	Selected examples from [84]
MD16	Benzyl alcohol	DBU/TU	CH ₂ Cl ₂	25	0 to 5	100	4000 to 13,500	1.06 to 1.07	Selected examples from [84]
MD12	Benzyl alcohol	DBU/TU	CH ₂ Cl ₂	40	5 to 20 min	50 to 150	8600 to 25,200	1.15 to 1.49	[99]
MD27	Benzyl alcohol	DBU/TU	CHCl ₃	RT	3 to 6	25 to 100	8100 to 25,600	1.07 to 1.11	[86]
MD28	Benzyl alcohol	DBU/TU	CHCl ₃	RT	8	100	23,700	1.11	[86]
MD29	Benzyl alcohol	DBU/TU	CHCl ₃	RT	24	100	28,200	1.10	[86]

a) SEC values; b) M/cat. ratio; c) not/partially soluble; d) low conversion.

MD monomers also allow the inclusion of isolated L-alanine units into PLA through copolymerization with lactide. This was comprehensively investigated for the DBU and TBD catalyzed, BnOH initiated copolymerization of L-lactide with 20 mol% **MD9** [100]. Detailed kinetic and thermodynamic analyses were based on variation of key parameters such as the temperature, initial total monomer concentration and solvent polarity. In-depth NMR studies of the resulting materials proved the absence of isolated PEA blocks in the copolymer. The combination of DBU and TU as a catalyst system was also applied in a copolymerization of **MD12** with L-lactide in feed fractions from 25 to 75 mol% [99]. The introduction of secondary alcohol-based chain ends through the lactide comonomer significantly decreased the polymerization rate of the MD monomer. As MD chain ends based on glycolic acid were more reactive compared to lactide chain ends, this resulted in gradient copolymers enriched with lactide in the beginning of the chain ($r_{LA} = 1.94 > 1 > r_{MD} = 0.26$, Finemann-Ross method). Noteworthy, creatinine acetate as a biogenic catalyst was also successfully utilized in the copolymerization of L-lactide with up to 10 mol% of the benzyl protected serine based **MD18** [87].

2.2.3. Application guided synthesis of MD containing polymers

Combining the individual features of different polymer classes enables the synthesis of tailor-made materials and can, therefore, be beneficial when targeting specific physicochemical properties. Besides solely relying on copolymerization, also more so-

phisticated morphologies such as (multi)block copolymers, covalently crosslinked hydrogels or material blends have been utilized to serve numerous purposes. The recent developments in the fabrication of polymers featuring MD are mostly application driven (Fig. 3), e.g. tailoring the of the degradation rates of polyesters, tissue engineering or shape memory materials, gene delivery platforms, or the encapsulation or conjugation of API. Such covalent functionalizations rely on post-polymerization modification reactions of PEA obtained through incorporation of MD monomers featuring functional moieties.

2.2.3.1. Bulk applications of MD containing polymers. Thermal properties, such as the glass transition temperature (T_g) or melting events of homo- or stereocrystallites represent macroscopic properties that have been tailored for MD containing polymers. Depending on the substituents (**MD1**, **MD8**, **MD11**, **MD12** and **MD14**) PEA are either amorphous or partially crystalline [101–104]. Among these PEA featuring either no or C₁ to C₄ substituents, only **PMD11** with an isopropyl substituent is unable to crystallize. PEA based on glycine (**PMD1**), alanine (**PMD8**) and leucine (**PMD12**) feature T_m values above 190 °C, whereas the T_m value of the isoleucine-derived **PMD14** is significantly lower at 74 °C. Expanding the field of MD based homopolymers, a study by Lendlein and coworkers described PEA with hexyl substituents featuring a relatively low T_g of around 35 °C [79]. This was achieved by the Sn(Oct)₂ catalyzed

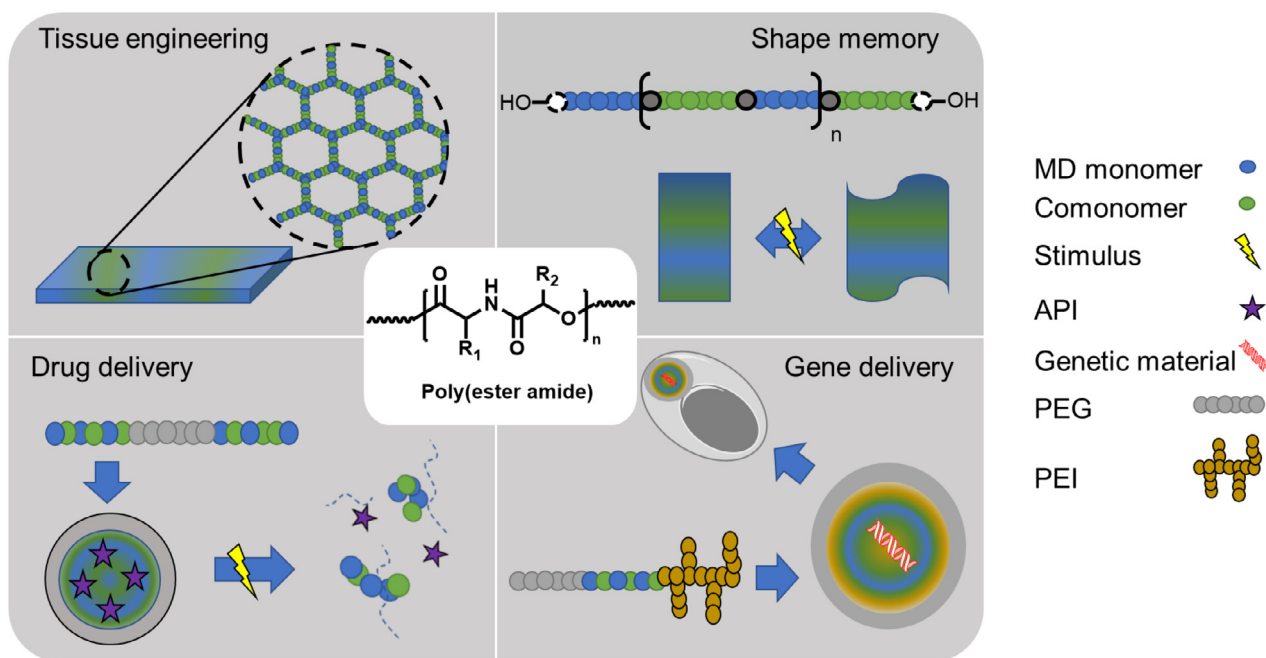


Fig. 3. Schematic overview of recent application fields of polymers derived from MD monomers.

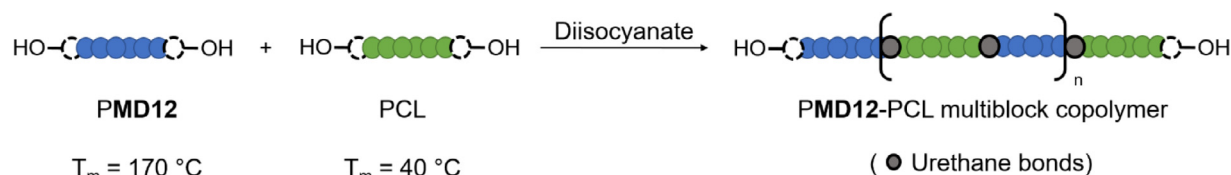


Fig. 4. Schematic representation of the synthesis approach towards PMD12-PCL multiblock copolymers.

bulk ROP of **MD15** and **MD10**, carrying a hexyl substituent in 3- or 6-position, respectively.

The copolymerization of **MD8** with a sterically demanding cyclic carbonate monomer resulted in thermal properties that were adjustable through **MD8** mass fractions from 18.5 to 100 wt% [81]. T_g values of the amorphous copolymers increased significantly with higher carbonate monomer content due to its rigid character. Tsuji et al. recently demonstrated the stereocomplexation of PLLA/PDLA comprising up to 13 mol% alanine units obtained by copolymerization of lactide with 20 mol% **MD9** featuring the respective stereocenter [105]. As typical for stereocomplexation, stereocrystallites featured increased T_m values compared to homocrystallites. Depending on the stereocomplexation conditions, the alanine units could be selectively included or excluded from the stereocrystallites.

The partial crystallinity of PEA derived from **MD12** was exploited for the generation of shape memory polymers. In this regard, Lendlein and coworkers focused on the development of multiblock copolymers fabricated by polyaddition of **PMD12** ($M_n = 9300 \text{ g mol}^{-1}$) and oligo- ϵ -caprolactone (PCL, $M_n = 2700 \text{ g mol}^{-1}$) polyols with trimethylhexamethylene diisocyanate (Fig. 4) [106]. The crystalline domains of the **PMD12** represented anchor points defining the permanent shape due to their high T_m value, whereas the crystalline PCL domains as well as the T_g of the **PMD12** were used for temporary shape fixation. After deformation to 200% strain, the material recovered efficiently the initial shape. Follow-up studies described the influence of the physical programming parameters on the shape memory ability of the multiblock copolymer [107], the tuning of the surface morphology [108], and potential applications in modern compression textiles [109].

PMD12-PCL multiblock copolymer based fibers were also modified with peptides aiming at enhanced HUVEC adhesion and proliferation and to reduce protein adsorption [110]. In addition, the multiblock copolymers were utilized as a matrix material for polyester-based microparticles for gene delivery [111]. The system was further improved by the incorporation of spider fibroin, thereby enhancing the mechanical properties and biocompatibility [112].

Materials for tissue engineering represent another application of MD containing polymers. Fig. 5 summarizes the applied synthetic strategies. Statistical copolymers comprising either hydrophobic or functional MD monomers were used for this purpose. Covalently crosslinked materials have been accessed through star-shaped MD containing macromonomers with methacrylate end groups.

The alanine-based **MD8** was utilized to improve the mechanical properties of PLGA nanofibers applied for vascular tissue engineering [113]. Introduction of up to 17.4 wt% **MD8** in a statistical copolymer lowered the tensile strength in the wet state and significantly increased the elongation at break. Cell proliferation of human vascular endothelial cells (HUVEC cells) was also improved, and cells penetrated the partially degraded subcutaneous implant prepared from the material.

MD monomers based on of L-Lys or L-Asp (**MD20** or **MD23**, respectively) were used to introduce 5% charged moieties in PLA [88]. PEA containing scaffolds loaded with physically entrapped growth factors for tissue regeneration indeed revealed a faster release than solely PLLA based scaffolds, presumably due to a higher hydrolysis rate of the PEA containing polymers. This resulted in enhanced cell proliferation and superior attachment of rat PC12 pheochromocytoma cells. In particular, the slightly posi-

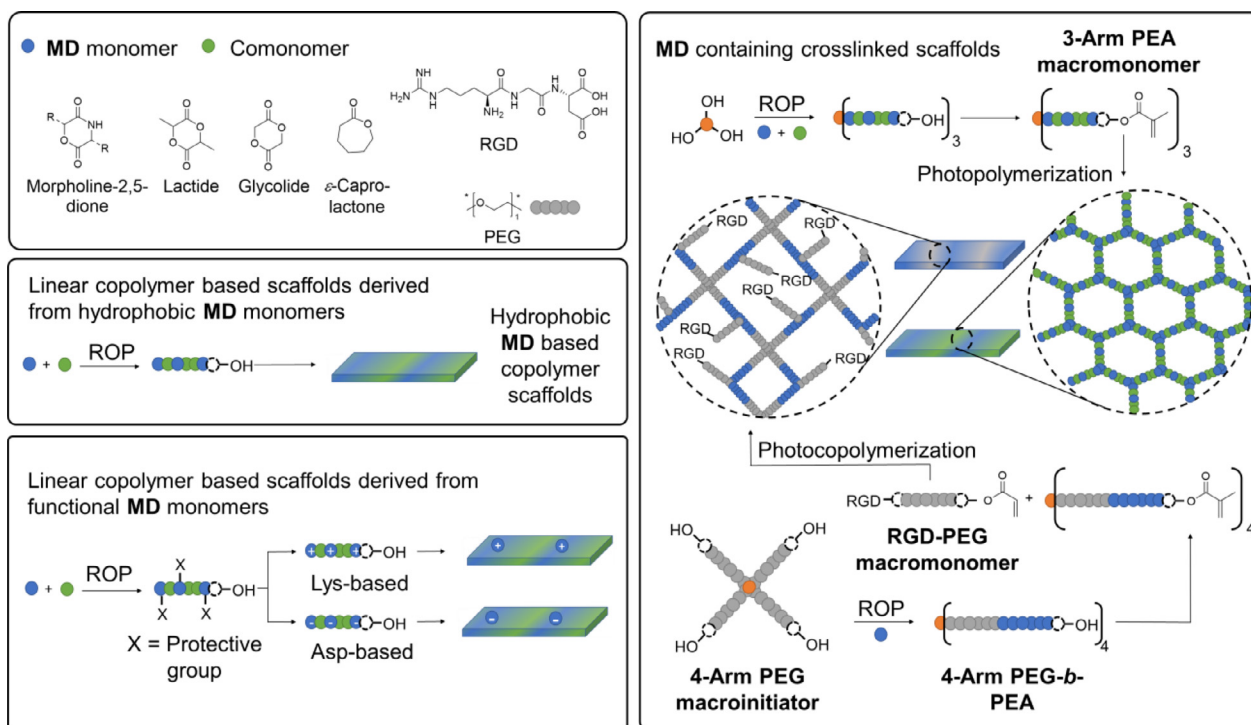


Fig. 5. Schematic depiction of recent synthesis strategies towards MD containing materials used for tissue engineering. Schematic representations of the key structural elements for the fabrication of such materials are depicted in the top left corner.

tively charged L-Lys-based copolymer scaffold promoted differentiation into nerve-like cells, emphasizing a potential use of this material for enhanced nerve regeneration.

Elomaa et al. reported the fabrication of crosslinked three-dimensional polymer scaffolds for tissue engineering by photopolymerization of **MD8** containing macromonomers [80]. Firstly, a three-arm macromonomer was synthesized by copolymerization of ϵ -caprolactone with up to 10 wt% **MD8**. Subsequent methacrylation of the hydroxyl end-groups enabled the photopolymerization process, resulting in a highly crosslinked polymeric scaffold. Biocompatibility was proven by incubation of the material with HUVEC. After treatment for seven days, a 10-fold amount of the initial cells was reported. For testing of the bone regeneration ability, C3H10T1/2 bone cells were seeded on the scaffolds, also revealing enhanced cell proliferation.

A four-arm PEG-*b*-(**MD8**-methacrylate)₄ macromonomer was utilized to fabricate high-density crosslinked hydrogels by visible light stereolithography [114]. For this purpose, a methacryl functionalized PEG-RGDS conjugate was copolymerized with the star-shaped macromonomer to enhance cell attachment due to the presence of the integrin-specific RGDS functions. In general, these hydrogels were softer compared to PEG hydrogels and their stiffness was in the range of natural tissue material. Initial *in vitro* degradation experiments revealed that the mass loss could be tailored by the applied photopolymerization time, *i.e.* the crosslinking density. The degradation of cell-laden hydrogels occurred throughout cell proliferation, thus enabling cell penetration into the scaffold.

2.2.3.2. MD containing polymers as drug delivery vehicles. The application of PEA made from MD monomers as drug delivery vehicles represents a highly emerging field. In general, the MD monomers serve two purposes (Fig. 6): a) Hydrophobic MD are utilized for particle formulation of PEA homopolymers or to tailor the degradation rate of polyester based materials through copolymerization. b) Functional MD allow access to macromolecular prodrugs, and the

attachment of targeting functions or hydrophilic “stealth” polymers *via* post-polymerization modifications. Alternatively, the latter can be introduced by using PEG or poly(2-oxazoline)s (POx) with hydroxyl end groups as macroinitiators for the ROP of MD monomers.

The bioavailability of hydrophobic API can be increased through formulation in nanoparticles composed of degradable hydrophobic polymers. PLGA represents the standard material utilized for this purpose. Nanoparticles made of PLA comprising 5 mol% of the leucine-based **MD12** (1 in Fig. 7) and ciprofloxacin hydrochloride facilitated similar drug release profiles as PLGA [115]. An initial burst release was followed by a sustained release over the course of 24 h, but the drug release rate was lower. A similar release profile was evident when rivastigmine [116] was encapsulated. In contrast, when naltrexone [117] was encapsulated, the release from PEA based microparticles was faster than for the PLGA control. Switching from nanoparticles to microparticles prolonged the sustained release to a period of 28 days [117]. Also nanoparticles composed of the homopolymer of the isoleucine-based **MD14** and dexamethasone featured similarly altered release properties [94]. The formation of hydrogen bonds between the PEA units and the drug significantly increased the drug content in the delivery vehicle, in particular when polymer films were compared. These films retained the drug much longer compared to PLGA films, most likely due to the slower degradation of the PEA as well as a deformation of the film throughout degradation. These studies highlight the possibility of the formation of stable nanocarriers that retain the drugs longer than the gold standard PLGA *via* the use of PEA derived from MD monomers.

Suitably protected MD monomers based on aspartic and glutamic acid (**MD23** and **MD24**, respectively) enabled access to PLA comprising 8 to 16% carboxylic acid groups after deprotection [89, 92, 93]. These were subsequently utilized to attach PEG sidechains *via* DCC/DMAP coupling (4 in Fig. 7) [89, 93]. The release rate of doxorubicin (DOX) encapsulated in micelles formed from these PLA-*graft*-PEG graft copolymers increased when longer PEG chains were used, presumably due to an enhanced permeation of water

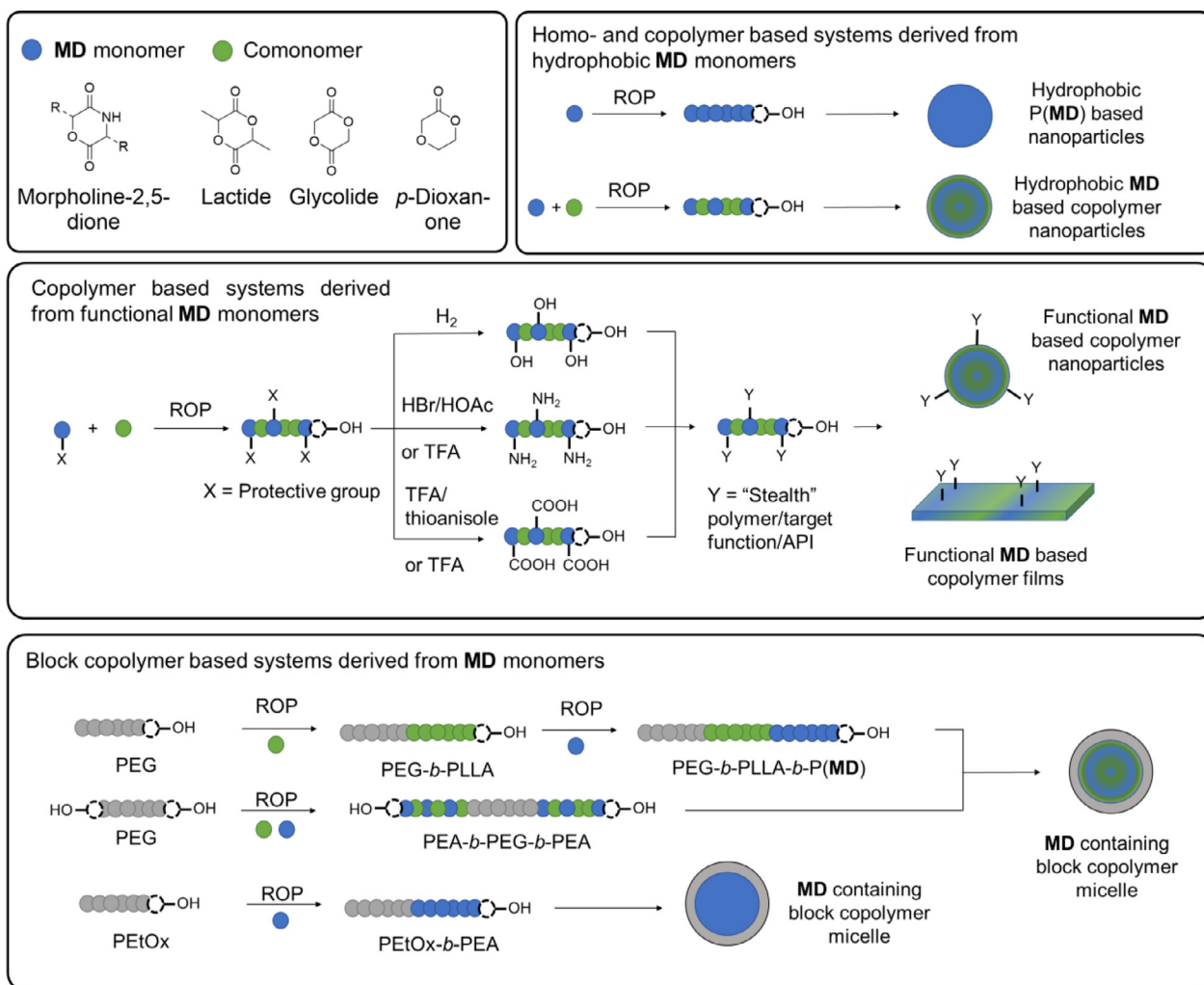


Fig. 6. Schematic representation of the synthesis strategies towards PEA based drug delivery systems derived from MD.

into the micelle core. When the grafting of PEG was only performed to 90% of the carboxylic acid groups, the residual 10% enabled the coupling of other, additional molecules [92]. Ohya and coworkers used these to couple levofloxacin resulting in a macromolecular prodrug (**3** in Fig. 7). The material was designed as an injectable gel, transitioning from the sol phase to the gel phase at physiological temperature and releasing the API in a sustained manner.

Aiming at a qualitative comparison of the release behavior of these PEA based drug delivery systems, Fig. 7 summarizes the API release regarding burst release and normalized sustained release. The following conclusions should be taken with a grain of salt due to the variety of applied API and polymer structures: (i) The sustained release rate of hydrogels and microparticles is lower compared to that of nanoparticles. (ii) The initial burst release can be suppressed by the incorporation of PEG. (iii) The overall release behavior of DOX is faster from micelles featuring longer PEG chains.

"Stealth" polymers such as PEG help to increase the blood circulation time of drug delivery vehicles. The fact that the ROP of MD monomers is initiated by alcohols enables the attachment of PEA to PEG in a straightforward manner *via* macroinitiator approaches. This methodology has already been applied in earlier literature as summarized by Feng [77]. Briefly, monohydroxyl or dihydroxyl end functional PEGs can be used as macroinitiators to result in AB or ABA block copolymers, respectively. Recent research is directed towards more sophisticated tri- or pentablock copolymers, as well as

the replacement of PEG by alternative materials. The latter originates from drawbacks afflicted with the use of PEG such as, e.g., the occurrence of PEG antibodies or anaphylaxis, presumably induced by this polymer. These issues are in addition recently observed subsequent to administration of the new vaccines against COVID-19, thus, highlighting the urgency to develop suitable alternative polymers [118].

Exposing a PETox shell from nanocarriers, in this regard, results in a similar "stealth" effect as that of the gold standard PEG [119]. Recently, poly(2-ethyl-2-oxazoline) (PETox) featuring an ω -hydroxyl end group was applied as a macroinitiator for the ROP of MD11 and MD14 [120]. For each monomer, three different block copolymers with varied fraction of the PEA block were synthesized (MD11: 71 to 87 wt%; MD14: 56 to 88 wt%). Although these materials have not yet been applied as nanocarriers, the PETox-*b*-PMD materials fulfilled the basic requirements since they formed well-defined nanostructures in aqueous suspension exposing the "stealth" polymer toward the outside, as confirmed by cryo-TEM.

Exploiting PEG as ROP macroinitiator enabled access to varying more sophisticated block copolymer structures. mPEG-*b*-PLLA-*b*-PMD8 ABC triblock copolymers were accessed utilizing mPEG as an initiator for the consecutive ROP of L-lactide and MD8 [121]. Paclitaxel (PTX) as a hydrophobic anti-tumoral API was encapsulated in micelles formed from these triblock copolymers. The PEA block prevented drug leakage that occurred for mPEG-*b*-PLLA diblock copolymer micelles, enhanced their stability, and increased

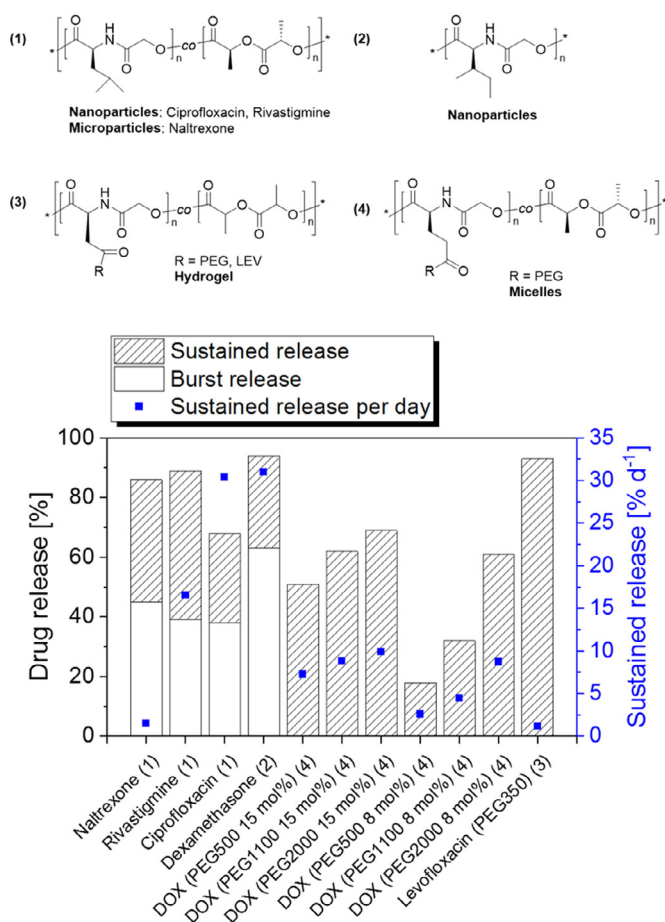


Fig. 7. API release behavior of drug delivery systems composed of polymers made by ROP of MD monomers (phosphate-buffered saline (PBS), pH = 7.4) and schematic representation of the polymer structures [89, 92–94, 115–117]. The sustained release was normalized to release per day since most studies performed *in vitro* drug release experiments in different timeframes. A linear course of the sustained release was assumed to simplify the calculation.

the cytotoxicity on the investigated cancer cell lines. Similar triblock copolymers, composed of PLGA instead of PLLA, were utilized to stabilize PEG-PLGA micelles containing 10-hydroxycamptothecin (HCPT) through preparation of mixed micelles [122].

The use of PEG-diol as macroinitiator for the ROP provides ABA triblock copolymers with a central PEG block in one step. DOX was successfully encapsulated and released from PEA-*b*-PEG-*b*-PEA ABA triblock copolymer nanoparticles [83, 123]. The PEG fraction was kept constant as 20 wt% and the PEA blocks in these studies were composed of the hydrophobic MD14 or MD8, either as homopolymer blocks or statistical copolymers with *p*-dioxanone (PDO). These combinations were favored, since pure PPDO revealed a rather slow hydrolytic degradation kinetics in earlier studies [124]. In addition, interactions between the amino acids helped to stabilize the nanocarriers. In a follow-up study, the material was further modified by attachment of a P(*N,N*-dimethylaminoethylmethacrylate) (PDMAEMA) block through atom-transfer radical polymerization (ATRP) using an ABA triblock copolymer based on PEG and statistical copolymers comprising MD12 and PDO [125]. The resulting pentablock copolymers were utilized for the co-encapsulation of ibuprofen (IBU) and DOX.

All these nanomaterials revealed sustained release, which could be controlled by the MD contents, and the polymer degradation was monitored utilizing size exclusion chromatography (SEC). Aiming at a direct comparison of these investigated systems, the re-

spective block copolymers with the highest and the lowest MD weight fractions were selected (Fig. 8). For the triblock copolymers (Fig. 8a and b), three general statements can be made. (i) The fastest degradation occurred for the block copolymers composed of PEG and the PEA homopolymer, (ii) the PEA segment bearing the methyl substituents hydrolyzed faster compared to that comprising *sec*-butyl substituents and (iii) the hydrolysis rate can be tailored by the weight fractions of PDO and MD in the respective PEA block. For the pentablock copolymers (Fig. 8c), a substantially higher relative molar mass remained due to the non-degradable P(DMAEMA) segments. However, the lowest and highest MD weight fractions (2 and 25 wt%) revealed rather similar degradation rates, pointing towards less adjustable hydrolysis rates compared to the ABA triblock copolymers.

2.2.3.3. MD containing polymers for gene delivery. Poly(ethylene imine) (PEI) is a commonly applied polymer for the immobilization of genetic material, either as linear (*l*PEI) or branched (*b*PEI) polymer. A hydrophobic segment is additionally advantageous when designing gene delivery vehicles. PEA homopolymers, statistical copolymers with lactide or glycolide, and block copolymers comprising the “stealth” polymer PEG have been utilized for that purpose. Most synthesis strategies exploit the hydroxyl end groups of the PEA for coupling to PEI via isocyanates or NHS-esters (Fig. 9). To enhance cellular uptake of these gene delivery vehicles, peptide sequences such as REDV or CAGW were attached additionally to the PEI building blocks.

Transfection using *l*PEI based conjugates to a PEA homopolymer composed of MD14 was investigated [126]. The strong interaction of the isoleucine-based PEA segments with each other on an intermolecular level enhanced the stability of the polyplexes. The materials were synthesized by ROP of MD14 in the presence of either benzyl alcohol or 1,8-octanediol, resulting in the respective mono- or di-hydroxyl end-functional PEA. In a second step, these moieties were converted to isocyanates and subsequently reacted with *l*PEI. Although *l*PEI represents a linear polymer, the conjugation reaction most likely occurred at secondary amines along the backbone, thereby resulting in swallowtail end groups. The best results regarding assembly parameters, plasmid DNA (pDNA) binding and transfection behavior were obtained for the material obtained from a bifunctional ROP initiator and 10 kDa *l*PEI, featuring the highest *l*PEI content.

Several consecutive studies by Wencheng and coworkers were concerned with optimization of the selective transport of pZNF580 DNA towards endothelial cells, thus enabling rapid endothelialization of artificial vascular implants by overexpression of the ZNF580 protein, which represents a key protein for cell migration. In order to access the migration and proliferation enhancement through the utilization of PEA based gene delivery materials, the recovery of artificial scratch tests of cell films as well as the protein overexpression was monitored. The materials consisted of the following segments: *b*PEI as the gold standard cationic polymer, PEG as a stealth polymer to reduce the cytotoxicity, and biodegradable MD containing polymers to enhance the polyplex stability. Initially, the hydrophobic block consisted of glycolide and the alanine-based MD8, and *b*PEI ($M_w = 1800 \text{ g mol}^{-1}$) was used [127]. The material self-assembled into sub 200 nm objects that were successfully loaded with the selected gene at various nitrogen to phosphorous (N/P) ratios. *In vitro* tests revealed a decreasing release rate with an increasing N/P ratio. Transfection in ECs was successful, thereby increasing the ZNF580 protein expression which led to an enhanced cell proliferation and migration behavior. In the following, hydrophobic cores ranging from pure P(MD8) over MD8-*co*-lactide to MD8-*co*-lactide-*co*-glycolide were compared systematically [128]. Fig. 10 summarizes the pDNA release, protein overexpression enhancement factors as well as the recovered areas from

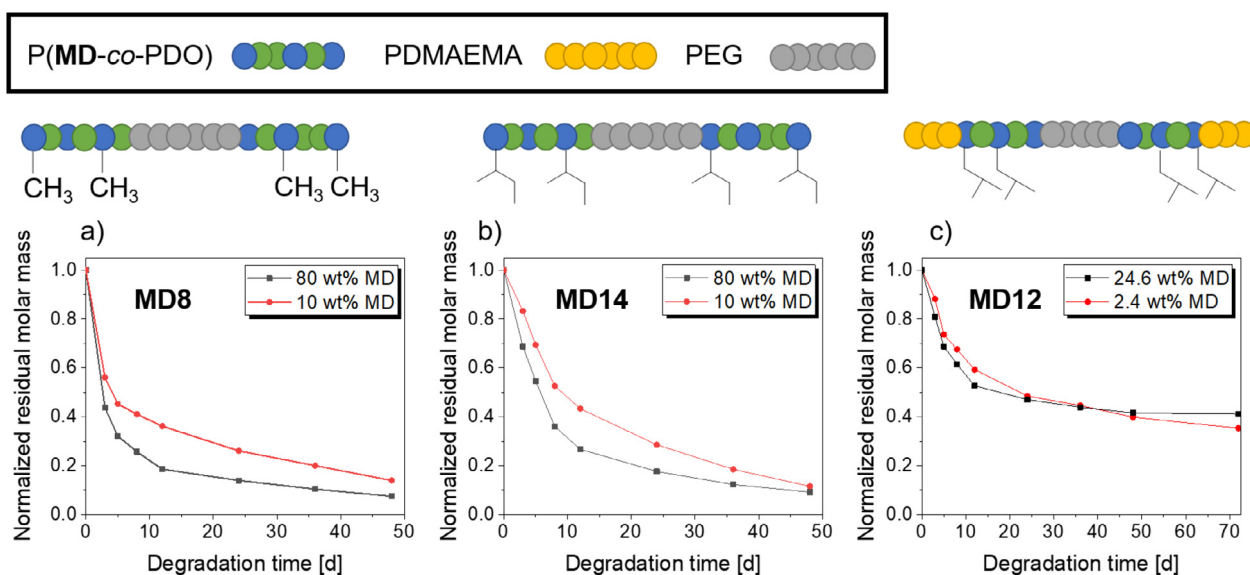


Fig. 8. Normalized residual molar masses of the PEA containing block copolymers obtained during *in vitro* degradation experiments in PBS buffer (pH = 7.4, T = 37 °C) [83, 123, 125].

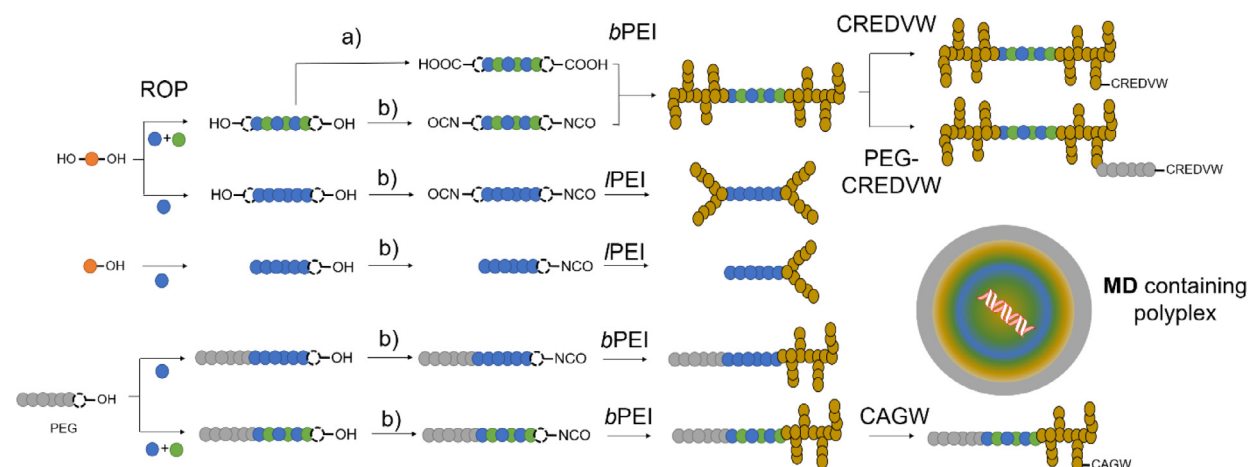


Fig. 9. Schematic representation of synthetic strategies towards MD containing materials for gene delivery. a) Succinic anhydride functionalization of the hydroxyl end groups and subsequent *b*PEI attachment by *N*-hydroxyl succinimide (NHS) coupling. b) Diisocyanate functionalization of the hydroxyl end groups.

scratch tests. When a copolymer with glycolide was used (1), *i.e.* the least sterically demanding hydrophobic copolymer block, the release of the pDNA as well as the corresponding protein expression exhibited the lowest overall values, whereas these low values did not affect the endothelialization and cell migration, reaching values about 80% recovery. Utilization of the PEA homopolymer as hydrophobic core (2) resulted in an enhancement of the cumulative pDNA release and overexpression of the factor. Additional improvement was achieved when copolymers with lactide (3) or a combination of lactide and glycolide (4) were used. The release rates and protein expression further accelerated, which also resulted in enhanced healing ability, reaching values up to 90%.

The CREDVW peptide sequence was attached to polyplex materials consisting of **PMD8** and *b*PEI by a Michael addition [129]. As the REDV peptide sequence enabled selective binding to the $\alpha_4\beta_1$ integrin receptor of endothelial cells (ECs), cellular uptake was enhanced. Cytotoxicity assays proved the biocompatibility of the material up to concentrations of 100 $\mu\text{g mL}^{-1}$. In artificial scratch-healing tests, up to 95% of the scratch area were recovered by ECs within a timeframe of 12 h when PEA containing polyplexes were used for transfection (PLGA based control: 85% were recovered).

The promising carrier system was further modified by incorporation of PEG spacers [130] and through attachment of the alternative active peptide CAGW to enhance adhesion of ECs [131]. For the latter, **MD8** containing materials proved superior to controls comprising only PLGA as hydrophobic segment.

Co-assembly of two different polymers simplifies the synthesis, purification and characterization. In such approaches, components composed of the hydrophobic block and PEI are mixed with block copolymers comprising the same hydrophobic block and the stealth polymer PEG. A micellar co-assembly of *b*PEI-P(**MD8-co-lactide**)-*b*PEI and mPEG-P(**MD8-co-lactide**) was utilized to investigate the impact of the polymer ratio on the efficacy of mixed micelle carriers [82]. It was demonstrated that high PEG contents decreased the DNA binding ability, presumably due to shielding of pDNA-*b*PEI interactions. Cytotoxicity and transfection efficiency could be adjusted by the mPEG and *b*PEI amount in the polyplexes. A subsequent study replaced linear PEG segments by poly(poly(ethylene glycol)methacrylate) (PPEGMA) [132]. After an initial ROP of **MD8** and L-lactide initiated by 1,8-octanediol, the hydroxyl end groups were converted into bromides, thus enabling a subsequent ATRP of PEGMA. The polymer was addition-

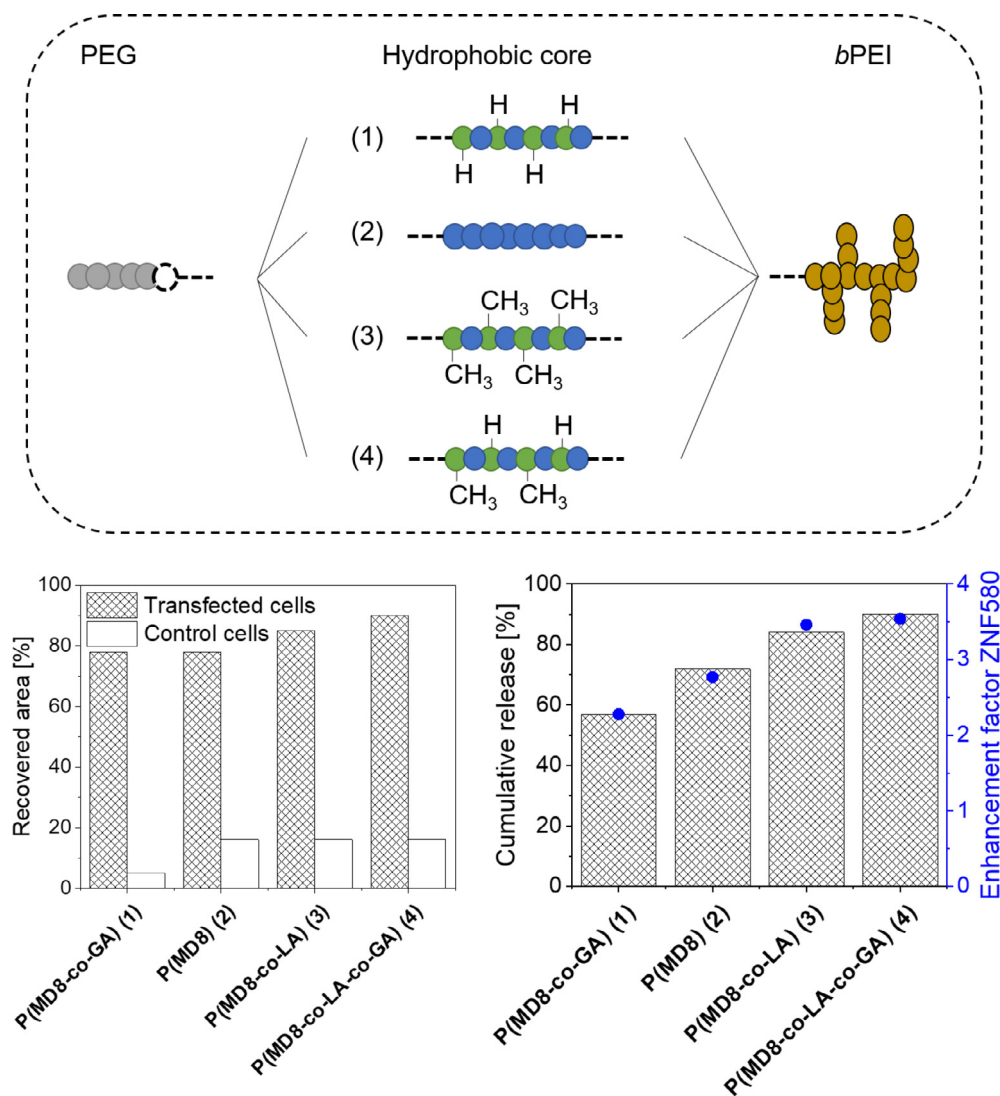


Fig. 10. Comparison of the efficiency of pZNF580 DNA loaded gene delivery vehicles featuring different MD containing hydrophobic cores [127, 128]. **Bottom left:** Recovered area after scratching experiments compared to the respective control groups. **Bottom right:** Cumulative pDNA release (columns) and protein overexpression (dots).

ally decorated with REDV units at the sidechain end groups of the PPEGMA block. A *b*PEI-P(MD8-co-lactide)-*b*PEI was used for micellar co-assembly and loading with the pZNF580 gene. As expected, the peptide decorated polyplexes revealed superior transfection and proliferation when compared to the unmodified control group.

3. Polyphosphoesters and analogues

PPEs and analogues represent highly interesting materials *e.g.* as flame retardants [133] or in biomedical research. Especially the latter is in focus here due to the biocompatibility as well as the adjustable biodegradability of these materials. The polymer backbone or sidechain can be varied by utilization of ester (P-O), amide (P-NH) or phosphonate/phosphate (P-C) based monomers, opening a broad variety of accessible phosphorous based polymers (Scheme 3). P-O bonds are degradable under alkaline conditions, whereas P-N bonds are labile in acidic environments [134, 135]. In contrast, P-C bonds feature enhanced hydrolytic stability but can be degraded by microorganisms [136].

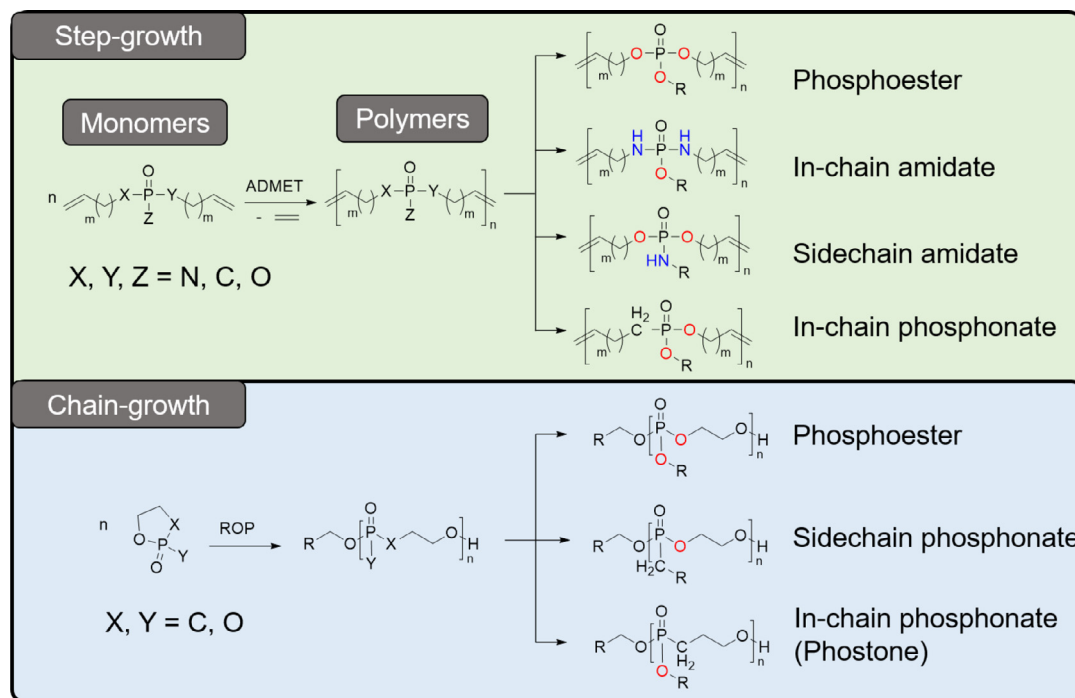
The most commonly applied syntheses of such materials can be categorized into step-growth polymerizations by metathesis polymerization and chain-growth polymerization by ROP. Recently,

Wurm and coworkers published a review highlighting the usage of hydrophilic PPE [137]. Because PPE have recently been reviewed comprehensively [24, 133, 138], the following chapter only briefly highlights latest reports about hydrophobic PPE synthesis and their biomedical applications.

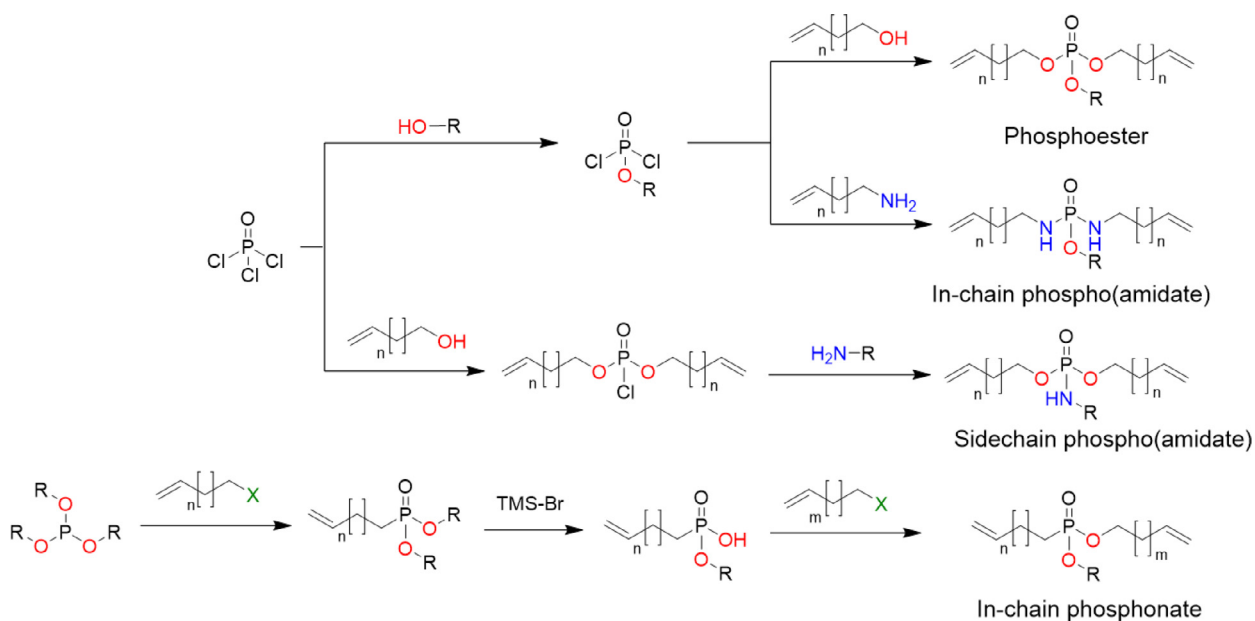
3.1. Phosphoester monomers for acyclic diene metathesis polymerization (IPE)

In general, PPE derived from ADMET can feature adjustable degradability, interesting thermal as well as mechanical properties. Therefore, some recent reports focus on the synthesis and thorough characterization of the polymers without specifying on a particular application since the materials are potentially suited for biomedical research as well as flame retardants.

From a structural perspective, IPE facilitate a broad variability in terms of building blocks. Besides adjustable methylene spacer lengths between the central phosphorous atom and the polymerizable alkene moieties, the covalent binding at the phosphorous atom can be based on different structural elements, such as esters, amides and phosphonates. These can be obtained by mainly two different synthesis routes (Scheme 4). Monomers featuring solely



Scheme 3. Schematic representation of the most commonly applied synthesis routes towards PPE and analogues.



Scheme 4. Schematic representation of synthesis approaches towards phosphoester monomers for acyclic diene metathesis polymerization (IPE).

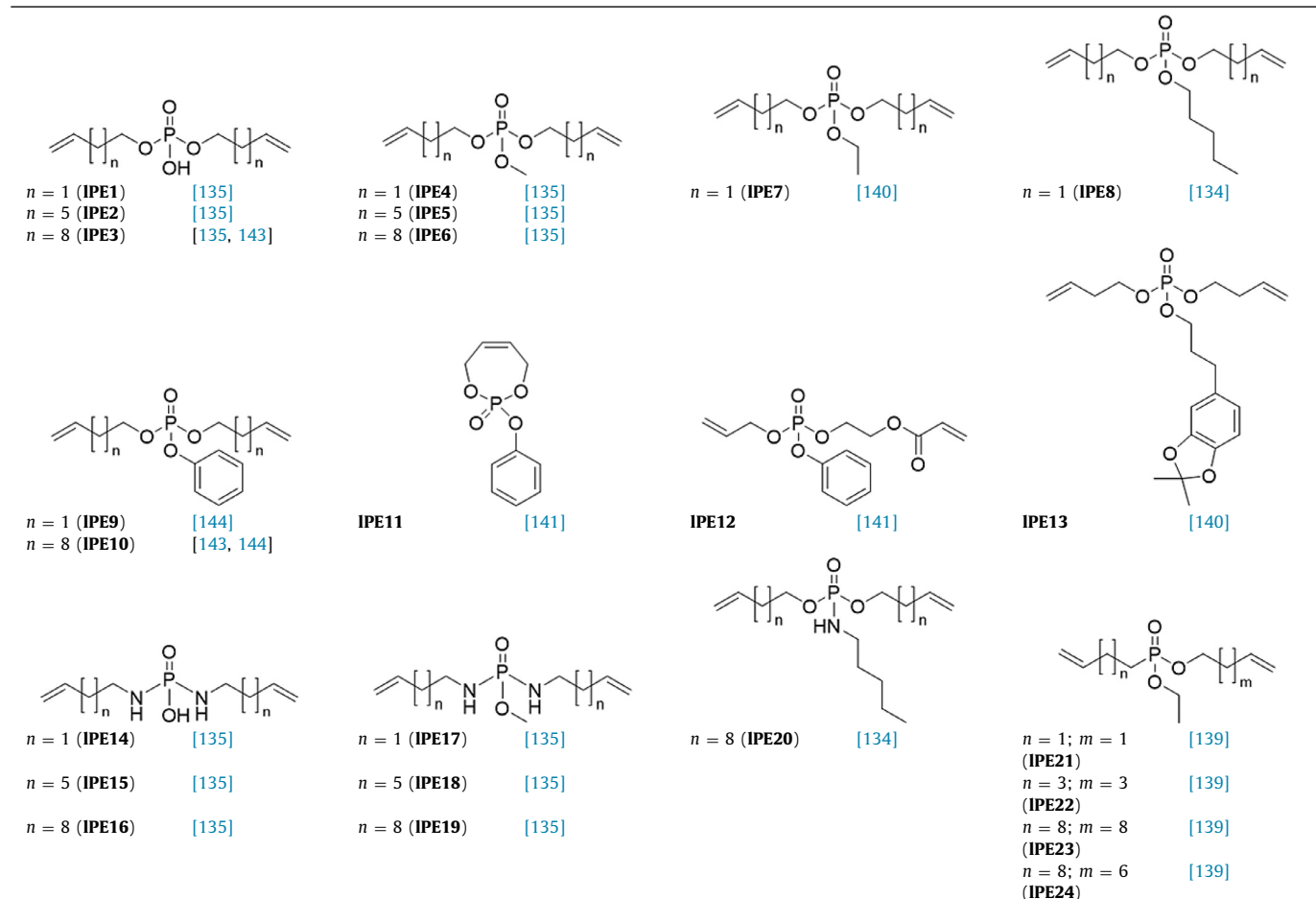
ester bonds and in-chain phosphoamidates featuring pendant ester functions are obtained in a two-step reaction starting from phosphoryl chloride. The initial step is a nucleophilic substitution of one chlorine atom by an alcohol. The remaining two chlorine atoms are subsequently exchanged utilizing ω -alkylene alcohols or amines. When aiming at sidechain phosphoamidates, the polymerizable groups are introduced prior to the pendant substituent.

For non-symmetrical in-chain phosphonates, phosphitesters serve as starting materials [139]. Initially, the P-C bond is formed through a Michaelis-Arbusov reaction, whereby the trivalent phosphorous is oxidized to a pentavalent form. One of the remaining ester bonds is cleaved by stoichiometric amounts of trimethylsi-

lyl bromide and subsequently reacted with a halide functionalized alkene.

The reader is directed to other reviews for a broader overview of the applied monomers as well as a summary about metathesis polymerizations, including ring-opening metathesis (ROMP) [24, 133]. **Table 3** only depicts IPE reported since 2015. Phosphoester monomers were varied regarding the methylene spacer lengths as well as the pendant substituents. The latter ranged from hydroxyl or methyl ester moieties of low steric demand to bulky hydrophobic phenyl esters. **IPE13** featured an isopropylidene protected catechol moiety that was deprotected in an acidic environment without backbone degradation subsequent to polymeriza-

Table 3
Schematic representation of recently applied IPE for the synthesis of PPE via ADMET polymerization.



tion [140]. IPE11 represents a 7-membered cyclic monomer that was polymerized by ring-opening metathesis polymerization for the synthesis of phosphorous based block and miktoarm polymers (*vide infra*) [141].

Recently polymerized in-chain phosphoamidate monomers comprise methylene spacers of varying lengths, with the pendant substituents of low sterical demand. Only one sidechain phosphoamidate monomer was utilized for ADMET polymerization. In-chain phosphonate dienes featured pendant ethyl esters with varying alkyl spacer lengths. The PPE resulting from polymerization of the IPE monomers contain main chain double bonds, which are usually hydrogenated to result in a fully saturated backbone, mostly to improve the flame-retardant properties of the materials. Other post-polymerization modifications such as triazolidione-ene coupling enable further modification of the PPE properties [142].

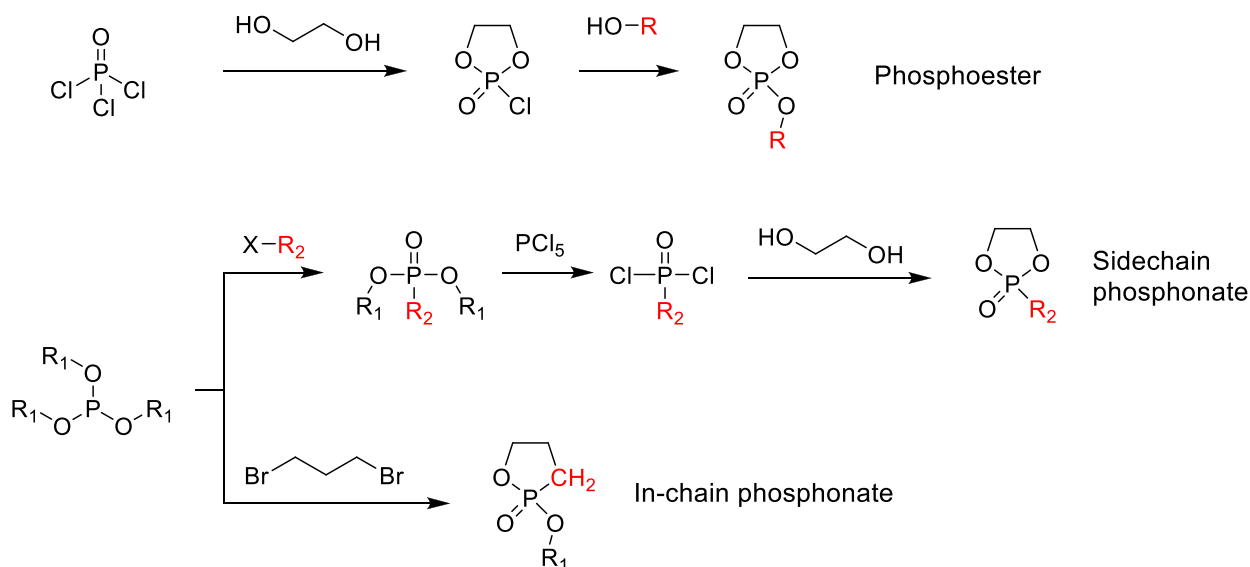
3.2. PPE derived from ADMET polymerization of IPE

The ADMET polymerization represents a step-growth polymerization. A variety of transition metal based catalysts were reported to catalyze this polymerization type, including tungsten-, molybdenum- and ruthenium complexes [145]. In particular, Ru-based Grubbs and Grubbs-Hoveyda catalysts facilitate selectivity towards olefins and tolerate many functional groups such as alcohols and carbonyl containing compounds [146]. During the polymerization, stoichiometric amounts of ethylene are formed. The re-

moval of this gaseous byproduct represents the driving force of the polymerization. The resulting polymers always feature α,ω -terminal double bonds. Addition of suitable alkenes subsequent to polymerization enables the introduction of tailored end groups. The approach was exploited for quenching of the homopolymerizations of IPE9 or IPE10, respectively, to obtain alcohol, carboxylic acid, halide, epoxide, or thioacetate PPE homotelechelic [144].

The enhanced hydrolytic stability of P-C bonds was exploited for the synthesis of in-chain phosphonate IPE with varying aliphatic spacer lengths (IPE21 to IPE24) [139]. Similar to the corresponding cyclic phosphonate monomers (*vide infra*), these monomers were stable at room temperature for several months. The polymerization of IPE21, featuring the shortest alkyne spacer, only resulted in the formation of oligomers, presumably since the short distance between the central phosphorous atom and the catalyst center subsequent to attachment of the monomer hampered further propagation. However, PPE with molar masses $> 10 \text{ kg mol}^{-1}$ were obtained from the non-symmetric monomers.

ADMET of the side-chain phosphoamidate IPE20 and the corresponding phosphoester based IPE8 resulted in materials with similar crystallization behavior [134]. However, the material comprising the pendant amidate moiety featured enhanced thermal stability. In addition, selective cleavage of the pendant amidate moieties under mild acidic conditions enabled access to pendant hydroxyl groups, making the resulting polymers polyphosphodiester.



Scheme 5. Schematic representation of synthesis strategies towards cPE monomers.

Despite the excellent group tolerance of the catalysts, these materials may be difficult to obtain by direct polymerization of the respective monomers **IPE1–3** or **IPE14–16** [135]. In contrast to monomers with pendant methyl ester moieties (**IPE4** to **IPE6**, **IPE17** to **IPE19**), the monomers with a free hydroxyl group failed to homopolymerize due to catalyst deactivation. However, copolymerization of the two monomer types was successful. The incorporation of phosphodiester moieties is useful because they act as hydrogen bond donors. As shown for copolymers of **IPE3** and **IPE10**, this enabled self-healing and shape memory properties, and enhanced adhesion to alumina devices [143]. Besides exploiting adhesive properties to magnetite particles, pendant hydroxyl moieties through incorporation of the catechol-based **IPE13** have also been used for covalent crosslinking reactions [140].

ADMET also allows the copolymerization with non-phosphorous containing monomers, as reported for the copolymerization of **IPE10** with a diacrylamide based on lysine [147]. The reactivity differences of the two monomer types resulted in alternating copolymers and molar masses up to 18,000 g mol⁻¹. The hydrophobic materials were used to encapsulate rifampicin in sub-100 nm particles.

3.3. Cyclic phosphoester monomers (cPE)

Although the key structural elements of different types of cPE are similar, the synthesis of solely phosphoester based monomers and the regioselective introduction of P-C bonds require individual synthesis strategies (Scheme 5). Phosphotriester monomers are synthesized starting from phosphoryl chloride. Reaction with ethylene glycol results in a five membered ring precursor, which can be readily functionalized with various alcohols at the phosphorous atom.

The Michaelis-Arbusow reaction represents the most commonly applied synthesis towards monomers featuring P-C bonds using phosphite esters as starting materials [148]. Sidechain phosphonate syntheses comprise of three steps: A nucleophilic attack of the lone electron pair of phosphite esters at an alkyl halide to introduce the P-C bond, chlorination using PCl_5 and subsequent ring closure with ethylene glycol. In contrast, in-chain phosphonates can be accessed in a one-step reaction by direct ring closure of phosphite esters using 1,3-dibromopropane.

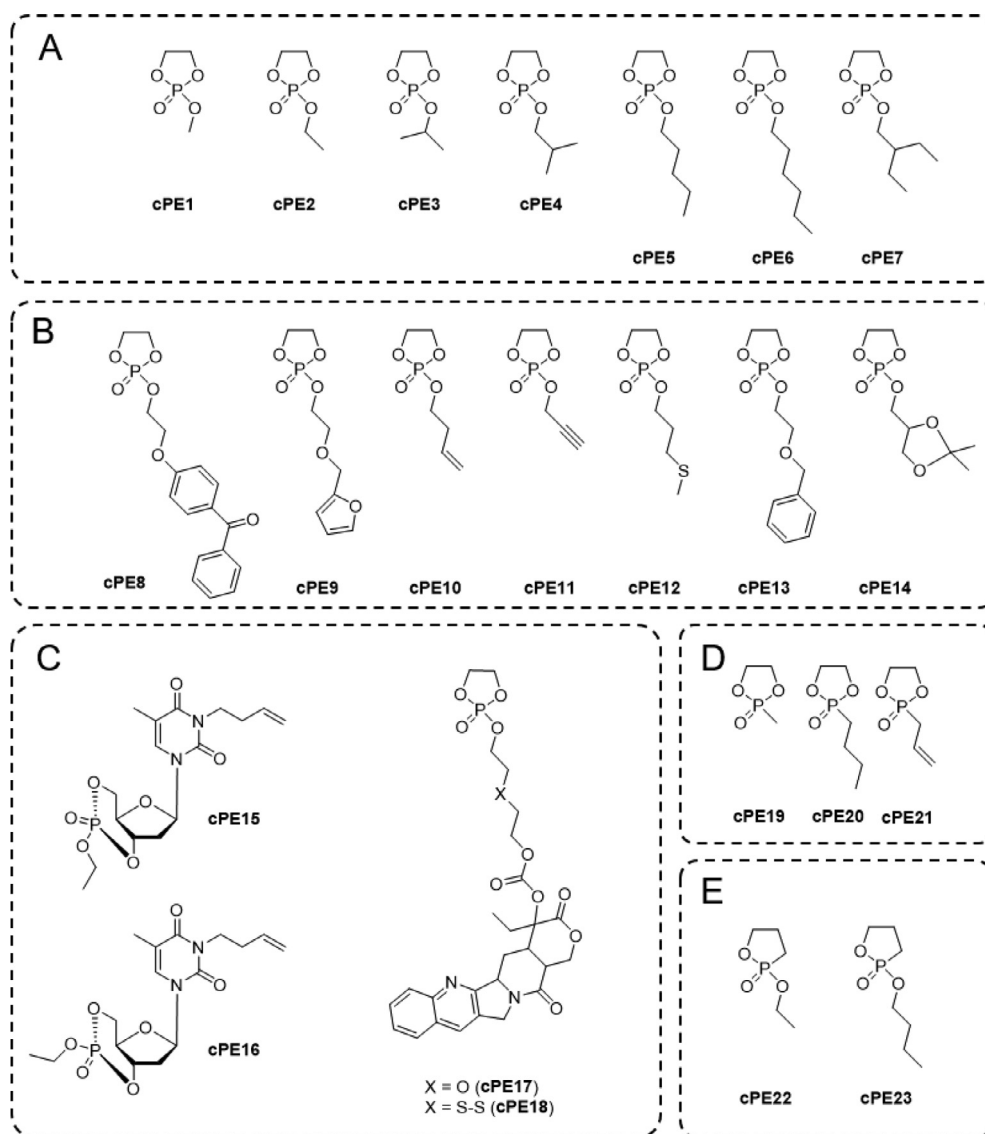
Scheme 6 depicts the respective cPE monomers recently applied for ROP. Phosphotriesters featuring alkyl substituents (**cPE1** to **cPE7**) comprise linear and branched moieties. Among these, **cPE1** and **cPE2** with methyl- or ethyl-ester moieties are hydrophilic. The hydrophobic character increases from the propyl substituted **cPE3** on. Their ROP, thus, potentially enables access toward PPE with tailored hydrophobicity.

In order to fabricate PPE materials featuring lower critical solution temperatures (LCST), the furfuryl functionalized **cPE9** was copolymerized with the hydrophilic **cPE1** or **cPE2** in various molar ratios (5 to 25 mol% **cPE9**, respectively) [149]. The cloud point temperature (T_{cp}) decreased with an increasing amount of the hydrophobic **cPE9**. The same concept was applied for sidechain phosphonate-based PPE through DBU catalyzed copolymerization of the hydrophilic **cPE19**, the hydrophobic **cPE20** and the allyl functionalized **cPE21** [150].

Since the ROP of cPE monomers proceeds in a similar fashion as that of MD, the utilization of functional monomers is limited. Non-saturated pendant substituents (**cPE10** to **cPE11**) are preferably introduced to enable post-polymerization modifications of PPE. For instance, a **cPE10** homopolymer featuring pendant allyl substituents was quantitatively modified by UV induced thiolene addition without the necessity of purification [151]. This kind of modification was also utilized for a copolymer comprising the propargyl functionalized **cPE11** for the attachment of protein repelling peptides [152]. The propargyl moiety of **cPE11** was moreover functionalized in a copper-catalyzed azide-alkyne reaction in order to introduce tertiary amino moieties [153]. The furfuryl moiety of **cPE9** allowed post-polymerization modification with a variety of maleimides via Diels-Alder reactions [149].

Due to the degradability of solely phosphoester-based materials under basic conditions, protection / deprotection strategies need to be based on orthogonal reaction conditions. **cPE13** featuring a benzyl protected hydroxyl moiety can be deprotected by hydrogenation, whereas the acetal moieties in **cPE14** can be removed in slightly acidic media. Both have been utilized to introduce pendant hydroxyl moieties into PPE [154]. In addition, a copolymer comprising both functional monomers was selectively deprotected without backbone degradation, allowing a potential stepwise functionalization.

The benzophenone decorated **cPE8** enabled crosslinking of PPE terpolymers and simultaneous covalent attachment to benzophe-



Scheme 6. Schematic representation of recently utilized cPE. A) Cyclic phosphotriesters featuring pendant alkyl esters. B) Cyclic phosphotriesters featuring functional moieties. C) Bulky cyclic phosphotriesters for the synthesis of artificial DNA or macromolecular prodrugs. D) Sidechain phosphonate cPE. E) In-chain phosphonate (phostone) cPE. The reader is referred to a more specialized review for a comprehensive list [133].

none modified glass substrates, which were further studied regarding the interactions of various PPE with proteins [155].

The camptothecin conjugates **cPE17** and **cPE18** were copolymerized with **cPE2**, yielding copolymers comprising up to 10 mol% of the prodrug monomer [156]. The API was connected to a spacer via a carbonate moiety and, therefore, released from both systems. The disulfide containing linker of **cPE18** additionally enabled a reduction triggered release, thereby enhancing the release rate. Thymidine functionalized cPE (**cPE15** and **cPE16**) were polymerized aiming at macromolecules with structural elements similar to DNA [157, 158].

Also cyclic phosphonate monomers featuring P-C bonds have been reported, resulting in side-chain (**cPE19** to **cPE21**) [150, 159] or in-chain polyphosphonates (phostones, **cPE22** and **cPE23**) [136].

3.4. ROP of cPE monomers

When aiming at the synthesis of PPE derived from ROP, typically low temperatures (-40 °C to room temperature) and high monomer concentrations (4 M) are applied, whereby the targeted molar masses can be adjusted by the applied monomer to initia-

tor (M/I). However, higher molar masses often come to the cost of slightly increased dispersity values (Table 4). In general, α -end groups can be pre-determined by choice of the initiating alcohol which can be either small molecule- or polymer-based. However, the end groups can also be intrinsically derived from the catalyst, as shown for methyl ytterbocene (Cp_2YbMe), which was applied in the ROP of aliphatic ester-based cyclic phosphates (**cPE1** and **cPE3**) and sidechain phosphonates (**cPE19** and **cPE20**) [159]. The successful group transfer from the catalyst was evident from MALDI MS measurements.

Similar to the organocatalyzed polymerization of MD, current literature is mainly focused on the utilization of “super-base” catalysts such as TBD or DBU, partly in combination with co-catalysts. Kinetics of the binary DBU/TU system for the ROP of **cPE4** and **cPE10** were particularly suited to develop continuous flow polymerization in microreactors, whereas the TBD catalyzed ROP of **cPE10** could not be adapted to the reaction setup [151]. Similarly, the binary catalysts DBU/TU and DBU/tris-urea efficiently catalyzed the ROP of the in-chain phosphonates **cPE22** and **cPE23** (pseudo-first order kinetics, $D \approx 1.5$) [136]. When solely TBD or metal-based

Table 4

Summary of the polymerization conditions and selected polymer characterization data of recent homopolymerizations of cPE (for the chemical structure refer to Scheme 6).

Monomer	Initiator	Cat.	T (°C)	t (min)	M/l	M _n (g mol ⁻¹)	Đ	Refs.
cPE4	Benzyl alcohol	DBU/TU or TBD	0 to 40	1 to 20	30	1100 to 2440	1.10 to 1.19	[151]
cPE10	Benzyl alcohol	DBU/TU or TBD	0 to 40	3 to 20	30	1400 to 3580	1.08 to 1.21	[151]
cPE22	2-(Benzyloxy)ethanol	DBU/TU or DBU/Tris-urea	0	ca. 24 h	20 to 170	3000 to 25,100	1.24 to 1.56	[136]
cPE23	2-(Benzyloxy)ethanol	TBD	-20 to 0	ca. 5 d	20 to 50	3900 to 8500	1.56 to 1.61	[136]
cPE15	4-Methoxybenzyl alcohol	TBD	RT	6 to 24 (h)	10 to 30	3200 to 6200	1.06 to 1.09	[157]
cPE19	-	Cp ₂ YbMe	-40	2 to 60	50	11,400 to 33,400	1.15 to 1.47	[159]
cPE20	-	Cp ₂ YbMe	-40	2 to 180	50	800 to 31,500	1.03 to 1.28	[159]
cPE1	-	Cp ₂ YbMe	-40	10	50	1900	1.21	[159]
cPE3	-	Cp ₂ YbMe	-40	2 to 60	50	500 to 8200	1.01 to 1.22	[159]

Table 5

Summary of recently synthesized statistical copolyphosphoesters. Schematic representations of the monomer structures are illustrated in Scheme 6. The color indicates the recently reported compositions of the copolymers (Green: Composed of two monomers. Orange: Composed of three monomers. Blue: Copolymers composed either of two of three monomers.). Monomer compositions that have not yet been explored are represented by the non-colored fields in the table.

cPE	1	2	5	7	8	9	10	11	13	14	17	18	19	20	21
1							[149]								
2		[155]	[155]	[155]	[149]	[155]	[152]	[154]	[154]	[156]	[156]				
5				[155]											
7					[155]										
8						[155]									
9							[155]								
10								[155]							
11									[154]						
13										[154]					
14											[154]				
17												[150]	[150]		
18														[150]	[150]
19															[150]
20															
21															

Statistical copolymers (Green)

 Statistical terpolymers (Orange)

 Co- and terpolymers (Blue)

catalysts (Sn(Oct)₂, ^{tbu}[salen]AlMe) were applied, ill-defined polymers were obtained.

Whereas recent literature regarding the homopolymerizations of cPE focused on aspects such as the polymerization behavior and access towards new PPE classes, copolymerization approaches focus on the incorporation of functional moieties to enable post-polymerization modifications of the resulting copolymers. In contrast to MD, which are mostly copolymerized with cyclic ester monomers, different cPE monomers are preferably copolymerized with each other utilizing the established metal- or organo-based catalysts (Table 5).

As the ROP of cPE monomers can be initiated by alcohols, utilization of PEG macroinitiators allows access to amphiphilic block copolymers featuring hydrophobic PPE blocks. This was exploited for photodynamic therapy, where the photosensitizer chlorin e6 was encapsulated in nanocarriers composed of a PEG-*b*-P(**cPE6**) block copolymer [160]. Similarly, PEG-*b*-(**cPE12**) was used for the encapsulation of chlorin e6 and PTX [161]. The chlorin e6 catalyzed singlet oxygen generation resulted in the *in situ* oxidation of the **cPE12** thioether moieties, thereby increasing the hydrophilicity of

the carrier. Due to the triggered disassembly of the micelles, the PTX release was accelerated.

Besides application oriented research, PPE synthesis strategies have become reliable enough to enable access to sophisticated polymer architectures, as was demonstrated by a combination of ROP, ROMP and ADMET yielding fully PPE based ABC block and miktoarm star terpolymers (Fig. 11) [141]. In contrast to ADMET of symmetrical monomers, ROMP allows the synthesis of heterotetrahelic polymers. The initial ROMP of **IPE11** was terminated utilizing 1,4-diacrylate-*cis*-2-butene to introduce an acrylate ω -end group. For the linear ABC block copolymer, the resulting material was used in a subsequent ADMET polymerization of the heterobifunctional **IPE11** that comprises an allyl as well as an acrylate moiety, thereby ensuring a selective head-to-tail orientation throughout the polymerization. Post-polymerization modification of the remaining acrylate ω -end group utilizing mercaptoethanol enabled the ROP of cyclic phosphate monomer **cPE2**. For the miktoarm star polymer synthesis, the ROMP polymer was modified with 3-mercapto-1,2-propanediol. One hydroxyl moiety was subsequently esterified utilizing acryloyl chloride, and the polymer was applied

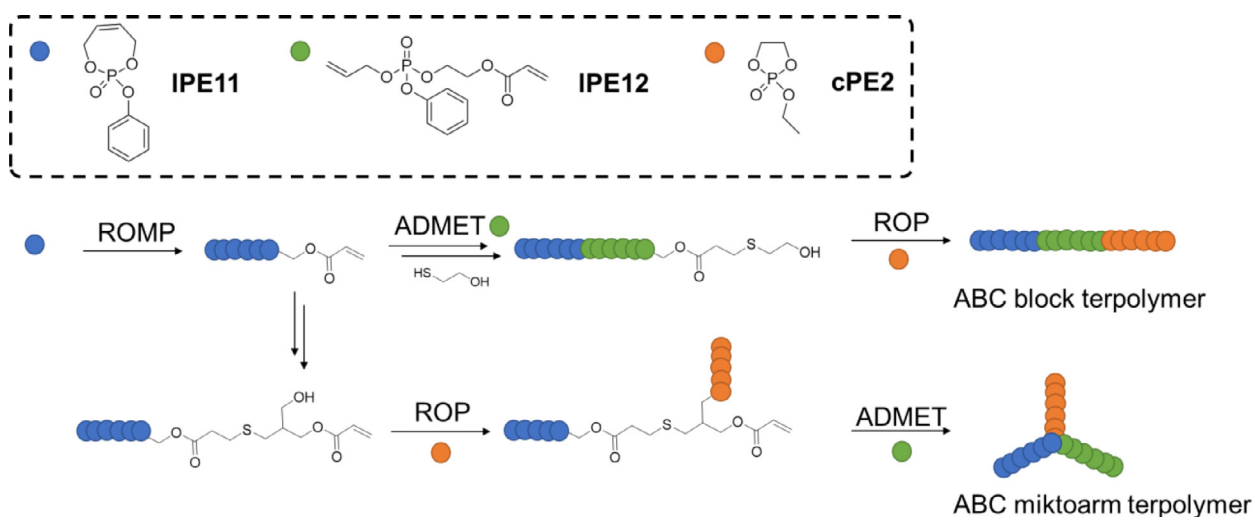


Fig. 11. Schematic representation of synthesis strategies applied for the generation of fully PPE based ABC block and miktoarm terpolymers [141].

as macroinitiator for the ROP of **cPE2**. The **IPE12** segment was introduced through ADMET polymerization.

4. Polyacetals

The nucleophilic addition of an alcohol to the carbonyl moiety of an aldehyde produces unstable hemiacetals, which usually react with a second alcohol molecule, thereby directly forming an acetal through condensation. When the reaction is performed starting with a ketone as carbonyl compound, a ketal is formed *via* the same mechanism. According to IUPAC, ketals are considered now a subclass of acetals [162]. We will hence use the term “ketal” to highlight significant structural effects but refer to both moieties as acetals for the sake of simplicity. Acetals are stable under basic conditions but hydrolysable under acidic conditions forming neutral degradation products, *i.e.* the initial carbonyl compound and alcohol.

Polyoxymethylene, also named polyformaldehyde, is one of the simplest and oldest polyacetals. The first report goes back to studies by A. M. Butlerov in 1859 [163] and was followed by extensive studies, among others by H. Staudinger in the 1920s [164]. The role of polyoxymethylene and developments in this field are summarized elsewhere and recommended to the interested reader [165, 166]. Since then, a variety of other polyaldehydes has been developed [167], and also polysaccharides such as, *e.g.* acetalated dextran [168] might be considered as polyacetals.

A variety of methods for the synthesis of manifold polyacetals was developed, ranging from straightforward step-growth polymerizations to controlled / living chain growth polymerizations. The utilized monomers cover a large parameter space facilitating access to hydrophilic as well as hydrophobic materials featuring different hydrolysis behavior. In consequence, different kinds of application exist that range from thermoplastics [25] to drug delivery systems [169, 170]. Due to the immense recent progress with respect to development of polyacetals designed for the latter, we focused our attention on new developments in the field of degradable main-chain polyacetals.

4.1. Step-growth polymerization

Polyacetals can be obtained by step-growth polymerization *via* two main synthetic strategies (Scheme 7). The acetal moieties can be directly incorporated through polyaddition of diols to divinyl ethers, as initially reported by Heller et al. in 1980 [171]. Established by Murthy and co-workers in 2004 [172], transacetalization

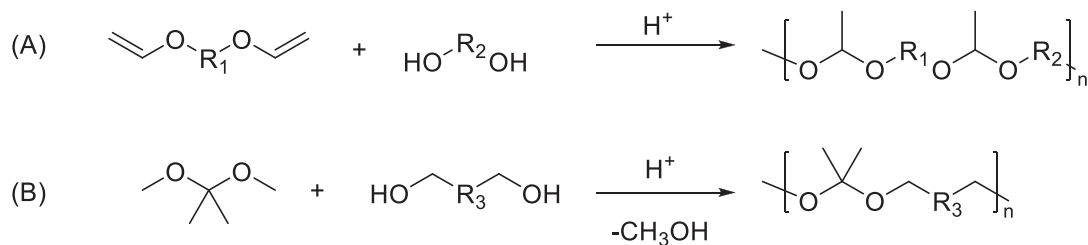
polymerization proceeds through an acetal exchange reaction between a diol compound and an acetal containing monomer such as 2,2-dimethoxy propane (DMP) (*i.e.* acetone dimethyl ketal). The newly formed volatile alcohol is removed from the reaction by simultaneous distillation thereby shifting the reaction equilibrium towards polymeric species. Both approaches rely on acidic catalysts such as toluene sulfonic acid or its pyridinium salt, as reviewed in 2013 [169, 170].

4.1.1. Linear polyacetals from polyaddition of diols and divinyl ethers

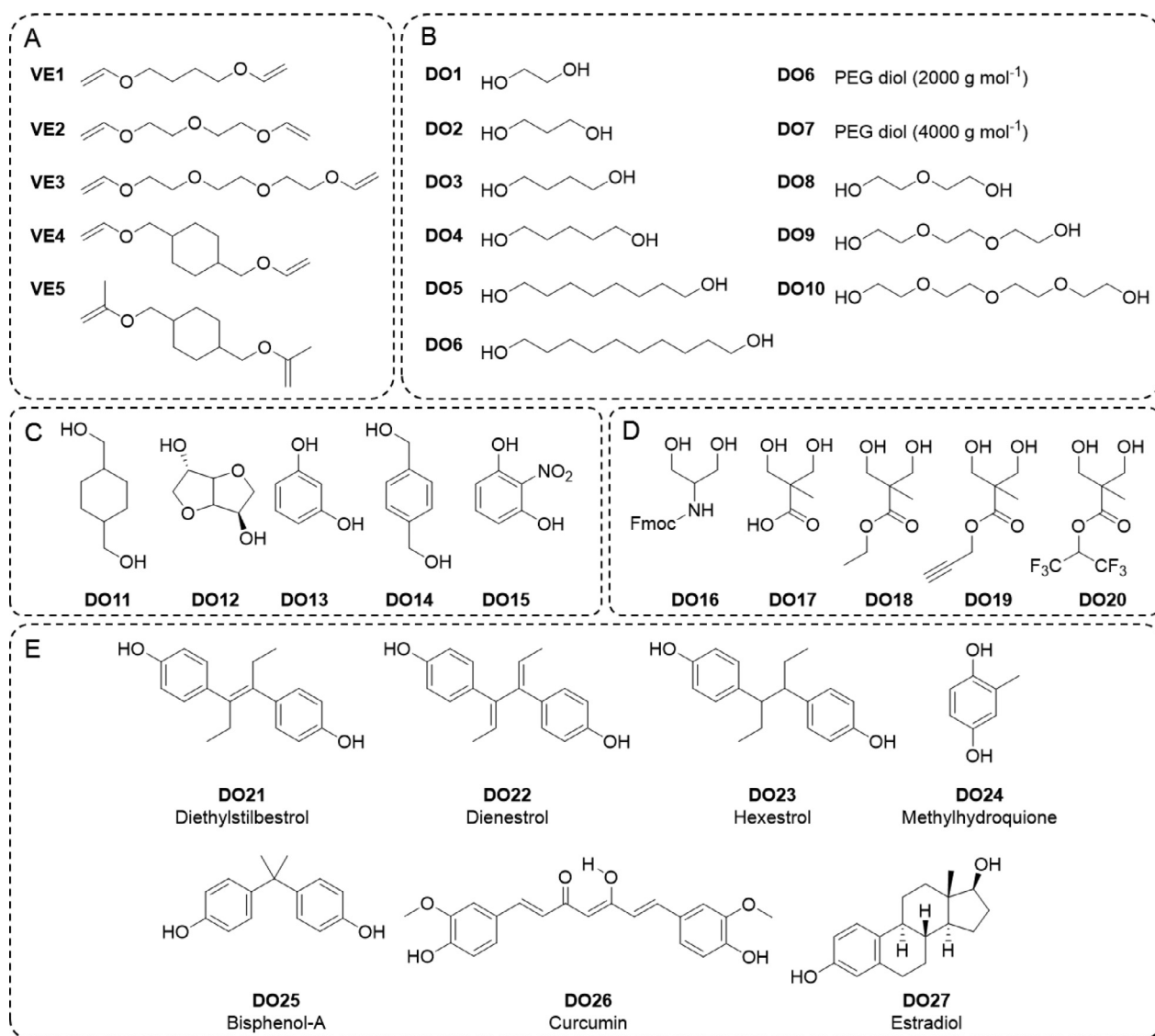
By AA+BB polyaddition of diols and divinyl ethers, hydrophilic, hydrophobic or amphiphilic polymers are accessible (Table 6). Aside from variation of properties through simple monomers, drugs with diol functionalities can directly be used as monomers (Scheme 8), as established in 2004 by Duncan and co-workers [173]. Further functional moieties such as esters or Fmoc protected amines were introduced through the diol monomer. Similarly, reactive ester or alkyne containing monomers enabled access to additional conjugation of proteins, drugs as well as targeting units *via* post polymerization modifications. If the monomer features a vinyl and a hydroxy function at the same molecule an AB step-growth polymerization can proceed, as reported for macromonomers.

4.1.1.1. Polyacetals comprising drugs in the backbone. The wide variety of diols and divinyl ethers represents an excellent platform for the variation of properties of polyacetals in a combinatorial manner, as reported by Koberstein and co-workers, who synthesized a 21-membered library [174]. A variety of hydrophobic aliphatic diols (**DO1** to **DO4**) as well as oligo(ethylene oxide) diols (**DO8** to **DO10**) and three divinyl ethers (**VE1** to **VE3**) were used for that purpose. The combination of hydrophilic and hydrophobic monomers resulted in polyacetals featuring LCST behavior in water in a temperature range from 6 to 80 °C. This behavior was further exploited as a polymer-gel matrix for antimicrobial compounds such as silver sulfadiazine or Neosporin in wound care applications [175].

The oligo(ethylene oxide) based monomers **VE3** and **DO10** represented the basis for the incorporation of hydrophobic Hypoxia Inducible Factor-1 (HIF-1) inhibitors for anti-cancer therapy into the polyacetal chains through copolymerization of the drug diols **DO21**, **DO24** and **DO25** [176]. Drug contents varied from 5 to 40%. Whereas **DO24** and **DO25** polymerized with full conversion, **DO21** was less reactive, resulting in polyacetals with only 20% drug content. The hydrophobicity of the drugs in the PEG-like polymer



Scheme 7. Schematic representation of the two main reaction pathways for acid-catalyzed step-growth polymerization yielding polyacetals. (A) Polyaddition of divinyl ethers and diols. (B) Polycondensation of 2,2-dimethoxypropane and diols.



Scheme 8. Schematic representation of recently utilized monomers for polyacetal synthesis. A) Divinyl ethers. B) and C) Hydrophobic and hydrophilic diols. D) Diols with functional groups. E) Diols used as active pharmaceutical ingredients.

led to LCST behavior, which could be adjusted by the copolymer composition. Promising candidates for hyperthermia-based targeting included poly(VE3-co-DO10/DO14_{15%}) with a T_{cp} of 40.7 °C, poly(VE3-co-DO10/DO25_{7.5%}) with a T_{cp} of 39.4 °C, and poly(VE3-co-DO10/DO21_{15%}) with a T_{cp} of 39.5 °C. As the drug formed part of the polymer chain, drug release was achieved by complete degradation of the polyacetal. Whereas the molar mass decreased by 50% after 5 h in a pH 5 PBS solution, the drug release was delayed. Only 20% of DO21 were released after three days.

Vicent and coworkers reported similar polyacetals based on PEG (DO6 or DO7) and VE2 comprising between 2.4 and 8.9 wt% DO21, DO22, DO23 as well as DO25 [177]. Detailed release studies of designed copolymer pairs showed that the release of bisphenol A (DO25) was significantly slower compared to that of diethylstilberol (DO21), and that the degradation of polyacetals with lower drug content or longer PEG spacers was faster. In contrast to the free drugs, the polymeric prodrugs were not or only slightly cytotoxic, thereby enhancing the drug therapeutic index.

Table 6
Selected characterization data of the polyacetals obtained via polyaddition of divinyl ethers and diols. Molar masses determined by SEC.

VE	DO	Drug or 2nd diol	M _n (g mol ⁻¹)	Application	Acidic degradation ^{a)}	Refs.
VE1-3	DO1-4, DO8-10		1000 to 17,300	LCST	VE1/DO10 : 50% of original M _n after 4 h at pH 5.5 (SEC)	[174]
VE1	DO1		12,400	Film forming	–	[175]
VE3	DO10 _{20%}	DO5 _{80%}	12,280	Film forming	–	[175]
VE3	DO10	DO21, DO24, DO25	7000 to 18,300	Drug conjugate	VE3/DO10 _{85%} / DO21 _{15%} : 50% of original M _n after 5 h at pH 5 (SEC)	[176]
VE2	DO6	DO21 _{2wt%}	17,600	Drug conjugate	50% drug release after 3 days at pH 5.5 (HPLC)	[177]
VE2	DO6	DO21 _{5wt%}	22,000	Drug conjugate	50% drug release after 15 days at pH 5.5 (HPLC)	[177]
VE	DO6	DO21 _{9wt%}	25,300	Drug conjugate	30% drug release after 45 days at pH 5.5 (HPLC)	[177]
VE2	DO7	DO22 _{4wt%}	25,800	Drug conjugate	–	[177]
VE2	DO7	DO23 _{4wt%}	22,700	Drug conjugate	–	[177]
VE2	DO7	DO21 _{5wt%}	22,500	Drug conjugate	50% drug release after 7 days at pH 5.5 (HPLC)	[177]
VE2	DO7	DO25 _{5wt%}	24,300	Drug conjugate	50% drug release after 13 days at pH 5.5 (HPLC)	[177]
VE3	DO7	DO21	20,800 to 24,400	Drug conjugate (Statistical structure)	VE3/DO7/DO21 _{4wt%} : 50% drug release after 3 days at pH 5.5 (HPLC)	[178]
VE3	DO7	DO21	16,700 to 24,200	Drug conjugate (Block structure)	VE3/DO7/DO21 _{4wt%} : 50% drug release after 3 days at pH 5.5 (HPLC)	[178]
VE2	DO7	DO26	26,600 to 45,400 (M _w)	Drug conjugate	VE2/DO7/DO26 _{4wt%} : 50% drug release after 24 h at pH 5.5 (HPLC)	[179]
VE2	DO6	DO21 DO26	11,200 to 40,100	Drug conjugate	VE2/DO6/DO21 _{1wt%} / DO26 _{5wt%} : Drug release at pH 5.5 after 7 days: 40% for DO26 and 10% for DO21 (HPLC)	[180]
VE5	DO27		6500	Drug conjugate	–	[181]
VE5	DO11	DO27 _{11wt%}	23,300	Drug conjugate	50% drug release after 3 days at pH 5.0 (HPLC)	[181]
VE5	DO11		–		–	[181]
VE5	DO11	DO6	49,800		–	[181]
VE5	DO3		47,800		–	[181]
VE5	DO6		193,100		–	[181]
VE5	DO12		45,300		–	[181]
VE3	DO7 _{60%}	DO16 _{40%}	6500	Protein conjugation	–	[182]
VE3	DO7 _{64%}	DO17 _{36%}	4900	Protein conjugation	–	[182]
VE1	DO18		16,000		–	[183]
VE1	DO20		5600	Drug conjugation	–	[183]
VE1	DO19		17,500	Drug conjugation	–	[183]
VE1	DO19 _{48%}	DO20 _{52%}	19,500	Drug conjugation	–	[183]
VE4	DO15	–	2800	For block copolymer synthesis	–	[184]
VE4	DO13		–	For block copolymer synthesis	–	[185]

^{a)} Additional degradation conditions and profiles are reported.

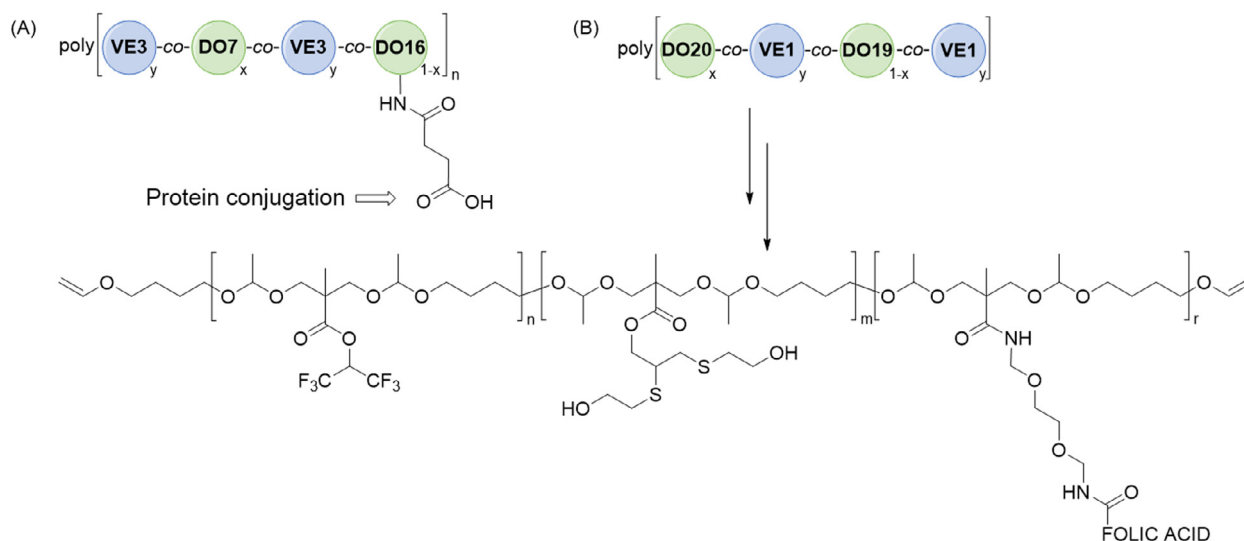
In a follow-up study, the influence of the distribution of the of **DO21** with respect to its position in the polyacetal chain was investigated [178]. In contrast to simple direct copolymerization of all comonomers to result in a statistical distribution of the drug in the polymer chain, a block-like architecture was achieved by a consecutive polymerization of **DO7** and **DO21** with **VE3**. Thereby, the drug content of water soluble polyacetals was increased from 6 to 9 wt%. A different assembly behavior of the two copolymers in water resulted in altered **DO21** release profiles: It was gradually released from the statistical copolymer but in a stepwise fashion from the block-like copolymer. The latter also featured enhanced cytotoxicity in selected prostate cancer cell lines.

Relying on the established PEG-based polyacetal formed from **VE2** and **DO7**, the antioxidant and anti-inflammatory drug curcumin (**DO26**) was copolymerized in drug loadings from 2 to 6 wt% [179]. Due to the hydrophobicity of the drug, well-defined nanocarriers of 90 nm size (DLS) were formed. Similar to diethylstilberol,

the conjugation of curcumin improved solubility, blood bioavailability, cytotoxicity as well as stability in comparison to the free drug to potentially enable treatment for acute and chronic spinal cord injury recovery.

To exploit a synergistic cytotoxic effect against LNCaP cells of both drugs, curcumin (**DO26**) and diethylstilbestrol (**DO21**) were copolymerized in a PEG-based matrix formed from **DO6** and **VE2** [180]. Due to the less stable curcumin acetal moieties, copolymers comprising increasing **DO26** amounts featured lower molar masses (40,100 g mol⁻¹ > M_n > 11,200 g mol⁻¹) and assembled into smaller nanocarriers (33 nm > D_h > 9 nm). Accordingly, **DO26** was released faster from the copolymers than **DO21**.

A substituent variation at the vinyl double bond results in different acetal or ketal repeating units than a the simple acetaldehyde-based acetal. Guo et al. reported the respective **VE5** to form acetone as degradation product of polyketals synthesized via polyaddition with a range of hydrophobic diol



Scheme 9. Schematic representation of conjugation strategies for the attachment of bioactive molecules to polyacetals obtained by step-growth polymerization.

monomers (**DO3**, **DO6**, **DO11**, **DO12**) [181]. The catalyst pyridinium *p*-toluenesulfonate yielded polymers with high molar masses between 45 and 193 kg mol⁻¹ ($1.7 < D < 2.2$) at room temperature. Estradiol (**DO27**) was used as a model drug for copolymerization, either as sole diol or with **DO11**. Degradation of microparticles formed from the terpolymer released the estradiol, avoiding or reducing the formation of acidic degradation products, as was shown by fluorescence mapping of the pH sensitive cargo LysoSensor Yellow/Blue dextran. Biocompatibility of the terpolymer microparticles was confirmed by *in vivo* experiments in rat with benign tissue reaction.

Whereas the approach represents an elegant way to release the drug through backbone degradation in its native form, it is intrinsically limited to drugs comprising two hydroxyl moieties. Reactivity differences of the hydroxyl moieties further complicate predictions of the final copolymer composition, which directly corresponds to the drug loading in this approach. However, detours such as functionalization of such drugs with acetal moieties that are additionally linked to other polymerizable moieties represent promising alternatives circumventing such problems, as recently reported for gemcitabine [186].

4.1.1.2. Polyacetals for conjugation of bioactive molecules. The incorporation of diol monomers with additional functional moieties enables access to polyacetals that can be used for the conjugation of bioactive molecules via post-polymerization modification approaches (Scheme 9). In particular, Fmoc-protected serinol (**DO16**) was frequently applied to yield amino functionalities to be exploited for fluorescence labeling, e.g. through NHS ester coupling [178, 179]. In addition, other functional diols such as the alkyne containing **DO19** or the active ester containing **DO20** offer alternative synthetic possibilities.

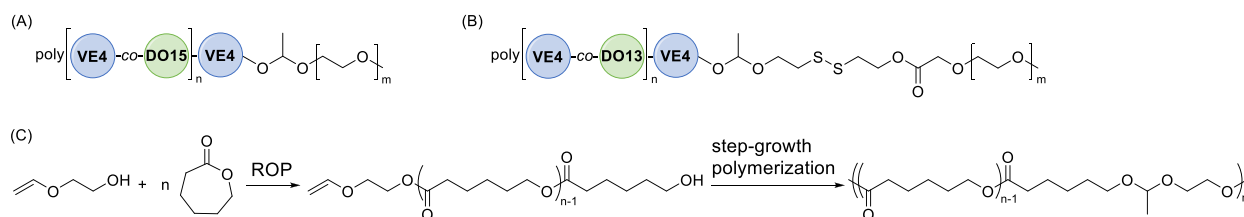
The serinol strategy was applied for conjugation of trypsin to a PEG-based polyacetal formed from the polyaddition of **VE3** and **DO7** [182]. The resulting polymer comprised 40% of the Fmoc-protected serinol (**DO16**) and was subject to a series of post-polymerization modifications involving the deprotection of the Fmoc group, the ring-opening of succinic anhydride through the nucleophilic amino moieties, and the conjugation of trypsin to the carboxylic acid functionalities with a C4-spacer (Scheme 9A). A terpolymerization of **VE3**, **DO7** and **DO17** yielded a corresponding polyacetal without the C4-spacer, which was less efficiently conjugated due to steric hindrance. Both integer polymers inhibited

the enzymatic activity of trypsin at pH 7.4 due to a masking effect, and released the protein at pH 6.5 due to polymer degradation, thereby restoring its activity. The so-called “polymer masked - unmasked protein therapy” (PUMPT) effect was also compared to a common PEGylated trypsin, revealing 2 to 3-fold higher activity for the polyacetal-based systems.

A conjugation strategy based on the use of ester functionalized diols was reported by Moreno et al. (Scheme 9B) [183]. The utilized monomers in the polyaddition included **VE1** and diols based on 2,2-bis(hydroxymethyl) propionic acid with different ester groups such as ethyl ester (**DO18**), propargyl ester (**DO19**) as well as hexafluoroisopropyl ester (**DO20**). These monomers enabled chemically orthogonal postpolymerization modifications. **DO19** was reacted with 2-mercaptoethanol by thiol-yne reaction in varying degrees of modification to tune the polymer hydrophilicity, size and critical aggregation concentration (CAC) of nanoparticles, which were used to encapsulate and release curcumin. Based on detailed development of the orthogonal functionalization of the active ester containing monomer **DO20**, a folic acid derivative was attached by amidation to decorate the nanocarriers with a targeting ligand.

4.1.1.3. Utilization of end groups. The polyaddition of diols and divinyl ethers results in polymers featuring hydroxyl or vinyl ether end groups. While reducing the molar mass [174], the use of one monomer in slight excess enables certain control of the end group type. However, a mixture of both end groups will likely be present when the two monomers are used in an equimolar ratio. Nevertheless, terminal vinyl ether moieties were utilized for attachment of a hydrophilic PEG block through addition of hydroxyl end functional PEG (Scheme 10A and B).

The approach was initially investigated using a polyacetal from **VE4** and **DO15** as light-controlled drug delivery system for photochemotherapy [184]. The coupling of mPEG (2000 g mol⁻¹) resulted in a clear shift of the SEC elugram, however, also in a range of degradation products, most likely formed through transesterification or hydrolysis of the initial polyacetal. The amphiphilic block copolymer (5000 g mol⁻¹) was used to encapsulate camptothecin and hematoporphyrin, which were released through pH value and light as triggers (photolysis at single (365 nm) and double (532 nm) photon excitation). The synthetic approach was adapted by Wang et al. who additionally included disulfide linkages between the two blocks, i.e. a hydrophobic polyacetal from



Scheme 10. Schematic representation of acetal-copolymer structures obtained by utilization of end groups.

Table 7

Selected characterization data of the polyacetals obtained via transacetalization of 2,2-dimethoxypropane (DMP) and diols. Molar masses determined by SEC.

Polyacetal	M_n (g mol ⁻¹)	API	Application	Acidic degradation	Refs.
DO11 + DMP	4100 (\mathcal{D} of 1.54)	SB239063	Loaded particles of 370 nm (SEM)	$t_{1/2}$ of 24.1 days at pH 4.5 by ¹ H NMR sample	[188, 189]
0.13 DO4 / 0.87 DO11 + DMP	2500 (\mathcal{D} of 1.43)	siRNA / microRNA	Loaded particles of 500 nm (SEM)	$t_{1/2}$ of 1.8 days at pH 4.5 by ¹ H NMR sample	[190–193]
DO14 + DMP	6700 (\mathcal{D} of 1.8)	–	Polymer film	Photochemical degradation after 10 min by UV irradiation	[194]
DO4, DO11 + DMP (ABA-block with PNVP)	5500 (\mathcal{D} of 1.16)	DOX, imatinib	Loaded particles of 42 to 49 nm (TEM)	M_n change by SEC: Detection of the mass for the hydrophilic block after 24 h	[195]
DO4, DO11 + DMP (ABA-block with PEG)	8500 (\mathcal{D} of 1.05)	DOX	Loaded particles of 70 nm (TEM)	M_n change by SEC: Detection of the mass for the hydrophilic block after 24 h	[196]

VE4 and **DO13** and mPEG (2000 g mol⁻¹) (**Scheme 10B**) [185]. The acetal and disulfide functionalities rendered the carriers acid and reduction sensitive, respectively, as demonstrated by degradation studies at various pH values and glutathione concentrations.

Fuoco obtained acetal and ester copolymers by a straightforward one pot polymerization with two subsequent steps combining a heterotelechelic macromonomer synthesis and AB polyaddition (**Scheme 10C**) [187]. The first step included ROP of ϵ -caprolactone yielding oligo(ϵ -caprolactone) with TBD as catalyst and ethylene glycol vinyl ether as initiator, featuring a vinyl ether functionality at the α -end and a hydroxyl functionality at the ω -end. These AB-monomers with molar masses between 300 and 10,200 g mol⁻¹ were then polymerized in a step growth approach by switching the catalyst through addition of an excess of diphenyl phosphate (DPP). The resulting multiblock copolymers featured increased M_n values from 2300 to 78,400 g mol⁻¹ ($1.6 < \mathcal{D} < 2.4$). To expand the proof of concept also other cyclic monomers such as trimethylene carbonate, *p*-dioxanone and L -lactide were utilized in the one pot approach. The degradation behavior of films formed from the poly(oligo(ϵ -caprolactone)-co-acetal)s with different DP of the ϵ -caprolactone sequences (6, 10, 18, 33) was investigated over eight days. The according mass losses were between 8% and 16%, whereby films with shorter ϵ -caprolactone sequences degraded faster.

4.1.2. Linear polyacetals from transacetalization polymerization

Recently published transacetalization polymerizations yielding polyacetals rely on DMP and hydrophobic diols initially utilized by Murthy in 2004 [172], i.e. **DO4**, **DO11**, and **DO14** (compare **Scheme 8**, **Table 7**). Hence, recent developments are mainly focused on exploiting their properties for new applications, such as the encapsulation and release of apoptosis inhibitors, siRNA, or chemotherapeutic agents.

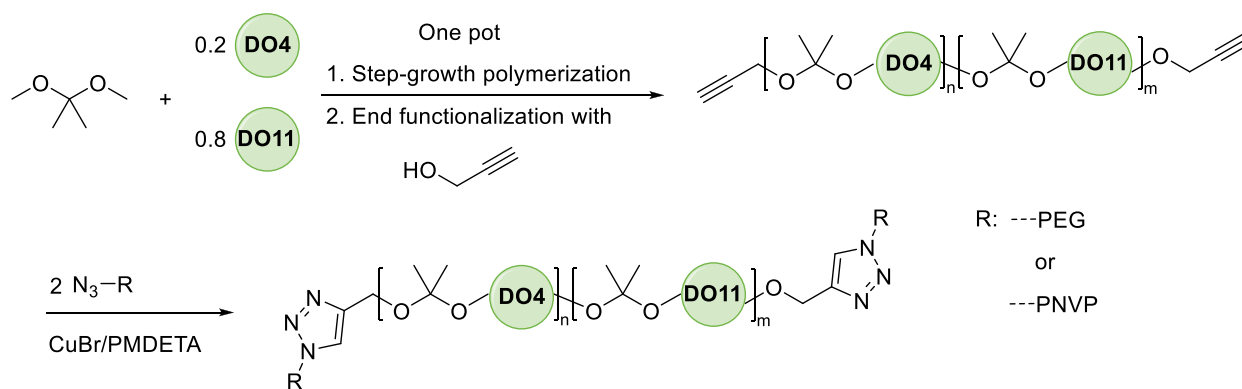
The polyacetal from the condensation of **DO11** and DMP [188] was formulated into *N*-acetylglucosamine (GlcNAc) decorated particles through use of a sugar functionalized surfactant [189]. A decoration degree of 9 wt% was achieved benefitting from the interaction of the surfactant's hydrophobic alkyl chain with the particle exposing the hydrophilic carbohydrate head group to the

aqueous phase. The GlcNAc decoration of particles loaded with the apoptosis inhibitor SB239063 led to increased cellular uptake into cardiomyocytes when compared to unfunctionalized particles. A reduction in apoptotic events as well as infarct size, and improved acute cardiac function were found in rats treated with the particles, whereas no acute effects of non-sugar-decorated particles were found [197].

For the delivery of genetic material such as siRNA, a copolymer based on two diols **DO4** as well as **DO11** with DMP [191, 192] was coformulated with the cationic lipid DOTAP and chloroquine to increase the endosomal escape [190]. An improvement of cardiac function of mice following myocardial infarction was achieved through uptake by cardiac macrophages, where released siRNA specifically silenced the Nox2 gene and inactivated the NADPH oxidase, thereby restoring acute cardiac function at a low dose of 5 $\mu\text{g kg}^{-1}$ animal. The same polyacetal was also applied to deliver microRNA for the reprogramming of cultured mouse bone marrow-derived mononuclear cells [193]. The microRNA released from particles containing 0.9 wt% of genetic material was specific towards embryonic stem cells and successfully activated pluripotency-associated genes (Oct4, Sox2 and Nanog) without permanent genetic manipulation after only eight days of treatment.

Polyacetals are also potentially photochemically degradable [194]. This was intensely investigated for polymers prepared via both step growth mechanisms, i.e. for a polymer from polycondensation of **DO14** and DMP as well as a polymer obtained via the polyaddition of **VE4** and **DO14** (compare Chapter 4.1.1.). Films from both polymers of roughly similar molar mass degraded fully after 10 min exposure to low energy UV irradiation at 193 nm as well as 248 nm. A photolysis mechanism was proposed, based on the heterolytic cleavage of the benzylic acetal moieties and subsequent rearrangement to carbonyl and hydroxyl products. The polymer films were used as photodegradable substrates for laser-mediated cell detachment and direct patterning of mouse fibroblast sheets through postculture laser ablation.

The step-growth synthesis was further expanded by the introduction of alkyne groups at both ends of the polyacetal backbone thereby enabling postpolymerization modification (**Scheme 11**) [195, 196]. For this purpose, the transacetalization polymerization



Scheme 11. Schematic representation of the synthetic strategy towards ABA polymers with a hydrophobic polyacetal middle block and hydrophilic outer blocks.

was performed as already established with a feed ratio of 20 mol% **DO4** and 80 mol% of **DO11**. After monomer conversion, propargyl alcohol was added in large excess to produce oligomeric acetals with claimed end groups ($M_n \approx 1800 \text{ g mol}^{-1}$; $D = 1.15$). Subsequently, ABA copolymers were synthesized by the alkyne-azide-click reaction with N_3 -poly(ethylene glycol) and N_3 -poly(*N*-vinyl pyrrolidone), respectively. Both ABA polymers formed nanocarriers of 4 to 6 nm size (TEM), which considerably increased upon loading with hydrophobic drugs such as DOX or imatinib (42 to 70 nm). Strong decrease of M_n was observed at pH values between 1.4 and 7.4 after 4 h. Despite complete degradation of the hydrophobic segments of the carrier polymers, drug release reached a plateau after ~ 10 h independent of the utilized polymer, drug or the pH value. This might point towards aggregation of the hydrophobic drugs upon degradation of the carrier, thereby impeding quantification in the used setup. *In vitro*, the loaded nanocarriers demonstrated tumoricidal activities against the parental and drug resistant lymphoma cells of murine and human origin with significant effects on cellular uptake, cytotoxicity, growth inhibition and apoptosis. *In vivo*, PEG-*b*-polyacetal-*b*-PEG+DOX reduced the lymphoma size and increased the life span of the treated mice with improved histopathological parameters.

4.1.3. Linear polymers from polyaddition of acetal containing monomers

In addition to synthesis of polyacetals by formation of the acetal moiety throughout the polymerization process, the acetal/ketal unit can already be present within the monomer structure and stay unaltered during the polymerization, thereby introducing the acetal into the polymer backbone while other functional groups react in a step-wise manner (**Scheme 12**).

This synthetic approach was successfully implemented by Murthy and coworkers (**Scheme 12A**) [198]. The alkyne-azide-cycloaddition was used to polymerize a diazide adamantane monomer together with a dialkyne ketal monomer to yield polyacetals with M_n of $49,500 \text{ g mol}^{-1}$ and D of 1.74. The adamantane group embedded into the backbone formed host guest complexes with β -cyclodextrin modified with *b*PEI (1800 g mol^{-1}). pDNA polyplexes of these materials increased transfection efficiency 60-fold in comparison to the uncomplexed β -cyclodextrin modified with *b*PEI while also reducing the cytotoxicity.

A similar approach was reported by Andrade-Gagnon et al. (**Scheme 12B**) [199]. The spirocyclic acetal monomer based on pentaerythritol was further functionalized with two (ethynoxy)aryl groups to be subsequently polymerized with diazide-PEG in a step-growth manner by the Cu(I)-catalyzed cycloaddition. Nanoaggregates with sizes of 400 to 460 nm formed from these amphiphilic polymers were hydrolysable at acidic pH value but stable at physiological pH value. However, the similar Nile Red release profiles at

both pH values pointed towards leakage effects, although the carriers were cytocompatible and taken up by epithelial cells.

The bifunctional monomer 2-methylene-1,3-dioxane-5-pene was used to synthesize a poly(acetal thioether) [200]. First, the anti-Markovnikov thiol-ene addition of the acetal ketene functionality with 1,6-hexanedithiol led to dimeric intermediates (**Scheme 12C**). Subsequently, the photoinitiated, radical polyaddition of the remaining endocyclic double bonds with the dithiol yielded polymers with backbone acetal functionalities. After reduction and capping of the thiol end groups, a polymer of M_n of 5900 g mol^{-1} and D of 3.8 was obtained.

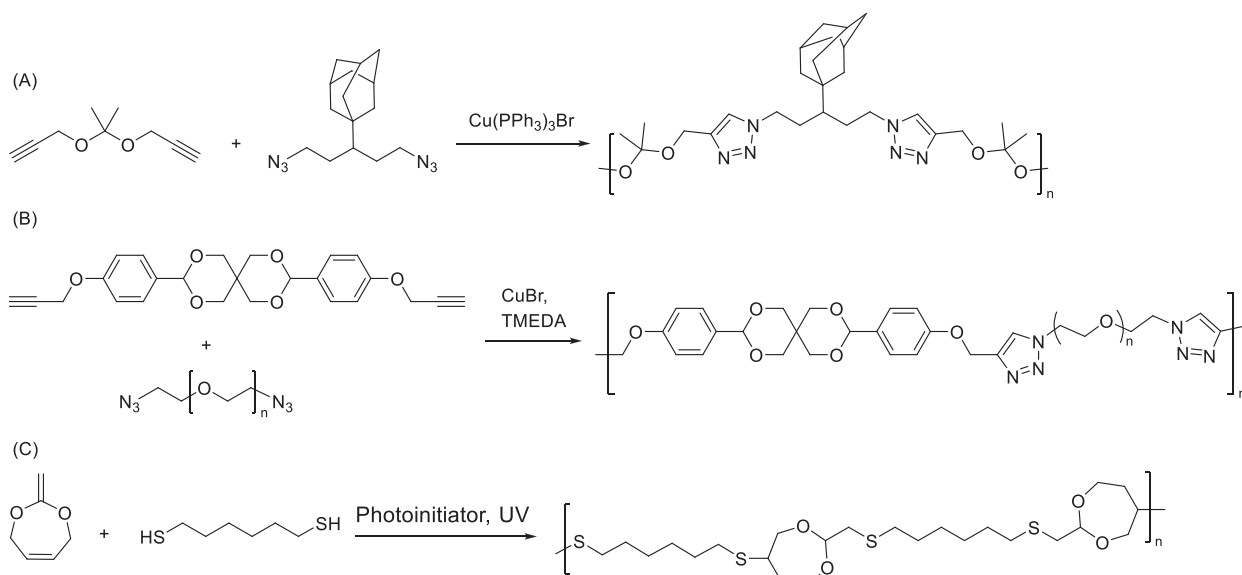
4.2. Chain growth polymerization

Over the last decade a range of different synthetic strategies was reported for the incorporation of acetal moieties into the polymer backbone. Besides the direct ROP of cyclic monomers, their copolymerization with lactones or vinyl ethers opened access to polymers with adjustable degradation behavior. In this regard, acetal functionalities in the polymer backbone are also formed in copolymerizations of vinyl ethers with carbonyl compounds or cyclic ethers when a crossover of the monomers takes place. In addition, cyclic hemiacetal esters enable access to polymers with repeating acetal and ester moieties. As many of these synthetic strategies are new, recent publications in this field mainly focus on polymerization mechanism, the design of new polymers as well as on detailed characterization approaches. The few applications reported so far include solid electrolytes in batteries, recyclable thermoplastics or drug delivery systems but rely mainly on well-established synthesis strategies such as the ROP of cyclic acetals based on formaldehyde.

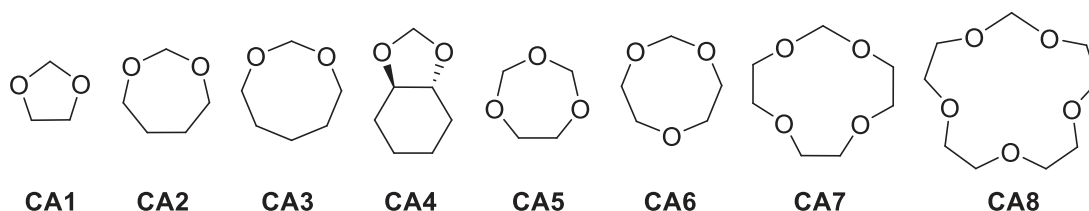
4.2.1. Polymerization of cyclic acetals

Cyclic acetal monomers (**Scheme 13**) represent a straightforward choice for obtaining polyacetals in a direct ROP approach. In fact such syntheses were already reported in the 1930s for the cationic ROP (CROP) of the seven-membered formaldehyde-based acetal **CA2** and the analogous eight membered ring **CA3** by Hill and Carothers [201]. The homopolymerization of **CA1** was patented in the 1940s [202]. Cyclic acetals based on (substituted) **CA1** and **CA2** were found to copolymerize with formaldehyde or 1,2,5-trioxane yielding polyoxymethylene copolymers with high industrial success that are today known as POM-C [165, 166, 203-210].

In addition to these formaldehyde and acetaldehyde based materials, additional early reports exist on the copolymerization of other substituted 1,3-dioxacycloalkanes with 1,2,5-trioxane [211-213]. Since then, aspects of polymerization conditions and mechanistic pathways have remained of great interest. The activated chain end mechanism during Brønsted or Lewis acid catalyzed



Scheme 12. Schematic representation of linear polyacetals from polyaddition of acetal containing monomers.



Scheme 13. Schematic representation of cyclic acetal monomers successfully polymerized *via* chain-growth processes to homopolymers.

CROP of such monomers promotes formation of cyclic polymers with overall low molar masses, which causes dispersity broadening and hampers the access to end-functionalized polyacetals. Intermacromolecular transacetalization represents another challenge to be met during the synthesis of tailor-made polyacetals [209].

The access to α,ω -hydroxy telechelic poly**CA1** was recently optimized in the triflic acid / ethylene glycol initiated CROP [214]. Low catalyst to initiator ratios in the solution polymerization were favorable. However, inter- and intramacromolecular transacetalization could not be avoided at conversions above 20%.

Other recent reports are concerned with achieving high molar mass poly**CA1**. The use of rare-earth triflates $[\text{RE}(\text{OTf})_3]$ ($\text{RE} = \text{Sc}, \text{Y}, \text{Gd}, \text{Tm}, \text{and Lu}$) led to poly**CA1** with molar masses up to $44,300 \text{ g mol}^{-1}$ as well as $D < 1.71$ [215]. Coates and coworkers described reversible-deactivation conditions during the CROP of cyclic acetals using halogenmethyl methyl ethers as initiators and indium(III) bromide as catalyst [216]. The living polymerization of five different cyclic acetals (**CA1** to **CA4**, **CA6**) based on formaldehyde yielded polymers with high conversions (up to 85%) and molar masses up to $230,000 \text{ g mol}^{-1}$. Dispersity values ranged between 1.51 and 1.74 due to the transacetalization as described above. Poly**CA1** was investigated in detail as a chemically recyclable thermoplastic, as it exhibited tensile strength comparable to commodity olefins such as isotactic polypropylene or high-density polyethylene. Depolymerization catalyzed by a strong acid was impressively shown as it was possible to recover the **CA1** monomer quantitatively by distillation from polymer bulk material or plastic waste mixtures.

In particular, the more hydrophilic poly(ether acetals) (**CA1**, **CA5** to **CA8**) are currently discussed as poly(ethylene oxide) (PEO) alternatives as polymer electrolytes in lithium-ion batteries [217–222]. The polymers can be synthesized from cyclic acetals containing in-

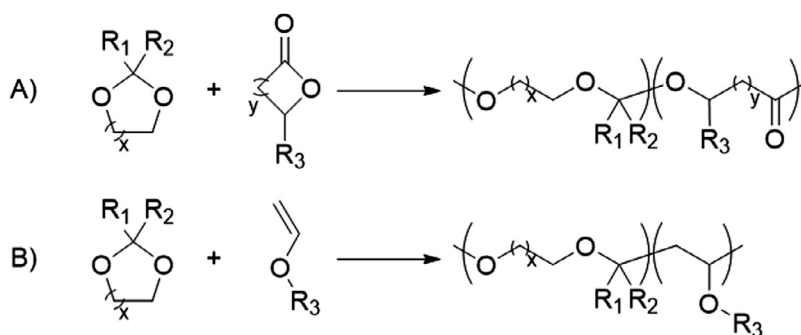
creased amounts of ethylene oxide in the ring structure, predetermining the ratio of ethylene oxide and methylene oxide repeating moieties in the resulting polymers [217]. The variation of the Li^+ coordination in the electrolyte, as in comparison to PEO, enhances the cation self-diffusion and, hence, influences the conductivity. Further optimizations are potentially possible through the use of miscible blends of, e.g., poly**CA6** and PEO [219]. In this context, it should also be noted that the monomer **CA1** can be used as solvent in Li ion batteries, whereby its electro- or cationic polymerization within the device creates a protective solid electrolyte interphase layer [220–223].

4.2.2. Copolymerization of cyclic acetals with lactones or vinyl ethers

The fact that cyclic acetals can be polymerized *via* CROP facilitates their copolymerization with other cationically polymerizable monomers such as lactones or vinyl ethers (Scheme 14, Fig. 12).

The copolymerization of L-lactide with **CA1** yielded copolymers comprising up to 27 mol% acetal moieties leading to increased acid sensitivity compared to the pure polyester [224]. For instance, a copolymer featuring a molar mass of 7500 g mol^{-1} degraded to oligomers of 1400 g mol^{-1} after 72 h.

Cyclic acetals represent isomers of hydroxyl functionalized vinyl ethers. 4-Hydroxybutyl vinyl ether (**VE21**) isomerized forming 2-methyl-1,3-dioxepane (**CA10**) within 5 min at 0 to $30 \text{ }^\circ\text{C}$ in the presence of ethanesulfonic acid (EtSO_3H), *i.e.* under cationic polymerization conditions [225]. Its copolymerization with ϵ -caprolactone yielded a variety of copolymers with tunable compositions and sequences depending on the initial monomer concentration. Poly(ϵ -caprolactone-*alt*-**VE21**) was obtained by removal of **CA10** at reduced pressure from a copolymer comprising 80 mol% **CA10**. During this degradation under vacuum *via* depolymerization



Scheme 14. Schematic representation of the cationic copolymerization of cyclic acetals with A) lactones and B) vinyl ethers.

M _n kg mol ⁻¹ /Đ										Behavior in copolymerization
	CA9	CA10	CA2	CA11	CA12	CA13	CA14	CA15	CA1	
VE9	15.6 /1.41	6.8 /1.65	11.2 /1.84	16.5 /1.85	7.2 /1.19		9.9 /1.19	5.2 /1.37		■ Copolymer <i>via</i> frequent crossover
VE8	13.0 /1.16	8.6 /1.36	4.5 /1.34	12.8 /1.16			9.9 /1.09			■ Occasional crossover / reduced polymerization control
VE14	8.5 /1.54						1.0 /1.26			■ Vinyl homopolymers
ϵ -Caprolactone	2.5 /2.20	15.2 /1.9	1.6 /3.24		16.1 /1.37			10.0 /3.10	23.3 /1.79	□ No data
L-Lactide									7.5 /2.0*	

M _n kg mol ⁻¹ /Đ								Behavior in copolymerization
	CA10 (VE21)							
CA10 (VE21)	14.5 /1.90**	1.3 /2.17	8.8 /1.92**		0.5 /2.21			■ Copolymer <i>via</i> frequent crossover
								■ Occasional crossover / slow reaction
								■ Not successful

* No crossover information, [L-lactide]/[CA1]:1.4
** Main peak value

Fig. 12. **Top:** Summary of copolymerization studies of a variety of cyclic acetals with the vinyl ethers and lactones. **Bottom:** Summary of the copolymerization study of 2-methyl-1,3-dioxepane (**CA10**) (generated *in situ* from 4-hydroxybutyl vinyl ether (**VE21**)) with a variety of lactones. Molar masses determined by SEC.

as well as random transacetalization, the molar mass decreased from 6300 g mol⁻¹ to 1900 g mol⁻¹. However, such copolymerizations were only possible with a few lactones [226]. Copolymerizations of **CA15** and L-lactide, β -butyrolactone, as well as β -hexanolactone failed; copolymerizations with ϵ -heptanolactone and β -propiolactone proceeded slowly yielding cyclic, low molar mass products. In contrast, γ -valerolactone and ϵ -caprolactone were copolymerizable with **CA10**. Other cyclic acetals were incorporated only in low amounts into PCL. Poly(δ -valerolactone-*co*-**CA15**) was subjected to a polymerization-depolymerization study controlled by the reaction temperature between 30 and 90 °C. Sequence transformation was achieved at higher temperatures shifting from 2:1 [**CA15**]:[δ -valerolactone] towards a 1:1 ratio of the monomers. Interestingly, this behavior was reversible, as the **CA15** monomer was reintroduced into the polymer backbone upon cooling.

The cationic copolymerization of several cyclic acetals derived from formaldehyde, acetaldehyde and acetone with the vinyl ethers **VE8** and **VE9** was intensively investigated (Fig. 12) [227, 228]. Among them, the 5-membered heterocycle **CA1** as well as the 7-membered rings **CA2** and **CA10** underwent homopolymerization or oligomerization under the conditions used in the copolymerizations (IBEA / TiCl₄ / SnCl₄ / ethyl acetate / DTBP, in toluene / CH₂Cl₂ at -78 °C), which is in agreement with earlier reports [201, 209]. In copolymerizations with the vinyl ethers, vinyl ether homopolymers were obtained for non-compatible VE-cyclic acetal combinations. However, several copolymer sequences such as

multiblock, random, or nearly alternating were realized for suitable monomer combinations. For copolymers with **VE9**, an increasing stability of the acetal-generated carbocation (primary < secondary < tertiary) also increased the efficiency of the crossover reaction as well as the polymerization rate. The more reactive **VE8** exhibiting a higher tendency to homopolymerize led to fewer successful **VE8**-cyclic acetal combinations with less frequent crossover reactions.

Trimethylsilyl vinyl ether (**VE14**) enabled access to polyvinyl alcohol through deprotection of the resulting polymer, which can be achieved at weak basic or acidic conditions but also with fluorides [229]. In a copolymerization with a cyclic acetal such as **CA9** (Fig. 13), the resulting vinyl alcohol repeating units form an unstable hemiacetal at positions in the polymer chain where a crossover took place. Applicable also in terpolymers of **VE14**, **CA9** and **VE9**, the strategy hence facilitated selective cleavage of these predetermined breaking points with fluoride ions, whereas the acetal moieties could be further degraded under acidic conditions.

4.2.3. Copolymerization of vinyl ethers with aldehydes

Over the last years, Aoshima and coworkers produced a large body of work on cationic copolymerization of vinyl ethers with aldehydes, oxiranes (as well as other cyclic ethers), and ketones as well as the combination thereof. Review articles concentrate mainly on mechanistic aspects of that research area and focus on living cationic polymerization in general as well as Lewis acid-base

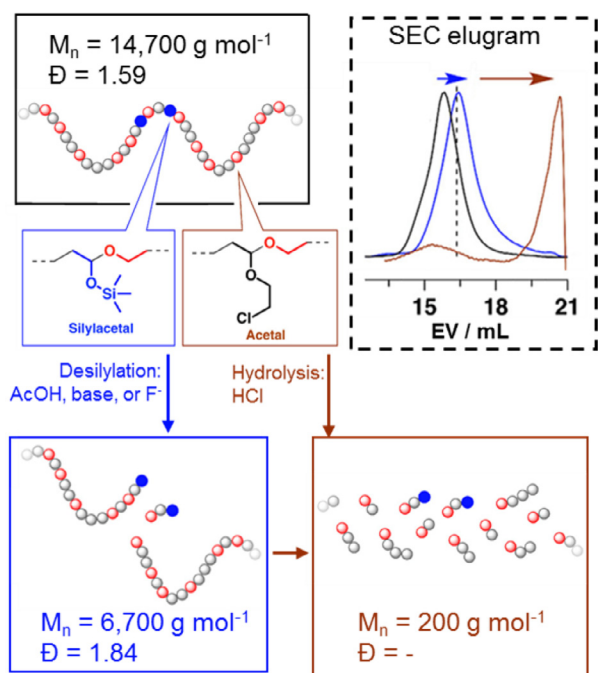
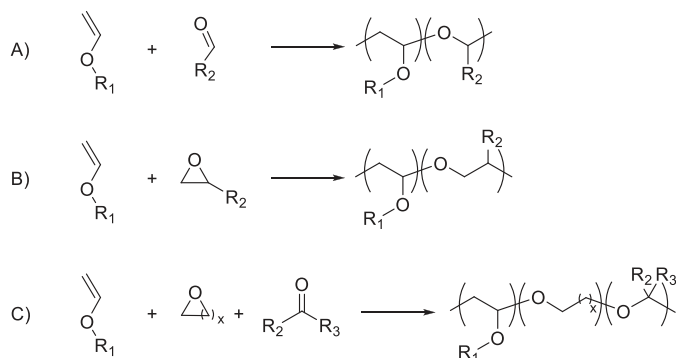


Fig. 13. Schematic representation the selective cleavage of hemiacetal moieties formed upon desilylation of trimethylsilyl vinyl ether repeating units in the terpolymer poly(**VE9-co-CA9-co-VE14**) as confirmed by SEC (EV: elution volume). Adapted with permission from [Kato R. et al. ACS Macro Lett. 2019;8:1498–503] [229]. Copyright 2019 American Chemical Society.



Scheme 15. Schematic representation of vinyl ether copolymerizations yielding polymers featuring acetal moieties.

pair catalysis, and are recommended to the interested reader [230, 231]. Whereas their degradability is seen as a tool to elucidate monomer sequences within these copolymers, biomedical use of the materials is not focused upon. The acetal functionality is introduced by the consecutive polymerization of a vinyl ether and, e.g., an aldehyde. Thereby one acetal oxygen atom is located in the backbone and one in the sidechain (**Scheme 15**). The degradability is not affected by this positioning and can even yield recyclable degradation products. In more recent studies a large variety of monomers was tested, mainly with the focus on achieving alternating or sequence controlled polymers (**Scheme 16**). In particular, the cyclotrimerizations represent frequent side reactions to be avoided. For that purpose, control parameters such as monomer structure and reactivity, Lewis acid, solvent, presence or absence of Lewis bases represent crucial factors.

4.2.3.1. General reaction scope / living polymerization. Earlier reports describe the establishment of the base-assisted cationic copolymerization of isobutyl vinyl ether (**VE8**) and benzaldehyde (**AL1**) ini-

tially utilizing EtSO_3H and EtAlCl_2 in toluene in the presence of 1,4-dioxane at -78°C [242, 243]. A subsequent systematic study investigating the structural effects was performed for cationic copolymerizations of benzaldehyde derivatives and various enol ethers with different structures under standard reaction conditions (**Table 8**) [232]. In addition to simple vinyl ethers such as **VE6** and **VE8**, acyclic monomers with methyl substituents involved the α -methyl substituted **VE11**, the β -monomethyl substituted **VE12**, and the β,β -dimethyl substituted **VE13**. Additionally, five- and six-membered cyclic enol ethers such as **VE23**, **VE24**, and **VE25** were investigated. Several benzaldehyde-based monomers (**AL1 / AL3 / AL4**) successfully copolymerized with **VE6**, **VE12**, **VE8**, **VE23** and **VE24**. Some copolymerizations were even well controlled, yielding alternating copolymers with controlled molar masses and dispersity values. However, monomers such as **VE11**, **VE13** or **VE25** either homopolymerized, underwent exclusive cyclotrimerizations with one benzaldehyde-based monomer, or prohibited any polymerization. Nevertheless, the possibility to achieve a successful alternating copolymerization in such cases through variation of the polymerization conditions was demonstrated for the copolymerization of **VE25** and **AL4**. In general, the molar masses of the poly(**VE-co-AL**) increased with increasing reactivity of the benzaldehyde-based monomer following $\text{AL1} < \text{AL3} < \text{AL4}$ due to the increasing ability to stabilize the cationic charge. In contrast, an ortho-substitution of the benzaldehyde-based monomer (**AL2**) resulted in loss of the defined properties, increase of side products, in particular for copolymerizations with β -substituted enol ethers. Among a variety of plant-derived, non-aromatic enals, in particular the copolymerization of **VE8** and myrtenal (**AL6**) was well controlled [234, 244].

The controlled cationic copolymerization of cinnamaldehyde (**AL7**) with **VE8** proceeded *via* the specific 1,2-carbonyl addition of the enal fragment and resulted in the alternating copolymer poly(**VE8-alt-AL7**) [233]. Its acidic hydrolysis yielded, among others, **AL8** as a degradation product. Despite the additional conjugated double bond, the copolymerization of **AL8** with **VE8** also proceeded mainly *via* the 1,2-carbonyl addition. The resulting copolymer likewise hydrolyzed to yield the extended conjugated aldehyde (*E,E,E*)-7-phenylhepta-(2,4,6)-trienal with $\sim 80\%$ yield. A chemical recycling system was hence established as overall three copolymerization-hydrolysis rounds were achieved taking into account the synthesis of poly(**VE8-alt-AL1**) and its hydrolysis giving the **AL7** monomer [242].

The synthetic sequence control was demonstrated through the controlled cationic copolymerization of **VE9** and **AL3** as well as **VE8** and **AL6** [235]. Up to three predetermined breaking points in form of alternating VE-AL sequences (*i.e.* acetal moieties) were introduced in the main chain by addition of at least five equivalents of the highly reactive **AL3** to the living cationic polymerization of **VE9**. Thereby, the fast aldehyde consumption facilitated the formation of homo-VE-sequences before and after aldehyde addition. Block-type copolymers with degradable VE-AL blocks were obtained by addition of 1.5 equivalents of **AL6** to the living cationic polymerization of the monomer **VE8**. Subsequently, the two monomers were consumed at the same rate yielding poly(**VE8**)-block-(**VE8-alt-AL6**). The livingness of such polymerizations was further exploited in order to obtain core-degradable star-shaped polymers, through addition of a bifunctional VE or aldehyde in the second step to enable crosslinking of the second block.

The sequential arrangement of monomeric units was further expanded to gradient copolymers made of tri(ethylene glycol) methyl vinyl ether (**VE18**) and **AL4** [236]. Use of a large excess of **VE18** ($[\text{VE18}]_0/[\text{AL4}]_0 = 11/1$) caused a gradual decrease in the instantaneous composition of the aldehyde units along the polymer. Alternating as well as block copolymers with the same monomers were obtained as described above. However, less reactive **AL6** as well

Table 8

Copolymerizations of vinyl ethers and aldehydes. Schematic representation of the monomer structures is depicted in **Scheme 16**. Deviations from the standard polymerization conditions (EtSO₃H / GaCl₃ / 1,4-dioxane in toluene at -78 °C) are noted accordingly. DTBP: 2,6-Di-*tert*-butylpyridine. Molar masses determined by SEC, unless indicated otherwise.

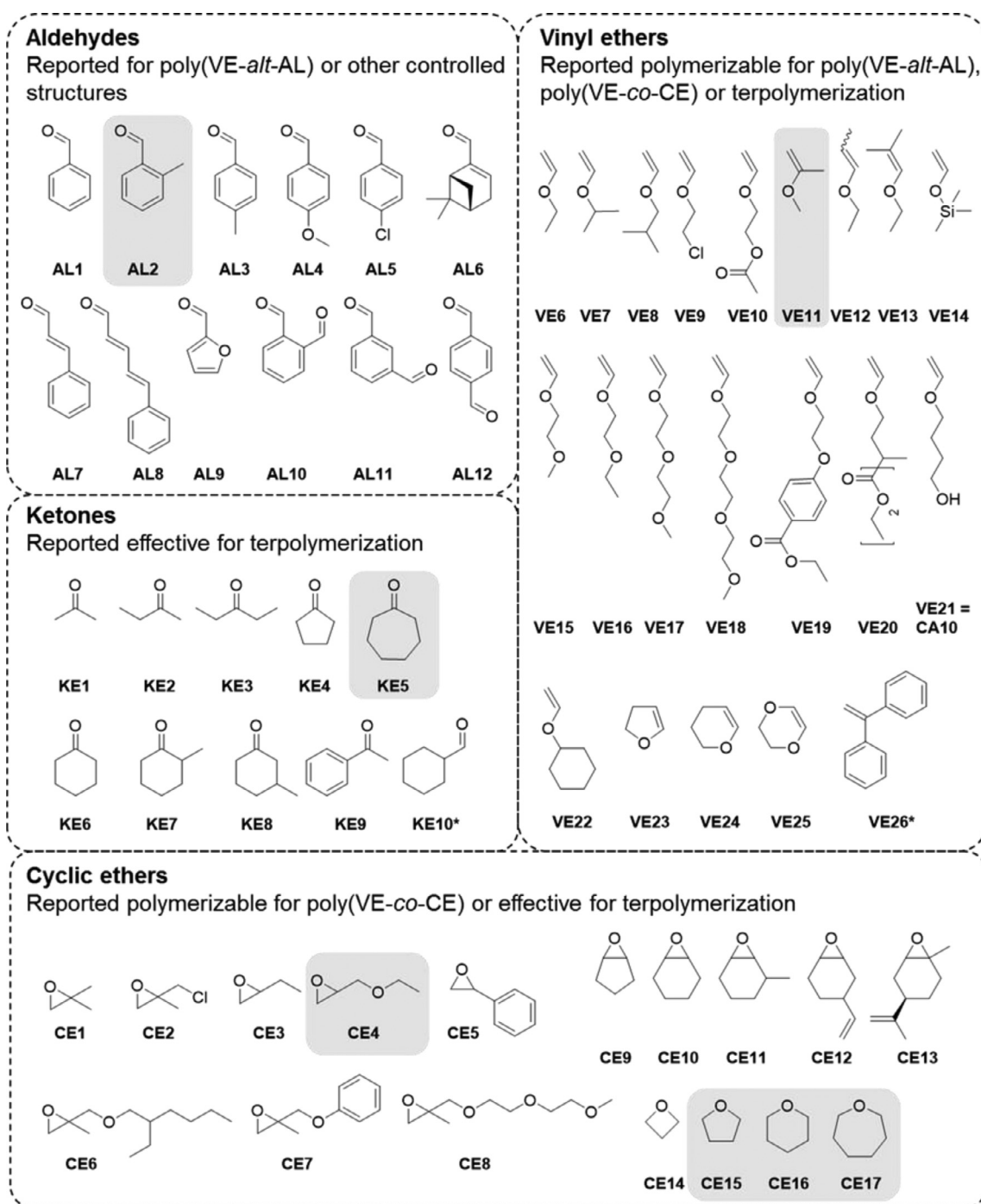
VE	AL	M _n (g mol ⁻¹)	D	Reaction conditions	Content AL (%)	M _n of degradation product ¹⁾ (g mol ⁻¹)	Refs.
VE11	AL1 / AL3 / AL4	4700 to 6500	1.40 to 1.59	Standard	<1	-	[232]
VE12	AL1 / AL3 / AL4	17,800 to 20,300	1.17 to 1.59	Standard	42 to 48	150 to 210	[232]
VE13	AL1 / AL3 / AL4	300 to 380	-	Standard	-	-	[232]
VE23	AL1 / AL3 / AL4	6000 to 18,400	1.72 to 2.40	Standard	44 to 48	190 to 200	[232]
VE24	AL1 / AL3 / AL4	3500 to 13,000	1.38 to 1.90	Standard	48 to 50	100 to 1000	[232]
VE25	AL4	21,100	1.62	GaCl ₃ in CH ₂ Cl ₂ at -78 °C	49	-	[232]
VE9	AL7	22,400	1.15	Standard	47	160	[233]
VE9	AL8	18,000	1.27	EtSO ₃ H / GaCl ₃ / 1,4-dioxane / DTBP in toluene at -78 °C	48	180	[233]
VE8	AL6	22,100	1.12	Standard	48%	180	[234]
VE9	AL1	10,000	1.08	Standard	5 (short block) ⁴⁾	5100	[235]
VE8	AL6	5100	1.17	Standard	~25 (block) ⁴⁾	3300	[235]
1. VE8 2. VE4	AL6	11,300	1.53	1. EtSO ₃ H / GaCl ₃ / 1,4-dioxane in toluene at -78 °C, 2. -40 °C	n.d.	1500	[235]
VE9	AL11	13,700 ²⁾	1.65	Standard	n.d.	690	[235]
VE18	AL4	33,900	1.27	EtSO ₃ H / GaCl ₃ / DTBP / 1,4-dioxane in toluene at -78 °C	48 (alt) ⁴⁾	170	[236]
VE18	AL4	17,900	1.21	EtSO ₃ H / GaCl ₃ / DTBP / 1,4-dioxane in toluene at -78 °C	14 (block) ⁴⁾	13,400	[236]
VE18	AL4	31,200	1.30	EtSO ₃ H / GaCl ₃ / DTBP / 1,4-dioxane in toluene at -78 °C	7 (gra-dient) ⁴⁾	3300	[236]
VE10	AL9	8100	1.51	Standard	48	285 / 389 / 433 ³⁾	[237]
VE10	AL9	5900	1.56	EtSO ₃ H / GaCl ₃ / 1,4-dioxane in CH ₂ Cl ₂ at -78 °C	40	-	[237]
VE9	AL9	5700	1.75	Standard	48	-	[237]
VE8	AL10	17,500	1.21	Standard	48	360	[238]
VE23	AL10	5400	2.12	Standard	-	-	[238]
VE24	AL10	9000	2.06	Standard	52	-	[238]
VE13	AL10	5800	1.69	Standard	50	260	[238]
VE9	AL11	2200	1.77	EtAlCl ₂ with THF or ethyl acetate in CH ₂ Cl ₂ at 0 °C	90 ⁴⁾	100	[239]
VE9	AL12	3600	2.39	EtAlCl ₂ with THF or ethyl acetate in CH ₂ Cl ₂ at 0 °C	87 ⁴⁾	-	[239]
VE13	AL11	3100	2.21	EtAlCl ₂ with THF or ethyl acetate in CH ₂ Cl ₂ at 0 °C	95 ⁴⁾	-	[239]
VE13	AL12	2500	1.99	EtAlCl ₂ with THF or ethyl acetate in CH ₂ Cl ₂ at 0 °C	n.d. ⁴⁾	-	[239]
VE26	AL11	2300	1.65	GaCl ₃ in CH ₂ Cl ₂ at -78 °C	n.d. ⁴⁾	-	[239]
VE18	AL4	33,900	1.27	EtSO ₃ H / GaCl ₃ / 1,4-dioxane / DTBP in toluene at -78 °C	48	170	[240]
VE19	AL1	14,800	1.15	EtSO ₃ H / GaCl ₃ / THF in toluene / CH ₂ Cl ₂ at -78 °C	42	190/150	[240]
VE20	AL1	12,700	1.12	GaCl ₃ / THF in toluene at -78 °C	46	150	[240]
VE9	AL1	16,700	1.19	Standard	45	-	[241]
VE9	AL3	27,300	1.28	Standard	49	-	[241]
VE9	AL4	5500	1.75	Standard	50	-	[241]
VE9	AL5	11,000	1.31	Standard	43	100	[241]

¹⁾ Indicative of the copolymer microstructure.

²⁾ Determined by laser light scattering.

³⁾ Determined by electrospray ionization mass spectrometry (ESI MS).

⁴⁾ % Cyclic trimerization.



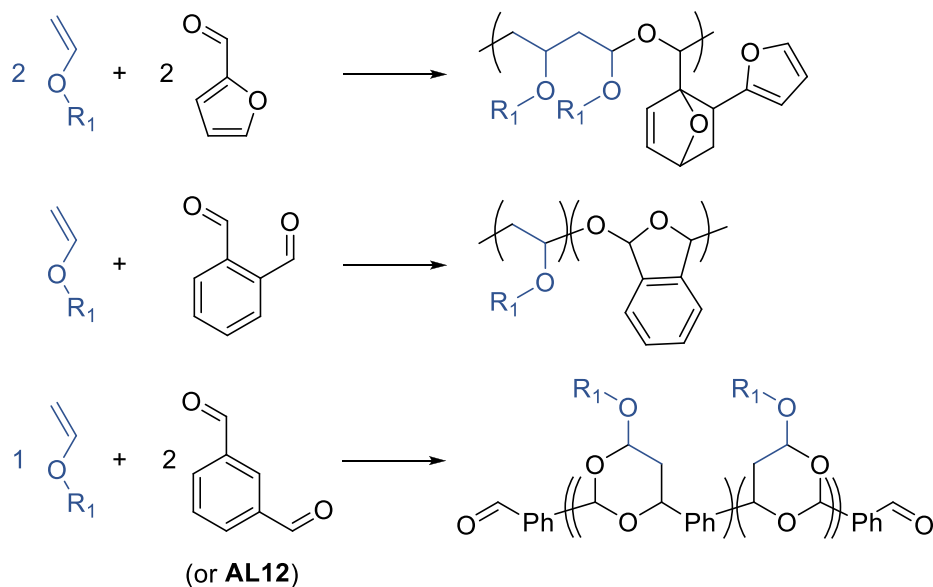
Scheme 16. Schematic representation of monomers tested for different chain growth polymerizations. Compounds marked in gray reported unsuccessful in the respective polymerization attempts. Compounds marked with an asterisk (*) are sorted according to their use in the polymerization instead of functionality. **VE21** isomerizes forming the cyclic acetal **CA10**.

as **AL1** hindered the crossover reaction the VE-derived propagation end to the aldehyde monomer.

In addition to being evident from the thermoresponsive properties of the materials, the successful synthesis of such tailored polymer architectures was confirmed by SEC after acidic hydrolysis of the respective breaking points at the specific positions [235, 236]. Whereas alternating copolymers fully degraded into low molar mass products, according polyVE fragments of higher molar mass were clearly evident for block, gradient and star-shaped polymers.

4.2.3.2. *More complex poly(VE-*co*-AL) from various aldehydes.* The aldehyde monomer scope was further expanded to more complex monomers such as furfural (**AL9**) [237], *o*-phthalaldehyde (**AL10**) [238], isophthalaldehyde (**AL11**) and terephthalaldehyde (**AL12**) (Scheme 17) [239].

The use of **AL9** in the copolymerization with 2-acetoxyethyl vinyl ether (**VE10**) as well as **VE9** resulted in a 2:(1 + 1)-type repeating sequence because every second **AL9** monomer reacted as dienophile in a Diels-Alder reaction with the pendant furan ring adjacent to the growing carbocation [237]. In contrast, the use



Scheme 17. Schematic representation of the copolymerization of vinyl ethers and furfural (**AL9**), *o*-phthalaldehyde (**AL10**), isophthalaldehyde (**AL11**) and terephthalaldehyde (**AL12**) yielding more complex structures.

of dialdehydes resulted in a variation of the backbone structure. The living copolymerization of **AL10** with **VE8** proceeded via the intramolecular cyclization of the two aldehyde moieties of **AL10** and frequent crossover propagation between **AL10** and **VE8** [238]. However, **AL10**'s tendency to form five-membered-rings also in cationic homopolymerization [245] was reduced when copolymerized with **VE23** as approximately 15% of the aldehyde units did not undergo intramolecular cyclization. On the other hand, **VE24** and **AL10** yielded a nearly alternating copolymer. Here, **AL10** probably helped to overcome the low homopolymerizability of the sterically hindered **VE24**. Furthermore, the sterically hindered **VE13**, which does not homo- or copolymerize with benzaldehyde derivatives, was also copolymerizable with **AL10** in an alternating fashion. **AL11** and **AL12** yielded six-membered rings when copolymerized with vinyl monomers such as **VE9**, **VE13** or **VE26** [239]. However, the use of the more reactive vinyl ethers **VE8** and **VE7** resulted in side reactions such as VE-homopolymerization and termination of the linear poly(cyclic acetal) chain.

4.2.3.3. Functional and stimuli responsive copolymers. Most copolymers of aldehydes and vinyl ethers represent hydrophobic materials, which is due to the use of the hydrophobic aldehydes during copolymerization that decreases the water solubility of the polyvinyl ether analogs, as the case for 2-(2-methoxyethoxy)ethyl vinyl ether (**VE17**) (A in **Scheme 18**) [236]. However, increased length of the pendant oligo(ethylene glycol) chain resulted in copolymers featuring LCST behavior in water (B in **Scheme 18**) [240]. Also hydrophilic copolymers featuring carboxylate moieties were accessible through use of ethyl ester functional vinyl ethers and subsequent deprotection at alkaline conditions (C-F in **Scheme 18**). The detour was necessary because the cationic polymerization mechanism prohibited the direct polymerization of the carboxylic acid functional monomers. Whereas F in **Scheme 18** was water soluble only at pH > 6.7, i.e. featured pH value responsive solubility behavior, the two carboxylate functionalities made (E) fully water soluble over the whole temperature range, potentially the only poly(VE-*alt*-AL) reported so far.

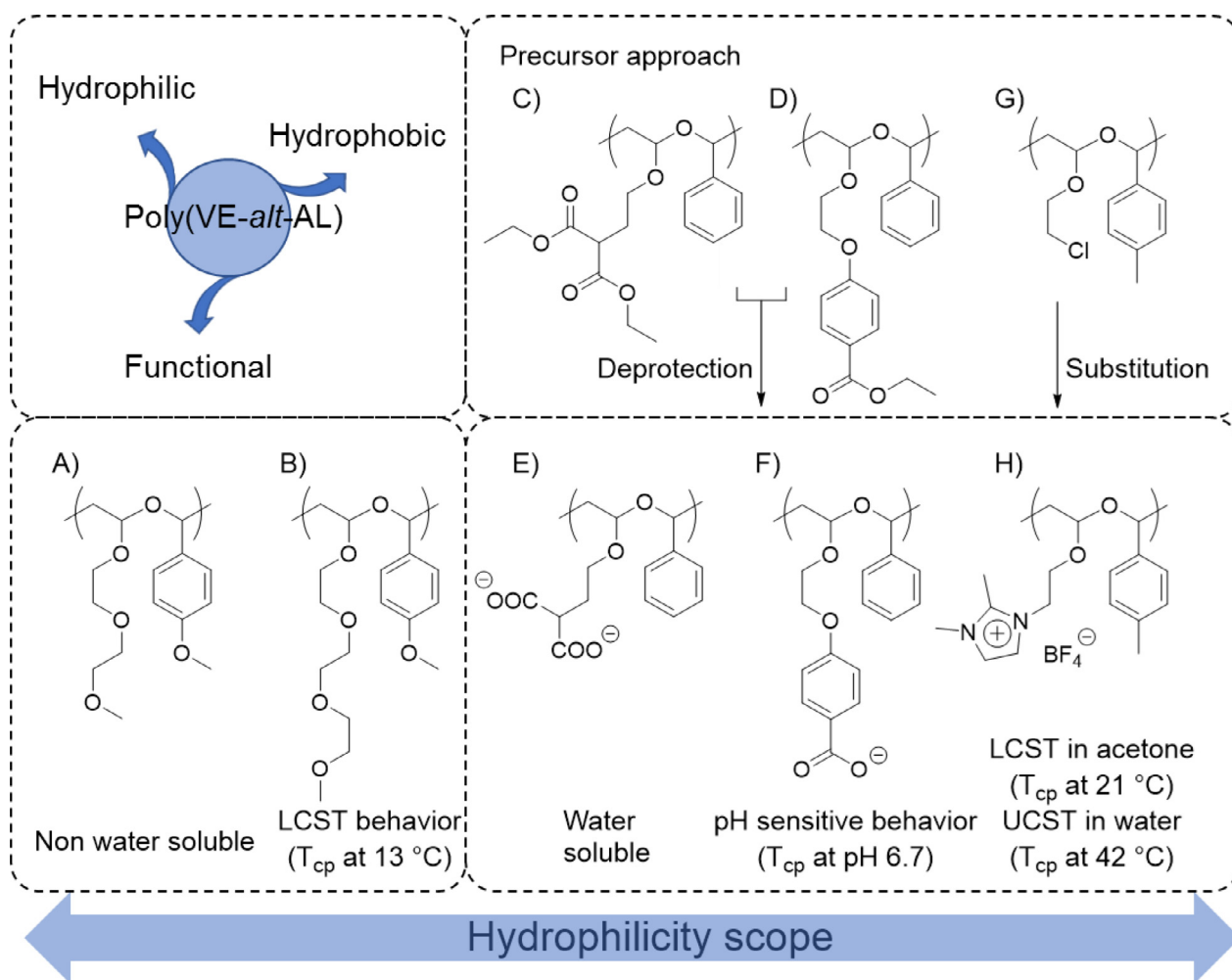
The use of the standard vinyl ether monomer **VE9** enabled access to further post-polymerization modifications through nucleophilic substitution of the pendant chlorine atom [241]. The ap-

proach was exploited for the attachment of dimethylimidazolium functionalities to copolymers of **VE9** with several aldehydes (96 to 100% efficiency). The resulting alternating polymeric ionic liquids featured UCST-type phase transitions in water, and several also LCST behavior, as investigated in detail by the authors. The LCST behavior of several copolymers in acetone was exploited for thermo-induced micelle and aggregate formation of a block copolymer comprising a poly**VE8** segment as a corona.

4.2.4. Copolymerization of vinyl ethers with oxiranes

Similar to the reaction of vinyl ethers with aldehydes, the strictly alternating polymerization of vinyl ethers and oxiranes would yield copolymers with an acetal group in the repeating unit by concurrent cationic vinyl-addition and ring-opening copolymerization (**Scheme 15 B**).

The excellent focus review [246] by Kanazawa et al. summarized different strategies for this polymerization approach. We hence briefly summarize key aspects and focus on very recent work (**Fig. 14**). So far poly(VE-*co*-oxirane) were obtained by copolymerization via frequent crossover reaction. Although the comonomers were not incorporated in a strictly alternating fashion, the VE-oxirane crossover per chain was sufficient to yield low molar mass degradation products after hydrolysis. The generation of a stabilized carbocation resulting from the ring opening of the oxonium ion derived from an oxirane was essential for successful crossover (**Fig. 14**, top). By implication, the frequency of crossover reactions in copolymerization depended on the frequency of the ring-opening reactions of oxonium ions and the nucleophilicity of the monomers. Substituents at the oxirane ring were hence found to be crucial for the successful copolymerization with alkyl VEs. In addition, a suitable Lewis acid catalyst generating a weakly coordinating counter anion was necessary. For instance, B(C₆F₅)₃ effectively initiated through the reaction with water traces, producing B(C₆F₅)₃(OH)⁻ and a proton that initiated the VE and/or oxirane polymerization [247–249]. Other parameters such as solvent polarity as well as the presence of additives also had a significant influence. A weak Lewis base such as ethyl acetate promoted the carbocation stability of the chain end and, thereby, facilitated the cross over reaction [250].



Scheme 18. Schematic representation of responsive and functionalized alternating copolymers of vinyl ethers and aldehydes.

Crossover reactions for the concurrent cationic vinyl-addition and ROP

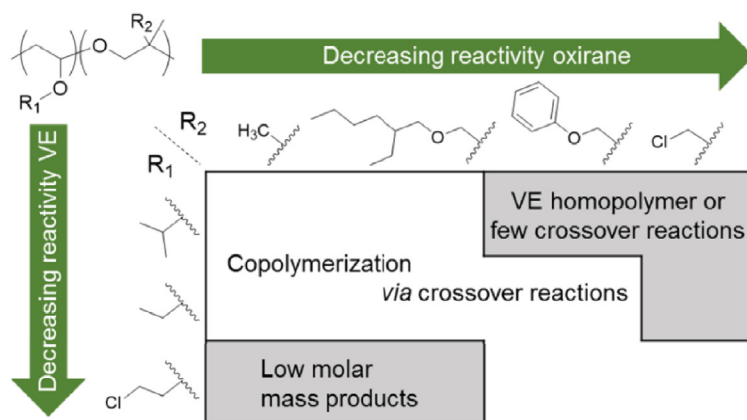
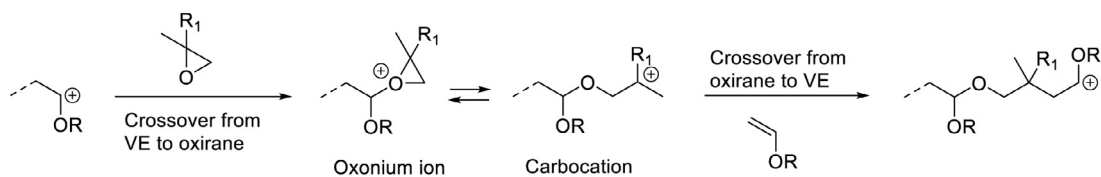


Fig. 14. Copolymerization of vinyl ethers and oxiranes *via* concurrent cationic vinyl-addition and ring-opening polymerization. (**Top**) Schematic representation of the monomer propagation in the different crossover reactions. (**Bottom**) The influence of the monomer substituents and reactivities on the copolymerization products. Triphenylmethyl tetrakis(penta-fluorophenyl)borate ($\text{Ph}_3\text{CB}(\text{C}_6\text{F}_5)_4$) was used as initiator at -78°C in CH_2Cl_2 (with 5 vol% hexane).

Table 9

Selected results of cationic co- and terpolymerization of vinyl ethers, cyclic ethers and carbonyl compounds. DP indicates number of repeating units per chain divided by the number of crossover events per chain. Molar masses determined by SEC.

VE _{DP}	Cyclic ether _{DP}	Carbonyl compound _{DP}	M _n (g mol ⁻¹)	D	M _n of the degradation product (g mol ⁻¹)	Refs.
VE7 ₃₀	CE1 _{5,1}	–	9500	2.20	2800	[251]
VE7 ₉₅	CE6 _{3,5}	–	16,200	1.97	7300	[251]
VE6 _{4,6}	CE1 _{6,6}	–	1900	2.04	900	[251]
VE6 _{7,4}	CE6 _{3,2}	–	7500	1.94	900	[251]
VE6 ₄₁	CE7 _{0,9}	–	4900	1.95	1900	[251]
VE9 _{2,9}	CE7 _{4,5}	–	2100	1.76	700	[251]
VE9 ₃₄	CE2 ₇	–	11,200	2.15	3300	[251]
VE6	CE8	–	3000	1.53	800	[251]
VE7 ₁₃	CE1 _{2,3}	–	5700	1.57	1500	[252]
VE7 ₁₇	CE1 ₃	–	4900	1.72	1700	[253]
VE9	CE2	–	5600	2.57	–	[253]
VE7 _{2,3}	CE10 _{2,1}	KE2 _{0,96}	2100	1.96	300	[257]
VE7 _{6,8}	CE1 _{1,6}	KE2 _{0,79}	4000	1.83	400	[257]
VE7 _{0,49}	CE10 _{7,3}	KE10 _{1,1}	9200	2.05	700	[257]
VE6 _{1,2}	CE12 _{1,4}	KE2 ₁	17,300	1.74	300	[255]
VE7 ₂₄	CE14 _{1,8}	KE2 _{0,82}	17,600	1.82	3400	[254]
VE6 ₁₂	CE14 _{1,7}	KE2 _{0,77}	12,000	1.94	–	[254]
–	CE1 _{2,7}	HAE2 ₁	4500	1.83	300	[256]
–	CE12 _{1,1}	HAE1 ₁	13,600	2.24	1200	[256]
–	CE12 _{6,7}	HAE2 _{0,95}	18,800	2.21	1100	[256]
–	CE12 _{9,9}	HAE3 ₁	6900	1.62	1300	[256]
VE7 _{6,3}	CE1 _{1,6}	HAE2 ₁	19,900	1.79	1800	[256]
VE7 ₁₂	CE12 _{3,8}	HAE3 ₁	12,600	1.20	1200	[256]

The scope of monomer reactivities was recently further expanded to combinations of alkyl VE and 2,2-disubstituted oxiranes featuring a methyl and a weakly electron-withdrawing substituent (Fig. 14, bottom) [251]. For the used oxirane monomers, the reactivity (or nucleophilicity) decreased in relation to the electron withdrawing effect of the substituents in the following order: CE1 > CE8 > CE7 > CE2. Analogously, the reactivity of the VE monomers decreased following VE7 > VE6 > VE9. For the successful copolymerization via crossover reaction the comonomer reactivities had to match. However, VE homopolymers with few crossover reactions were obtained when the reactivity of the VE was higher compared to that of the oxirane. Accordingly, low molar mass products with short homooxirane sequences were isolated when the reactivity of the oxirane exceeded that of the vinyl ether. Table 9 summarizes selected successful copolymerization results including the sequences from efficient crossover reactions.

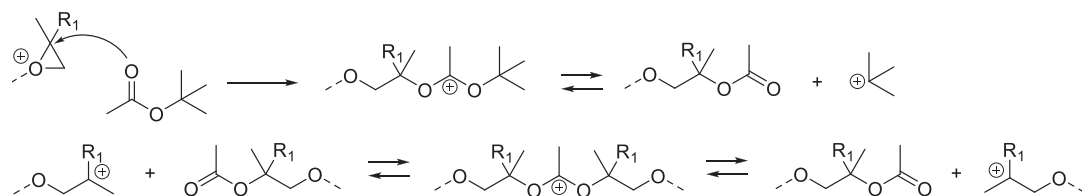
Current efforts are directed to improve the copolymerization of vinyl ethers and oxiranes by screening of initiators aiming at generation of a “living” species during the cationic polymerization [252]. Among the variety of initiators or catalysts such as CF₃SO₃H, (CF₃SO₂)₂NH, 1,1,2,2,3,3-hexafluoropropane-1,3-disulfonamide, B(C₆F₅)₃, Ph₃C⁺B(C₆F₅)₄⁻, Ph₃C⁺PF₆⁻, IBVE-HCl / SnCl₄, CF₃SO₃H / *n*-Bu₄NI, only trifluoromethyl sulfonate decreased the frequency of side reactions, thereby enabling molar mass control of the copolymers. A reversibly cleavable, covalent carbon-triflate bond formed exclusively at the CE1-derived propagating end of for polyVE7-co-CE1 and generated a dormant state. Whereas the reaction conditions were optimized for the monomer pair VE7 / CE1, the copolymerization of several other monomer pairs involving cyclohexyl VE (VE22), limonene oxide (CE13), and styrene oxide (CE5) remained to be improved. Another strategy to increase the control of the cationic copolymerization of oxiranes and vinyl ethers included the use of *tert*-butyl esters as reversible chain transfer agents (CTA) (Scheme 19) [253]. The proposed mechanism was based on nucleophilic attack of the ester at the CE1-derived oxonium species, the formation of an intermediate cation and the subsequent generation of a relatively stable *tert*-butyl cation that initiated a new chain. The ester derived polymer ω-chain end acted as a CTA and promoted reversible chain transfer. Among a variety of potential CTAs, in particular *tert*-butyl

acetate efficiently decreased the polymerization rate, was able to control the molar mass and produced up to 94% acetoxy ω-end groups, thereby validating the proposed mechanism. Besides being successful for the monomer pairs VE7 / CE1 and VE9 / CE2, the approach was also applicable with acetoxy endfunctional poly(*p*-methylstyrene) as a macro CTA enabling access to block copolymers.

4.2.5. Terpolymerization of vinyl ethers with cyclic ethers and ketones

As described above, esters such as ethyl acetate acted as weak Lewis bases and promoted the ROP of the oxirane-derived carbocation or acted as CTAs similar as *tert*-butyl acetate. However, carbonyl compounds such as ketones were also able to act as comonomers in combination with VEs and cyclic ethers (Scheme 15C) [246]. The polymerization mechanism includes the concurrent cationic vinyl-addition, ring-opening and carbonyl-addition terpolymerization through crossover reactions in, potentially, a one-way cycle (Fig. 15, right). The sequence control occurs from the preferential reaction of vinyl ethers with cyclic ethers, cyclic ethers with ketones and ketones with vinyl ethers. However, vinyl ethers as well as cyclic ethers are also homopolymerizable, resulting in a possible occurrence of short homoblocks of these monomers and a general sequence block for the terpolymer according to [(vinyl ether)_x - (cyclic ether)_y - (ketone)_z]_n. Usually performed with B(C₆F₅)₃ in CH₂Cl₂ at -78 °C, other initiators [254] or reaction conditions were also favorable to suppress homopropagation yielding ABC-type terpolymers [255]. As described above, the VE-cyclic ether crossover reaction introduces an acetal functionality in the main chain rendering the terpolymers hydrolysable. However, also the utilization of hydrolysable monomers such as HAE2 [256] (Fig. 15, left) or crossover reactions from carbonyl compound to oxiranes can introduce hydrolysable moieties to the main chain. A summary of promising monomer combinations is provided in Table 9.

Initially successful for the comonomer combination VE7, cyclohexene oxide (CE10) and methyl ethyl ketone (KE2), which yielded poly(VE7-₂-CE10-₂-KE2) (M_n = 2.100 g mol⁻¹; D = 1.96), other monomer combinations such as CE1 / VE7 / KE2 or CE10 / VE7 / KE10 resulted in terpolymers featuring longer polyoxiran or poly(vinyl ether) sequences [257]. The orthogonality of the terpoly-



Scheme 19. Schematic representation of the reversible chain transfer mechanism in the *tert*-butyl acetate mediated cationic copolymerization of vinyl ethers and oxiranes.

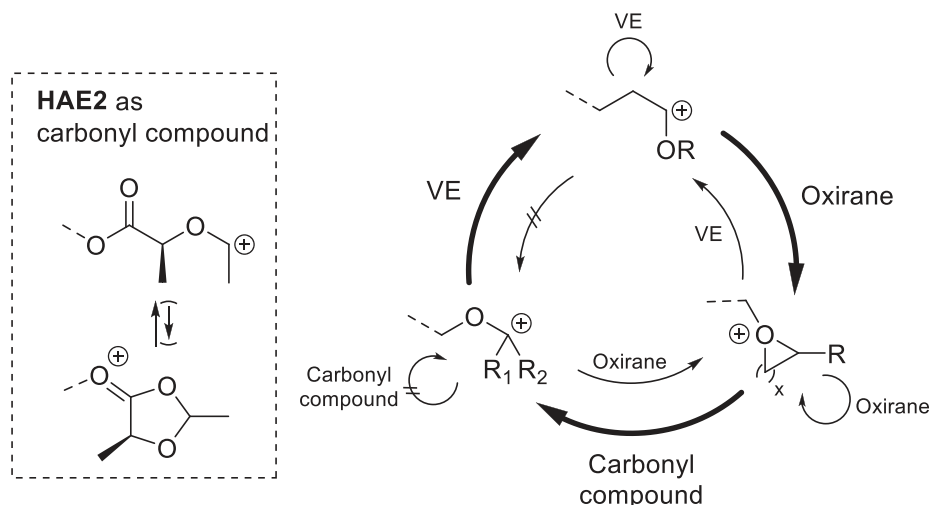


Fig. 15. Schematic representation of the propagation reactions during the cationic terpolymerization of vinyl ethers, oxiranes (as well as cyclic ethers) and carbonyl compounds. Mostly ketones were reported, but also an aldehyde and cyclic hemiacetal esters such as, e.g., **HAE2** were applied. Targeted reactions to achieve sequence control in a one-way-cycle are depicted in bold (clockwise direction). Counter clockwise side reactions were (mostly) suppressed.

merization was hence screened using a large variety of monomers (ten VEs, nine cyclic ethers and nine ketones) [255]. Substitution pattern and the thereby induced steric hindrance, ring strain, intrinsic homopolymerizability, and nature of the generated cationic propagation chain end affected the ability of each monomer type to be terpolymerized in ABC periodic sequences. Moderate but sufficiently high relative reactivities were required for VEs and cyclic ethers to suppress homopropagation, facilitate the frequent crossover reactions and generate polymers with sufficiently high molar masses. In particular cyclic ketones such as cyclohexanone (**KE6**) promoted the formation of ketals in the main chain. The frequency of cross over reactions increased at high ketone concentrations and when polymerizations were performed in less polar solvents such as toluene at lower temperatures ($-100\text{ }^{\circ}\text{C}$). Under such optimized conditions, the cationic terpolymerization of **VE6**, **CE12** and **KE2** yielded the ABC pseudo-periodic poly(**VE6**_{1,2}-**CE12**_{1,4}-**KE2**_{1,0}) with a high molar mass of $M_n = 17,300\text{ g mol}^{-1}$ ($D = 1.74$).

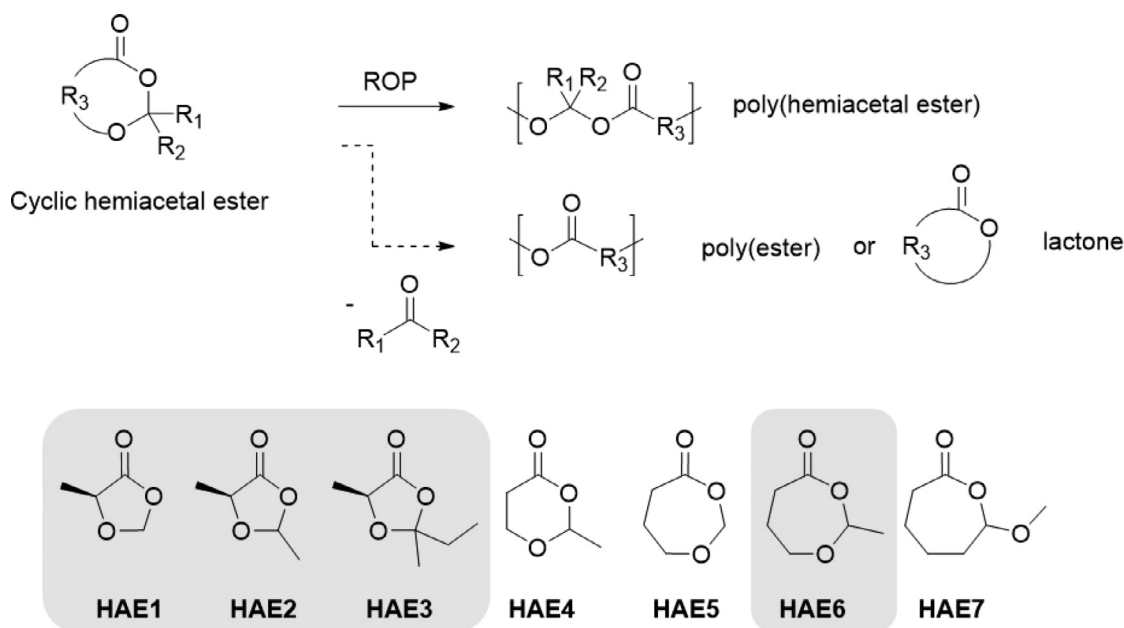
The scope of the carbonyl-based monomer was further expanded to 1,3-dioxolan-4-ones, i.e. lactic acid derivatives with formaldehyde, acetaldehyde and methyl ethylketone, respectively (**HAE1** to **HAE3**, **Scheme 20**) [256]. Although these cyclic hemiacetal esters did not homopolymerize cationically, and copolymerizations with **VE7**, **VE9**, **VE6** or styrene derivatives failed, copolymerizations with **CE1** and **CE12**, or the terpolymerization **VE7** / **CE1** / **HAE2** were successful.

4.2.6. Ring opening polymerization of hemiacetal esters

The ring-opening polymerization of hemiacetal esters would enable the synthesis of poly(hemiacetal ester)s (**Scheme 20**). As mentioned above, the homopolymerization of **HAE1** to **HAE3** via cationic ROP using different Lewis acid catalysts or reaction tem-

peratures was unsuccessful [256]. In fact, also homopolymerization using aluminum salen catalysts [258, 259] or Sn(II)octanoate [260] failed or yielded polyesters due to elimination of the carbonyl compound [261]. Similar problems arose when high catalyst amounts of diethylzinc (ZnEt_2) were used for the ROP of 2-methyl-1,3-dioxan-4-one (**HAE4**) [262]. However, a reduction of the catalyst amount facilitated access to the poly(hemiacetal ester)s with M_n s of 8000 to 34,000 g mol^{-1} . Whereas a variety of other catalysts caused monomer decomposition, DPP was identified as a very versatile catalyst for the ROP of **HAE4**. Polymerizations without additional initiators proceeded via an activated chain end mechanism, where initially high molar mass polymers were formed that decreased their molar mass due to backbiting reactions throughout the course of the reaction. Addition of various alcohols as initiators introduced a competing activated monomer mechanism, enabling access to well-defined poly(hemiacetal ester)s with predetermined end groups. DPP was hence further utilized for the synthesis of block copolymers utilizing mPEG-OH as macroinitiator [263]. The variation of the DP of the hydrophobic block resulted in micellar assemblies of varying sizes (26 to 142 nm) in aqueous phosphate buffer solution. Whereas poly**HAE4** alone degraded surprisingly slow (half the original M_n at pH 4.4 after 75 h) [262], the micelles degraded considerably faster. For instance, complete degradation occurred after 3 h at pH 5.7 as well as pH 10.8. The core shell micelles were able to solubilize the hydrophobic Nile Red (94 nm by DLS) as well as AdiFectinTM, an amphiphilic immune stimulatory TLR-7 agonist. The drug accessibility was thereby increased and hence increased TLR stimulation activity of the RAW blue macrophages as determined *in vitro* studies in comparison to the free drug alone.

Aiming at favorable ROP thermodynamics, Neitzel et al. further continued their studies on 7-membered ring analogues of



Scheme 20. (Top) Schematic representation of the ROP of cyclic hemiacetal esters yielding poly(hemiacetal ester)s. Release of the carbonyl compound as side reaction (dashed arrow) results in polyesters or lactones. (Bottom) Schematic representation of the cyclic hemiacetal ester monomers. Compounds marked in gray reported unsuccessful for homopolymerization.

HAE4, i.e., 2-methyl-1,3-dioxepan-4-one (**HAE6**), 1,3-dioxepan-4-one (**HAE5**) as well as 7-methoxyoxepan-2-one (**HAE7**) [264, 265]. Although the high reactivity due to the ring strain of **HAE6** as well as **HAE5** complicated their handling as frequent decomposition or autopolymerization occurred during monomer purification, **HAE5** was successfully polymerized applying DPP and benzyl alcohol yielding the respective poly**HAE5** with a molar mass of 6000 g mol^{-1} ($D = 1.3$). In contrast, the polymerization of **HAE5** with diethylzinc and benzyl alcohol failed and instead yielded γ -butyrolactone and formaldehyde. To avoid the release of a volatile aldehyde during its ROP, **HAE7** featuring an exocyclic hemiacetal ester was investigated [265]. Whereas poly**HAE7** was successfully obtained by the cationic ROP using HCl / benzyl alcohol or triflic acid, the molar mass could not be controlled. However, cationic reversible addition-fragmentation chain-transfer polymerization with a photocatalyst and three different dithiocarbamate or trithiocarbonate CTAs was successful in this respect, also in a copolymerization with **VE8**.

5. Summary

Poly(ester amide)s (PEA), polyphosphoesters (PPE) and polyacetals represent promising alternative polymer classes for the substitution of polyesters in biomedical applications. This is due to a broad parameter space, enabled by the highly variable structural design and, in return, adjustable degradation behavior. For all three polymer classes, well-established step growth syntheses exist that have led to materials that are currently broadly applied. Whereas there is a clear focus on materials for biomedical applications in particular for PEA and polyacetals, the use of PPE in this respect is in its infancy.

A considerable variety of polymer architectures exists within the polymer classes, which is due to the necessity to attach stealth polymers or biologically active molecules in materials potentially applicable in drug delivery applications. However, multi-step syntheses approaches make the exact structural identification of the final polymers difficult, in particular due to their degradability. The fact that biological data are sometimes nevertheless reported might cause misleading interpretation regarding their performance.

We hence encourage the complementation of a spectroscopic characterization with at least size exclusion chromatography during each step to verify the covalent attachment of all building blocks.

In fact, this point of view seems to find its way into the community and is strengthened through the current immense progress in the development of chain growth polymerizations for all three polymer classes. This is due to the use of organocatalysts for ring-opening polymerizations (ROP) enabling access to well-defined PEA, PPE, and to a certain extent also polyacetals. For the latter, in particular cationic copolymerizations of vinyl ethers with cyclic ethers, aldehydes or cyclic ketals represents a very promising alternative route. As such new synthetic developments are usually accompanied by in-depth structural characterization approaches, we expect the variety of well-defined polymer architectures to thrive.

The question of degradability is addressed from different viewpoints within the polymer classes: Whereas the hydrolysis of acetal moieties is often used to determine the copolymer microstructures of new copolymers from vinyl ethers with, e.g., carbonyl compounds, it is often seen as a prerequisite to promote drug release from more established carrier materials. The reasoning is straightforward when API's are covalently attached, e.g., within the main chain of polyacetals. However, additional leakage effects are likely to contribute when actives are encapsulated. At this point, the additional hydrogen bonding options in PEAs are promising, either to increase drug loading or to sustain the release in comparison to standard polyester materials. In particular, the option to tailor the degradability of PPEs through incorporation of P-O, P-N or P-C bonds is expected to be exploited in future with respect to release kinetics.

Such future studies will likely be accompanied by a careful characterization of degradation products, which is a necessity taking into account that they will be of biological relevance as well. Additional upcoming biological investigations utilizing such new materials will clearly benefit from that viewpoint, bringing the application of polyester alternatives to the next level.

Declaration of Competing Interest

The authors declare no competing interest.

Funding Sources

The work was financially supported by the Deutsche Forschungsgemeinschaft (DFG, German Research Foundation) - project number 316213987 - SFB 1278 (projects A01 and Z01) and the Federal Ministry for Education and Research of Germany (BMBF) (project NextPEG, 13XP5049C).

References

- [1] Geyer R, Jambeck JR, Law KL. Production, use, and fate of all plastics ever made. *Sci Adv* 2017;3:e1700782.
- [2] Aklonis JJ. Mechanical properties of polymers. *J Chem Educ* 1981;58:892–7.
- [3] Nunes RW, Martin JR, Johnson JF. Influence of molecular weight and molecular weight distribution on mechanical properties of polymers. *Polym Eng Sci* 1982;22:205–28.
- [4] Bicerano J. Prediction of the properties of polymers from their structures. *J Macromol Sci Part C* 1996;36:161–96.
- [5] Li WC, Tse HF, Fok L. Plastic waste in the marine environment: a review of sources, occurrence and effects. *Sci Total Environ* 2016;566–567:333–49.
- [6] Milošević M, Kučić Grgić D, Bolanča T, Š Ukić, Cvetnić M, Očelić Bulatović V, et al. Ecotoxicological assessment of microplastics in freshwater sources—a review. *Water (Basel)* 2021;13:e56.
- [7] Schneiderman DK, Hillmyer MA. 50th anniversary perspective: there is a great future in sustainable polymers. *Macromolecules* 2017;50:3733–49.
- [8] Haider TP, Völker C, Kramm J, Landfester K, Wurm FR. Plastics of the future? The impact of biodegradable polymers on the environment and on society. *Angew Chem Int Ed* 2019;58:50–62.
- [9] Ikada Y, Tsuji H. Biodegradable polyesters for medical and ecological applications. *Macromol Rapid Commun* 2000;21:117–32.
- [10] Baumann A, Tuerck D, Prabhu S, Dickmann L, Sims J. Pharmacokinetics, metabolism and distribution of PEGs and PEGylated proteins: quo vadis? *Drug Discov Today* 2014;19:1623–31.
- [11] Englert C, Brendel JC, Majdanski TC, Yildirim T, Schubert S, Gottschaldt M, et al. Pharmapolymer in the 21st century: synthetic polymers in drug delivery applications. *Prog Polym Sci* 2018;87:107–64.
- [12] Molavi F, Barzegar-Jalali M, Hamishehkar H. Polyester based polymeric nano and microparticles for pharmaceutical purposes: a review on formulation approaches. *J Control Release* 2020;320:265–82.
- [13] Pappalardo D, Mathisen T, Finne-Wistrand A. Biocompatibility of resorbable polymers: a historical perspective and framework for the future. *Biomacromolecules* 2019;20:1465–77.
- [14] Maitz MF. Applications of synthetic polymers in clinical medicine. *Biosurf Biotechnol* 2015;1:161–76.
- [15] Sung H-J, Meredith C, Johnson C, Galis ZS. The effect of scaffold degradation rate on three-dimensional cell growth and angiogenesis. *Biomaterials* 2004;25:5735–42.
- [16] Wong DY, Hollister SJ, Krebsbach PH, Nosrat C. Poly(ϵ -caprolactone) and Poly(L-lactic-co-glycolic acid) degradable polymer sponges attenuate astrocyte response and lesion growth in acute traumatic brain injury. *Tissue Eng* 2007;13:2515–23.
- [17] Li S. Hydrolytic degradation characteristics of aliphatic polyesters derived from lactic and glycolic acids. *J Biomed Mater Res* 1999;48:342–53.
- [18] Fu K, Pack DW, Klivanov AM, Langer R. Visual evidence of acidic environment within degrading poly(lactic-co-glycolic acid) (PLGA) microspheres. *Pharm Res* 2000;17:100–6.
- [19] Woodard LN, Grunlan MA. Hydrolytic degradation and erosion of polyester biomaterials. *ACS Macro Lett* 2018;7:976–82.
- [20] Trofymchuk K, Valanciunaite J, Andreiuk B, Reisch A, Collot M, Klymchenko AS. BODIPY-loaded polymer nanoparticles: chemical structure of cargo defines leakage from nanocarrier in living cells. *J Mater Chem B* 2019;7:5199–210.
- [21] Xu P, Gullotti E, Tong L, Highley CB, Errabelli DR, Hasan T, et al. Intracellular drug delivery by poly(lactic-co-glycolic acid) nanoparticles revisited. *Mol Pharmaceutics* 2009;6:190–201.
- [22] John J, Mani R, Bhattacharya M. Evaluation of compatibility and properties of biodegradable polyester blends. *J Polym Sci Part A* 2002;40:2003–14.
- [23] Ostafinska A, Fortelny I, Nevalova M, Hodan J, Kredatusova J, Slouf M. Synergistic effects in mechanical properties of PLA/PCL blends with optimized composition, processing, and morphology. *RSC Adv* 2015;5:98971–82.
- [24] Steinbach T, Wurm FR. Poly(phosphoester)s: a new platform for degradable polymers. *Angew Chem Int Ed* 2015;54:6098–108.
- [25] Hufendiek A, Lingier S, Du Prez FE. Thermoplastic polyacetals: chemistry from the past for a sustainable future? *Polym Chem* 2019;10:9–33.
- [26] Pirsas S, Kurush AS. A review of the applications of bioproteins in the preparation of biodegradable films and polymers. *J Chem Lett* 2020;1:47–58.
- [27] Manavitehrani I, Fathi A, Badr H, Daly S, Negahi Shirazi A, Dehghani F. Biomedical applications of biodegradable polyesters. *Polymers (Basel)* 2016;8:20.
- [28] de Jongh PAJM, Paul PKC, Khoshdel E, Wilson P, Kempe K, Haddleton DM. High Tg poly(ester amide)s by melt polycondensation of monomers from renewable resources; citric acid, D-glucono- δ -lactone and amino acids: a DSC study. *Eur Polym J* 2017;94:11–19.
- [29] Triki R, Bougarech A, Tessier M, Abid S, Fradet A, Abid M. Furanic-aliphatic polyesteramides by bulk polycondensation between furan-based diamine, aliphatic diester and diol. *J Polym Environ* 2018;26:1272–8.
- [30] Winnacker M, Rieger B. Poly(ester amide)s: recent insights into synthesis, stability and biomedical applications. *Polym Chem* 2016;7:7039–46.
- [31] Nyambo C, Misra M, Mohanty AK. Toughening of brittle poly(lactide) with hyperbranched poly(ester-amide) and isocyanate-terminated prepolymer of polybutadiene. *J Mater Sci* 2012;47:5158–68.
- [32] Yin T, Sun HY, Zhao JB, Zhang ZY, Yang WT. Synthesis and characterization of aliphatic polyesteramides mainly composed of alternating diester diamide units from N,N'-bis(2-hydroxyethyl)-oxamide and diacids. *Polym Eng Sci* 2014;54:756–65.
- [33] Douka A, Vouyiouka S, Pappaspyridi L-M, Pappaspyridis CD. A review on enzymatic polymerization to produce polycondensation polymers: the case of aliphatic polyesters, polyamides and polyesteramides. *Prog Polym Sci* 2018;79:1–25.
- [34] Rusu G, Rusu E. Evaluation of thermal and mechanical behavior of some anionic polyesteramide copolymers. *J Polym Res* 2013;20:e308.
- [35] Ahmad S, Ashraf SM, Zafar F. Development of linseed oil based polyesteramide without organic solvent at lower temperature. *J Appl Polym Sci* 2007;104:1143–8.
- [36] Killi N, Pawar AT, Gundloori RVN. Polyesteramide of neem oil and its blends as an active nanomaterial for tissue regeneration. *ACS Appl Bio Mater* 2019;2:3341–51.
- [37] Pin J-M, Misra M, Mohanty AK. Cross-linkable liquid-crystalline biopolyesteramide as a multifunctional polymeric platform designed from corn oil side-stream product of bioethanol industry. *Macromol Rapid Commun* 2019;40:e1900093.
- [38] Muniandy A, Lee CS, Lim WH, Pichika MR, Mak KK. Hyperbranched poly(glycerol esteramide): a biocompatible drug carrier from glycerol feedstock and dicarboxylic acid. *J Appl Polym Sci* 2021;138:e50126.
- [39] Guo K, Chu CC. Synthesis, characterization, and biodegradation of novel poly(ether ester amide)s based on L-phenylalanine and oligoethylene glycol. *Biomacromolecules* 2007;8:2851–61.
- [40] Lu D-D, Yuan J-C, Lei Z-Q. High molecular weight biodegradable poly(lactic acid-glycolic acid- ϵ -caprolactam) copolymer: direct polycondensation of lactic acid, glycolic acid and ϵ -caprolactam using Sn(II)-organic anhydride as catalysts. *Polym Adv Technol* 2009;20:536–40.
- [41] Tsitlanadze G, Kviria T, Katsarava R, Chu CC. In vitro enzymatic biodegradation of amino acid based poly(ester amide)s biomaterials. *J Mater Sci: Mater Med* 2004;15:185–90.
- [42] Bonillo Martínez AD, Margarit Bellver MV, Rodríguez Galán IC. Matrix tablets based on amino acid-derived polyesteramide containing release modifiers. *J Drug Deliv Sci Technol* 2017;42:307–14.
- [43] Andrés-Guerrero V, Zong M, Ramsay E, Rojas B, Sarkhel S, Gallego B, et al. Novel biodegradable polyesteramide microspheres for controlled drug delivery in ophthalmology. *J Control Release* 2015;211:105–17.
- [44] Peters T, Kim S-W, Castro V, Stingl K, Strasser T, Bolz S, et al. Evaluation of polyesteramide (PEA) and polyester (PLGA) microspheres as intravitreal drug delivery systems in albino rats. *Biomaterials* 2017;124:157–68.
- [45] Tellegen AR, Rudnik-Jansen I, Pouran B, de Visser HM, Weinans HH, Thomas RE, et al. Controlled release of celecoxib inhibits inflammation, bone cysts and osteophyte formation in a preclinical model of osteoarthritis. *Drug Deliv* 2018;25:1438–47.
- [46] Rudnik-Jansen I, Schrijver K, Woike N, Tellegen A, Versteeg S, Emans P, et al. Intra-articular injection of triamcinolone acetonide releasing biomaterial microspheres inhibits pain and inflammation in an acute arthritis model. *Drug Deliv* 2019;26:226–36.
- [47] Rudnik-Jansen I, Woike N, de Jong S, Versteeg S, Kik M, Emans P, et al. Applicability of a modified rat model of acute arthritis for long-term testing of drug delivery systems. *Pharmaceutics* 2019;11:e70.
- [48] Ali Mohamed A, Salhi S, Abid S, El Gharbi R, Fradet A. Random and quasi-alternating polyesteramides deriving from ϵ -caprolactone and β -alanine. *Eur Polym J* 2014;53:160–70.
- [49] Salhi S, Mahfoudh J, Abid S, Atanase L-I, Popa M, Delaite C. Random poly(ϵ -caprolactone-L-alanine) by direct melt copolymerization. *Polym Int* 2020;69:1161–8.
- [50] Ali Mohamed A, Salhi S, Abid S, El Gharbi R, Fradet A. Quasi-alternating polyesteramides from ϵ -caprolactone and α -amino acids. *J Appl Polym Sci* 2016;133:e44220.
- [51] Basterretxea A, Gabirondo E, Sanchez-Sanchez A, Etxeberria A, Coulembier O, Mecerreyes D, et al. Synthesis and characterization of poly(ϵ -caprolactam-co-lactide) polyesteramides using Brønsted acid or Brønsted base organocatalyst. *Eur Polym J* 2017;95:650–9.
- [52] Deshayes G, Delcourt C, Verbruggen I, Trouillet-Fonti L, Touraud F, Fleury E, et al. Novel polyesteramide-based diblock copolymers: synthesis by ring-opening copolymerization and characterization. *Macromol Chem Phys* 2009;210:1033–43.
- [53] Deshayes G, Delcourt C, Verbruggen I, Trouillet-Fonti L, Touraud F, Fleury E, et al. Novel polyesteramide-based di- and triblock copolymers: from thermo-mechanical properties to hydrolytic degradation. *Eur Polym J* 2011;47:98–110.
- [54] Douhi A, Fradet A. Study of bulk chain coupling reactions. III. Reaction between bisoxazolines or bisoxazines and carboxy-terminated oligomers. *J Polym Sci Part A* 1995;33:691–9.

- [55] Huang CQ, Luo SY, Xu SY, Zhao JB, Jiang SL, Yang WT. Catalyzed chain extension of poly(butylene adipate) and poly(butylene succinate) with 2,2'-(1,4-phenylene)-bis(2-oxazoline). *J Appl Polym Sci* 2010;115:1555–65.
- [56] Néry L, Lefebvre H, Fradet A. Chain extension of carboxy-terminated aliphatic polyamides and polyesters by arylene and pyridylene bisoxazolines. *Macromol Chem Phys* 2004;205:448–55.
- [57] Seppälä JV, Helminen AO, Korhonen H. Degradable polyesters through chain linking for packaging and biomedical applications. *Macromol Biosci* 2004;4:208–17.
- [58] Xu SY, Shi YH, Zhao JB, Jiang SL, Yang WT. Chain extension of adipic acid and (or) succinic acid/butanediol polyesters with 2,2'-(1,4-phenylene)-bis(2-oxazoline) and adipoylbiscaprolactamate combined chain extenders. *Polym Adv Technol* 2011;22:2360–7.
- [59] Kagiya T, Narisawa S, Maeda T, Fukui K. Preparation of a crystalline poly(ester-amide) by the polyaddition reaction of bisoxazoline and a dicarboxylic acid. *J Polym Sci B Polym Lett* 1966;4:257–60.
- [60] Wilsens CHR, Willems NJM, Gubbels E, Yao Y, Rastogi S, Noordover BAJ. Synthesis, kinetics, and characterization of bio-based thermosets obtained through polymerization of a 2,5-furandicarboxylic acid-based bis(2-oxazoline) with sebacic acid. *Polym Chem* 2015;6:2707–16.
- [61] Muljajew I, Erlebach A, Weber C, Buchheim JR, Sierka M, Schubert US. A polyesteramide library from dicarboxylic acids and 2,2'-bis(2-oxazoline): synthesis, characterization, nanoparticle formulation and molecular dynamics simulations. *Polym Chem* 2020;11:112–24.
- [62] Muljajew I, Chi M, Vollrath A, Weber C, Beringer-Siemers B, Stumpf S, et al. A combined experimental and *in silico* approach to determine the compatibility of poly(ester amide)s and indomethacin in polymer nanoparticles. *Eur Polym J* 2021;156:e110606.
- [63] Lustoň J, Kronek J, Kleinová A, Janigová I, Valentová H, Nedbal J. Synthesis and polymerization reactions of cyclic imino ethers. VI. Polymers with biphenyl structure. *J Polym Sci Part A* 2012;50:3936–43.
- [64] Culbertson BM. Cyclic imino ethers in step-growth polymerizations. *Prog Polym Sci* 2002;27:579–626.
- [65] Kempe K. Chain and step growth polymerizations of cyclic imino ethers: from poly(2-oxazolines) to poly(ester amide)s. *Macromol Chem Phys* 2017;218:e1700021.
- [66] Chevallier P, Soutif J-C, Brosse J-C, Rincón-Guerrero A. Poly(amide-ester)s from 2,6-pyridine dicarboxylic acid and ethanolamine derivatives for metal ion complexation. Synthesis via bis(2-oxazoline)-diacid reaction. *Eur Polym J* 1998;34:767–78.
- [67] Kronek J, Nedbal J, Valentová H, Neubert M, Janigová I, Petrenčíková N, et al. Thermal stability and structural anisotropy of semiaromatic poly(ester amide)s from aromatic bis(2-oxazolines) and aliphatic dicarboxylic acids. *Polym Test* 2018;68:1–7.
- [68] Li S, Tao M. Preparation and properties of copolymer resins based on phenolphthalein benzoxazine-benzoic acid and bisoxazoline. *J Therm Anal Calorim* 2013;113:633–9.
- [69] Lustoň J, Kronek J, Markus O, Janigová I, Böhme F. Synthesis and polymerization reactions of cyclic imino ethers. 3. Poly(ester amide)s of the AA+BB type on the basis of 2-oxazolines. *Polym Adv Technol* 2007;18:165–72.
- [70] Mansour IB, Alouani K, Chauveau E, Martin V, Schiets F, Mercier R. Synthesis and characterisation of poly(ester-amide)s from aromatic bisoxazoline precursors. *Eur Polym J* 2010;46:814–20.
- [71] Sano Y. Polymerization of bis(2-oxazoline) compounds with dicarboxylic acids. *J Polym Sci Part A* 1989;27:2749–60.
- [72] Erlebach A, Muljajew I, Chi M, Bückmann C, Weber C, Schubert US, et al. Predicting solubility of small molecules in macromolecular compounds for nanomedicine application from atomistic simulations. *Adv Theory Simul* 2020;3:e2000001.
- [73] Führer FN, Schlaad H. ADMET Polymerization of amino-acid-based diene. *Macromol Chem Phys* 2014;215:2268–73.
- [74] Medel S, Martínez-Campos E, Acitores D, Vassileva-Tonkova E, Grabchev I, Bosch P. Synthesis and spectroscopic properties of a new fluorescent acridine hyperbranched polymer: applications to acid sensing and as antimicrobial agent. *Eur Polym J* 2018;102:19–29.
- [75] Helder J, Kohn FE, Sato S, van den Berg JW, Feijen J. Synthesis of poly[oxyethylidenecarbonylimino(2-oxoethylene)] [poly(glycine-D,L-lactic acid)] by ring opening polymerization. *Macromol Rapid Commun* 1985;6:9–14.
- [76] Basu A, Kunduru KR, Katzhendler J, Domb AJ. Poly(α -hydroxy acid)s and poly(α -hydroxy acid-co- α -amino acid)s derived from amino acid. *Adv Drug Delivery Rev* 2016;107:82–96.
- [77] Feng Y, Lu J, Behl M, Lendlein A. Progress in decapeptide-based biomaterials. *Macromol Biosci* 2010;10:1008–21.
- [78] Fonseca AC, Gil MH, Simões PN. Biodegradable poly(ester amide)s – a remarkable opportunity for the biomedical area: review on the synthesis, characterization and applications. *Prog Polym Sci* 2014;39:1291–311.
- [79] Peng X, Behl M, Zhang P, Mazurek-Budzyńska M, Razaq MY, Lendlein A. Hexyl-modified morpholine-2,5-dione-based oligodepsipeptides with relatively low glass transition temperature. *Polymer* 2016;105:318–26.
- [80] Elomaa L, Kang Y, Seppälä JV, Yang Y. Biodegradable photocrosslinkable poly(depsipeptide-co- ϵ -caprolactone) for tissue engineering: synthesis, characterization, and *in vitro* evaluation. *J Polym Sci Part A* 2014;52:3307–15.
- [81] Feng Y, Chen C, Zhang L, Tian H, Yuan W. Synthesis and characterization of novel copolymers based on 3(S)-methyl-morpholine-2,5-dione. *Trans Tianjin Univ* 2012;18:315–19.
- [82] Lv J, Yang J, Hao X, Ren X, Feng Y, Zhang W. Biodegradable PEI modified complex micelles as gene carriers with tunable gene transfection efficiency for ECs. *J Mater Chem B* 2016;4:997–1008.
- [83] Zhang L, Feng Y, Tian H, Shi C, Zhao M, Guo J. Controlled release of doxorubicin from amphiphilic decapeptide-PDO-PEG-based copolymer nanosized microspheres. *React Funct Polym* 2013;73:1281–9.
- [84] Shi C-X, Guo Y-T, Wu Y-H, Li Z-Y, Wang Y-Z, Du F-S, et al. Synthesis and controlled organobase-catalyzed ring-opening polymerization of morpholine-2,5-dione derivatives and monomer recovery by acid-catalyzed degradation of the polymers. *Macromolecules* 2019;52:4260–9.
- [85] Franz N, Klok H-A. Synthesis of functional polydepsipeptides via direct ring-opening polymerization and post-polymerization modification. *Macromol Chem Phys* 2010;211:809–20.
- [86] Lian J, Li M, Wang S, Tao Y, Wang X. Organocatalytic polymerization of morpholine-2,5-diones toward methionine-containing poly(ester amide)s: preparation and facile functionalization. *Macromolecules* 2020;53:10830–6.
- [87] Pang Z, Li H, He P, Wang Y, Ren H, Wang H, et al. Controllable ring-opening copolymerization of L-lactide and (3S)-benzyloxymethyl-(6S)-methyl-morpholine-2,5-dione initiated by a biogenic compound creatinine acetate. *J Polym Sci Part A* 2012;50:4004–9.
- [88] Ohya Y, Matori J, Ouchi T. Preparation of growth factor-loaded biodegradable matrices consisting of poly(depsipeptide-co-lactide) and cell growth on the matrices. *React Funct Polym* 2014;81:33–9.
- [89] Yu Z, He B, Long C, Liu R, Sheng M, Wang G, et al. Synthesis, characterization, and drug delivery of amphiphilic poly{(lactic acid)-co-[(glycolic acid)-alt-(L-glutamic acid)]-g-poly(ethylene glycol)}. *Macromol Res* 2012;20:250–8.
- [90] Naolou T, Lendlein A, Neffe AT. Influence of metal softness on the metal-organic catalyzed polymerization of morpholine-2,5-diones to oligodepsipeptides. *Eur Polym J* 2016;85:139–49.
- [91] Yu H, Guo X, Qi X, Liu P, Shen X, Duan Y. Synthesis and characterization of arginine-glycine-aspartic peptides conjugated poly(lactic acid-co-L-lysine) diblock copolymer. *J Mater Sci: Mater Med* 2008;19:1275–81.
- [92] Takahashi A, Umezaki M, Yoshida Y, Kuzuya A, Ohya Y. A macromolecular prodrug-type injectable polymer composed of poly(depsipeptide-co-lactide)-g-PEG for sustained release of drugs. *Polym Adv Technol* 2014;25:1226–33.
- [93] Yu Z, He B, Sheng M, Wang G, Gu Z. Novel PLGGE graft polymeric micelles for doxorubicin delivery. *Chin Sci Bull* 2012;57:3994–4004.
- [94] Brunacci N, Neffe AT, Wischke C, Naolou T, Nöchel U, Lendlein A. Oligodepsipeptide (nano)carriers: computational design and analysis of enhanced drug loading. *J Control Release* 2019;301:146–56.
- [95] Peng X, Behl M, Zhang P, Mazurek-Budzyńska M, Feng Y, Lendlein A. Synthesis of well-defined dihydroxy telechelics by (co)polymerization of morpholine-2,5-diones catalyzed by Sn(IV) alkoxide. *Macromol Biosci* 2018;18:e1800257.
- [96] Pratt R, Dove A, Lohmeijer B, Culkun D, Waymouth R, Hedrick J. Extending the reactivity of N-heterocyclic carbenes to polymerization of functional and biomimetic monomers. *Polym Prepr* 2005;46:902.
- [97] Pratt RC, Lohmeijer BG, Mason AF, Waymouth RM, Hedrick JL. Organocatalytic ring-opening polymerizations of morpholine-2, 6-diones: a route to functionalized poly(lactide)s and pseudopeptides. *Polym Prepr* 2006;47:101–2.
- [98] Dirauf M, Bandelli D, Weber C, Görls H, Gottschaldt M, Schubert US. TBD-catalyzed ring-opening polymerization of alkyl-substituted morpholine-2,5-dione derivatives. *Macromol Rapid Commun* 2018;39:e1800433.
- [99] Burton TF, Pinaud J, Giani O. Rapid and controlled organocatalyzed ring-opening polymerization of 3S-(isobutyl)morpholine-2,5-dione and copolymerization with lactide. *Macromolecules* 2020;53:6598–607.
- [100] Kivijärvi T, Pappalardo D, Olsén P, Finne-Wistrand A. Inclusion of isolated α -amino acids along the polylactide chain through organocatalytic ring-opening copolymerization. *Eur Polym J* 2020;131:e109703.
- [101] Feng Y, Klee D, Höcker H. Synthesis and characterization of new ABA triblock copolymers with poly[3(S)-isobutylmorpholine-2,5-dione] and poly(ethylene oxide) blocks. *Macromol Chem Phys* 1999;200:2276–83.
- [102] Feng Y, Klee D, Höcker H. Lipase-catalyzed ring-opening polymerization of 3(S)-sec-butylmorpholine-2,5-dione. *Macromol Biosci* 2001;1:66–74.
- [103] In 't Veld PJA, Dijkstra PJ, van Lochem JH, Feijen J. Synthesis of alternating polydepsipeptides by ring-opening polymerization of morpholine-2,5-dione derivatives. *Makromol Chem* 1990;191:1813–25.
- [104] In 't Veld PJA, Shen Z-R, Takens GAJ, Dijkstra PJ, Feijen J. Glycine/glycolic acid based copolymers. *J Polym Sci Part A* 1994;32:1063–9.
- [105] Tsuji H, Sato S, Masaki N, Arakawa Y, Kuzuya A, Ohya Y. Synthesis, stereocomplex crystallization and homo-crystallization of enantiomeric poly(lactic acid-co-alanine)s with ester and amide linkages. *Polym Chem* 2018;9:565–75.
- [106] Yan W, Fang L, Noechel U, Kratz K, Lendlein A. Influence of deformation temperature on structural variation and shape-memory effect of a thermoplastic semi-crystalline multiblock copolymer. *Express Polym Lett* 2015;9:624–35.
- [107] Yan W, Fang L, Noechel U, Kratz K, Lendlein A. Influence of programming strain rates on the shape-memory performance of semicrystalline multiblock copolymers. *J Polym Sci B* 2016;54:1935–43.
- [108] Yan W, Fang L, Weigel T, Behl M, Kratz K, Lendlein A. The influence of thermal treatment on the morphology in differently prepared films of an oligodepsipeptide based multiblock copolymer. *Polym Adv Technol* 2017;28:1339–45.
- [109] Yan W, Rudolph T, Noechel U, Gould O, Behl M, Kratz K, et al. Reversible actuation of thermoplastic multiblock copolymers with overlapping thermal transitions of crystalline and glassy domains. *Macromolecules* 2018;51:4624–32.

- [110] Bai L, Zhao J, Li Q, Guo J, Ren X, Xia S, et al. Biofunctionalized electrospun PCL-PIBMD/SF vascular grafts with PEG and cell-adhesive peptides for endothelialization. *Macromol Biosci* 2019;19:e1800386.
- [111] Feng Y, Liu W, Ren X, Lu W, Guo M, Behl M, et al. Evaluation of electrospun PCL-PIBMD meshes modified with plasmid complexes *in vitro* and *in vivo*. *Polymers (Basel)* 2016;8:e58.
- [112] Bai L, Li Q, Duo X, Hao X, Zhang W, Shi C, et al. Electrospun PCL-PIBMD/SF blend scaffolds with plasmid complexes for endothelial cell proliferation. *RSC Adv* 2017;7:39452–64.
- [113] Feng Y, Lu W, Ren X, Liu W, Guo M, Ullah I, et al. Electrospun poly(lactide-co-glycolide-co-3(S)-methyl-morpholine-2,5-dione) nanofibrous scaffolds for tissue engineering. *Polymers* 2016;8:e13.
- [114] Elomaa L, Pan C-C, Shanjanji Y, Malkovskiy A, Seppälä JV, Yang Y. Three-dimensional fabrication of cell-laden biodegradable poly(ethylene glycol-co-depsipeptide) hydrogels by visible light stereolithography. *J Mater Chem B* 2015;3:8348–58.
- [115] Pagar KP, Vavia PR. Poly[LA-(Glc-Leu)] copolymer as a carrier for ocular delivery of ciprofloxacin: formulation, characterization and *in vivo* biocompatibility study. *Ther Deliv* 2013;4:553–65.
- [116] Pagar K, Vavia P. Rivastigmine-loaded L-lactide-depsipeptide polymeric nanoparticles: decisive formulation variable optimization. *Sci Pharm* 2013;81:865–88.
- [117] Pagar KP, Vavia PR. Naltrexone-loaded poly[La-(Glc-Leu)] polymeric microspheres for the treatment of alcohol dependence: *in vitro* characterization and *in vivo* biocompatibility assessment. *Pharm Dev Technol* 2014;19:385–94.
- [118] Rimmel A. COVID vaccines and safety: what the research says. *Nature* 2021;590:538–40.
- [119] Fam SY, Chee CF, Yong CY, Ho KL, Mariatulqabtiyah AR, Tan WS. Stealth coating of nanoparticles in drug-delivery systems. *Nanomaterials* 2020;10:e787.
- [120] Dirauf M, Erlebach A, Weber C, Hoepfner S, Buchheim JR, Sierka M, et al. Block copolymers composed of PET/Ox and polyesteramides based on glycolic acid, L-valine, and L-isoleucine. *Macromolecules* 2020;53:3580–90.
- [121] Zhao Y, Li J, Yu H, Wang G, Liu W. Synthesis and characterization of a novel polydepsipeptide contained tri-block copolymer (mPEG-PLLA-P-MMD) as self-assembly micelle delivery system for paclitaxel. *Int J Pharm* 2012;430:282–91.
- [122] Yin S, Li J, Li N, Wang G, Gu X. Preparation and characterization of long-circulating PELMD/mPEG-PLGA-mixed micelles for 10-hydroxycamptothecin. *J Nanoparticle Res* 2014;16:e2274.
- [123] Lv J, Zhang L, Khan M, Ren X, Guo J, Feng Y. Biodegradable depsipeptide-P-DO-PEG-based block copolymer micelles as nanocarriers for controlled release of doxorubicin. *React Funct Polym* 2014;82:89–97.
- [124] Bai W, Chen D, Li Q, Chen H, Zhang S, Huang X, et al. *In vitro* hydrolytic degradation of poly(para-dioxanone) with high molecular weight. *J Polym Res* 2009;16:471–80.
- [125] Zhang L, Feng Y, Tian H, Zhao M, Khan M, Guo J. Amphiphilic depsipeptide-based block copolymers as nanocarriers for controlled release of ibuprofen with doxorubicin. *J Polym Sci Part A* 2013;51:3213–26.
- [126] Wang W, Naolou T, Ma N, Deng Z, Xu X, Mansfeld U, et al. Polydepsipeptide block-stabilized polyplexes for efficient transfection of primary human cells. *Biomacromolecules* 2017;18:3819–33.
- [127] Shi C, Yao F, Huang J, Han G, Li Q, Khan M, et al. Proliferation and migration of human vascular endothelial cells mediated by ZNF580 gene complexed with mPEG-b-P(MMD-co-GA)-g-PEI microparticles. *J Mater Chem B* 2014;2:1825–37.
- [128] Shi C, Yao F, Li Q, Khan M, Ren X, Feng Y, et al. Regulation of the endothelialization by human vascular endothelial cells by ZNF580 gene complexed with biodegradable microparticles. *Biomaterials* 2014;35:7133–45.
- [129] Shi C, Li Q, Zhang W, Feng Y, Ren X. REDV peptide conjugated nanoparticles/pZNF580 complexes for actively targeting human vascular endothelial cells. *ACS Appl Mater Interfaces* 2015;7:20389–99.
- [130] Yang J, Liu W, Lv J, Feng Y, Ren X, Zhang W. REDV-polyethyleneimine complexes for selectively enhancing gene delivery in endothelial cells. *J Mater Chem B* 2016;4:3365–76.
- [131] Hao X, Li Q, Wang H, Muhammad K, Guo J, Ren X, et al. CAGW modified polymeric micelles with different hydrophobic cores for efficient gene delivery and capillary-like tube formation. *ACS Biomater Sci Eng* 2018;4:2870–8.
- [132] Li Q, Hao X, Lv J, Ren X, Zhang K, Ullah I, et al. Mixed micelles obtained by co-assembling comb-like and grafting copolymers as gene carriers for efficient gene delivery and expression in endothelial cells. *J Mater Chem B* 2017;5:1673–87.
- [133] Bauer KN, Tee HT, Velencoso MM, Wurm FR. Main-chain poly(phosphoester)s: history, syntheses, degradation, bio- and flame-retardant applications. *Prog Polym Sci* 2017;73:61–122.
- [134] Cankaya A, Steinmann M, Bülbül Y, Lieberwirth I, Wurm FR. Side-chain poly(phosphoramidate)s via acyclic diene metathesis polycondensation. *Polym Chem* 2016;7:5004–10.
- [135] Steinmann M, Wagner M, Wurm FR. Poly(phosphorodiamidate)s by olefin metathesis polymerization with precise degradation. *Chem Eur J* 2016;22:17329–38.
- [136] Bauer KN, Liu L, Andrienko D, Wagner M, Macdonald EK, Shaver MP, et al. Polymerizing phosphonates: a fast way to in-chain poly(phosphonate)s with adjustable hydrophilicity. *Macromolecules* 2018;51:1272–9.
- [137] Pelosi C, Tinè MR, Wurm FR. Main-chain water-soluble polyphosphoesters: multi-functional polymers as degradable PEG-alternatives for biomedical applications. *Eur Polym J* 2020;141:e110079.
- [138] Yilmaz ZE, Jérôme C. Polyphosphoesters: new trends in synthesis and drug delivery applications. *Macromol Biosci* 2016;16:1745–61.
- [139] Bauer KN, Tee HT, Lieberwirth I, Wurm FR. In-chain poly(phosphonate)s via acyclic diene metathesis polycondensation. *Macromolecules* 2016;49:3761–8.
- [140] Becker G, Ackermann LI-M, Schechtel E, Klapper M, Tremel W, Wurm FR. Joining two natural motifs: catechol-containing poly(phosphoester)s. *Biomacromolecules* 2017;18:767–77.
- [141] Qiu J, Zhang J, Yu F, Wei J, Ding L. Novel ABC miktoarm star terpolyphosphoesters: facile construction and high-flame retardant property. *J Polym Sci Part A* 2016;54:692–701.
- [142] Becker G, Vlaminck L, Velencoso MM, Du Prez FE, Wurm FR. Triazolinedione-“clicked” poly(phosphoester)s: systematic adjustment of thermal properties. *Polym Chem* 2017;8:4074–8.
- [143] Tee HT, Koynov K, Reichel T, Wurm FR. Noncovalent hydrogen bonds tune the mechanical properties of phosphoester polyethylene mimics. *ACS Omega* 2019;4:9324–32.
- [144] Steinmann M, Marsico F, Wurm FR. Reactive poly(phosphoester)-telechelics. *J Polym Res* 2015;22:e143.
- [145] Hilf S, Kilbinger AFM. Functional end groups for polymers prepared using ring-opening metathesis polymerization. *Nat Chem* 2009;1:537–46.
- [146] Grubbs RH. The development of functional group tolerant ROMP catalysts. *J Macromol Sci A* 1994;31:1829–933.
- [147] Peres LB, Preiss LC, Wagner M, Wurm FR, de Araújo PHH, Landfester K, et al. ALTMET polymerization of amino acid-based monomers targeting controlled drug release. *Macromolecules* 2016;49:6723–30.
- [148] Bhattacharya AK, Thyagarajan G. Michaelis-Arbuzov rearrangement. *Chem Rev* 1981;81:415–30.
- [149] Becker G, Marquetant TA, Wagner M, Wurm FR. Multifunctional poly(phosphoester)s for reversible Diels-Alder postmodification to tune the LCST in water. *Macromolecules* 2017;50:7852–62.
- [150] Wolf T, Rheinberger T, Wurm FR. Thermoresponsive coacervate formation of random poly(phosphonate) terpolymers. *Eur Polym J* 2017;95:756–65.
- [151] Baeten E, Vanslambrouck S, Jérôme C, Lecomte P, Junkers T. Anionic flow polymerizations toward functional polyphosphoesters in microreactors: polymerization and UV-modification. *Eur Polym J* 2016;80:208–18.
- [152] Pranantyo D, Xu LQ, Kang E-T, Mya MK, MB Chan-Park. Conjugation of polyphosphoester and antimicrobial peptide for enhanced bactericidal activity and biocompatibility. *Biomacromolecules* 2016;17:4037–44.
- [153] Yao X, Du H, Xu N, Sun S, Zhu W, Shen Z. Fully degradable antibacterial poly(ester-phosphoester)s by ring-opening polymerization, “click” chemistry, and quaternization. *J Appl Polym Sci* 2015;132:e42647.
- [154] Müller LK, Steinbach T, Wurm FR. Multifunctional poly(phosphoester)s with two orthogonal protective groups. *RSC Adv* 2015;5:42881–8.
- [155] Becker G, Deng Z, Zober M, Wagner M, Lienkamp K, Wurm FR. Surface-attached poly(phosphoester)-hydrogels with benzophenone groups. *Polym Chem* 2018;9:315–26.
- [156] Jin H, Sun M, Shi L, Zhu X, Huang W, Yan D. Reduction-responsive amphiphilic polymeric prodrugs of camptothecin-polyphosphoester for cancer chemotherapy. *Biomater Sci* 2018;6:1403–13.
- [157] Tsao Y-YT, Wooley KL. Synthetic, functional thymidine-derived polydeoxyribonucleotide analogues from a six-membered cyclic phosphoester. *J Am Chem Soc* 2017;139:5467–73.
- [158] Tsao Y-YT, Smith TH, Wooley KL. Regioisomeric preference in ring-opening polymerization of 3',5'-cyclic phosphoesters of functional thymidine DNA analogues. *ACS Macro Lett* 2018;7:153–8.
- [159] Wang Q, Chen S, Deng B, Wang Y, Dong D, Zhang N. Rare earth metal-mediated ring-opening polymerisation of cyclic phosphoesters. *Polym Chem* 2019;10:2101–5.
- [160] Ding F, Li H-J, Wang J-X, Tao W, Zhu Y-H, Yu Y, et al. Chlorin e6-encapsulated polyphosphoester based nanocarriers with viscous flow core for effective treatment of pancreatic cancer. *ACS Appl Mater Interfaces* 2015;7:18856–65.
- [161] Wang J, Li D, Tao W, Lu Y, Yang X, Wang J. Synthesis of an oxidation-sensitive polyphosphoester bearing thioether group for triggered drug release. *Biomacromolecules* 2019;20:1740–7.
- [162] Moss GP, Smith PAS, Tavernier D. Glossary of class names of organic compounds and reactivity intermediates based on structure (IUPAC Recommendations 1995). *Pure and Applied Chemistry* 1995;67:1307–75.
- [163] Butlerow A. Ueber einige Derivate des Jodmethylen. *Justus Liebigs Ann. Chem.* 1859;111:242–52.
- [164] Staudinger H, Lüthy M. Hochpolymere Verbindungen. 3. Mitteilung. Über die Konstitution der Poly-oxymethylene. *Helv. Chim. Acta* 1925;8:41–64.
- [165] Kern V, Jaacks V. Die Bedeutung der Polyoxymethylene für die Entwicklung der makromolekularen Chemie. *Kolloid-Z u Z Polymere* 1967;216:286–98.
- [166] Vogl O. Addition polymers of aldehydes. *J Polym Sci Part A* 2000;38:2293–9.
- [167] Köstler S. Polyaldehydes: homopolymers, block copolymers and promising applications. *Polym Int* 2012;61:1221–7.
- [168] Bachelder EM, Pino EN, Ainslie KM. Acetalated dextran: a tunable and acid-labile biopolymer with facile synthesis and a range of applications. *Chem Rev* 2017;117:1915–26.
- [169] Binauld S, Stenzel MH. Acid-degradable polymers for drug delivery: a decade of innovation. *Chem Commun* 2013;49:2082–102.
- [170] Carmali S, Brocchini S. Polyacetals. In: Kumbar SG, Laurencin CT, Deng M, editors. *Natural and synthetic biomedical polymers*. Burlington, MA: Elsevier Inc.; 2014. p. 219–33.
- [171] Heller J, Penhale D, Helwing R. Preparation of polyacetals by the reaction of divinyl ethers and polyols. *J Polym Sci B* 1980;18:293–7.

- [172] Heffernan MJ, Murthy N. Polyketal nanoparticles: a new pH-sensitive biodegradable drug delivery vehicle. *Bioconjugate Chem* 2005;16:1340–2.
- [173] Vicent MJ, Tomlinson R, Brocchini S, Duncan R. Polyacetal-diethylstilboestrol: a polymeric drug designed for pH-triggered activation. *J Drug Target* 2004;12:491–501.
- [174] Samanta S, Bogdanowicz DR, Lu HH, Koberstein JT. Polyacetals: water-soluble, pH-degradable polymers with extraordinary temperature response. *Macromolecules* 2016;49:1858–64.
- [175] De Silva CC, Israni N, Zanwar A, Jagtap A, Leophairatana P, Koberstein JT, et al. Smart™ polymer enhances the efficacy of topical antimicrobial agents. *Burns* 2019;45:1418–29.
- [176] Samanta S, De Silva CC, Leophairatana P, Koberstein JT. Main-chain polyacetal conjugates with HIF-1 inhibitors: temperature-responsive, pH-degradable drug delivery vehicles. *J Mater Chem B* 2018;6:666–74.
- [177] England RM, Masiá E, Giménez V, Lucas R, Vicent MJ. Polyacetal-stilbene conjugates—The first examples of polymer therapeutics for the inhibition of HIF-1 in the treatment of solid tumours. *J Control Release* 2012;164:314–22.
- [178] Giménez V, James C, Armiñán A, Schweins R, Paul A, Vicent MJ. Demonstrating the importance of polymer-conjugate conformation in solution on its therapeutic output: diethylstilbestrol (DES)-polyacetals as prostate cancer treatment. *J Control Release* 2012;159:290–301.
- [179] Requejo-Aguilar R, Alastrue-Agudo A, Cases-Villar M, Lopez-Mocholi E, England R, Vicent MJ, et al. Combined polymer-curcumin conjugate and ependymal progenitor/stem cell treatment enhances spinal cord injury functional recovery. *Biomaterials* 2017;113:18–30.
- [180] Plyduang T, Armiñán A, Movellan J, England RM, Wiwattanapatapee R, Vicent MJ. Polyacetal-based combination therapy for the treatment of prostate cancer. *Macromol Rapid Commun* 2018;39:e1800265.
- [181] Guo S, Nakagawa Y, Barhoumi A, Wang W, Zhan C, Tong R, et al. Extended release of native drug conjugated in polyketal microparticles. *J Am Chem Soc* 2016;138:6127–30.
- [182] Escalona GR, Sanchis J, Vicent MJ. pH-responsive polyacetal – protein conjugates designed for Polymer Masked–Unmasked Protein Therapy (PUMPT). *Macromol Biosci* 2018;18:e1700302.
- [183] Moreno A, Lligadas G, Ronda JC, Galia M, Cadiz V. Orthogonally functionalizable polyacetals: a versatile platform for the design of acid sensitive amphiphilic copolymers. *Polym Chem* 2019;10:5215–27.
- [184] Pasparakis G, Manouras T, Vamvakaki M, Argitis P. Harnessing photochemical internalization with dual degradable nanoparticles for combinatorial photo-chemotherapy. *Nat Commun* 2014;5:e3623.
- [185] Wang P, Wang JX, Tan HW, Weng SF, Cheng LY, Zhou ZP, et al. Acid- and reduction-sensitive micelles for improving the drug delivery efficacy for pancreatic cancer therapy. *Biomater Sci* 2018;6:1262–70.
- [186] Zhong H, Mu J, Du Y, Xu Z, Xu Y, Yu N, et al. Acid-triggered release of native gemcitabine conjugated in polyketal nanoparticles for enhanced anticancer therapy. *Biomacromolecules* 2020;21:803–14.
- [187] Fuoco T. Degradation in order: simple and versatile one-pot combination of two macromolecular concepts to encode diverse and spatially regulated degradability functions. *Angew Chem Int Ed* 2021;60:15482–9.
- [188] Lee S, Yang SC, Heffernan MJ, Taylor WR, Murthy N. Polyketal microparticles: a new delivery vehicle for superoxide dismutase. *Bioconjugate Chem* 2007;18:4–7.
- [189] Gray WD, Che P, Brown M, Ning X, Murthy N, Davis ME. N-Acetylglucosamine conjugated to nanoparticles enhances myocyte uptake and improves delivery of a small molecule p38 inhibitor for post-infarct healing. *J Cardiovasc Transl Res* 2011;4:631–43.
- [190] Somasuntharam I, Boopathy AV, Khan RS, Martinez MD, Brown ME, Murthy N, et al. Delivery of Nox2-NADPH oxidase siRNA with polyketal nanoparticles for improving cardiac function following myocardial infarction. *Biomaterials* 2013;34:7790–8.
- [191] Lee S, Yang SC, Kao C-Y, Pierce RH, Murthy N. Solid polymeric microparticles enhance the delivery of siRNA to macrophages *in vivo*. *Nucleic Acids Res* 2009;37:e145.
- [192] Yang SC, Bhide M, Crispe IN, Pierce RH, Murthy N. Polyketal copolymers: a new acid-sensitive delivery vehicle for treating acute inflammatory diseases. *Bioconjugate Chem* 2008;19:1164–9.
- [193] Sohn Y-D, Somasuntharam I, Che P-L, Jayswal R, Murthy N, Davis ME, et al. Induction of pluripotency in bone marrow mononuclear cells via polyketal nanoparticle-mediated delivery of mature microRNAs. *Biomaterials* 2013;34:4235–41.
- [194] Pasparakis G, Manouras T, Selimis A, Vamvakaki M, Argitis P. Laser-induced cell detachment and patterning with photodegradable polymer substrates. *Angew Chem Int Ed* 2011;50:4142–5.
- [195] Mitra K, Hira SK, Singh S, Vishwakarma NK, Vishwakarma S, Gupta U, et al. *In vitro* anticancer drug delivery using amphiphilic poly(N-vinylpyrrolidone)-b-polyketal-b-poly(N-vinylpyrrolidone) block copolymer as micellar nanocarrier. *ChemistrySelect* 2018;3:8833–43.
- [196] Hira SK, Mitra K, Srivastava P, Singh S, Vishwakarma S, Singh R, et al. Doxorubicin loaded pH responsive biodegradable ABA-type amphiphilic PEG-b-aliphatic polyketal-b-PEG block copolymer for therapy against aggressive murine lymphoma. *Nanomedicine* 2020;24:e102128.
- [197] Sy JC, Seshadri G, Yang SC, Brown M, Oh T, Dikalov S, et al. Sustained release of a p38 inhibitor from non-inflammatory microspheres inhibits cardiac dysfunction. *Nat Mater* 2008;7:863–8.
- [198] Maity S, Choudhary P, Manjunath M, Kulkarni A, Murthy N. A biodegradable adamantane polymer with ketal linkages in its backbone for gene therapy. *Chem Commun* 2015;51:15956–9.
- [199] Andrade-Gagnon B, Belanger-Bouliga M, Nguyen PT, Nguyen THD, Bourgault S, Nazemi A. Degradable spirocyclic polyacetal-based core-amphiphilic assemblies for encapsulation and release of hydrophobic cargo. *Nanomaterials* 2021;11:e161.
- [200] Herwig G, Dove AP. Synthesis of rapidly surface eroding polyorthoesters and polyacetals using thiol–ene click chemistry. *ACS Macro Lett* 2019;8:1268–74.
- [201] Hill JW, Carothers WH. Cyclic and polymeric formal. *J Am Chem Soc* 1935;57:925–8.
- [202] Gresham WF. Preparation of polydioxolane. 1946;US2394910A
- [203] Jaacks VV. Über die thermische Stabilität von Copolymeren des 1,3,5-Trioxans. *Makromol Chem* 1965;84:250–60.
- [204] Jaacks VV. Anomalien bei der kationischen Copolymerisation von Trioxan. *Makromol Chem* 1967;101:33–57.
- [205] Kern W, Jaacks V. Some kinetic effects in the polymerization of 1,3,5-trioxane. *J Polym Sci* 1960;48:399–404.
- [206] Lüftl S, Visakh P. Polyoxymethylene: state of art, new challenges and opportunities. In: Lüftl S, Chandran S, Visakh P, editors. Polyoxymethylene handbook. Scrivener Publishing; 2014. p. 1–19.
- [207] Offermanns H. C 1-Chemie: formaldehyd und seine polymere. *Chem Unserer Zeit* 2020;54:242–8.
- [208] Price MB, McAndrew FB. The polymerization and copolymerization of trioxane. *J Macromol Sci A* 1967;1:231–42.
- [209] Reibel LC, Durand CP, Franta E. Cationic polymerization of 1,3-dioxolane and 1,3-dioxepane. Application to graft and block copolymer synthesis. *Can J Chem* 1985;63:264–9.
- [210] Walling CT, Brown F, Bartz KW. Copolymers; 1962. US3027352A.
- [211] Weissermel VK, Hermann HD, Burg KH. Die Copolymerisation des Trioxans mit substituierten 1,3-Dioxacycloalkanen. *Makromol Chem* 1967;107:149–57.
- [212] Penczek S. Cationic ring-opening polymerization (CROP) major mechanistic phenomena. *J Polym Sci Part A* 2000;38:1919–33.
- [213] Szymanski R, Kubisa P, Stpenczek. Mechanism of cyclic acetal polymerization. End of a controversy? *Macromolecules* 1983;16:1000–8.
- [214] Coenen AM, Harings JA, Ghazanfari S, Jockenhoevel S, Bernaerts KV. Formation of cyclic structures in the cationic ring-opening polymerization of 1,3-dioxolane. *RSC Adv* 2020;10:9623–32.
- [215] Qiu H, Yang Z, Köhler M, Ling J, Schacher FH. Synthesis and solution self-assembly of poly(1,3-dioxolane). *Macromolecules* 2019;52:3359–66.
- [216] Abel BA, Snyder RL, Coates GW. Chemically recyclable thermoplastics from reversible-deactivation polymerization of cyclic acetals. *Science* 2021;373:783–9.
- [217] Halat DM, Snyder RL, Sundararaman S, Choo Y, Gao KW, Hoffman ZJ, et al. Modifying Li⁺ and anion diffusivities in polyacetal electrolytes: a pulsed-field-gradient NMR study of ion self-diffusion. *Chem Mater* 2021;33:4915–26.
- [218] Zheng Q, Pesko DM, Savoie BM, Timachova K, Hasan AL, Smith MC, et al. Optimizing ion transport in polyether-based electrolytes for lithium batteries. *Macromolecules* 2018;51:2847–58.
- [219] Gao KW, Loo WS, Snyder RL, Abel BA, Choo Y, Lee A, et al. Miscible polyether/poly(ether–acetal) electrolyte blends. *Macromolecules* 2020;53:5728–39.
- [220] Sahadeo E, Wang Y, Lin C-F, Li Y, Rubloff G, Lee SB. Mg²⁺ ion-catalyzed polymerization of 1,3-dioxolane in battery electrolytes. *Chem Commun* 2020;56:4583–6.
- [221] Zhong H, Wang C, Xu Z, Ding F, Liu X. A novel quasi-solid state electrolyte with highly effective polysulfide diffusion inhibition for lithium-sulfur batteries. *Sci Rep* 2016;6:e25484.
- [222] Liu F-Q, Wang W-P, Yin Y-X, Zhang S-F, Shi J-L, Wang L, et al. Upgrading traditional liquid electrolyte via *in situ* gelation for future lithium metal batteries. *Sci Adv* 2018;4:eaat5383.
- [223] Wang Y, Sahadeo E, Rubloff G, Lin C-F, Lee SB. High-capacity lithium sulfur battery and beyond: a review of metal anode protection layers and perspective of solid-state electrolytes. *J Mater Sci* 2019;54:3671–93.
- [224] Kost B, Basko M. Synthesis and properties of L-lactide/1,3-dioxolane copolymers: preparation of polyesters with enhanced acid sensitivity. *Polym Chem* 2021;12:2551–62.
- [225] Higuchi M, Kanazawa A, Aoshima S. Tandem unzipping and scrambling reactions for the synthesis of alternating copolymers by the cationic ring-opening copolymerization of a cyclic acetal and a cyclic ester. *ACS Macro Lett* 2019;9:77–83.
- [226] Higuchi M, Kanazawa A, Aoshima S. Unzipping and scrambling reaction-induced sequence control of copolymer chains via temperature changes during cationic ring-opening copolymerization of cyclic acetals and cyclic esters. *J Polym Sci* 2021;59:2730–41.
- [227] Shirouchi T, Kanazawa A, Kanaoka S, Aoshima S. Controlled cationic copolymerization of vinyl monomers and cyclic acetals via concurrent vinyl-addition and ring-opening mechanisms. *Macromolecules* 2016;49:7184–95.
- [228] Maruyama K, Kanazawa A, Aoshima S. Controlled cationic copolymerization of vinyl monomers and cyclic acetals via concurrent vinyl-addition and ring-opening mechanisms: the systematic study of structural effects on the copolymerization behavior. *Polym Chem* 2019;10:5304–14.
- [229] Kato R, Kanazawa A, Aoshima S. Desilylation-triggered degradable silylacetal polymers synthesized via controlled cationic copolymerization of trimethylsilyl vinyl ether and cyclic acetals. *ACS Macro Lett* 2019;8:1498–503.
- [230] Aoshima S, Kanaoka S. A renaissance in living cationic polymerization. *Chem Rev* 2009;109:5245–87.
- [231] Hong M, Chen J, Chen EY-X. Polymerization of polar monomers mediated by main-group Lewis acid–base pairs. *Chem Rev* 2018;118:10551–616.

- [232] Ishido Y, Kanazawa A, Kanaoka S, Aoshima S. Controlled cationic alternating copolymerization of various enol ethers and benzaldehyde derivatives: effects of enol ether structures. *J Polym Sci Part A* 2014;52:1334–43.
- [233] Ishido Y, Kanazawa A, Kanaoka S, Aoshima S. Chemically recyclable alternating copolymers with low polydispersity from conjugated/aromatic aldehydes and vinyl ethers: selective degradation to another monomer at ambient temperature. *Polym Chem* 2014;5:43–7.
- [234] Ishido Y, Kanazawa A, Kanaoka S, Aoshima S. New degradable alternating copolymers from naturally occurring aldehydes: well-controlled cationic copolymerization and complete degradation. *Macromolecules* 2012;45:4060–8.
- [235] Kawamura M, Kanazawa A, Kanaoka S, Aoshima S. Sequence-controlled degradable polymers by controlled cationic copolymerization of vinyl ethers and aldehydes: precise placement of cleavable units at predetermined positions. *Polym Chem* 2015;6:4102–8.
- [236] Matsumoto S, Kanazawa A, Kanaoka S, Aoshima S. Dual stimuli-responsive copolymers with precisely arranged degradable units: synthesis by controlled alternating copolymerization of oxyethylene-containing vinyl ethers and conjugated aldehydes. *Polym Chem* 2019;10:4134–41.
- [237] Matsumoto S, Kanazawa A, Kanaoka S, Aoshima S. Tandem reaction of cationic copolymerization and concertedly induced hetero-Diels-Alder reaction preparing sequence-regulated polymers. *J Am Chem Soc* 2017;139:7713–16.
- [238] Hayashi K, Kanazawa A, Aoshima S. Exceptional copolymerizability of *o*-phthalaldehyde in cationic copolymerization with vinyl monomers. *Polym Chem* 2019;10:3712–17.
- [239] Naito T, Kanazawa A, Aoshima S. Polyaddition of vinyl ethers and phthalaldehydes via successive cyclotrimerization reactions: selective model reactions and synthesis of acid-degradable linear poly(cyclic acetal)s. *Polym Chem* 2019;10:1377–85.
- [240] Aoshima S, Oda Y, Matsumoto S, Shinke Y, Kanazawa A, Kanaoka S. Efficient design for stimuli-responsive polymers with quantitative acid-degradability: specifically designed alternating controlled cationic copolymerization and facile complete degradation. *ACS Macro Lett* 2014;3:80–5.
- [241] Yokota D, Kanazawa A, Aoshima S. Alternating degradable copolymers of an ionic liquid-type vinyl ether and a conjugated aldehyde: precise synthesis by living cationic copolymerization and dual rare thermosensitive behavior in solution. *Macromolecules* 2019;52:6241–9.
- [242] Ishido Y, Aburaki R, Kanaoka S, Aoshima S. Well-defined alternating copolymers of benzaldehydes with vinyl ethers: precision synthesis by cationic copolymerization and quantitative degradation to cinnamaldehydes. *Macromolecules* 2010;43:3141–4.
- [243] Ishido Y, Aburaki R, Kanaoka S, Aoshima S. Controlled cationic copolymerization of benzaldehyde with isobutyl vinyl ether using base-assisting system. *J Polym Sci Part A* 2010;48:1838–43.
- [244] Ishido Y, Kanazawa A, Kanaoka S, Aoshima S. Selectively degradable alternating copolymers of isobutyl vinyl ether and plant-derived aldehydes with acyclic side chains: effects of side group structures on copolymerization behaviors. *J Polym Sci Part A* 2013;51:4684–93.
- [245] Aso C, Tagami S, Kunitake T. Polymerization of aromatic aldehydes. II. Cationic cyclopolymerization of phthalaldehyde. *J Polym Sci Part A* 1969;7:497–511.
- [246] Kanazawa A, Aoshima S. Concurrent cationic vinyl-addition and ring-opening copolymerization of vinyl ethers and oxiranes. *Polym J* 2016;48:679–87.
- [247] Piers WE, Chivers T. Pentafluorophenylboranes: from obscurity to applications. *Chem Soc Rev* 1997;26:345–54.
- [248] Ishihara K, Yamamoto H. Arylboron compounds as acid catalysts in organic synthetic transformations. *Eur J Org Chem* 1999:527–38 1999.
- [249] Erker G. Tris(pentafluorophenyl)borane: a special boron Lewis acid for special reactions. *Dalton Trans* 2005:1883–90.
- [250] Kanazawa A, Aoshima S. Frequency control of crossover reactions in concurrent cationic vinyl-addition and ring-opening copolymerization of vinyl ethers and oxiranes: specific roles of weak Lewis bases and solvent polarity. *Polym Chem* 2015;6:5675–82.
- [251] Miyamae Y, Kanazawa A, Tamaso K-i, Morino K, Ogawa R, Aoshima S. The influence of the substituents of oxiranes on copolymerization with vinyl ethers via concurrent cationic vinyl-addition and ring-opening mechanisms. *Polym Chem* 2018;9:404–13.
- [252] Hotta D, Kanazawa A, Aoshima S. Generation of “living” species using perfluoroalkylsulfonic acids in concurrent cationic vinyl-addition and ring-opening copolymerization via crossover reactions. *Macromolecules* 2018;51:7983–92.
- [253] Hotta D, Kanazawa A, Aoshima S. *tert*-Butyl esters as potential reversible chain transfer agents for concurrent cationic vinyl-addition and ring-opening copolymerization of vinyl ethers and oxiranes. *Macromol Rapid Commun* 2021;42:e2000479.
- [254] Kanazawa A, Aoshima S. Cationic terpolymerization of vinyl ethers, oxetane, and ketones via concurrent vinyl-addition, ring-opening, and carbonyl-addition mechanisms: multiblock polymer synthesis and mechanistic investigation. *Macromolecules* 2017;50:6595–605.
- [255] Mimura M, Kanazawa A, Aoshima S. ABC pseudo-periodic sequence control by cationic orthogonal terpolymerization of vinyl ether, oxirane, and ketone. *Macromolecules* 2019;52:7572–83.
- [256] Hyoi K, Kanazawa A, Aoshima S. Cationic ring-opening co- and terpolymerizations of lactic acid-derived 1,3-dioxolan-4-ones with oxiranes and vinyl ethers: nonhomopolymerizable monomer for degradable co- and terpolymers. *ACS Macro Lett* 2019;8:128–33.
- [257] Kanazawa A, Aoshima S. Exclusive one-way cycle sequence control in cationic terpolymerization of general-purpose monomers via concurrent vinyl-addition, ring-opening, and carbonyl-addition mechanisms. *ACS Macro Lett* 2015;4:783–7.
- [258] Cairns SA, Schultheiss A, Shaver MP. A broad scope of aliphatic polyesters prepared by elimination of small molecules from sustainable 1, 3-dioxolan-4-ones. *Polym Chem* 2017;8:2990–6.
- [259] Xu Y, Perry MR, Cairns SA, Shaver MP. Understanding the ring-opening polymerization of dioxolanones. *Polym Chem* 2019;10:3048–54.
- [260] Martin RT, Camargo LP, Miller SA. Marine-degradable polylactic acid. *Green Chem* 2014;16:1768–73.
- [261] Bandelli D, Alex J, Weber C, Schubert US. Polyester stereocomplexes beyond PLA: could synthetic opportunities revolutionize established material blending? *Macromol Rapid Commun* 2020;41:e1900560.
- [262] Neitzel AE, Petersen MA, Kokkoli E, Hillmyer MA. Divergent mechanistic avenues to an aliphatic polyesteracetate or polyester from a single cyclic esteracetate. *ACS Macro Lett* 2014;3:1156–60.
- [263] Bixenmann L, Stickdorn J, Nuhn L. Amphiphilic poly(esteracetate)s as dual pH- and enzyme-responsive micellar immunodrug delivery systems. *Polym Chem* 2020;11:2441–56.
- [264] Neitzel AE. Ring-opening polymerization of cyclic hemiacetal esters for the preparation of hydrolytically and thermally degradable polymers [Ph.D. dissertation]. Minneapolis, MN: University of Minnesota; 2018.
- [265] Neitzel AE, Barreda L, Trotta JT, Fahnhorst GW, Haversang TJ, Hoye TR, et al. Hydrolytically-degradable homo- and copolymers of a strained exocyclic hemiacetal ester. *Polym Chem* 2019;10:4573–83.